

UNIVERSITÀ DEGLI STUDI DI PADOVA

INSTITUTO SUPERIOR TÉCNICO



Università degli Studi di Padova

CENTRO INTERDIPARTIMENTALE *"Centro Ricerche Fusione"*

Universidade Técnica de Lisboa

INSTITUTO SUPERIOR TÉCNICO

JOINT RESEARCH DOCTORATE IN FUSION SCIENCE AND ENGINEERING

CYCLE XXV

Study, analysis, design and diagnostics of plasma and beam facing components of fusion devices

Coordinator: Ch.mo Prof. Piero Martin

Supervisors: Ch.mo Prof. Piergiorgio Sonato

Dott. Ing. Samuele Dal Bello

Dott. Ing. Mauro Dalla Palma

Doctoral student: Emanuele Sartori

Summary

Neutral Beam Injection is the horse-power of present and future fusion devices. Modeling plays a fundamental role in anticipating/predicting the performance of the injector and optimizing its behaviour. Successful design can only be achieved through integrated approach between physics and engineering. In the last three years, my research activity has been carried out at *Consorzio RFX*, where the ultimate neutral beam test facility is being designed and constructed. This PhD thesis has sought to address issues critical for the design and operation of such injectors. As the dynamics of beam acceleration and transport are dominated by the density of the background gas, I developed a reliable code for simulating its distribution in high vacuum systems. The density topic is strictly connected to the characteristics of the gas cell where the beam is neutralised before reaching the fusion plasma. Consequently I developed the final design of the Neutraliser and performed the thermo-mechanical verifications, a critical task because of the high power load interesting the beam facing component. I considered also other issues related to the study of beam components - e.g. the beam source in its operating thermal conditions. The development and application of methods and models, the experimental validation and benchmarking, are described in the perspective of a practical use in neutral beam engineering.

Sommario

Gli iniettori di neutri sono e saranno il principale sistema di riscaldamento nelle macchine da fusione. La modellazione numerica gioca un ruolo fondamentale nel predirne le prestazioni ed ottimizare il suo funzionamento, ed un buon design nella fisica e ingegneria può essere raggiunto solo tramite un apporoccio integrato tra i due. Nei tre anni trascorsi, ho svolto la mia attività di ricerca presso il *Consorzio RFX*, dovesarà installato e testato il più grande iniettore di neutri al mondo, ed il suo design è in corso. Questa tesi di dottorato ha affrontato aspetti critici per il design e le operazioni di questa tipologia di iniettori. Poiché le dinamiche di accelerazione e trasporto del fascio di particelle sono dominate dalla presenza di gas residuo, ho sviluppato un codice robusto ed affidabile per simulare la sua distribuzione e flusso nei sistemi di alto vuoto; questo argomento è strettamente legato alle caratteristiche ed il design della cella di gas dove il fascio deve venire neutralizzato prima di raggiungere il plasma da fusione, di

cui ho sviluppato il *final design* ed ho eseguito le verifiche termomeccaniche, che presentano tutte le difficoltà di componenti affacciati ad un fascio di particelle ad alta energia. Altri aspetti hanno riguardato lo studio di componenti e diagnostiche del fascio. Vengono trattati lo sviluppo e l'applicazione di metodi e modelli, e la loro eventuale validazione sperimentale; i risultati sono valutati nella prospettiva di un uso pratico nella ingegneria degli iniettori di neutri.

Sumário

Os injetores de neutros são e serão o principal sistema de aquecimento nas máquinas de fusão. A modelagem numérica desempenha um papél fundamental em predizer as prestações e otimizar o seu funcionamento, e um bom design na física e engenharia pode ser alcançado somente através de uma aproximaçao integrada entre os dois. Nos três anos de trajetória, eu fiz a minha atividade de pesquisa no Consorzio RFX, onde está instalado e testado o maior injetor de neutros do mundo, e o seu design está em andamento. Esta tese de doutorado enfrentou aspectos críticos sobre o design e as operações deste tipo de injetor. Já que as dinâmicas de aceleração e transporte da viga de partículas são dominadas pela presença de gás resídual, eu desenvolvi um código robusto e confiavél para simular a sua distribuição e uso nos sistemas de alto vazio; este argomento é extremamente ligado as características e ao design da cela de gás onde o feixe tem que ser neutralizado antes de alcançar o plasma de fusão, do qual eu desemvolvi o "final design" e fiz também as verificações termomecânicas, que apresentam todas as criticidades dos componentes e diagnósticos do feixe. São tratados: o desemvolvimento e a aplicação de métodos e modelos, com possíveis validações experimentais; os resultados são avaliados em uma perspectiva de uso pratico na engenharia dos injetores de neutros.

Contents

Summary iii

Contents x

Introduction 1
Neutral Beams for Fusion . . . 3
Motivations for the study . . . 7
Thesis outline . . . 9

1 Short introduction to NBI Systems 11
1.1 Negative Ion Beam Sources . . . 11
1.1.1 Negative ion production . . . 12
1.1.2 Negative ion destruction . . . 13
1.1.3 Plasma generation . . . 13
1.1.4 Negative ion extraction and acceleration . . . 14
1.2 Negative Beam Neutralisation . . . 19
1.2.1 Dumping of the residual ions . . . 20
1.3 Road to the Full scale Plasma Source for ITER NBI . . . 21
1.3.1 BATMAN MANITU ELISE . . . 21
1.3.2 SPIDER . . . 22
1.3.3 The ITER HNB prototype: MITICA . . . 23

I DENSITY DISTRIBUTION 27

2 Much Ado About Nothing 29
2.1 Vacuum for dummies . . . 30
2.1.1 Gas . . . 30
2.1.2 Pressure . . . 30
2.1.3 Temperature: the Maxwell-Boltzmann distribution . . . 30
2.1.4 Mean free path . . . 30
2.1.5 Flow regimes . . . 31
2.1.6 Laminar and turbulent flow . . . 32
2.1.7 Vacuum ranges . . . 32
2.2 Vacuum in Fusion Devices . . . 33
2.2.1 Vacuum in Neutral Beam Injectors for Fusion . . . 35
2.3 Analytical and numerical tools for vacuum systems . . . 36
2.4 Objectives of AVOCADO . . . 38

3 AVOCADO **41**
3.1 Governing equations . . . 41
3.1.1 Equilibrium flows in the view factor method . . . 42
3.1.2 Non-equilibrium flows and temperature accommodation: a new consistent model . . . 44
3.2 Numerical methods for the definition of the equation system . . . 48
3.2.1 View factor calculation . . . 48
3.2.2 Implementation and optimization . . . 55
3.2.3 Mesh format and access to mesh database . . . 58
3.3 Numerical methods for the solution . . . 59
3.3.1 Sparse matrix implementation . . . 59
3.3.2 Mirroring or transposing . . . 61
3.3.3 Data structures and data access . . . 62
3.3.4 Solution scheme for the linear system . . . 62
3.3.5 Solution scheme for the coupled systems . . . 63
3.4 Pre- and Post-processing . . . 64
3.4.1 Pre-processing . . . 64
3.4.2 Post-processing of gas properties in the volume . . . 65
3.4.3 Visualization of the solution . . . 66
3.5 Benchmarking and applied cases . . . 66
3.5.1 Benchmarking of constant temperature model against analytical cases . . . 66
3.5.2 Applications and benchmarking of the temperature accommodation model . . . 69
3.5.3 Thermal Accommodation Factor . . . 75

4 Experimental validation in ARIANNA **79**
4.1 Description of the ARIANNA experiment . . . 81
4.1.1 Description . . . 81
4.1.2 In-vacuum components . . . 81
4.1.3 Pumping system . . . 81
4.1.4 Measurement systems . . . 81
4.1.5 Gas properties . . . 83
4.2 Experimental results in ARIANNA . . . 84
4.2.1 Experimental set-up n.1 - preliminary measurements . . . 84
4.2.2 Experimental set-up n.2 . . . 86
4.2.3 Exp set-up n.3 - multigrid set-up . . . 94
4.2.4 Exp set-up n.4 - multigrid set-up with lateral conductance 98
4.3 Discussion of the results in ARIANNA . . . 102

5 Applications **105**
5.1 MITICA Beam Source . . . 105
5.1.1 Mono-beamlet models . . . 109
5.1.2 Numerical characterizations for a lumped model . . . 111
5.1.3 Slice models: Preliminary study and Comparison between different frame designs . . . 111
5.1.4 Consistent temperature . . . 120
5.1.5 1/4 model . . . 125
5.1.6 Comments and future work . . . 132
5.2 MITICA Beam Line . . . 132

5.2.1 General description and challenges of the model 133
5.2.2 Challenges and general considerations 137
5.2.3 Result I - Density profiles and expected neutralisation . . 143
5.2.4 Result II - Effect of LED panels 150
5.2.5 Result III - Density at tomography and BES cross-sections 154
5.2.6 Result IV - Boundary conditions for the submodel of the Beam Source 157
5.2.7 Comments 157
5.3 Benchmarking with MANITU 160
5.3.1 Density profiles in the simplified geometry 160
5.3.2 Comments 163
5.4 RFX-Mod pumping system 166
5.4.1 Characterization of the pumping system 166

II MITICA Neutraliser and Electron Dump 169

6 The MITICA Neutraliser: thermohydraulic and thermomechanical design 171
6.1 Design requirements 172
6.1.1 Beam optics 172
6.1.2 Beam operation 172
6.1.3 Cooling Parameters 173
6.1.4 Coordinates, position and alignment 173
6.2 Regulatory documents and standards 174
6.2.1 Primary and secondary stresses 174
6.2.2 Thermomechanical criteria and rules for the design 175
6.2.3 Structural Materials 176
6.2.4 Thermohydraulic correlations 176
6.2.5 Pressure Equipment Directive 177
6.3 Steps of the design 177
6.3.1 Thermomechanical design at component-level 178
6.3.2 Load cases to be verified 178
6.3.3 Technological Issues 178
6.4 Design description 180
6.4.1 Wall Panels 184
6.4.2 Support of the Wall Panels 184
6.4.3 Leading Edge Elements 185
6.4.4 Electron Dump 185
6.4.5 Piping assembly 187
6.5 Assembly procedure description 188

7 Calculation of thermal loads and power density maps 191
7.1 Power deposited by the beam . . . 191
7.1.1 Beamlet definition . . . 192
7.1.2 Beam Modelling . . . 193
7.1.3 Geometry definition and mesh . . . 193
7.1.4 Interaction with the solid surfaces . . . 193
7.1.5 Post-processing . . . 195
7.1.6 Implementation of the tools . . . 195
7.2 Power deposited by co-accelerated electrons . . . 197
7.3 Application to the NED . . . 198
7.3.1 Geometry of the wall panels . . . 198
7.3.2 Vertical positioning of the Neutraliser component . . . 198
7.3.3 Vertical positioning of the Electron Dump . . . 202
7.3.4 Total heating power . . . 204
7.3.5 Power density maps and most thermally loaded elements 204

8 Heat removal 209
8.1 Overview of the cooling system of beam heated elements . . . 209
8.2 Thermal loads . . . 210
8.3 Parameters of the Hydraulic Circuits . . . 210
8.4 Finite Element model . . . 212
8.5 Thermal-hydraulic Results . . . 214
8.5.1 Influence of Vertical Tilting and Horizontal Misalignment 214
8.5.2 Influence of Water Inlet Temperature . . . 217
8.5.3 Influence of LEE Internal Diameter . . . 217

9 Thermal and mechanical analyses and verifications 219
9.1 Neutraliser wall panels . . . 219
9.1.1 Load cases . . . 219
9.1.2 Preliminary analyses . . . 220
9.1.3 Model description . . . 220
9.1.4 Results . . . 222
9.1.5 Comments . . . 228
9.2 Leading Edge Elements . . . 228
9.2.1 Optimization of the Leading Edge Elements . . . 228
9.2.2 Verifications . . . 230
9.3 Floors and wall spacers . . . 230
9.3.1 Model description . . . 231
9.3.2 Results . . . 232
9.4 Electron Dump panels . . . 233
9.4.1 Thermo-mechanical model . . . 234
9.5 Piping assembly . . . 235
9.5.1 Requirements and preliminary remarks . . . 236
9.5.2 Design of the bellows restraining device . . . 238
9.5.3 Design and verifications of the piping assembly . . . 239
9.5.4 Design and verification of the Panel Expansion Joints . . 242
9.5.5 Draining and drying pressure . . . 244
9.6 Support structure . . . 245
9.6.1 Load cases . . . 245
9.6.2 Model description . . . 245
9.6.3 Results for the side plate . . . 248
9.6.4 Results for the tie-rods . . . 252

10 Thermal diagnostics **259**
10.1 Inertial termocouples . . . 260
10.1.1 Dependency on beam source tilting . . . 260
10.1.2 Dependency on horizontal misalignment . . . 261
10.1.3 Dependency on beam core divergence . . . 261
10.1.4 Identification of PD peak positions . . . 262
10.1.5 Proposed Layout . . . 263
10.2 Calorimetric thermocouples . . . 264
10.2.1 Proposed Layout . . . 265
10.3 Boiling detectors . . . 265
10.3.1 Proposed Layout . . . 265
10.4 Discussion . . . 265

11 The Gas Injection system **267**
11.1 Design description and injection requirements . . . 268
11.2 Flow regions . . . 269
11.2.1 Gas flow in the vacuum . . . 269
11.2.2 Gas expansion at the injection . . . 270
11.2.3 Gas expansion in the vacuum . . . 271
11.2.4 Gas flow in the injection channels . . . 272
11.3 Models . . . 272
11.3.1 CFD characterization of the discharge coefficient . . . 273
11.3.2 Model of the injection channels and nozzles . . . 274
11.3.3 Model for transient analyses . . . 277
11.4 Discussion . . . 277

III SPIDER **279**

12 Thermally induced misalignments and stresses in SPIDER **281**
12.1 SPIDER description . . . 281
12.1.1 Conceptual description of the Grid Supporting Structure 282
12.2 Design requirements . . . 284
12.2.1 Operating scenarios and thermal load cycles . . . 284
12.3 Thermal Contact Conductance . . . 285
12.4 Thermal characterization of the structure . . . 286
12.4.1 Summary of the analyses . . . 286
12.4.2 Frame Conditioning System (2D model) . . . 287
12.4.3 Plasma Grid and Bias Plate fastenings (3D model) . . . 287
12.4.4 Horizontal section of the PG frame (2D model) . . . 288
12.4.5 Extraction Grid fastenings and frames (3D model) . . . 289
12.5 Transient thermal lumped model of SPIDER beam source . . . 289
12.5.1 Lumped model description . . . 290
12.5.2 Imposed operating conditions . . . 292
12.5.3 Daily-based thermal behaviour . . . 292
12.6 Analysis of SPIDER structure deformations . . . 294
12.6.1 Boundary conditions and use of sub-model . . . 295
12.6.2 Global integrated model . . . 296
12.7 Post-insulator probability of failure analysis . . . 298
12.7.1 Verification of ceramic material . . . 298
12.7.2 Finite Element analysis . . . 299
12.7.3 Comments . . . 302
12.8 Discussion and open issues . . . 303

Conclusions and perspective **305**
Gas distribution modeling 305
MITICA Neutraliser and Electron Dump 306
SPIDER thermal deformations 306
Other activities 307
Further developments 307

Appendixes **307**

A Magnetic field in the extraction region of MITICA ion source **311**

B Application of Trigo to the MITICA Calorimeter **315**

Publications **319**

References **320**

References - RFX Technical Notes **330**

to Arianna and the sons of her sons
may they find a better world

Introduction

Substantial advantages over other forms of innovative energy generation distinguish nuclear fusion, in terms of environmental protection, fuel availability and safety. Far from being commercially available, the practical production of energy from nuclear fusion could mitigate the shortage of energy supply and the emissions of carbon dioxide. A great worldwide effort, international and well coordinated, is put on the subject.

The construction of a nuclear fusion device for energy production is among the most ambitious projects mankind ever attempted. Those who say that man-made fusion replicates the energy of the sun are mistaken: the sun - with a mass of 2×10^{30} kg - produces an extremely low specific energy, in the orders of 10^{-4} watts per kilogram, whilst in a man-made fusion machine, a deuterium-tritium mixture should produce thousands of MW per kg of reactants, in the range of 10^{10} W/kg.

The fusion research followed two paths, inertial confinement fusion and magnetic confinement fusion. An interesting historical review is given by Meade [12]. One of the most promising candidates for producing thermonuclear fusion is the tokamak magnetic configuration; some 40 different tokamaks were built and operated since 1956. In a tokamak, both the externally generated toroidal magnetic field and the poloidal magnetic field generated by plasma current play a role in the confinement [13]. The process that generates the toroidal current relies on the transformer effect, which is the inductive coupling between the central solenoid and the toroidal plasma itself; this Ohmic Heating (OH) regime is limited in maximum current and duration, and only allows pulsed operations. Auxiliary heating systems can be used: nowadays most of the experiments make use of both Neutral Beam Injection systems (NBI) and several variants of Radio Frequency (RF) heating. It has been found that the auxiliary heating allows the access to high-confinement regimes (so called H-mode). It is also commonly understood that the auxiliary heating systems, ideally speaking, can maintain the plasma current indefinitely by Current Drive (CD); their use is mandatory to achieve long steady-state operations, and therefore they will be part of the future fusion power plants.

When thermonuclear fusion as an energy source was first conceived, insufficient understanding and excessive optimism determined false expectations and bad predictions, but sixty years from then, the progresses that have been made in fusion are unquestionable. Mapping the most important tokamak experiments in a topographical map that defines the conditions required for deuterium-tritium plasmas to achieve a specific fusion gain (Lawson criterion defined back in 1957 [14]), we find out that the progresses towards an exothermic steady-state op-

eration have been inexorable (figure 1). The *triple product* of ion density and temperature in the plasma core and energy confinement time $n_i \tau_E T_i$ increased by $\sim 10^7$ since 1958.

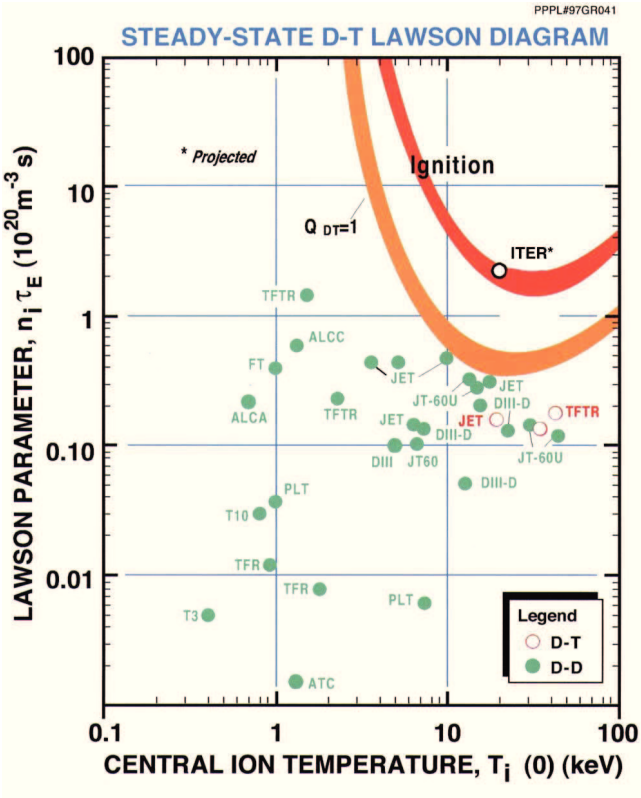


Figure 1: The "Lawson Criterion" for energy gain in D-T plasmas, (PPPPL [15]) [16]

The fusion power grows with the dimensions of the plasma, depending on the major radius R_0 and minor radius a as $P \sim {R_0}^{3/2} a^{1/2}$ [17]. This is the reason for the dimensional growth of the past experiments, and the future devices. In figure 2 the size of some operating and future devices are compared.

Seeking for an early realization of fusion energy, a road map was internationally agreed few years ago, tracked towards the future construction of a demonstration reactor. The road map identifies first the construction of a major experimental device, ITER, and the achievement of its nominal operational parameter, as key accomplishments, on which the international efforts on the nuclear fusion research shall be focused. Based on a "fast track approach", the European Union and Japan set out also a broader approach, which allows the parallel development of the engineering (component technology) and fusion plasma research.

ITER shall demonstrate the scientific feasibility of fusion as energy source [18]. It is a magnetic confinement machine of tokamak configuration, whose engineering design started in 1992 [19]. Since the initial collaboration agreement signed in 1985, the nominal requirements demanded to ITER have been revised

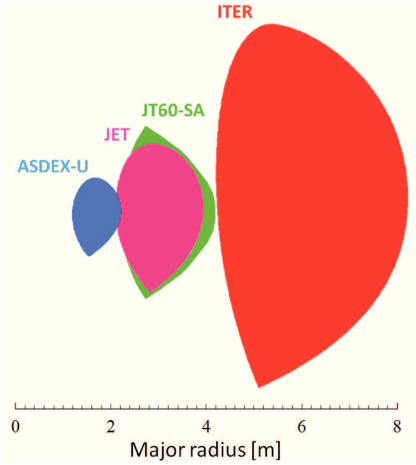


Figure 2: plasma section and scaling of some present and future tokamak devices

several times, basically reducing the claimed performances [20, 21], while the overall projected cost ramped up.

The recent agreements, the events of the recent decades, and the history of the research in this field, show altogether the difficulties of fusion; but even more, they indicate the scientific and political will to successfully achieve it. Fusion also leads research on other fields, such as new materials and technologies, plasma physics and numerical modelling, and many other implications that will eventually contribute to a widespread progress.

In this scenario, the development of high-power, high-efficiency, high-energy and high-reliability NBI systems is essential. The design of these devices, starting from their physical requirements, up to the engineering requirements, presents challenging difficulties and open issues. This area of study constitutes the basis of this work.

Neutral Beams for Fusion

Experiments of neutral-beam heating in tokamaks were first conducted on the Adiabatic Toroidal Compressor (ATC) in 1973. Most of the neutral beam technology at that time had been developed for the mirror confinement devices, which relied on neutral beams for energy and density build-up. In the early applications, the NBI power was a small fraction of the ohmic heating power; the beam energy was in the range of 15-25 keV. In ATC for instance, with a plasma density n_e=1.5×10^{13} cm^{-3}, the ion temperature could increase from 1.6 keV to 2.8 keV by using two beams totaling 60kW, while no electron heating was observed.

In the late 1970's, the new generation of tokamaks brought an upgrade in the neutral beam heating systems, with an order of magnitude increase in beam power and pulse length, and an acceleration voltage of approximately 60 kV. In the Princeton Large Torus (PLT), with a total injection power up to 3MW, it was possible for the first time to increase the electron temperature, and to reach ion temperatures up to the minimum Lawson criterion temperature of 10

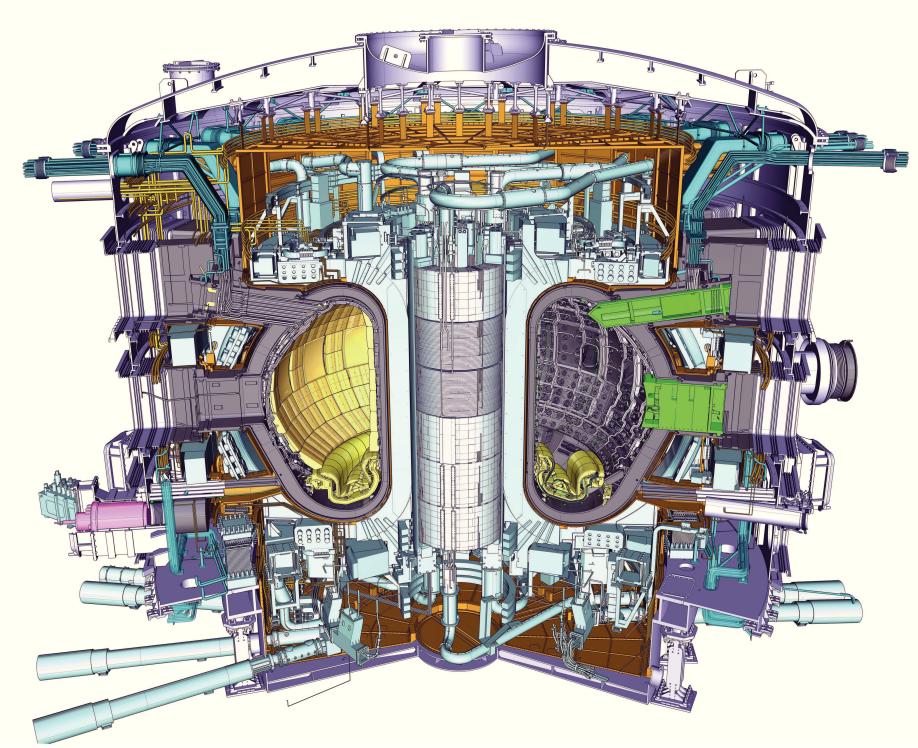


Figure 3: D cutaway model of ITER torus and cryostat

keV in 1978. A brief overview of the first ten years of NBIs in fusion devices is given by Eubank [22].

Since then, the NBIs were employed as the dominant auxiliary heating system in tokamaks, as shown in table 1).

In 1982 in the ASDEX tokamak, the NBI heating caused the spontaneous transition to a regime with higher confinement, which was called H-mode, with a transport barrier at the plasma edge [23]. Since the fusion output is proportional to the square of the plasma pressure (∼temperature×density), in H-mode, the plasma pressure increases by a factor two with respect to the case without any pedestal (called low confinement mode, L-mode) and the fusion output increases by a factor four. Nowadays the H-mode is the baseline tokamak discharge scenario.

In the Tokamak Fusion Test Reactor (TFTR), with a minor radius a =85 cm, the beam energy was in the range of 120 keV for the D_0 beams. There were four NBIs installed. The efficiency of these systems was, in terms of input AC power and neutral power delivered to the plasma, of about 20%. The NBI had also been used for tritium fueling during the D-T campaign in 1994.

In the Joint European Torus (JET), two identical NBI units are installed, each composed by 8 independent ion sources and neutralisers. After a recent upgrade, a total of 34 MW heating power is installed. In figure 4(a), the size of the NBI is shown to be comparable with that of the torus itself. In figure 4(a), the NBI components are illustrated: the ion beam is extracted from the plasma source, in many independent beamlets; it becomes a neutral beam by passing

	R0 [m]	a [m]	Ip [MA]	Bt [T]	PNBI [MW]	NNBI [MW]	ECRH [MW]	ICRH [MW]	LH [MW]
ITER	6.2	2.0	15	5.3	-	33	20	20	-
JET	2.96	1.25	4.8	3.45	34	-	-	10	7
JT-60U	3.4	1.1	5	4.2	40	3	4	7	8
JT-60SA	2.97	1.17	5	2.25	24	10	7	-	-
TFTR	2.4	0.8	2.2	5	40	-	-	11	-
EAST	1.7	0.4	1.0	3.5	-	-	0.5	3	4
DIII-D	1.67	0.67		2.1	20	-	5	4	-
ASDEX-U	1.65	0.65	1.2	3.1	20	-	6	8	-

Table 1: Summary of Tokamaks and installed heating power [24].

through a cloud of gas in the neutraliser; the residual fraction of ions is removed from the beam by the Residual Ion Dump; a Calorimeter takes care of this removed fraction, and of the full beam power when the beam does not enter the tokamak. The highest fusion power output (16.1 MW) shot in JET was obtained with 3.1 MW of ICRH power and 22.3 MW of beam power (with injection of 155 keV T and 80 keV D) [25].

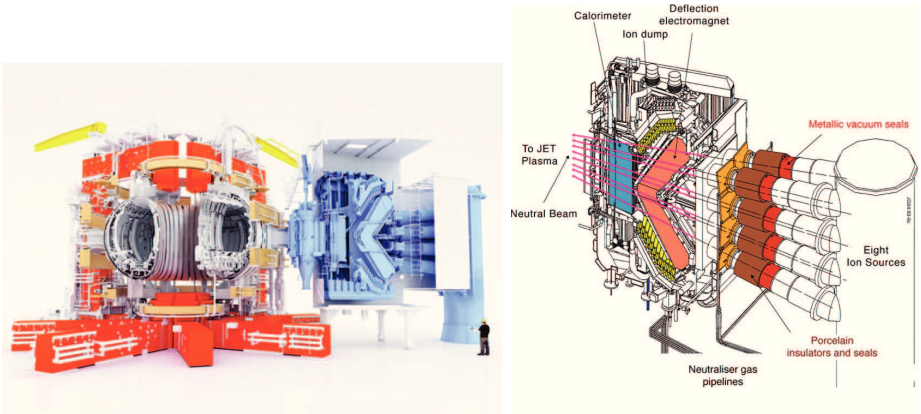


Figure 4: Left: A 3D illustration of the JET vessel and the Neutral Beam injection box, note the relative dimension of the P-NBI system and the torus itself. Right: Detail of the JET P-NBI components. [26].

Given the importance of the heating systems and in prospect of the continuous current drive, at this point it had been understood that the only viable option to realize NBIs of higher energy and efficiency was the use of negative ions, since the binding energy of the electron in D^- is weak (0.75 eV). The community of the negative ion sources and accelerators was well established, with an already existing dedicated symposium. At the beginning of the 1980's, negative ion beams in the 1-2 A range were under experimental investigation; in this context, also Laser neutralisation by photodetachment, for instance, was proposed at the beginning of the 1980's.

The Japan Torus JT-60, in operation since 1985, after the original upgrade used 14 Positive NBI units (P-NBI) at 95 keV and 2 Negative NBI units (N-NBI) at 500 keV. This device holds the record of fusion triple product $n_i \tau_E T_i$, thanks to the huge NBI power available. The NBI systems were also capable

of running a high performance plasma with full non-inductive plasma current drive [27, 28]: the dominant direction of the beam can drive current in the plasma. The construction of the JT-60 Super Advanced, in which niobium-titanium superconducting coils will be used, is currently on going; it employs 12 P-NBI at 2 MW each and one N-NBI at 10 MW. The N-NBI unit uses *Kamaboko* type filament-arc negative ion sources; the performances of the accelerators have been improved and now the pulse duration of these systems has exceeded the initial 10s pulse duration limit, and eventually sustains the acceleration voltage of 490 kV [29].

Three N-NBIs operate in the Large Helical Device (LHD) since 2001, with a total injection power of 16 MW at energies in the range of 180 keV. Each injector has two cesium-seeded filament-arc discharge negative ion source, with external magnetic filter. The pulse duration reaches 10s, but it is only 1.6 s at full power [30].

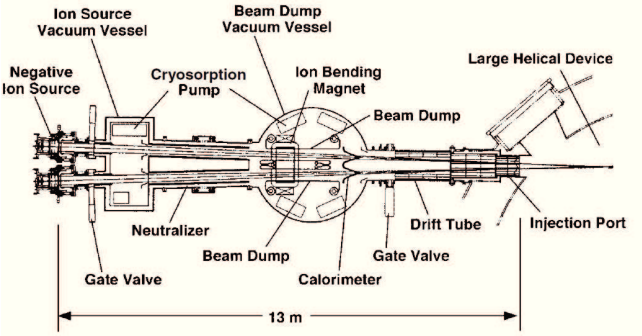


Figure 5: Horizontal section of the N-NBI installed in LHD [30].

At present, the only operating N-NBIs are those installed at LHD and JT-60U, but the N-NBI technology has paramount importance in the future scenarios. The beam energy is transferred to the tokamak plasma by first ionization and consequent thermalization. The higher the energy per amu is, the longer the path the beam can travel reaching the core of the plasma; on the other hand, the ion beam neutralization by charge exchange process in gas neutralisers becomes very inefficient at high energies for positive ions (see figure 6). Therefore negative-ion based beams must be used for beam energies >300 keV.

Steady-state operation of ITER is foreseen to be with 100% non-inductive current drive at moderate plasma current. Two Heating and Current Drive (H&CD) N-NBI will be installed, with the possibility of a third. The present design of the N-NBI for ITER is shown in figure 7. The required D_0 beam power is 16.7 MW/beamline, obtained with a 40 A, 1MeV D^- beams; the initial operation will be in H_0 at 0.87 MeV. The very demanding performances requested to the injector are summarized in table 2 (the low extracted current density indicates the difficulty of operating negative ion sources; in JET NBI sources for comparison, $j_+ \sim 200$ mA/cm^2).

The acceleration voltage, the extracted current density, the duration of the beam-on phase are requirements that have been accomplished separately by other devices, but never together at the same time. For this reason, a dedicated Neutral Beam Test Facility (NBTF) was foreseen, in order to test the injector

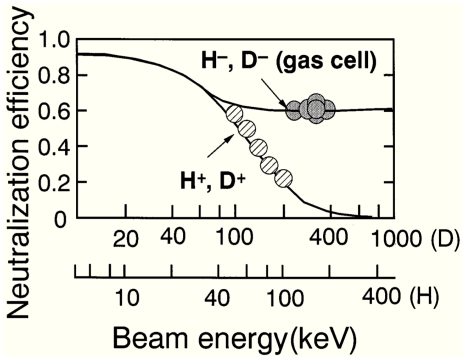


Figure 6: Neutralization efficiency of hydrogenic ions as a function of energy per amu, measured in the NBIs at JT-60U [31]

and reach the nominal performances before ITER starts the operations. This facility is now called PRIMA and is under construction in Padova at the Consorzio RFX. PRIMA will house two experiments. The "Megavolt ITer Injector and Concept Adancement" MITICA is the full scale ITER injector [1] ; the full scale ion source and extractor will be first tested in the "Source for Production of Ion of Deuterium Extracted from Rf plasma" SPIDER.

Motivations for the study

The delivery of efficient heating and current drive systems is of paramount importance if fusion energy is to become reality. In particular, the development of efficient neutral beam injectors for ITER presents several challenging issues of physics and technology. Since 2003 an extensive activity has been performed by many European and Japanese associations; it aimed to revise and update the NBI design for ITER and bring the design to a built to print level.

The purpose of this thesis is the contribution to the design of the ITER negative neutral beam injector and its testbed, MITICA, in a context of integrated approach from physics to engineering disciplines. The following key challenges have been identified:

Design of beam facing components A critical issue for present fusion ma-

D^0 Beam energy	1000 keV
Acceleration current	40 A
Delivered power	16.5 MW
Maximum Beam source pressure	0.3 Pa
Apertures	1280
Extraction area	$\sim 0.2 m^2$
Extracted current density	~ 30 mA/cm^2
Co-extracted j_{e-}/j_{D-}	<1
Beam current density	20 mA/cm^2
Beamlet divergence	≤ 7 mrad
Beam on time	3600 s

Table 2: Requirements for ITER H&CD NBI operations in deuterium [32].

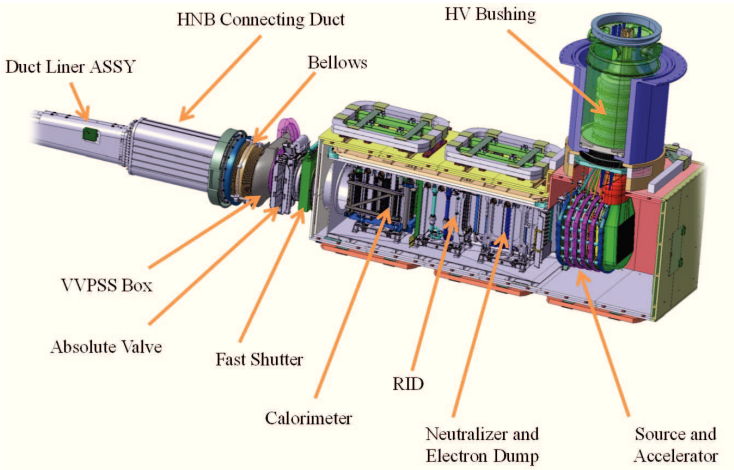


Figure 7: A 3D illustration of the ITER NBI system and its components [2].

chines, and even more for next generation ITER and reactor prototypes, is the reliability of plasma and beam facing components that is highly correlated to their material properties and heat exchange capability. The engineering problem is very challenging and the research in this field requires a large number of multidisciplinary competences as thermo-mechanical and thermo-hydraulic, together with the knowledge of materials able to resist to thermal fatigue cycles under intense radiation for very long periods in presence of enhanced creep and aging phenomena. Additionally, position and alignment tolerances often must be respected under heavy heat fluxes originating thermal deformations.

Investigation on the beam efficiency In nowadays NBI technology, the efficiency of the beam is dominated by the interaction with the background gas; whether it is called neutralisation or stripping, the phenomena has the same origin. The knowledge of the density distribution inside the injector influences the physics design, and is valuable in the engineering design, since it is at the origin of the heat loads on the beam line components.

Study of beam-surface interactions The estimates of power deposition and thermal energy exchange from plasma to facing components, and even between boundary components, needs further knowledge of plasma/beam behaviour, plasma/beam interactions with components, chemical and physical sputtering, and in-vacuum thermal contact resistance.

Numerical models, analyses, design optimization, monitoring during operations, development of dedicated numerical tools and possible execution of R&D and tests for benchmarking, are the METHODS of my research activities. I have addressed the following points:

- *The study of the density distribution in MITICA*. The design of all the components along the path of the beam (beam line components, BLCs) is influenced by the presence of background neutral gas: it is by interaction with it that most of the beam losses occurs, and different kinds of

causes of power deposition originate. Vice-versa, the geometry and overall dimensions of the BLCs and the negative ion accelerator affect the gas flow. A deep understanding of the gas dynamics is advisable to evaluate the consequence of design choices. A study of these phenomena, including the development and validation of three-dimensional numerical codes, is needed to support the MITICA design.

- *The detailed design of MITICA Neutralizer and Electron Dump (NED).* The Neutralizer is the first beam line component and is subjected to heating by beam particles: analyses are required to perform a detailed design and verification. The interaction of the beam particles with the Neutraliser shall be modelled considering the beam emittance diagram. The power deposition shall be quantified, and the requirement of the hydraulic cooling circuit shall be consequently defined in different configurations and operating conditions. Integrating these results, the thermal behaviour of the NED elements need evaluating: not only the elements directly intercepting the beam (such as the wall panels, the leading edges, the ion and electron baffles) but also all the elements participating in the heat removal and the structural support (supporting structure, and others). The NED shall be instrumented for diagnostic purposes, coherently with the physical quantities the simulations foresee. Additionally, the Neutraliser is the main gas source in the injector, and the design of the component directly affect the gas density distribution, also because of the presence of external panels intercepting divergent electrons. A deep understanding of the gas flux mechanism is advisable to evaluate the consequence of design choices. The design of the NED in any aspect shall proceed iteratively taking into account the results of these studies.

- *The study of the heat fluxes and thermal deformations in the grids' support structure of SPIDER.* Given the critical importance of position tolerances in the accelerator grid alignment, analyses in realistic operating conditions of the SPIDER accelerator support frame have been carried out with the purpose of predicting the deformations of the accelerator structure and identifying the critical aspects of the frame supports; this also comprises the verification of the fragile ceramic post-insulators against structural deformations.

Thesis outline

The purpose of this thesis is to face with an integrated multidisciplinary approach the design of SPIDER and MITICA, starting from physical requirements up to the development of the engineering requirements. This thesis is articulated into three parts, which deal with the three macroareas of my research.

This section has introduced the context and the motivations for this thesis. Chapter 1 will contain a more detailed description of negative neutral beam injectors for fusion, and the fundamental aspects of the physics and technology of the subject, without pretension to be exhaustive; it will also give an overview of the recent and future experiments related to the development of the ITER H&CD NBI, focusing the attention on MITICA in particular.

PART I describes the development of the numerical code AVOCADO to model gas distibutions in vacuum systems, and its application to MITICA. Chapter 2 will introduce the importance of vacuum in fusion devices and an overview of the existing codes for gas calculations. Chapter 3 will detail the development of the accurate and versatile code for gas distribution calculation in three dimensional geometries of molecular flows, also describing the implemented techniques. After the initial benchmarking on analytical solutions, the experimental validation is described in Chapter 4, as it was performed in the Adaptable Rarefied Instrumented Atmosphere for Neutral iNjection Applications (ARIANNA) using geometries relevant to electrostatic multi-aperture accelerators. Finally Chapter 5 will give the results of AVOCADO applications to MITICA Beam source and Beam Line, highlighting the results and the indications obtained for the design of components and diagnostics, and to the existing devices.

PART II deals with the design of the Neutraliser and Electron Dump (NED) of MITICA. In Chapter 6, the component will be described calling the attention on the peculiarities and issues of its thermohydraulic and thermomechanical design. Chapter 7 will present the techniques developed and used to evaluate the power deposition due to interactions with the beam; the methods were used to propose a new beam channel geometry and the arrangement of the Electron Dump. Chapter 8 will show the solutions for cooling each subsystem, and the overall parameters of the hydraulic system. These results are followed by the description of the mechanical verifications carried out on the most loaded elements of the NED, on the piping assembly and on the support structure, which are reported in Chapter 9. The diagnostics, in particular thermocouples, foreseen for safe operation and possibly beam diagnostics are the subject of Chapter 10. In Chapter 11, the gas injection system is described and some methods for its study and an optimized configuration are proposed.

PART III covers the activities on the full-scale negative ion source experiment, SPIDER. In Chapter 12, the functional description of the SPIDER structure will be followed by its thermal modelling; two consequences are then evaluated, one concerning the grids' aperture misalignment, the other being the failure probability of the ceramic post-insulators which have a fundamental structural role.

The Conclusion will summarize my research activity, showing how some gaps identified in the existing knowledge have been filled and describing the main results achieved.

1

Short introduction to NBI Systems

This introductory chapter gives an overview of the NBI systems, describing their main functional components, and explains the main phenomena at the basis of their operation.

The components of a Neutral Beam Injection systems are functional to the generation of a powerful ion beam, its neutralization, and to the transport of the neutral beam to the tokamak plasma. The Beam Source generates the ion beam; the beam passes through a Neutraliser, but some residual charges need to be stopped on a dedicated Residual Ion Dump (RID). The beam proceeds through a duct to the tokamak, but a Calorimeter to absorb its power is necessary in the case the beam shall not be coupled with the plasma.

1.1 Negative Ion Beam Sources

In this section, the main elements and an overview of the physics at the basis of the negative ion beam sources is presented. The term beam source indicates the assembly of:

- *ion source*, often *plasma-based*, where the ions are generated and delivered to the extraction region;
- *extractor*, where an electrostatic field extract the ions;
- *accelerator*, in which the ion beam is accelerated and reaches the maximum potential.

Often the term ion source is used to indicate the beam source as a whole. In the following the phenomena involved in the beam generation are described. A schematic of a beam source, in the particular case of RF plasma source with magnets for filter field and local suppression field at the extraction is shown in figure 1.1.

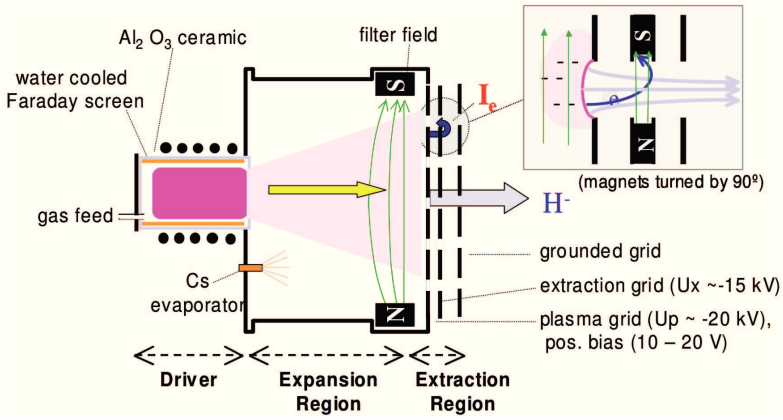


Figure 1.1: Scheme of a RF ion source [33]

1.1.1 Negative ion production

A negative ion is formed by physical mechanisms in which an atom or molecule captures an electron into an electron affinity level from an electron source [34]. Three mechanisms are classified according to the source of electrons into: *surface production* for electrons in the conduction band of a metal, *volume production* for plasma electrons, and *charge transfer* for free particles.

Charge transfer

In the charge transfer mechanism, alkali metals are used as electron donors for negative ion production, because of their large charge transfer cross section.

Volume production

In the volume production a highly vibrationally-excited hydrogen molecule captures a low energy plasma electron, to form a negative hydrogen ion through dissociative electron attachment process $H_2 + e^- \rightarrow H^- + H$. This can be seen as a two steps process, in which a high energy electron ($\sim$10 eV) vibrationally excite a hydrogen molecule later dissociated by a low energy electron ($\sim$2 eV). The simple dissociative electron attachment from a molecule in the ground state has very low cross-section.

By the use of a magnetic filter, the region where this process occurs shall be separated from the region for the molecule excitation, where electrons of high energy are needed.

Surface production

An atom emitted energetically from a low work function metal surface may leave in the form of negative ion. The electron at the Fermi level in the conduction band of the metal shifts by tunneling to the electron affinity level of the atom or molecule which is approaching the surface. The probability is greatly enhanced by the work function of the metal surface.

Two processes are involved: light particle reflection and heavy particle sputtering by positive ions, which are a thermodynamic equilibrium surface ionization and non-thermodynamic equilibrium surface ionization.

The negative ion production probability depends on the ion production probability density function $P(v)$, where v is the velocity of the sputtered particle [35]:

$$P(v) = \frac{2}{\pi}\exp\left(\frac{-\phi + E_a}{(2av\cos\theta + B)/\pi}\right) \tag{1.1}$$

where ϕ is the work function of the metal surface, E_a is the electron affinity (0.75 eV for negative hydrogen ions), θ is the ejection angle of the emitted particle, and a is the decay factor (2×10^{-5} eV/m for hydrogen). When the particle velocity is low (heavy particles) the factor $B = k_B T_{eff}$ is used, being T_{eff} an effective temperature function of the emitted particle mass. This process was discovered in the 80's by Belchenko [36].

The most widely used method for reducing the work function ϕ is deposition of a cesium layer on the surface. The minimum work function after cesium coverage of a metal surface is a semi-empirical relation [37]:

$$\phi_{min} = 0.62(V_i + E_a) - 0.24\phi_0[\text{eV}] \tag{1.2}$$

being ϕ_0 the work function of the metal surface, and V_i and E_a the first ionization potential and electron affinity of the adsorbed material on the metal: for cesium, $V_i + E_a = 4.35$ eV, which is the smallest of all elements. The work function of the base material is generally between 4.5 and 6 eV, and can be reduced to minimum values between 1.4 and 1.8 eV with a Cs coverage of about 0.6 atomic layers [38].

This to say, in any case the surface production strongly depends on the work function, and low work function cesiated metal surface is essential for high efficiency negative ion production.

1.1.2 Negative ion destruction

Many volume destruction processes occurs in the volume: mutual neutralization in collision with positive ions ($H^- + H^+(H_2^+, H_3^+) \rightarrow H + ...$), electron detachment in collision with electrons ($H^- + e \rightarrow H + 2e$) and associative detachment in collision with atoms ($H^- + H \rightarrow H_2(v") + e$).

In the energy ranges relevant to source plasmas, the cross section for the sole single-electron-detachment collisions is such that, across 0.1 m, few more than 1/1000 negative ions survive if the pressure is higher than 1 Pa. Therefore the pressure in the plasma production chamber should be as low as possible.

During the transport from the production region, the negative ion current is decreased by a factor $exp(-n_0 L\sigma_d)$, where n_0, L and σ_d are respectively the neutral gas density, the transport length and the electron detachment cross section.

The path of the negative ions shall be minimized to avoid their destruction.

1.1.3 Plasma generation

An adequate hydrogen plasma source shall have the following characteristics:

- high ion flux density (tens A/cm^2), with high fraction of atomic ions, delivered to the ion source chamber over a wide area;
- uniformity in space, and uniformity in time on long pulses;
- low content of impurities and therefore radiative losses;
- minimum requirements in terms of maintenance.

An additional advantage is the possibility to operate at low source pressures when the plasma source is coupled with Cs-seeding and magnetic filter.

Hot cathode sources

The source plasma is generated in arc discharges. Electrons emitted from the hot cathodes are accelerated by electrostatic potentials around 100 V, and hydrogen ionization follows. Numerous configurations evolved over 25 years of operation and testing [39]. The many filaments have limited thermal cycle life and require continuous replacement. The power of the arc discharge cannot be controlled. The concept of Arc ion source for ITER NBIs was abandoned in 2009.

RF sources

The RF source, or driver, utilizes the inductively coupled plasma (ICP) approach to generate the source plasma. The coupling is setup first with the free electrons, starting a cascade ionization. Typical frequencies are around 1 MHz, with RF power of 100 kW. As proven in many years of operation of the RF driven P-NBI in ASDEX, the RF sources have long lifetime, allow beam modulation thanks to the direct response of the ion density in the source to changes of the RF input power, and simplify the construction of the beam source with few electrical connections. The RF ion source also includes a series of auxiliary systems: the electric circuit for power input, the cooling circuits for the actively cooled Faraday shield, the gas supply system, starter filaments to initiate the plasma and several diagnostic sensors.

1.1.4 Negative ion extraction and acceleration

The formation of the beam occurs in the electrostatic extractor and accelerator, which is generally constituted by a set of grids at potentials decreasing from the plasma potential. A schematic of the negative ion extraction and acceleration process is shown in figure 1.2. The domain of the problem can be divided into regions: (1) hot plasma region, in which the electron temperature is high ($T_e = 5 \div 10$ eV) and the plasma is unaffected by the electrode potential; (2) a pre-sheath region, in which only colder electrons ($T_e = 1 \div 2$ eV) can diffuse through the filter field B_f; plasma quasi-neutrality hold when also negative ions are accounted; in the thin sheath close to the surface of the PG the potential falls and the meniscus is formed; (3) the beam region is dominated by the electrostatic field; the extraction field B is used to get rid of the co-extracted electrons; space charge by the beam should be considered too.

Meniscus formation

In the absence of a solid boundary, the plasma protect its neutrality forming a sheath against no static surface, but a free boundary facing the beam. The shape

of this boundary is defined by the balance of the characteristics of the plasma and the intensity of the electric field. The *meniscus* is the equipotential surface corresponding to the zero electric field; its shape is fundamental in defining the beam characteristics as its particles are accelerated from here. The quantity of available negative ions immediately before the meniscus is another complication.

Perveance

A limit to the extracted current is given by the space-charge. The extracted current I depends on the applied electrostatic potential V, but it is also related to the geometric properties of the system, such as the aperture diameter a, the length of the region in which the electric field acts on the ions L, but also to the charge Z and mass number M of the extracted ion. These parameters can be written as a term independent from the potential, the perveance P:

$$P = \frac{I}{V^{3/2}} = C \cdot \sqrt{\frac{Z}{M}} \left(\frac{a}{L}\right)^2 \tag{1.3}$$

where C is a constant. The term L is limited by breakdowns (there exist a minimum gap for a given potential), and therefore multi-apertures electrodes are used to subdivide into circular beamlets the beam, allowing for the same accelerator length elevated extracted current. Also the homogeneity is enhanced.

Divergence

The divergence of a beamlet is the angle with which the ions exit the accelerator with respect to the beamlet axis. The divergence is often visible on the emittance diagram, which presents the divergence ω (often indicated in mrad) as a function of the distance from the axis r (often in mm). An example in the case of SPIDER is shown in figure 1.3(a); the associated equipotential lines and trajectories are shown in figure 1.3(b). There is an analogy between the curved electrostatic potential lines and the optic lenses and how they focus and defocus the beamlet.

For a given geometry of the extractor and accelerator, there exist an optimum electrostatic potential associated with the ion flux from the ion source. This optimum shall be verified in any aperture and acceleration grid gap; variations in the ion current density delivered by the ion source cause degradation of the divergence. The divergence is typically studied in single-beamlet models.

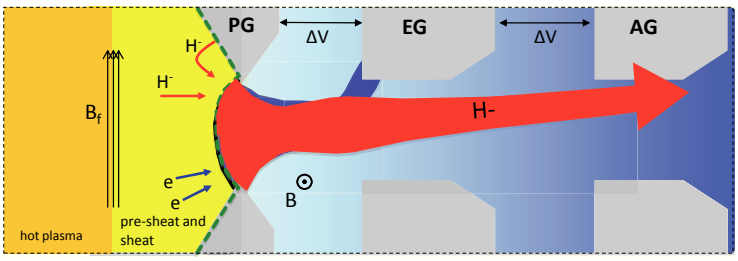
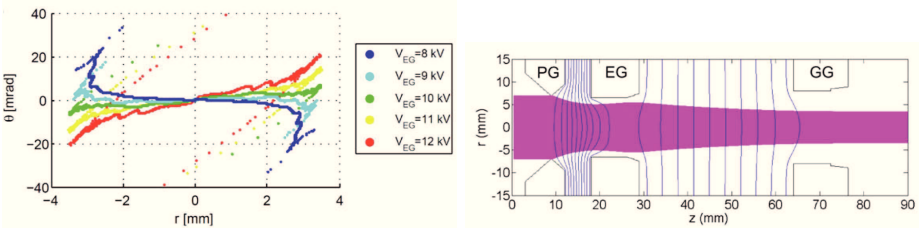


Figure 1.2: Extraction of negative ions.



(a) (b)

Figure 1.3: (a) emittance diagram and (b) equipotential lines and ion trajectories calculated for SPIDER (V_{EG}=9.4 kV and V_{GG}=100 kV) [40]

It is observed experimentally that some particles of the beamlet have larger divergence angle than the average. These particles form the so-called halo surrounding the core of each beamlet. This occurs also in condition of perveance match. It could originate from two causes: aberrations in the electrostatic lenses of the accelerator, or negative ions emitted from the downstream the PG aperture (in particular on the surface of the diverging cone. According to the available experimental data for lower energy beamls and the results of the model calculations, are that about 85% of the power will be in the core fraction, and 15% of the power will be in the halo; in addition, for the reference ITER NBI beamlet it is assumed a core 1/e divergence of 5 mrad, and the halo 1/e divergence of 15 mrad. These values of divergence and power fractions are based on bi-gaussian approximations, as widely discussed in section 7 of this thesis.

Magnetic field

A magnetic field $\vec{B}$ acts on moving charged particles a force $\vec{F} = q(\vec{v} \times \vec{B})$. The velocity given to the charge along a path $\mathrm{d}z$ is:

$$v_\perp = \frac{1}{m} \int qvB_\perp \, \mathrm{d}t = \frac{q}{m} \int B_\perp \, \mathrm{d}z \tag{1.4}$$

The axial velocity of a charge at the exit of the electrostatic accelerator of potential U is $v = \sqrt{2qU/m}$; the ratio between v and the transverse velocity due to the magnetic field $v_\perp$ will be proportional to the beamlet deflection, if the second order lens effects at the apertures are neglected.

Multi-beamlet aiming

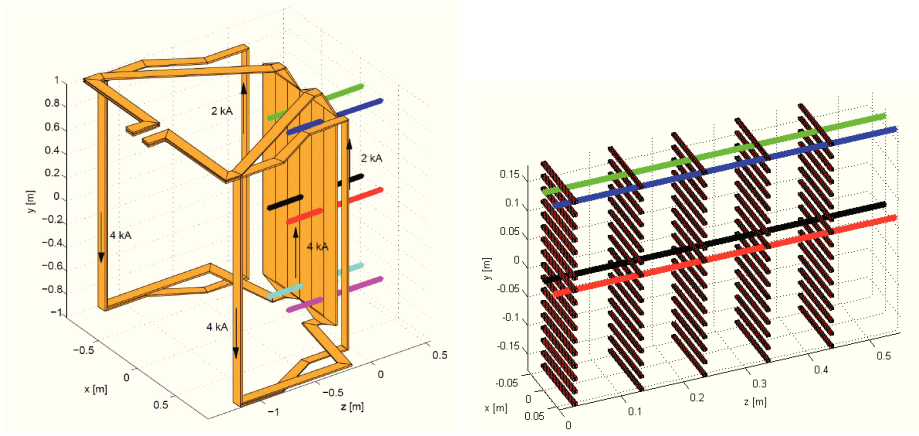
The beam footprint depends on the divergence of the single beamlets and the nominal direction of their trajectory, but also on the beamlet-beamlet interaction. The aiming or steering is the correction of these effect, and is performed on the single beamlets, on groups of beamlets or on the whole beam. The aiming must be studied on multi-beamlet models.

Stripping losses

A fraction of the accelerated ions is lost inside the accelerator by charge changing processes involving the background gas, or stripping. The main charge changing processes in the beam are listed in table 1.1.

$\underline{\mathrm{H}}^- + \mathrm{H}_2$	$\rightarrow$	$\underline{\mathrm{H}}^0 + e + \mathrm{H}_2$
$\underline{\mathrm{H}}^- + \mathrm{H}_2$	$\rightarrow$	$\underline{\mathrm{H}}^+ + 2e + \mathrm{H}_2$
$\underline{\mathrm{H}}^0 + \mathrm{H}_2$	$\rightarrow$	$\underline{\mathrm{H}}^+ + e + \mathrm{H}_2$
$\underline{\mathrm{H}}^0 + \mathrm{H}_2$	$\rightarrow$	$\underline{\mathrm{H}}^- + \mathrm{H}_2^+$
$\underline{\mathrm{H}}^+ + \mathrm{H}_2$	$\rightarrow$	$\underline{\mathrm{H}}^0 + \mathrm{H}_2^+$
$\underline{\mathrm{H}}^+ + \mathrm{H}_2$	$\rightarrow$	$\underline{\mathrm{H}}^- + 2\mathrm{H}^+$
$\underline{\mathrm{e}} + \mathrm{H}_2$	$\rightarrow$	$\underline{\mathrm{e}} + \mathrm{H}_2^+ + e$

Table 1.1: Main charge changing processes in the beam and cross sections; the last two do not modify the beam fractions [41].



(a) (b)

Figure 1.4: Analysis of the magnetic field produced by (a) currents in PG and return and lateral bars (b) analysis of the field produced by the embedded magnets [166]

The stripping loss, L_s, is a figure of merit for the gas flow conditions in the BS. It can be quantified as:

$$L_s = \int n(x)\sigma(E(x))\,\mathrm{d}x \tag{1.5}$$

Both the gas density, n, and the energy of negative ions, E, depends on the distance from the plasma source x, and so does the stripping cross section ω which depends on E.

Codes for modelling

The SLACCAD code estimates the electric field inside an electrostatic accelerator by integrating the Poisson's equations in cylindrical geometries [42]. It is a modified version of the SLAC Electron Trajectory Program, adapted to include ions, a free plasma boundary and the charge exchange processes [43].

PerMag [44] is a two-dimensional magnetostatic code that can ben used to calculate the magnetic field generated by the permanent magnet embedded in the EG and the filter field magnets.

NBIMAG [45] can be used to calculate the long range magnetic field produced by the current running through the PG and on the return bars, see figure 1.4.

The commercial finite element (FEM) code ANSYS [46] solves on discretized volumes the magnetic field produced by permanent magnets and currents.

The electrostatic and magnetostatic fields are used by the code EAMCC [47], which is a relativistic particle tracking code that compute the trajectories of the macroparticles, the collisions and the secondary particle production processes. The collisions that are accounted are the ones between the particles and the grids, the negative ion single and double stripping and the ionization of the background gas. The reference for the cross section is the ORNL Redbooks [41]. An example of its application is shown in figure 1.5.

Opera is a commercial code [48]. It calculates the beam trajectory by launching a large number of macroparticles, calculate the magnetic field and the space charge deposition of beam particles, including also stripping losses.

Bypo [49] and BACKSCAT [3] were developed at Consorzio RFX, together with the code for calculating the gas density distribution AVOCADO (see part I of this thesis).

Approach to the design

The region immediately before the first electrostatic grid, called Plasma Grid (PG), is typically "protected" by a filter magnetic field, which should create an ion-ion plasma by removing the lighter electrons. In this way, the extracted electron density is lower, but most of all the negative ion density is higher, and the high energy electron are prevented from destructing the negative ions.

The second electrostatic grid is the Extraction Grid (EG). The electric field between the PG and the EG penetrates the plasma source chamber through the PG apertures. Electrons are co-extracted as well, and their trajectories subjected to the magnetic fields constitute a source of heat load on the electrostatic

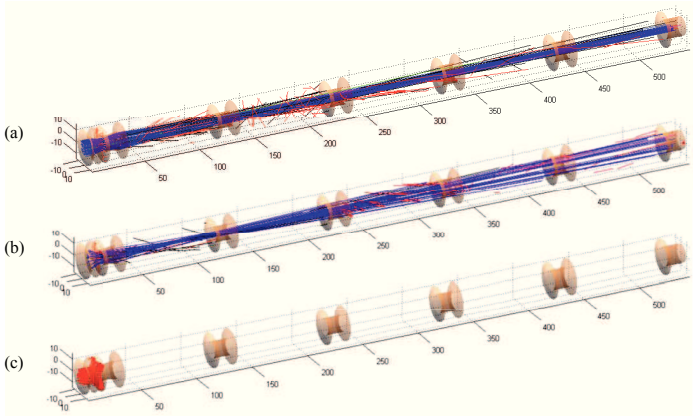


Figure 1.5: Simulation with EAMCC of MITICA relevant accelerator design [166]: (a) negative ions and related particles, (b) halo particles and (c) coextracted electrons. The colors represent: blue D^-, red e^-, black D^0, magenta D^+, green D_2^+.

grids, especially if they reach the full acceleration energy. They are removed as soon as possible, typically in recent applications by a magnetic field between PG and EG created locally by magnets embedded in the EG; for this reason the EG must be cooled as it receive this continuous electron thermal load. Various Acceleration Grid (AGs) can follow; typically the last one is at ground potential and is called Grouded Grid (GG). Electrons are generated as well along the path of the beam inside the accelerator by stripping, and are removed by magnetic means, either using local or long range fields. The actual trajectory of the ions, bent by these magnetic fields, must be taken into account. In the case of stripping, whichever charge changing process that generate positive ions is dangerous, because a positive ion is accelerated back and hits the backplate of the plasma source with energies up to the full acceleration potential.

Generally speaking, many solutions are available for multibeamlet aiming. *Kerbs* are thickening of the grid on the side of the apertures; they bend the equipotential lines causing a focusing effect of beamlet groups if placed at their side. *Oblique* or *displaced apertures* cause a net deflection of the beamlet; if properly designed, the electrostatic deflection they originate can create the whole optic of the beam. Subdivision in grid segments and *tilting* of the segments is an easy way of realizing a vertical focusing. The use of long range or local *suppression magnetic field* can be used to remove the unwanted electrons in any position along the accelerator. A different *aperture diameter* in each grid can be used to redistribute the heat load, while a general reduction of the *neutral gas density* heals any problem related to secondary particle generation. Table 1.2 summarize different applicable solutions.

		POSSIBLE SOLUTION / CONTROL PARAMETER											
#	ISSUE	kerbs	oblique apertures	displaced apertures	grid segments vertically tilted	grid segments vertically offset	non-flat grid segments	embedded secondary electron suppression magnets	long-range magnetic field	rotated beam source	horizontal aperture centring	neutral gas density reduction	different AG aperture sizes
1	Uniform magnetic field in accelerator							X	X				
2	Uniform heat loads on AGs							X	X			X **	X
3	Low AG heat loads due to secondary particles							X	X			X **	X
4	Horizontal beamlet aiming	X	(X)	X							X *		
5	Space charge deflection	X	(X)	X									
6	Zigzagging beamlet rows due to EG magnets			X – EG							X *		
7	Vertical beamlet group aiming				X	X							
8	Horizontal beamlet group aiming			X – AGs *			X *						
9	Vertical displacement due to SESF					X *				X **			

Table 1.2: Possible solutions that can be used to correct common issues of optics and aiming in a beam source.

1.2 Negative Beam Neutralisation

The beam negative ions are converted to neutral particles by single-electron-detachment collisions or to positive ions by double-electron-detachment collisions; the cross-sections are indicated as $\sigma_{\bar{1}0}$ and $\sigma_{\bar{1}1}$ respectively. Stripping

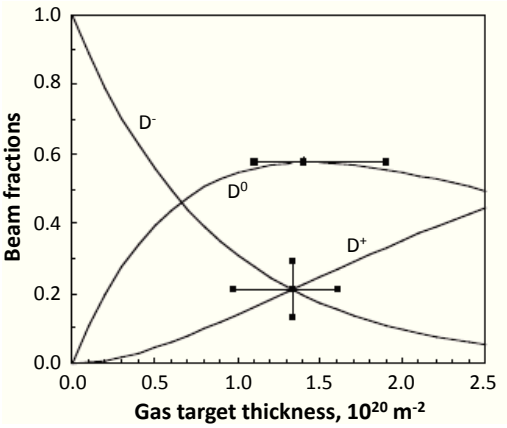


Figure 1.6: Beam fractions as a function of the gas target thickness [50]

processes have a very bad connotation in any part of a NBI, apart from the neutraliser, where it is welcome and named neutralisation.

Above 80 100 keV/nucleon, the maximum conversion efficiency to neutrals is slightly more than $\sim 55\%$, and it is essentially independent of the beam energy, as depicted in figure 6.

The proper gas target thickness, calculated as $\int n(x)\,\mathrm{d}x$ [m^{-2}] shall be provided to the beam through the gas cell of the neutraliser (see figure 1.6). At sligthly lower target thickness than the one of maximum efficiency, the fraction of negative and positive ions are equal, and operation at this neutralisation target make easier the dumping of the residual ions.

For the ITER heating neutral beam (HNB) the stripped electrons are not thermalised and pass out of the neutraliser with the neutral beam; in this case the gas heating is predicted to be negligible [51].

Other options for neutralisation have been proposed in the past, such as plasma neutraliser or laser neutraliser. It is known that the bottleneck to the efficiency of an NBI is in the limited beam neutral fraction achievable with gas neutralisers, and therefore future efforts will be put on the development of new, reliable technology for the component.

1.2.1 Dumping of the residual ions

After the incomplete neutralisation, the beam fraction of positive and negative ions is about 1/5 each. There are two possible approaches, one magnetic, the other electrostatic. In an E-RID, the charged fractions are deflected by electrostatic fields between parallel panels, capable of accepting dumped power at the expected PD.

In the multi-channel E-RID of MITICA, the panels are at negative potential or are grounded; the strength of the field oscillates in order to move the region of maximum power density on the panels. The impact of fast positive ions with the panels at negative potential generates electrons due to secondary electron emission. The secondary electrons are accelerated to and dumped at the opposite panels at ground potential. The value of the secondary emission coefficient for the typical ion impact angle and energy in the RID is assessed to be in a

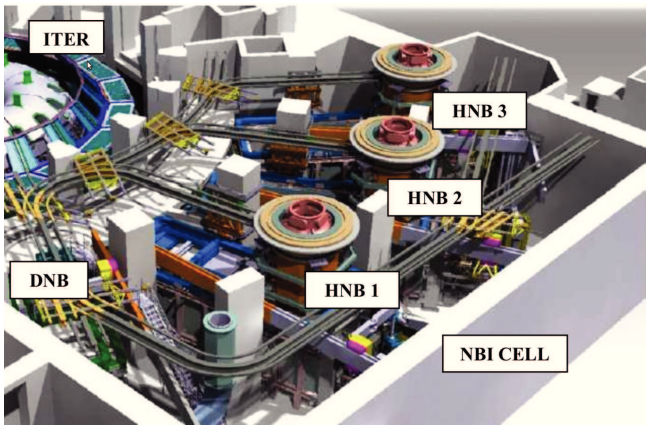


Figure 1.7: ITER NBI cell with DNB and three HNB injectors

range of 67 electrons/ion, the other source of electrons being the detachment processes in the Neutraliser. The design of a multichannel E-RID is short and compact.

A M-RID deflect the charged fractions by magnetic means on single, longer panels located on the side of the the beam; typically it is somehow longer than the E-RID and requires more space in the vacuum vessel.

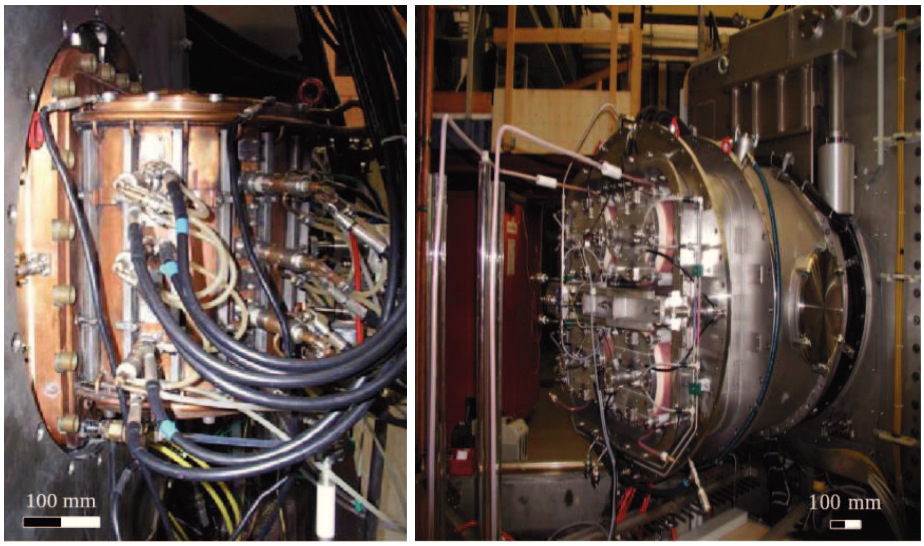
1.3 Road to the Full scale Plasma Source for ITER NBI

The requirements of the ITER H&CD NBI (figure 1.7) have been presented in table 2. As already said, the required beam properties have been accomplished in past experiments, but never altogether at the same time, on the same device. The road to the ITER NBI that is being followed started from different conceptual designs of the beam source (kamaboko or RF type, see figure 1.8), of the accelerator setup (single acceleration gap SinGap or multi-grid setup MaMuG), and of the RID (magnetic or electrostatic).

The different strategies were tried, on dedicated experiments of increasing complexity. The final step before the operation in ITER will be the full scale injector MITICA. A brief overview is given in the following.

1.3.1 BATMAN MANITU ELISE

The RF driver was developed at the Max-Plank-Institut für plasmaphysik, where it has been recently tested in various facilities for the production of negative ion sources [52, 53]. The BATMAN and MANITU were intermediate experiments with single RF driver. ELISE [54] is a test facility that will test the extraction of a half-size source. This test facility is an intermediate step between the small one-driver sources and the full size, 1.6 m high and 0.6 m large, ITER NBI source; so, the target extracted current is 20 A, with an extraction voltage around 10 kV and a total acceleration of 60 kV. The facility will demonstrate 1 hour operations of the RF drivers.



(a) (b)

Figure 1.8: Negative ion sources developed for ITER: (a) Kamaboko III arc driven ion source (b) Half-size ITER RF circuit with source installed on the RADI facility

1.3.2 SPIDER

SPIDER is the full scale ITER H&CD NBI source. It is equipped with eight radio-frequency drivers, followed by a plasma expansion and ion extraction region [55, 56].

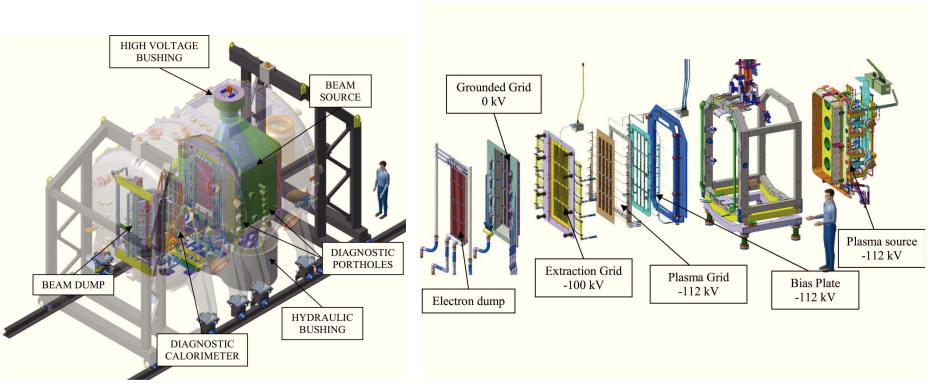
In the driver coils, fed with 1 MHz RF current, the electrons become sufficiently energetic (15-30 eV) to cause collisional ionization and dissociation of the injected gas (H_2 or D_2). The resulting plasma is mainly constituted by the species e^-, H, H_2, H^+, H_2^+ (and the analogous for deuterium); it expands in the expansion region where the electrons are cooled down by a magnetic filter field, which is produced by a current vertically running through the PG itself.

In the source chamber, the production of the negative ions is dominated by the volume process and surface processes described above. The surface processes dominate: negative hydrogen/deuterium ion production is mainly due to the presence of atomic neutrals which combine with electrons, mostly at the cesiated surface of the PG.

The negative ions beamlets are extracted through 1280 apertures, organised in 16 groups that are, in pairs, faced to a single driver; each group has 16 rows and 5 columns of beamlets. Upstream of the PG, a copper bias plate (BP) guarantees the same reference potential all around each beamlet group.

The acceleration grid (EG) is biased at 10 kV with respect to the PG. The grounded grid (GG), further downstream, will provide the ions with the last acceleration step of 90 kV. All the physical processes described so far evolve with a timescale of the order of tens of milliseconds.

A figure of the SPIDER experiment and a sketch of its main components is shown in figure 1.9(a) and 1.9(b).



(a) (b)

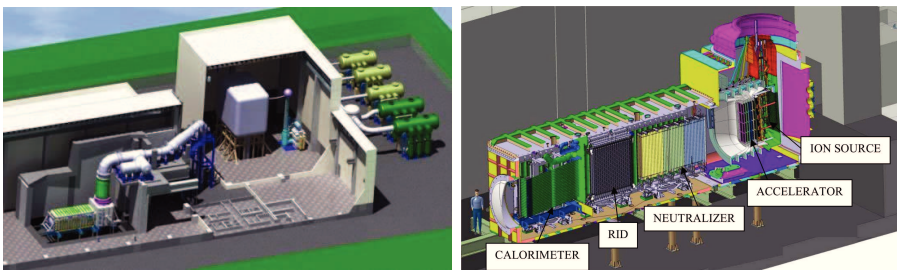
Figure 1.9: (a) SPIDER experiment with transparent vessel and (b) exploded view of the SPIDER Beam Source.

1.3.3 The ITER HNB prototype: MITICA

The prototype for the ITER heating neutral beam (HNB), MITICA, will be installed in the PRIMA facility in Padova at Consorzio RFX together with SPIDER (see figure 1.10).

Differently from the case of SPIDER, where more flexibility was allowed, the technical requirements of MITICA are shared with the HNB to be installed in ITER, a nuclear facility with strict regulations. The parameters listed in table 1.3 complete the general requirements for the beam already presented in table 2. The MITICA Beam Source is shown in figure 1.11; the concept of the ion source is the same as SPIDER, but the complexities are much more challenging because of the higher voltages involved and the many acceleration grids. The other components of the beam line are:

- the Neutraliser and Electron Dump (NED), which is divided into 4 vertical channels constituting the gas cells, and stops the unwanted electrons exiting the source with steered trajectories;



(a) (b)

Figure 1.10: (a) MITICA installed in PRIMA buildings and (b) its main components.

- the Electrostatic Residual Ion Dump (E-RID), which is divided into 4 channels in which an electric field deflect the partially positive and partially negative residual ions. The power load of about 18 MW is expected on the component.
- the Calorimeter, is located downstream the RID and is constituted by two panels, in a V shape, of 96 tubes each parallel to the beam. The neutral power dumped onto the calorimeter can be measured, and in the ITER NBI, the V calorimeter will open and the deuterium beam of 16.5 MW power will travel the duct until the ITER plasma.
- Cryopumps are placed on each side of the beam path and the beamline components to reduce to the minimum the pressure of the background gas. The pressure downstream the accelerator must be low in order to minimize losses in the accelerator. The pressure downstream of the neutralizer must be low in order to minimize re-ionization of the D_0.

The most heated elements, such as the Neutraliser leading edges facing the source, the Calorimeter tubes, and the E-RID panels make use of Swirl Tape Elements (STE) to enhance the heat transfer coefficient (HTC) between the cooling water and the cooling channel surface

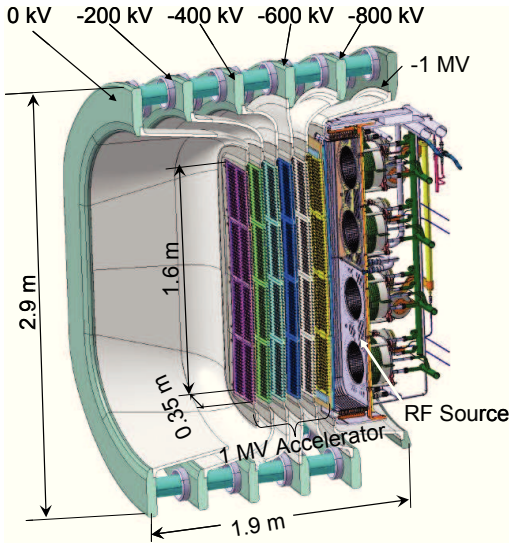


Figure 1.11: Vertical section view of the MITICA beam source; dimensions and electric potential of the grids and the plasma source are indicated.

Two modes of operations are foreseen for the NBI, the plasma operation mode, and the commissioning/conditioning mode in which the NB is dumped on the calorimeter. The pulse duration and the beam cycles are listed in table 1.4.

Beam Physics Parameter	**Value**
Max Halo power	15%
Max Halo divergence [mrad]	30
Vertical tilting [mrad]	49.2±10
Horizontal misalignment [mrad]	2
Vertical misalignment [mrad]	4
Vertical beamlet focal length [m]	8
Vertical beamlet group focal length (from the GG) [m]	25.479 ± 2.55
Horizontal beamlet focal length (from the GG) [m]	7.2 ± 0.72
Horizontal beamlet group focal length (from the GG) [m]	25.479 ± 2.55

Table 1.3: Physical parameters of the beam

Beam Mode	Number of pulses	Number of pulses @ each pulse length					
		3600s	1000s	400s	200s	50s	10s
Plasma Operation	40000	1000	3000	30000	2000	2000	2000
Commissioning	2000	5	15	80	400	500	1000
Conditioning	8000	0	0	0	1000	5000	2000
TOTAL	50000	1005	3015	30080	3400	7500	5000

Table 1.4: Pulse duration and beam cycles

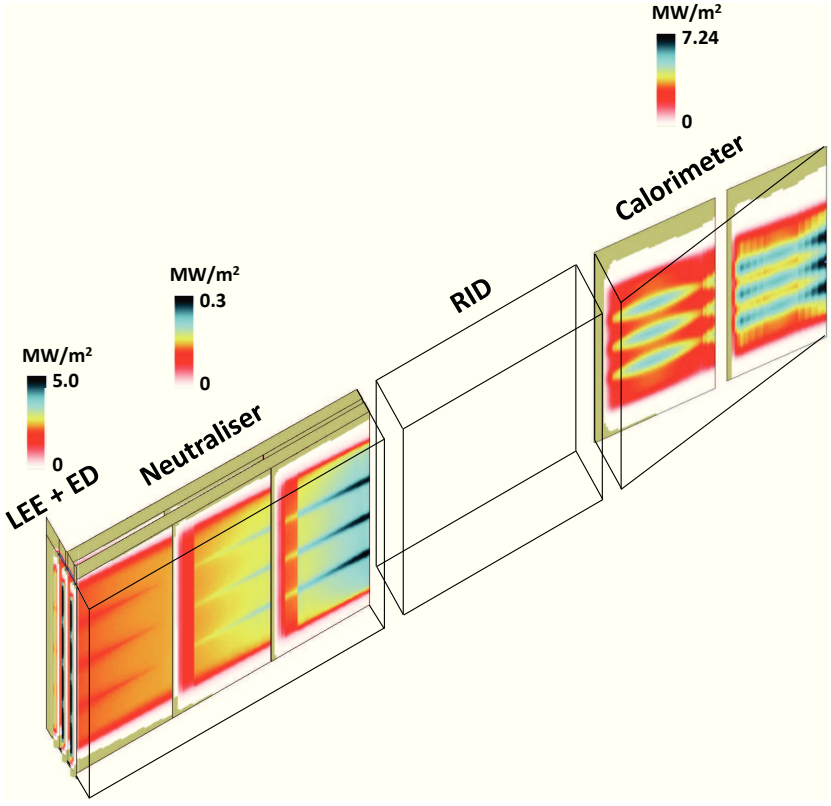


Table 1.5: Power density deposited on the Neutraliser and the Calorimeter, see section 7

Part I

DENSITY DISTRIBUTION

2

Much Ado About Nothing

At the heart of the Scientific Revolution in the seventeenth century, the void, the vacuum, represented one of the key issues of the dispute on the constitution of the universe and of the matter. The debate on the void had been constricted into the dogmas of the Christian faith and the reinterpreted ideas of Aristotele; then, in 1644 Torricelli performed his mercury experiment, causing a great sensation all around Europe: it was the first time that the existence of the vacuum was convincingly proven by experimental evidence. The greatest scientists, theologians and philosophers tackled the existence of the void and its scientific and cosmological implications; within ten years, the void, or vacuum, had been replicated across Europe and became a common topic of conversation in cultural gatherings and salons; also, it took only ten years for the invention of the air-pump, that succeed in making better vacuums, which encouraged experimentation. The Torricelli result was epoch-making: it leaded to great transformations, and prompted deep reflections and debates about the "*nothing*", the vacuum.

With the same prodigious impetus, nowadays the vacuum continues to boost the scientific advances. Over the last 50 years, the development of increasingly larger and more sophisticated devices for physics research, has been strongly coupled to the development of the science and technology of ultrahigh vacuum. Particle accelerators, magnetic fusion devices and gravity wave observatories were made possible thanks to progresses in the vacuum technology. In this fervent context, with the growing complexity of the applications, the gas distribution modelling in high vacuum conditions offers an increasingly substantial help in the engineering design; in the case of ITER HNB&CD injector and the MITICA, the density of the background gas shall be accurately controlled along the path of the beam; at different positions, opposite densities are required, to minimize stripping losses on one hand or to cause the beam neutralisation on the other.

As part of my phd activity, I developed a numerical tool for gas pressure and density calculations in high vacuum systems. The code, named AVOCADO, simulates neutral gas flow in molecular regime inside complex/difficult geometries

such as the whole vessel of MITICA or the electrostatic accelerator. AVOCADO is the acronym for "A View-factOr Code to Analyze gas DistributiOn".

2.1 Vacuum for dummies

The word *vacuum* simply refers to part of the pressure scale. Its definition is not precise, but it is commonly taken to mean pressures below, and often considerably below, atmospheric pressure. In the following, the essential informations required to introduce the rarefied gases are provided.

2.1.1 Gas

A gas shows a number of macroscopic properties: it occupies a volume, has a temperature and exert a pressure to the walls, and these properties are related by an equation of state. In addition, a gas originates frictional forces thanks to its viscosity, transfers heat thanks to its thermal conductivity, and diffuses molecules. Each of these properties can be explained from the microscopic behaviour by means of the kinetic theory of gases, which considers the statistical behaviour of the very large number of particles composing the gases. All collisions between the particles and with the the walls of the container are elastic, and therefore the energy is conserved, but cause changes in velocity. The simplest form of the kinetic theory makes use of hard-speres with fixed diameter that do not attract themselves.

2.1.2 Pressure

An example is the calculation of the pressure. Assuming N particles move chaotically in a cubic volume with velocity v, 1/3 of them will move along one direction with v_x if the velocity is isotropically distributed. Before colliding with the wall, the particle momentum is mv_x, and after colliding it leaves the wall with a momentum $-mv_x$, totaling a momentum variation of $2mv_x$. Between consequent collisions, the particle will travel twice the width of the container d, and the collision frequency with the same wall will be $v_x/(2d)$. The force at the wall is the product of momentum change and collision frequency; the pressure results $2mv_x \cdot v_x/(2d) \cdot 1/d^2$. Considering the number of particles hitting the wall, the pressure exerted on the wall is given by

$$p = \frac{N}{3}\frac{mv_x^2}{V} \tag{2.1}$$

since the volume V equals d^3. This is an example of the applicatio of the kinetic theory of gases to derive a macroscopic property. Some of the assumptions that were made are too simplistic, among them: the wall has surface roughness and the rebounds are not perfect reflections, the fact that the particles collide between themselves, the single velocity for the particles.

2.1.3 Temperature: the Maxwell-Boltzmann distribution

2.1.4 Mean free path

In the hard-sphere model, two particles collides when the distance is equal to their diameter. In the collision, the particles change the value and direction of

their velocity, and therefore they follow a zig-zag path. Statistically, an average path length that a particle travels between two collisions can be calculated and is referred to as mean free path (m.f.p.) λ. The total effective collision area for a moving particle among stationary ones is given by the number of particles N and the collision area of each one πd^2; the number of particle is the number density n multiplied by the cross section of the volume A and its thickness t; one collision will occur when the total collision area is equal to the geometric area, therefore $nAt\pi d^2 = A$ and the m.f.p. λ is the thickness of the volume:

$$\lambda = \frac{1}{n\pi d^2}$$

More collisions occur when all the particles are in motion, and Maxwell added the term $1/\sqrt{2}$ to the equation:

$$\lambda = \frac{1}{\sqrt{2}n\pi d^2} \tag{2.2}$$

2.1.5 Flow regimes

A flow, or flux, of gas is a movement of substance; in a gas it is determined by the thermal motion as well as macroscopic forces due to pressure difference, and its behaviour is determined by pressure itself and viscosity. Taking the case of gas flow in a tube, different types of flow regimes may arise:

Molecular regime The mean free path of the particles is high compared to the cross dimensions of the tube in low pressure cases: the collisions between particles is unlikely. This is a single-particle motion dominated by the thermal velocity, and is called *molecular flow*.

Viscous regime The mean free path of the particles is much smaller than the cross dimensions of the tube under high pressure. The continuous collisions redistribute energy and momentum even in small volumes, thus the gas behaves as a continuum, and the flow is the result of pressure gradients. The situation is that of a *continuum flow* or *viscous flow*.

Transitional regime The intermediate case, in a medium-pressure range, occurs when the number of mutual collisions between the particles is comparable with the number of collisions with the walls, determining a transition between the two types of flow presented before. This regime is referred to also as *Knudsen flow*.

The criteria for a flow to occur in a particular regime is the ratio between the m.f.p. and the characteristic dimension L of the geometry, and is called Knudsen number:

$$Kn = \frac{\lambda}{L} \tag{2.3}$$

The Kn ranges corresponding to the three regimes are [57]:

$$\begin{array}{cc} Kn > 0.5 & \text{molecular regime} \\ 0.5 > Kn > 0.01 & \text{transitional regime} \\ Kn < 0.01 & \text{viscous regime} \end{array} \tag{2.4}$$

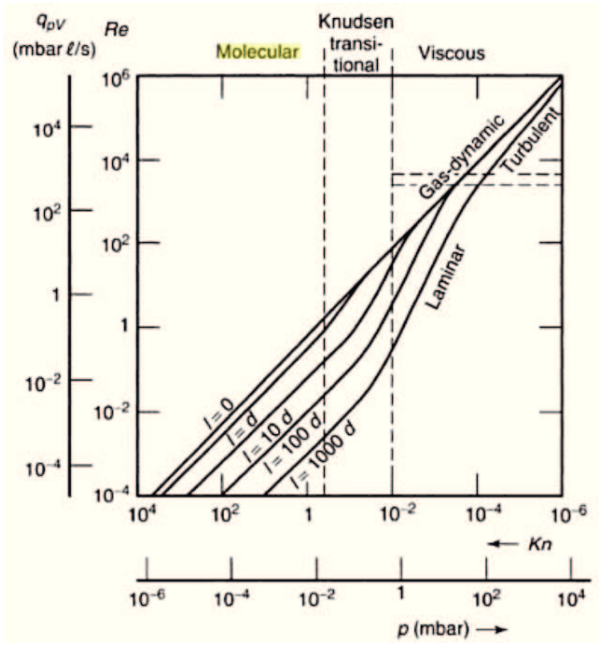


Figure 2.1: Air flow in tubes with circular cross-section, 1 cm diameter ; inlet pressure in abscissa [57]

In a gas with average particle velocity $\bar{c}$, the Knudsen number can be written also as a function of the dynamic viscosity $\eta = \rho\bar{c}\lambda/2$ [Pa s]:

$$Kn = \frac{\pi}{4}\frac{\bar{c}\eta}{pL} \tag{2.5}$$

2.1.6 Laminar and turbulent flow

In the case of viscous flow, a distinction is made between laminar and turbulent flow, respectively occurring at low speed and higher flow speed. The occurrence of the turbulent flow is contingent upon the Reynolds number, which reads

$$Re = \frac{\rho}{\eta}vL \tag{2.6}$$

for a flow of velocity v and density ρ; the dynamic viscosity is denoted with η The flow will be laminar up to values of $Re < 2300$ and fully turbulent above $Re > 4000$.

2.1.7 Vacuum ranges

According to the American Vacuum Society, a distinguish between up to seven pressure ranges is possible. A rough classification of the vacuum, that gives the flavor of the nature of the matter, distinguish between three ranges:

- Low vacuum covers a range from 10^5 to 10^3 Pa.
- Medium vacuum is in the range from 10^3 to 10^{-1} Pa and can be achieved using, for instance, inexpensive rotary pumps.

- High vacuum lies between about 10^{-3} and 10^{-5} Pa which is made possible by two different classes of pumps, the diffusion pumps and the turbomolecular pumps; generally speaking, the m.f.p. in this pressure range should be longer than the size of the chamber.
- Ultrahigh vacuum represents state of the art performance in today experimental surface science. Pressures from 10^{-5} down to 10^{-10} Pa and below are routinely achieved using mass produced standard parts and ion pump systems.

2.2 Vacuum in Fusion Devices

The appropriate vacuum environments for accelerating particle beams, or for heating and confining high temperature plasmas, evolved together with the vacuum technology incorporated into these machines, including vacuum pumps, instrumentation and control, surface cleaning and conditioning procedures, sealing and appropriate vacuum materials. In the following, a brief historical survey of the vacuum systems and procedures used in fusion devices is given. An interesting review is also offered by Dylla in [16].

In the early 50's, Lyman Spitzer from Princeton University conceived the figure-8 stellarator confinement and a plan to move the technology along. When the third planned stellarator, Model C, was commissioned in 1961, its stainless steel vacuum vessel became the largest UHV system built to date. [58] Less than fifty years after their invention by W. Gaede (1913), two large mercury diffusion pumps, isolated from the torus by lead-sealed valves and freon-cooled traps, pumped the system in the 10^{-10} Torr range. Mercury was chosen as the pumping fluid because its presence could be easily detected by spectroscopy technique and, with equal simplicity, removed during bakeout; the system to be baked to 450°C thanks to special gold wire flange seals. While the performance of the Model C vacuum system was a huge success, the experiment was quickly converted to tokamak design eight yeas later.

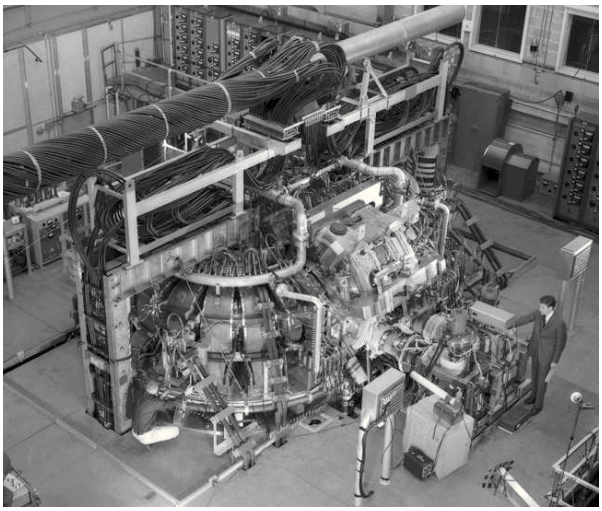


Figure 2.2: PPPL Model C stellarator (1962), S.S. vacuum vessel with gold wire flange seals, bakeout at 450 °C, base pressure 10^{-10} Torr.

The Princeton Large Torus (1975) had 0.5 m plasma radius, with a 6400l vacuum vessel. A turbomolecular pump vacuum system composed by four vertical shaft, oilbearing, 1500 l/s turbomolecular pumps could provide a net pumping speed of 3000 l/s for H2. [59]

In the mid-70's, pure hydrogen plasmas were archieved, by successful wall conditioning (titanium evaporation) and pulse discharge cleaning. Removing the low-Z carbon and oxygen, the edge plasma improved so much that new materials had to be introduced in the first wall: in particular, high Z tungsten limiters were replaced by high purity graphite.

In the early 80's, PDX at Princeton and ASDEX at Garching had vacuum vessels larger than the plasma volume (≈ 36 m^3) to contain the divertor structure. The divertor requires high capacity pumping in that volume; in those machines. it was equipped with Ti evaporation sources to provide up to 200000 l/s of hydrogenic pumping; in both tokamaks, glow discharge techniques were developed for cleaning complicated vacuum vessels, originally studied on accelerator structures.

When three large tokamaks were constructed to demonstrate energy breakeven in the 80's, the achievements in plasma temperature moved together with the impurity suppression and removal techniques. The TFTR vacuum vessel was protected with graphite tiles, replaced with CFC material; JT-60U upgraded to CFC as well; JET replaced graphite with Be in high flux areas. In many other tokamaks, the first wall property was improved with thin boron-carbide layer coating. In D-T operations, the requirement to pump tritium presents significant design problems.

In TFTR [60], by utilizing eight 3500 l/s turbomolecular pumps, liquid helium cryogenic pumps in the NBIs, bake-out up to 150 °C, plasma discharge cleaning and various wall-coating techniques, this volume was maintained at a pressure less than 2×10^{-8} Torr. By adding internal ZrAl surface pumping, the base pressure could drop in the 10^{-10} Torr range.

In JET [61], there were four turbomolecular pumps connected in pair in two turbo-pump stations, basically an L-shaped tube 1.2 m of diameter that was used also as an human access to the torus. The nominal pumping speed was 2900 l/s of N_2, totallying 8500 l/s for H_2. Leaks as small as 3×10^{-9} mbar l/s were detected and repaired; All the flanges use metal seals. The torus octants are all-metal all-welded, and can be baked to a temperature up to 520°C to remove physically bound impurities such as H_2O, N_2 and CO_2 from the inner surface (about 1000 m2); further conditioning is obtained by glow discharge cleaning GDC to remove chemically bounded impurities, namely C and O. The vessel is double-walled with an independent pumping system of the enclosed volume, which is used also for the baking (hot or cold He gas flowing inside). A partial pressure for hydrogen of 4×10^{-7} mbar and below 4×10^{-9} for the impurities is can be reached.

The improvements in the first wall materials and treatments rely on the UHV standards of the second wall, that is, the vacumm vessel with its many access ports; it must withstand the strong eddy currents and the many thermal cycles required for baking. The standard pumping is nowadays constituted by non-contaminating turbomolecular pumps, whose capacity grew up to 3500 l/s.

The ITER vacuum vessel, with a volume of 1400 m^3, is among the largest vacuum systems ever built. The tokamak will be fuelled at a time averaged rate of up to 200 Pa·m^{3}s^1, requiring neutralised gas in the divertor to be pumped, to

balance the fuelling and remove the fusion helium and other impurities in the exhaust. In the lastest design [62], six large bespoke cryo-sorption pumps are foreseen; during operation, there will be always 4 pumping and 2 regenerating pumps. According to tests with ITER-relevant exhausts mixture on testbed at KIT [63], a pumping speed of 1 l/s cm^2 can be exeeded. Complex tritium recovery systems are also foreseen.

2.2.1 Vacuum in Neutral Beam Injectors for Fusion

Two vacuum requirements, one being the low base operating pressure of the NBI systems, the other being the gas throughput to be pumped, originate from the following considerations.

The beam neutralisation with the present technology makes use of clouds of gas where a fraction of high energy ions become neutral by charge exchange. The minimum gas density, or gas target thickness when integrated along the path of the beam, is obtained by continuous gas injection. At the same time, the background gas in regions other than the neutraliser gas cells is detrimental. In the accelerator, it causes early neutralisation and therefore incomplete acceleration of the ions, or double charge exchange and acceleration in the opposite direction; after the neutralisation and the dumping of the residual ions, the high energy neutrals may re-ionize and deflect on the beam duct walls, because of the interaction with the magnetic fields of the torus. The high power neutral beam heating systems drove the design of large He cryocondensation pumps with speeds exceeding 10^6 l/s for hydrogenic species.

An alternative technology is used in ASDEX [64], the Titanium getter pump. The main advantages are the simplicity of operation, the long operation without maintenance, the cheaper cost. They are made of two components: titanium evaporator and the sorption substrate onto which the titanium is evaporated. The pumping speed for gas sorption is $S \propto \sigma A$, where σ is the adhesion coefficient, i.e. the sticking probability $\sigma = n/n_0$ of gas impinging on the sorption surface A. In the case of H_2 on Ti sorption surfaces, the $\sigma = 0.2$ at -196 °C.

In JET [61], each NBI systems is pumped by cryopumps of $S = 8{\cdot}10^{+6}$ l/s of hydrogen. The cryopumps cover the entire side walls of the vacuum box, with a total pump entrance area of 40 m^2 divided in 20 modules 350 mm wide and 6 m high. Every liquid Helium (LHe) cooled surfaces are screened by liquid nitrogen (LN_2) plates, totaling 4 t of aluminum alloy 2.3. After pumping down to 10^{-4} mbar, the cool down of the 80K surfaces requires about two hours of LN_2 circulating, after which Hydrogen is injected in the box in order to enhance the cool down of the LHe plates by gas contact instead of pure radiation: the procedure is shorten by 17 hours. The LHe starts to circulate, and the whole cool down requires about 11 h. Regeneration, carried out in about 6 hours, is required after 500 bar.l hydrogen load, a retention that is reached after about one week of operations. With this pumping system, the pressure downstream the beamline is kept at $5x10^{-5}$ mbar, even with a throughput of 250 mbar l/s per NBI from the many neutraliser cells.

There are extraordinary high demands on the vacuum system for ITER HNBs. The two operational tasks are the high pumping speed, with required pressures down to 10^3 Pa in the beam line vessel, and the high gas loads to be pumped, with up to one hour of continuous beam operation. The beam line components are considerable sources of gas and thermal radiation. The

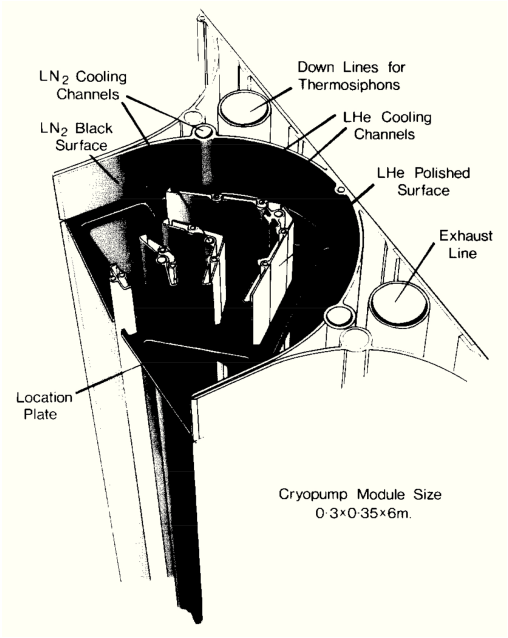


Figure 2.3: Schematic of a cryopump module in JET [61].

design was driven by two competing requirements [65] as the high thermal heat loads ask for a closed pump, the need of a high pumping speed ask for an open structure.

2.3 Analytical and numerical tools for vacuum systems

Much of modern experimental physics is carried out under vacuum, and the performances often depend on the vacuum system and its design. Nowadays, many computational schemes and tools are available to the vacuum scientists and engineers, to support the design and analysis of the vacuum system [66]; the vacuum system is addressed with methods of increasing complexity, according to the necessities.

Usually, analytical calculations as well as computer simulations rely on the following assumptions:

- stationary flow;
- no collisions between particles;
- diffuse angular distribution after collision with walls (cosine distribution).

The typical approach to vacuum system design is to use monodimensional models, where vessels, pumps and pipes are reduced to points and lines. To describe the molecular flow in many vacuum components, analytical or approximate solution exists; analytical expressions for the transmission probability can be found for apertures, and ducts of circular, rectangular and elliptical cross section [67, 57, 68]. The intrinsic conductance of a component C is the product of the conductance of the aperture of the entrance cross-section C_A and the transmission probability P, $C = C_A P$. This quick-and-clean method is useful

in simple cases or at concept design level; in the presence of distributed sources and sinks instead, or in the case of complex vacuum system geometry, the semi-empirical conductance formulas fail in describing the effective conductance C, and pressure anisotropy cannot be investigated. The analytical approach can fail in the proper estimation of pressure.

Lumped models can be assembled, for instance in resistor network simulations [69], using the conductance C of each element of the vacuum system, or better their resistance $R = 1/C$. Any program solving resistor networks, such as any of the Spice family [70], can be used to deal with vacuum systems.

The Monte-Carlo method has been used extensively for the calculation of the gas distribution in vacuum systems for which analytical or approximate solutions do not exist [71, 72]. A reference MC program doesn't exist yet; in large majority of the cases, the problem had to be solved once for all, and therefore the program code was designed specifically and written ad-hoc [73]. There are different applications to the simulation of the gas distribution; an interesting review of the Monte Carlo methods for the simulation of gas flows is given in [74].

The distinguishing feature of the Test Particle Monte Carlo (TPMC) is that the molecular trajectories are generated serially rather than simultaneously. The method is suitable for collisionless regimes, for which intermolecular interaction is negligible. The method was introduced by Davis [75].

The Direct Simulation Monte Carlo (DSMC), originally proposed by Bird [76], generates particles one by one and simultaneously tracks them from source to sink. The simulation always starts from an equilibrium flow. In the case of collisional models, the interaction between particles is based on probabilistic models rather than on deterministic basis, as it is the case for the Molecular Dynamics methods (MD). This restrict the method to diluite gas, in which the average distance between molecules is larger than their diameter.

In the following, a brief overview of the existing numerical tools for pressure calculations is given. There exist a number of specific codes currently available. Some are used in the ITER project.

MOLFLOW is a three-dimensional test-particle Monte-Carlo simulator for ultra-high vacuum systems. The development is currently carried on by CERN, and the code is freely available on the CERN website [77]. The original author is R. Kerservan [72].

MOVAK3D and PROVAC3D MOVAK3D is a computer program for simulating the trajectories of particles (e.g. atoms, photons) in a definable vacuum system with the Test Particle Monte Carlo TPMC method. The basic idea is the generating of particles on sources, reflecting them on different surfaces and the finishing of the particles track on absorbers or sources [78]. The model generation is based on predefined surface elements or bodies, with given properties, such as an orientation (direction of the surface normal), the kind of reflection (e. g. source, absorber, diffusely reflecting) and a reflection coefficient; the particles are generated serially, with a start weight of one, that will be reduced by reflecting on adsorbing surfaces. The result of a simulation is the total weight of adsorbed particles for every source or absorber [79]. Originally developed at KIT (formerly FZK) for fusion applications, now the code is - to the author understanding - commercialized.

FEM Three-dimensional gas domains are solved by means of commercial programs which implement the radiative heat exchange calculation can be adapted thanks to the mathematical analogy between the radiative exchange and the molecular flow between surfaces. The pressure is equal to the radiation temperature T^4 and the gas flow Q to the heat flow q. The limits of this approach are: the calculation of the view factor matrix may be poor; the time-consuming convergence of the radiation simulations, which is linearized but not linear; the absence of customization in the algorithm, which is limited to the calculation of the pressure and cannot consider the non equilibrium flows (variation of the gas temperature for instance); and finally the gas pressure is only defined at solid surfaces.

ITERVAC It is an example of computer program to calculate the mass flow and the pressure drop in a complex system of characterized vacuum ducts. Developed by KIT, the typical scope of ITERVAC is the transition pressure range under isothermal conditions. Nevertheless, it works also in molecular flow regime. The vacuum system is described by a block diagram, consisting of elements and nodes. Elements are the presentation of the real ducts, some of them special designed for the ITER vacuum system, some for general problems. Every element has a set of properties, like the channel type, cross section type and measurements [80].

2.4 Objectives of AVOCADO

A tool for routine computation of gas distribution and flow in molecular regime is to be developed to handle simulations of vacuum systems. Such a code can be applied to any facility which operates in vacuum, but it is especially meant to simulate systems of high complexity, such as multi-aperture electrostatic accelerators. The application of the code, named Avocado, will be primarily the ITER NBI and its test facility MITICA, but it must be versatile and allow its use to any kind of application. In order to minimize the possibility of programming mistakes, the code is to be validated: initially against analytical results and later in a dedicated test facility, named Arianna.

This target has given the project a multi-disciplinary connotation, and required the development of competences and research efforts in different areas:

1. study of existing numerical algorithms suitable to model the molecular regime, and development of a new method accounting for the physics of non-equilibrium flows in temperature varying domains;

2. use of parallel algorithms and program techniques to support high-perfor mance computing;

3. implementation of robust and efficient state-of-the-art numerical solvers and methods;

4. integration with meshing and post-processing tools, in order to allow a simple and versatile use of the code;

5. acquisition of competences in the planning and execution of experimental activities and measurements.

The code shall be tailored to the workstation and HPC facilities made available by the Consorzio RFX.

3
AVOCADO

In this section, I describe the development of the efficient and accurate ViewfactOr Code to Analyze gas Distribution AVOCADO, for calculation in high vacuum systems. I will give an insight of the used methods and algorithms. The work is oriented mainly towards Hydrogen and Deuterium gas applications, in geometries difficult to reduce to simple gas conductance formulae.

3.1 Governing equations

In high vacuum environments, simplified mathematical models are typically used instead of solving the Boltzmann kinetic equations. Gas-gas interaction is reasonably negligible when the elastic mean free path λ is greater than the typical length scale L of the system: in such a non-collisional regime, only the walls and their properties are significant. The Knudsen number $Kn = \lambda/L$ is a good indicator of the flow regime, as discussed in section 2.1. The pressure at the wall is created by the momentum deposition by molecules. The gas molecules hitting the wall are briefly absorbed by the wall, and then randomly emitted with a direction that does not depend on the previous trajectory, but follows Lambert's cosine law. This simple scattering operator was originally assumed by Knudsen, but it continues to be widely used to describe gas scattering on weakly adsorbing surfaces [81]. Hence a mathematical analogy exists between the law of molecular flow and radiative exchange between surfaces, and the same numerical methods can be adopted [71].

Starting from these considerations, only the domain boundaries may be considered for modelling the propagation behaviour of the gas, and this is the case of the view-factor or angular coefficient method [82]. Even though the Monte Carlo MC method is a more widespread numerical method, which directly implements the kinetic theory equations, the view factor method is a well-known [71, 83] valuable alternative that allows for very fast analyses once the geometry has been fully characterized. The main advantage is that it can be used in the very complex geometries of vacuum systems and its statistical validity is based on the scattering operator [84, 85], while the MC method is typically limited to geometries easy to represent mathematically and it must consider

a large number of particles; in addition, it may not be trivial to prepare an appropriate random number generator. A complete gas-wall interaction model would typically account for different phenomena. In particular, the prolonged retention of the gas molecule by the surface, due to a simple sticking event or to a condensation event, reduces the fluxes leaving the solid surfaces. The incident flux shall be reduced by this adsorbed fraction. In the case of non-condensable gases, such as H_2, D_2, T_2, Helium and noble gases, the outgoing fluxes coincide with the incoming ones, and the sticking probability is therefore zero.

3.1.1 Equilibrium flows in the view factor method

A mathematical analogy exists between the law of molecular flow and radiative exchange between surfaces. The solution of a molecular flow problem is, from any point of view, similar to the problem of heat exchange by radiation. In molecular flow regime, a particle in a closed volume is continuously bouncing from one surface to the other, since the elastic m.f.p. is larger than the dimensions of the system: therefore only collisions with solid walls shall be considered. A scalar quantity of pressure is assigned to elements at discretized surfaces, which are related to one another by view factors calculated using Knudsen's cosine law [81]. The set of governing equations is derived on the basis of the fact that the geometry dominates molecular flow, and that the pressure distribution is obtainable by surface discretization and calculation of mutual exchanges due to molecular trajectories. In the equations, m and T are parameters describing the gas properties and do not vary. The pressure at the surface can be written as a function of the incoming particle flux. In the kinetic theory of gases, considering a particle flux Φ [molec/m^2 s] we can write the pressure p [Pa] as:

$$p = \Phi(2\pi m k_B T)^{1/2} \tag{3.1}$$

The cosine law is the simplest scattering operator describing the gas-wall interaction, which gives substantially correct results and is therefore commonly used [82]. The probability of a gas molecule leaving a solid surface in a given direction is proportional to $cos\theta\,\mathrm{d}\omega$, where θ is the angle between the direction and the normal to the surface, and the velocity directions after the interaction are within the solid angle $\mathrm{d}\omega$; in addition, the distribution of scattered velocities is independent of the incidence angle. The cosine law can be used to derive a view factor between two surface elements (see figure 3.1, which can be written considering the reciprocity relationship as:

$$F_{1,2} = F_{2,1} = \int F_{1\to 2}\,\mathrm{d}\Sigma_1 = \int \frac{cos\theta_1 cos\theta_2\,\mathrm{d}\Sigma_1\,\mathrm{d}\Sigma_2}{\pi l_{1,2}^2} \tag{3.2}$$

Derivation of a linear system in matrix form

By assuming that the walls are discretized into surface elements the flow rate of molecules $\phi_{1\to 2}$ [molec/s] rebounding from a surface element of area $\mathrm{d}\Sigma_1$ and directed towards a second surface element $\mathrm{d}\Sigma_2$ at distance l can be written as $\phi_{1\to 2} = \Phi_1 F_{1,2}$. At the same time, a similar expression can be written for the second surface element. Hence, a balance of net particle exchange between two surface elements occurs, and can be written in the general form:

$$\phi_{net_i,j} = (\Phi_i - \Phi_j)F_{i,j} \tag{3.3}$$

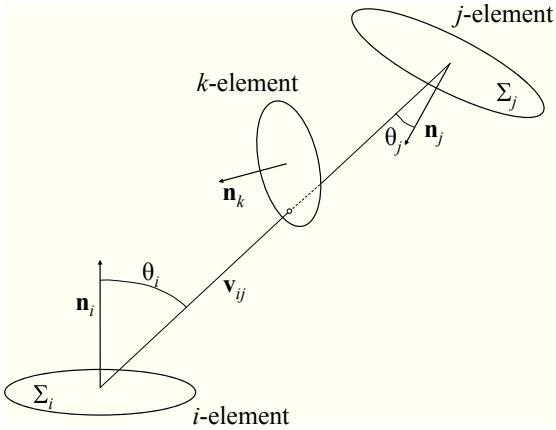


Figure 3.1: View factor calculation with hidden surface determination problem

A continuity equation, based on bouncing and throughput, can be written for every surface element constituting the boundary of the system. Combining 3.1 and 3.3, the flux term and the source term can be identified when two surface elements 1, 2 are considered. The equation of net fluxes (function of scalar, cell centred variable pressure p) between two surface elements is given by:

$$\phi_{net_i,j} = (\Phi_i - \Phi_j)F_{i,j} = \frac{p_i - p_j}{(2\pi m k_B T)^{1/2}} F_{i,j} \tag{3.4}$$

While the equation of sources of a surface element (function of scalar, cell centered variable throughput Q [Pa m3/s]) is expressed ($k_B T$ [J]) as:

$$\phi_{source_i} = \frac{Q_i}{k_B T} \tag{3.5}$$

At steady state, the net balance of source terms combined with mutual fluxes of all the elements in the domain shall be zero. Combining together fluxes and source terms, we obtain a set of N equations:

$$\frac{p_i}{(2\pi m k_B T)^{1/2}} \sum_{j \neq i} F_{i,j} - \sum_{j \neq i} \frac{p_j}{(2\pi m k_B T)^{1/2}} F_{i,j} = \frac{Q_i}{k_B T} \tag{3.6}$$

with N number of elements. The vector of throughputs can be written $\mathbf{Q}$, while the vector of pressures can be written $\mathbf{p}$, both of size N. All the other terms in the equation are constants, or parameters correcting the geometry-depending term of the $\mathbf{F}$ matrix, symmetric and composed by the terms $F_{i,j}$. Rewriting the equation using the elements $M_{i,j}$ of a coefficient matrix $\mathbf{M}$, the set of linear equations has the general form

$$\sum_{j \neq i} p_i M_{ij} - \sum_{j \neq i} p_j M_{ij} = p_i \sum_{j \neq i} M_{ij} - \sum_{j \neq i} p_j M_{ij} = Q_i \tag{3.7}$$

In particular, the coefficient $M_{i,i}$ multiplying p_i is given by the sum of all the elements of $\mathbf{M}$ in a row with $j \neq i$. Eq. 3.7 may be expressed as:

$$\begin{aligned} Q_i &= p_i M_{i,i} - \sum_{j \neq i} p_j M_{i,j} \\ M_{i,j} &= \frac{1}{(2\pi m k_B T)^{1/2}} F_{i,j}, \quad M_{i,i} = \textstyle\sum_{j \neq i} M_{i,j} \end{aligned} \tag{3.8}$$

The reciprocal view factor calculated for each pair of elements $F_{i,j}$ is stored in a sparse triangular matrix $\mathbf{F}$. This matrix must be symmetric, since the reciprocal VF between pairs of elements is the same, and thus the number of operations required to populate the matrix is in the order of $N^2/2$. The diagonal terms are zeroes, since the view factor of a surface with itself is zero. In the next step, the diagonal terms are populated, according to eq. 3.8, with the sum of the terms in a row (or column) with opposite sign. The matrix now fully describes the meshed domain, that is, the geometry of the system as modelled. The gas properties (m and T) are then used to correct all the terms in the matrix.

Let $\mathbf{M} \cdot \mathbf{x} = \mathbf{b}$ define the linear set of equations to be solved. The vector of unknowns $\mathbf{x}$ initially contains the pressure at the surface elements, so that $\mathbf{x} = (p_1, ..., p_N)^T$. The constant vector term $\mathbf{b}$ initially contains fluxes, that is, inlet/outlet surface elements where throughput is assigned as boundary condition, and therefore $\mathbf{b} = (Q_1, ..., Q_N)^T$. The boundary conditions (BCs) imposed at surfaces are then considered. If a surface element (i=1) represents an inlet section at fixed pressure, the throughput is moved from the constant vector to the vector of unknowns, and the relative matrix column, multiplied by the fixed pressure, is moved to the constant vector on the right hand side:

$$\begin{bmatrix} -1/k_BT & M_{1,2} & \dots & M_{1,N} \\ 0 & M_{2,2} & \dots & M_{2,N} \\ \vdots & \vdots & \ddots & \vdots \\ 0 & M_{N,2} & \dots & M_{N,N} \end{bmatrix} \begin{bmatrix} Q_1 \\ p_2 \\ \vdots \\ p_N \end{bmatrix} = \begin{bmatrix} -M_{1,1}p_1 \\ Q_2 - M_{2,1}p_1 \\ \vdots \\ Q_N - M_{N,1}p_1 \end{bmatrix} \tag{3.9}$$

The same procedure holds if a specific throughput $\tilde{Q} = Q_i/\Sigma_i$ [Pa m/s] is considered instead of Q_i, and the element area Σ_j is moved from the constant vector $\mathbf{b}$ to the matrix of coefficients. Three boundary conditions are applicable to the domain boundaries, for instance to an i-th surface element: fixed pressure p_i [Pa], fixed specific throughput $\tilde{Q}$ [Pa m/s], and fixed specific volumetric flux (velocity) $\tilde{S}$ [m/s]. In the latter case, the linear system is easily corrected by adding a $-S_i/k_BT$ term to the relative diagonal term $M_{i,i}$.

3.1.2 Non-equilibrium flows and temperature accommodation: a new consistent model

The view-factor technique for the modeling of collisionless molecular gas flows [71, 85, 86] had a primary limitation with respect to the Monte Carlo methods [87, 76] and their recent implementations [88], since it do not allow a consistent treatment of the temperature and density of the gas. In order to deal with the molecular gas flows in which the energy accommodation by collision of a particle with a solid surface plays a role, the typical/standard view-factor scheme shall be improved. This is the objective of this section.

In rarefied gas dynamics, accurate description of the energy exchange at the gas-solid interface are important for studying non-equilibrium flows. This energy exchange is historically expressed in terms of energy accommodation coefficient (EAC), as it was firstly conceived by Maxwell and introduced by Smoluchowski (1898) [89] as a constant to quantify the exchange of energy between a stream of gas molecules striking a solid surface. In free molecular flow or transition regime ($Kn > 0.5$), Knudsen [81] formally defined the EAC in rarefied gases, to

explain the incomplete energy exchange between gases and walls, as

$$\alpha_E = \frac{E_i - E_r}{E_i - E_w} = K_{ac} \tag{3.10}$$

where E is the average kinetic energy of gas molecules in gas-wall interaction, and the subscripts i and r represent the incident and reflected particles. E_w is the average kinetic energy of particles reflected in equilibrium with wall at temperature T_w, which is, in three-dimensional case, $E_w = 2k_B T_w$. The EAC is basically a measure of the efficiency with which the striking particle comes into equilibrium with the surface. A considerable effort has been spent by many researchers to measure the EAC (also known as thermal accommodation coefficient TAC). The accommodation coefficient is sensitive with the surface conditions, surface roughness or temperature for instance, or the presence of surface adsorbents. Therefore the coefficient given by experiments depends on the specific treatment of test conditions [90, 91, 92, 93, 94], and nowadays numerical simulations are the main means of investigating energy exchange at the gas-solid interface [95, 96, 97, 98].

A model has been derived to correlate the pressure with the state of the gas before and after the collision, which makes use of the accommodation factor as a parameter. The iterative scheme to solve the energy distribution together with the density has been implemented in Avocado. The local pressure at walls and the mutual fluxes can be solved linearly if no energy variation for the gas occurs; but the code applicability has been extended to heterogeneous gas energy distribution, and the system is solved iteratively.

This section presents our rationale for extending the method to a consistent and comprehensive gas model, in which the collisions with solid walls modify the particle's trajectory but also its energy. Let's consider only the velocity component v_x normal to a surface. The pressure at the wall is due to the variation of the gas particle momentum, that is to be calculated at instant t before the wall collision and $t + \Delta t$ immediately after.

The average volume of particles $< V >$ that will hit the surface is related to the velocity probability distribution $P(v_x)$:

$$\langle V \rangle = \int_0^\infty V P(v_x)\, \mathrm{d}v_x = A\Delta t \int_0^\infty v_x P(v_x)\, \mathrm{d}v_x \tag{3.11}$$

Multiplying $< V >$ by the number density of particle $n = N/V$, yields the number of collisions occurring in the time Δt. At steady state, the number of particles N that collided must equal the number of particles that will collide.

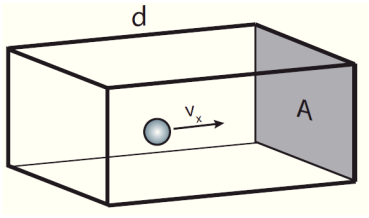


Figure 3.2: The average volume of particles that will hit the surface is related to the velocity v_x

Considering the volume of particle that in the same time interval had collided with the surface $< V' >$

$$\langle V \rangle = \int_{-\infty}^{0} VP(v_x)\,\mathrm{d}v_x = A\Delta t \int_{-\infty}^{0} v_x P(v_x)\,\mathrm{d}v_x \tag{3.12}$$

and having N collision in the time interval, the number density after collision will be different from the one before. At the target surface, the pressure at the surface is due to the momentum before and after the collision, that is, is due to the gas state before and after the strike.

If we take $p = nk_BT$, the two contribution to pressure $p = p' + p''$ given by the particle fluxes Φ are respectively

$$\begin{array}{ll} p' = \Phi_{IN}\sqrt{\pi m k_B T_{IN}/2} & \text{and} \\ p'' = \Phi_{OUT}\sqrt{\pi m k_B T_{OUT}/2} & . \end{array}$$

For the mass conservation, the particle flux Φ during collision with a solid wall is constant at steady state for non-condensable gases, and the number of collisions at walls takes the form:

$$\Phi = \frac{p}{T_{IN}^{1/2} + T_{OUT}^{1/2}}\sqrt{\frac{2}{\pi m k_B}} \tag{3.13}$$

The pressure is expressed in Pa and the particle flux in [1/m^2·s].

Derivation of a linear system in matrix form

As discussed before, the pressure at surfaces is determined by the particle flux and the state of the gas immediately before and after the hits at solid walls. In order to calculate the particle flow, the view factors are used to create mutual relations of particle exchange between discretized surface elements. These terms are used in the two continuity equation, the conservation of mass at walls:

$$\phi_i = \Sigma_i \tilde{\phi}_i = \frac{p_i}{T_{IN,i}^{1/2} + T_{OUT,i}^{1/2}}\sqrt{\frac{2}{\pi m k_B}}\sum_{j\neq i} F_{i,j} - \sum_{j\neq i}\frac{p_j}{T_{IN,i}^{1/2} + T_{OUT,i}^{1/2}}\sqrt{\frac{2}{\pi m k_B}}F_{i,j} \tag{3.14}$$

and the throughput at the open boundaries:

$$Q_i = \Sigma_i \tilde{Q}_i = \frac{k_B T_{OUT,i} p_i}{T_{IN,i}^{1/2} + T_{OUT,i}^{1/2}}\sqrt{\frac{2}{\pi m k_B}}\sum_{j\neq i} F_{i,j} - \sum_{j\neq i}\frac{k_B T_{OUT,i} p_j}{T_{IN,i}^{1/2} + T_{OUT,i}^{1/2}}\sqrt{\frac{2}{\pi m k_B}}F_{i,j} \tag{3.15}$$

The conservation of mass shall be used at wall surfaces, and the throughput equation at the open boundaries (inlets and outlets with known $\tilde{Q}$): therefore, the majority of the surface elements are typically solid surface, hence mostly $\tilde{\phi} = 0$ or $\tilde{\phi} = \tilde{\phi}_{\text{degassing}}$ conditions shall be used. In the case of open boundaries, this condition is replaced by equation $\tilde{Q} \neq 0$, when the throughput or the pressure is given. The reader is warned that, according to these definitions, there is no direct relation between the energy per unit time Q [W], and the net number of particles ϕ [1/s] entering the domain from an inlet. In fact, the particles crossing the inlet boundary enter or exit with different energies;

so, there could be a zero balance in terms of mass flow, but still a net energy income.

Instead of $\mathbf{M}$, two matrices can be built up, which define the pair of linear systems $\mathbf{M_Q} \cdot \mathbf{p} = \mathbf{Q}$ and $\mathbf{M_\phi} \cdot \mathbf{p} = \boldsymbol{\phi}$, with terms:

$$M_{Q,ij} = k_B T_{OUT,i} M_{\phi,ij} \tag{3.16}$$

and:

$$M_{\phi,ij} = \begin{cases} \dfrac{1}{T_{IN,i}^{1/2} + T_{OUT,i}^{1/2}} \sqrt{\dfrac{2}{\pi m k_B}} \displaystyle\sum_j F_{i,j} & \text{if } i = j \\ \dfrac{1}{T_{IN,j}^{1/2} + T_{OUT,j}^{1/2}} \sqrt{\dfrac{2}{\pi m k_B}} \cdot F_{i,j} & \text{if } i \neq j \end{cases} \tag{3.17}$$

An appropriate combination of the two matrices is therefore used to calculate the solution, as

$$\mathbf{p = M^{-1} \cdot b}. \tag{3.18}$$

The combined matrix $\mathbf{M}$, has terms $M_{i,j} = M_{\phi\ i,j}$ if the i-th element is a solid wall, or $M_{i,j} = M_{Q\ i,j}$ if the i-th element is an open boundary (inlet or outlet). In a similar way, the source vector $\mathbf{b}$ is built up by the terms $b_i = \phi_i$ (typically equaling zero) or $b_i = Q_i$, respectively in the case of solid wall or open boundary. For instance, if element 1 is an open boundary through which particle can flow, the matrix product becomes:

$$\begin{bmatrix} M_{1,1}^Q & M_{1,2}^Q & \dots & M_{1,N}^Q \\ M_{2,1}^\phi & M_{2,2}^\phi & \dots & M_{2,N}^\phi \\ \vdots & \vdots & \ddots & \vdots \\ M_{N,1}^\phi & M_{N,2}^\phi & \dots & M_{N,N}^\phi \end{bmatrix} \begin{bmatrix} p_1 \\ p_2 \\ \vdots \\ p_N \end{bmatrix} = \begin{bmatrix} \tilde{Q}_1 \Sigma_1 \\ \phi_1 \\ \vdots \\ \phi_N \end{bmatrix} \tag{3.19}$$

Afterwards, the degrees of freedom of the system are inverted accordingly to the boundary conditions, as described before:

$$\begin{bmatrix} -\Sigma_1 & M_{1,2}^Q & \dots & M_{1,N}^Q \\ 0 & M_{2,2}^\phi & \dots & M_{2,N}^\phi \\ \vdots & \vdots & \ddots & \vdots \\ 0 & M_{N,2}^\phi & \dots & M_{N,N}^\phi \end{bmatrix} \begin{bmatrix} \tilde{Q}_1 \\ p_2 \\ \vdots \\ p_N \end{bmatrix} = \begin{bmatrix} -M_{1,1}^Q p_1 \\ \phi_2 - M_{2,1}^Q p_1 \\ \vdots \\ \phi_N - M_{N,1}^Q p_1 \end{bmatrix} \tag{3.20}$$

Again, the vector of the unknowns $\mathbf{x}$ in which the solution is stored and updated will look like a mixture of pressures and fluxes; the same consideration holds for the source terms $\mathbf{b}$. The average energies of the incoming and outgoing gas particle at walls are extensively used to determine the terms of $\mathbf{M}$. These energies are strictly related to the temperature at solid walls and the energy exchange occurring during collisions. The temperature T_w can be defined as the temperature the gas would have if during the rebounds at the wall no variations of temperature occurs, it is given as boundary condition and stored in $\mathbf{T_w}$ for each surface element; as stated before, in order to relate the average incoming T_{IN} and outgoing T_{OUT} gas temperature the accommodation factor K_{ac} is used. The average temperature of the incoming gas can be calculated as:

$$T_{IN,i} = \frac{\sum_j T_{OUT,j} \phi_{j \to i}}{\sum_i \phi_{jtoi}}, \tag{3.21}$$

while the average temperature for the gas leaving the surface reads

$$T_{OUT,i} = T_{IN,i} - K_{ac}(T_{IN,i} - T_{w,i}). \tag{3.22}$$

The average temperature of the outgoing gas is obtained by iterating or, alternatively, inverting

$$\mathbf{M_T} \cdot \mathbf{T_{OUT}} = \mathbf{b_T},$$

where the matrix $\mathbf{M_T}$ and the source terms $\mathbf{b_T}$ are defined as:

$$\begin{aligned} &M_{T_i,i} = 1\ , \qquad M_{T_i,j} = -(1 - K_{ac})\frac{\phi - j \to i}{\sum_j \phi_{j \to i}}, \\ &\mathbf{b_T} = K_a c \cdot \mathbf{T_w} \end{aligned} \tag{3.23}$$

3.2 Numerical methods for the definition of the equation system

3.2.1 View factor calculation

The view factor of two surface elements is an integral quantity that gives an index of their geometrical coupling. One can choose between the hidden and non-hidden methods: the non-hidden method calculates view factors from every element to every other element, regardless of any blocking ones; the hidden method (default) uses an algorithm to determine which elements are reciprocally visible. Coupling verification, based on the hidden surface determination, is associated to the view factor calculation; the computational cost of the latter algorithm is a small fraction of the former one. The following methods were taken into account:

z-buffering, is the management of image depth coordinates in three-dimensional (3-D) graphics; it is one solution to the visibility problem which considered the projected distance along the normal to the i-th element to compare overlapping j-th elements.

radiosity method the j-th element is projected on a hemisphere of unit radius enclosing the i-th element; to calculate the form factor, a predetermined number of rays are projected to the projected elements. The view factor is the ratio of the number of rays incident on the projected surface to the number of rays emitted by the viewing element.

projection methods on a mapped 6-face emicube enclosing the i-th element, the j-th element is projected; the distance from the centroid of i determines which element should occupy the "pixel" of the hemicube. Each pixel is associated with a solid angle and then view factor.

ray tracing a straight line connects directly the i and j-elements, and it must be verified if it intersect a surface.

The implemented solution is a *discrete ray tracing*, that is a reciprocal, direct calculation of the view factors considering the centroids of the surface elements. When the element centroids are used for discrete view factor calculation as concentrated areas, the view factor F_{ij} expressed in vector form is given by

$$F_{i,j} = \frac{\mathbf{v}_{i,j} \cdot \mathbf{n}_i}{\|\mathbf{v}_{i,j}\| \cdot \|\mathbf{n}_i\|} \frac{\mathbf{-v}_{i,j} \cdot \mathbf{n}_j}{\|\mathbf{v}_{i,j}\| \cdot \|\mathbf{n}_j\|} \frac{\|\mathbf{n}_i\| \cdot \|\mathbf{n}_j\|}{\pi \|\mathbf{v}_{i,j}\| \cdot \|\mathbf{v}_{i,j}\|} \tag{3.24}$$

where the vector connecting the centroids of the elements is $\mathbf{v}_{ij}$ normal to surface elements is $\mathbf{n_i}$ as shown in figure 3.1, and its norm equals the element area $\|\mathbf{n_i}\| = \Sigma_i$. In this way, the problem of the VF calculation with discretized surfaces shares issues and methodologies with ray-tracing or particle tracking codes. More accurate ("second order") space discretization consists on the subdivision of the surface of the element pair (see figure 3.3). The element sub-division is easily realized at run-time and does not imply the generation of a new mesh. By dividing each element into 4 sub-elements, the computational cost is multiplied by 16 times in the case of quadrilateral elements (9 times in case of two triangular elements), but the error in the calculation is reduced by about 30%. This error value was obtained by comparing analytical results with FE results of two perpendicular surfaces that share an edge, this being the worst case. This method was preferred to the direct integration in order to reduce the calculation time.

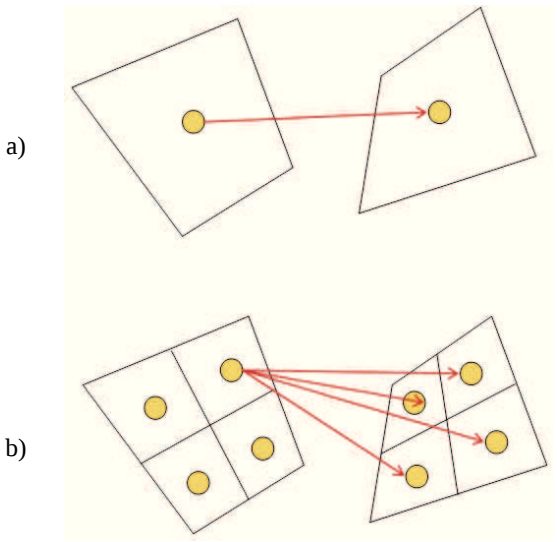


Figure 3.3: "First" (a) and "second order" (b) view factor calculation between quadrilateral elements.

Hidden surface determination

Hidden surface determination or Visible surface determination (VSD) is a process in 3D computer graphics used to determine which surfaces and parts of surfaces are not visible from a certain viewpoint. The coupling of surface elements must account for the real geometry, with concavities and interposed convexities.

A preliminary classification can be done by the user to identify the surfaces between which the gas flux can occur. Performed during the preparation of the model, this classification of flux-exchanging elements is gross and more oriented towards the reduction of computational cost by creating closed environments generally called *enclosures* (see also section 3.2.2); in complex geometries, the mutual coupling of surface elements on the mere basis of user-defined enclosures does not suffice. In order to additionally reduce the operations to be performed,

during the preparation of the model the user can prepare a partial selection of surfaces that will cause "shadowing" or hide part of the surfaces.

The presence of an interposed surface between two i, j surface elements can be resolved in finite elements with the existence of a third surface element k exactly intercepting the vector $\mathbf{v}_{ij}$. The shadowing surface could be more complex than a four-node element, for instance a polygon collecting many surface elements laying on the same plane; in that case, the hidden surface determination process would have a computational cost $1/2N^2f$, proportional to the number of polygonal faces f, instead of $1/2N^3$, with N number of elements. Basically, an algorithm that has to verify possible shadowing of element j wrt element i has to follow this procedure:

1. Operate a backface culling preparing a partial selection of j-elements: the surface elements are hollow shells, and the back side of the elements will not be considered in the calculation. This operation shall not be done for the occluding k-element;
2. Calculate the vector connecting the centroids, $\mathbf{v}_{ij} = \mathbf{c}_j - \mathbf{c}_i$;
3. Calculate the intersection of the direction of $\mathbf{v}_{ij}$ and the plane where the k-element lays: The point of intersection of a vector and a plane is easily calculated. By assuming that the plane is defined by a normal to the surface $\mathbf{n}_k$ applied to a vector point $\mathbf{c}_k$, and the intersecting vector $\mathbf{v}_{ij}$ is applied to the point $\mathbf{c}_i$, the intersection has coordinate

$$\mathbf{v}_I = \mathbf{c}_i + \left(\frac{\mathbf{c}_k \cdot \mathbf{n}_k}{\mathbf{v}_{ij} \cdot \mathbf{n}_k} \right) \mathbf{v}_{ij}; \tag{3.25}$$

4. Solve a three-dimensional Point-in-polygon (PIP) problem for point $\mathbf{v}_I$ (see next section).

PIP problem in 2D

PIP problem asks whether a given point in the plane lies inside, outside, or on the boundary of a polygon. Testing whether a point is inside a polygon is a basic operation in computer graphics. There are convex and non-convex polygons, and for each of these categories suitable algorithms exist:

Convex polygons if the intersection point is always on the same side of the set of oriented edges of the element, the point must be inside the polygon (see figure 3.4). Cross product is used: multiplying the oriented edge and the vector connecting a vertex to the point to test, a vector is obtained, whose direction is compared to the normal of the element. If one of the cross product has an opposite direction with respect to the others, the point is out of the polygon. Pro: at the first incoherence the algorithm stops; Contra: it may require up to 4 external products and it is only applicable to convex polygons.

Polygons For what concern the general algorithms for polygons, an interesting article by Haines [99] compares the efficiency of various methods. The so-called crossing number or even-odd rule algorithm is general and quick. In two dimensions, the algorithm counts the times the edges are crossed

by a half-line starting from the intersection point. Consider the case of figure 3.5): the point to test is the red one. Two tests are needed: one to verify if an edge has his nodes on opposite side of the blue line (one on top, the other on bottom); the second test is to verify if the intersection point (blue dots) are on the chosen side (left side in this case) of the intersection point (red dot). Many special cases or exceptions could be identified. In order to avoid test failure, a good criteria is to assign top flag to nodes that lies *on* the intersections (blue dots, figure 3.5 at the right-bottom).

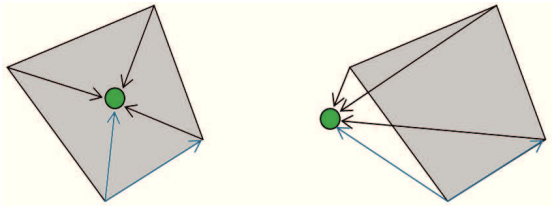


Figure 3.4: Method for convex polygon (the green dot is the intersection point in the plane of the element).

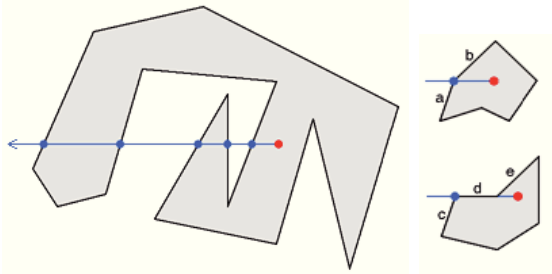


Figure 3.5: General method for non-convex polygons and two special cases.

PIP problem in 3D

Convex polygons The test for convex polygons (each element for instance) is valid in three dimensions: the test if the intersection point is always on the same side of the set of oriented edges of the element is performed using cross product, and it is verified if the tested point lays on the same plane of the polygon.

Non-convex polygons The method used in 2D cases has been generalized to 3D, and two methods have been tried. The first method makes use of *if* statements, considering the projection of the planar polygon on a plane of the global coordinate system (**A**); the second one uses the equation of planes to perform a similar test, but the planes are chosen as those defining the ray $\mathbf{v}_{i,j}$ (**B**). The two generalizations are described in the following.

A Crossing number algorithm generalized to 3D cases:

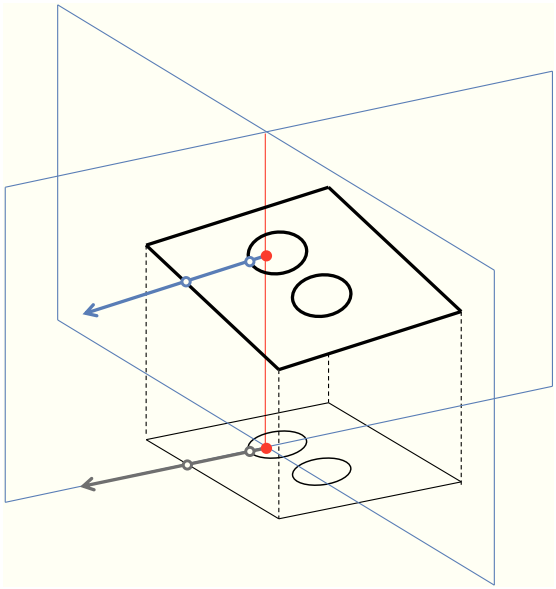


Figure 3.6: Three dimensional generalization of the PIP problem: the direction of minimum extension of the polygon is simply neglected.

1. During pre-processing, the direction of minor extension of the face and the two directions of major extension (normal to the planes in Figure 7.2) shall be identified with respect to the global coordinate system;
2. Once the intersection point has been calculated, all the edges are tested to verify if they cross one of the two planes, i.e. $x_1 \geq x_o, x_2 < x_o$ if x is one of the minor extension axes and x_o is the coordinate of the intersection; then a flag top or bottom is assigned to the edge nodes. Many special cases or exceptions can be identified, and in order to avoid failures, a good criteria is to assign top flag to nodes that lie on the intersections as for the 2D case;
3. the intersections with the edges are then compared to the other major extension direction, in order to account only for intersections on one side of the half-line;

Pro: No vector operations; Contra: Need to cycle over all the edges. In the case of convex polygons (four or less edges), exit as soon as two edges are crossed.

B Alternative algorithm generalized to 3D cases:

1. define ray $R = \mathbf{c}_i + \mathbf{v}_{i,j}$ as intersection of two planes:

$$P_1 : a_1 x + b_1 y + c_1 z + (-a_1 o_x - b_1 o_y - c_1 z) = 0$$

$$P_2 : a_2 x + b_2 y + c_2 z + (-a_2 o_x - b_2 o_y - c_2 z) = 0$$

where coefficients a,b,c are components of two vectors $\mathbf{n}_1, \mathbf{n}_2$ normal to the ray, chosen or calculated as:

$$\mathbf{n}_1 = (-v_{ij,2}, v_{ij,1}, 0)$$

$$\mathbf{n}_2 = (0, -v_{ij,3}, v_{ij,2}), \text{ or}$$

$$\mathbf{n}_2 = \mathbf{n}_1 \times \mathbf{v}_i j = (-v_{ij,1} \cdot v_{ij,3}, v_{ij,2} \cdot v_{ij,3}, -v_{ij,22} - v_{ij,12})$$

2. Substitute face vertex $\mathrm{N}_k = (X, Y, Z)$ to x, y, z in the plane equations, determining if the vertex are on one side or the other of the plane.
3. The general method for non-convex polygons can be used, substituting for instance the test $X > x$ with $\mathrm{P}_1(\mathrm{N}) > 0$ and $Y > y$ with $\mathrm{P}_2(\mathrm{N}) > 0$, where X, Y are the vertex coordinates and x, y the intersection point coordinates. Pro: No vector operations; Contra: Many operations to test the relative position of vertexes. This alternative method demonstrated to be between 50% and 70% slower.

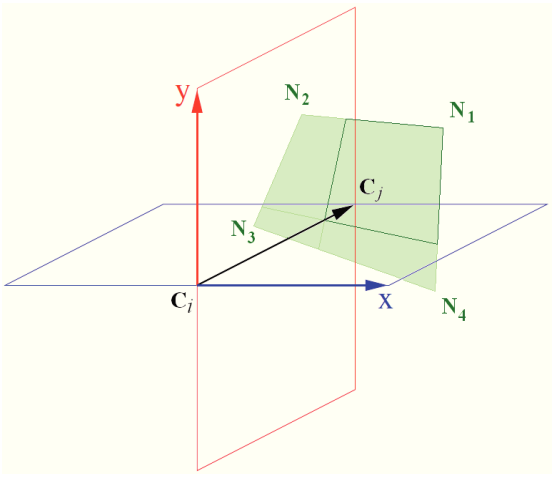


Figure 3.7: Use of cross-related enclosures

Face reconstruction

A polygonal, unstructured mesh is a collection of vertices, edges and elements that define the shape of polyhedral objects. In the passage from a CAD model to the FE meshed model, the information about faces is lost. However, these high level geometries are useful to the purposes of this code: the use of a single planar face instead of the great number of elements constituting it can strongly reduce the number of iterations in the shadowing test for interposed elements. Indeed, the hidden surface test is a nested cycle of third level and is carried out for every shadowing item. The use of faces leads to a strong reduction in computational cost per element, because even if the shadowing items are non-convex and a slower algorithm must be used, the number of items to test is typically reduced by orders of magnitude. The planar face re-composition is done in the pre-processing phase of the simulation. A set of operations of edge collapse

are performed, aimed at the reconstruction of polygonal face edges. Similar processes are used in visualisation and computer graphics [10], [11]. Additional data concerning element and node connectivity is required, since the procedure uses the connectivity definition of all the items (nodes and elements). The node connectivity in particular consists in a anti-clockwise list of elements sharing the node. The following operations are needed for the face reconstruction process, as all the elements are considered one by one:

a. edge collapse: Nearby elements with the same normal are joined in new faces or added to existing faces; the list of face edges is modified by replacing the common edge with the remaining edges of the nearby element, listed anti-clockwise; in this step the two elements are replaced by a face, and similar operations will be carried out on it. If an element does not have co-planar neighbours, it is a face by itself.

b. edge collapse: Nearby faces with the same normal are merged; once the common edge is identified, the list of edges is updated by replacing it with the edges of the nearby face;

c. recursive path removal: If the list of edges of a face contains recursive paths (e.g. capital letters are nodes: A→B, B→C, C→B, B→A), they are removed;

d. internal edge removal: If the list of edges of a face contains twice an edge with opposite direction (... A→B ... B→A ...) they are both removed. Recursive paths are created in this process, and then removed (see previous step: c). Note that consecutive edges lying on the same line are grouped into a single edge.

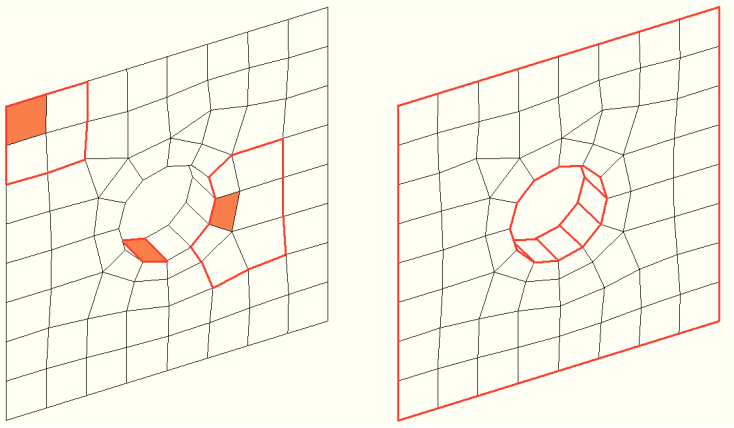


Figure 3.8: Example of face reconstruction: on the left, in the initial phase new faces (red lines) are created starting from the elements (three elements highlighted in the example) using vertex connectivity; on the right, the final step when only the external edges of each face are kept, after edge merging and removal

3.2.2 Implementation and optimization

The code is written in C++. All variables are expressed in S.I. measurement units. In the early implementation, the code demonstrated its capabilities but also disappointing slowness. A deep optimization campaign was carried out since then, basically following various steps:

1. removing "decisional ifs" but maintain customizability;
2. parallelization of the construction of the view factor matrix;
3. use of a high-performance compiler;
4. optimization of the algorithms and use of partial selection of elements;
5. mesh simplification;

Customizability

The implementation of Avocado allows the combination of different methods and algorithms. This versatility was necessary for testing purposes, but also to solve any specific problem with the methods most suitable to the case. A versatile construction could be obtained using various strategies:

- instances of a class inheritance, that is, the declaration of one of the classes that implement the chosen method;
- pointers to function, that are associated at run-time to the method requested by the user in the command line;
- customizable compiling, using preprocessor directives.

The first two options allow to accept optional command-line parameters; the latter instead requires to re-compile the binary file each time a different customization is required. In order to be compatible with OpenMP [100] versions prior to 3.0, for which no privatization of class objects is allowed, the first strategy could not be followed in the parallel part of the code: in the original implementation, Avocado was written as an Object Oriented (OO) code, but later it was rewritten using pointers to function to provide the same versatility. In order to solve for instance the electrostatic accelerator of MITICA, customized binaries were compiled, using the preprocessor directives (#ifdef, #endif) to add particular rules for the shadowing in that complex geometry.

Parallelization techniques

A single term in the view factor matrix $\mathbf{F}$ does not depend on any other. For this reason, the procedure that produces the matrix is natively parallelizable. In parallel softwares, there are operations that can be executed in parallel and part of the code that is executed serially. When the parallel part begins, many threads are instantiated. Various degrees of parallel implementation are possible, according to the algorithm and the interdependence of the parallel processes.

The techniques for programming parallel computers and the application programing interfaces (APIs) that were created can generally be divided into classes according to the memory architecture:

Shared memory: the communication between parallel processes is archived manipulating shared memory variables. These protocols are best used in multi-processor computers that share the same memory. An example of this class of APIs is Open Multiprocessing (OpenMP [100]).

Distributed memory: message passing protocols are required to achieve the interoperability of the independent threads. This class of parallel paradigms is best used in the case of processes executed on different machines, and the less the processes are dependent one on the other and the communication is minimized, the more the parallelization is efficient. An example of this class of APIs is the Message Passing Interface (MPI).

In C++, the two common parallelization paradigms (OpenMP and MPI) can be easily implemented, sometimes also combining the peculiarities of both of them. In AVOCADO, OpenMP was initially implemented, limiting to a single machine at a time the execution of the code. Using OpenMP , parallelization of threads on shared memory is archived while implementing slight modifications to the code. From the point of view of efficiency, the cpu time required for a simulation decreases linearly with the number of threads. Nevertheless, it has been found that the parallel speedup has a maximum around 10/12 threads and is far from the ideal speedup. The expected linear progression is probably limited by the continuous access to memory and in particular to shared variables carried out by the code, when reading mesh data.

Successively, a third valuable alternative was implemented, consisting in the division the VF matrix into independent regions and launching independent threads. This solution is somewhat similar to the MPI paradigm, in the sense that the parallel processes use different unshared variables; but the complete independence of the processes is allowed. The extension of the VF matrix regions is calculated by assuming a homogenously dense matrix. The VF matrix is symmetric and therefore only half of it shall be calculated. The triangular matrix is thus divided by rows into slices, or better trapezia, with about the same number of elements: by executing independent processes on non-shared memory to calculate these matrix sections, a much better speedup was obtained as shown in figure 3.9, when the VF matrix is divided into a sufficient number of regions. This at the cost of a minimum increase of memory consumption (due to the mesh data propagation for every process). Analogously with the division of a triangle into slices of equal areas, the parallel speedup is ideal, in the case of homogeneously dense matrix, because each independent process calculate the same number of entries.

This approach is obtained by bash scripting and background execution of the code. The user defines the number of divisions of the matrix, and the number of threads to be launched that can be much higher. The script uses the Portable Batch System (PBS) [101] for job scheduling, to assign the processors on the server network that are to be occupied by the job; the independent processes are launched, and once a process terminates, another one is launched, to calculate all the regions of the VF matrix.

High-performance compiler

A consistent gain in computational time was obtained by using a high-performance oriented compiler, such as Intel *icc* [102]. There are parameters that tells the

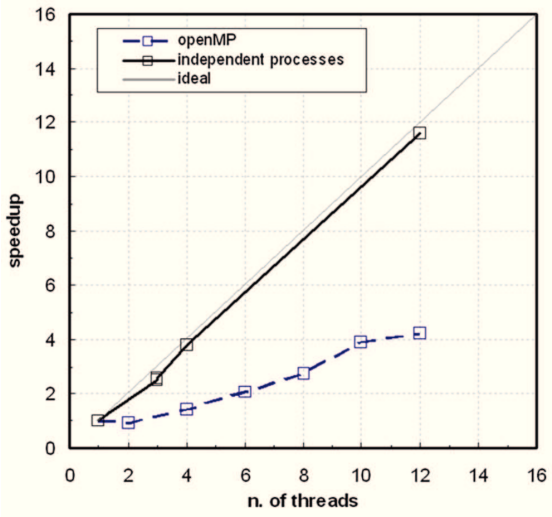


Figure 3.9: Speedup of the view factor matrix parallel calculation

compiler to optimize the binary for large memory bandwidth (useful in the case of parallel access to the memory, such as using OpenMP) and vectorization of *for* cycles and loops. In particular, I estimated a reduction by about 75% computational time over the standard g++ compiler [14] for some applications.

General optimization of the algorithms

Alternative, quicker algorithms were developed for line-of-sight interception, and the removal of decisional ifs in the core cycles were replaced by pointers to functions. In addition, variable initializations in the core cycles were minimized (variables are passed by reference to cyclic sub-routines). Operations in the core of the three nested cycles are very time consuming given the number of times they are repeated, independently from the efficiency of the algorithms themselves.

The use of partial selection of elements can reduce the calls to the inner routines and thus reduce the computational cost per element. The pre-selection of elements is operated by the user during the preparation of the model or the meshing phase. Two selections were devised:

- a set of elements that must be considered for shadowing (i.e. external boundary elements not to be included);
- a number of *enclosures*, sets of elements between which reciprocal gas flow is possible.

The combination of the two selections is also possible, in such a way that only shadowing surfaces that are part of the same enclosure shall be considered. The partial selection of shadowing elements is important because it reduces the number of iterations inside the third nested cycle. This operation is very useful in the case of walls dividing two chambers (both surfaces are modeled, but one suffices to the purpose of shadowing), but must be used carefully if convex/concave geometries are involved in the structure.

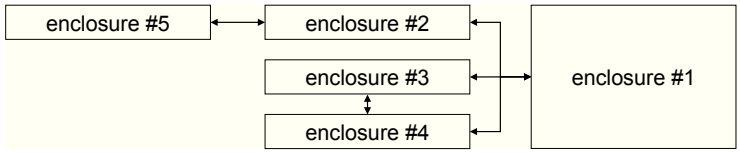


Figure 3.10: Use of cross-related enclosures

Enclosures are a way of dividing the meshed geometry in zones between which gas flow, in the molecular dynamic, is expected; this preliminary division is easy to guess and completely avoid the third nested cycle to be executed. When an enclosure is defined, the molecular flow from i-element is limited to j-elements belonging to the same enclosure, or an enclosure to which it is explicitly associated by the user. The program can be executed with or without this feature enabled.

3.2.3 Mesh format and access to mesh database

The collection of vertices, elements and their properties that constitute the polygonal mesh is contained in a single mesh object. Mesh data structure is defined in a class. The mesh object is first instantiated in the main routine, then populated in data access subroutines, and then used for the view factor calculations. A pointer to the instance of the class is passed by reference to every sub-routine, and this is the way the mesh data is shared in the code. The structure of node and element data is defined in the code by means of structures. The structure of Face data is a little more complex and is defined in a class. Nodes are vertexes defined by index, coordinates, and element connectivity (a list of elements surrounding the node in anticlockwise order, reconstructed in the pre-processing phase). A surface element is defined by set of nodes listed in anticlockwise order with respect to the normal. The stored data about elements is composed by: index; node connectivity (a list of 3 or 4 node numbers, depending on the shape of the element); coordinates of the element centroid; area of the element; normal vector to the element (not the normal unity vector); material number; face number; enclosure number; shadowing quality (whether it constitutes a solid barrier to gas flowing). The face object lists the following data: list of elements; list of ordered edges (anticlockwise); two axes of minimum bulk dimensions. In addition, the face object, defined in a class, contains a number of methods used for face reconstruction and simplification. For instance, during the face recomposition procedure, edges are continuously added, merged and removed to the edge list of the face; this removal routine requires also ordering methods (i.e. bubblesort algorithms [103] vol. 3). In order to minimise the access to memory, the relational map of the enclosures is implemented using a symmetric square bitset matrix. A *bitset* is a special container class that is designed to store bits (elements with only two possible values: 0 or 1). For instance, if gas exchange between enclosure 2 and 4 is foreseen, elements (2, 4) and (4, 2) of the bitset array are populated with 1. In this way, no cycles with decisional ifs are executed at run-time.

3.3 Numerical methods for the solution

The view factor matrix $\mathbf{F}$ is sparse, symmetric ($a_{ij} = a_{ji}$) with zero diagonal terms; but in AVOCADO, only the upper triangular part of the view factor matrix $\mathbf{F}$ is parallel computed using an arbitrary number of independent processes. The vector $\mathbf{b}$ could be sparse in case that few fluxes and no pressures are set as BCs.

The square coefficient matrix $\mathbf{M}$ must be prepared starting from $\mathbf{F}$. $\mathbf{M}$ is sparse and, unlike $\mathbf{F}$, non-symmetric and weakly diagonally dominant ($|a_{jj}| = \sum_{i=1}^{n} a_{ij},\ j = 1, .., n$).

The steps toward the solution of the system are:

1. the mirroring (basically a transposing operation) of $\mathbf{F}$.
2. Successively, the diagonal terms shall be added.
3. Then, an efficient method to solve the system shall be used;
4. in the case of temperature-varying simulations, the proper iterative schemes and convergence criteria shall be used.

According to these requirements, the solutions presented in the following were identified.

3.3.1 Sparse matrix implementation

Sparse matrix technology includes the data structures to represent the matrices, the techniques for manipulating them, but also the algorithms and the efficient mapping of the data structures and algorithms to high performance and parallel machines. In scientific computing, it was one of the most important "enabling" developments. A sparse matrix is one with most of its entries equal to zero, or "one with enough zeros to take advantage of"*.

Typically sparse matrices are used to solve partial differential equations (PDE's) that arise from almost all discretization methods (finite differences, finite volumes, finite elements, spectral elements); only "boundary element" methods give dense matrices. The view factor method at the basis of AVOCADO is a middle ground between the finite element and the boundary element method: in principle, in a simple geometry such a sphere there exist a reciprocal view factor exists for all the elements, but in the case of many interposed bodies and hidden surfaces, there will be a large fraction of zero out-of-diagonal terms.

The numer of non-zeroes in a matrix is commonly written nnz, with n number of rows and column. In general any components of a sparse matrix that are exactly 0.0 should not be stored, but in some cases it is more computationally efficient to allow a few to be included. Each sparse storage method has advantages and disadvantages. For instance, the row major order is usually preferred since it gives great advantages in the matrix-vector multiplication.

COO Coordinate-wise [nnz sizeof(float) and 2 nnz sizeof(integer)]. For each nonzero entry, its value, row i and column j index are stored in three arrays (ia, ja, val) of size nnz. It is easy to use, understand, debug; easy to add terms, rows/columns access is equally easy and need not be ordered in any way. Matrix-vector products $\mathbf{y} = \mathbf{A} \cdot \mathbf{x}$ looks like:

```
Initialize y(1:n) = 0
for k = 1 to nnz
   y(row(k)) = y(row(k)) + val(k)*x(col(k))
end for
```

CSR Compressed Sparse Row [nnz sizeof(float) and $nnz + n + 1$ sizeof(integer)] stores the column indices and values in nnz size vectors, but entries must be listed one row after another. A third vector of size $n + 1$ records: n informations about where the n rows begin in the first two vectors, and the total number of entries $nnz + 1$. This technique requires entries from a row to be consecutively located in data structure (row-major order) and the row access easy, column access difficult as well as transpose matrix operation. Matrix-vector products $\mathbf{y} = \mathbf{A} \cdot \mathbf{x}$ looks like:

```
Initialize y(1:n) = 0
for i = 1 to n
   for k = row(i) to row(i+1)-1
     y(i) = y(i) + val(k)*x(col(k))
   end for
end for
```

MSR Modified Sparse Row [min nnz+1 sizeof(float) and nnz+1 sizeof(integer)] is somewhat similar to CSR, except that the row pointers and column indices are both stored in a single integer array *bindx* and the diagonal entries are stored first in the array of values *val*, which means that even if a diagonal entry is zero, it must be explicitly stored as zero.

In *bindx*, the first n entries store the indices where each row's off-diagonal entries begin; The $n + 1$ entry has value one more than the size of *bindx* and *val* required, so that the matrix-vector product can be written with a single nested loop and no special cases handled for the last row of the matrix; the successive entries of *bindx* store the column index.

In *val*, the n diagonal entries are stored first (*val*[0] to *val*[n-1]), then skips a single unused entry in position $n+1$, followed by the off-diagonal entries, row-by-row. Matrix-vector products $\mathbf{y} = \mathbf{A} \cdot \mathbf{x}$ looks like:

```
Initialize y(1:n) = 0
for i = 0 to n-1
   y(i) = val(i) * x(i)
   for k = bindx(i) to bindx(i+1)-1
     y(i) = y(i) + val(k) * x(bindx(k))
   end for
end for
```

BCSR Block Compressed Sparse Row, or the more recent Compressed Block Storage, would be an interesting option, since very often the view factor matrices are block-sparse i.e. have square area of zeroes. It is more difficult to use and slightly less efficient to do vector-multiplication with.

Modified Sparse Row

Among the many ways of storing a sparse matrix, the modified sparse row (MSR) [104] has been preferred. The MSR offers better compression in the

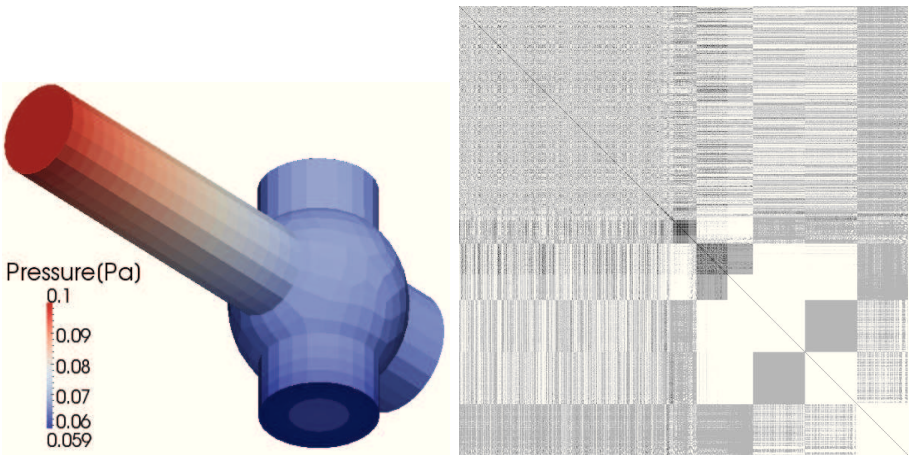


Figure 3.11: On the left, model of the pressure distribution in the RFX-MOD pumping port with a 1000 l/s turbomolecular pump attached at the bottom circular surface; on the right, the corresponding view factor matrix; the elements of the same planar surfaces are distinguishable as the square-blocks of zeroes.

applications, such as in this case, in which the diagonal terms are always present; the row-major order improves the many matrix/vector operations.

A view factor matrix is shown as an example in figure 3.11. It is calculated for a vacuum pumping port of the fusion device RFX-MOD [105]. The domain has a relatively low shadowing, basically it is a closed volume with a single inlet and outlet surface; the symmetry of the matrix - in this case relatively dense - is clearly visible. There are 1500x1500 surface elements; please find the complete discussion about this problem in section 5.4.

The square blocks of zeroes in regular pattern on the right-bottom area are the mutual VF of elements on the same plane surface, while the square dense blocks of non-zeros are the interaction between these plane surfaces. The diagonal has been already populated with the sum of the corresponding row/column terms.

3.3.2 Mirroring or transposing

It is an issue to perform the mirroring of a matrix efficiently when only sparse storage is possible. A difficult optimization of this procedure for very large matrices has been carried out. Mirroring is a case of transpose calculation in the case of triangular matrix that shall become symmetric. A large bibliography exists on the procedures to calculate the transpose of a matrix. Many of them require sorting, and typically the best algorithms are the *divide and impera* algoritms over the *bubblesort* methods [103]. A possible option would have been to use compressed block storage CBS [106], which do not require sorting of huge vectorized data.

An algorithm with a predictive approach has been developed to load and mirror on-the-fly the matrix $\mathbf{F}$, in MSR format. The diagonal terms n and the out of diagonal terms $nnz - n$ are estimated in a first reading from the COO-stored data file, together with the number of non zeroes in each i-th row

nElInRow(i) and j-th column *nElInColumn(j)*. The *bindx* array is populated with the coordinates of the non-zeroes before the values are actually read, as

```
Initialize val(0:nnz)=0.0, bindx(0:nnz)=0
for i=0 to n-1
    nElInRowTot(i)=nElInRow(i)+nElInColumn(j)
end for
for i=0 to n-1               //diagonal terms
       bindx(i)=bindx(i-1)+nElInRowTot(i-1)
       val(i)=0;
end for
bindx(n)=nnz+1
nextFreeRowIndex(n)=nnz+1
do while not eof             //out of diagonal terms
    read from file (value, i, j)
    val[nextFreeRowIndex[j]]=value
    bindx[nextFreeRowIndex[j]]=i
    nextFreeRowIndex[j]=nextFreeRowIndex[j]+1
    val(bindx[i]+nElInColumn[i]+cumulativeInRow]=value
    bindx(bindx[i]+nElInColumn[i]+cumulativeInRow]=j
    cumulativeInRow++
loop
```

3.3.3 Data structures and data access

The data structures are implemented in dedicated classes written on purpose: *matrix* and *Vector* classes for the dense data structures, while *Vector*and *iVector* class implements the *bindx* composed index array. The methods to access the data from the disk storage are implemented in the *dataaccess* class.

3.3.4 Solution scheme for the linear system

There is a variety of numerical methods available [107] for the solution of the system. The properties of the $\mathbf{M}$ matrix presented above shall be considered to select the algorithm to be implemented in AVOCADO.

The Biconjugate Gradient Stabilized (BiCGstab) algorithm [108] is a method for the solution of non symmetric linear systems. The Bi-Conjugate Gradient (Bi-CG) was implemented also, even if the former method has better performances. The algorithms are methods of the *solver* class.

Two versions of the two algorithm, for dense matrix and sparse matrix calculations, have been implemented as well. Furthermore, it is possible to use the modified algorithms for preconditioned systems.

Preconditioner

A preconditioner is any form of implicit or explicit modification of an original linear system which makes it easier to solve by a given iterative method. A system

$$\mathbf{P^{-1}Ax} = \mathbf{P^{-1}b} \tag{3.26}$$

which has the same solution as the original system is called a preconditioned system and $\mathbf{P}$ is the preconditioning matrix or preconditioner. The Jacobi preconditioner is the simplest one, in which it is chosen to be the diagonal of the matrix:

$$\mathbf{P} = diag(\mathbf{A}) \ . \tag{3.27}$$

It is efficient for diagonally dominant matrices.

With regards to the model in figure 3.11, the CPU time required to reach 10^-20 is 1.20 s; by using the Jacobi preconditioner, it reduces to 0.93 s. This is a particular case and this shall not be intended as a general behaviour; a higher improvement has been verified in the case of larger, less dense matrices.

Jacobi-preconditioned BiCGstab method for sparse matrices

The vector of unknowns $\mathbf{x}$ is found by means of an efficient algorithm for iterative solving, the Jacobi-preconditioned BiCGstab algorithm for sparse matrix. The method attempts to solve the system of linear equations. The matrix-vector and vector-vector operations are optimized for sparse population; the matrix is preconditioned using Jacobi preconditioner, which proved to highly increase the convergence stability in the applied cases. When the requested residual ϵ is reached, the vector of pressure $\mathbf{p}$ and the vector of throughputs $\mathbf{Q}$ are reconstructed from $\mathbf{x}$ and $\mathbf{b}$ vectors. The solution data is cell-centred.

Convergence criteria

The residual is:

$$\mathbf{r} = \mathbf{b} - \mathbf{A}\mathbf{x} \tag{3.28}$$

The stopping criterion used is that the 2-norm of the residual, $\delta i = ||\mathbf{r}||$ be reduced by a user-defined factor of ϵ relative to the 2-norm of the initial residual. A maximum number of iterations can be set as well. Both ϵ and the maximum number of iteration is set from the command line.

3.3.5 Solution scheme for the coupled systems

After the pre-processing described in the previous section, two subsystems, one corresponding to the molecular flow equations in closed volumes (1), and the other one being the gas temperature equations (2), are solved in a weakly coupled manner using the robust bi-conjugate gradient biCGstab method [107] with Jacobi preconditioner, which demonstrate to improve the convergence. The global linear system to be solved is:

$$\begin{bmatrix} \mathbf{M} & 0 \\ 0 & \mathbf{M}_T \end{bmatrix} \begin{bmatrix} \mathbf{x} \\ \mathbf{T} \end{bmatrix} = \begin{bmatrix} \mathbf{b}_1 \\ \mathbf{b}_2 \end{bmatrix} \tag{3.29}$$

An iterative solution is needed to solve temperature-varying gas domains.

Both matrices $\mathbf{M}$ and $\mathbf{M}_T$ have to be constantly updated: the gas temperature in the former, and the fluxes in the latter. In the iterative scheme, a different convergence criterion can be used for the two systems; in addition, initially they are updated after preliminary coarse convergence of both the systems, in the attempt to reduce the time necessary for the iterative solution.

The reduction of the number of iterations for the outer loop, would not be worth enough compared to the effort for the linearization of the equations, in order to solve $\mathbf{M}$ and $\mathbf{M_T}$ at the same time. In the present implementation, the coefficient matrix $\mathbf{M}$ is reassembled after convergence of the bi-CGstab method is reached. A global residual is used as convergence criteria, considering in particular 2-norm of both temperature and pressure. In figure 3.12, the

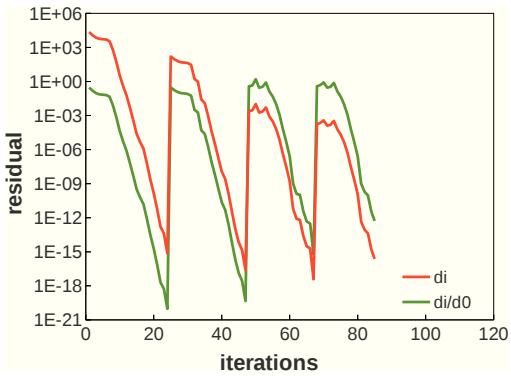


Figure 3.12: Residual of the biCGstab algorithm until convergence of the outer iteration is reached, relevant to the model in figure 3.11.

biCGstab residual ramp up when M is updated. In this case, the convergence criterion $\epsilon = 10^{-20}$ is exaggerated for the biCGstab, as the convergence criterion of the outer loop is smaller. The error at the exit is different as the convergence residual of the inner iterations varies: in this particular case, the error

$$\text{err} = \frac{||\tilde{\mathbf{x}} - \mathbf{x}||}{||\mathbf{x}||} \tag{3.30}$$

at the exit is shown in table 3.1 as a function of ϵ; for $\epsilon < 10^{-}15$ the error is dominated by the convergence criterion of the outer cycle.

3.4 Pre- and Post-processing

The gas pressure and temperature distribution is defined at the boundary surfaces of the gas domain, and the results of a simulation can be visualized in three dimensions using scientific data visualization tools. In the gas domain, especially in the cases when large gradients occurs and the gas properties change abruptly, it may be extremely helpful to know how they vary and where the gradients are located. This operation can be done in AVOCADO in the post-processing phase.

3.4.1 Pre-processing

The mesh is generated using commercial meshing tools, such as ANSYS [46]. In the early implementation the code could import the mesh from ANSYS but also create structured meshes on geometries composed by keypoints and planar surfaces. Nevertheless, the complexity of the applications and the necessity of making AVOCADO a versatile and user-friendly tool integrated in the design process of vacuum systems, forced to use only the powerful meshing capability of

ϵ	1.0e-11	1.0e-12	1.0E-13	1.0E-14	1.0E-15
err	9.47e-007	2.96e-012	2.17e-013	1.28e-014	0

Table 3.1: Error at converged solution as a function of the convergence criterion of the internal loop. Data refers to the model in figure 3.11

specialized programs. In particular, the ESURF command [46] is used in ANSYS APDL to generate the surface elements from the meshed solid bodies. Output redirecting is then used to create the list of nodes and surface elements, that will be imported in AVOCADO. According to the user selections, some element properties are modified as they will be interpreted as presented in table 3.2. The surface properties or "material", the enclosure number, and the "shadowing" flag is assigned to named selections (CM and CMSEL commands) and exported by using material number, "real constant" number and "section" number in the list of elements.

3.4.2 Post-processing of gas properties in the volume

One can easily imagine applications in which some processes occur in the center of a vacuum chamber, but the pressure measurements are made at recesses of the vessel surface; it becomes important to extend the information on the pressure; this is the case for instance of the applications to MITICA. It is also the case of the beam diagnostics, for instance the Beam Emission Spectroscopy, or Tomography, applied to accelerated particle profiling: the measured signal is proportional to the background/neutral gas density, and its uniformity or non-homogeneity must be taken into account (see section 5.2.5).

When a simulation has finished, the neutral gas distribution at boundary surfaces is at disposal; the gas leaving a surface i-element has temperature $T_{OUT,i}$ and density $n_{OUT,i} = p_{OUT,i}/k_B T_{OUT,i}$. At a test point G in the volume, the gas properties clearly depend on these quantities at all the surfaces that can be seen; a weighted average can be used therefore, the weight being the solid angle occupied by each surface element, of a unit sphere centered in G. This is a direct consequence of the non-collisionality (no collisions are considered indeed), since the whole method applies only to flows in molecular regime.

In the Avocado code, the solid angle was estimated as $\omega = cos\theta \, \mathrm{d}\Sigma l^{-2}/\pi$. By this definition, the sum of the solid angle equals 4 (instead of 4π), and this value can be used as an indication of the mesh quality around the test point and the quality of the interpolation. Gas temperature, density and pressure can be calculated in the same way. The scalar density at G point, for instance, reads:

$$n_G = \frac{\sum_i \Phi_i \sqrt{2\pi m/(k_B T_{OUT,i})} \cdot \omega_i}{\sum_i \omega_i} \tag{3.31}$$

A definition of n as a vector giving an indication of the anisotropy of the local density is also possible: this is obtained by multiplying the density inside the sum at numerator by the unit vector that defines the direction from the surface towards the test point. The obtained vector $\mathbf{n}_\mathrm{G}$ has little to do with the density: it is the net particle flow at a point in the volume, and can be used to show the flow field across the vacuum system.

ANSYS	MAT	TYPE	REAL	SECT
AVOCADO	$m, T_{in}, P, Q, S, T_{wall}$	yes/no	shadowing/not	enclosure number

Table 3.2: Element properties in ANSYS associated with element properties in AVOCADO; a unique TYPE number determines whether or not the element is a surface element to be considered as a boundary in the gas domain.

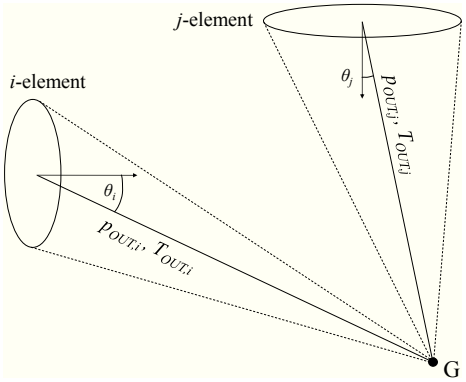


Figure 3.13: Interpolation of the gas properties in the volume from an existing pressure distribution

Generally speaking, performing this interpolation in the post-processing phase, allow thorough and deep investigation both of the vacuum system and the quality of the numerical results.

3.4.3 Visualization of the solution

The complexity of the solution in 3D geometries requires a good tool to view and analyze the results of simulations: results are converted to the VTK format [109], which is a standardized scientific format. It can be used to store scalar or vector data on unstructured grids, made of triangular or quadrilateral elements. Data can be associated both with cells (cell centered data) or vertices: scalar, vector, and tensor field storage and visualization is possible.

There are many open source viewers that are able to read the VTK format. Among them, ParaView [110] is an open-source, multi-platform, extensible application designed for visualizing large data sets [111].

3.5 Benchmarking and applied cases

The constant temperature model is benchmarked against analytical cases, and some sensitivity analyses against the mesh quality are carried out and briefly presented in the following section 3.5.1. A more complete discussion of the basic benchmarking cases is given in the technical note [167].

Also the accommodating temperature model is applied to some paradigmatic cases and benchmarked against simple cases in section 3.5.2.

3.5.1 Benchmarking of constant temperature model against analytical cases

In this section, the validity of the code is demonstrated by benchmarking with available analytical or experimental formulae. The implemented algorithms have been validated in simple cases against analytical formulae, in particular gas conductance of straight tubes with circular or rectangular cross-section, in the presence of elbows, and in the presence of chambers at the two ends [57, 112]. The gas conductance of tubes of circular cross section can be calculated as

$$C = 3.81\alpha(T/M)^{1/2}d^3/l. \tag{3.32}$$

AR of longitudinal elements	n. of elements on side edges	tube length / side edge side edge	num[m^3/s] numerical result	[m^3/s] analytical result	1-C_{num}/C
1	2	4	1.592	1.665	0.04
1	2	8	0.918	0.954	0.04
1	2	16	0.503	0.488	0.03
1	4	16	0.486	0.488	0.01
1	4	32	0.258	0.264	0.02
1	4	64	0.133	0.136	0.02
1	4	100	0.086	0.089	0.03
2	4	100	0.087	0.089	0.02
2	8	100	0.088	0.089	0.006
2	4	200	0.044	0.044	0.01
4	4	200	0.042	0.044	0.05

Table 3.3: Gas Conductance across a square pipe of variable length, calculated for various element sizes, using first order space discretization on very coarse meshes. Both the aspect ratio of longitudinal elements and the element size in transverse direction can affect the results.

Lengths (d, a, b, l), gas bulk temperature T, molar mass M and conductance C are expressed respectively in cm, K, g and l/s; α is a correction factor to be used for conducts shorter than $l/d = 100$, typically $\alpha = 1/(1 + 4d/3l)$; in the case of rectangular cross section, the equation becomes

$$C = 0.970\alpha K_f (T/M)^{1/2} a^2 b^2/(la + lb), \tag{3.33}$$

where K_f is a form factor that accounts for the shape of the cross-section, and varies with the ratio of the duct sides a/b.

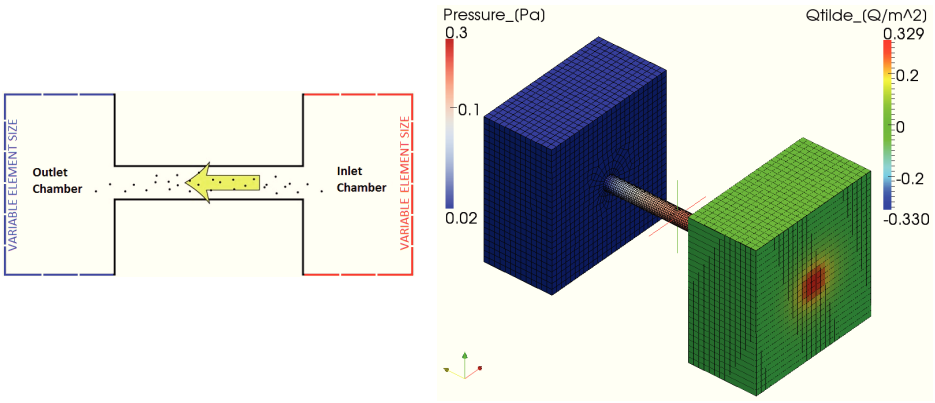
The conductance values obtained from analytical formulae have to be compared with the numerical estimates, which are extrapolated from numerical results by considering the throughput Q [Pa·m^3/s] and the pressures at the inlet p_1 and outlet p_2 [Pa] sections C_{num}[m^3/s]=$Q/(p_1 - p_2)$.

The comparison with the analytical results is presented in the case of raw mesh and first order element discretization in Table 3.3, for tubes of variable length and square cross section with 10 cm side. These are limit cases, presented to show that coarse meshing of models can give results within a reasonably low error interval ($< 10\%$ in these cases). Please note that the use of second order discretization gives the same result as doubling the number of divisions of the edges, and strongly reduce the error.

In the case of long (l/d=100) straight tubes (see table 3.4), the applied Boundary Conditions were chosen as: inlet p =0.3 Pa, outlet p =0.02 Pa. The throughput was obtained by integrating the specific throughput over the outlet elements. Different gas parameters were considered (gas type and temperature); the tube cross-section was varied as well, investigating also the dependency on element size and the dependency on the element Aspect Ratio (AR). Both in the case of long circular or square tubes, for molecular or atomic hydrogen or deuterium at different temperatures, the error is less than 4% even with elongated elements of row meshes (square tube with 4 elements per side, AR of the longitudinal elements up to 8). In the case of long circular tube with a 90° turn and l/d=200, the analytical solution is given by correcting the effective tube lenght: $L_{eff} = L_{ax} + 1.33d$. For hydrogen gas H_2 at 293 K, the numerical solution has a negligible error (0.3%) with respect to the analytical one.

Case	n. of elements	C_{num}[m3/s] numerical	C[m3/s] analytical	1-C_{num}/C
Square, straight 1m tube	6432	6.11e-4	6.27e-4	0.026
	3101	6.47e-4	6.28e-4	0.030
Circular, straight 1m tube	3101	4.63E-4	4.45E-4	0.040
Circular tube, two segments 1m long with 90° elbow	7200	2.298E-4	2.291E-4	0.003

Table 3.4: Gas conductance across long tubes, with length over diameter ratio l/d=100; hydrogen gas at 273K.



(a) (b)

Figure 3.14: Model of two connected chambers: (a) sketch with the surfaces of variable element size highlighted and (b) pressure distribution and the specific throughput at the outlet.

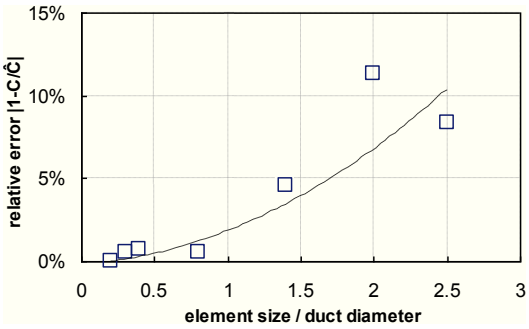


Figure 3.15: Sensitivity analysis for element size with respect to the dimension of the main geometric feature (tube diameter). The relative error is referred to the numerical result C_{num} calculated with the smallest element size.

Another case that has been tested is the gas flow between two connected chambers at different pressure (see figure 3.14). This more articulated geometry is meshed with different detail level, in order to test the effect of the element size on the results. The boundary conditions are similar to those of the previous cases, with uniform inlet pressure applied to the five open surfaces of the parallelepiped inlet chamber and uniform pressure applied to the five open boundaries of the outlet chamber. The sensitivity analysis shown in Figure 3.15 suggests that a suitable choice of the element dimension is that below the characteristic geometric feature size; for instance, the tube diameter in this case. The capability to solve correctly the conductance depends in particular on the element size on certain areas, such as the surfaces in front of the tube apertures. Note that the error is the same for any gas type and parameter.

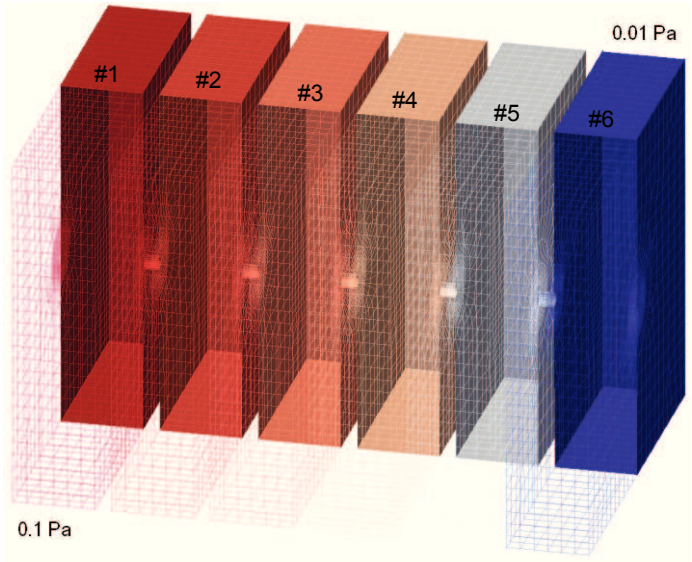


Figure 3.16: Model of six chambers connected by circular aperture, $l/d = 1.0625$.

In the case of deuterium gas flow through six chambers, connected in series by a circular aperture of $l = 17$mm and $d = 16$mm, a fine mesh with 13992 surface elements (shown in figure 3.16) required 570s CPU time for view factor matrix calculation (56 sec wall time with 12 parallel threads) and 32 s to solve the system. In table 3.5 the pressure calculated in the gaps is listed. In table 3.6, and the analytical conductance calculated with short tube correction α is compared to the numerical values Cnum. Results obtained with much a coarser mesh of 4252 elements, solved in 11 s wall time on 12 threads, differ by 5% maximum.

3.5.2 Applications and benchmarking of the temperature accommodation model

The equilibrium reached between two connected chambers 1, 2 showing unequal temperature T_1 and T_2 is different according to the flow regime. In the viscous

Chamber	#1 (source)	#2	#3	#4	#5	# 6 (tank)
p [Pa]	0.1	0.08185	0.064	0.0462	0.0283	0.01

Table 3.5: Gas flow through six chambers, pressure in the gaps. The calculated D_2 throughput was 0.605E-3 Pa·m^{3}s^{-1}.

aperture between	#1→#2	#2→#3	#3→#4	#4→#5	#5→#6
C [m^{3}s^{-1}], $\alpha = 1/(1 + 4d/3l)$	0.0349	0.0349	0.0349	0.0349	0.0349
C [m^{3}s^{-1}], α Clausing [22]	0.0315	0.0315	0.0315	0.0315	0.0315
C_{num} [m^{3}s^{-1}]	0.0333	0.0339	0.0340	0.0338	0.0331

Table 3.6: Gas flow through six chambers, comparison of numerically calculated conductances $C_{num,i} = Q/(P_i - P_{i+1})$ with analytical conductances C; The calculated D_2 throughput was 0.605E-3 Pa·m^{3}s^{-1}.

range, at equilibrium the chambers will have equal pressure $p_1 = p_2$; but at lower pressures, between the two connected environments at different temperatures, the *thermal transpiration effect* [57, 113] causes a pressure difference, depending on pressure range, geometry and gas. Clearly, this is the common case of a capacitance transducer, operating at a stabilized temperature, which measures a vessel at room temperature. In the molecular flow limit, the ratio of the two pressures is the Knudsen's value [81]:

$$\frac{p_2}{p_1} = \sqrt{\frac{T_2}{T_1}} \tag{3.34}$$

AVOCADO and the non-equilibrium method it implements are only applicable to the molecular regime in stationary regime. In the following this result will be verified.

A first application of the the temperature accommodation model is shown in Figure 3.17. The schematic shows the model used to verify the thermal transpiration effect. A duct of variable length connects two chambers, the tank (1) and the test chamber (2). The walls of the small test chamber are maintained at the fixed temperature of 373 K. On the other hand, the surfaces of the vacuum chamber and the connecting duct are at room temperature (296 K). Using arbitrarily varying accommodation factors, we performed a sensitivity analysis also changing the ratio between the duct radius and the test chamber radius (r/R): the spherical geometry of the test chamber gives the possibility to evaluate aspects of the flow that in the case of a thin, cylindrical volume may not be clear. We assume that the geometry of the vacuum chamber do not influence the process. We tested Hydrogen gas, which is non condensable, at steady state.

In many analyses concerning how the thermal transpiration effect affects measurements of capacitance diaphragm gauges, the accommodation factor is simply set to unit, meaning that the gas immediately thermalise to the wall energy: this assumption is made by many authors [114, 115]. We believe that this assumption holds well in these cases, because the temperature smoothly

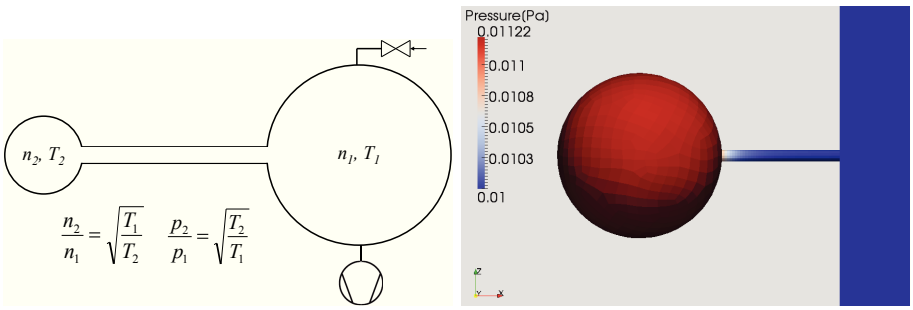


Figure 3.17: Model to test the thermal transpiration: on the left, the schematic of the model and on the right the simulated pressure

varies along the vacuum connection tube, and because of the very small size of the duct with respect to the diaphragm chamber. If we extend the problem to sudden variations of temperature, we expect the gas properties to vary smoothly if they require more than one collision to reach the energy level of the wall material.

Therefore, going beyond the approximation that one collision suffices for the gas to thermalise with the wall, brings us up against more realistic and sophisticated models, which nonetheless require experimental data on the subject. The energy accommodation of low energy atoms (below 1 eV) on surfaces is therefore an important issue, in particular in the case of large temperature variations; in that condition, the influence of the accommodation factor may be important indeed.

The pressure profiles along the axis of the duct are presented in figure 3.18, for various duct diameters (1÷20 mm ID) but fixed duct length (10 mm) and diameter of the spherical chamber (20 mm), and an energy accommodation factor of 0.2 and 1. Indeed, we see that the gas temperature varies through the duct: by energy exchange at the walls, the hot gas proceeding from the heated test chamber is cooled down, and the longitudinal extent of this process depends on the accommodation factor. This is the cause of the pressure reduction, even though, as shown before, the density is increasing along the same direction.

The walls in this model have infinite heat capacity, therefore their temperature is constant and they can provide the required heat to warm up the particles. Knudsen's ratio of pressure is correctly calculated by Avocado. In figure 3.19, the density profile along the axis of the duct is shown. With the assigned temperature drop of 77 °C, the gas density along the axis of the duct has the opposite behaviour of the pressure. In particular, we see that in the case of $K_{ac} = 0.2$ and duct diameter/length ratio of 0.5, the gas density at the outlet of the duct on the cold tank do not reach the undisturbed value, and still about 1/7 of the total density difference remains. Typically, the thermal non-homogeneities that cause thermal transpiration are experimentally associated with outgassing from non-baked surfaces, and therefore might be difficult to experience or to quantify experimentally.

A second application of the the temperature accommodation model is a simple, straight pipe shown in figure 3.20, which is used to compare the flows when the thermal boundary conditions are varied; the tube is 1 m long with

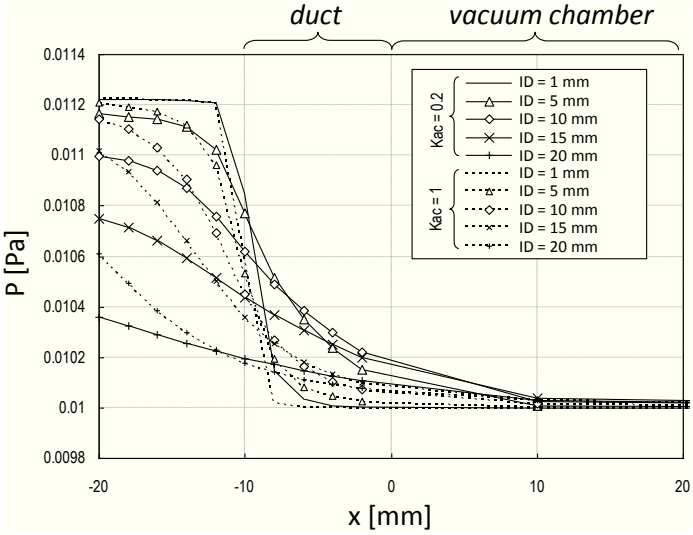


Figure 3.18: Pressure profiles along the axis of the duct, from 20 mm inside the tank (20 mm) up to the centre of the spherical test chamber (-20mm). The dependence on the diameter of the duct (1, 5, 10, 15 and 20 mm ID) and the accommodation factor (0.2 and 1) is shown.

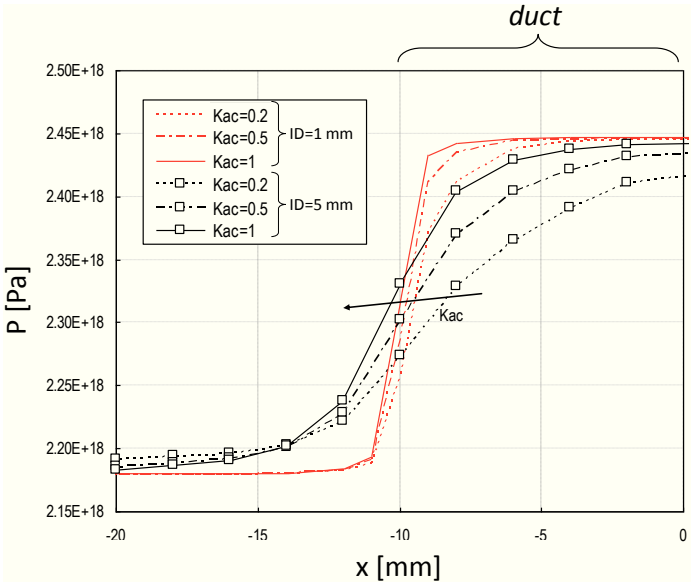


Figure 3.19: Density profiles along the axis of the duct, from the entrance of the duct on the side of the tank (0 mm) up to the centre of the spherical test chamber (-20mm). The dependence on the diameter of the duct (red line: 1 mm ID, black line: 5 mm ID) and the accommodation factor (0.2, 0.5, 1) is shown.

a diameter of 20 mm, with a nominal conductance at room temperature of $C_{an} = 9.63 \times 10^{-4}$ m^3/s if the correction $\alpha(l/d = 50) = 0.97$ for short pipes is used. The following cases were compared:

Orange The gas is cold and thermalised with the walls of the tube ($T_{wall} = T_{in} = T_{out}$ =297 K); there is a pressure difference between the two apertures $p_{in} = 0.02$ Pa and $p_{out} = 0.01$ Pa and the tube conductance C_{orange} is calculated indifferently as $Q/\Delta p$ or $\phi/\Delta n$. This is a preliminary run of the code; it gives $C_{\text{orange}} = 9.59 \times 10^{-4}$ m^3/s, with an error within 0.5%.

Red The gas is hot and thermalised with the walls of the tube ($T_{wall} = T_{in} = T_{out}$ =333 K); there is a pressure difference between the two apertures $p_{in} = 0.02$ Pa and $p_{out} = 0.01$ Pa, and the tube conductance $C_{\text{red}} = 1.015 \times 10^{-3}$ m^3/s is calculated indifferently as $Q/\Delta p$ or $\phi/\Delta n$; as expected, $C_{\text{red}} = C_{\text{orange}}\sqrt{T_{\text{red}}/T_{\text{orange}}}$.

Blue A hot duct (T_{wall} =333K) connects two cold chambers ($T_{in} = T_{out}$ =297K) at the equal pressure of 0.01Pa. As the temperature of the gas varies along the duct, different gas pressure and density are reached, according to the thermal transpiration. No net particle flux occurs, as $\phi_{\text{blue}}/\phi_{\text{orange}} < 10^{-5}$, but $Q < 0$ at the two apertures: the gas particles exiting the system have higher energy than those entering. The pressure in the center of the tube reaches 0.010588 Pa, correctly in the ratio $\sqrt{(T_{wall}/T_{in})}$.

Green The same temperature conditions (T_{wall} =333 K; $T_{in} = T_{out}$ =297 K) are imposed but $p_{in} = 0.02$ Pa and $p_{out} = 0.01$ Pa. A net particle flux is verified; the conductance calculated as $\phi/\Delta n$ is $C_{\text{green}} = 9.59 \times 10^{-4}$ m^3/s, while the $Q < 0$ on both sides of the tube as there is a net power exiting the domain. This conductance is equal to the *orange* case; apparently only the gas temperature at the sides of the duct are significant to the calculation of the gas conductance.

Violet The hot inlet chamber is connected by a hot duct to a cold chamber (T_{wall}, T_{in} =333K, T_{out} =297K), and $p_{in} = 0.02$ Pa and $p_{out} = 0.01$ Pa. The conductance calculated as $\phi/\Delta n$ is $C_{violet} = 1.087 \times 10^{-3}$ m^3/s. If the gas properties at the inlet are converted to 297 K by $p'_{in} = \sqrt{297/T_{in}}p_{in}$, $n'_{in} = p'/(k_B T)$, it results $\phi/\Delta n' = C_{orange}$.

The pressure and density profiles along the tube are presented in figure 3.21. From the results presented, it appears that only the gas temperature at the entrance and exit of a duct determines its molecular conductance C. In addition, heterogeneous conditions between the connected chambers can be reduced to homogeneous ones, and the analytical values of C are found thereafter. It results:

$$C_H = \frac{\phi}{(n_{out} + \phi \cdot C_C)\sqrt{\dfrac{T_{in,C}}{T_{in,H}}} - n_{out}} \tag{3.35}$$

where the subscripts H, C indicate respectively Hot and Cold cases (e.g. Violet and Orange); the cold case is at the temperature T_{out}.

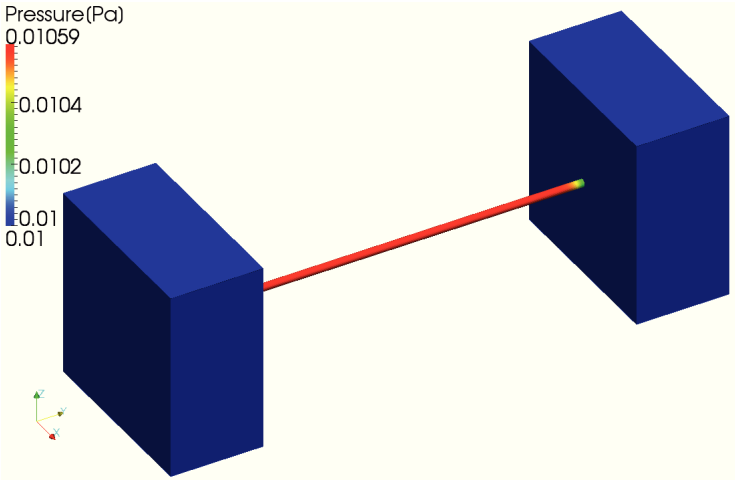


Figure 3.20: Normalized density profiles along the axis of the duct: the slope of the four cases is better comparable (case: blue).

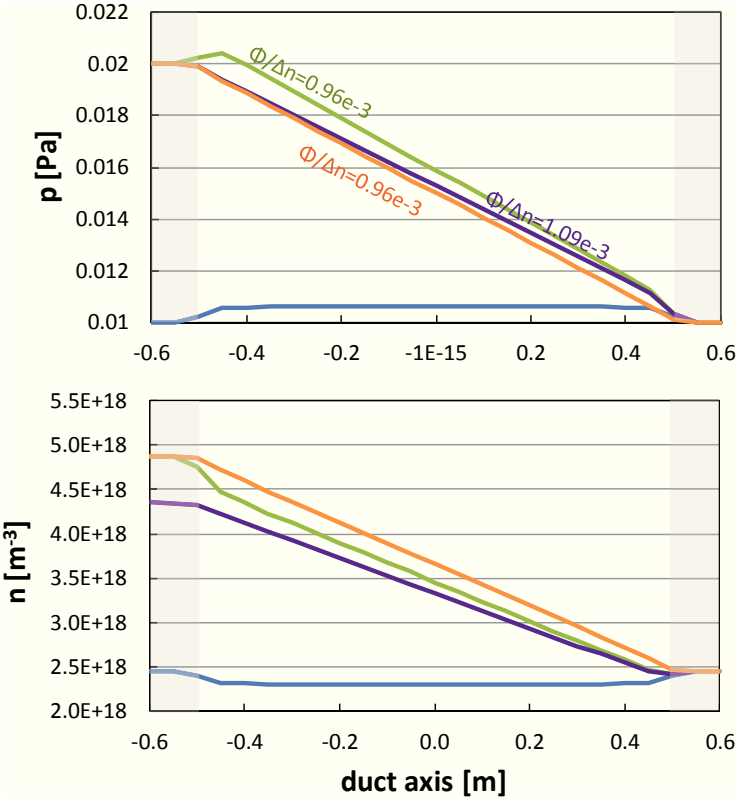


Figure 3.21: Pressure and density profiles along the axis of the duct, various cases

3.5.3 Thermal Accommodation Factor

The theory for clean surfaces dates back to 1914 [116]. The exchange of translational kinetic energy between two hard sphere molecules was considered, and this derived the expression[1]

$$\alpha_c = \frac{2\mu}{(1+\mu)^2} \tag{3.36}$$

where $\mu = M_g/M_w$ is the ratio between the molecular weight of gas and solid; when $\mu = 1$, this formula gives the maximum $\alpha_c = 0.5$. α_E is indicated as α_c as it is calculated for clean surfaces.

A more accurate expression [117] is

$$\alpha_c = \frac{2.4\mu}{(1+\mu)^2} \tag{3.37}$$

The accommodation coefficient may be greatly influenced by temperature and surface structure (roughness for instance).

The surface roughness can increase the value of α_c, as it determines n multiple collisions:

$$\alpha_c = 1 - (1 - \alpha_{E0})^n \tag{3.38}$$

When the gas adsorb to the solid wall, the accommodation coefficient strongly varies, as a net fraction of the interaction will be with already adsorbed gas instead of particles from the solid. In fully-adsorbed conditions, a fit of experimental data gives [92]:

$$\alpha_a = \frac{M_g}{6.9M_g} \tag{3.39}$$

and in the case of biatomic molecules:

$$\alpha_a = \frac{1.4M_g}{4.9 \cdot 1.4M_g} \tag{3.40}$$

In intermediate conditions, where F is the surface coverage by adsorbed gas, it results:

$$\alpha = F\alpha_a + (1-F)\alpha_c \tag{3.41}$$

the fraction F depends on the surface temperature.

According to this simple model, at room temperature the accommodation factor for H_2 on Cu is $\alpha_c = 0.07$ and $\alpha_a = 0.36$, values that give, for a 50% coverage, $\alpha_E \approx 0.21$

A wide discussion on the EAC is given by Goodman in [118].

Studies on the thermal accommodation factor by molecular dynamics

Nowadays in many applications, the accommodation coefficients are calculated by molecular dynamic (MD) simulations, mostly in material science and modeling of biomolecules. In MD, the Newton's equation of motion are solved for the whole set of interacting molecules. The basic ingredients of these simulations are therefore the interactions between particles, that is, the force fields

[1] in this paragraph, the accommodation factor is indicated as α_E instead of $K_a c$, in order to be in accordance with bibliography

(Van der Waals interactions, electrostatic force if relevant, harmonic springs to model solid metals as for the Einstein model).

I developed a simple model, in order to investigate this numerical approach and its applicability to the practical calculation of $K_a c$, trying to reproduce in particular the results for Ar on Pt found in [98].

NVT ensemble A MD simulation can be performed in different ensembles, of which the most common are:

- Microcanonical Ensemble, where the constaints are fixed number of particles N, fixed volume V and constant total energy E (NVE)
- Canonical Ensemble, where the constaints are fixed number of particles N, fixed volume V, and conserved temperature T (NVT)

In NVT ensemble, a thermostat is required to avoid non-local energy artifacts and carry out the microscale simulation at the required macroscopic temperature. Possible thermostats are: Popular techniques to control temperature include velocity rescaling, the Nos-Hoover thermostat, the Berendsen thermostat and Langevin thermostat.

The particle impact with the solid wall is solved in NVT, as the wall is maintained at a prescribed temperature during the time interval simulated.

Force field and solid wall model The Lennard Jones potential is used for the interaction between the gas and wall atoms. The force is obtained spatially deriving the potential:

$$F_{LJ}(r) = -\frac{dU(r)}{dr} = 24\frac{\epsilon}{\sigma}\left(2\left(\frac{\sigma}{r}\right)^{13} - \left(\frac{\sigma}{r}\right)^{7}\right) \tag{3.42}$$

The parameters describing the interaction between different atoms are determined by one of the following combination rules:

$$\begin{aligned}
&1. \quad \epsilon_{ij} = \sqrt{\epsilon_i \epsilon_j} && \sigma_{ij} = \sqrt{\sigma_i \sigma_j} \\
&2. \quad \epsilon_{ij} = \sqrt{\epsilon_i \epsilon_j} && \sigma_{ij} = \frac{\sigma_i + \sigma_j}{2} \\
&3. \quad \epsilon_{ij} = \frac{2\sigma_i^3 \sigma_j^3 \sqrt{\epsilon_i \epsilon_j}}{\sigma_i^6 + \sigma_j^6} \sqrt{\epsilon_i \epsilon_j} && \sigma_{ij} = \left(\frac{\sigma_i^6 + \sigma_j^6}{2}\right)^{1/6}
\end{aligned} \tag{3.43}$$

The solid walls are built based on the Einstein model. The atoms vibrate around their lattice sites in a face centered cube (FCC), by harmonic springs:

$$k = \frac{m_w k_B^2 T_E^2}{\hbar^2} \tag{3.44}$$

Where $\hbar$ is the reduced plank's constant, T_E is the Einstein temperature for the material, m_w is the mass of the atoms.

The initial velocities vibrational state of each wall particle is obtained from Maxwell Boltzmann distribution for the given temperature. A random number from Maxwell Boltzmann distribution can be calculated using the Johnk's algorithm [119].

Covalent bonds are modeled by springs. The bond potential is $U(r) = 2k(r - r_0)^2$, and therefore the force reads $F(r) = k(r - r_0)$. This would apply

in the case of bi-atomic molecules, for instance.

Thermostat The use of velocity scaling methods determines a sudden reduction of the vibrational state after the initial strike, when some energy is transferred from the projectile to the wall. The following thermostats [120] have been evaluated:

- Langevin thermostat: based on the idea that the temperature is maintained by collision with an underneath heat bath of particles. Difficult to find the correct damping coefficient 1/taud. The method to obtain a random number from a general normal distribution is derived from Box-Muller transformation [119]. Scaling from the standard normal distribution is required considering sigma.
- Berendsen thermostat: derive towards temperature, correction factor depends on the characteristic time for thermalization and the time step. This method gives an exponential decay of the system towards the desired temperature. The change in temperature between successive time steps is:

$$\Delta T = \frac{dt}{\tau}(T_0 - T(t)) \tag{3.45}$$

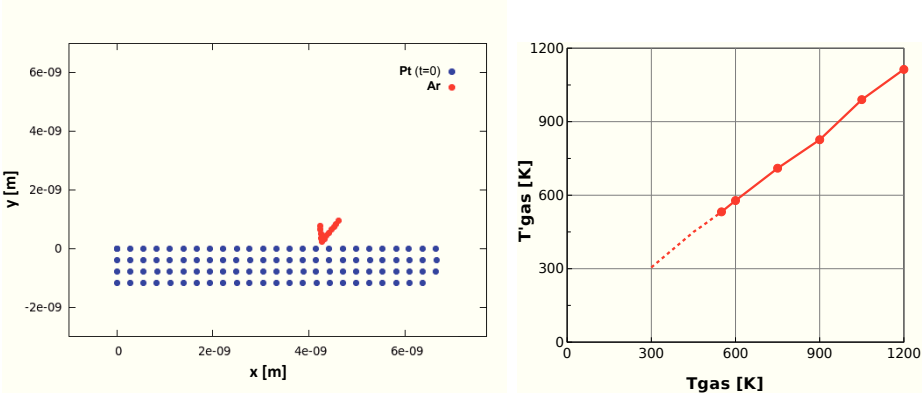
  Thus this lead to a modification of the momenta $p_i \rightarrow \lambda p_i$ where λ is the scaling factor:

$$\lambda^2 = 1 + \frac{\Delta t}{\tau_T}\left(\frac{T_0}{T} - 1\right) \tag{3.46}$$

  and τ_T is the coupling time constant.

In these schemes, the system is weakly coupled to a heat bath with some temperature. The Berendsen thermostat was implemented and tuned in order to have a small deviation from the prescribed wall temperature during a simulation.

Method Two-dimensions are considered, with the configuration (110) of a FCC lattice as shown in figure 3.22(a); the vertical distance between layers



(a) (b)

Figure 3.22: (a) layout of a simulation, 2D FCC (110) lattice and (b) average gas temperature after rebound at different temperatures.

is $\sqrt{2}\sigma_{Pt}$. Leap-frog-Verlet integration is used [121]. The chosen time step is about 0.5 fs (0.0005 ps). The simplified approach is to model the collision of one single atom at a time. Simulating a large statistics of incoming velocities and angle, and impact position, the scattered angle and velocity are memorized for each run.

Results for Ar - Pt The results for Ar particles impacting on Pt are: negligible variations of EAC are verified for different gas equivalent temperatures in the range 400÷1050 K (see figure 3.22(b)); the average value is ~ 0.089, which is in line with the value calculate in [98]. This value, nevertheless, does not coincide with the value predicted by the simple model described before, as it results $\alpha_c \approx 0.28$. For scattered angles above 75°, generally speaking, the accommodation seems to be minimum.

The developed MD model was simply a preliminary modelling of the phenomena, prepared in order to gain a better understanding of the phenomena involved in the accommodation.

Comments

In the case of bi-atomic molecules, an accommodation factor can be identified for the internal degrees of freedom. Translational, rotational and vibrational EAC shall be used, by introducing the "partial effective temperatures" corresponding to them. Apparently, only the translational EAC should concern the molecular flow, but energy exchange between the degree of freedom can occur at the collision with the surface. Therefore, in the applications of AVOCADO of the following chapter, the accommodation factor K_{ac} will be a parameter of many simulations, in a range that is considered reasonable (0.1÷0.3).

4

Experimental validation in ARIANNA

The Adaptable Rarefied Instrumented Atmosphere for Neutral iNjection Applications (ARIANNA) experiment has been set up as complementary service in the beam source modelling activity. ARIANNA supported the development and validation of the AVOCADO code for molecular flow and density distribution analysis.

The AVOCADO code has been validated in this experiment. In particular, the aims of this activity are listed in the following: 1. Demonstrate the capability of resolving the correct mass flow from the pressure differences; 2. Evaluate the correctness of the predicted pressure distribution in the volume; 3. Study the applicability of the code to systems in thermal non-equilibrium.

This activity has sought to fulfill these aims by the following strategies: 1) Measure at the same time the mass flow rate of the injected gas and the pressure difference between key locations in the domain; 2) Measure the pressure in as many points as possible in known conditions; the use of multiple capacitance heads, or different ducts for the same head, or manipulators for the pressure probe is advisable; 3) verify the adequacy of the mesh around the grid apertures.

An additional aim is to 4) Measure the pressure difference and the mass flow rate after the internal components of the vacuum vessel had been heated to known temperatures, and thermal transpiration effect must be considered; this activity is ongoing.

The complete documentation of the experimental campaign carried out in ARIANNA is reported in the RFX technical note [168].

This chapter deals with the validation activity based on the experimental campaign. In section 4.1, the experimental setup is described, listing the many subsystems involved in the vacuum production and measurement. Section 4.2 contains the results of the measurement campaigns: both the successful results and the unsuccessful ones are reported, followed by a discussion of the necessary improvements or the quality of the measurements. A summary of the experimental validation is given in section 4.3.



Figure 4.1: ARIANNA experiment

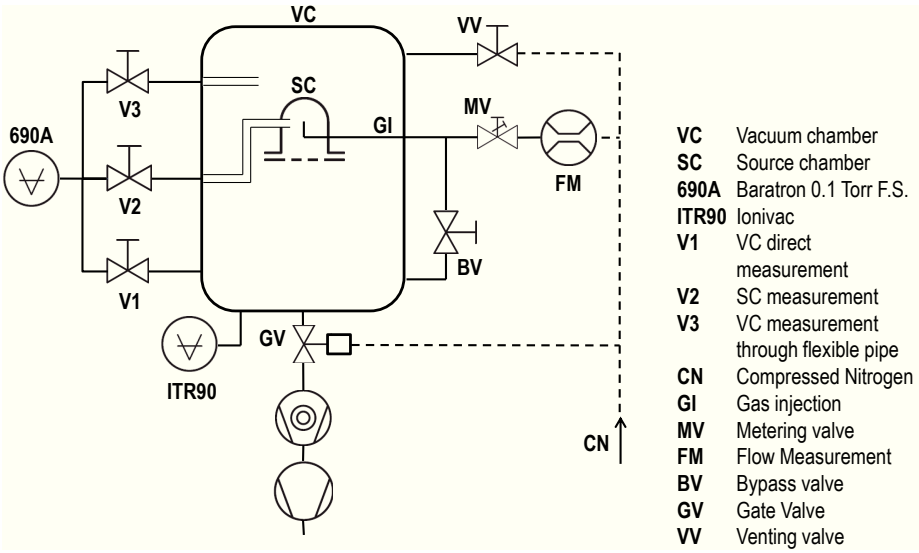


Figure 4.2: ARIANNA vacuum diagram

4.1 Description of the ARIANNA experiment

4.1.1 Description

An existing 600mm ID, 700 mm high vacuum vessel is used to prepare an instrumented atmosphere in which perform pressure measurements in gas flowing conditions. The vessel (or vacuum chamber) has 4 radial ports about 100 mm wide and 8 bottom ports. The vacuum is produced by using a 1000 l/s turbomolecular pump, which is connected to the main port of the vessel at the bottom.

In order to reproduce a configuration similar to that of an electrostatic accelerator, a gas is injected in a closed volume, separated from the chamber by a 5x5 aperture grid. The gas injection is regulated.

The experimental set-up has been incrementally modified during various measurement campaigns.

4.1.2 In-vacuum components

The in vacuum components are the following:

- Cylindrical gas source (shown in figure 4.3);
- Multi-aperture grids (shown in figure 4.4);
- Support structure (not considered in numerical models for benchmarking);
- Protection grid, before the turbopump (also not modelled);
- Ducts for gas injection and measurement.

4.1.3 Pumping system

The duct is 160mm internal diameter. The pump is a TURBOVAC 1100C, with flange 250 ISO-K (nominal S(N2) 1050 l/s). The pre-vacuum is done by a EcoDry M oil free vacuum pump.

4.1.4 Measurement systems

MKS Type 690A Pressure transducer

The pressure measurement for temperature-regulated capacitance manometers shall be corrected, for the thermal transpiration effect:

$$p = p_c \sqrt{\frac{T}{T_c}} \tag{4.1}$$

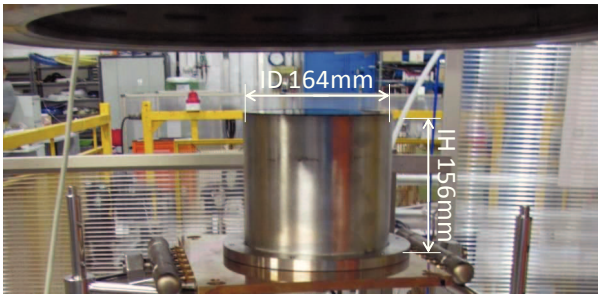


Figure 4.3: Cylindrical gas source chamber

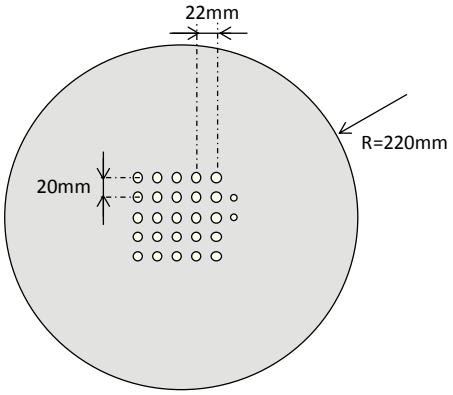


Figure 4.4: Sketch of the multi aperture grids

where the c subscript refers to the capacitance manometer. Correction factors for temperatures relevant to the ARIANNA experiments are listed in table 4.1.

$T_{BARATRON}$ [K] ([°C])	$T_{CHAMBER}$ [K] ([°C])	$p_{CHAMBER}/p_{BARATRON}$
318 (45)	293 (20)	0.960

Table 4.1: Correction for thermal transpiration effect

Total uncertainty when measuring in the range of 1E-4 Torr: 6E-7 Torr (8E-05 Pa).

MKS Type 615A Pressure transducer

The measurement oscillates.

LEYBOLD ITR90 (IONIVAC)

The ITR90 gives a continuous measurement of the vacuum in a wide range of pressures, by switching from Pirani to ionization sensor.

MASS FLOWMETER and MKS 246B Single Channel Readout

The mass flow meter reads equivalent nitrogen standard litres per minute (slm). The Gas Correction Factor GCF is used to indicate the ratio of flow rates of different gases which will produce the same output signal from a mass flow meter. Nitrogen has GCF = 1. The gas correction factor for X gas reads:

$$GCFx = \frac{0.3106 \cdot s}{dx \cdot cpx_c} \tag{4.2}$$

where: cpx is the specific heat of gas X, expressed in cal/g°C; dx is the standard density of gas X, in g/l; s is a correction factor that depends on the molecular structure (1.030 for monoatomic gases, 1.000 for diatomic gases, 0.941 for triatomic gases). In the case of Argon gas, the values in Table 4.2 shall be used. Three different flow meters were used as listed in 4.3.

s	1.030
dx	1.784
	520 J/kg·K
cpx	124.2 cal/kg·K
	0.1242 cal/g·K

Table 4.2: Correction for the gas type

experimental set-up	**mass flow meter**
1	10000 sccm (10 slm)
2	1000 sccm (1 slm)
3	200 sccm (0.2 slm)
4	200 sccm (0.2 slm)

Table 4.3: Various mass flow meters used in ARIANNA

Signal conditioners, controllers and readouts

The signal conditioners, controllers and readouts of the experimental apparatus are shown in figure 4.5

4.1.5 Gas properties

In the following, gas properties are listed, in the tables 4.4, 4.5 and 4.6. The elastic mean free path (m.f.p.) is calculated for various combinations of gas, pressure and temperature; the consequent Knudsen number is considered to define the limits of molecular flow regime in the chamber and the gas source in the experiment.

Gas	Standard Atomic weight	Atomic mass unit	mass [kg]	σ [m]
H	1.00794	1.6605E-27	1.6737E-27	
H_2	2.01588	1.6605E-27	3.3474E-27	2.73E-10
D_2	4.03176	1.6605E-27	6.6949E-27	
N	14.00310	1.6605E-27	2.3253E-26	
N_2	28.00620	1.6605E-27	4.6505E-26	3.74E-10
He	4.00260	1.6605E-27	6.6465E-27	2.18E-10
Ar	39.9480	1.6605E-27	6.6335E-26	3.62E-10

Table 4.4: Properties of some gases

	σ [pm]	σ [m]
H_2	273	2.73E-10
He	218	2.18E-10
N_2	374	3.74E-10
O_2	357	3.57E-10
Ar	362	3.62E-10
CO_2	456	4.56E-10

Table 4.5: Collisional data of gases

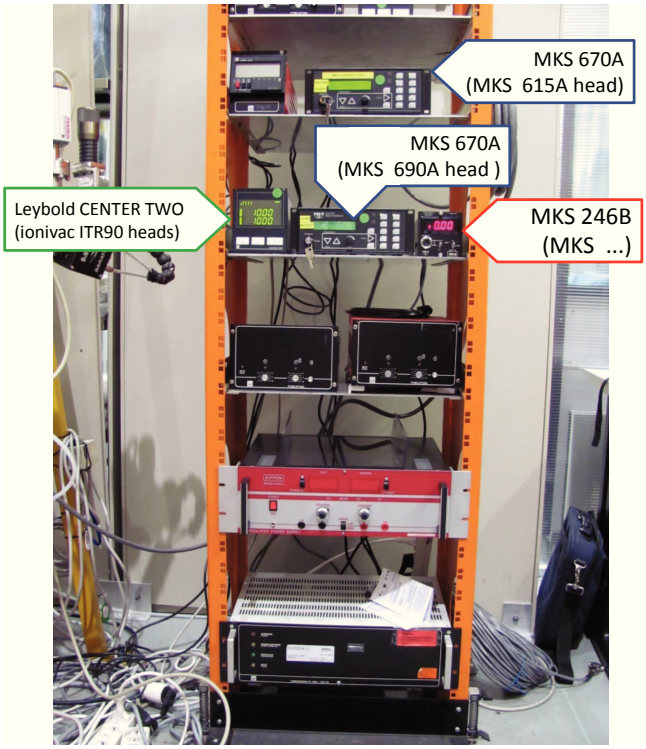


Figure 4.5: Signal conditioners, controllers and readouts

	Hydrogen gas H_2		Nitrogen gas N2		Argon Ar	
T [K]	293	293	293	293	293	293
p [Pa]	0.245	0.049	0.133	0.027	0.139	0.028
p [mbar]	2.45E-03	4.9E-04	1.33E-04	2.67E-04	1.39E-04	2.79E-04
L [m]	0.1	0.5	0.1	0.5	0.1	0.5
σ [m]	2.73E-10	2.73E-10	3.70E-10	3.70E-10	3.62E-10	3.62E-10
mfp [m]	0.050	0.250	0.050	0.250	0.050	0.250
Kn	0.5	0.5	0.5	0.5	0.5	0.5

Table 4.6: Mean free path and Knudsen number, pressures and dimensions of interest

4.2 Experimental results in ARIANNA

This section contains all the measurements that were carried out. Various configurations were prepared, and for some of them many measurement campaign were performed. The ARIANNA configurations are listed in table 4.13.

4.2.1 Experimental set-up n.1 - preliminary measurements

This section describes the initial experimental setup and highlights the problems encountered. In figure 4.6 the experimental set-up of the internal components and the injection system are shown; the blue hoses are made of Rilsan PA11. There were three different measurement ducts, in various areas of the vacuum,

experim. set-up	configuration	measur. points	mass flow meter	tubes
1	single grid	fixed	10000 sccm (10 slm)	Rislan PA11
2	single grid	fixed	1000 sccm (1 slm)	S.S.
3	multi grid	fixed	200 sccm (0.2 slm)	S.S.
4	multi grid	movable	200 sccm (0.2 slm)	S.S.
5 (foreseen)	multi grid, heating	movable	200 sccm (0.2 slm)	S.S.

Table 4.7: List of experimental sessions

and three valves to switch from one measurement to the other. At the very beginning, the capacitive head (Baratron) was connected to damaged electronics; no F.S. regulation was allowed, no control of the Baratron heating system. When we tried a measurement of the gas conductance in the three regimes, molecular, transition, and viscous, we found out the problem with the electronics. The mass flow was measured by the flow meter, but regulated with a calibrate valve.

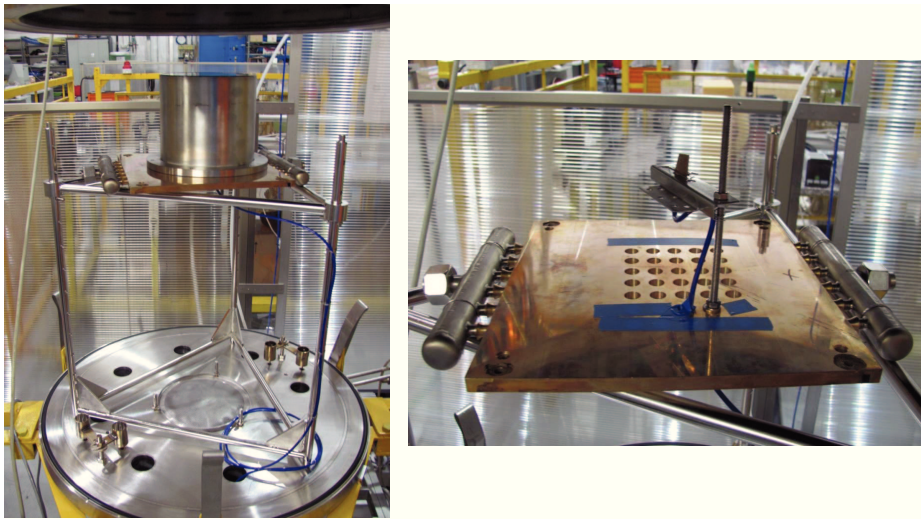


Figure 4.6: Set-up #1: in-vacuum components (left) and detail of the gas injection inside the source chamber (right)

After the initial measurements, the following problems were identified:

- 0.1Torr capacitance head gives wrong readings. The electronics had to be replaced (MKS 670 A) and the issue was solved;
- The F.S. of the Flow meter (10000 sccm) is too high: only one significant digit can be used in the range of throughput required. A new flow meter was used in the following campaigns.
- The measured pressure is strongly influenced by the degassing of the Rilsan PA11 hoses. Purely vacuum-compatible materials shall be used, even if the expected operating pressure are in the range of a relatively low vacuum.

4.2.2 Experimental set-up n.2

Thanks to the experience gained in the first attempt, in this new setup the following solutions were implemented:

1. Replaced tubes by vacuum compatible S.S. tubes;
2. Valves and external ducts were heated for surface cleaning (reducing surface degassing);
3. Adhesive tape removed (used to reduce the number of apertures of the grid), replaced by alluminium thin sheets, vacuum compatible;
4. Cleaning with acetone of vacuum components;
5. Micrometric diffuser removed:
6. Reduce to the minimum the volume of the tubes between the capacitance manometer and the vacuum vessel.
7. New flow meter: 1000 sccm (1 slm).

The pictures of the key components are presented in figure 4.7: it is possible to see the three measurement tubes and related valves (V1, V2, V3).

In the following of this section, the AVOCADO models are presented and the dependence on the mesh is evaluated. Many measurement campaign were performed under different vacuum conditions.

AVOCADO models

The gas source is a cylinder, 164mm ID and 156 mm high. The gas is injected in the gas source through a circular surface, centered in the volume of the source. The turbopump modelled as a circular ring, with given pumping speed S. In the molecular flow, the conductance is linear and therefore a single simulation is sufficient to characterise the system.

Two meshes have been considered, a coarse and a fine one: the difference is in the discretization of the grid's apertures, and is visible comparing figures 4.9 and 4.10. The rest of the model (respectively shown in figures 4.8(a) and 4.8(b)) is not varied. The results of the coarse mesh are presented in tables 4.8, 4.9, 4.10. The results of the fine mesh are listed in tables 4.11, 4.12. The conductance differs by only 0.5%, meaning that the discretization into 3 elements along the cylinder length and the additional 2 elements in the chamfered edge are enough to properly resolve the gas flow through the apertures.

Measurement procedure

During the measurement campaign, there is a drift in the pressure measurement. At the end of each gas injection phase, the zero pressure measurement p_{s0} in the gas source chamber varies; and two subsequent measurements with the same mass flow do not give the same result. If a proper procedure is not defined, this could be a limit to the reproducibility of the measurement. When the value of pressure measurement seems to reach a steady state, a minor pressure drift is still present. The measurements are performed in a transient condition; the cause of the different pressure measured for the same injection rate could be due to

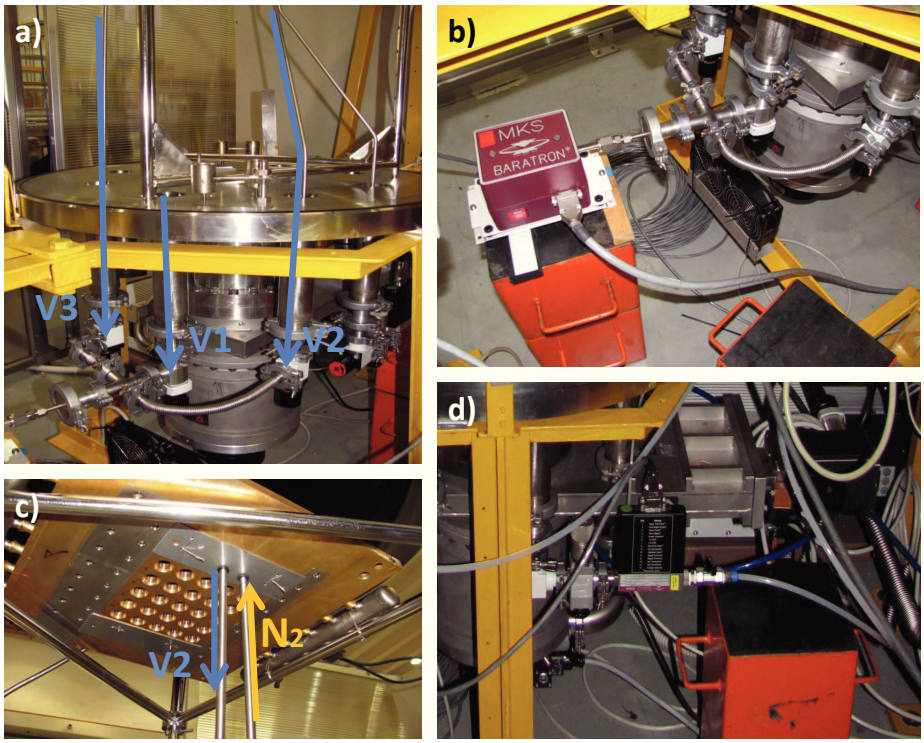
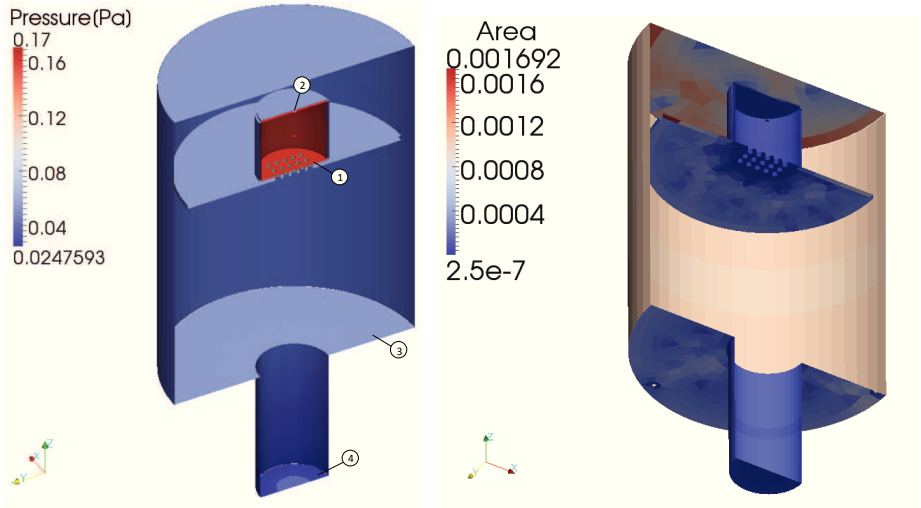


Figure 4.7: Set-up #2: (a) pressure measurements system with three tubes and valves for independent measurements, (b) measurements system with the capacitance head connected, (c) gas injection (nitrogen in this case) and measurement in the gas source, and (d) mass flow meter and controller, F.S. 1000 sccm



(a) (b)

Figure 4.8: (a) AVOCADO model with measurement points highlighted and (b) Fine mesh: Area of the elements.

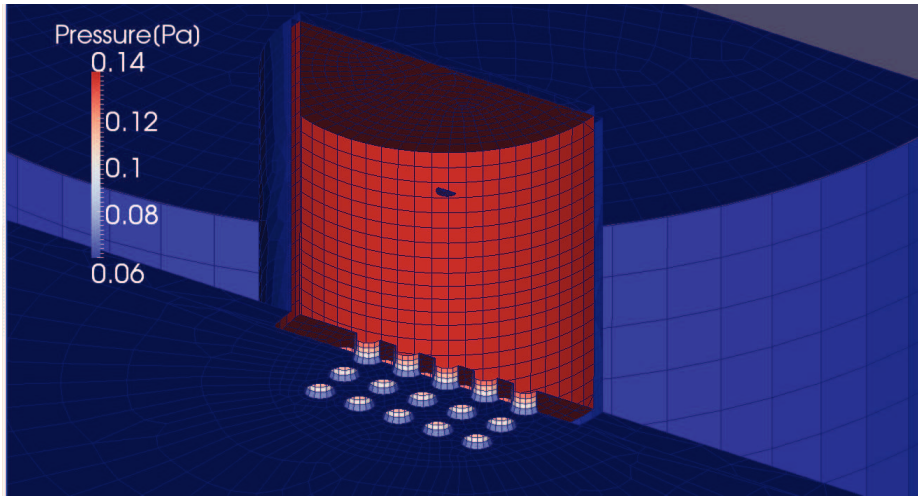


Figure 4.9: Coarse mesh, detail of the source chamber and the multiaperture grid.

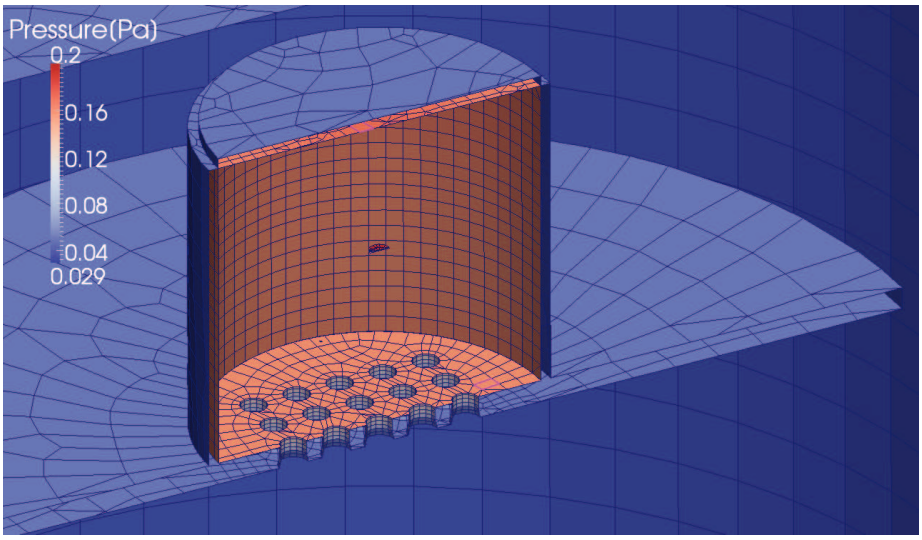


Figure 4.10: Fine mesh: detail of the source chamber and the multiaperture grid.

Data for Nitrogen gas N_2	**Value**
Turbopump S [m3/s]	-1
Turbopump A [m2]	0.01761
Turbopump $\tilde{S}$ [m/s]	-56.7811
Throughput Q [Pa m^3/s]	0.0254
Source pressure @1 (BML) [Pa]	0.1641
Max source pressure @2 [Pa]	0.1769
Chamber pressure @3 (BML) [Pa]	0.0542
Turbopump surface @4 (area averaged) [Pa]	0.0255

Table 4.8: Coarse mesh, simulation results (BML = Baratron Measurements Location)

Gas	Conductance between	@	C [m3/s]
Nitrogen gas, N_2	Source (BML) / Chamber (BML)	1-3	0.2314
	Source (Max) / Chamber (BML)	2-3	0.2072
	Source (BML) / Turbopump	1-4	0.1835
Argon, Ar	Source (BML) / Chamber (BML)	1-3	0.1938
	Source (Max) / Chamber (BML)	2-3	0.1735
	Source (BML) / Turbopump	1-4	0.1536

Table 4.9: Coarse mesh, conductance results at 297K

T [K]	297	293
C [m^3/s]	0.231	0.229

Table 4.10: Coarse mesh, conductance results, Nitrogen gas, N2, @1-3

Gas	Conductance between	@	C [m3/s]
Nitrogen gas, N_2	Source (BML) / Chamber (BML)	1-3	0.2314
	Source (Max) / Chamber (BML)	2-3	0.2072
	Source (BML) / Turbopump	1-4	0.1835
	Source (Probe 10mm from the grid) / chamber (BML)	5-3	0.2332

Table 4.11: Fine mesh, conductance results at 297K

T [K]	297	293
C [m^3/s]	0.234	0.232

Table 4.12: Fine mesh, conductance results, Nitrogen gas, N2, @1-3

local surface conditions in the measurement assembly. For instance, the surface adsorption of the nitrogen gas may not be balanced with desorption and thus the pressure measurement drifts in time; the cause could be as well the accumulation of water in the volume of the measurement assembly. A standard measurement procedure has been defined, as shown in table XX, in order to properly account for this pressure drift. To perform each measurement, 2 minutes are waited after varying the injection rate. Phase (3) is replaced with measurements with 1Torr F.S. Capacitive Head. This measurement is problematic, since the reading oscillates continuously: from campaign #4 the pressure measurement in the chamber is performed with 690A Head.

	gas injection	**V1**	**V2**	**V3**	**measurement**
(1)	OFF	CLOSE	OPEN	CLOSE	p_{s0}
(2)	ON	CLOSE	OPEN	CLOSE	p_s
(3)	ON	OPEN	CLOSE	CLOSE	p_c
(4)	ON	CLOSE	CLOSE	OPEN	p_{c2}
(5)	OFF	CLOSE	OPEN	CLOSE	p'_{s0}

Table 4.13: Standard measurement procedure

The source pressure p_s is corrected accounting for the bias:

$$\tilde{p}_s = p_s - p_{s0} \tag{4.3}$$

In the case of the 690A, the thermal transpiration shall also be considered:

$$p = \sqrt{\frac{T}{T_{690A0}}} p_{690A} \tag{4.4}$$

The pressure difference between the chamber and the source is then calculated as:

$$\Delta p = \tilde{p}_s - p_c \tag{4.5}$$

Experimental errors

In the case of few measurement points, the following formula to propagate the error holds:

$$x = x_2 - x_1 \tag{4.6}$$

$$\pm\, \Delta x = |\Delta x_1| + |\Delta x_2| \tag{4.7}$$

As said before, the bias pressure drifts during the injection test. In addition, it is affected by the length of time the V1 valve is opened, which directly (with a large conductance) connects the measurement assembly to the pumping system. In the measurement procedure, the bias pressure is measured immediately before the gas injection. This is therefore the best possible estimation of p_s0, even though the p_s measurement lasts 2 minutes and during this period the surface conditions can vary and therefore the instantaneous bias. For this reason an additional error, which is due to the apparatus and the measurement procedure, affects the measurements of $\tilde{p}_s$.

$$p_s \pm \Delta p_s \tag{4.8}$$

$$\tilde{p}_s \pm (|\Delta p_s| + |\Delta p_{s0})$$

The value $p'_{s0} - p_{s0}$ is typically positive, and is the range in which the instantaneous bias at the instant of p_s acquisition should be. The error affecting the value of Δp is therefore:

$$\Delta p = \tilde{p}_s - p_c \pm (|\Delta p_s| + |\Delta p_{s0} + |\Delta p_c|) \tag{4.9}$$

In the case of the 690A, the uncertainty of Δp is 0.00025 Pa.

Measurement campaigns with this experimental set-up

measurement campaign #1 The 1000 sccm F.S. flow meter has been used in this campaign. The instrument was new and just calibrated. Pressure in the chamber is measured with a 1 Torr F.S. capacitance head, in a different location. In addition the instrument measures oscillate (the 10^{-5} mbar digit is not significant due to this oscillation). Only pressure measurements from 690A instrument are corrected for the thermal transpiration. Correction for the thermal transpiration effect: 0.96. Conductance fit gives 0.2152 Pa m^3/s. It is noticed that the chamber pressure measurements are 2e-5 mbar lower than measurements through V1. Accounting for this difference, the conductance results 0.2187 Pa m3/s. The mass flow is measured using 1000 sccm mass flow meter. The results are shown in figure 4.11.

measurement campaign #2 The chamber pressure measurements are performed with the 1Torr F.S. instrument, and 2e-5 mbar are added to this measurements. Correction for the thermal transpiration effect: 0.96. The results are shown in figure 4.12.

measurement campaign #3 Correction for the thermal transpiration effect: 0.96. The results are shown in figure 4.13.

measurement campaign #4 Argon gas. Correction for mass flow as described in section 4.1.4. Correction factor for the thermal transpiration effect: 0.96. The results are shown in figure 4.21.

measurement campaign #5 A more appropriate flow meter has been used in this campaign: a 200 sccm F.S. (0.2 slm). There was no calibration certificate for this instrument. The number on the three digit display of the flowmeter shall be converted in slm (for instance 0.01 equals 0.0002 slm). This value is obtained considering not the ideal maximum digits (i.e. 9.99) but the maximum experimentally obtained (9.92). Dividing the nominal F.S. of 0.2 slm by this value, a conversion factor of 0.02016 is obtained. The interpolated data with correction for thermal transpiration is shown in figure 4.17. The linear fit crosses 0,0 point, the vertical error bar is given by the sensitivity of the mass flow meter, that converted in slm is 0.0002 slm. The error bars are smaller but the dispersion of the measured points around the ideal, linear conductance is higher than in the previous campaigns.

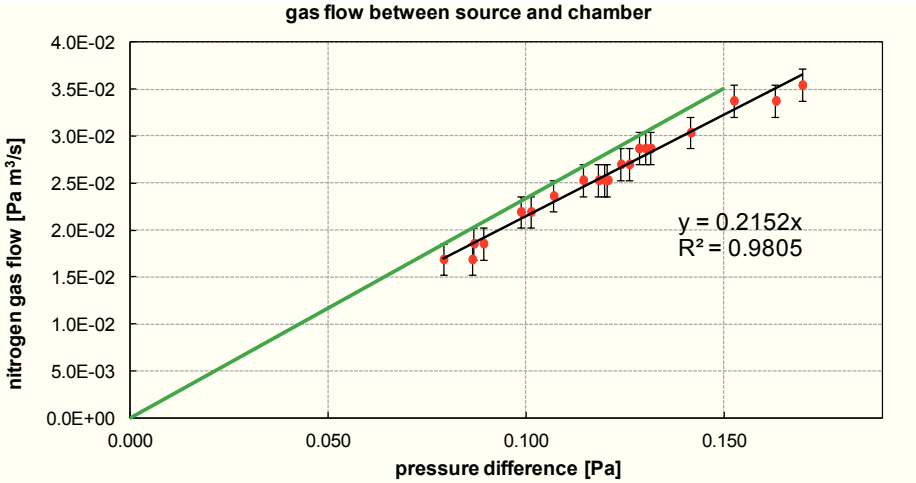


Figure 4.11: interpolated data with correction for thermal transpiration and fit of conductance. The linear fit crosses 0,0 point. Vertical error bars are calculated on the basis of the uncertainty of the flow-meter instrument.

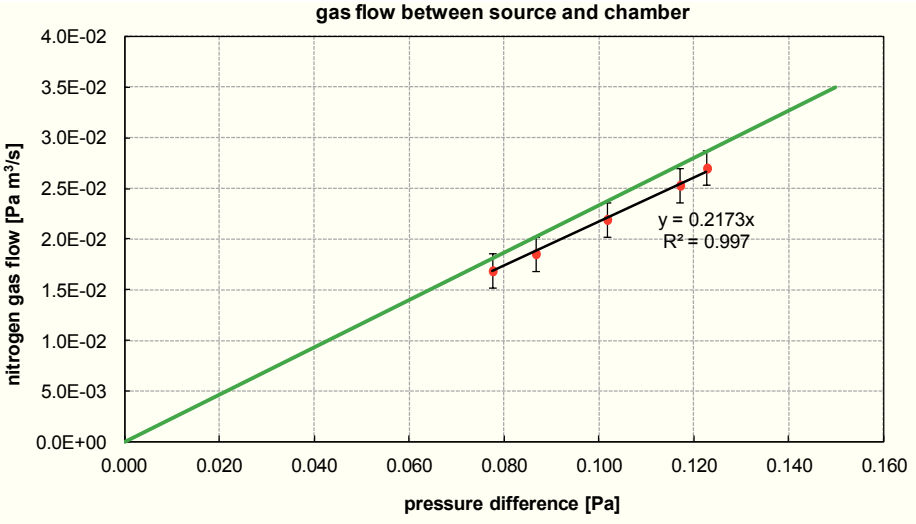


Figure 4.12: interpolated data with correction for thermal transpiration and fit of conductance. The linear fit crosses 0,0 point. Vertical error bars are calculated on the basis of the uncertainty of the flow-meter instrument.

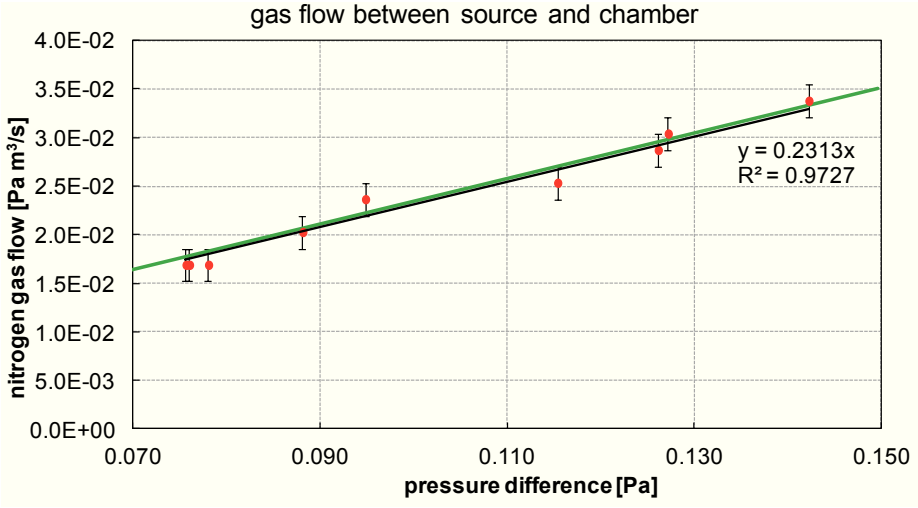


Figure 4.13: interpolated data with correction for thermal transpiration and fit of conductance. The linear fit crosses 0,0 point. Vertical error bars are calculated on the basis of the uncertainty of the flow-meter instrument.

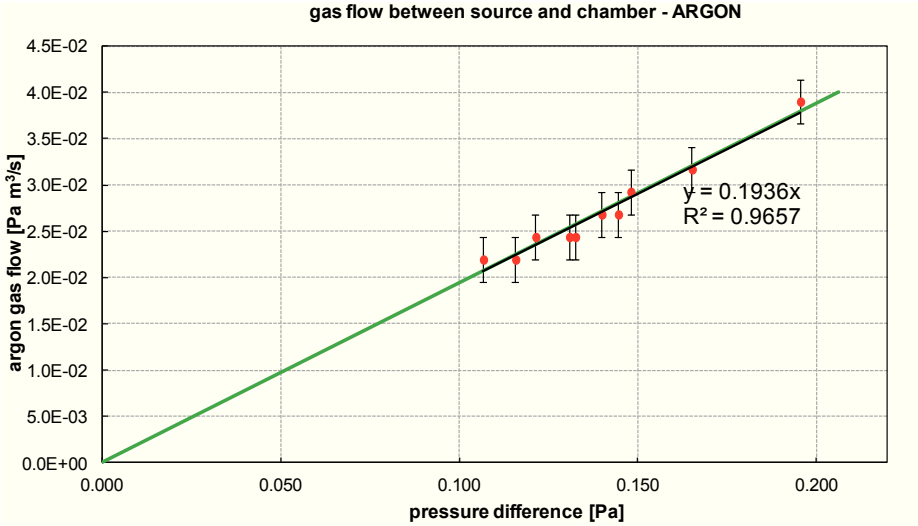


Figure 4.14: interpolated data with correction for thermal transpiration and fit of conductance. The linear fit crosses 0,0 point. Vertical error bars are calculated on the basis of the uncertainty of the flow-meter instrument.

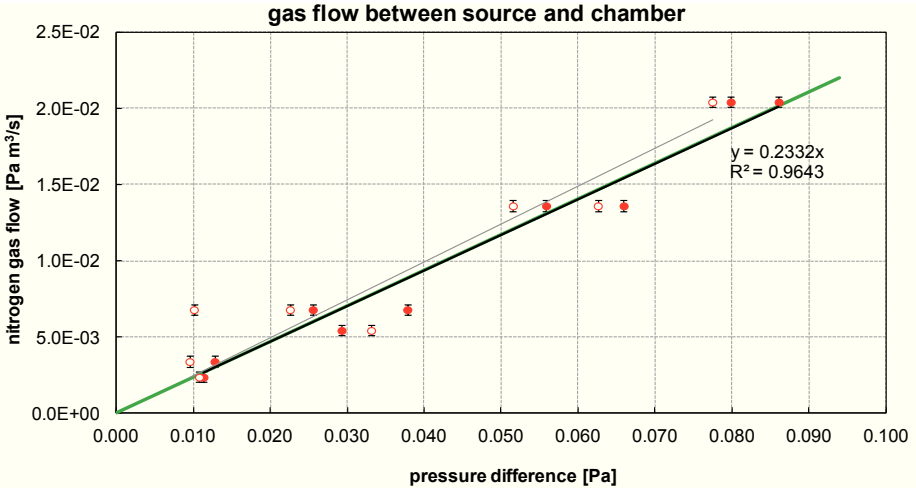


Figure 4.15: interpolated data with correction for thermal transpiration and fit of conductance. The linear fit crosses 0,0 point. Vertical error bars are calculated on the basis of the uncertainty of the flow-meter instrument.

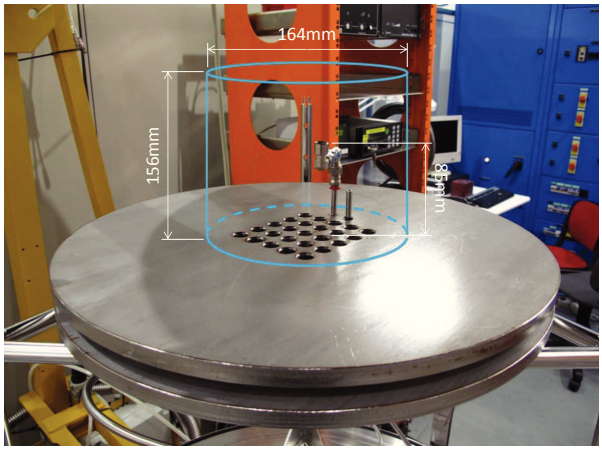


Figure 4.16: Scheme of the source chamber on top of the first grid

4.2.3 Exp set-up n.3 - multigrid set-up

This is a multigrid setup, in which two AISI 304L plates are coupled together with a closed cylindrical duct between them.

AVOCADO models

Applying 0.2 Pa uniform pressure at the top surface of the gas source chamber, a total throughput Q=1.91E-2 Pa m3/s is obtained at 297K. The probe points are shown in figure 4.18. The details of the mesh at the source chamber and the grids are shown in figures 4.19, 4.20, together with the position of the probe point n.3 which accurately reproduces the position of the measurement duct.

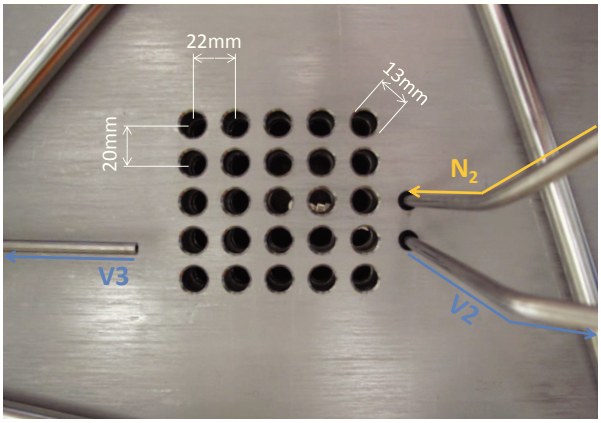


Figure 4.17: Ducts for gas injection and measurements, view from the bottom

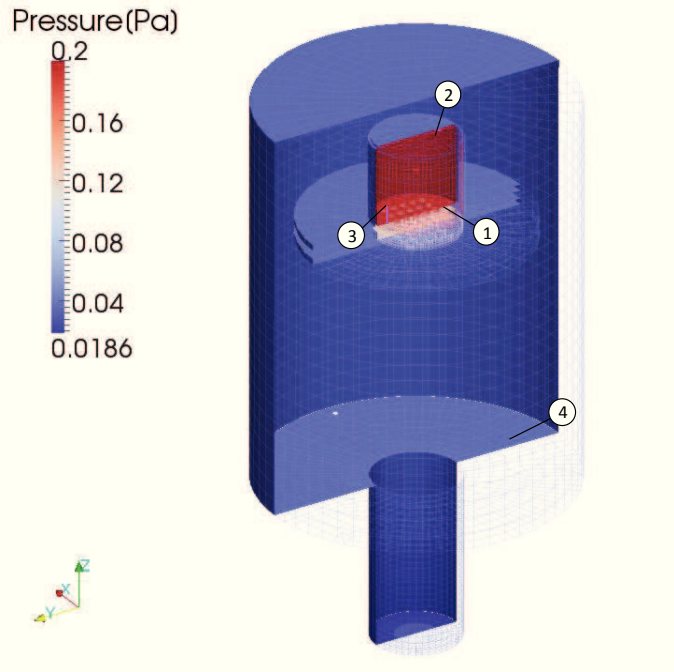


Figure 4.18: Pressure distribution and probe points in AVOCADO model

Extrapolated conductances are listed in table 4.14. Measurements at Baratron Measurement Location BML are to be preferred for comparison with the experimental data. In this experimental setup, the BML in the source is positioned 30mm higher than the first grid; in the model, the pipe cylinder is neglected, and a small surface, normal to the pipe, is placed at the pipe end, oriented in the proper direction. The conductance results are presented in tables 4.14 and 4.15.

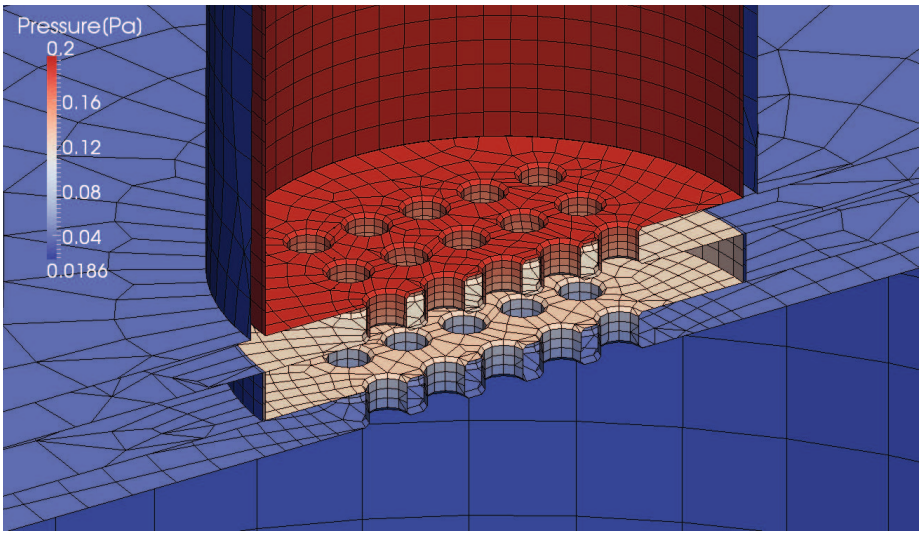


Figure 4.19: Detail of the mesh and pressure distribution in AVOCADO model

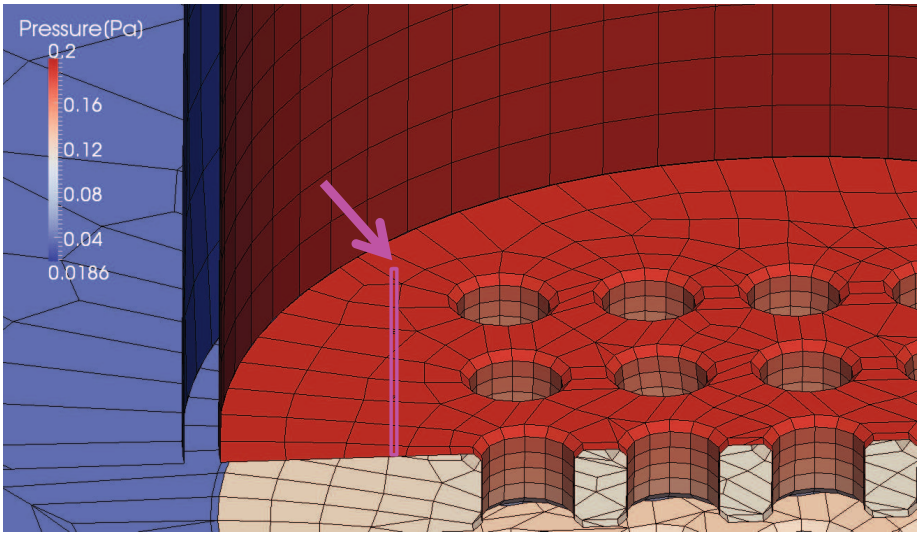


Figure 4.20: Probe point n.3 in AVOCADO model

Gas	Conductance between	@	C [m^3/s]
Nitrogen gas, N_2	Source (grid surface) / Chamber (BML)	1-4	0.1242
	Source (Max) / Chamber (BML)	2-4	0.0.120
	Source (BML) / Chamberl (BML)	3-4	0.1238

Table 4.14: Conductance results at 297K

T [K]	297	295
C [m^3/s]	0.1238	0.1234

Table 4.15: Conductance result, Nitrogen gas, N_2, @3-4

Measurement procedure

Same as 4.2.2.

Experimental errors

As said before, the bias pressure drift during the injection test. In addition, it is affected by the length of time the V1 valve is opened, which directly (with a large conductance) connects the measurement assembly to the pumping system. In the measurement procedure, the bias pressure is measured immediately before the gas injection. This is therefore the best possible estimation of ps0, even though the ps measurement last 2 minutes and during this period the surface conditions can vary and therefore the instantaneous bias. The pressure bias in the source is measured also after the injection, p's0. For this reason an additional error, which is due to the apparatus and the measurement procedure, affects the measurements of $\tilde{p}_s$. For the sake of completeness, instead of considering it as an experimental error, we simply fit an upper limit for the conductance, by using $\tilde{p}'_s$, which is calculated considering the pressure bias p'_{s0}. In the case of few measurement points, the following formula to propagate the error holds:

$$\begin{gathered} p_s \pm \Delta p_s, p_{s0} \pm \Delta p_{s0} \\ \tilde{p}_s \pm (|\Delta p_s| + |\Delta p_{s0}|) \\ \tilde{p}'_s \pm (|\Delta p_s| + |\Delta p'_{s0}|) \end{gathered} \tag{4.10}$$

The value $p'_{s0} - p_{s0}$ is typically positive, and is the range in which the instantaneous bias at the instant of ps acquisition should be. The error affecting the value of Δp is therefore:

$$\begin{aligned} \Delta p &= \tilde{p}_s - p_c \pm (|\Delta p_s| + |\Delta p_{s0} + |\Delta p_c|) \\ \Delta p' &= \tilde{p}'_s - p_c \pm (|\Delta p_s| + |\Delta p'_{s0} + |\Delta p_c|) \end{aligned} \tag{4.11}$$

In the case of the 690A, the uncertainty of p is 0.00025 Pa.

Measurement campaigns with this experimental set-up

measurement campaign #6 Using bias source pressure p_s0, the black linear fit of figure Figure 3 data with correction for thermal transpiration and fit of molecular conductance. The linear fit crosses point (0,0). is obtained, interpolating the red dots. If bias source pressure p's0 is used instead (open red circles), the grey linear fit is obtained. These two lines are the boundaries of the experimental conductance. The black fit is to be preferred, since ps0 is measured immediately before the injection and the measurement of ps, while p's0 is measured after the chamber pressure is measured through V1 and V3. Thermal transpiration correction (22°C) factor is 0.963. The linear fitted conductance is included between 0.1232 m3/s (suggested value) and 0.1259 m^3/s. The value predicted with AVOCADO is 0.1234 m^3/s.

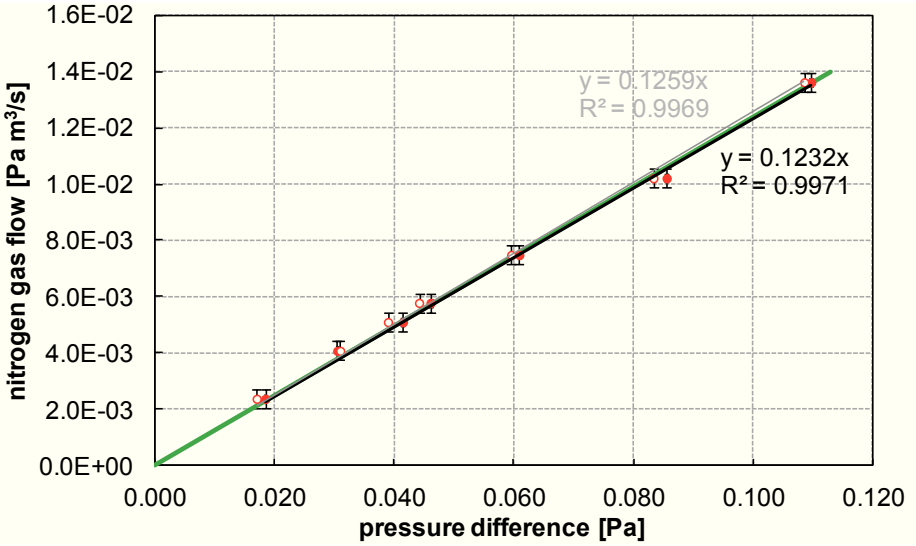


Figure 4.21: interpolated data with correction for thermal transpiration and fit of conductance. The linear fit crosses 0,0 point. Horizontal error bars are calculated on the basis of the uncertainty of the flow-meter instrument.

4.2.4 Exp set-up n.4 - multigrid set-up with lateral conductance

This is a two-grids setup, in which the drilled AISI 304L plates are used as grids with controlled molecular conductance. The grids are 55 mm apart (distance calculated between the two facing surfaces). Later, the set-up has been slightly modified: a radial manipulator has been installed to the lateral ports of the vessel. A 1 m long pipe is suspended exactly in between the grids, which have been moved downwards to allow this. A 1Torr MKS 690A head is attached at the manipulator port; it is not supported from a structure, since any unnecessary force acting non-constantly on the capacitance head influences the measurement. Vibrations during movements occurs, and the measurements are affected; typically, waiting for stabilization is sufficient, but in some cases, calibration/zero reference was lost when not paying enough attention. The accuracy in the position of the movable probe is in the order of 10 mm. The accuracy shall be referred to the center of the apertures array.

AVOCADO models

The detail of the source chamber and the grids in the AVOCADO models are shown in figure 4.23, with - highlighted in pink - the discrete pressure probes along the path of the movable duct (manipulator probe). The axis of the manipulator duct is aligned along the diagonal of the array of 5×5 apertures.

The results, in terms of conductances, are presented in table 4.16.

Moving downwards the grids basically has no effect on the calculated conductances, which are the same. The calculated pressure profile along the path of the manipulator probe is shown in continuous blue line in figure 4.28.

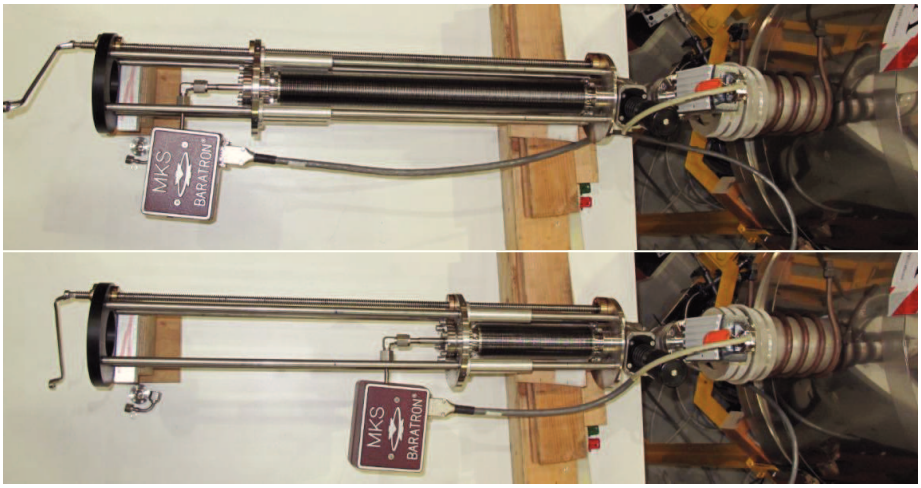


Figure 4.22: Manipulator installed radially on the ARIANNA experiment, in extended (on top) and withdrawn (at the bottom) positions. The travel of the probe is 30 cm.

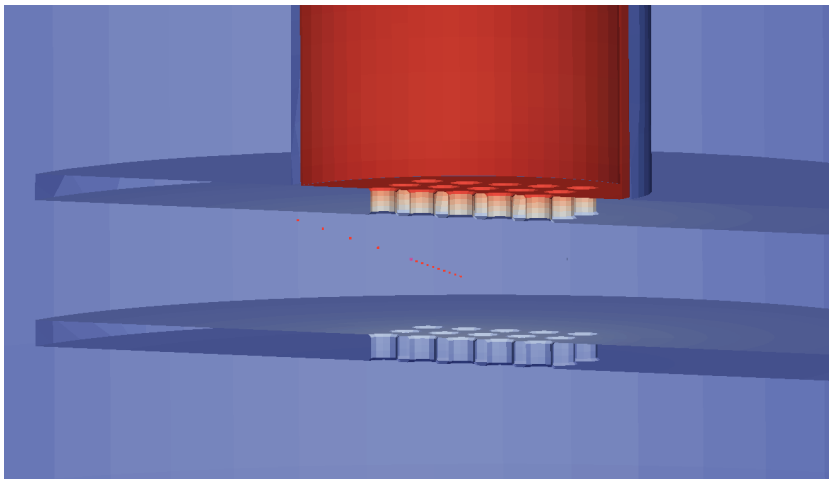


Figure 4.23: Model in AVOCADO of set-up n. 4: pressure distribution and, highlighted, the probe points along the path of the manipulated probe.

	source/ chamber	between grids/ chamber	source/ between grids
Valves in ARIANNA	V2-V1	V3-V1	V2-V3
C [m^3/s]	0.205	1.752	0.232

Table 4.16: AVOCADO-calculated conductances

Measurement campaigns with this experimental set-up

measurement campaign #7 The measurements and the processed conductances are presented in figure 4.24. The measurement of the zero pressure

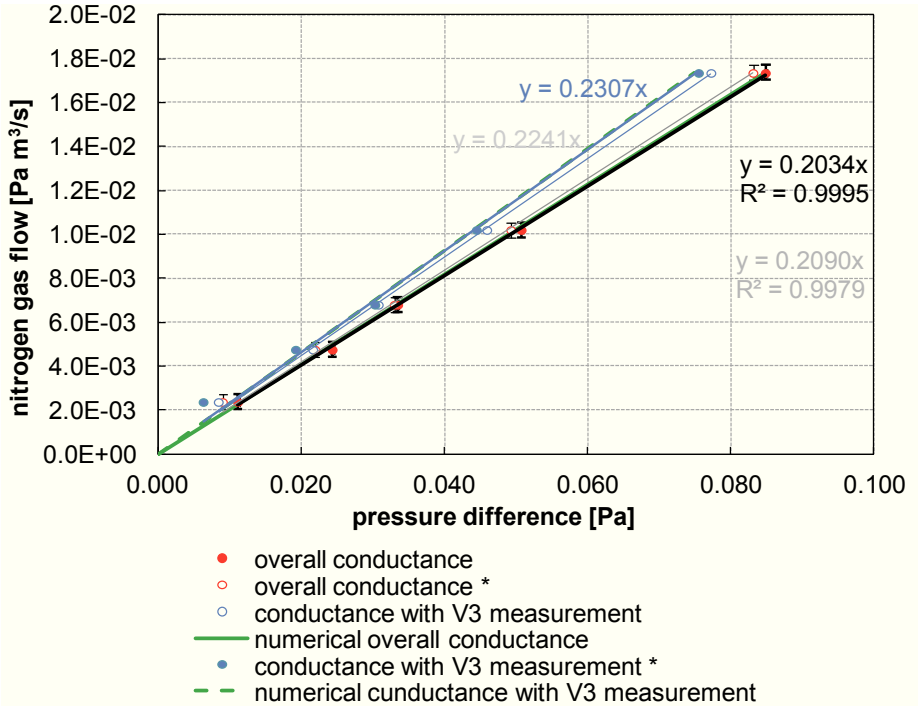


Figure 4.24: Comparison between experimental conductance and numerical results.

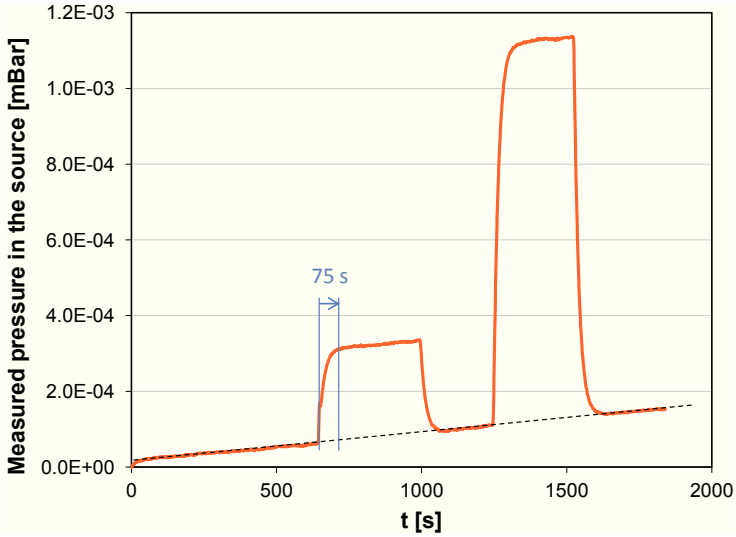


Figure 4.25: Pressure measurement in the source, obtained with the new acquisition system. Two gas injections were performed; the bias pressure is rising linearly. This is probably a long-scale transient, due to surface conditions of the measurement pipe assembly. The time scale for the pressure transient due to the injection is about 75s; the two minute waiting used until now is enough.

(bias) is done at the beginning and at the end of the injection; in the case of the source pressure, the measurement before injection is closer (in time) and is preferred (solid red dots). In the case of the measurement between the grids, the zero measured after the injection is closer and therefore preferred (solid blue dots). The results marked with a * are the other measurements. An acquisition system has been prepared and the measurement procedure has been verified thanks to that; in figure 4.25, the pressure drift is clearly visible. The measurement system reached steady state when directly connected to the chamber; when changing valves to measure the source, a quick transient occurs as expected, followed by a transient with a much longer characteristic time apparently a drift.

measurement campaign #8 The pressure measured for zero throughput is unexpectedly high; the degassing rate has been calculated, assuming a constant value among all the surface ("source" walls and grid surfaces). The total degassing surface that participate in creating the bias pressure in the volume between the grids is about 0.42 m^2. The pressure in the center of the volume is 1e-4 mbar, which equals the pressure increase in that point when a throughput of about 0.05 mbar l/s is injected in the source; distributing the same throughput on the surfaces, the degassing rate would be about 0.12 mbar l s^{-1} m^{-2} (for comparison, this value is orders of magnitude higher than the typical values for stainless steel after one hour pumping). This is possibly due to the rough surface finishing of the laminated grid plates. Having to experimentally live with this, the only possibility is to subtract the zero pressure measurement to each measurement, whatever be the cause of this bias. In figure 4.26, the measured pressure during the campaign is shown. The pressure drift is seen to decrease after the first two nitrogen injections. The measured pressure along the transverse direction is shown for various gas throughtputs in figure 4.27. On one hand, in the volume between the grids, a pressure of about 1E-3 mbar is at the boundary of Kn=1 value; on the other hand, given the high pressure bias in that volume, a pressure as high as possible is preferable. For these reasons, the orange profile in figure 4.27 has

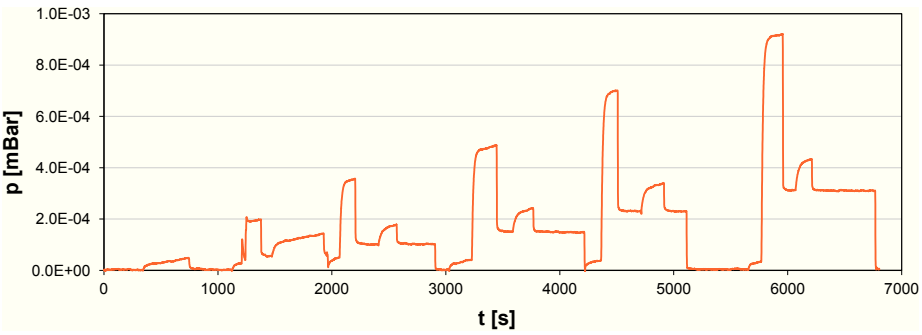


Figure 4.26: Measurement session with various gas injection throughputs; for each throughput, the pressure in the source the chamber and between the grids has been measured with the same capacitive head. The pressure drift is seen to decrease after the first two nitrogen injections.

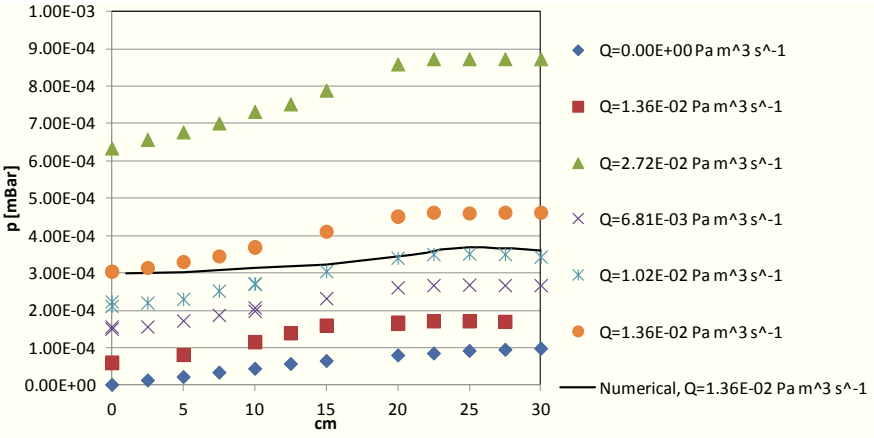


Figure 4.27: Measured pressure along the path of the moveable sensor, for various throughput; the numerical result is given for a single case.

been used for comparison with the numerical data. The difference between the open circles and the blue line could be due to the fact that the main degassing source could be the surface of the grids, therefore moving outward the bump of the profile. On average, the difference between the experimental and numerical data is 3%, according to table 4.17.

4.3 Discussion of the results in ARIANNA

The set-up of the ARIANNA experiment demonstrated a good versatility. The multiple accesses of the vessel allowed many, qualitatively different, measurements. The Avocado code was profitably applied to the various arrangements of the injection chamber (source) and the multi-aperture grids.

The measurement campaigns were performed under various conditions in four experimental configurations. Multiple measurements were performed on the same arrangements in different conditions of the vacuum and with different gases (Nitrogen, Argon).

The results of the Avocado validation are summarized in 4.18, in terms of gas molecular conductance. The initial set-up is not considered here, because

Position [cm]	Corrected measurement [mBar]	Numerical [mBsr]	difference
0	3.03E-4	2.98E-4	2%
5	3.08E-4	3.03E-4	2%
10	3.24E-4	3.13E-4	4%
15	3.46E-4	3.23E-4	7%
20	3.72E-4	3.47E-4	7%
22.5	3.77E-4	3.59E-4	5%
25	3.68E-4	3.68E-4	0%
27.5	3.67E-4	3.67E-4	0%
30	3.64E-4	3.59E-4	1%

Table 4.17: Comparison of numerical results with experimental data

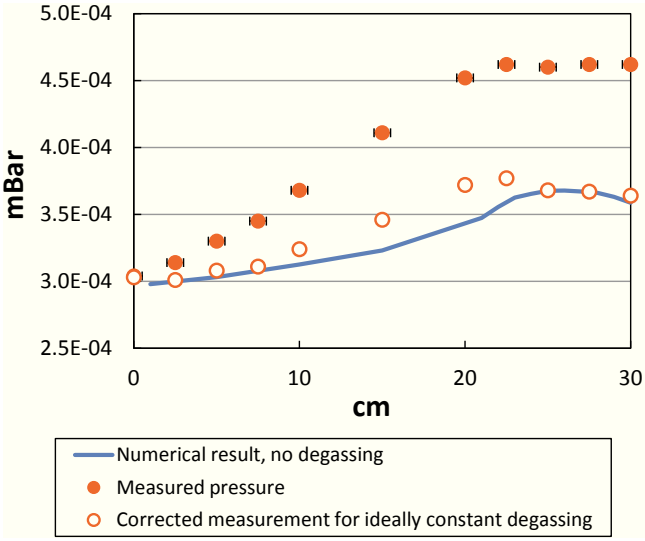


Figure 4.28: Comparison between numerical and experimental profiles, with correction for degassing. An unverified, large error may be involved in subtracting the measured "zero": the degassing rate is a function of the pressure itself. Pressure profile calculated for $Q = 0.0137$ Pa m^3 s^{-1}

of the many problems encountered with that set-up. With the second set-up, the results of the first two campaign measurements gave a large error; if the measurement errors are considered, the difference between the numerical and the experimental values is in the same range of the other campaigns (about 1%). An averaged difference is considered in the case of the pressure profile measured in campaign #8.

These results indicate that the code Avocado is a good tool to calculate the gas distribution in geometries relevant to the electrostatic accelerators.

experim. set-up	measurement campaign #	numerical conductance [l/s]	experimental conductance [l/s]	diff. %
1	1	232	215.2	8% *
	2	232	217.3	7% *
2	3	232	231.3	0%
	4	193.8	193.6	0%
	5	232	233.2	1%
	6	123.4	123.2	0%
3	7	205	203.4	1%
	7	232	230.7	1%
4	8	various points, averaged		3%

Table 4.18: Comparison of numerical results with experimental data; * in the measurement campaign #1 and #2, the measure error is about 7%.

5 Applications

AVOCADO has been applied to the study of various aspects of gas flow and distribution in the ITER NBI and its test facility, MITICA. There are two areas of interest; the sole beam source (BS) and the whole injector. The gas distribution shall be studied to a different detail in the two systems, which share common boundaries and are coupled.

The main purpose of the analyses of the BS is to quantify the efficiency of the ion source and the collateral thermal loads, which originate from the same physical processes that go by the name of stripping. The stripping is linearly dependent on the background gas density, and therefore the gas simulations are very important to support the design of the ion source. The analyses of the MITICA BS are presented in section 5.1.

The analyses of the whole NBI system may give indications on the design of some components that strongly affect the gas conductance towards the cryopumps, or clarify some open issues regarding the transverse homogeneity of the background gas. For instance, the non-homogeneity at the cross sections where the diagnostics are located affect the measurements; of course, also the neutralisaztion may be different for different gas target thickness. The analyses of the injector are presented in section 5.2.

In addition, a benchmarking activity to the MANITU experimental data has recently started. MANITU was an RF driven negative ion source active at IPP during the last few years, and part of the devices aimed at the development of reliable RF divers for the use in ITER NBI. The benchmark of AVOCADO is indirect and is carried out as part of a set of numerical codes that are currently used in the design of MITICA extractor and accelerator. The preliminary results of the benchmarking are presented in section 5.3

5.1 MITICA Beam Source

Unwanted particles - such as electrons and positive ions - are massively produced in the negative ion accelerators, as a result of the charge exchange processes, or stripping, between the high-energy ions and the background gas they encounter

along their drift. In the electrostatic field, these charged particles are accelerated. The electrons are strongly deflected by the presence of the magnetic field B, and take curved trajectories and hit the grids or exit the accelerator spreading heat loads on the beam line components and the cryopumps; the positive ions are counter-accelerated, and focus onto hot-points on the backplate of the plasma source. Therefore, stripping causes both loss of efficiency, with a net reduction of fully-accelerated negative ions, and detrimental effects on the many in-vessel components. The stripping loss L_s can be calculated as described in 1.1.4.

In the framework of the activities aimed at the optimization of the MITICA BS and its final design, the gas analyses played an important role. The first approach that can be considered is the used of lumped circuits exploiting the analogy between gas conductance in molecular flow and conductance in electric circuits. The three-dimensional geometry can be correctly evaluated only using more complex methods, such as numerical gas analyses with Monte Carlo codes. The latter approach used by Krylov and Hemsworth [122] was used as a reference during the design of the accelerator; moving from the conceptual design to the (next) final design, radical changes in the design were introduced and new analyses were necessary.

My activity on the beam source modelling started in year 2011 in concomitance with the development of the Avocado code. From its first implementation, the code has been applied to this study; along with its development and optimization, the models of MITICA accelerator progressively grew in size and complexity. The BS modelling was at the basis of a continuous, challenging increase of simulation requirements, both in terms of quality of the modelled physics and versatility and efficiency of the numerical implementation. Many models were developed, representing the problem at a different scale.

A major move forward in the modelling was the implementation, in the Avocado, of a consistent solution of the gas temperature, as a degree of freedom that is affected by the wall temperature; this is an original contribution to the molecular flow solvers based on the view factor methods. In the particular case of MITICA accelerator, this shall be considered a key feature; the deuterium or hydrogen gas temperature decrease through the system, from the high temperature in the plasma source (up to 1300K) to the room temperature of the Beam Source Vessel (BSV). Our understanding of the issues also evolved during this year. When first facing the gas simulation in MITICA operating condition, the simulation techniques had to be determined; the definition of filling pressure and the procedure used by IPP to operate the RF sources were at the basis of this (see section 5.1.4). Another example is the definition of the gas temperature that shall be properly used as boundary condition in the plasma source; according to most recent measurement interpretations by IPP [123], it shall be about 1150K before the plasma grid (PG) in deuterium. Early simulations were performed assigning 2000K as gas temperature in the plasma source. A lower temperature in the plasma source means an overall higher density along the beam path. In the meanwhile, the Avocado code has been validated (molecular flows in constant temperature) in a dedicated experiment (Arianna, A Rarefied Instrumented Atmosphere for Neutrals iNjection Applications), with very good results in different geometries relevant to electrostatic accelerators. The benchmarking activity has now moved to the study of Manitu, together with the complete set of codes used at Consorzio RFX for beam modelling.

The new contributions of my activities are:

- The modelling of the MITICA BS using a different technique than in the past; the AVOCADO results are consistent with previous results, and in addition have a very good spatial discretization.
- The calculation of the gas distribution in up-to-date geometries, and the support of the design comparing different designs and solutions;
- The evaluation of the transverse non-homogeneity of the gas density and therefore the stripping losses;

This chapter is divided into four sections. Two simple models are presented in section 5.1.1, to offer comparison with analytical results and evaluate the applicability of simplified lumped models. Section details the mono-beamlet models that were initially used to gain a better understanding of the gas flow A simple approach, that is to build a lumped circuit with numerically calculated conductances, is described in section 5.1.2. Also a preliminary study regarding a simplification of the models is commented, that is, the influence of the post insulators in the lateral pumping of the accelerator is evaluated. Section 5.1.3 reports the simulations carried out on slice models of increasing size. The geometries at three design stages are also compared at room temperature. From spring 2012, AVOCADO could solve consistently the gas temperature and density; its application to the 1/8 model is presented in section 5.1.4. The model of 1/4 of the beam source, which at last comprises the vertical conductance of the support frames, is presented and discussed in section 5.1.5.

In less than two years, the number of elements in the BS models grew from 10100 of a mono-aperture slice (10 apertures, April 2011) to 183000 of a 1/4 model of the source (320 apertures, October 2012).

Beam Source geometry: a challenge of complexity

The geometry of the BS is shown in figure 5.1. The neutral gas flows out of the ion source at higher pressure (0.3 Pa nominal maximum pressure) through the 1280 plasma grid (PG) apertures, and reaches the low-pressure vessel (0.02 Pa nominal pressure) by going across the grid apertures, but mostly through the lateral conductances offered by the support frames. The negative ions, extracted by the extraction grid (EG) and accelerated by the five acceleration grids (AGs), suffer stripping losses along their path. The gas distribution is thus important to quantify and optimize the accelerator efficiency.

The operating pressure of an RF-source is defined at room temperature as the filling pressure pf , which is foreseen to be maximum 0.3 Pa in the ITER HNB ion sources. The deuterium D2 throughput in the ion source is regulated in the absence of plasma until this target pressure is reached [124]. The pressure distribution as well as the gas throughput when gas enters the system at room temperature is important to characterize the behaviour of the accelerator.

The details of the geometry, such as the distance between the grids, the diameters and the shapes of the apertures, evolved during the optimization of the beam optics; but the following general issues of the BS model the can be identified:

1. there is a number of apertures that shall be detailed to a good level in the gas simulations;

2. the curved shape of the support frame;

3. there are many minor features: the non co-planarity of the grids, the cylindrical post-insulators...;

4. a large number of meshes shall be used: when calculating the view factors, the numerical complexity grows at least with the power of 2 of the number of meshes.

An additional difficulty is the fact that many features were continuously modified in the optimization of the beam optics: the shape of the apertures, the distance between the grids and their thickness.

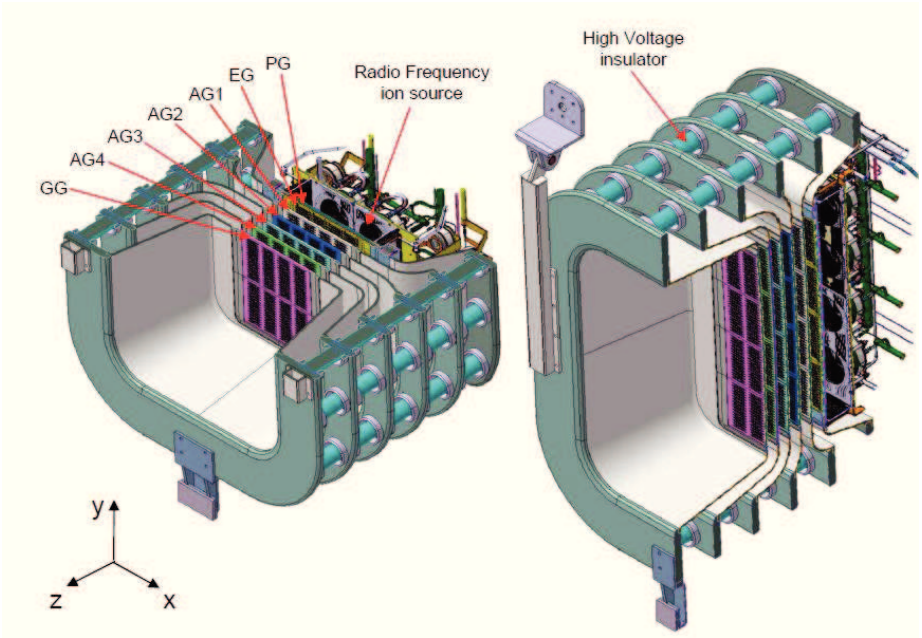


Figure 5.1: Horizontal and vertical sections of the MITICA beam source (BS), in a recent design (2012). The gaps between the support grids are clearly visible; they constitute a lateral conductance to the beam source vessel (BSV).

Applicability of a collisionless solver

The mean free path can be calculated as described in section 2.1.4. The resulting Knudsen number Kn as a function of pressure p is, in the case of H_2 flow in this domain, is shown in figure 5.2, based on the equation:

$$\mathrm{Kn}(p) = \frac{k_B T}{\sqrt{2}\pi d_{D_2}^2 p} \cdot \frac{1}{L} \tag{5.1}$$

In the accelerator, the elastic m.f.p. is in the range of 10 cm. The Kn number is around 1 considering a characteristic length of 0.1 m, and it goes above 1 if the diameters of the apertures is considered instead. Across longer distances, gas-gas interaction can actually occur.

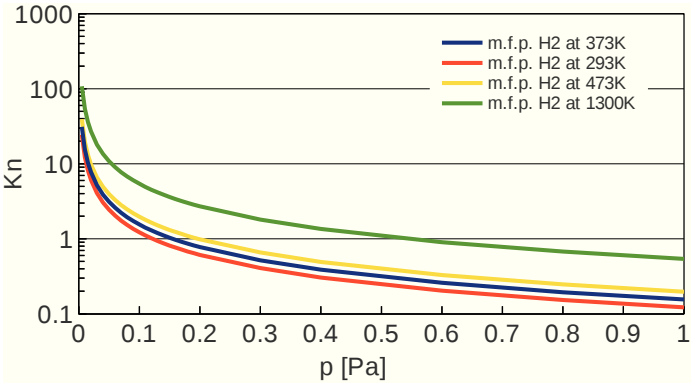


Figure 5.2: Knudsen number Kn, H_2 gas, 0.1 m characteristic length.

5.1.1 Mono-beamlet models

In order to offer a quick comparison with analytical results, two handy, simple models have been prepared, representing the path of a single beamlet across the apertures of the accelerator. Molecular flow is a linear problem, and the extrapolated gas conductance is a constant value, not depending on the pressures or throughputs set as boundary conditions.

Figure 5.3-a shows a single beamlet model with no lateral conductance: the grid gaps are closed chambers, connected by single grid apertures, and the neutral gas can only exit from the AG5. The diameters and lengths of the grid apertures are those presented in Fig.1 (b). The AGs are 17mm long, with apertures of 16mm diameter. The gap between grids is 85mm wide, 6mm in the case of PG-EG. The gaps in the model have a width/length ratio of at least 4, in order to minimize any boundary effect creating a chamber in which only the grids' parallel surfaces matter.

The model was finely meshed with 16000 surface elements, and required 52 min CPU time for view factor matrix calculation (350 sec wall time with 14 parallel threads) and 3 minutes to solve the system. Results obtained with much a coarser mesh (5000 elements, 20 sec wall time on 14 threads), refined only at the apertures, differ by 6% maximum. On average, in this case the neutral gas exits the system after a great number of surface rebounds (80000). The total D2 throughput calculated at room temperature (295 K) is 1.388 Pa·m^{3}s^{-1}. The conductance C between connected chambers can be calculated from the numerical results as $C = Q/(P1 - P2)$.

In table 5.1, numerical results are presented together with the expected, analytical conductance C_{anal}. The conductance of cylindrical, short ducts is calculated as $C_{anal} = 3.81\alpha d^3(T/M)^{1/2}/l$ [8], where the diameter d and length l of the aperture are expressed in cm, M is the molar mass, T is the temperature in Kelvin; correction factor $\alpha = 0.44$ [8] is used for short tubes. In the case of conical apertures, the effective conductance is obtained dividing the length of the cone into cylinders of intermediate diameter. The numerical conductances between adjacent gaps, conform to the analytical values in the case of the AGs. A higher difference is appreciated in the case of the first grid (PG). This difference is due to the technique used to reduce the cone to analytically solvable discontinue cylinders (see figure 5.3-b), which is an imprecise and unpractical

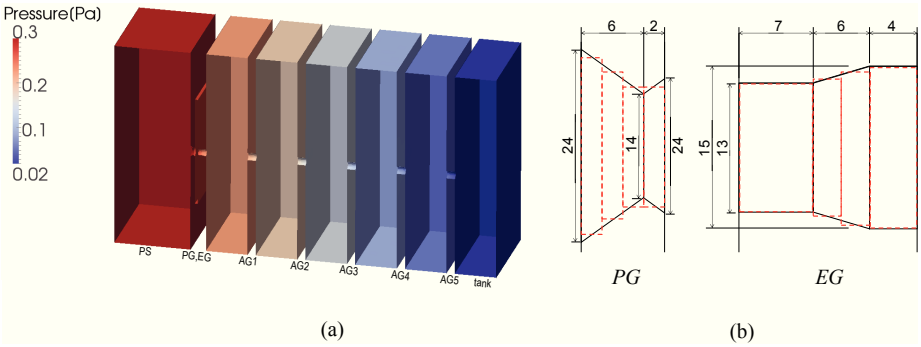


Figure 5.3: Single beamlet model used for comparison with analytical conductances (a): the gas flows from the plasma source PS on the left , out to the vessel on the right; dimensions (in mm) and reduction of conical apertures to cylindrical ducts, in the case of the PG and EG grids (b).

	source	**PG, EG**	**EG, AG1**	**AG1, AG2**	**AG2, AG3**	**AG3, AG4**	**AG4, AG5**	**tank**
p [Pa]	0.3	0.279	0.220	0.179	0.140	0.101	0.061	0.02

aperture:	**PG**	**EG**	**AG1**	**AG2**	**AG3**	**AG4**	**AG5**
C_{num} [$m^3 s^{-1}$]	0.062	0.023	0.033	0.034	0.034	0.033	0.033
C_{anal} [$m^3 s^{-1}$]	0.041	0.023	0.034	0.034	0.034	0.034	0.034

Table 5.1: Pressure in gaps and comparison of numerically calculated conductances C_{num} to analytical conductances C_{anal}, Deuterium gas.

procedure.

Figure 5.4 shows a single beamlet model that has been used to quantify the importance of the molecular beaming effect, from the beam source chamber towards each grid gap. This model was prepared to test the applicability of lumped models: they are a common approach to vacuum system modeling, but may easily lose validity, in the case of complex geometries, but even in simpler cases when molecular beaming effect is expected. It occurs in molecular flows when the gas finds a preferential way along the axis of a duct of a certain length, or co-aligned apertures. In this small model, deuterium cannot cross the grid apertures after rebounding on the grid surfaces, and this gives a quantitative indication of this effect.

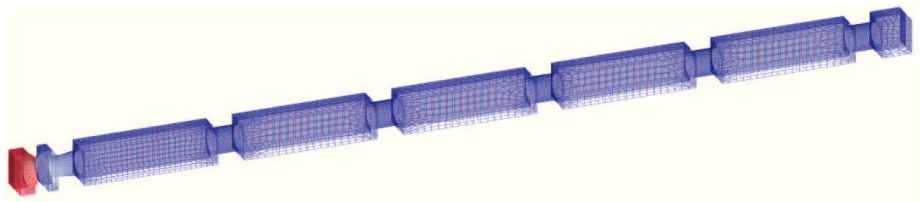


Figure 5.4: Single beamlet model (horizontal section) used to quantify the molecular beaming effect. Between the circular apertures, the rectangular boxes are virtual boundaries at constant pressure, from which the gas particles only exit.

By increasing the EG thickness, the flow partitioning is redistributed, but in any configuration tested, less than 0.5% of the gas flow is directly canalized through the AG1, without bouncing at the planar surfaces of the grid. Thickening the EG grid from 11mm to 17mm, the gas fraction exiting from PG-EG gap increase from 74% to 77% and that from EG-AG1 gap decrease from 25% to 22.5%. Simplified analytical calculation confirms, for instance, the quota beamed to EG-AG1 gap: assuming the gas enters from the center of the plane of minimum cross-section of the PG aperture, with cosine distribution $F = cos\theta/\pi dA$ projected on a unit sphere of surface area $dA = sin\theta d\theta d\phi$, the gas fraction beamed will be

$$\int_0^{2\pi} \int_0^{\theta} \frac{cos\theta}{\pi} sin\theta d\theta d\phi = sin^2\theta \tag{5.2}$$

Using the proper distances and aperture radius, it results that 8% molecules are directly beamed out of the EG aperture, and half of the 32% hitting the aperture's internal surface will bounce forward, confirming the numerical percentage of 24%. The outcome of this simple study is that the beaming effect is basically negligible after the AG1 gap: the axial conductances of the acceleration grids are independent, while the PG and EG apertures are coupled by molecular beaming effect. This result justifies the use of lumped models to estimate the gas flow through the accelerator as a first approximation, on condition that the PG-EG apertures be treated as an unicum. But with this technique, only an average pressure of each gap between the grids could be obtained, relevant to a central beamlet. Non-homogeneity along transverse directions cannot be appreciated, and neither the coupling between near apertures. Furthermore, the lumped parameters should be accurately calculated: parallel surfaces may hardly approximate the drilled grids, and the shape of the support frame, similar to that of bathtubs, determines lateral conductances towards the beam source vessel that should be calculated with care. For these reasons, an integrated model of the accelerator gas domain is to be preferred, despite the complexity and computational cost it implies.

5.1.2 Numerical characterizations for a lumped model

To ensure the voltage holding, the structural support of two subsequent grids is provided by 18 ceramic breaks, the so-called post-insulators, placed all around the support frame. In order to simplify the accelerator models, we tested the influence of their presence on the lateral conductance. The particular case of the AG4-AG5 support frames is shown in figure 5.5: with the post-insulators cylinders, the conductance between the volume between the grids (0.3 Pa assigned at beamlet group surfaces) and the lateral exit surface (tank pressure) is reduced only by 3%, being the calculated lateral conductance of 33.4 instead of 34.1 $m^3\ s^{-1}$ in the case of D_2 at room temperature.

5.1.3 Slice models: Preliminary study and Comparison between different frame designs

As stated before, the models of MITICA accelerator progressively grew in size together with the capabilities of the Avocado code. In this section, these intermediate progresses are reported and commented. In section 5.1.3, the evolution

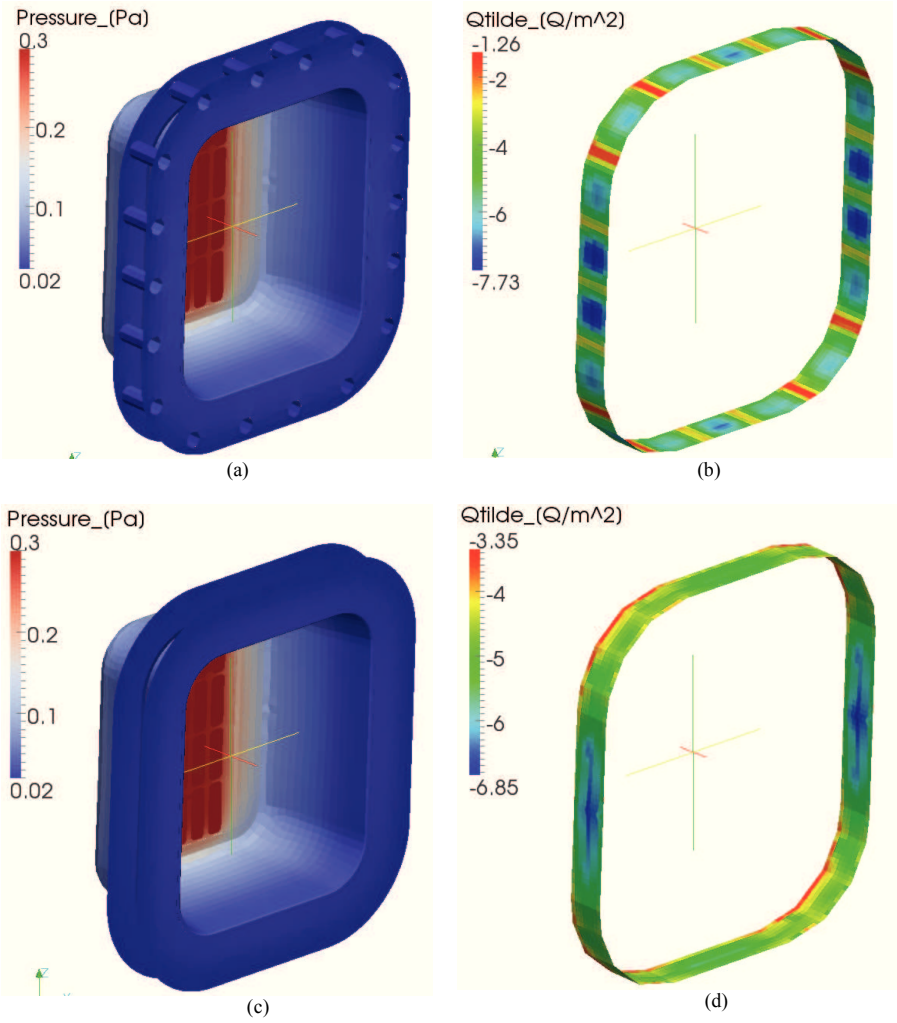


Figure 5.5: Horizontal and vertical sections of the MITICA beam source (BS), in a recent design (2012). The gaps between the support grids are clearly visible; they constitute a lateral conductance to the beam source vessel (BSV).

of the Beam Source support frames and grid thickness is also reported from the point of view of the AVOCADO simulations.

Horizontal slices of the accelerator were modelled and tested. The simulations are run with domains of increasing size and number of elements, until the maximum acceptable mesh dimension is reached in terms of computational time and cost. The frame and support structure design is updated to April 2011.

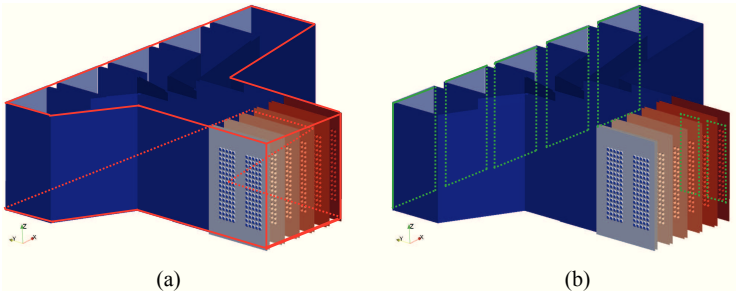


Figure 5.6: Boundary conditions applied: (a) symmetry and (b) constant pressure p_{tank}=0.02 Pa. The different colors represent the various "materials" used in AVOCADO to model the different boundaries, and the grids.

The slice models all share the same geometry, the 2010 design (Geom A). The accelerator has a thin, 11 mm thick extraction grid, 20 mm thick acceleration grids, and the support frame design as of 2010. The slice models also share the same BCs (those shown in figure 5.6):

- Pressure 0.3 at the knife edge of the PG apertures (in correspondence of the narrowest section);
- Pressure 0.02 at AG5 aperture (exit section);
- Pressure 0.02 at frame lateral apertures;
- Symmetry at the bottom and top planes.

The boundary condition at the inlet is imprecise, and the whole PG aperture should be modelled; as discussed later, the gas conductance is increased by some 8% in this way.

Boundary condition of Symmetry

The options that have been evaluated to represent a symmetry boundary were:

- to model the plane of symmetry using solid surfaces (with zero throughput);
- not to model the symmetry plane.

Generally speaking, a fully implemented boundary condition of symmetry (or periodic repetition) would not reduce the computational complexity, since each surface element would be virtually mirrored doubling in this way the computational cost. On the other hand, according to our understanding, the simple symmetry condition (neglecting the elements beyond the symmetry plane) is inapplicable to the used method of the view factors: correctly there will be no net flux across the symmetry plane, but the gas fluxes will be partially neglected.

Therefore a quasi-symmetry condition, for which the condition "no net gas flux crossing it" is verified, is possible. We have decided not to model the symmetry plane. If no symmetry plane is modelled, no net flux occurs at the symmetry plane; no molecular flow towards the symmetry plane is considered at all in the system of equations. Therefore, the total flux from the existing boundaries in the proximity of the symmetry plane is probably reduced. The distance of the boundaries from critical areas of the geometry is therefore a key factor that has an influence on the results. The presence of this boundary condition may have strong effect on the results. The first applied cases (thin slices) presented in this section might have little physical meaning and are only aimed at the understanding of various aspects of the problem; by increasing the volume/boundary ratio we can have a hint of this effect at the edges of the domain.

As stated before, no net flux occurs across a symmetry plane; no molecular flow towards the symmetry plane is considered at all in the system of equations. This means that in a "slice model" the effective lateral conductance is underestimated since only a small part of lateral conducting boundary is modelled. As a consequence of this, increasing the dimensions of the domain up to the height of a grid segment, the pressure inside the gaps progressively decreases. This trend is also verified in the quarter model.

Overview of the preliminary models

The four models developed along with the AVOCADO code are presented in figure 5.7 and discussed in the following. The gas is molecular hydrogen H_2, with molecular mass 3.347e-27 kg, at constant temperature of 293 K. A quick comparison between the models is proposed in figure 5.9, where three pressure profiles along the accelerator are plotted.

Slice model #1, single aperture high This analysis was carried out on an unstructured mesh that reproduces a horizontal section of the MITICA accelerator geometry. The beamlet groups (16x5 beamlets) were reduced to groups of 1x5 beamlets. This test may have little physical meaning, but was a good and quick test for the code. The pressure distribution is presented in figure 5.7(a). The mesh has 10123 elements, 224 of which are triangular.

Slice model #2, five aperture high The height of the slice has been increased, and the model now reproduces groups of 5x5 beamlets (figure 5.7(b)). The used mesh has 36596 elements, 705 of which are triangular. Some post-processing was carried out on this model: the pressure distribution on the downstream face of the PG together with the linearized profile along the transverse direction, for instance. The PG-EG gap is connected, laterally, with the EG-AG1 gap and the gas can exit from the side; the strong pressure gradient that is seen in the plot is due to this reason. The PG-EG gap is closed in the later designs. The gas specific throughput at each PG aperture was also calculated, obtaining a non-homogeneity of about 50% between the inner apertures and the lateral ones; this difference is necessary to balance the pressure gradient immediately downstream.

Slice model #3, one row of apertures, one segment high The height of the slice has been increased to the height of a grid segment (about 400

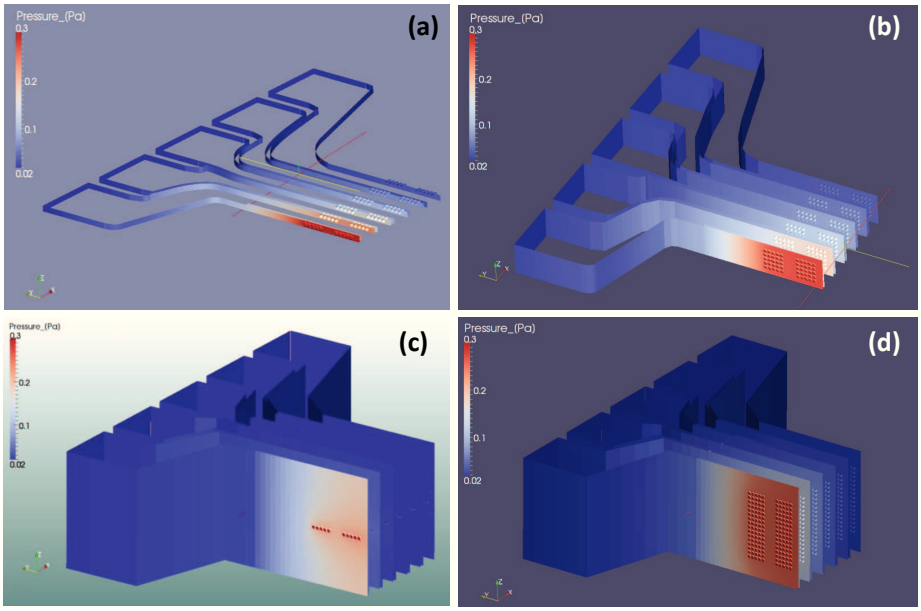


Figure 5.7: Four preliminary models: (a) slice model #1, 10 apertures; (b) slice model #2, 50 apertures; (c) slice model #3, 10 apertures, one grid-segment height; (d) slice model #4, model of one grid segment.

mm), but only one row of apertures was modelled. This model was, in part, aimed at studying the effect of the imprecise boundary condition of symmetry, and evaluating the mesh size around the grid apertures. Focusing in the zone on top and bottom of the aperture row, the pressure distribution indicates that an additional gradient along vertical direction exists in the area immediately on top and bottom of the aperture row. This effect is only partially due to the vertical extension of the lateral conductance; since there is no gas flow exiting the domain through the top or bottom of the model, the apertures of the successive grid exert an effective suction on that area, up to a certain angle. This pressure gradient is slightly detectable, in the horizontal direction, even between the two beamlet groups (see figure 5.7(c)) The pressure profile between the grids and the values of conductance of this model are not directly comparable with results from previous simulations, given the notable difference of lateral conductance.

Slice model #4, 160 apertures, one segment high A horizontal half of the grid is modelled (figure 5.7(d)), together with the support structure. This domain has been represented in a lumped model, in order to have an indication of its validity. The lumped conductances were calculated considering the same height. The comparison between the results is given in figure 5.8. This model is discussed also in the following, when the comparison between different designs of the beam source are compared.

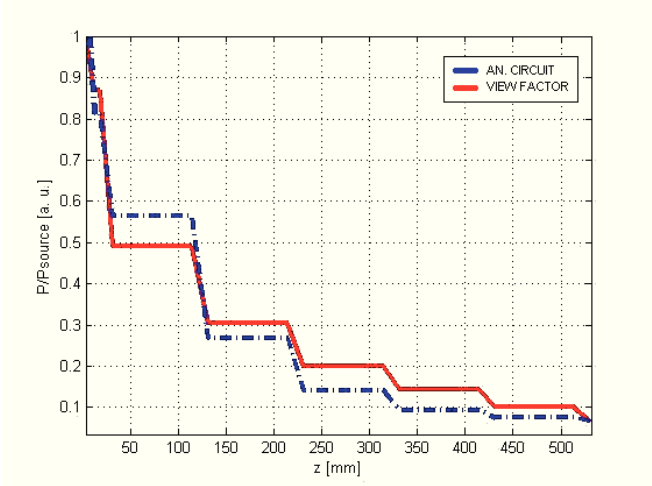


Figure 5.8: Comparison between slice model #4 and a lumped model of an analogous gas domain. The lateral conductance were calculated considering rectangular slits, and the curves of the support frames were accounted considering the proper angle [169].

Comparison between different frame designs

During the design optimization of the MITICA multi-gap accelerator, various geometric combinations have been studied by using the slice model. Figure 5.10 shows how the slice models are applied to the beam source.

The shape and thickness of the extraction grid and the five accelerator grids, the distance between them, and most important the aperture diameters, which greatly influence the gas conductance. Three case studies are presented in the following, which share identical boundary conditions and are therefore fully comparable:

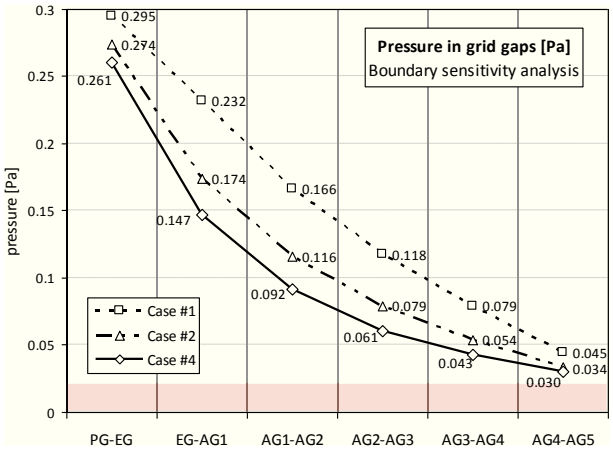


Figure 5.9: Pressure calculated in the grid gaps with the three slice models: the pressure decreases with the increasing of the lateral conductance.

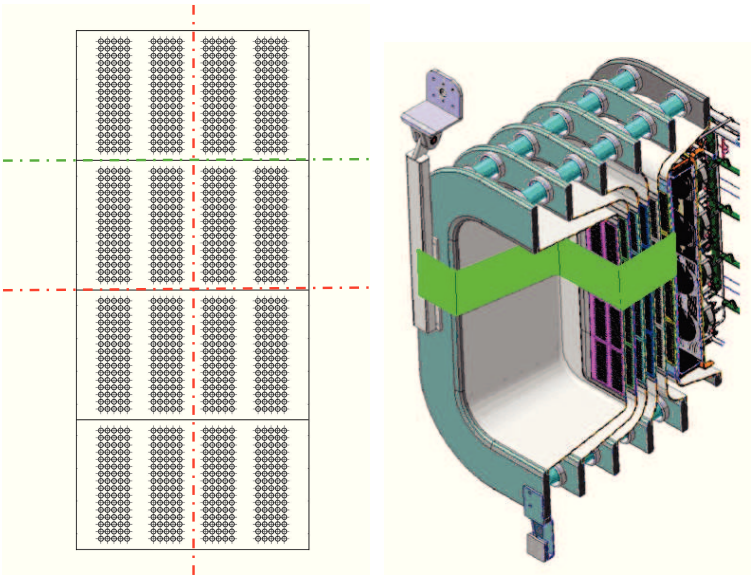
1. The gas temperature is set to 297 K, with no variation allowed inside the domain;

2. The tank pressure at the lateral boundaries and downstream the AG5 is 0.02 Pa, which is in line with the requirements for the neutral gas pressure between beam source and neutralizer in the ITER HNB vessel (H_2 0.025 Pa, D_2 0.02 Pa [125];

3. In the first 3 cases presented in the following, the source pressure pf has been applied at the knife edge (section of minimum diameter) of the PG aperture, in order to reduce the computational complexity: that said, a conductance in series of the 1280 converging cones should be added to the results of in the following, thus reducing the total conductance and throughput. The results of a fourth, complete model (accelerator and plasma source) are also presented;

4. The geometry had to be simplified. For symmetry reasons, the accelerator model is limited to half a slice 500mm high, and no net flow out of the domain across the top and bottom boundaries is allowed: these boundary conditions should represent the conditions of a central grid, yielding an upper limit of the neutral gas pressure distribution.

5. The curved support frames were reduced to planar segments, which simplify the hidden surface determination, reducing the computational cost while maintaining the correct lateral gap allowance/clearance. Figure 4 shows the comparison of two designs simplified for calculations (2010 and present frame design compared).



(a) (b)

Figure 5.10: (a) Four grid segments and (b) section of the beam source, with the region represented by the slice model highlighted in green.

The grids' support frames have been redesigned in 2011, moving forward the concave support frames, in the attempt to enhance the lateral conductance of the first two gaps, being these the most influencing lateral conductances. The new design is showed in figure 5.11, together with the previous one.

Geom A The 2010 design (Geom A) has a thin, 11 mm thick extraction grid, 20 mm thick acceleration grids, and the support frame design as of 2010. According to our calculations, at room temperature about 47% of the mass flow exits from the first lateral gap (24% from the second).

Geom B The intermediate design (Geom B) has 15 mm thick extraction grid and the present support frames. With the new frame design, the gas exiting from the first gap is 43% and 26% from the second: even though the new design was aimed at enhancing these lateral conductances, the gas fraction exiting from the first gap is reduced because there is no more an open gap between the PG and the EG connected to the EG-AG1 gap.

Geom C features the same characteristics of the present accelerator design, with equal thickness grids (EG and AGs) of 17mm (same geometry described in fig 1 (b). In this case, the fractions of gas flowing out the first gaps are 41% and 26%.

Geom C+PS The slice model of the accelerator with the plasma source chamber is Geom C+PS: pressure reductions are appreciable also immediately before the PG and inside its apertures and the total throughput is reduced by about 7%.

In table 5.2, the total throughput calculated for each case is presented. The slice models that were used represent only 1/8 of the accelerator, and there-

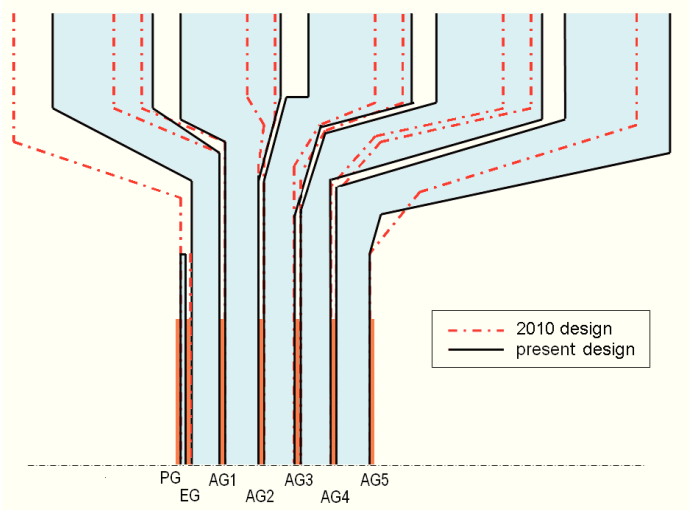


Figure 5.11: Simplified sketch of the horizontal sections used to represent the support frames: the gas domain between the grids and the frames is highlighted in blue, the 2010 design is shown in red.

Case name	A	B	C	C+PS
EG, AGs thickness [mm]; (support frame)	11, 20 (2010 design)	15, 20 (2012 design)	17, 17 (2012 design)	
total Q_{D_2} [Pa m^3 s^{-1}]	3.76	3.68	3.64	3.39
$\bar{p}_{gap,PG-EG}$ [Pa]	0.261	0.259	0.260	0.243
$\bar{p}_{gap,EG-AG1}$ [Pa]	0.144	0.142	0.137	0.128

Table 5.2: Calculated total throughput for considered configurations.

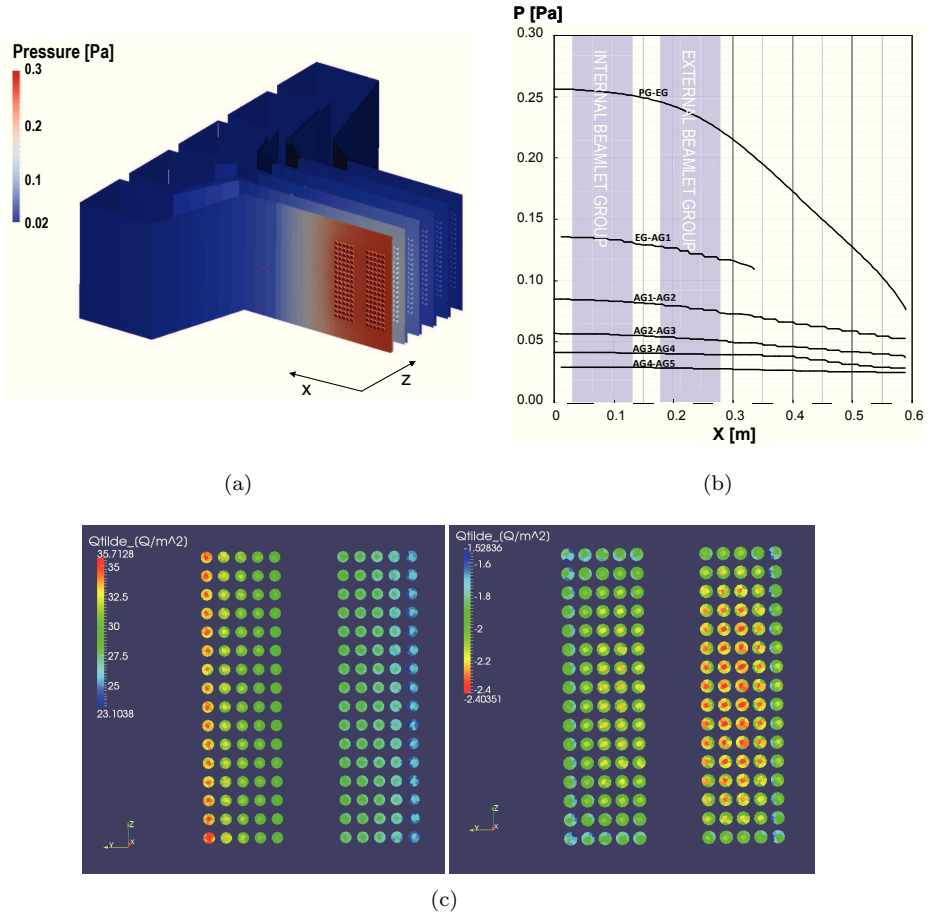


Figure 5.12: Geom A: pressure distribution at room temperature (a) and pressure profiles on downstream grid surfaces along the transverse directions x (b); the gas throughput at the inlet apertures is shown (c) together with the gas throughput at the outlet apertures at the AG5 (d)

fore the throughputs have been multiplied by a factor 8 to calculate the total throughputs.

The Avocado code provides a spatially detailed resolution, allowing the pressure profiling on surfaces to evaluate non-homogeneities. Figure 5.12 (a) and (b) presents the pressure profiles along the transverse direction on the surface of the grids and the frames for Geom A. The D2 throughput across the PG where the boundary condition of constant pressure is assigned is not uniform between different apertures. Across the external grid apertures (closer to the lateral conductance to the vessel), the throughput is 8% higher than across the inner apertures, thus balancing the slightly lower pressure downstream. The low throughput at the innermost apertures is an effect of the imprecise implementation of the symmetry condition, which underestimate the net gas fluxes even though the pressure distribution is acceptably resolved.

In figure 5.14, the pressure profile along the axis of a beamlet is shown, comparing Geom C and Geom C+PS. It is clear that the complete modelling of the PG aperture plays an important role and should not be neglected. With these analyses, the evolution of the BS models reaches a more mature level.

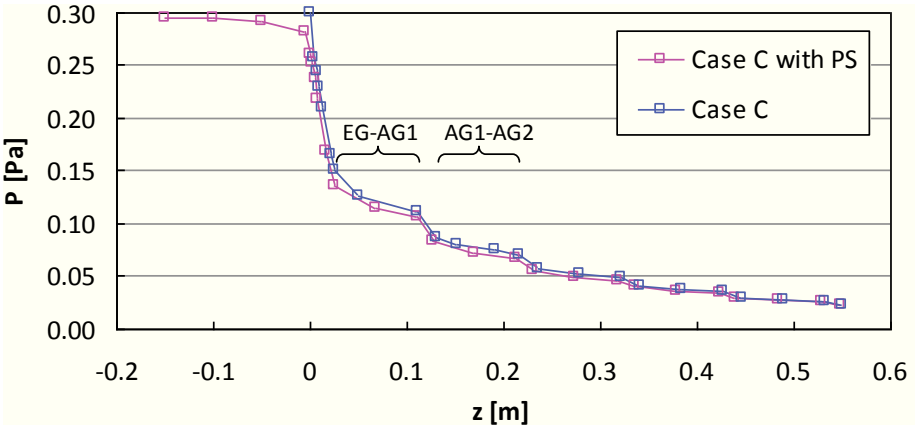


Figure 5.13: Pressure profile along the path of the 8th beamlet (numbering from the centre beamlet 1st to the outermost 10th), Geom C: in this case the zero is located at the knife edge of the PG aperture.

5.1.4 Consistent temperature

Some considerations on the gas temperature variations inside MITICA beam source were done also before this development. The approach that was tried is based on the calculation of the average number of rebounds per particle at the solid walls of the grids and the support frames. An average temperature can be calculated for each grid gap on the basis of the temperature accommodation factor and the average number of rebounds. The method has been discussed in an RFX technical note [170]. The results were in line with the lumped circuit approach, because both use average temperatures for chambers treated independently one from the other. The experience gained in this activity leaded to the definition of new requirements for the Avocado code. The main new required features were:

1. the capability to solve the gas temperature consistently with the gas fluxes and the energy exchange at the solid walls: the temperature variations are strong in very short length, and cannot be solved using averaged temperature in the first two grid gaps;

2. the capability to calculate the gas state at given coordinates in the volume: the pressure calculated at the solid walls was not the one required for stripping calculations.

According to these specifications, the Avocado solver has been rewritten in order to iteratively solve the gas temperature. As described in section 3.1.2, the capabilities of AVOCADO were improved implementing a consistent set of equations to account for the temperature evolution of the gas during the rebounds at the walls. The simulations with AVOCADO deal with the temperature variations in a continuous way, and each surface element has its own average temperatures of the incoming and outgoing particle fluxes.

The second requirement was fulfilled as well, and the extrapolation of the gas properties at given points inside the gas domain is now possible in the post-processing phase starting from the solution data.

In the following, a sensitivity analysis on various parameters and boundary conditions of the simulation is presented. It was performed on a slice model. The results are an upper limit in terms of pressure and density, since the vertical conductance is not modelled; but the indications and general trends this parametric study gives are correct.

Consistent mass flow rate

The gas injected in the plasma source is regulated at room temperature in order to obtain the required filling pressure p_f in the source. MITICA and ITER HNB will operate with a maximum pressure in the plasma source of 0.3 Pa. It is defined in the absence of plasma in the ion source, when all the experimental settings are carried out, hydrogen or deuterium mass flow rate included. In the presence of plasma, the throughput at the injection is maintained constant during operations and therefore $Q = Q_f$.

Since the gas temperature varies from the injection to the plasma source region, a proper pressure rescaling is needed to estimate the pressure in the source during operating conditions. If gradients in the source are neglected, the thermal transpiration effect will give the equilibrium in the region.

For what concern the conservation of mass, the continuity equation between the injection at the RF drivers and the PG will be expressed in terms of particle flux ϕ [molec/s]. This molecular flow rate is easily calculated, being $\phi = Q/(k_B T)$. The throughput Q is not a conserved quantity: it is expressed in W and the gas is heated in the plasma source.

The gas distribution in the BS in the presence of the plasma will be obtained with a two steps approach, as it is in the experiments:

1. a simulation at room temperature setting the filling pressure as boundary condition will give the nominal filling throughput Q_f. This throughput is conserved in this conditions and is the same at each forced cross section of the system.

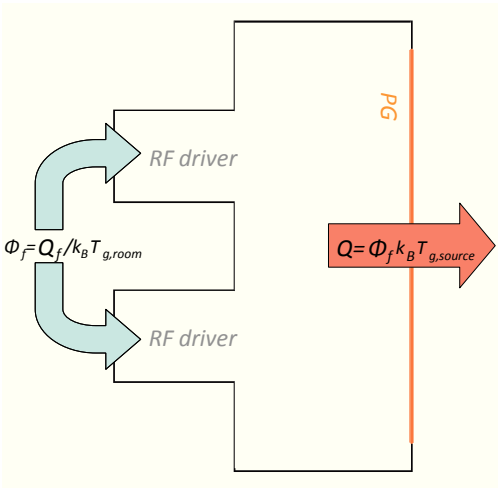


Figure 5.14: The Conservation of mass shall be applied for the two gas temperatures in the plasma source: at room temperature and in operating conditions, the mass flow will be the same according to the definition of filling pressure p_f.

2. After the expected temperatures has been imposed at the walls (i.e. at the surfaces of the PG, EG, and so on) and the proper temperature in the plasma source $T_{g,source}$ has been assigned, the pressure in the PS is varied until the correct throughput Q is obtained, which is calculated as

$$Q = Q_f \frac{T_{g,source}}{T_f} \tag{5.3}$$

   Alternatively, the particle flux at room temperature ϕ_f can be used as target variable of this iterative process. The other option would be to vary the type of boundary condition, and directly use the specific throughput; but it is preferable to use the same kind of boundary condition, in order to maintain the same spatial distribution of the throughput or of the pressure.

The gas temperature in the source $T_{g,s}$ in the presence of the plasma has been investigated in RF driven sources at IPP [126]. Neutral gas temperature measurements are performed at a distance of about 2 cm from the PG in the source by means of Optical Emission Spectroscopy (OES). Latest results in Batman experiment [123] show that a good value for D_2 and H_2 temperature could be 1150K and 1050K respectively. These values were obtained in the case of 70 kW RF diver power.

Effect of some parameters on the density profiles in MITICA beam source

After the model had been extended to the PS, the complete PG was part of the model (see 5.15). The properties of the gas in the PS are now applied to two planar surfaces (on the back of the PS, and on the side), as the symmetry plane are not modelled as in the rest of the accelerator. The gas temperature that shall be matched with the experimental results is, instead, that of the gas in front of the PG. Gas temperatures in the range 10001200K are simulated

at that location, depending to the chosen energy accommodation factor K_{ac}, when $T_{g,s}$ is 1300K. Note that, in the model, the neutral gas temperature is strongly influenced by the presence of the water-conditioned PG conditioned at 150 °C ($T_{w,PG}$=423K, uniform and constant). In the following, the effects of some parameters is discussed.

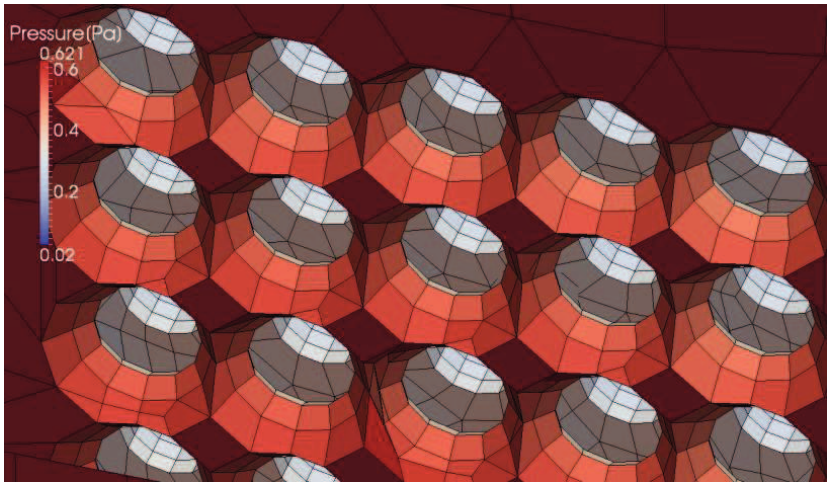


Figure 5.15: Close-up of the upstream face of the plasma grid. The quality of the mesh is visible.

T_s=1300K, variable K_{ac} Keeping constant the gas temperature T_s assigned at the inlet BC, the pressure along the volume of the PS varies as the accommodation factor of the gas to the solid surfaces is modified. The results are presented in table 5.3 and in figure 5.16. The temperature calculated 2 mm before the PG, where the gas temperature has been measured in the IPP experiments, varies with the accommodation factor.

$T_{s,OES}$=1150K, variable K_{ac} After other iterations were done, the same gas temperature at a distance of 20 mm from the PG: precisely, 1150K for D_2. The required Ts and the other calculated properties are listed in table 5.4 and the density and tempearture profiles are presented in figure 5.17.

K_{ac}=0.2, variable T_s Two cases are presented in figure 5.18, obtained with different gas temperature in the PS. The higher is the temperature at the source, the lower is the density profile.

Beamlet position There is an horizontal non-homozeneity that, between the inner beamlets and the lateral one, has been quantified in about 8%. The influence of the beamlet position will be better discussed on the basis of the results of the 1/4 model in section 5.1.5.

K_ac	T_s [K]	P_s [Pa]	n_s [m^{-3}]	$T_{s,OES}$ [K]	$P_{s,OES}$ [Pa]	n_{OES} [m^{-3}]
0.1	1300	0.612	3.50e+19	1173	0.568	3.50e+19
0.2	1300	0.604	3.55e+19	1102	0.552	3.63e+19
0.3	1300	0.594	3.58e+19	1045	0.537	3.72e+19

Table 5.3: Calculated pressure and other gas properties in the source and at the LOS of the OES, D_2 gas

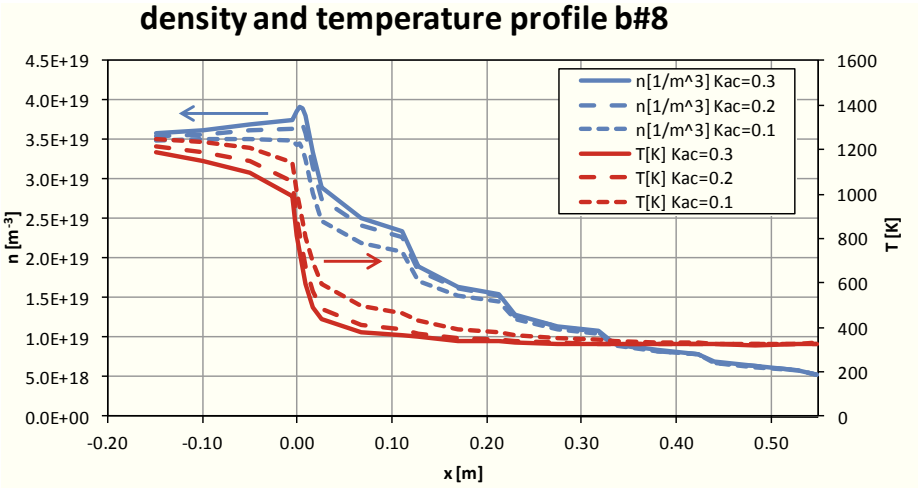


Figure 5.16: Density and temperature profile for beamlet #8, K_{ac} between 0.1 and 0.3, T_s=1300K

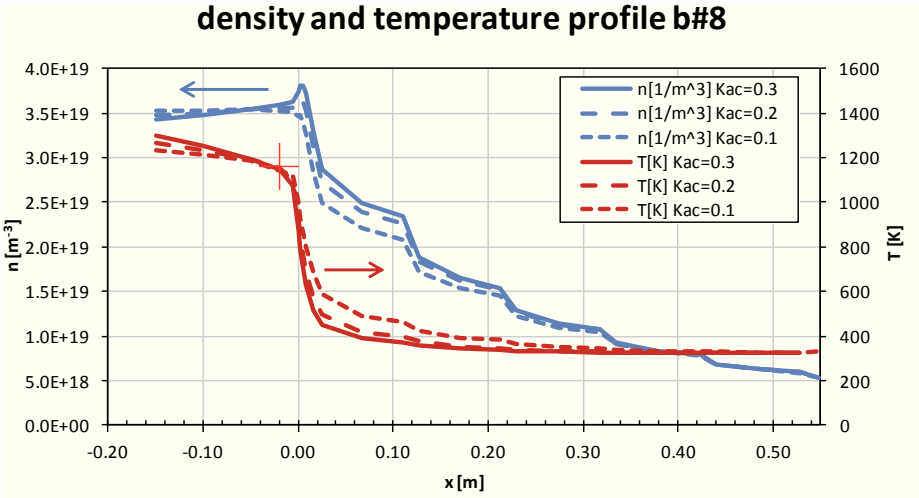


Figure 5.17: Density and temperature profile for beamlet #8, K_{ac} between 0.1 and 0.3, $T_{s,OES}$=1150K

$K_a c$	T_s [K]	P_s [Pa]	n_s [m^{-3}]	$P_{s,OES}$ [Pa]	n_{OES} [m^{-3}]
0.1	1275	0.612	1156	0.563	3.52e+19
0.2	1356	0.615	1175	0.570	3.57e+19
0.3	1430	0.622	1172	0.570	3.59e+19

Table 5.4: Calculated pressure and other gas properties in the source and at the LOS of the OES, D_2 gas

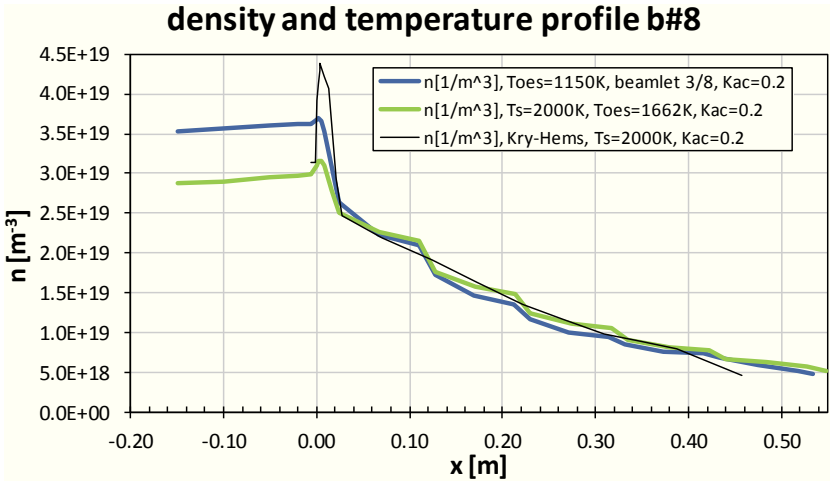


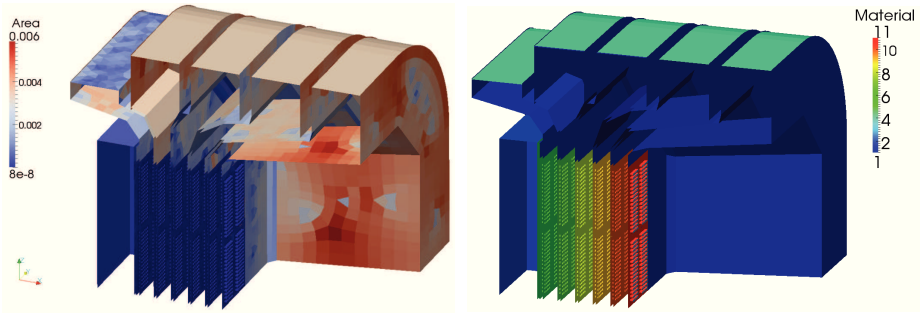
Figure 5.18: Density and temperature profiles for beamlet #8, comparison between two source gas temperature: T_s ≈2000K and $T_{s,OES}$=1150K. The profile from [122] is presented for comparison of the case $T_s \approx 2000$ K, even though it was obtained for a different accelerator.

5.1.5 1/4 model

After the improvements in the physics implemented in AVOCADO, the code developments were aimed at allowing the simulation of bigger models. In this section, the simulation of 1/4 of the beam source is presented.

The AVOCADO executable was customized to solve this model, adding rules for the particle interception. The "shadowing" between cylindrical apertures of the same grid was realized by introducing additional rectangular surfaces, horizontal and vertical, between each aperture row and column. Instead of about 10 faces per cylinder, totaling 10x32x10=3200 faces (depending on the angular number of divisions of the cylinder), only 33 horizontal and 10 vertical planes had to be considered in the calculation. The x coordinate (beam axis in this case) is also tested considering the grid thickness. There are 183000 surface elements in this model. The wall time for VF calculation is reduced to 97h 30', reduced by a factor 4.5 (expected). The matrix mirroring and inversion required less than an hour. The geometry is that of EQ-GAPS-23 [171, 166], as described in table 5.5

In figure 5.19(a), the meshed model is presented, showing the area of the surface elements;: there is a large variation between the meshes of the drilled grids and the support frames. The surface "materials" used are 11, as shown in figure 5.19(b); The inlet, outlet and grid surfaces have different material



(a) (b)

Figure 5.19: (a) area of surface elements and (b) material assignment to the boundaries of gas domain (11 different materials).

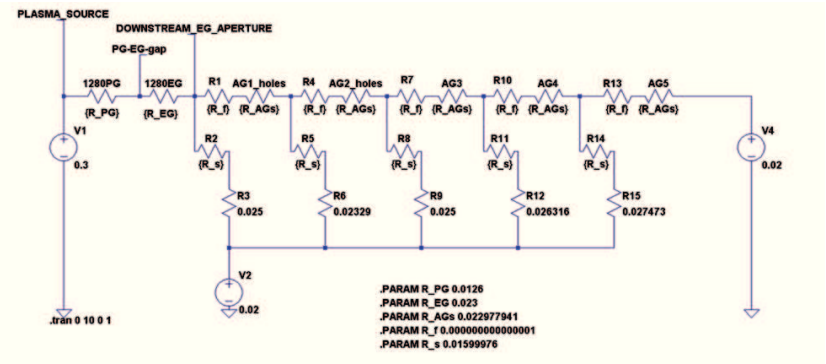
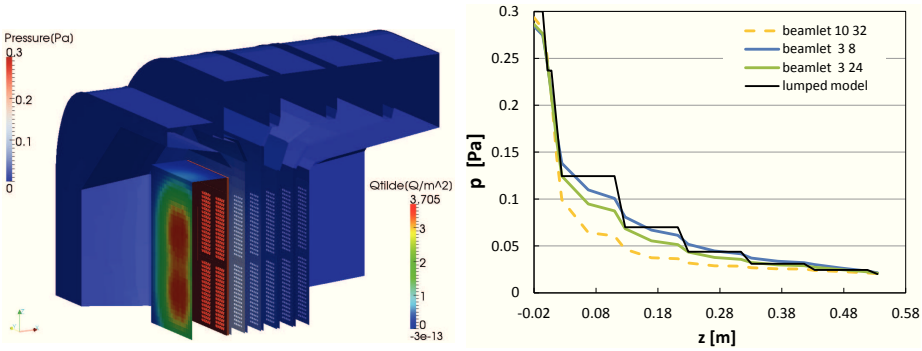


Figure 5.20: Lumped model solved in LTspice [70].



(a) (b)

Figure 5.21: Results for filling pressure 0.3 Pa, room temperature: (a) pressure distribution and specific gas throughput at the inlet and (b) pressure profiles along the path of three beamlets, compared to the results from the lumped model shown in figure 5.20

Aperture	Geometry Description
Plasma Grid (PG)	8mm thick, max. aperture 24mm, diameter at knife edge 14mm, divergent cone max. diameter 16mm;
Extraction Grid (EG)	diameter of inlet cylinder 13mm, 7mm long; conical segment 6mm long; diameter of the outlet cylinder 15mm, 4mm long;
Acceleration Grids (AGs)	17mm long, 16mm diameter;
Grid gap (PG-EG)	6 mm
Grid gap (EG,AGs)	85 mm

Table 5.5: Main parameters of the considered geometry.

assignments and properties.

Filling pressure

The simulation of deuterium gas at room temperature is carried out using the materials assignments listed in table 5.6. The calculated total throughput from the BS is 3.838 Pa m^3 s^{-1} (obtained multiplying by 4 the throughput from the simulation). This value is in line with those obtained with the slice models, and in the past by others [122, 127]. The view factor matrix is mirrored, in MSR format, in 60 min and then solved in 37 min on a single processor.

Material n.	Element	Boundary condition	
		T [K]	P [Pa]
1	Support frame	293	-
2	Plasma Source	293	0.3
3	AG5 apertures	-	0.02
4	Lateral apertures	-	0.02
5	PG	293	-
6	EG	293	-
7	AG1	293	-
8	AG2	293	-
9	AG3	293	-
10	AG4	293	-
11	AG5	293	-

Table 5.6: Boundary conditions for the simulation of the filling pressure

The pressure distribution and the throughput from the PS is shown in figure 5.21(a); it is clear that the symmetry boundary condition as it is used is not adequate to properly solve the gas fluxes (even though the pressure should be correctly solved) as the gas throughput is underestimated near to the symmetry planes.

The pressure profiles for three beamlets are presented in figure 5.21(b). The beamlets are numbered i, j where i is the beamlet number in the horizontal direction starting from the center and j is the beamlet number in the vertical direction. The pressure in the EG-AG1 gap differs by up to 40% between the corner beamlet 10,32 and the beamlet 3,8 at the center of one central beamlet group. The lumped model shown in figure 5.20 uses conductances calculated in simpler models, in particular the axial conductances are taken from table 5.1 and the lateral conductances have been characterized as described in section 5.1.2.

On the center axis of the BS, the pressure in the PG-EG gap is 0.232 Pa, and the pressure in the EG-AG1 gap is 0.115 Pa.

Deuterium operation with $T_{s,OES}$ ≈1150 K

The temperature of the gas 2mm before the PG is approximately $T_{g,2mm}$ ≈1150 K if the temperature of the gas entering the domain from the inlet surface of the PS is at about $T_{g,s}$ =1300 K. The precise values of temperature and pressure were found by iteration. The boundary conditions used in this simulation, such as the grid temperatures, are summarized in table 5.7. The iterative solution requires about 3 hours on a single processor to reach a residual of 1e-27. The gas exits the BS as detailed in table 5.8.

Material n.	Element	Boundary condition	
		T [K]	P [Pa]
1	Support frame	313	-
2	Plasma Source	1280	0.607
3	AG5 apertures	-	0.02
4	Lateral apertures	-	0.02
5	PG	423	-
6	EG	323	-
7	AG1	323	-
8	AG2	323	-
9	AG3	323	-
10	AG4	323	-
11	AG5	323	-

Table 5.7: Boundary conditions for the simulation of the operating conditions

	EG-AG1	AG1-2	AG2-3	AG3-4	AG4-5	AG5
Avocado [123]	50%	26%	12%	6%	1%	4%
Kry/Hems [122]	50%	21%	13%	5%	1%	10%

Table 5.8: Mass flow partitioning between the five lateral apertures and the AG5 apertures

In figure 5.24 the average temperatures of the gas before and after rebounding are shown in a section of the model. The gas temperature is reduced in the PS from the inlet to the PG, since it is determined by the particles proceeding in both the directions $\pm x$, with a fraction that already accommodated with the PG and its temperature. This is the reason why the gas temperature at the inlet is different from the gas temperature 2 mm before the PG. The pressure distribution and the four beamlets that are considered for the post-processing are shown in figure 5.22; the related temperature and density profiles are plotted in figure 5.23. There results a diagonal non-homogeneity of about 12% in the gap between EG-AG1, which would be higher if the corner beamlet were considered. In figure 5.25, the profile of the central beamlet group is compared with the density profile by Krylov-Hemsworth which was the reference density profile used until now for the MaMuG accelerator. The resulting stripping losses are listed in table 5.9. The mass flow rate fraction exiting from the domain are listed in table 5.11.

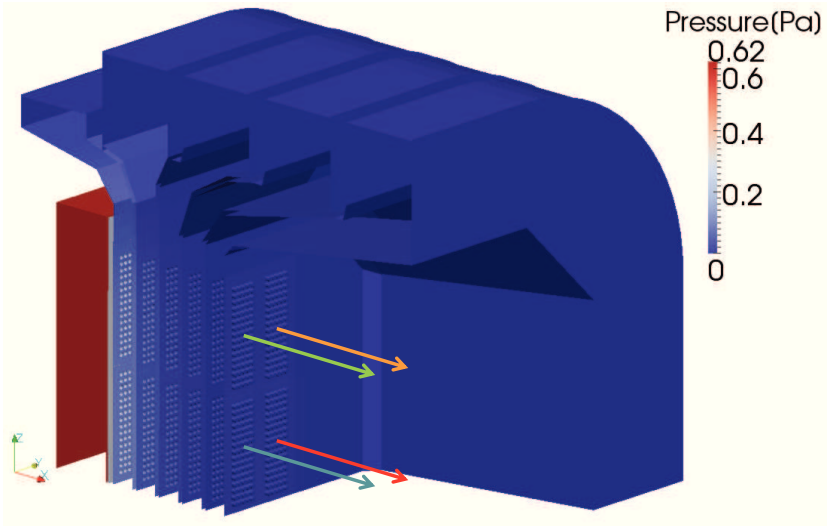


Figure 5.22: Pressure distribution in the case $T_{s,OES}$ ≈1150 K: four centerbeamlets are indicated.

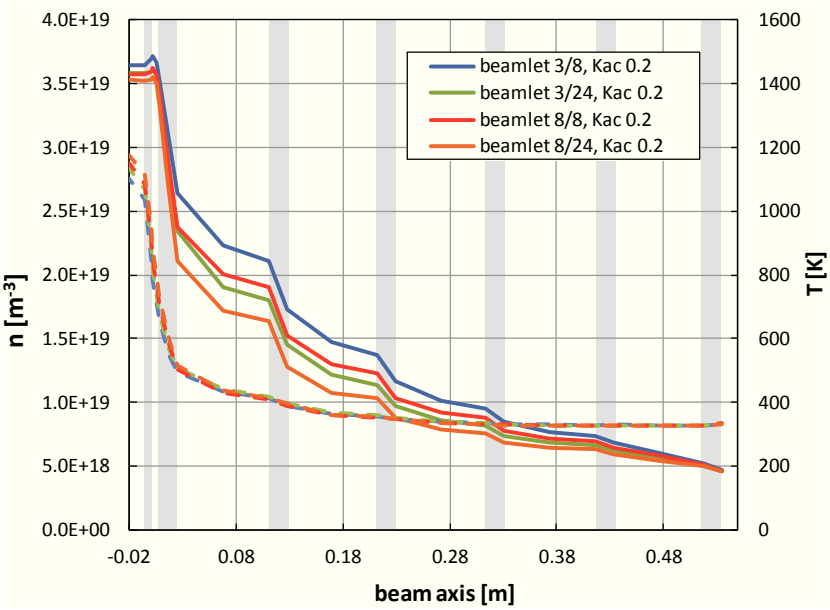


Figure 5.23: Calculated density (solid lines) and temperature (dashed lines) profiles in correspondence of the four centerbeamlets indicated in figure 5.22.

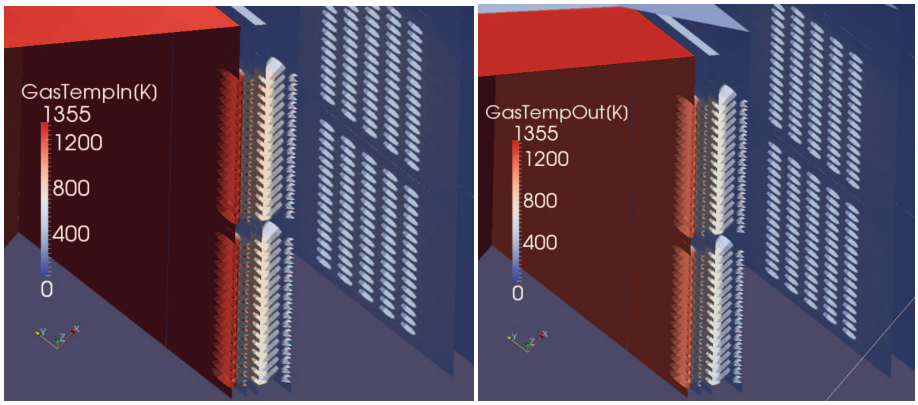


Figure 5.24: Gas temperature before and after accommodation with the wall ($K_a c$=0.2).

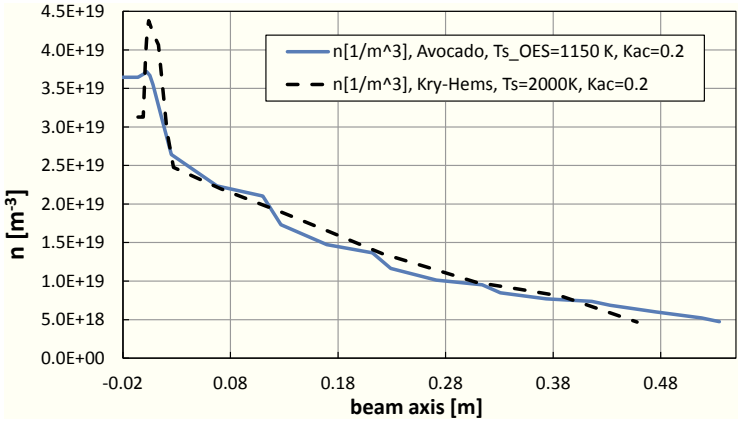


Figure 5.25: Comparison with the profile from [122], obtained for a different accelerator and different boundary conditions.

Position	Color	Total stripping losses [%]
Central	Blue	27.7
Side	Red	25.5
Top	Green	26.6
Corner	Orange	23.7

Table 5.9: Influence of beamlet position on stripping losses. See RFX tech. note [166].

Enhanced lateral conductance

It is clear that the density profiles are dominated by the pumping between the EG and AG1. The higher is the lateral conductance of this gap, the lower the density in the EG-AG1 gap and in the PG-EG. It has been suggested to realize slots in the AG1 support frame in order to enhance this conductance. Unluckily, these slots cannot create a direct path between the 1 MV area and the ground

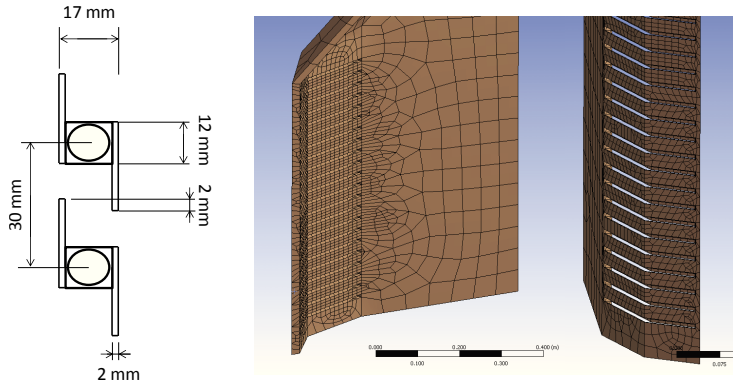


Figure 5.26: Sketch of the horizontal slits in the AG1 support frame (on the left) and its meshed model (on the right).

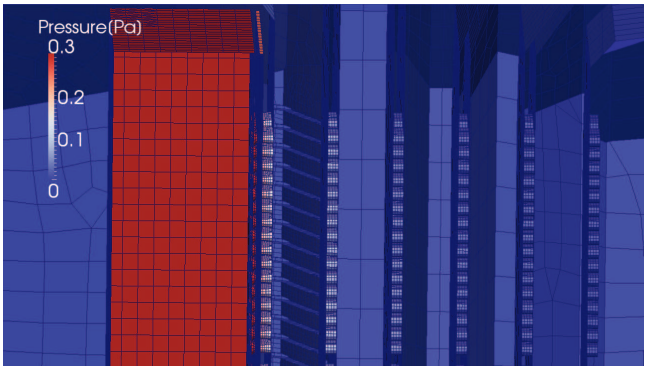


Figure 5.27: Pressure distribution, detail of the slits in the AG1 support frame.

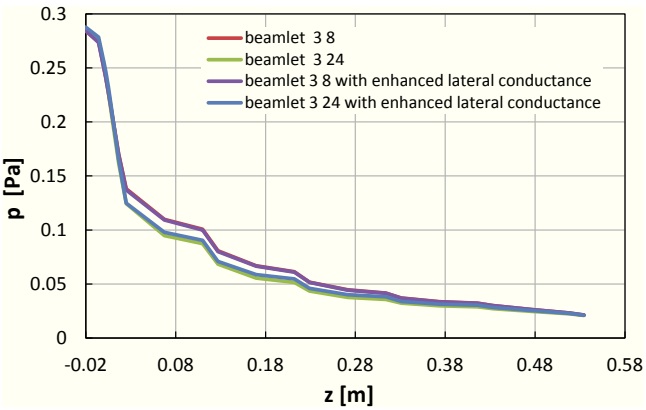


Figure 5.28: Operating conditions, the mass flow will be the same according to the definition of filling pressure p_f.

potential of the vessel; a "Z" shaped slot (see figure 5.26(a)) is a solution that fulfill both requirements.

The support frame has been modified and now houses 42 of these slots; the number of elements is 189500. The mesh is shown in figure 5.26(b).

A detail of the solution is shown in figure 5.27 and the pressure profiles, compared to those of the original model, are shown in figure 5.28. There is no indication that the slits in the AG1 frame enhance the lateral conductance towards the vessel.

5.1.6 Comments and future work

The gas distribution in the beam source of MITICA has been simulated with Avocado with many models of increasing complexity. The results have been compared with lumped models and previous researches, and the results demonstrated a qualitative and quantitative similarity: the pressure profiles and the gas throughputs are similar to those calculated in the past for different beam source designs.

The accuracy the pressure distribution is solved with was not achived before. The Avocado models supported the design of the BS, and has gaven important indications on the non-homogeneities of the density profiles between different beamlets.

The BS model is one quarter of the beam source but shall be enlarged and comprise the whole geometry, avoiding in this way the approximations due to the "not-so-appropiate" symmetry conditions. This could be possible with small modifications to Avocado and to the finite element model. The latest designs of the grid apertures - in particular of the EG, which plays a fundamental role in the gas conductance - shall be considered in the next gas model.

The effect of some main parameters has been investigated, such as the source gas temperature and the accommodation factor. The importance of the latter in the gas dynamics in the first few centimeters of the beamlet path is such that it will require some deepened research. The benchmark activity that is being carried out on Manitu data is also aimed at this study.

The dissociated atoms are neglected in the calculation of the stripping losses, while it is known that the D or H atoms have a cross section for the charge exchange processes that is comparable, at low energies (8 keV/amu), to those of their molecular counterparts.

5.2 MITICA Beam Line

In this section, the activity regarding the gas density simulations in MITICA. The analysis of the gas distribution inside MITICA, either aimed at the estimation of the beam neutralisation or at the calculation of the total gas throughput, or at evaluating the influence of some design choices on the gas distribution and the overall performance of the NBI, must be performed taking into account the whole gas domain. Increasing progressively the completeness and complexity, a satisfactory model of MITICA has been developed using Avocado. Data on the density distribution is already available: from the work by Krylov and Hemsworth [122] and the analyses described in the appendix n.3 of the ITER HNB DDD 5.3 [50, App. 3], up to more recent results by KIT [127]. The new contributions of my study consist in:

1. The updated geometry of the Beam Line Components (BLC) is considered in the simulations. In particular, the gas analyses supported the design of the Lateral panels of the Electron Dump (LED) during this year.

2. The Beam Emission Spectroscopy and the Tomography are key beam diagnostics, which in other NBI test-beds demonstrated their importance [128, 129]. The density distributions at the diagnostic planes have been calculated.

3. The submodelling of the Beam Source (BS) up to now used a uniform tank pressure of 0.2 Pa in the Beam Source Vessel (BSV), both at the lateral conductance and downstream the Grounded Grid (GG). With this model, different pressures are calculated at these boundaries, the lateral gaps of the BS and the GG surface.

In the following, the main results obtained are presented and discussed. First, in section 5.2.2, the challenges of such a task are summarized, together with some considerations concerning how the boundary conditions affect the results. The density profile for neutralisation and the calculated beam fractions are presented in section 5.2.3. In section 5.2.4, the effects of the lateral electron dump (LED) panels are discussed. The density distribution at the transverse sections where the beam diagnostics are is shown in section 5.2.5. The submodel of the Beam Source (BS) has boundaries in common to this model; the gas throughput coming from the beam source is used as boundary condition for this model, and the calculated pressure (section 5.2.6) at the common boundaries can be used as boundary condition for the BS submodel.

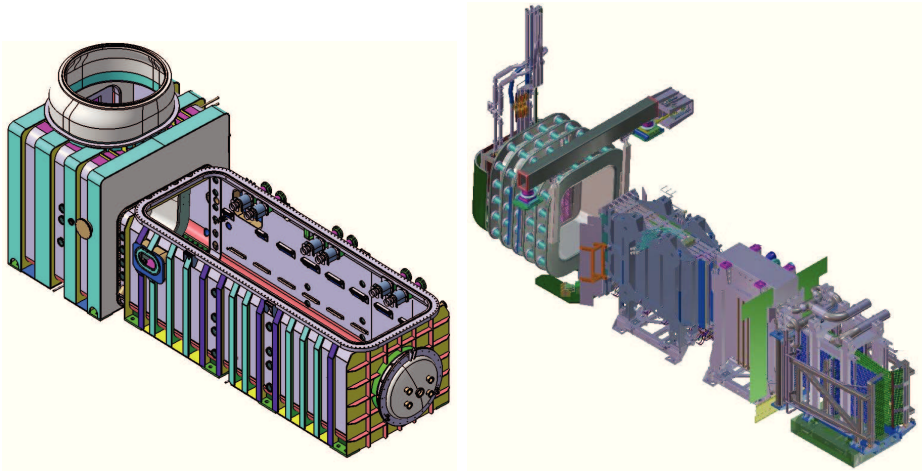
5.2.1 General description and challenges of the model

Geometry description

The external boundaries are given by the vessel: the MITICA vessel is divided into two main functional parts, the Beam Source Vessel (BSV) and the Beam Line Vessel (BLV). The internal components are the Beam Source (BS) and the Beam Line Components (BLC). Accuracy must be used in modelling key details, such as the shape of the Neutraliser channels. The following geometric features affect the gas distribution and will be considered:

- The internal dimensions of the MITICA Vessel. A CAD picture is shown in figure 5.29.
- The overall dimensions of the internal components, considering their bounding box, as reported in Figure 5.30.
- The geometry of the beam channels of both the Neutraliser and the RID are of paramount importance to the quality of the simulation; their dimensions are listed in table 5.10.
- The position of the gas injection: there will three separate injection feedlines in MITICA, with three possible injection positions at 50%, 60% and 70% of the Neutraliser length. The positions at 50% and 70% have been tested with Avocado.
- The panels of the Lateral Electron Dump (LED) on the two sides of the Neutraliser: these elements affect the gas conductance from the BSV to the cryopumps.

- The gas baffle, foreseen at the downstream side of the RID, is modelled as well; basically, the gas density before the Neutraliser or before the RID should not be affected by this element.
- The high voltage connections of the beam source up to the transmission line are not modelled.



(a) (b)

Figure 5.29: CAD model of (a) MITICA vessel and (b) its internal components.

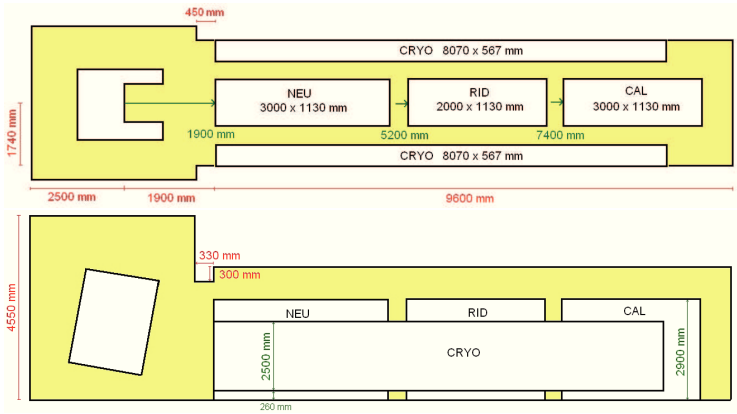


Figure 5.30: Sketch showing the overall dimensions of the vessel and the internal components: on top, vertical section; on bottom, horizontal section.

Coordinate system

The coordinates are given with respect to the center of the GG. The X axis is the projection on a horizontal plane of the beam axis, the Z axis is normal to this plane, Y is perpendicular to the beam axis and parallel to the horizontal axis.

Component	channel edge	front Y coord.	rear Y coord.
Neutraliser	1	±274.2	±240
	2	±170.1	±146
	3	±126.1	±112
	4	±22	±17
E-RID	1	±237.8	±213.04
	2	±133.23	±121.46
	3	±114.15	±101.53
	4	±9.5	±9.97
Component	**coord.**	**front**	**rear**
Calorimeter	x	7757	10157.5
	y	±235	0

Table 5.10: Width of the beam channels of the Neutraliser and the RID and of the internal space of the Calorimeter. Dimensions in mm.

Meshed model

A finite element model with up to 40846 surface elements has been created, 38 of whose are triangular. The actual number of meshes varies depending on the presence or not of the LED and the gas baffle at the downstream side of the RID. The elements are included in 139 planar faces, partially used for shadowing calculations.

Gas sources and sinks

The gas throughput injected in the neutraliser is such that any other gas source could be, as a first approximation, neglected; as a second order approximation, also the gas from the plasma source should be included, as well as recombining processes in the RID and Calorimeter which produce neutral gas. The degassing from solid surface is neglected in the model. The sources of gas in MITICA were calculated in various analyses in the past (see [122, 127, 130]). The main gas sources and their nominal gas throughputs are:

- the Neutraliser (19 Pa m^3 s^{-1})
- the Beam Source (3.9 Pa m^3 s^{-1})
- the RID (expected 0.38 Pa m^3 s^{-1})

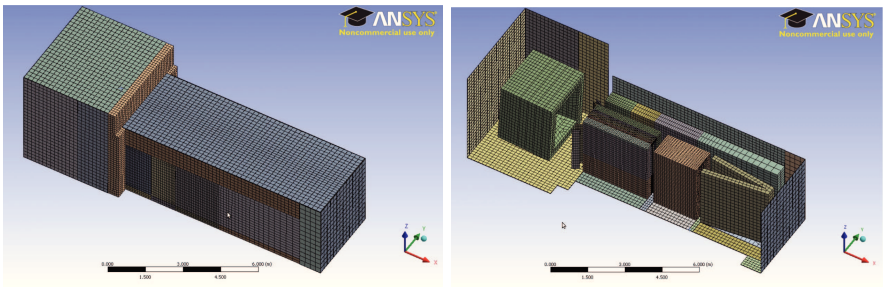


Figure 5.31: ANSYS meshing capability were used, where possible, to mesh with mapped grids the surfaces

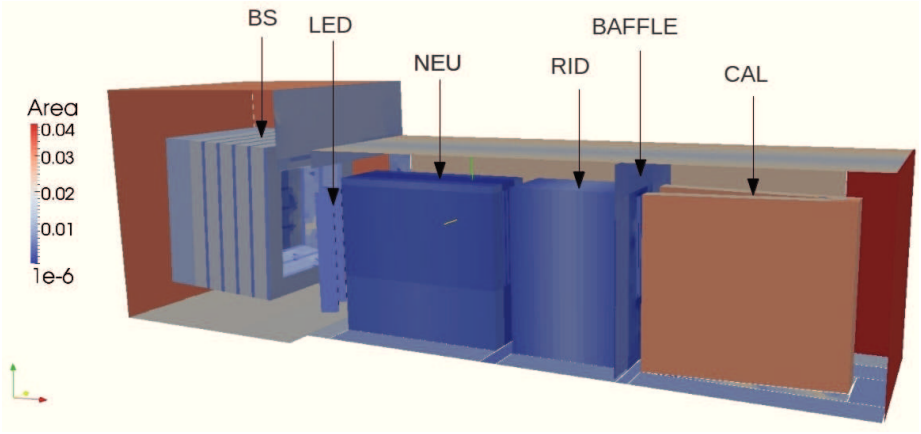


Figure 5.32: Meshed model of the vessel and its internal components (element area in m^2).

Location	A [m^2]	Q [Pa m^3/s]	Q %	Q[Pa m/s]
EG-AG1	3.1378	1.6856	43.0%	0.537192
AG1-AG2	3.1378	1.0016	25.6%	0.319205
AG2-AG3	3.1378	0.52	13.3%	0.165721
AG3-AG4	3.1378	0.2448	6.2%	0.078016
AG4-GG	3.1378	0.116	3.0%	0.036969
GG	0.748	0.35024	8.9%	0.468235

Table 5.11: Repartition of the nominal gas source throughput between the lateral conductance and the front apertures of the grounded grid (Q_{BS}=3.9 Pa m3/s (1/8 BS gives partial Q=0.49 Pa m3/s).

In this model, the gas throughput that originates at the RID and the Calorimeter is neglected. The gas throughput proceeding from the BS flows mainly through the lateral conductance of the accelerator support [122]. By iterating with the simulation of the Beam Source submodel, the throughput fractions listed in table 5.11 are imposed at stripes around the modelled BS.

In the case the temperature is included as a variable in the simulation, the effective throughput to be set at the inlet varies. The injection channels are drilled inside the wall panels, whose temperature is expected to rise during operations, and the surface temperature of these channels is expected to be about 100 °C. See section 5.2.2.

The injection apertures are meshed as octagons, and thus the specific throughput $\tilde{Q}$ to be assigned to these elements has been calculated in accordance to:

$$A_{octagon} = 2\sqrt{2}r^2 \tag{5.4}$$

The influence of the diameter of the injection nozzles has been evaluated considering the two cases listed in Table 2 Gas sources from the Neutraliser: QNEU=19 Pa m3/s. No remarkable difference was appreciated; it has a greater influence, for instance, the dimension and position of the meshes in front of the nozzle.

The gas exits the domain from the two front surfaces of the cryopumps. The appropriate choice of boundary condition to be set there is discussed in the following.

	A [m^2]	Q [Pa m^3/s]	Qtilde [Pa m/s]
single injection nozzle	1.13137E-05	0.95	83969

Table 5.12: Gas sources from the Neutraliser (Q_{NEU}=19 Pa m3/s).

5.2.2 Challenges and general considerations

Gas Species

Only H_2 or D_2 are considered in the model. The other gas species in the NBI are in negligible percentages with respect to the neutralisation gas. There is no indication that any kind of impurity should affect the beam performance in normal operations. In the case of accident, a leak from the gas-insulated transmission line could occur.

Applicability of collisionless methods

AVOCADO solves free molecular flows, and the applicability of the code to the case shall be proven, paying particular attention in the evaluation of the high pressure regions, in correspondence of the gas injection in the Neutraliser.

The issue of collisions between molecules inside the neutraliser is mitigated by considering the narrow channel width dominating the gas flow, and thus using the channel width as length scale. In general, it is a challenge to calculate collisional gas flow in complex systems, and up to now, free molecular flow regime has been considered in the Neutraliser of ITER and MITICA NBI [122, 50, 127]. A different approach (continuous fluid) has been followed also [131] and recently a DSMC collisional model has been applied to the Neutraliser 2D section [132].

The gas is injected in the beam channels by five nozzles aligned along vertical lines. The transition between the viscous regime of the injection feedlines and the vacuum occurs through these nozzles and the following expansion region in the gas cells. The flow is chocked at the nozzles, which are simple cylindrical holes, and the expansion occurs in the volume of the gas cells downstream. This is a region of compressible flow, and its extension will be verified in a dedicated model in section 11. The region is limited to the immediate proximity of the aperture.

Figure 5.33 shows the pressure distribution calcualted with AVOCADO inside a middle channel of the Neutraliser (highest pressure in the domain). A vertical non-uniformity can be appreciated in correspondence of the five injection apertures. The pressure distribution inside the Neu Channels (Figure 2-75) is similar to that obtained by Lou (F4E presentation, 2011).

The width of the channel (perpendicular to the plane of the figure) is about 0.1m. The mean free path can be calculated as described in section 2.1.4: the resulting Knudsen number Kn as a function of pressure p is, in the case of H_2 flow in this domain, is shown in figure 5.2, based on eq. 5.1:

In the case of H_2 gas at 100 °C, Kn crosses the value of 1 at 0.155 Pa; at 0.3 Pa, Kn equals 0.52. Given these results, we know that there is region where the molecular collisionality starts to affect the flow also at a macroscopic scale inside the Neutraliser.

Bearing in mind this limit, the code is applied to the case. The solution of the transition regime is approached from the molecular limit, to which anyway the

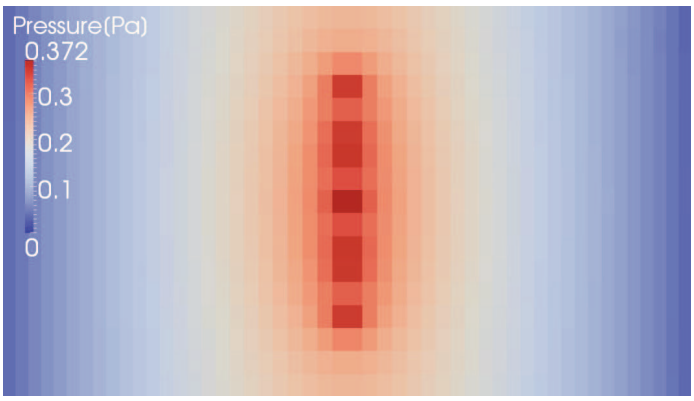


Figure 5.33: Pressure distribution inside one middle channel of the Neutraliser, in the case of channel walls at room temperature (297K). The maximum pressure would be 0.383 Pa in the case of hot channel walls (373K).

condition is very close. The injection nozzles are modelled with circular surfaces, whose effective (meshed) area is that of an inscribed octagon ($A_{oct} = 2\sqrt{2}r^2$). It has been verified that the diameter of these inlet surfaces negligibly affect the pressure distribution in the channels; doubling the diameter the variations of the maximum pressure are well below 1%. The boundary condition of these surfaces is that of a constant specific throughput:

$$\tilde{Q} = Q/A_{oct} = \frac{Q}{2\sqrt{2}r^2} \tag{5.5}$$

The profiles in figure 5.34 are calculated along the centerline of one of the middle gas cells of the Neutraliser, in the case of Deuterium injection at 0.5 of the channel length (Q=19 Pa m^3/s) and uniform specific pumping speed at the cryopanels (S=3800 m^3/s). Various profiles are shown; the centerline is exactly in correspondence of the gas injection, and therefore the peak pressure of these profiles is the peak pressure in the whole MITICA vacuum system. A Knudsen number above 0.5 indicates that collisions between gas particles are negligible in the gas flow. The minimum value in this case is about 0.4, meaning that the gas flow is entering the transition regime between molecular and viscous flow. A possible approach is to model the transition regime at this high value of Kn as molecular flow.

It has been recently calculated [132] that the error in the effective gas target thickness is overestimate by 10% in the case of collisionless solvers with respect to collisional DSMC methods, if a path crossing exactly the injection nozzles is considered; in particular the pressure peak at that location is calculated to be up to 25% less. The shape of the density profile remains the same, and also the density at the edges of the beam channels is the same. Bearing these considerations in mind, the collisionless method is applied in this document. Most of the results concern the zones where the molecular regime is fully developed.

Gas temperature in the Neutraliser

The gas temperature in the gas cells of the Neutraliser is determined by the combination of three factors: (a) the interaction with the beam (b) the inter-

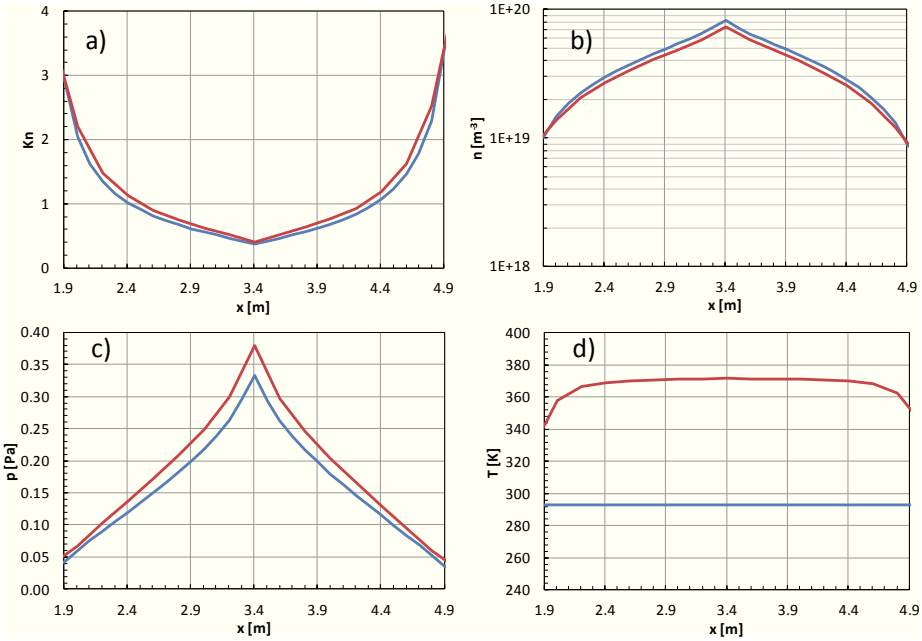


Figure 5.34: Various centerline profiles in one of the central gas cells of the Neutraliser: (a) Knudsen number, (b) density, (c) pressure and (d) temperature. The gas is D_2.

action with the solid walls and (c) the injection temperature. Avocado in its present implementation is not the appropriate model to evaluate (a). The other two contributions are discussed in the following. Qualitatively speaking, the gas temperature profile in the gas cells is similar to models that account for the interaction with the beam [51, 133].

Gas temperature in the Neutraliser: wall temperature

By assigning higher temperature to the boundaries of the narrow neutraliser channels, the temperature of the gas itself is modified. A higher temperature means a higher conductance, proportionally to $\sqrt{T/T_{old}}$, and therefore an overall lower gas target thickness: the conductance at 100 °C is higher than at room temperature by 13%. This effect has been evaluated, and many pictures reported in the following show it (figure 5.34 for instance).

Gas temperature in the Neutraliser: injection temperature

The gas is injected in the neutraliser cells through S.S. pipes that partially exchange heat by radiation with the cryopanels; the last segment of the injetion channels is drilled inside the neutraliser wall panels, which shall operate at a surface temperature up to 130°C in the region of the injection (see for instance figure 9.2).

The internal surface of the injection channel should be averaged between this temperature and the water temperature of the cooling channels few cm aside. Therefore, at each of the three injection position the surface of the injection

channel could have a slightly different temperature. That said, the gas in laminar flow regime - such as the flow in the injection channel - exchanges heat at a certain rate with the channel wall.

All these variable are not addressed in this model. Two injection temperatures were considered, in order to acquire a certain sensitivity on this parameter: the gas enters the molecular flow domain at room temperature (300 K) or at 100 °C (373 K), coherently with the imposed wall temperature. It is advisable to use the same temperature as that imposed at the channel walls, because the gas flow in the gas cells is dominated by their temperature in the simulation; and with slight modifications due to the choice of the accommodation factor, the volume affected by the injection temperature is very small. The accommodation factor to be properly used in this case is, somehow, an uncertain value.

The gas throughput is commonly given at room temperature. The mass flow rate [kg/s] and throughput [Pa m^3 s^{-1}] are related by the following equation, which consider the gas temperature T:

$$Q = \frac{\dot{m}}{m} k_B T \tag{5.6}$$

Assuming the gas arrives at the injection holes perfectly thermalized with the channel surface, a throughput of 19 Pa m3 s-1 measured at room temperature becomes $Q_{373K} = Q_{293K} \cdot 373/293 = 24.2$ Pa m^3 s^{-1}. The number of deuterium molecules entering the gas cells is 4.69E+21 s^{-1}.

Gas sink: boundary conditions at the cryopanels

In the simulation, among the possible boundary conditions to be imposed at their surfaces, there is the uniform pressure, whose absolute value shall be identified in a conservative estimate.

Another possibility is to use the nominal pumping speed of the cryopump, uniformly distributed at the surfaces. The sticking probability of hydrogen hisotopes on the charcoal ranges from 0.7 for H_2 and 1.0 for D_2. For the present design of the cryopumps, using these coefficients, it has been calculated by Dremel [65] that the capture probability would range from 29.8 in the case of H_2 and 33.7 in the case of D_2, with an overall pumping speed of respectively 5000 m^3/s and 3800 m^3/s.

In order to assess the effects and sources of uncertainties in the interest of creating a robust model, a sensitivity analysis has been performed to investigate the effects of the condition imposed at the outlet boundary. Three cases are presented in the following. (a) A fixed pressure of 0.01 Pa is assigned uniformly to both the cryopannels' surfaces; (b) the uniform pressure is reduced to 0.001 Pa; (c) the nominal, total pumping speed S of 3800 m^3/s is used to calculate the specific pumping speed $\tilde{S} = S/A = 105 m/s$, which is then imposed to the surface [134].

In the model, the cryopanels are at room temperature. Concerning this, the following considerations can be drawn:

- The main advantage is that the nominal pumping speed S can be used, without converting into mass flow rate by local average temperatures at the boundary;

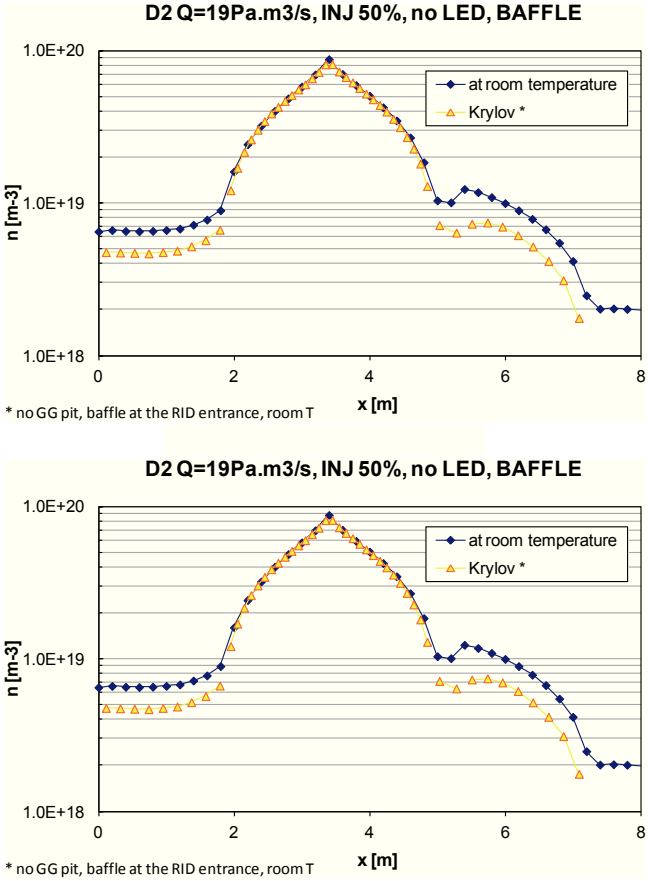


Figure 5.35: Density profiles along the path of a central beamlet, calculated assigning at the cryopanels respectively 0.001 Pa uniform pressure (on top) and uniform pumping speed of 3800 m^3/s (bottom). The Avocado results are compared with a result by Krylov.

- The gas temperature of the gas re-entering the domain from the outlet boundary only causes small perturbation to the averaged quantities in the high-density regions, in particular along the path of the beam.

In figure 5.47 the Avocado results in the cases (b) and (c) are shown compared with the density profile calculated by Krylov in one similar case. The known differences in the Avocado model are:

- The BLC are boxes with larger transverse (Y) width;
- The Gas baffle is located at the exit of the RID, in Krylov's model it is at the entrance;
- The calorimeter panels have no transparency and are in closed position.

Energy accommodation coefficient

The temperatures of the solid boundaries that may be considered in this simulation ranges from about 80K up to 373K. The energy accommodation coefficient

EAC of 0.2 is assumed, even though it may be an imprecise value. The effect it has may in this case be small:

- since the Neutraliser channels are narrow and the transition to a higher gas temperature occurs shortly;
- a small amount of gas enter the domainbackstreaming from the cryopanels, and its effect may be neglected for the high density regions of the domain.

If the area of the calorimeter were to be studied in detail, this effect shall be included, among other necessary improvements.

BLC geometry approximations

The Neutraliser and the RID have been accurately modelled in terms of overall dimensions and geometry of the internal channels. Also the LED and the gas Baffle had to be accurately modelled, because they modify the gas distribution in the domain. A different story is that of the Calorimeter, in the closed position. It is approximatively modelled as a "V" shaped volume of constant height, with no transparency across its panels. The conductance in molecular flow is geometry limited and the minimum pressure that can be reached at the pumping boundary and the gas density along the path of the beam is higher than what would be observed with a proper modelling of the listed aspects. No effort was put on this activity, and the results discussed in the following are limited to the domain volume up to the RID. In figure 5.36, a detail of the Calorimeter and the specific throughtput at cryopanels is shown; the approximate shape of the component and the minimum pressure and flux is reached at the pumping boundary in its area.

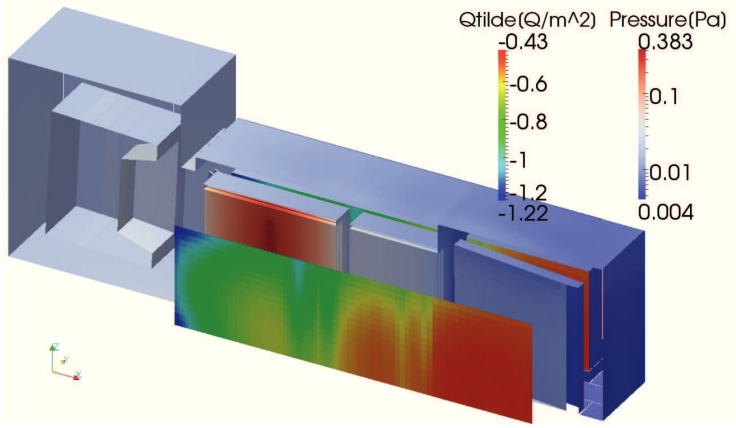


Figure 5.36: Detail of the Calorimeter and the specific throughput Pa m/s at the cryopanel surfaces. Imposed BC at outlet: S=3800m3/s, hot beam channel walls in the Neu and RID.

Vertical and transverse uniformity

In the horizontal direction, the transverse uniformity is affected by the division of the Neutraliser into four independent gas cells, the lateral ones being

better pumped. The improved pumping is noticeable at a higher degree in the drift region immediately before and after the Neutraliser. There can be also a non-homogeneity of the gas target thickness along the vertical direction, since the injection point are five discrete apertures inside the gas cells, as shown in figure 5.33. Additionally, the Neutraliser front section and the LED constitute a obstacle, which causes a higher gas conductance and can determine a better pumping on the top. Some results will be discussed in section 5.2.3.

5.2.3 Result I - Density profiles and expected neutralisation

The proper gas flow shall be maintained inside the beam channels in order to obtain an optimum neutralization. This condition is different in the case of H^- or D^- beams. Not all the charge changing processes listed in table 1.1 play a role at the energy range applicable to the MITICA Neutraliser, and only the dominating processes listed in table 5.13 will be considered. The cross sections as a function of the energy and the atomic mass unit (amu) of the projectiles in the case of Hydrogen are shown in figure 5.37.

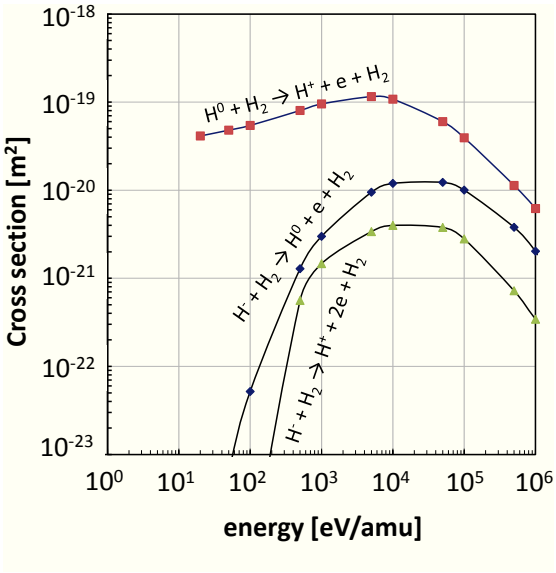


Figure 5.37: Cross sections for hydrogen and deuterium particles as reported in the ORNL Redbooks [41]: cross sections for single-electron-detachment collision of a neutral (red), double-electron-detachment collisions (green) and single-electron-detachment collisions (blue) of negative ions.

The number density n_n of neutrals (H_2 or D_2) inside the Neutraliser channels is a function of the longitudinal x coordinate. The beam species flux Γ_i varies according to:

$$\frac{\mathrm{d}\Gamma}{\Gamma} = \pm\sigma n_n(x)\mathrm{d}x \tag{5.7}$$

This very simple equation has been used to calculate the beam fractions along the neutraliser channels, by discrete numeric integration. If we consider

Charge changing process	**Cross section σ [m^2] at 1 MeV**	
	Hydrogen	Deuterium
$H^- + H_2 \rightarrow H^0 + e + H_2$	6.19e-21	1.13e-20
$H^- + H_2 \rightarrow H^+ + 2e + H_2$	3.43e-21	7.22e-22
$H^0 + H_2 \rightarrow H^+ + e + H_2$	2.03e-21	3.79e-21

Table 5.13: Main charge changing processes involving the beam in the MITICA Neutraliser, and cross sections at 1 MeV [41].

gas	D_2
injection throughtput	19 Pa m^{3}s^{-1}
injection temperature	300 K
Neutraliser wall temperature	100 °C
RID wall temperature	70 °C
EAC (K_{ac})	0.2
beam energy	1 MeV

Table 5.14: Parameters of the simulation

each i path step of length Δx for each reaction k, the flux of each s species Γ_s is calculated as:

$$\left(\frac{\Delta\Gamma_{k,s}}{\Gamma_s}\right)_i = \sigma_k \cdot (x_i - x_{i-1}) \cdot \frac{1}{2}(n_{n,i} + n_{n,i-1}) \tag{5.8}$$

$$\Gamma_{s,i} = \Gamma_{s,i-1} + \sum_k \left(\frac{\Delta\Gamma_{k,s}}{\Gamma_s}\right)_i \cdot \Gamma_{s,i-1} \tag{5.9}$$

A particular case is presented and discussed here to explain the procedure that can be used. This is the case of D_2 gas, injected at 50% of the channel length, with the nominal Q=19 Pa m^{3}s^{-1}. The complete parameter list is reported in table 5.14; this is the same case of the green curve in figure 5.47.

It is interesting that, by imposing a very simple boundary condition such as uniform temperature at the neutraliser walls, a temperature distribution qualitatively similar to that obtained with CFD methods by Porton [133] is calculated.

Density and temperature profiles, with the relative local beam fractions, were calculated in various cases: some significant results are presented in figure 5.38, 5.39, 5.40, and 5.41.

Homogeneity of the density profiles

The homogeneity of the gas target thickness may differ from bemalet to beamlet. According to Avocado simulations, there is a quite good vertical homogeneity; there is a transverse non-homogeneity that is concentrated in the drift region before and after the Neutraliser, where the transverse density gradient is due to the lateral pumping. This effect in front of the Neutraliser is mitigated by the presence of the LED. Results are shown in figure 5.42 and 5.43.

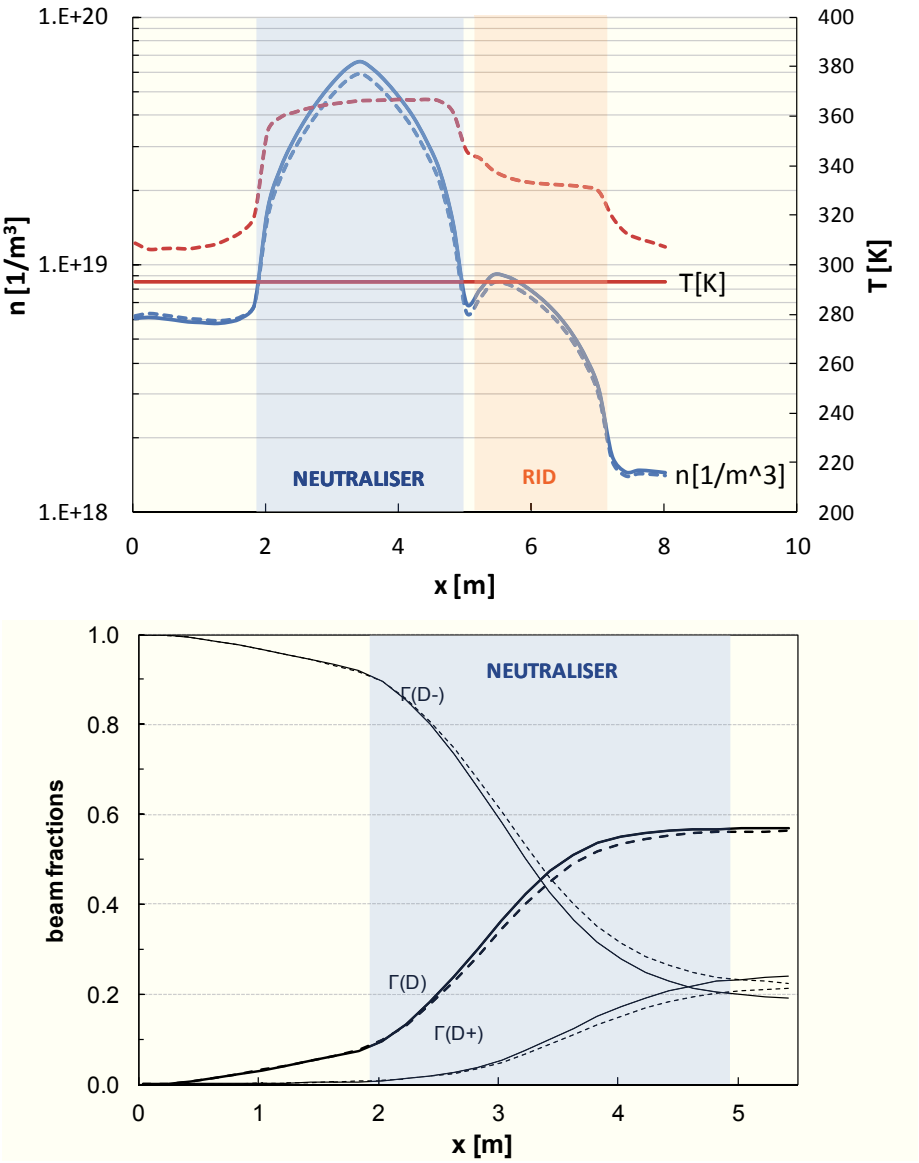


Figure 5.38: Comparison between the case of gas at constant temperature (solid lines) and the case of variable temperature (dashed lines): Gas density and temperature profiles (top) and beam fractions (bottom) up to the RID entrance along the path of a central beamlet, nominal deuterium injection throughput of 19 Pa m^3s^{-1} at 300K or 24.2 Pa m^3s^{-1} at 373 K, Neu wall panels at 25 °C or 100 °C, RID panels at 25 °C or 70°C respectively, uniform pressure at the cryopanels (0.001 Pa). The LED panels are considered.

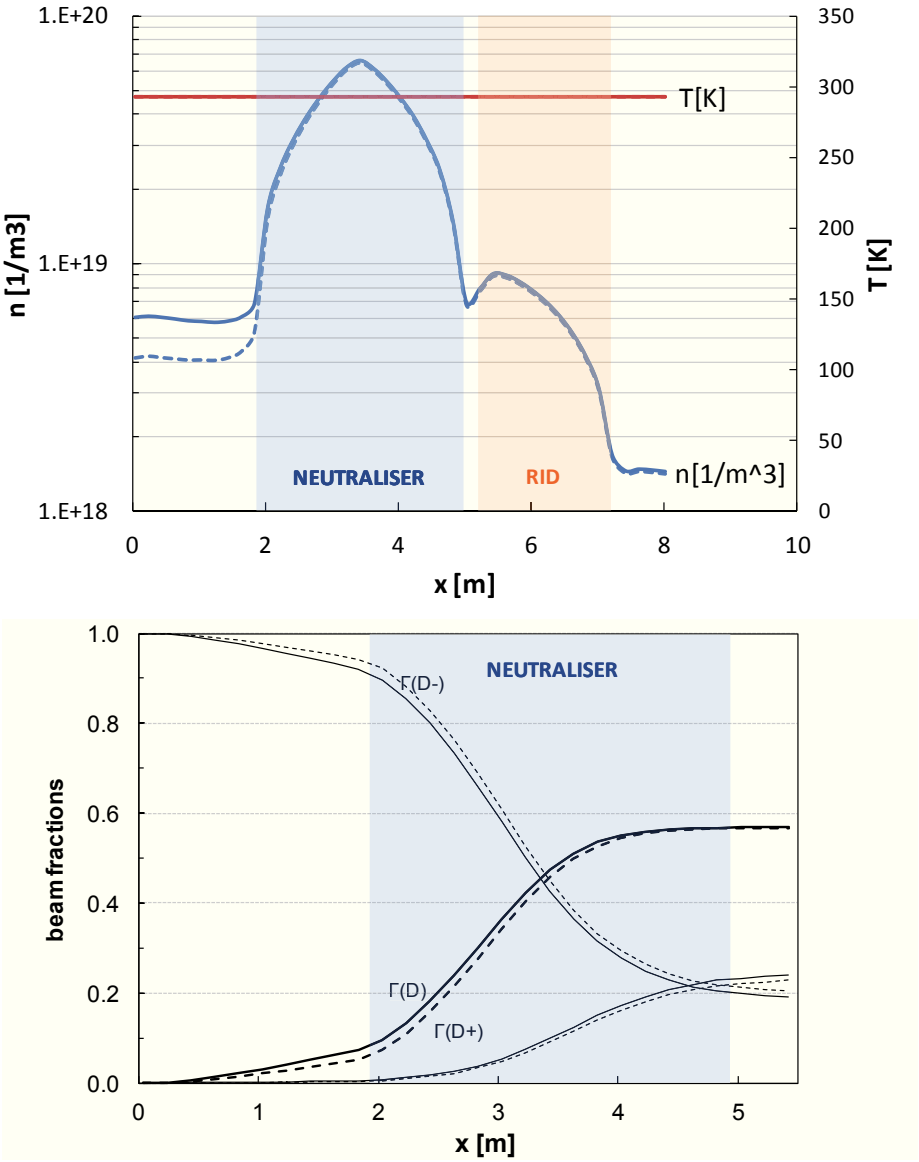


Figure 5.39: Comparison between the density profiles in the presence of the LED (solid lines) or not (dashed lines): Gas density and temperature profiles (top) and beam fractions (bottom) up to the RID entrance along the path of a central beamlet, in the case of nominal deuterium injection throughput of 19 Pa $m^3 s^{-1}$, gas at room temperature and uniform 0.001 Pa pressure at the cryopanels.

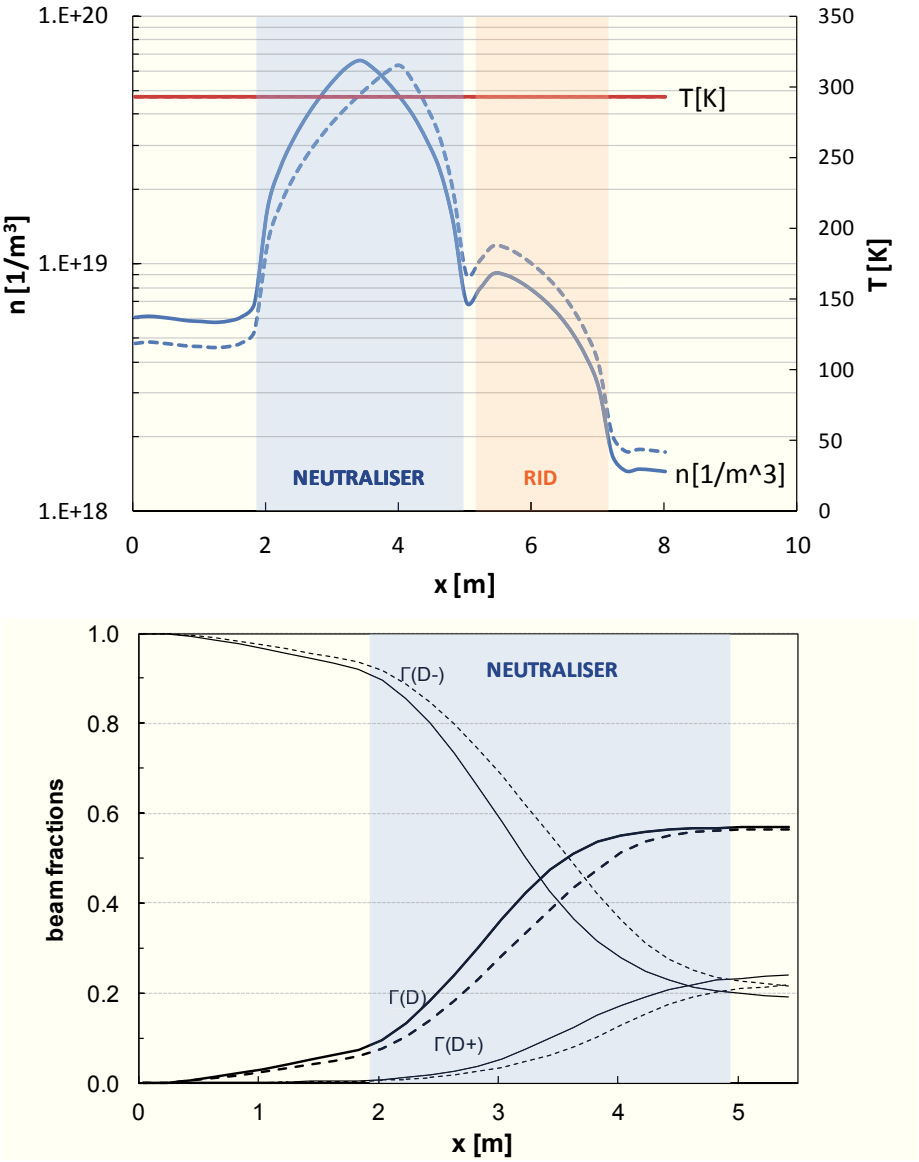


Figure 5.40: Comparison between the injection at 0.5 (solid lines) and 0.7 (dashed lines) of the Neutraliser length: Gas density and temperature profiles (top) and beam fractions (bottom) up to the RID entrance along the path of a central beamlet, in the case of nominal deuterium injection throughput of 19 Pa $m^3 s^{-1}$, gas at room temperature, uniform pressure at the cryopanels (0.001 Pa).

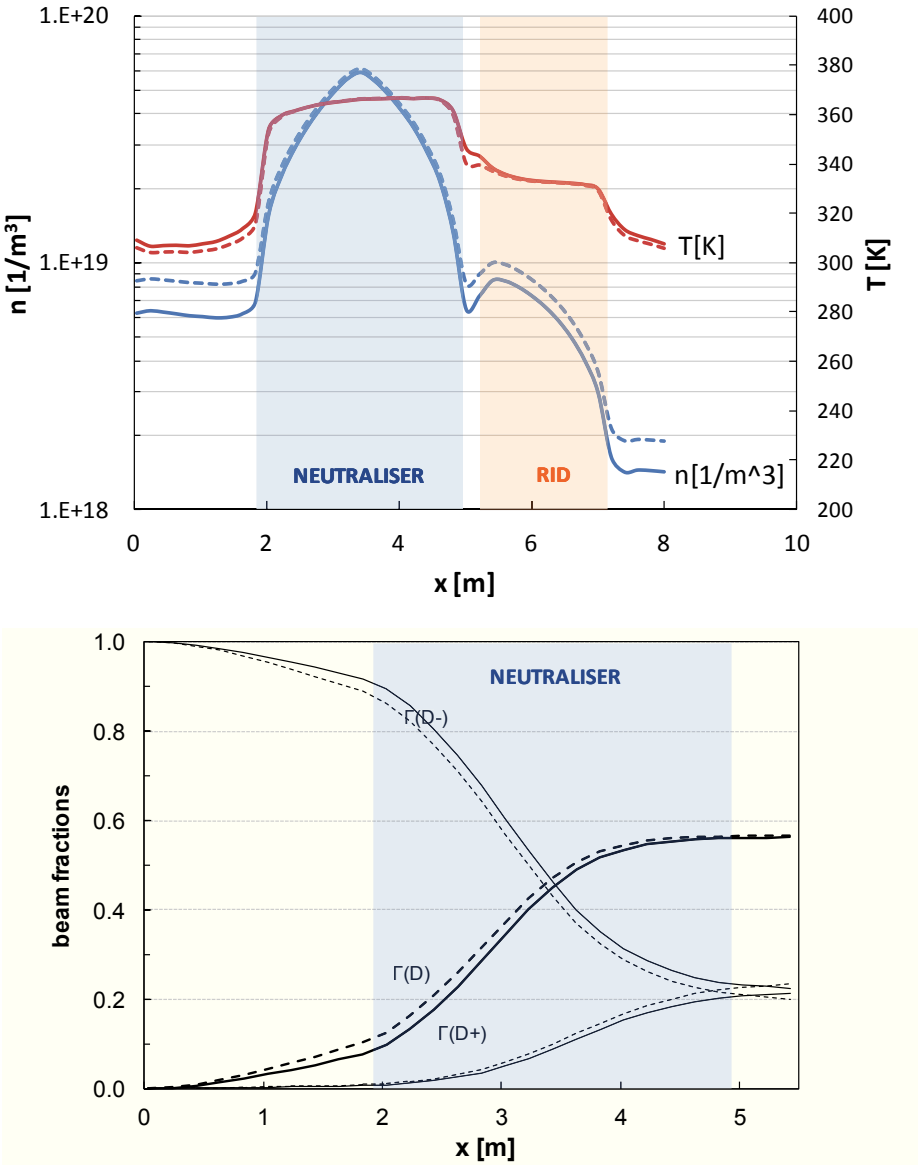


Figure 5.41: Comparison between the boundary condition at the cryopanels: 0.001 Pa (solid lines) and 3800 m^3/s (dashed lines): Gas density and temperature profiles (top) and beam fractions (bottom) up to the RID entrance along the path of a central beamlet, in the case of nominal deuterium injection throughput of 19 Pa $m^3 s^{-1}$ at 0.5 of the neutraliser length, hot walls of the neutralsier and the RID.

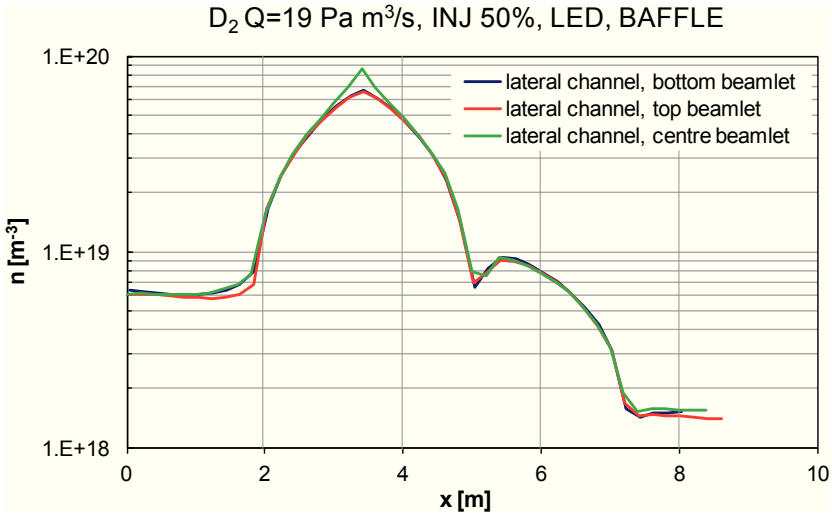


Figure 5.42: Density profies along the path of theree beamlets in the lateral channel of the neutraliser; nominal deuterium injection throughput of 19 Pa m^3s^{-1}, uniform pressure at the cryopanels (0.001 Pa). The LED panels are considered.

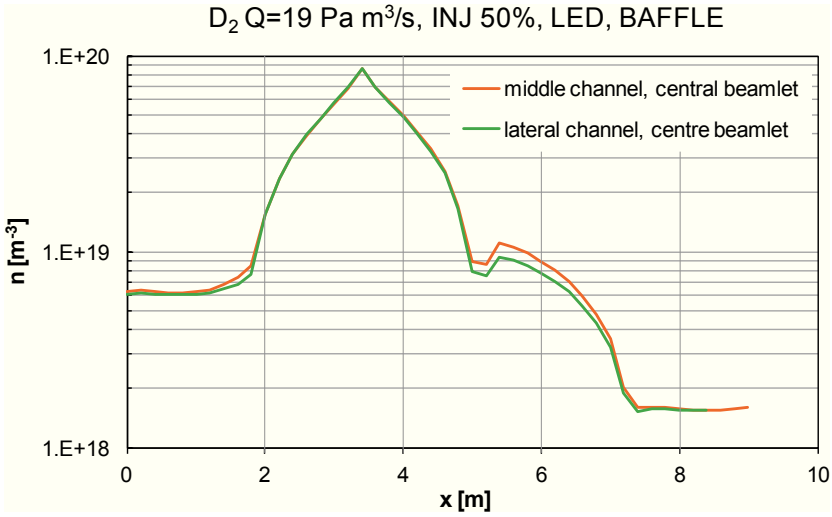


Figure 5.43: Density profies along the path of the centerline of the middle and lateral channel of the neutraliser; nominal deuterium injection throughput of 19 Pa m^3s^{-1}, uniform pressure at the cryopanels (0.001 Pa). The LED panels are considered.

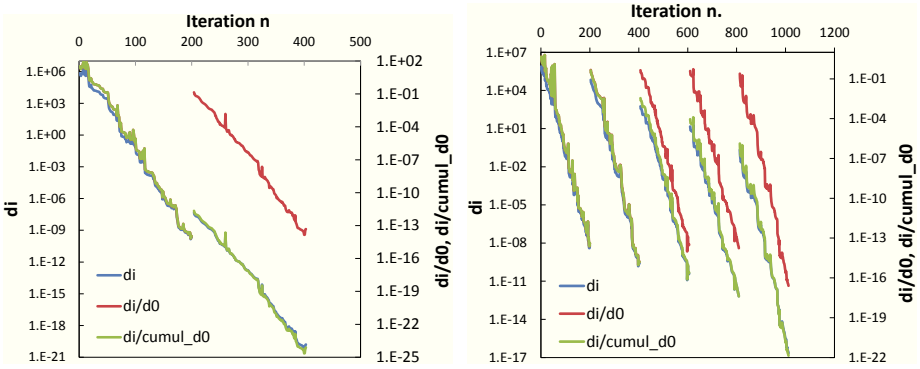


Figure 5.44: Convergence history for the simulation of the MITICA vessel, in the case of constant room temperature (left) and in the case of variable wall and gas temperature (right). The value of the residual calculated on the pressures, when normalized to the initial value, drops by tens of order of magnitude; during each iteration, the convergence is reached when the partial residual goes below, in this case, 10e-13.

5.2.4 Result II - Effect of LED panels

High-divergence or scattered energetic particles may reach the MITICA cryopanels, originating heat loads that at cryogenic temperatures are costly removed. As the beam optics and the solutions adopted to stop the co-accelerated electrons evolved, the divergence of these particles and the average trajectory changed. In this phase, a continuous conceptual re-design of the electron dump was necessary.

The major drawback of the LED is that it reduces the gas conductance between the BSV and the cryopump. One should notice that the striping losses in the accelerator directly depend on the gas density, as discussed in section 1.1.4, and therefore on the pumping capability and the tank pressure in the BSV.

In the early design for instance, the lateral Electron Dump was imagined with three vertical panels oriented towards the BS, with an angle that had been chosen to maximize the gas flow and efficiently stop the incoming particles. The vertical extension of the panels was such that any linear trajectory exiting from the GG apertures would have been stopped. At the end of 2011, the design was slightly modified. Two foldable panels on each side, inclined by 60°, directly intercept the trajectories oriented to the cryopanels, and an internal panel completes the protection. At the end of 2012, the LED was updated, and the panels prolonged down to the bottom of the vessel. The gas density analyses with AVOCADO supported the conceptual design of the electron dump, by studying the three design configurations and their effects.

Early design

In the early design, the three LED panels were about 2 m high, and a sensitivity study on the influence of their vertical extension was performed. The following boundary conditions were used: (a) constant pressure of 0.001 Pa or 0.01 Pa at the Cryopump surfaces ; (b) gas throughput at room temperature from

the five circular apertures in each channel, located at 70% of the neutraliser length, of 4mm diameter; (c) a constant gas temperature of 293 K everywhere. The reference points used for comparing the three cases are highlighted in figure 5.46. The pressure calculated at these locations are used to compare the gas distribution with or without the LED.

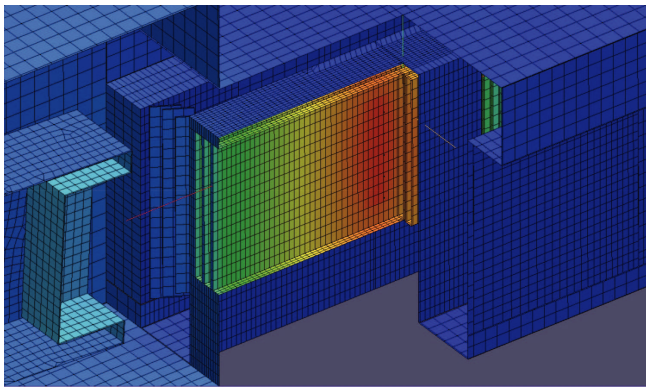


Figure 5.45: First design: detail of the LED and pressure distribution in log scale.

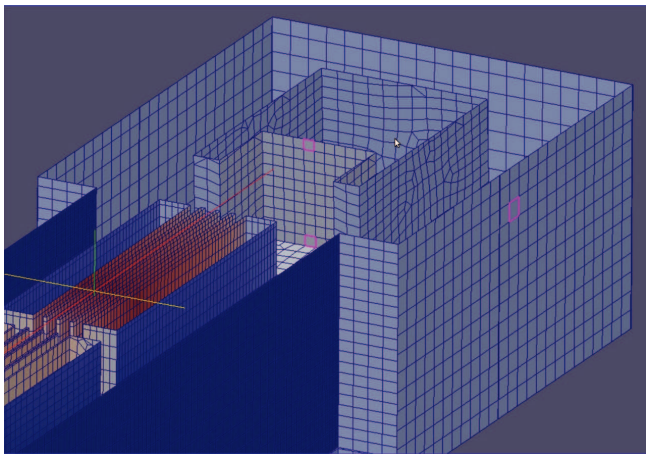


Figure 5.46: The highlighted elements in figure are the reference elements used for evaluating the variations of pressure caused by the LED panels

The main results are listed in table 5.15. Pressure calculated at different position (on the GG, on the lateral wall of the BSV...) are affected differently by the LED, since the geometry greatly affect the molecular conductance. The general trend, which is independent on the gas species, is an increase of about one quarter in terms of gas pressure.

Present design

A more mature design of the LED was reached in 2012. The foldable panels were reduced to two, and moved forward towards the BS. In the associated gas model,

		pressure increase		
LED vertical extension	no LED	80% height	100% height	120%
GG surface, center	ref.	+19.0%	+22.9%	+25.6%
GG surface, bottom	ref.	+18.5%	+21.7%	+24.1%
BSV side wall, center	ref.	+23.4%	+29.9%	+34.4%

Table 5.15: First design: effect of the LED panels on the gas distribution: pressure at test cells

the new geometry of the LED was taken into account, but also the geometry of the BLCs and the BS in the model was improved: (a) the overall dimensions of the Neu were revisited; (b) a new simplified geometry was adopted for the BS; (c) the geometry of the BSV and the flanged interface between it and the BLV was modelled properly; (d) the parallelepiped representing the Calorimeter was replaced by a V shaped volume. The simulation quantified the detrimental effect of the LED on the pressure distribution. The results are listed in table 5.16: the clear indication is that the LED increases the pressure in the BSV by about 30%.

BCs	position	no LED	LED	%
$p_{cryo} = 0.001$ Pa, Q=19 Pa m^3/s, D_2	GG surface, center [Pa]	0.0136	0.0175	+28.6
	GG surface, bottom [Pa]	0.0146	0.0185	+26.7
	BSV Side wall, center [Pa]	0.0077	0.0099	+28.8
	(Max Press at Neu Walls)	0.383	0.385	+0.4
$p_{cryo} = 0.001$ Pa, Q=43 Pa m^3/s, H_2	GG surface, center [Pa]	0.0212	0.0274	+29.4
	GG surface, bottom [Pa]	0.0228	0.0290	+27.4
	BSV Side wall, center [Pa]	0.0118	0.0153	+30.1
	(Max Press at Neu Walls)	0.613	0.615	+0.4

Table 5.16: Intermediate design: effect of the LED panels on the gas distribution: pressure at test cells

In year 2012, the physics and engineering design of the accelerator moved towards a solution with a long-ranged horizontal magnetic field, whose effect is a net deflection of the electrons toward the bottom of the BLV. The LED panels had to be extended to the bottom of the vessel, in order to directly intercept most of the electrons but also to stop the electrons scattered back, as described in section 7 and in [3]. A new analysis was carried out in order to compare the new design with the previous and with a configuration without LED. The simulations were performed considering deuterium nominal throughput (19 Pa m^3 s^{-1}) and, at the cryopanels, the pumping speed of 3800 m^{3}s$^-$1. The gas is at constant room temperature, 297 K in this case. The results shown in table 5.17 are different than those obtained before (in table 5.16), because the Boundary Condition at the outlet is changed. The absolute pressure at the surface of the cryopanels is different, and the percentage variation should account for the differential value of the pressure and not the absolute one. Nevertheless, it is not easy to choose a reference value of the pressure at the cryopanels when the constraint is given in terms of specific pumping speed: in other words, it is not clear where to read the pressure value (max, min, averaged on the cryopanels...). In figure 5.50, the smooth convergence history for one of these simulations is shown. The absolute residual (green line) drops by 28 orders of magnitude in

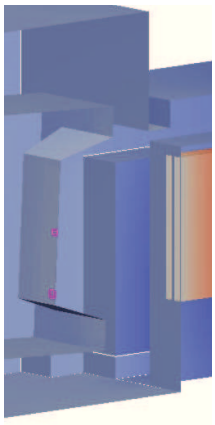
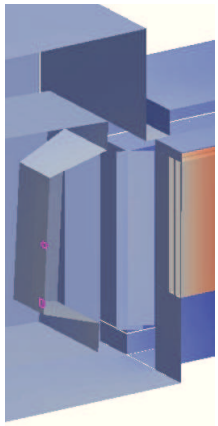
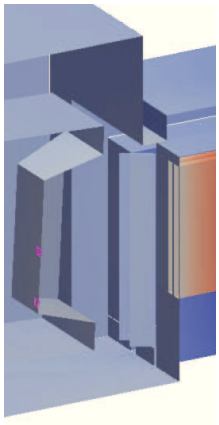
	Position			
				
A	GG, centre	0.0199 Pa	0.0268 Pa +35%	0.0282 Pa +42%
	GG, bottom	0.0200 Pa	0.0274 Pa +37%	0.0286 Pa +43%
	BSV, side	0.0149 Pa	0.0192 Pa +29%	0.0205 Pa +38%
B	GG, centre	0.0288 Pa	0.352 Pa 22%	0.0365 Pa +27%
	GG, bottom	0.0290 Pa	0.0357 Pa 23%	0.0368 Pa +27%
	BSV, side	0.0239 Pa	0.0276 Pa 15%	0.0288 Pa +21%

Table 5.17: Comparison between three solutions: no LED (on the left), LED in the intermediate design (middle), and the final design of the LED (right). The simulations were performed in the following conditions: (**A**) nominal D_2 throughput (19 Pa m^3 s^{-1}) and uniform pressure 0.001 Pa at the cryopanels, (**B**) nominal D_2 throughput (19 Pa m^3 s^{-1}) and uniform pumping speed totaling 3800 m^3/s.

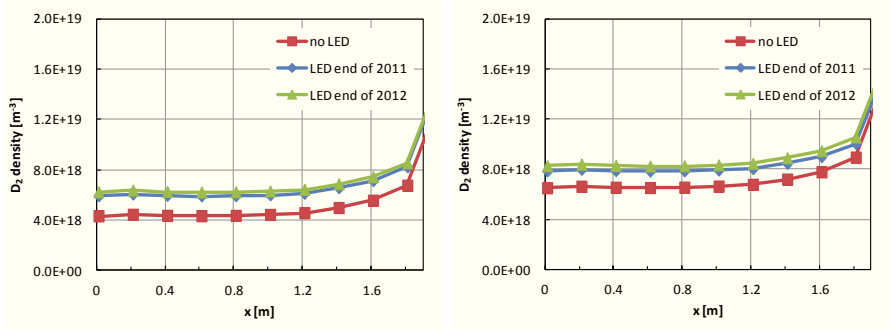


Figure 5.47: Density profiles calculated along the path of the same beamlet in the drift region before the Neutraliser, for the three cases: no LED, intermediate design, and present design. The boundary condition at the cryopanels is also considered: uniform pressure of 0.001 Pa (left) and uniform pumping speed of 3800 m^3/s (right). The gas is D_2 with nominal throughput.

400 iterations.

5.2.5 Result III - Density at tomography and BES cross-sections

The extracted beam is probed by beam emission spectroscopy, to measure the beam homogeneity, divergence and stripping losses. This technique has been used extensively in the past, and in MANITU at IPP, and will be used in SPIDER and MITICA [135]. Observing the emission of a selected spectral line with a sufficient number of lines-of-sight will allow a tomographic reconstruction of the two-dimensional beam emission, which is proportional to the beam density. The balmer line that is typically observed is the H_α emission,and the main processes [5,6] that contribute are basically:

$$H^- + H_2 \rightarrow H^0(n=3) + e + H_2$$

$$H^0 + H_2 \rightarrow H^0(n=3) + H_2$$

$$H^0 + H_2 \rightarrow H^0 + 2H(n=3)$$

The signal intensity is therefore proportional to $n_{gas} n_{beam} < \sigma^{\alpha}_{gas,beam} v >$, where n_{beam} can be n_{H^-} or n_{H^0}. These beam diagnostics interpret a signal that is proportional to both the beam and the background gas density, and clearly the homogeneity of the latter cannot be disregarded.

Pressure Probes

In the following, the analyses carried out to study the background gas homogeneity at the diagnostic planes (see an example in figure 5.49 are presented. In particular, the planes before and after the Neutraliser are considered in the case of Deuterium injected at 50% of the length is discussed, comparing the gas distribution with or without the LED and the gas baffle. The gas is assumed at constant room temperature, with nominal Q_{D_2} 19 Pa m^3 s^{-1} injected at 50% of Neu length. The qualitative result, in terms of uniformity, is valid also in the case of hydrogen gas; instead, this result might be partially sensitive to the boundary condition at the cryopumps p_{cryo}=0.001 Pa. A more complete discussion of the results can be found in the relative technical note [172].

A probe array was prepared at the positions of the diagnostics. Before the implementation in avocado of the post-processing utility for extrapolation of gas properties in the volume, small cubic elements were used as pressure probes. Using cubic elements, anisotropy in the velocity distribution is accounted; in order to give a single value, the values of pressure and densities at the six surfaces are averaged. Two Pressure Probe Arrays (PPA) were included in the model:

- PPA 1 is located at X=1.4 m, on a plane normal to the X axis between the BS and the NEU. The horizontal distance between probes is Y=37.5 mm, and the vertical one is Y=360 mm, defining 6 equally spaced rows made by 19 probes each.
- PPA 2 is located at X=5 m, on a plane normal to the X axis between the NEU and the RID. The horizontal distance between probes is Y=32 mm, and the vertical one is Y=330 mm, defining 6 equally spaced rows made by 19 probes each.

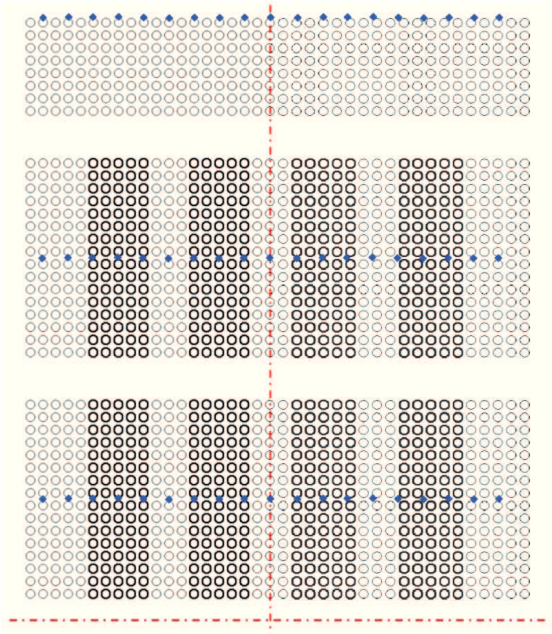


Figure 5.48: Position of the PPAs with respect to the beamlets

Position	Z [m]					
PPA1	0.825	0.465	0.105	-0.255	-0.615	-0.975
PPA2	0.579	0.249	-0.081	-0.411	-0.741	-1.071

Table 5.18: Vertical position of pressure probe rows

The diagnostic plane between RID and Calorimeter was not studied; this analysis requires a much more detailed modelling of the Calorimeter. The blue dots in figure 5.48 are the positions of the PPAs with respect to the position of the beamlets. The probe array is very dense along the horizontal line, given the geometry of the system: there are narrow, vertical channels, and the pumping is lateral.

Results and discussion

The density map has been reconstructed at the tomography planes after the BS and after the NEU. The gas temperature assumed constant at 293K; nevertheless, the gas exiting the Neutraliser channels is probably at a higher temperature, both because of the temperature of the Neu walls (on average, at about 373K), and because of the plasma that originates by interaction with the beam. These effects are neglected, and the density profiles calculated are, ideally, relevant to the beam-off condition.

In the case of the first PPA between BS and NEU, the background gas density at the edge beamlet groups is on average 10% less than the density at the central beamlet groups. In the present design of the neutraliser, four lateral panels are foreseen to protect the cryopumps, the Lateral Electron Dump LED. Considering these panels, the gas density at PPA 1 is slightly higher (about

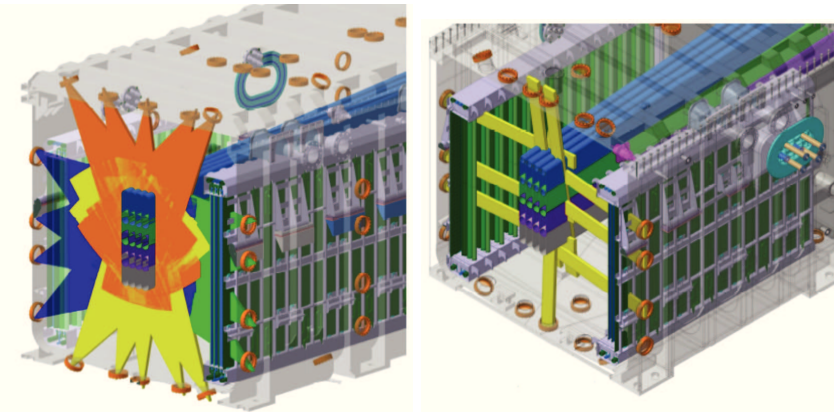


Figure 5.49: Example of Tomography (left) and BES LOS (right) in MITICA, both on planes slightly inclined with respect to the beam. [173]

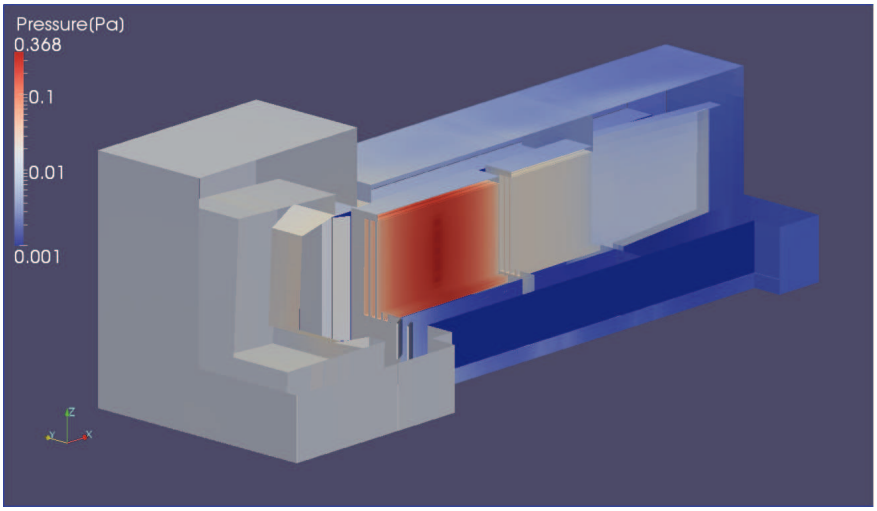


Figure 5.50: Pressure distribution and specific throughput resulting at the cryopump (LED and Gas Baffle, gas at constant room temperature, nominal Q_{D_2} 19 Pa m^3 s^-1 inected at 50% of Neu length, p_{cryo}=0.001 Pa)

+30%), but the diagonal non-homogeneity is the same. Only discrete vertical positions were considered as shown in figure 5.48, and therefore along the path of the the edge beamlets the density could be different.

In the case of gas injection at 70% of NEU length, the gas flow exiting the Neutraliser channels is less equally parted between the front and rear exit. This condition also has been analyzed; the profiles are not shown here in detail, but the non homogeneity is summarized in table 5.19

The calculated pressure distribution and the specific throughput are presented in figure 5.52 and figure 5.53, respectively considering the LED and the Gas Baffle and without considering these surfaces. The horizontal density profiles at the two PPAs are shown in figure 5.51(b),5.54 in the presence of the LED; as a reference, the profiles without LED in front of the Neutraliser are

injection (% NEU length)		50%	70%
LED	BS-NEU	Δn ~11%	Δn ~11%
	NEU-RID	Δn ~22%	Δn ~23%
no LED	BS-NEU	Δn ~14%	Δn ~13%
	NEU-RID	Δn ~22%	Δn ~13%

Table 5.19: Diagonal non-homogeneity.

shown in figure 5.51(a).

5.2.6 Result IV - Boundary conditions for the submodel of the Beam Source

The effective pressure at the lateral pumping of the BS have been estimated in the last configuration of the NBI, that is with the present design of the LED. As a consequence of the results obtained (see in particular figure 5.40), two cases have been considered: the injection at 0,5 and 07, of the Neutraliser length. The gas throughput exiting from these surfaces is that reported in table 5.11, post-processed at the surface elements highlighted in figure 5.55. The results are listed in table 5.20.

5.2.7 Comments

The vacuum environment of the MITICA injector has been modelled, considering updated dimensions of the first two beam line components. This model has been simulated using AVOCADO. The results have been compared with previous researches, with which the density profiles are fully compatible. The applicability of this kind of collisionless methods to MITICA has been evaluated and discussed. The complexity of a collisional solver is probably unnecessary in this domain, unless a deep understanding of the gas injection were necessary. The Knudsen number in the gas cell is as low as 0.4 in the proximity of the injection; having in mind this limit, and under the adequate assumption, Avocado results

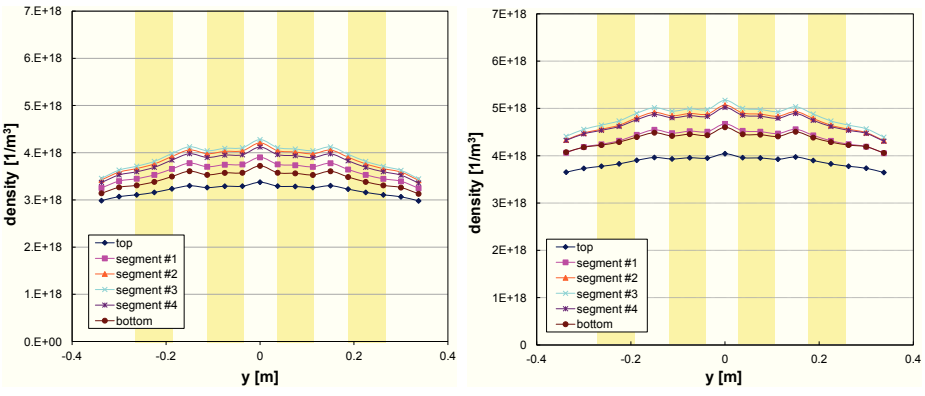


Figure 5.51: Pressure profile at the tomography plane before the NED, Gas Baffle, gas at constant room temperature, nominal Q_{D_2} 19 Pa m^3 s^{-1} inected at 50% of Neu length, p_{cryo}=0.001 Pa: (a) no LED, (b) LED.

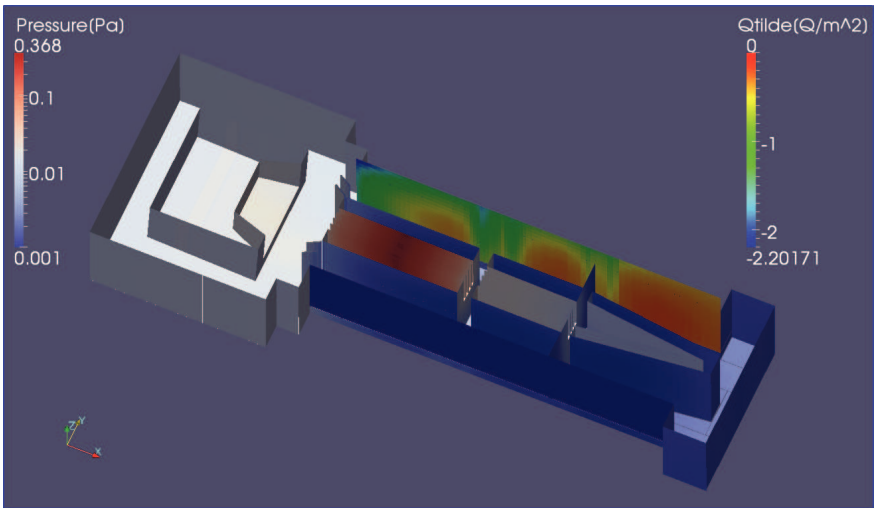


Figure 5.52: Pressure distribution and specific throughput resulting at the cryopump (LED and Gas Baffle, gas at constant room temperature, nominal Q_{D_2} 19 Pa m^3 s^-1 inected at 50% of Neu length, p_{cryo}=0.001 Pa)

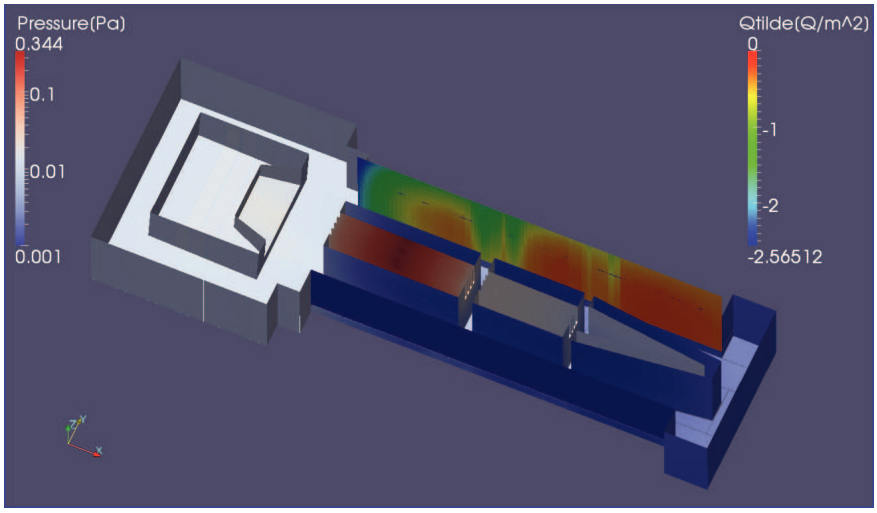


Figure 5.53: Pressure distribution and specific throughput resulting at the cryopump (no LED, no Gas Baffle, gas at constant room temperature, nominal Q_{D_2} 19 Pa m^3 s^-1 inected at 50% of Neu length, p_{cryo}=0.001 Pa)

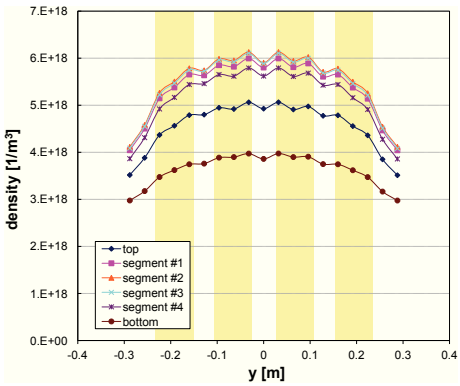


Figure 5.54: Pressure profile at the tomography plane between the NED and the RID, and Gas Baffle, nominal Q_{D_2} 19 Pa m^3 s^{-1} inected at 50% of Neu length, p_{cryo}=0.001 Pa; the influence of the LED is negligible in this case.

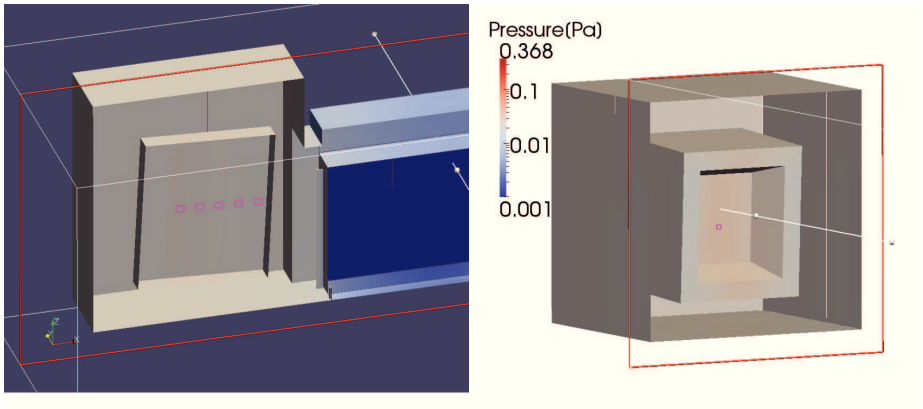


Figure 5.55: Surface elements considered.

Location	**Pressure [Pa]**	
	injection at 0,5	injection at 0,7
EG-AG1	0.0223	0.0187
AG1-AG2	0.0216	0.0179
AG2-AG3	0.0210	0.0173
AG3-AG4	0.0206	0.0169
AG4-GG	0.0203	0.0167
GG	0.0282	0.0223

Table 5.20: Background gas pressure to be used as BC in the BS submodel. The LED is considered, the nominal deuterium throughput is used and a uniform pressure of 0.001 Pa is assigned at the cryopanels.

have been applied to the calculation of the beam neutralisation; the method has been applied to the study the effect on the beam neutralisation of the wall temperature, as well as the effect of the lateral electron dump that reduce the conductance towards the cryopumps, and the position of the injection nozzle. In the simulations, the boundary condition applied to the cryopump surfaces has

strong influence in the gas density in the drift region in front of the Neutraliser; a sensitivity analysis has been performed to evaluate this effect. Further investigations are required on this issue. The gas density in the volume before the Neutraliser is affected by the lateral electron dump. Three LED designs have been compared; in the present design, the density is calculated to increases by 43% or 26% depending on the boundary condition at the cryopanels, and in one of this cases the requirement of 0.025 Pa maximum pressure in this area is not verified. The beam diagnostics interpret the emissions generated by the interaction of the beam with the background gas. The knowledge of the density distribution at the cross-sections where two beam diagnostics are located (before and after the Neutraliser) is therefore fundamental. With this model of MITICA gas flow, the homogeneity at these planes has been assessed, and a diagonal non-uniformity of about 22% has been quantified between the center of the beam and the corners.

5.3 Benchmarking with MANITU

The long pulse stability has been demonstrated at the test facility MANITU, able to operate with ITER relevant parameters. In the framework of the activities supporting the development of the ITER HNBs, a comprensive set of codes is being used at Consorzio RFX, aiming at simulating the most important aspects of the negative ion accelerators: electrical and magnetic fields, beam aiming and optics, pressure and density of the background gas, stripping reactions [129]. These codes are used for the engineering design optimization of the overall injector and its components, as well as for the prediction of the operating conditions and the interpretation of the experimental results: SLACCAD, EAMCC (see section 1.1.4).

The extraction and acceleration system in MANITU is composed by PG, EG and GG. The potential of the EG and GG is variable between respectively 2.5÷9.0 and 18÷29 kV. The beam diagnostics that will provide most of the data to be compared with the numerical results is the beam emission spectroscopy (BES).

AVOCADO has been used to calculate, in a simplified geometry of the extraction and acceleration system, the density profile to be used in the EAMCC code. The results of various cases and the preliminary interpretation is presented in the following.

5.3.1 Density profiles in the simplified geometry

The MANITU grids have 262 apertures. In H_2 and D_2 operations, the filling pressures of 0.44÷0.46 Pa and 0.33÷0.34 Pa respectively are obtained by a throughput of 5.6÷5.7 mbar l/s and 2.9÷3 mbar l/s.

A simplified cylindrical model with only 7 beamlets has been developed in order to calculate the density profiles across the accelerator length. This simplification is based on the fact that no lateral pumping occurs between the grids, since the accelerator is closed at the sides. The validity of this model has, nonetheless, a limit in the presence of lateral walls all around the system.

The gas properties in the PS are assigned to the boundaries of the cylinder. The side boundaries are included. The same approach was followed to model

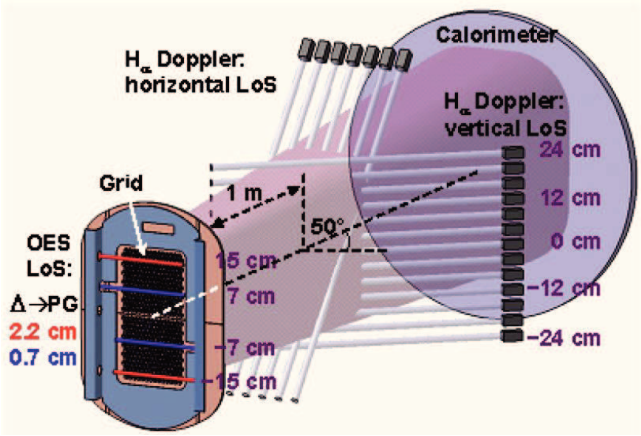


Figure 5.56: Beam Emission Spectroscopy set-up in MANITU [136].

grid	T [K]
PG	443
EG	300
GG	300

Table 5.21: Temperature assigned to the grids

the downstream tank. The tank pressure is as low as 0.001 Pa, even though the measured pressure of this region in MANITU is even lower.

Apart from the case at room temperature, the surface temperature assigned at the three grids is listed in table 5.21.

Three cases are presented in the following.

1) Room temperature, deuterium the model is shown in figure 5.57(a). The density profiles and the temperature and pressure profiles are presented in figure 5.57 (b) and (c).

2) Ts=1300 K and low pressure A preliminary calculation of the density profile is performed using the filling pressure with a temperature expected in the presence of plasma (gas temperature in the source of about 1300 K). The results for the cases of hydrogen and deuterium are presented in figure 5.58.

3) Ts=1300 K and same mass flow rate as at room temperature the measurements of pressure performed in the PS has to be modified accounting for the thermal transpiration. The approach that has been followed to calculate the density profiles in this case is to vary the pressure until the same mass flow rate (or molecular flux) as in case (1) is reached. It results $p_{PS} \approx 0.6$ Pa for deuterium. The accommodation factor slightly affects the value of pressure at convergence; the profiles are shown in figure 5.59. Since the beamlet cross-section is circular, the uniformity of the density profile was assessed in the cylinder, comparing three paths on the axis and off-axis (see figure 5.59); there is a negligible non-uniformity.

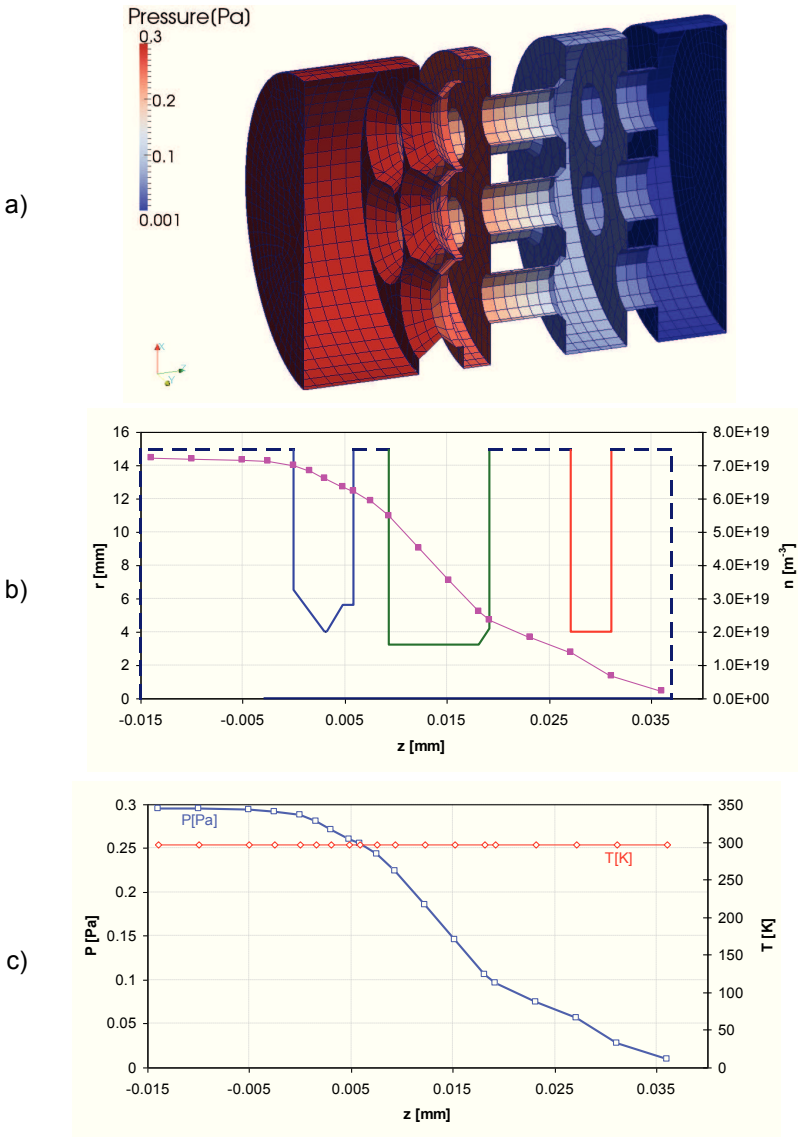


Figure 5.57: Case 1: A section of the model shows the pressure distribution (a); the cylindrical geometry of a single aperture and the density profile (b); the temperature and pressure profile (c). The simulation considers deuterium at room temperature.

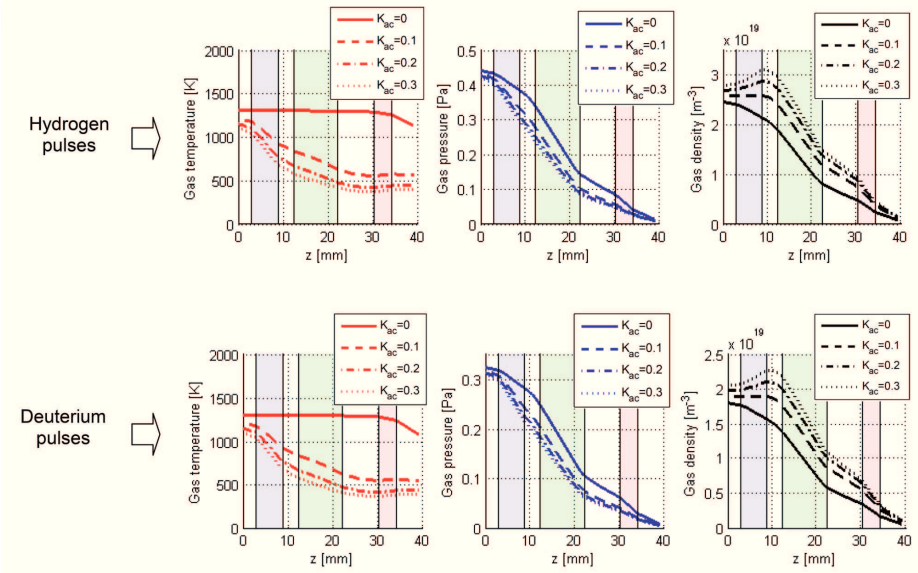


Figure 5.58: Case 2: from left to right, Temperature, pressure and density of the background gas along the axis of the beamlets. Hydrogen and deuterium cases are presented parametrized on the accommodation factor K_{ac}. The simulation is performed assigning gas temperature of 1300 K in the plasma source, and pressures are reported in the measurement data.

Up to these days, the eight results of case (2) have been analyzed with EAMCC, computing the stripping losses as n_{H^0}/n_{H^-}. The numerical results are presented in figure 5.61, where the range of experimental stripping is also shown.

5.3.2 Comments

The density profile have a peak after the PG when the accommodation factor is sufficiently high. The stripping losses calculated with EAMCC are generally higher than the experimental values. The reason for the mismatch is under investigation.

The very low stripping losses estimated in MANITU are correctly anticipated by the numerical codes only in the case of very low accommodation factor K_{ac}. This is reasonable in the case of hydrogen gas, because, as general rule, the lighter is the particle with respect to the atoms of the solid walls, the smaller is the accommodation. In the case of biatomic molecule, the fraction of the accommodated kinetic energy may be difficult to estimate, since in the rebound there can be an exchange of energy between the modes - translational, vibrational and rotational. A deeper investigation on the experimental data related to the accommodation factors shall be carried out.

The BES measurement gives a wave length spectrum, that is interpreted at IPP identifying three components: the steady background gas at a wavelength around 656.2, a Gaussian peak at the wavelength corresponding to the full acceleration energy and a small Gaussian around the wavelength around the extraction potential. The common interpretation in a three-grid accelerator is

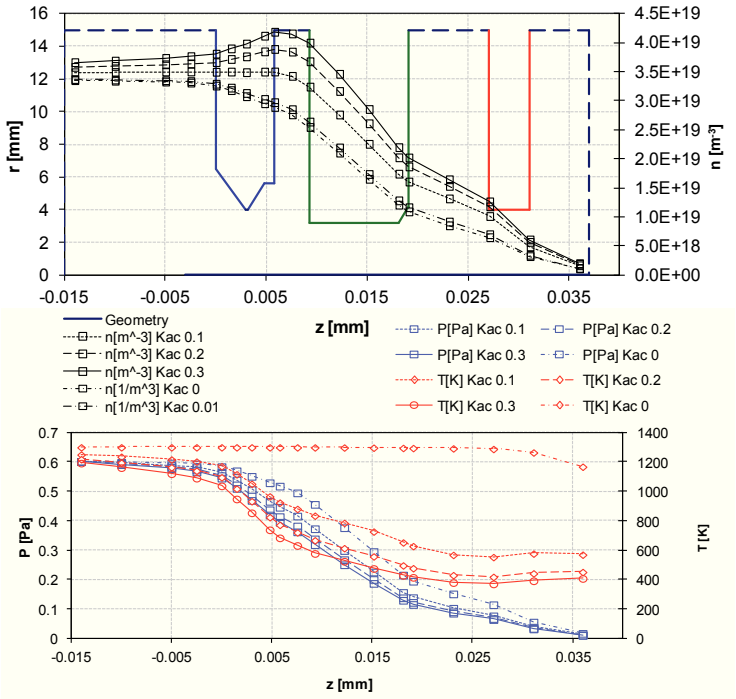


Figure 5.59: Case 3: density profiles calculated for different accommodation factors (a) and the corresponding temperature and pressure profiles (b).

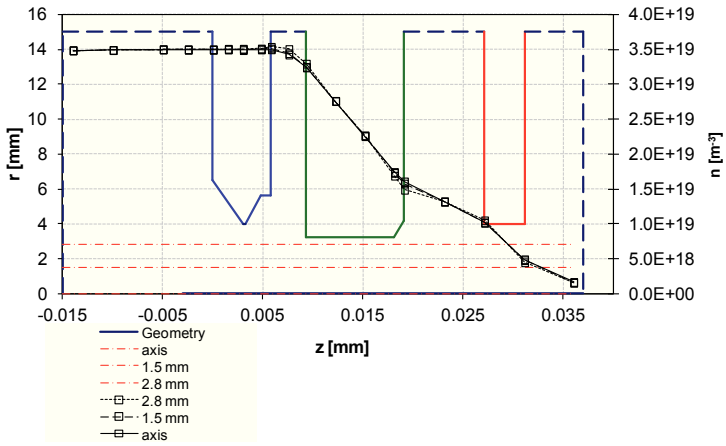


Figure 5.60: Case 3: density profiles calculated along three paths: on the axis, 1.5 mm off -axis, and 2.8 mm off-axis.

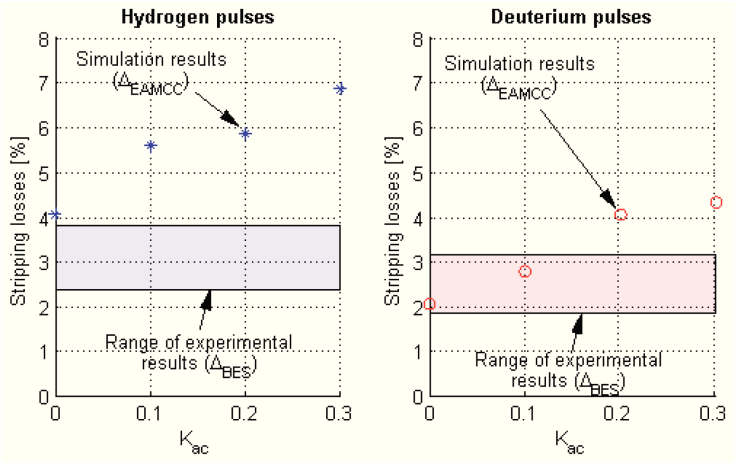


Figure 5.61: Stripping losses caused by the background gas density, calculated considering case (2) [174].

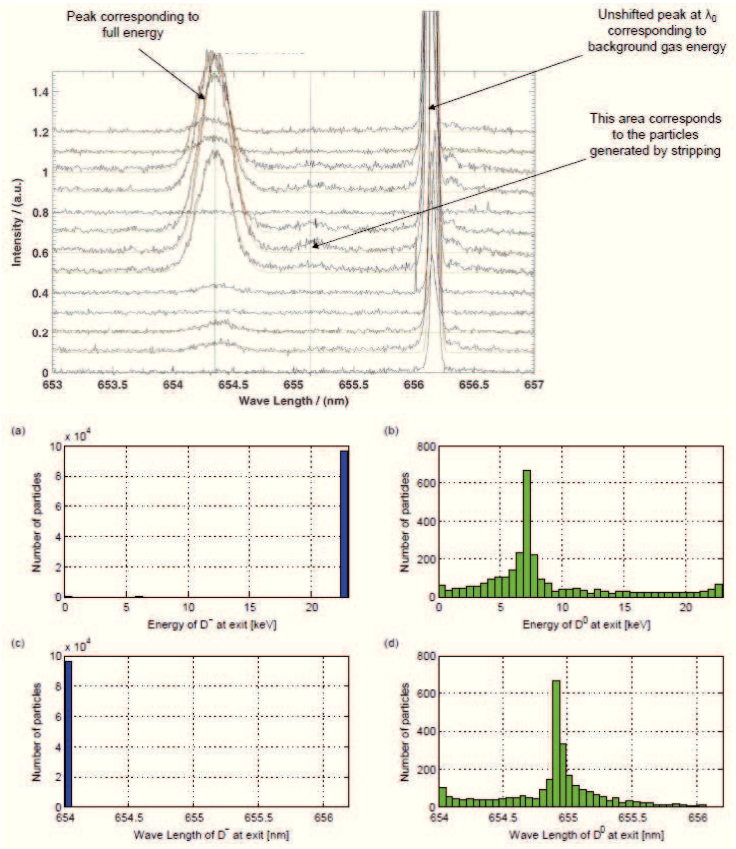


Figure 5.62: Measured wavelength spectrum (on top) and numerical spectrum (at the bottom): energy (a) and wavelength (b) spectrum of the negative ions and energy (a) and wavelength (b) spectrum of the neutral atoms. [174].

that most of the stripping occurs at low beam energies in the region before and around the EG. The numerical results have been processed to reconstruct this wave length spectrum [174]. Both the measured and simulated spectrum are presented in figure 5.62: the experimental stripping is calculated integrating the normal distribution in a width ± 0.25 nm around the extraction potential wavelength, and the comparison with the numerical data shall be carried out bearing this in mind. A deeper understanding of the experimental procedures and measurement parameters shall be carried out before any further speculation.

This concerning the interpretation of results from case (3), which are not presented here, even though it is expected to follow the correct approach.

5.4 RFX-Mod pumping system

The base pressure of the RFX machine is in the range of 10^{-7} Pa at room temperature. The pumping speed of several cubic meters required to reach this UHV pressure range is obtained by 10 turbomolecular pump (1 m^3/s for N_2 each) connected to the pumping port shown in figure 5.63 by means of an angle connector, as shown in figure 5.63. The pressure in this connector, called "sphere", is measured in the machine. The following analysis has been carried out to understand the behaviour of the pumping system, in variable pressure ranges. The transient regime could be characterised by measurements after the numerical model characterized the molecular conductance.

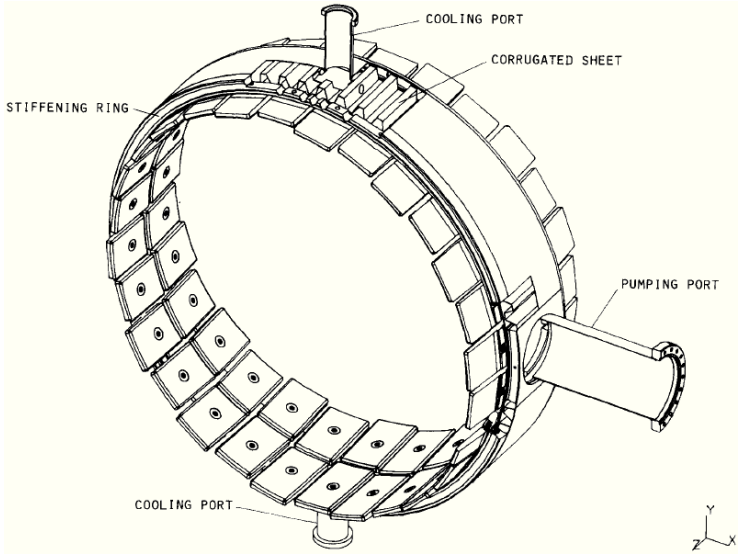


Figure 5.63: One of the 12 pumping section of the RFX vessel. [105]

5.4.1 Characterization of the pumping system

The gas conductance in molecular regime has been calculated with AVOCADO. The limits of the molecular regime have been also estimated considering the diameter of the pumping ports.

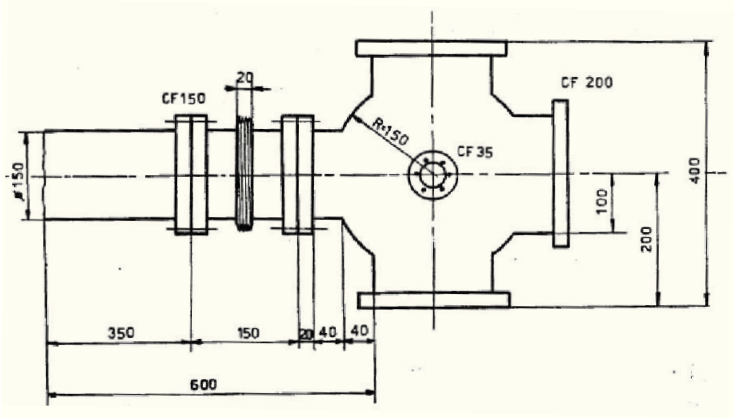


Figure 5.64: Sketch of the pumping port: a turbomolecular pump is connected to the bottom flange of the sphere.

The characterization is carried out simulating the following conditions: (A) uniform pressure at the connection with the toroidal chamber p_A and (C) uniform pumping speed S=1000 l/s at the effective pumping surface of the turbopump. The gas pressure and temperature at (A) has been changed, in order to calculate the conductance C under various operating conditions. The surfaces where the boundary conditions are applied and where the pressure can be measured in the machine (B) are shown in figure 5.65.

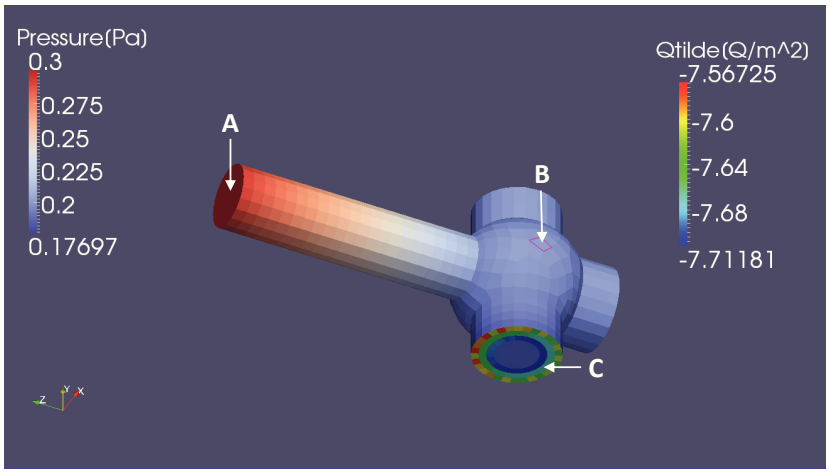


Figure 5.65: Calculated pressure distribution and specific throughput at the effective pumping surface of the turbopump. In figure also the locations where the boundary conditions are applied are shown.

The boundaries of the molecular regime have been calculated considering eq. 5.1 and a characteristic length of 0.15 m. In the case of hydrogen gas, the maximum pressure is 0.085 Pa, which rises to 0.105 if a gas temperature of 100 °C is considered. In the case of helium, the limits are respectively 0.155 and 0.194 Pa under the same assumptions. In the simulations of the different

gas and gas temperature has been performed assuming constant and uniform wall temperature of 297 K.

The conductance is calculated as $C = Q/\Delta p$, but the throughput had to be corrected in order to account for the mass flow (or the particle flux ϕ). The pressure at the outlet surface (C) is calculated integrating the result over the pumping surface.

The results in terms of throughput and conductances are listed in table 5.22 for inlet pressure $p_A = 0.1$ Pa; C is clearly higher when the gas enters the duct at higher temperature. The pressure that can be measured at (B) and the pressure at the inlet of the turbopump (C) is plotted in figure 5.66 as a function of the pressure in the torus.

The total N_2 pumping speed at the 10 pumping ports results 4 m^3/s in molecular regime. At the moment, the model is limited to the geometry described above, but it should include the torus pumping section, to properly model the complete UHV system.

gas	T [K] in the torus	p_C [Pa]	p_B [Pa]	C [m^3/s]
H_2	297	0.0596	0.067	1.48
H_2	373	0.0551	0.062	1.53
He	297	0.051	0.060	1.04
He	373	0.047	0.055	1.12

Table 5.22: Temperature assigned to the grids

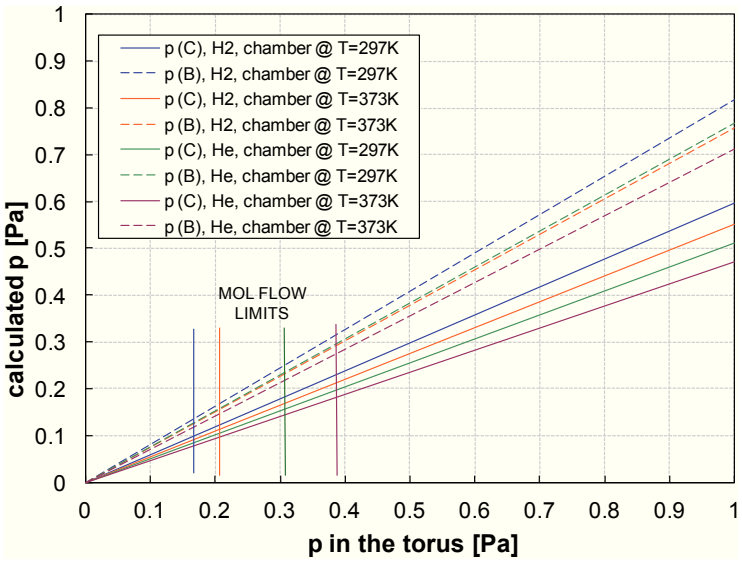


Figure 5.66: Calculated pressure as a function of the pressure in the torus. The validity of the results is ideally limited to the molecular limit indicated for each case.

Part II

MITICA Neutraliser and Electron Dump

6

The MITICA Neutraliser: thermohydraulic and thermomechanical design

One of the most critical issues for present and future fusion machines is the reliability of plasma and beam facing components, that is highly correlated to their material properties and the heat exchange capability of their design. The engineering problem is challenging and the research in this field requires a large number of multidisciplinary competences as thermo-mechanical and thermo-hydraulic, together with the knowledge of materials able to resist to thermal fatigue cycles.

In the case of beam-facing components, the estimates of power deposition and thermal energy removal from facing components, and even between boundary components, needs further knowledge of many aspects: from the beam behaviour to its the interactions with the materials, the chemical and physical sputtering, and in-vacuum thermal contact resistance.

Among the components of an NBI, the Neutraliser plays an important role. In particular, the Neutraliser and Electron Dump (NED) is the first Beam Line Component (BLC) of MITICA. It is subjected to heating by beam and co-accelerated particles. The performance and the reliability of the NED depends on many functional and system requirements, which shall be considered since the design phase. These general requirements are analysed and developed, obtaining engineering and technological requirements that are at the basis of the design of the NED.

I faced these problematics in my research activity for the design of the Neutraliser of the MITICA and ITER Neutral Beam Injector. I carried out the analyses for the design and verification of the many NED components, by using numerical models, analyses, design optimization, and tests. A wide documentation has been prepared, constituted by RFX technical reports [175, 176, 177, 178, 179, 180, 181, 182, 183, 184, 185, 186, 187, 188, 189, 190, 191, 192, 193].

6.1 Design requirements

The requirements of the NED system are summarized in the following to recognize the relevant requirements that impact the design and the manufacturing of the component. As for the other ITER components, there exists a Design Requirement Document [194] where the requirements are summarized.

6.1.1 Beam optics

The NED has been designed for the case of maximum extracted beam power, considering the present configuration of multi-grid ion source. The beam parameters listed in table 6.1 complete the information given in table 2. The thermo-mechanical verifications assume these beam parameters as those causing the maximum power deposition on the Neutraliser and Electron Dump. In addition, the geometry of the wall panels has to be compatible with the beam aiming [137]; the nominal position of the Neutraliser along the beam line corresponds to a distance of 1900 mm between the grounded grid centre and the Neutralizer entrance section (panels' edges).

Beam Physics Parameter	**Value**
Beam core divergence [mrad]	7
Halo power	15%
Halo divergence [mrad]	30
Vertical tilting [mrad]	49.2 (nominal) ±10 (tilting)
Horizontal misalignment [mrad]	± 2

Table 6.1: Physical parameters of the beam which determine the highest thermal load on the NED

6.1.2 Beam operation

The thermal cycles on the mechanical components determining thermal fatigue that are of two kinds:

1. cycles of beam-on/beam-off cycles, for pulses at full power: this cycle implies the full thermal excursion from the coolant temperature to the maximum temperature at the surface;

2. cycles of breakdowns in the beam source, associated with the loss of voltage holding and consequent loss of beam; this type of cycle has a duration typically much shorter than the thermal time constant of the component and causes a partial temperature decrease.

The NED has been designed for the number and frequency of beam breakdowns reported in table 6.2, which are directly derived from the operational requirements for the beam operations presented in table 1.4. The same number of beam cycles is foreseen for the NED operating in MITICA and in the ITER HNBs.

Parameter	Value
Total number of pulses	5.0×10^4
Total beam on time [s]	1.98×10^7
Total number of breakdowns	4.5×10^5
Breakdown (BD) frequency	Plasma operation: f=0.020 Hz (72 BDs/hr) Commissioning: f=0.20 Hz (720 BDs/hr)

Table 6.2: cycles of beam operations: total parameters

6.1.3 Cooling Parameters

The water for cooling will be provided to the NED component with the properties described in table 6.3. As clearly visible, a slight difference is expected between the cooling parameters in MITICA or in the ITER HNB, which has been accounted in the design. During beam-off, the NED will be fed with a trickle flow of cooling water to avoid freezing-up when required. The trickle flow will be maintained by a pressure drop of 0.1 MPa across the NED. In MITICA, the NED will be dried and drained independently of the other BLCs, by using the component drying facility.

Coolant Parameter	MITICA condition	ITER condition
Flow rate [kg/s]	80 (maximum)	100 (nominal)
Inlet Pressure [MPa]	2.0	2.4
Outlet Pressure (MIN) [MPa]	0.8	0.8
Optimum Pressure Drop [MPa]	$\approx$0.55	$\approx$0.55
Inlet temperature (MIN - MAX) [°C]	20 - 55	20 - 35
Outlet Temperature (MAX) [°C]	100	100
Water resistivity at 25 °C [M$\Omega\cdot$ cm]	1.0$\div$2.0	$\geq$ 2.0

Table 6.3: Cooling parameters

6.1.4 Coordinates, position and alignment

The cartesian coordinate system that defines the geometric positions within the MITICA beam line is the Grounded Grid (GG) coordinate system: the origin is the GG center, z is the vertical direction, and the x-axis is the projection of the beam axis on a horizontal plane.

The NED has been positioned and aligned, verifying its horizontal and vertical position. The NED shall be positioned, with respect to the coordinate system, within the following tolerances:

a) $\pm$10mm x-axis (longitudinal direction);

b) $\pm$1mm y-axis (transversal direction);

c) $\pm$5mm z-axis (vertical direction).

The manufacturing and positioning errors of the NED will be compensated by carrying out some adjustments at the Adjustable Bed in order to set the final position within $\pm$10 mm with reference to the nominal one. The vertical position of the Neutraliser has been fixed to -178 mm with respect to the Grounded Grid centre, and will be discussed in section 7.3.3 considering different criteria. The

size and positioning of the NED relative to the cryo-pumps is included inside a specified envelope to avoid freeze-up of components: 100 mm is the reference distance from cryo-pumps.

6.2 Regulatory documents and standards

The regulatory documents and standards applicable to the NED design can be categorized into three groups:

Regulatory documents European "Pressure Equipment Directive" (PED)

Design codes and standards ASME section VIII (pressure vessel) [138], ASME B31.3 (piping), RCC-MR (nuclear components, high temperature structures) [139].

ITER codes and standards Structural Design Criteria for In-vessel Components (SDC-IC) [140], and various ITER handbooks: Vacuum Handbook (VH), Remote Handling Code of Practice (IRHCOP), Material Properties Handbook (MPH) [141].

In particular the ASME VIII and the ITER SDC-IC define criteria for the thermo-mechanical verification, which will be discussed in the following.

6.2.1 Primary and secondary stresses

The classification in stress categories is based on the consequences of exceeding the yield strength.

The *primary stress* P is not self-limiting, as it is caused by the application of a mechanical force, pressure or moment; a failure can occur as a result of a single application of the loading. By contrast, *secondary stress* Q is caused by stress concentration from a nearby constraint, geometrical discontinuities, or self-constraint of the structure; as the strength of the material is reached, yielding eliminates the source of the stress and determines stress redistribution after the first application of the load but no failure or gross distortion. Secondary stresses are also called "deformation controlled" stresses, while "load controlled" are the primary stresses; the latter will continue to increase proportionally to the applied load irrespectively to the stress-strain curve.

In a membrane, such as the walls of a pressure vessel, an additional classification of the primary stresses is possible, when considering the linear stress distribution across the thickness of the wall (stress classification line through a shell). The *primary membrane stress* P_m is the average value through the wall, such that load redistribution cannot occur and loading beyond the yield strength determines failure; a *local primary membrane stress* P_L instead refers to limited extensions where the yield strength can be exceeded, but do not belong to secondary stresses. The *primary bending stress* P_b have the same bending moment as the actual stress distribution, and are somewhat proportional to the distance from the effective center of the wall thickness. The *peak stress* F is the increment of stress added by a stress concentration that does not cause noticeable distortion. The *total stress* is used in fatigue analysis.

In the elastic analysis, stresses are calculated, combined, and compared to limits, which are multiples of some material properties: there are the *allowable primary membrane stress intensity* S_m, which is 2/3 of the *minimum yield*

strength $S_{y,min}$ or 1/3 of the *minimum ultimate tensile strength* $S_{u,min}$; the *allowable primary plus secondary membrane stress intensity* S_e, proportional to $1/3S_{u,min}$ with or without a correction factor.; and the *allowable total stress intensity* S_d.

As said before, this classification is done considering the consequences originated by the stress type: in the same fashion, different rules shall be verified, each related to a particular consequence. The design rules are presented in table 6.4, which includes the criterion as of SDC-IC. These conditions will be verified for the elements that form the NED.

6.2.2 Thermomechanical criteria and rules for the design

The conditions a component undergoes during various operation phases can be classified into categories according to many considerations, including probability of occurrence and consequences. For each component, it must be specified what load case apply to it and which type of criteria shall be verified:

Category I, II, III, and IV which is basically and index of the likelihood of the load case with associated the acceptable damage limits;

Criteria level A, C, D section of the Structural Design Criteria for the ITER in-vessel components (SDC-IC) which identifies, basically, the safety margins required for the load case.

The two are combined as reported in table 6.5. Among others, the possible loads originates from:

- internal and external pressure;
- weight and the static and dynamic loads originated internally of the component;
- weight and the static and dynamic loads originated outside the component;

Criterion	Rule	Condition
Immediate plastic collapse and plastic instability (IC 3211)	Primary membrane and bending stress	$\overline{P_m} \le S_m(T_m, \phi t_m)$ [MPa]
		$\overline{P_L + P_b} \le K_{eff} S_m(T_m, \phi t_m)$ [MPa]
	Local primary membrane stress	$\overline{P_L} \le \min\left[1.5S_m(T_m, \phi t_m), S_{y,\min}(T_m, \phi t_m)\right]$
		$\overline{P_L} \le 1.1 S_m(T_m, \phi t_m)$ [MPa]
Immediate plastic flow localization (IC 3212)	Primary plus secondary membrane stress	$\overline{P_L + Q_L} \le S_e(T_m, \phi t_m)$ [MPa]
Local fracture due to exhaustion of ductility (IC 3213)	Total stress, including peak stress	$\overline{P_L + P_b + Q + F} \le S_d(T, \phi t, r_2)$ [MPa]
	Total stress, excluding peak stress	$\overline{P_L + P_b + Q} \le S_d(T, \phi t, r_3)$ [MPa]
Fast fracture (IC 3214)	Global fast fracture	$K_I \le 0.33 K_C(T_m, \phi t_m)$ [MPa m$^{1/2}$]
	Local fast fracture	$K_I \le 0.67 K_C(T_m, \phi t_m)$ [MPa m$^{1/2}$]

Table 6.4: Verification criteria as of SDC-IC [140]

Loading Category		Category Conditions	SDC-IC criteria level
I	Operational	Normal	A
II	Likely	Upset	A
III	Unlikely	Emergency	C
IV	Extremely unlikely	Faulted	D

Table 6.5: Load category and relative criteria

- electromagnetic loads;
- temperature effects;
- irradiation induced effects;
- earthquakes.

6.2.3 Structural Materials

The thermal, mechanical monotonic and cyclic propertiesof AISI 304L, AISI 316LN, OFHC Copper are defined in the ITER Material Properties Handbook [141].

All the materials properties have been implemented in the FE models as polynomial equations in temperature of the 3rd or 4th degree. These equations have been used by the FE code for the nonlinear calculations during the numerical solution processes.

6.2.4 Thermohydraulic correlations

Water properties

The fluid used to cool the NED and the NB Test Facilities is demineralized water with ultrapure grade. Accurate thermophysical properties of water have been obtained from the NIST database [142] to generate polynomial formulations. The thermo-physical properties are related to the liquid phase in saturation conditions in the range of temperatures from 0.01 °C to 370.01 °C with increments of 5.00 °C. The collected properties are: thermal conductivity, specific heat, pressure, mass density, dynamic viscosity.

Convective Heat Transfer Coefficient

The heat flux at the walls of the cooling channels is calculated as a function of the water bulk temperature T_b and the surface temperature T_w:

$$q = \alpha(T_w - T_b) \tag{6.1}$$

In FE models, the Sieder-Tate correlation is used for the calculation of the convective Heat Transfer Coefficient (HTC) α at the wetted surfaces [143], which depends also on the internal diameter ID:

$$\alpha = Nu\frac{k}{ID} \tag{6.2}$$

It depends on the Nusselt number Nu, which on turn depends on Reynolds number Re (see eq. 2.6) and Prandtl number Pr:

$$Pr = \frac{c_p \mu_b}{k} \tag{6.3}$$

in which the water thermal conductivity k and specific heat at constant pressure c_p are considered. The Nusselt number depends also on the local dynamic viscosity μ in the water bulk and at the surface μ_w, and reads

$$Nu = 0.027 Re^{0.8} Pr^{0.33} \left(\frac{\mu}{\mu_w}\right)^{0.14} \tag{6.4}$$

The correlation holds in the ranges $0.7 < Pr < 160$ and $Re > 10^4$, and for channels with length/diameter ratio greater than 60.

Pressure losses

The pressure drop Δp along a cooling channel of length L is calculated as:

$$\Delta p = 4f \frac{L}{ID} \rho \frac{v^2}{2} \tag{6.5}$$

In laminar flows, $f = 16/Re$ is the Fanning friction factor. The Colebrook-White [144] formula can be used to calculate the friction factor f in turbulent flows:

$$\frac{1}{\sqrt{4f}} = -2log_{10}\left(\frac{2.51}{Re\sqrt{4f}} + \frac{\varepsilon_r}{3.71}\right) \tag{6.6}$$

where $\varepsilon_r = \varepsilon/ID$ is the reduced roughness, function of the surface roughness ε and the duct diameter.

The localized pressure drops at inlet and outlets are estimated as $0.5 \div 1.0$ of the kinetic load.

6.2.5 Pressure Equipment Directive

The assessment of the PED hazard class according to the European directive was part of the topics influencing the design, in particular considering the water pressure and temperature during beam-on normal operation and the gas pressure during draining and drying procedures. The considerations related to the PED classifications are developed in a dedicated technical note [190].

6.3 Steps of the design

The design of the NED up to the Final Design Review (FDR) has to be carried out. To support the design, a set of multi-physics analyses has to be carried out, covering a wide spectra of applications, from the conceptual and functional point of view, up to the mechanical verifications of the components.

Many Analyses have been carried out and are presented in the following chapters, each with different purpose. Preparatory and general analyses are used to identify the components to study in detail and to obtain local boundary conditions; the analyses that evaluate alternative designs guided the component improvements up to the current design; and finally the mechanical verifications are carried out on the NED components, as it was modelled. Also NED assembly, maintenance and testing are considered, together with some technological issues that could be fixed by carrying out some R&D activities before the construction of the NED. The analyses can be categorized into:

System-level analyses include general studies preparatory to the detail design, or analyses required to identify the components to study in detail, and to obtain boundary conditions for the next steps. This category contains the simulations described in section 7 and 8.

Component-level analyses include the set of analyses that evaluates alternative designs and guided the improvements up to the current design, and the structural assessment and the thermo-mechanical verifications that are carried out on the NED components as designed. The simulations described in section 9, 11 and 10 pertains to this group.

6.3.1 Thermomechanical design at component-level

The thermomechanical design shall consider:

- thermomechanical strength of the components (verifications of stress and strain limits, thermal fatigue and creep damages, maximum material temperature);
- thermal control of the components;
- power density dumping due to stripped and co-extracted electrons;
- performance related to the gas flow control in the beam channels.

Thermo-hydraulic and thermo-mechanical numerical FE and analytical calculations have been carried out to verify the compliance with the above criteria and to reduce the need for realizing three-dimensional mock-ups to prove system performance.

The local heat transfer conditions for thermal control are evaluated carrying out coupled nonlinear thermo-hydraulic analyses with local calculation of the Convective Heat Transfer (CHT) coefficient during the transient analyses.

The nonlinear thermo-mechanical analyses have been carried out implementing the elasto-plastic stress-strain curves of the materials, in particular the cyclic stress-strain curves for fatigue verification.

6.3.2 Load cases to be verified

The conditions that impact the design of the component determines the load cases, during the service life of the NED (operational conditions and other events), that are described in the Load Case Table (see table 6.6). The *load case table* uses code keys that are explained in table 6.8. The design of the NED systems has been developed to withstand loading conditions.

The design verifications to be carried out for each NED element have been identified and are presented in Table 6.7, named the *component verification table*, which follows the same structure as the load case table. Nonlinear FE thermal-hydraulic and mechanical analyses have been carried out in order to verify the load cases marked with X in table. The compliance with ITER Structural Design Criteria for In-vessel Components (SDC-IC) will be then verified.

6.3.3 Technological Issues

Some technological issues required to be fixed by carrying out some R&D activities before the construction of the NED. These technological issues are common for many elements of the BLCs and they are:

Load case No.		Condition or event	Loading category	Damage limit	SDC-IC criteria level	Loads										Duty cycle or frequency of the event
						Inertial				Pressure		Thermal				
						Gravity	Bed position adjusters	Mechanical handling	Seismic	Cooling circuit	Vessel	Power density	Coolant	Volumetric heating	Cryogenics	
1. Operational loadings	1.1	Beam operation	I	Normal	A	G				CP1	Vac	PD	CT1		CR1	Beam-on / beam-off and breakdown cycles
	1.2	Standby - trickle flow of coolant	I	Normal	A	G				CP2	Vac		CT2		CR1	Potentially once per beam pulse
	1.3	Cryopump regeneration	I	Normal	A	G				CP2	Vac		CT1		CR2	
	1.4	Drying	I	Normal	A	G				CP3	Atm		CT3			
2. Likely loadings	2.1	Seismic event (investment protection level)	II	Upset	A	G			SL-1	CP1	Vac	PD	CT1		CR1	Once only: duration of exposure to the power density will be determined by the speed of response of safety system
	2.2	Small leak of coolant event during operations	II	Upset	A	G				CP4	Vac	PD	CT1		CR1	
3. Unlikely loadings	3.1	Large leak of coolant event during operations	III	Emergency	C	G					Vac	PD	CT1		CR1	Assumes all coolant is lost
	3.2	Loss of coolant during operations (pump failure)	III	Emergency	C	G					Vac	PD	CT1		CR1	Assumes coolant is present but not flowing
	3.3	Loss of coolant during operations (Flow interception)	III	Emergency	C	G				CP5	Vac	PD	CT1		CR1	Assumes coolant is present but not flowing and at max pressure
4. Extremely unlikely loadings	4.1	Seismic event (safe shutdown)	IV	Faulted	D	G			SL-2	CP1	Vac	PD	CT1		CR1	Note: 1.1 loads + SL-2
5. Test / Commissioning loading	5.1	Coolant pressure proof test	Test	Normal	Test	G				CP6						
	5.2	Coolant vacuum leak test	Test	Normal	Test	G				Vac	Atm					
	5.3	Bake out	I	Normal	A	G				Vac	Vac			Bak		
	5.4	Installation / removal	I	Normal	A	G		Lift			Atm					
	5.5	Bed position adjustment	I	Normal	A	G	BA				Atm					Initial installation only

Table 6.6: Load Case Table. Code keys are listed in table 6.8

Load case No.		Condition or event	Wall Panels			LEEs			Top-Bottom Floors			Baffles			Cooling pipework			Support Structure				Remarks
			T	M	C	T	M	C	T	M	C	T	M	C	T	M	C	T	M	C	S	
1. Operational loadings	1.1	Beam operation	X	X	X	X	X	X	X	X	X	X	X	X	X	X	X	Beam-on/off	Max temp	Beam-on/off		If not otherwise specified, all beam-on/off and breakdown cycles shall be verified
	1.2	Standby - trickle flow of coolant	X			X			X			X						CT2	CT2			Potentially once per beam pulse
	1.3	Cryopump regeneration	X			X			X			X						X				
	1.4	Drying	X			X			X			X						X	X			
2. Likely loadings	2.1	Seismic event (investment protection level)																X			X	Once only: duration of exposure to the power density will be determined by the speed of response of safety system
	2.2	Small leak of coolant event during operations	X			X			X			X										
3. Unlikely loadings	3.1	Large leak of coolant event during operations	X			X			X			X										Transient analysis with dried cooling channels
	3.2	Loss of coolant during operations (pump failure)	X			X			X			X										Transient analysis considering latent heat of coolant
	3.3	Loss of coolant during operations (Flow interception)	X	X		X	X		X	X		X	X									Transient analysis considering latent heat and pressure of coolant
4. Extremely unlikely loadings	4.1	Seismic event (safe shutdown)																X			X	Once only: duration of exposure to the power density will be determined by the speed of response of safety system
5. Test / Commissioning loading	5.1	Coolant pressure proof test		X			X			X			X			X						
	5.2	Coolant vacuum leak test		X			X			X			X			X						
	5.3	Bake out	X	X		X	X		X	X		X	X		X	X		X	X			
	5.4	Installation / removal																	X			
	5.5	Bed position adjustment																	X			Initial installation only

Table 6.7: Component Verification Table. The verification types are: **T**hermal verification, **M**onotonic-type verification, **C**yclic-type verification, and **S**eismic verification.

G	Gravity load (acceleration 1 g)
BA	Maximum bed adjustment mechanical loads
Lift	Mechanical loads due to lifting with RH crane
SL-1	Seismic Load 1 as defined in the ITER MQP Load Specifications [145]
SL-2	Seismic Load 2 as defined in the ITER MQP Load Specifications [145]
CP1	Normal operating coolant inlet pressure
CP2	Trickle flow coolant inlet pressure (differential inlet-outlet Δp= 0.1 MPa)
CP3	Maximum drying gas pressure = 2.0 MPa
CP4	Reduced coolant inlet pressure due to leak
CP5	Maximum coolant inlet pressure (relief valve pressure) = 3.0 MPa
CP6	Cooling circuits proof test pressure = 3.5 MPa
Vac	Normal vessel vacuum pressure
Atm	Normal atmospheric pressure
PD	Power density
CT1	Maximum operating coolant inlet temperature = 55 °C
CT2	Minimum coolant inlet temperature = 20 °C
CT3	Maximum drying gas temperature = 210 °C
BAK	Bakeout temperature = 240 °C
CR1	Normal cryopump heat load
CR2	Cryopump regeneration peak heat load

Table 6.8: Code keys for table 6.6.

1. deep drilling of panels: Neutraliser leading edge elements (CuCrZr), Neutraliser panels (Cu), ERID beam stopping elements (CuCrZr);
2. twist tape manufacture and installation: Neutraliser leading edge elements, ERID beam stopping elements, Calorimeter swirl tube elements;
3. manifold outlet extrusion tests: all the beam line components;
4. heterogeneous joints: all the beam line components;
5. mineral insulated cable of thermocouples: all the beam line components.

6.4 Design description

Isometric views and component naming of the assembly are shown in figure 6.1 and figure 6.2. The neutralization reaction occurs in the Neutralizer along four vertical channels of rectangular cross-section, each 3 m long and 1.7 m high laterally delimited by walls and at the top and bottom side by floors. The walls (one centre, two middle, and two side walls) are formed by panels (three 1 m long panels for each wall, 15 panels in total) made of OFHC copper (figure 6.6).

Each Wall Panel is cooled with demineralized water flowing inside 14 vertical channels. These channels will be manifactured by deep-drilling [], as some R&D test for the drilling executed from two sides has been carried out successfully on OFHC []. Plugs will be welded in order to realize the closed cooling circuit.

The five edges of the neutralizer channel walls are subjected to high heat loads due to power deposition from accelerated beam ions (D_2 or H_2) and electrons that are stripped in the accelerator: therefore the surfaces of the front panels facing the beam (beam entrance section) are protected by Leading Edge Elements (LEEs) 1.7 m long and made of CuCrZr-IG alloy.

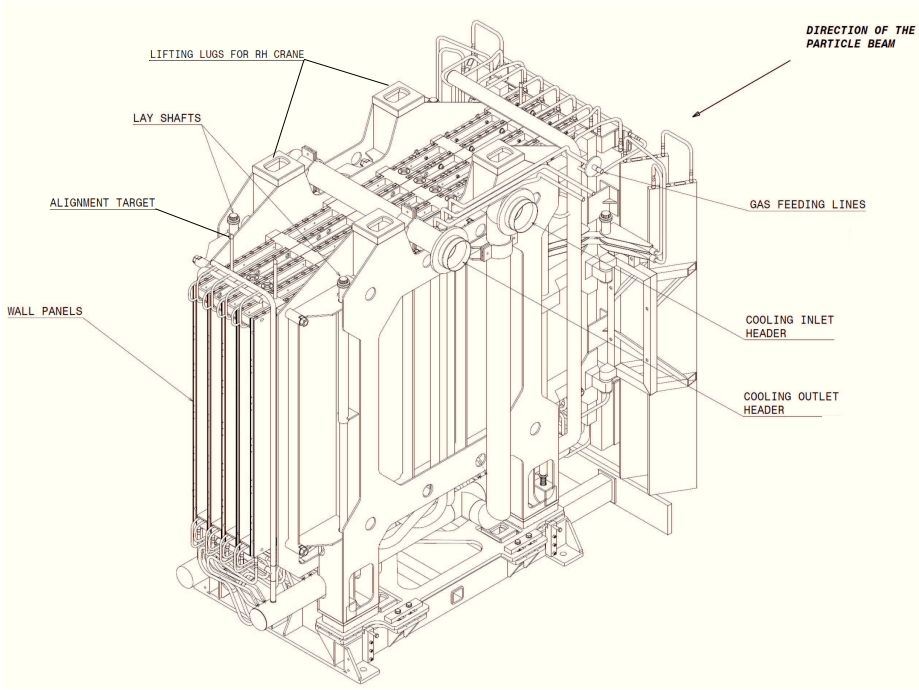


Figure 6.1: Front-bottom view of the NED and description of the main visible elements

The required gas target thickness is determined by continuous gas flow from the injection holes to the cryo-panels (see Figure 2 6). The gas (D_2 or H_2) is fed by gas feeding lines interfaced with the Gas Injection System (GIS) at the ex-vessel side and with vertical channels realized in the middle and rear panels.

Additional panels (see figure 6.1) are placed out of the Neutraliser main cross-section, constituting the Lateral Electron Dump (LED). They constitute a protection against accelerated particles with diverging trajectories for the cryopumps, which are located at the side of the Beam Line Components and would be otherwise heated considerably. Moreover, actively cooled Top and Bottom baffles (Ion and Electron Dump) absorb the power deposited by the beam. The presence of additional baffles out of the Neutraliser overall envelope may strongly affect the background gas distribution.

The NED panels are sustained by the Support Structure (see figure 6.3) consisting mainly of the Side Plates and of the Wall. The Support Structure integrates the RH lifting frame and lugs for the NED lifting/lowering. The NED pads at the Support Structure are interfaced with the Adjustable Bed that allows the NED position adjustment after positioning in the Beam Line Vessel by means of RH crane.

The NED will be instrumented with thermal sensors, boiling detectors and electrostatic probes. The purpose of these sensors and the layout are described

Signals generated at the sensing elements will be transmitted via cables up to the ex-vessel interface; intermediate connectors are foreseen in order to allow cables disconnection before and after maintenance and replacement operations of the NED.

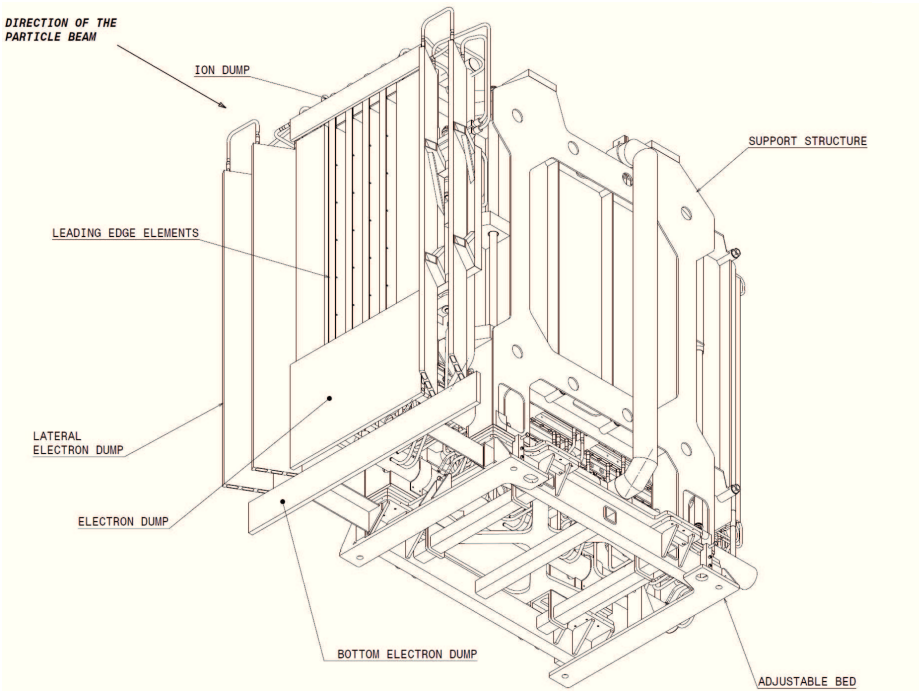


Figure 6.2: Rear-top view of the NED and description of the main visible elements

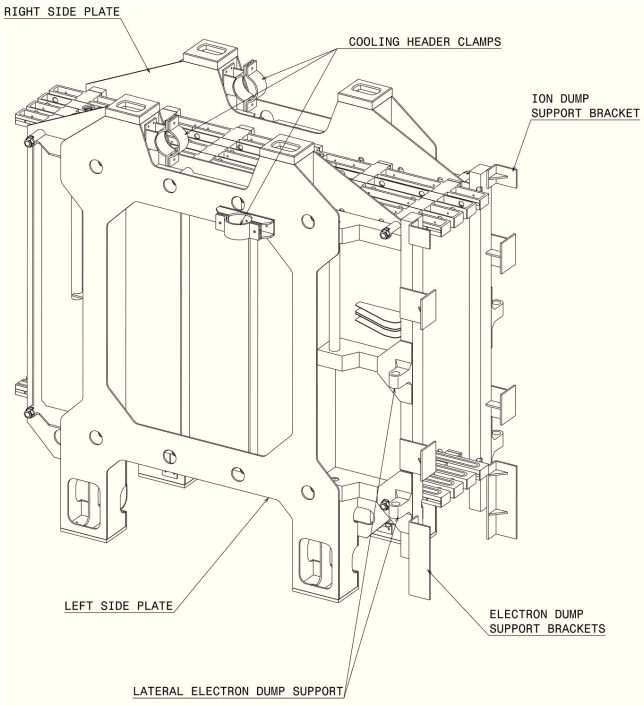


Figure 6.3: Sub-assembly of the support structure and its main elements

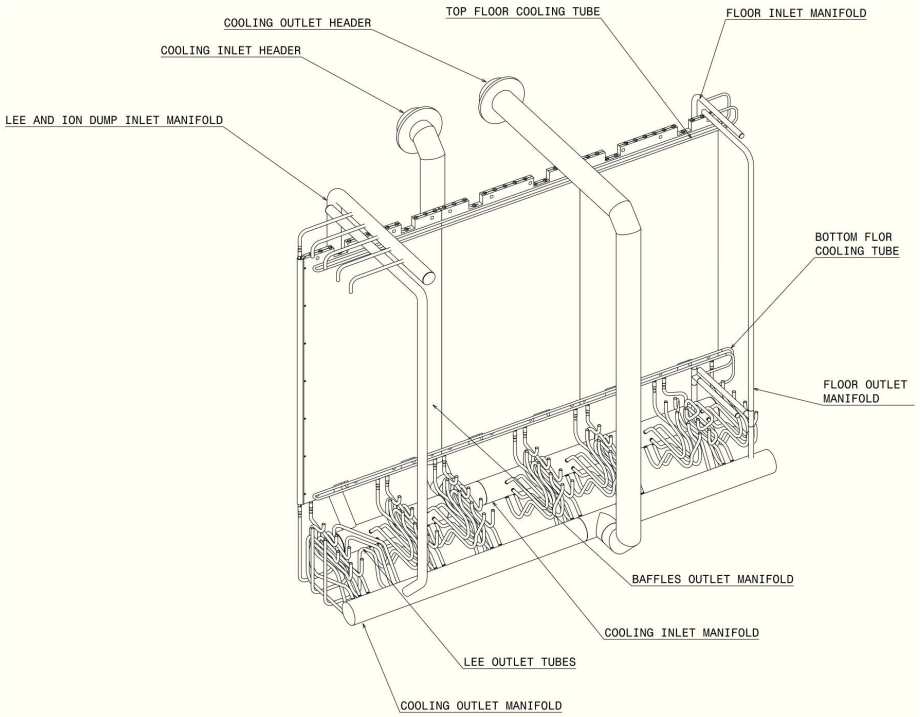


Figure 6.4: Sub-assembly of the cooling piping and its main elements; three panels of the left wall are also shown.

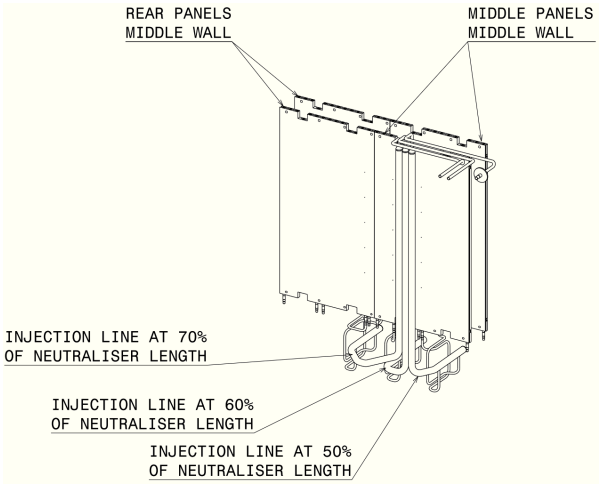


Figure 6.5: Sub-assembly of the gas injection: three independent injection lines are used to test three injection length in the test facility MITICA, while in ITER NBIs only one will be used.

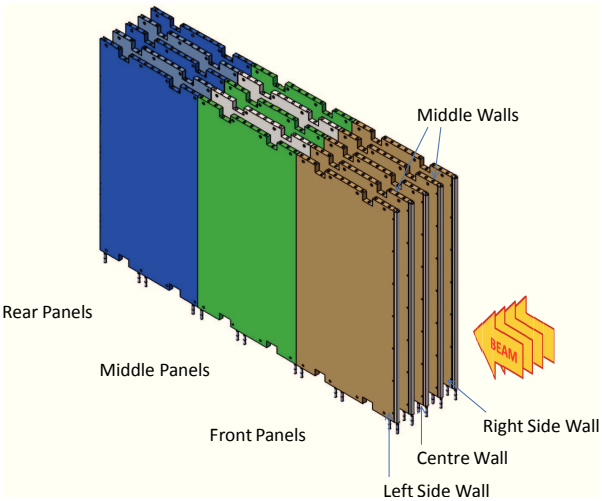


Figure 6.6: Naming and layout of the wall panels and the leading edge elements (beam entering from the right).

Only the Adjustable Bed interface has been taken into account in the design of the side plate pads.

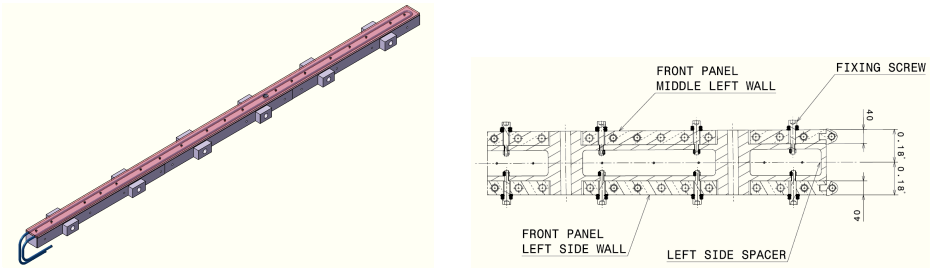
6.4.1 Wall Panels

The panels are made of OFHC Copper. As described in section 7.3.1, the panels have rectangular sections in a horizontal plane, instead of the trapezoidal sections defined in the DDD 5.3 [50]; the rectangular sections are inscribed inside the allowable trapezoidal sections defined by the beam aiming [137]. Their thickness decrease from 43 mm in the case of the front panels, to 40 mm, to 37 mm in the case of the rear ones. A gap of 2 mm between the panels allow relative thermal deformations; an imbricate geometry is realised between the pair of subsequent panels in order to limit the gas conductance through this gap.

6.4.2 Support of the Wall Panels

The panels' weight is supported by the *wall spacers* from the bottom of the assembly, and screws with belville washers keep the panels in position while allowing adjustments and thermal deformations. Thus, their main role is to sustain the weight of the walls, holding the pack of cooled panels compact, and keep the wall panels in position within strict tolerance in the transverse direction.

At the same time, the surfaces of the wall spacers exposed to the beam are protected by actively cooled Copper plates, called *channel floors*. These elements dump the impinging particles; by direct contact, they also thermally control the wall spacers. The cooling circuit of each floor/spacer assembly consists of a U shaped tube housed inside grooves, realized on the wall spacer and on the heat sink floor, as sketched in figure 9.11. With the purpose of reducing design complexity and heterogeneous welding, SS tubes (ID=8mm, OD=12mm) are used to cool the heat sink floor.



(a) (b)

Figure 6.7: Wall spacers protected by actively cooled Copper plate (a) and detail of the panel fixing (b).

6.4.3 Leading Edge Elements

The five edges of the Neutraliser channel walls are subjected to high heat loads due to power deposition from accelerated beam ions (D_2 or H_2) and electrons that are co-extracted or stripped in the accelerator. The front faces of the front panels (beam entrance section of the Neutraliser) are protected by Leading Edge Elements (LEEs) 1.7 m long and made of CuCrZr-IG alloy. The LEEs are designed with a front rounded part connected to the rear massive region with inclined surfaces in to spread the particle thermal load on wide surfaces. The thermal gradient from the front to the rear region will cause differential thermal deformations with bending along the axial direction; this thermal bending deformation will be opposed by realising a stiffening web on the rear side. The peak PD on the LEEs can reach values up to 7 MW/m^2 that recommends the use of active cooling by elements with water in nucleate boiling conditions to increase the heat transfer coefficient. These heat transfer conditions are realized in the LEE cooling channels with Swirl Tube Elements (STEs) that increase the water coolant turbulence. Each STE has its own inlet/outlet water tube connections to the main manifolds. The nucleate boiling conditions and the thermo-mechanical behaviour of the LEEs are simulated with a customized ANSYS code [146]. The analyses have been carried out identifying new geometries and cooling parameters that could be adopted in order to increase as much as possible the allowable peak power loads on the LEEs.

6.4.4 Electron Dump

Power deposition analyses pointed out the necessity of locating additional protections downstream the Beam Source, out of the Neutraliser cross section. These baffle shall be able to collect ion beam halo, co-extracted electrons, and stripped electrons; the diffuse and steered trajectories of the electrons must be stopped before reaching the cryopump panels. Also the ions of the beam halo will travel with high divergence out of the core Neutraliser cross section. Concerning the reference value for the design, it has been considered that the electrons exiting the accelerator carry about 600 kW due to stripped or co-extracted electrons [192] (originating from the beam core). According to present estimates (up to EQGAPS32 design [166]), this power can be lower ($490 \div 570$ kW), but also an 8% halo fraction must be considered, adding about $150 \div 180$ kW.

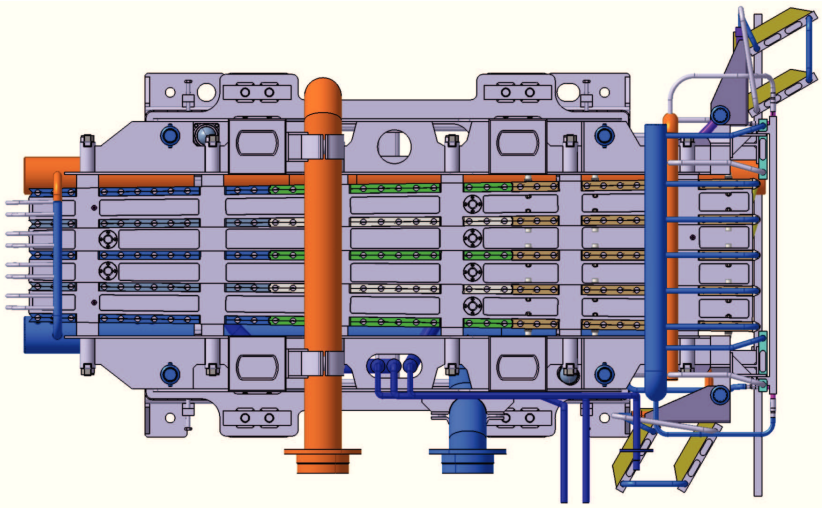


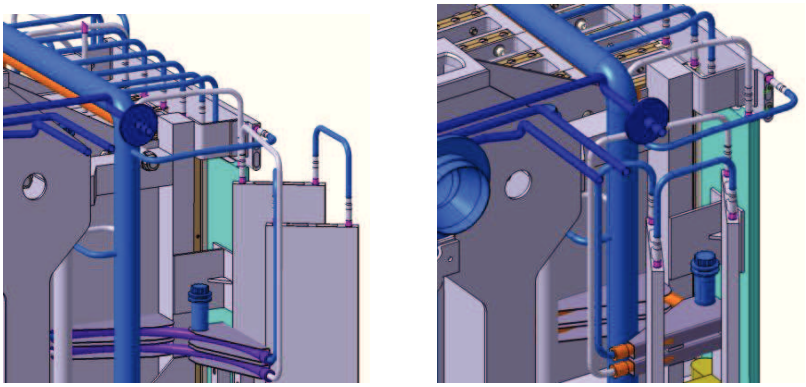
Figure 6.8: Foldable Lateral Electron Dump (LED) in open (on top) and close (at the bottom) position.

The numerical codes used for the development of the design of the Ion and Electron Dump are:

- Trigo for the ion beam power deposition;
- BACKSCAT for the co-accelerated electron power deposition;
- AVOCADO for the pressure investigations;
- ANSYS for the thermo-mechanical analyses.

Each of the particle dump panels is made of OFHC copper. In the present design, the top and bottom baffles are realized with actively cooled copper plates with 740 mm width: the top baffle is high 80 mm, the bottom one 590 mm. The plates are drilled with holes of 18 mm diameter and minimum 6 mm of bulk thickness between each couple of holes. Welded plugs connect one horizontal segment of the circuit with the next, making a cooling circuit connected in series inside each baffle. Because of the low value of power, the cooling channels inside the top and bottom baffle can be fed by a single water line, and the two baffles operate hydraulically in parallel. Only the cooling channels located close to the panel floors are swirl tube elements with inserted twisted tape in order to prevent burnout when the local power density will be very high. The total mass flow rate for the couple of particle baffles is 3 kg/s: 1.3 kg/s for the electron dump at the bottom and 1.7 kg/s for the ion dump at the top of the beam entrance section.

Each cryopump is protected by three panels, two of which are hydraulically connected in series. In order to allow the removal of the NED from the vessel during maintenance, the LED must be folded as shown in figure 6.9 thus reducing the overall dimensions and increasing the clearance with the cryopumps. The geometry and position of the LED has been optimized also considering gas conductance for pumping of the Beam Source Vessel.



(a) (b)

Figure 6.9: Foldable Lateral Electron Dump (LED) in open (a) and close (b) position.

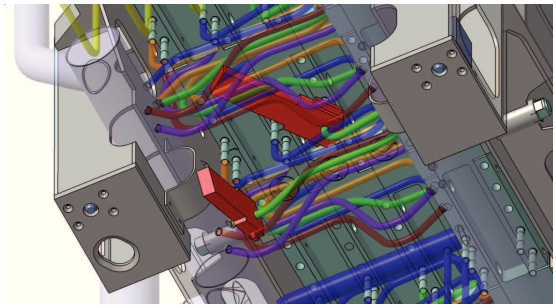


Figure 6.10: Welding of the flexible elements between the panels and the manifolds by automatic welding system; the overall dimensions required for the use of automatic heads are taken into account in the design.

6.4.5 Piping assembly

The cooling pipework shall supply the coolant to the actively cooled elements, from the interface at the vacuum vessel. Pipes and headers require flexible joints at the following interfaces:

1) at the Neutraliser-Vacuum Vessel, bellows that are properly selected from the Witzenmann catalogue [147] as described below;

2) Panel adaptors to accommodate the manufacturing/positioning errors and free thermal expansions of cooling and gas pipes.

Interface 2) consists of curved or curled tubes. The ends of these curled tubes will be welded to the manifold by using automated welding heads in order to realise reliable welding. The layout of the curled tubes proposed in the Neutraliser design consists of:

i. 100mm/65mm minimum distance between cooling tube axes at the manifold/adaptor side where the automated welding head will be positioned (see figure 6.10;

ii. 35mm minimum distance between the gas and cooling tube axes at the adaptor side where gas tubes will be welded using manual welding process;

iii. tubes will have 19mm outer diameter to satisfy coolant flow requirements, 0.5mm minimum wall thickness to maximise the flexibility satisfying coolant proof test, 50mm minimum bend radius for technological bendability.

Considering the above requirements and characteristics, the geometry of the curved tubes have been developed as detailed in the model. This layout is proposed as first proposal and it doesn't represent a mandatory solution; the manufacturer could develop a final solution under customer approval.

6.5 Assembly procedure description

The study of the assembly procedure started from the functional elements of the Neutraliser, the wall panels. As described before, its support is realized by means of spacers between the walls, which stick together thanks to tie-rods: the assembly procedure has been conceived following the precise sequence of piling the panels wall by wall. When the stack is completed and the tie-rods are tightened, the assembly can assume the vertical position as presented in figure 6.11. The design of the NED is totally compatible with this procedure.

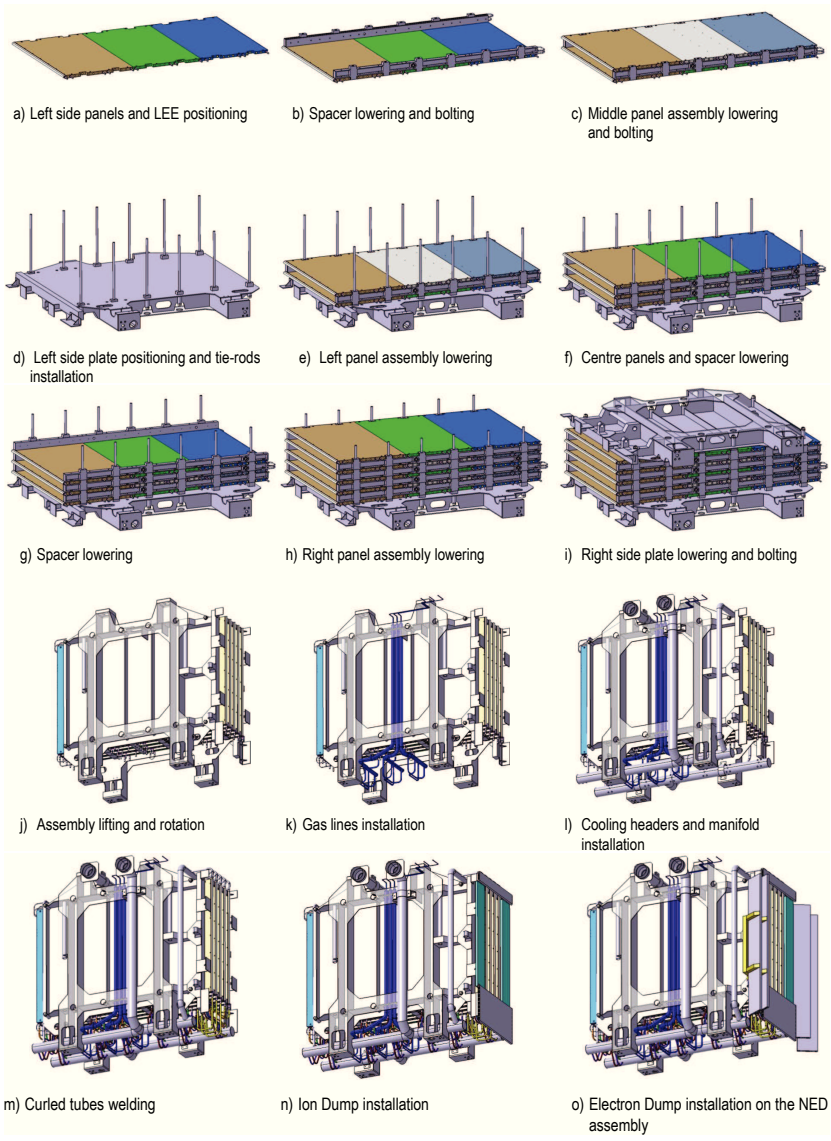


Figure 6.11: Assembly procedure.

7

Calculation of thermal loads and power density maps

The design of the Beam Line Components of the MITICA experiments is determined by many engineering, physical, and technological issues that are in part still open. Among them, one of the main issues is the evaluation of the Power and Power density load due to accelerated particles. The mechanical verifications - in order to satisfy the thermo-hydraulic and thermo-mechanical criteria are typically carried out using FE modelling for thermo-mechanical analyses, for which the thermal loads are a critical input. In the framework of MITICA design and development, a set of applications were developed at Consorzio RFX. They were mainly used to calculate beam-component interaction and heat deposition, as widely reported in many technical notes [191, 178, 193].

In this section, two numerical code aimed at the calculation of the ion beam power deposition is described. I developed the code to be integrated in the analysis procedure for the thermal verifications of BLCs, in particular the Neutraliser, and the results it produces can be easily exported to ANSYS environment. Additionally, a code aimed at extending the electron trajectories out of the beam source has been used to design the geometry of the Electron dump and its main results are presented here. This activity was also published in [3].

7.1 Power deposited by the beam

In order to carry on the design and thermomechanical verifications of the Beam Line Components (BLCs) concurrently with the design of the beam source, a simplified model of the beamlets defines the common ground on which the requirements are based. This simplified model describes the power carried by the beam with respect to the divergence angle using a bi-gaussian interpolation; for each Gaussian, the divergence and the fraction of power is given as a range of acceptable (or plausible during operations) values. The mechanical components interacting with the beam must withstand the worst condition in terms of beamlet divergence, which is different and shall be identified case by case for each BLC.

The numerical code named "Trigo" is a vector code aimed at the calculation of ion beam power deposition on the beam line components (BLCs), which uses this model for the verification of the thermomechanical requirements. The code was developed to be integrated in the analysis procedure for the thermal verifications of BLCs, in particular the Neutraliser, and the results it produces can be easily exported to ANSYS environment. Despite the name, the code uses vector analysis equations. It has been implemented in MS Visual Basic, a programming language that allows very quick development of applications with simple interface and easy graphics generation. A MITICA Thechnical Note [191] details the development of the code.

The code has been developed with the following objectives:

1. describe the entire complex assembly of the NED surfaces within a single simulation.

2. shadowing effect resulting from the surfaces assembly, with an algorithm that consider for each surface element if a beamlet is intercepted by other surfaces/bodies.

3. use of rotation matrix **R** for the GG apertures from where the beamlets proceeds, together with a translation vector **T** that considers the effective geometry and constraints of the Beam Source tilting system.

4. export the results for post-processing in file/tabular format and pictures; the pictures produced by the code have been widely used in the reports regarding Neutraliser design development [176].

The results produced by the codes were validated against similar codes (in particular APDP by Aleksander Panasenkov) and some maps by BTR [148].

7.1.1 Beamlet definition

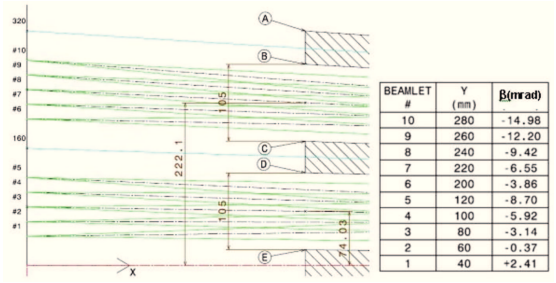
There are 1280 beamlets divided into 16 beamlet groups, each consisting in 5 x 16 apertures. The beamlets are defined as a list in a text file. The definitions are complete of:

- Coordinates of the aperture centre at the Grounded Grid (GG);
- Unit Vector of each beamlet aiming.

The code assumes the GG apertures lay in a plane surface. The GG surface is then oriented considering the vertical tilting, while the horizontal aiming angle is corrected in order to consider the horizontal misalignment. The position of the GG centre and the normal of its equivalent surface, wrt the tilting axis are obtained from the CAD design. The beamlet definition is consistent with DDD 5.3 drawings [50] as shown in 7.1.

The code uses a rotation matrix **R** for the GG apertures from where the beamlets proceeds, together with a translation vector **T** that considers the effective geometry and constraints of the Beam Source tilting system:

$$R = \begin{bmatrix} \cos\alpha & 0 & \sin\alpha \\ 0 & 1 & 0 \\ \sin\alpha & 0 & \cos\alpha \end{bmatrix}, T = \begin{bmatrix} -L \cdot \cos(\pi/2 - \gamma) \\ 0 \\ L \cdot \sin(\pi/2 - \gamma) \end{bmatrix} \tag{7.1}$$



BEAMLET #	Y (mm)	β(mrad)
10	280	-14.98
9	260	-12.20
8	240	-9.42
7	220	-6.55
6	200	-3.86
5	120	-8.70
4	100	-5.92
3	80	-3.14
2	60	-0.37
1	40	+2.41

Figure 7.1: Nominal optics of the beamlets as for DDD 5.3 drawings [50, 137]

Where α is the tilting angle, γ is the corresponding GG rotation angle, and L is the distance between the tilting axis and the GG centre. The rotation matrix is used to move the beamlet focus together with the coordinates of the GG apertures; the translation vector moves the points from where the beamlets exit the accelerator.

7.1.2 Beam Modelling

The code developed at RFX (aka "Trigo") is a vector code that calculates the Power density map on surfaces of the Beam Line Components, taking into account their interaction with the ion beam. The simulation code is based on a bi-gaussian approximation of beamlets, as detailed in [50, App. 2]. It is based on the assumption that the expected power density on the footprint of a beamlet is approximately a bi-Gaussian. Each of the Gaussian distribution represents a fraction of the beam: one is used for the beam core fraction with divergence ω_h, the second is used for the beam halo fraction with divergence ω_h. The power carried by each component is f for the latter and $1 - f$ for the former [50].

$$\frac{P(\omega)}{P_{tot}} = \left\{ \frac{1-f}{\pi(X\omega_c)^2} \exp\left[-\left(\frac{\omega}{\omega_c}\right)^2 \right] + \frac{f}{\pi(X\omega_h)^2} \exp\left[-\left(\frac{\omega}{\omega_h}\right)^2 \right] \right\} \tag{7.2}$$

7.1.3 Geometry definition and mesh

The mesh is created as a structured, regular grid on plane surfaces. The "faces" are listed in a text document. They are defined by four "keypoints" previously defined; the faces are rectangular plane surfaces, oriented in the 3D space, and their definition is complete with the number of divisions of the two pairs of edges. Each face shall have a unique name, in order to perform partial selection during visualization, or to export table results to ANSYS environment. The entire complex assembly of the NED surfaces is considered within a single simulation. The shadowing effect is simulated and account for every defined face resulting from the surfaces assembly. The algorithm considers, for each surface element, if a beamlet is intercepted by other faces.

7.1.4 Interaction with the solid surfaces

In a plane intercepting the beam, the integral of the power density fraction (volume of the bi-Gaussian) is 1.

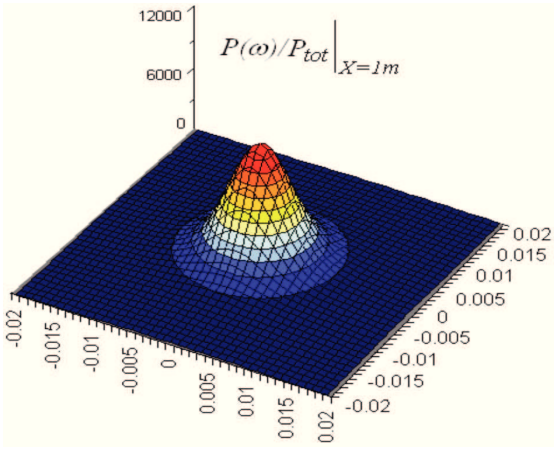


Figure 7.2: Example of Bi-Gaussian distribution with beam core and beam halo fractions. Coordinate in mrads.

Let's consider figure 7.3. The green arrow represent the axis of a j-th beamlet; the blue and dark blue arrows connect the beamlet origin to the centroids of the surface elements. Taking into account the distance X from the beamlet origin at the Grounded Grid, one can compute the power density intercepted by a i-th surface element positioned and oriented in the space with normal vector n originating from the centroid at a certain distance d from the beamlet axis. The value of $A_{i,\perp}$ is the element area projected on a plane perpendicular to the vector originating from the beamlet origin and directed to the element centroid, which define a divergence angle ω and originates an angle θ with $\mathbf{n}$. The area $A_{i,\perp}$ is simply calculated considering cos θ.

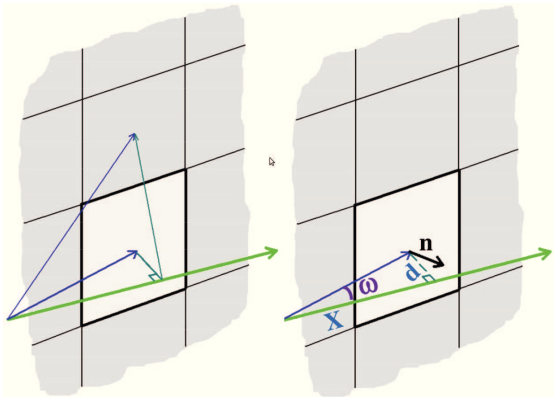


Figure 7.3: Geometrical representation of the beamlet interaction with a single element

All surfaces are modelled and discretized in elements. The power deposition on a given i-th element is obtained by summing up the contribution of any

beamlet j:

$$Pd_i[\mathrm{W/m^2}] = \sum_j \left(\frac{P(\omega)}{P_{tot}} \right)_j \cdot P_{tot} \cdot \frac{A_{i,\perp}}{A_i} \tag{7.3}$$

In the case other surfaces shadow the element from interacting with a j-th beamlet, a Hidden surface determination proccess shall be undertaken, and the same methods discussed in section 3.2.1 applies to the issue. Since the geometry is created bottom-up, the faces are rectangular: after the intersection point is calculated (eq. 3.25, the method for convex polygons can be applied. If the intersection point is always on the same side of the set of oriented edges of the element, the point must be inside the polygon (see figure 3.4) and therefore the beamlet already deposited its power at the solid angle occupied by the i-th element.

7.1.5 Post-processing

It is possible to view the results as a picture or to export the them for post-processing in file/tabular format, ready for the load application in ANSYS.

The pictures and the table data produced by the code have been widely used in the reports of the analyses of the Neutraliser and Electron Dump, and in the development of a neutron diagnostic for MITICA Calorimeter [195]. An example of the power density map as imported in ANSYS is shown in figure 7.4.

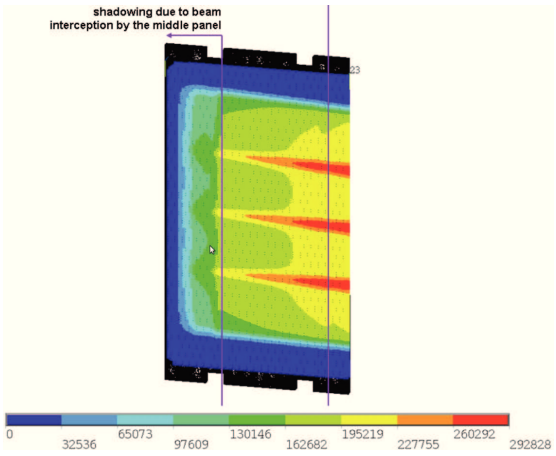


Figure 7.4: Power density applied in an ANSYS model of the Centre Wall - Rear Panel (on-axis 39.2 mrad vertical tilting, 0 mrad horizontal misalignment).

7.1.6 Implementation of the tools

Three independent applications were developed in MS Visual Studio environment:

- An application creates a finite element mesh starting from an input file that contains information on the geometry of the components;
- A second application is the solver and calculates the beamsurface interactions, considering various beam parameters;

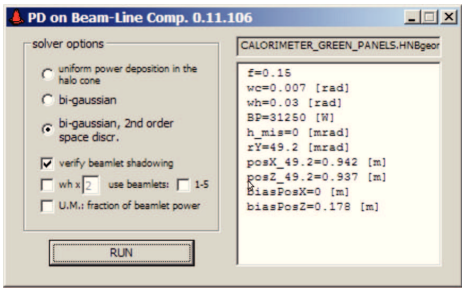


Figure 7.5: Pre-processing of analyses. Settings include beamlet divergence and power, vertical tilting of the beam source wrt to a pivot point, horizontal misalignment of the beam, space discretization, cropping of the Gaussian tail end, or a partial selection of beam channels.

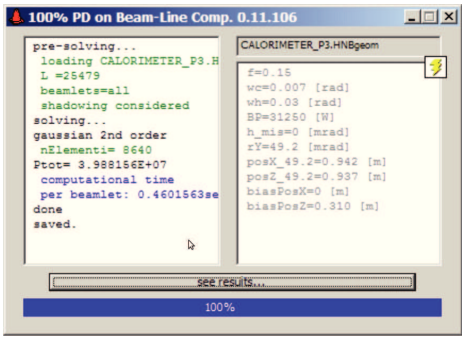


Figure 7.6: Solver at the end of a simulation.

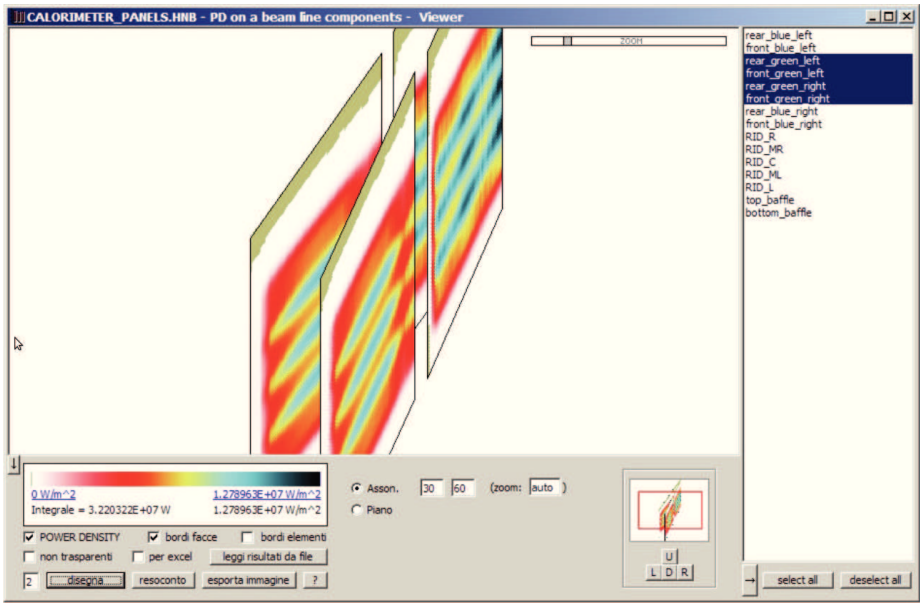


Figure 7.7: Results Viewer uses axonometric projection to represent the models, with user-defined angles and color contour.

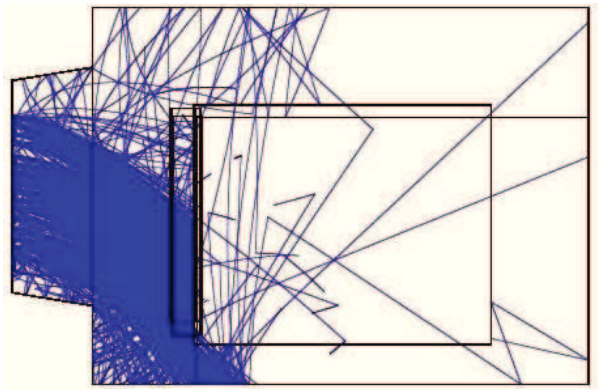


Figure 7.8: Example of calculated trajectories, side wiew of the drift region between the source and the NED [3].

- A third application is used to display the results and perform post-processing.

The file extension ".HNBinp" defines a text file that contains the geometry description and meshing procedures. The file extension ".HNBgeom" defines the meshed model, and the file extension ".HNB" contains geometry and Power Density results. The results are calculated on the centroid of the elements and not on the nodes, thus the scalar data is cell-centred. When executing the Solver program, one can use the text box on the right to change settings and beam properties (see Figure 7.5). Once the simulation has started, some information on the model is listed on the left (see Figure 7.6).

At the end of the simulation, a result file are created with extension ".HNB". These files can be opened with the viewing application (figure 7.8). The viewer may be used to obtain images, reports, and text tables of the power deposition on faces. The pre- and post-processing features include the capability of:

- prepare power density pictures in axonometric projections, with different power density contours and selectable colour scales;
- evaluate the quality of the mesh;
- perform power integration on faces and prepare reports of power and power distribution
- export power density tables on faces with mapped meshes.

The user can set the angles at which the view deviates from the orthogonal in order to use isometric or oblique projection, but also set the colour scale and the scale limits.

7.2 Power deposited by co-accelerated electrons

The approach followed in the development of the BACKSCAT code [3], developed in COMSOL environment, is different from what presented before. The code simulates the trajectories of the co-accelerated electrons from the exit of the GG, most of which with relativistic velocities, and takes into account the reflection at the walls (scattering). Macroparticles are considered. The trajectories, subjected to the long-range magnetic field of the beam source and

the residual magnetic field, are calculated until the electrons hit a component, then the power deposition and the backscattering with a new trajectory is calculated. The probability of the electron being backscattered is a function of the impacting angle and its energy; the fraction of energy left at the surface, based on experimental data, is a function of the initial energy of the electron and the incidence angle before and after the impact, being the latter randomly calculated.

7.3 Application to the NED

7.3.1 Geometry of the wall panels

The geometry of the wall panels has been simplified, from trapezoidal to rectangular section. The incidence angle of the impinging particles is now smaller (with respect to the perpendicular direction), but the slightly higher power density is compensated by the protection of the leading edges thanks to the greater thickness of the upstream panels (see section 7.9).

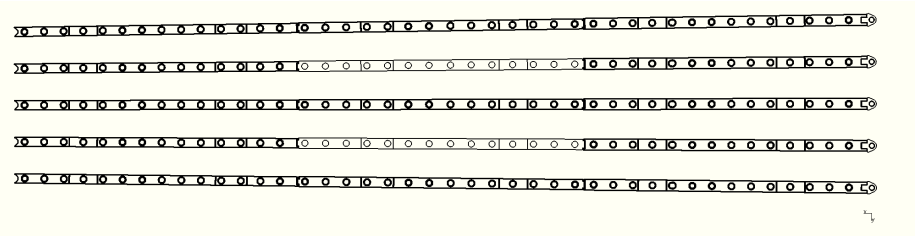


Figure 7.9: The wall panels have parallel surfaces, and the leading edge of one is protected by the one upstream it.

The power deposition maps, visible for instance in figure 7.13, show a peculiar contour, with a stepped increase of power density along the X direction. There are five steps, of increasing width, that can be easily identified. This behaviour is due to the shadowing originated by the panel before: there are 5 columns of beamlets in each beam channel, and the closer a beamlet is to the wall, the longer the shadow, thus the further the beamlet will interact with the surface.

7.3.2 Vertical positioning of the Neutraliser component

A correct vertical positioning of the NED will prevent direct beam interception and possible burnout of components due to over-heating at the maximum beam power. The position of the Neutraliser has been defined as result of an optimization process, which satisfies different criteria developed on the basis of various hypotheses and considerations.

The position of the Neutraliser is the same considering both the operations inside the MITICA and ITER HNBs injectors, so the evaluations carried out below do not distinguish between the two destinations. The vertical position has been calculated by assuming the following data:

1. the height of the beam channel between the top and bottom wall panels is fixed at 1700 mm;

2. the beam vertical tilting can range between 39.2 mrad and 59.2 mrad wrt the nominal orientation (49.2 mrad);

3. the beam source tilts around a rotation axis that is positioned at the top of the accelerator at the coordinates x = 942 mm, y = 0 mm, z = 937 mm (figure 7.13(a)).

Using the code Trigo, two approaches have been followed to calculate the optimum vertical position, and additionally to evaluate the positioning tolerance for the NED along the vertical direction: a tolerance of ±5 mm is found to be appropriate, and this value is consistent with the requirements. A third, analytical approach is used to verify the results.

Threshold of Beam Power Density

The beam power density on intercepting target planes is used as index of the fraction of beam power allowed to go beyond a certain beam line component; however, it is not directly related to the power deposited on the component itself. A threshold of the beam power density has been defined in order to centre the beam at the entrance and exit section of the Neutraliser; the estimation has been carried out by means of a finite element method and the results depend on the surface discretization.

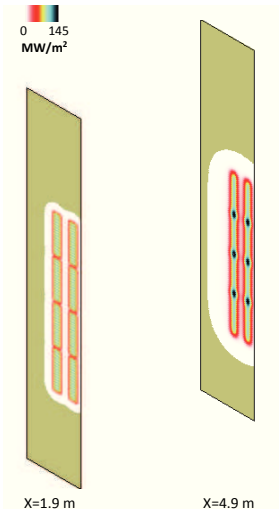


Figure 7.10: Beam power density maps on intercepting target planes at the Neutraliser entrance (left) and exit (right).

In order to be sure that the intercepted halo fraction (in terms of power density) is comparable between the beam entrance and the exit section of the Neutraliser, simulations have been done using the two surfaces (Entrance at Xentrance = 1900 mm and Exit at Xexit = 4900 mm) simultaneously exposed to the beam; this means that the surfaces are considered as non-shadowing targets. The power density profiles along two vertical lines, defined by the intersection with the middle plane of one beam channel, are plotted in figure 7.11. The threshold of power density equal to 2.0 MW/m^2 has been defined as reference and the corresponding vertical (Z) coordinate has been identified; the

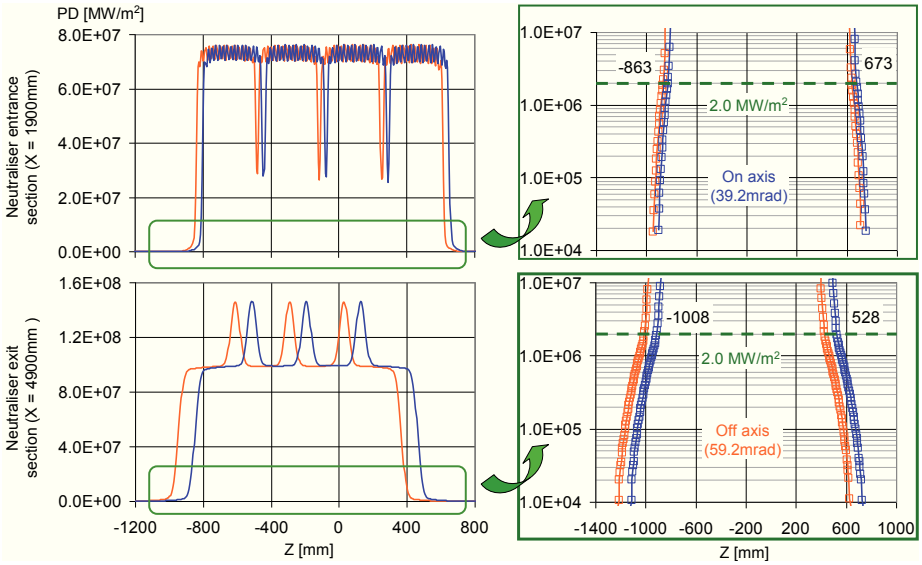


Figure 7.11: Definition of the power density threshold in order to centre the beam at the entrance (top graphics) and at the exit (bottom graphics) section of the Neutraliser

greatest absolute value of Z shall be used between 39.2 and 59.2 mrad tilting configuration respectively at the upper and at the lower side. Then, the mean value of the two Z coordinates identifies a plane where the middle plane of the Neutraliser entrance/exit shall lie. Despite the poor accuracy, this method is quick to be applied and gives good indications on the matter. The average value of Z is about -178 mm.

Intercepted Beam Power and vertical tolerance

The vertical positioning of the NED should minimize the beam power interaction with the component. A certain amount of beam particles will not pass through the beam channels defined by the Neutraliser wall panels; these intercepted particles will hit the top and bottom floors of the Neutraliser. The correct position is found by equating the power intercepted on the four bottom floors with the one deposited on the top baffle. The power deposited on any surface of the Neutraliser is calculated, as represented in figure 7.12(a) and (b). The bottom floor of a channel, and the corresponding part of the top floor as wide as the channel, have been considered. The maximum power density and the total power on these two surfaces vary with the shift of the Neutraliser along the vertical position, as plotted in figure 7.12(c).

The thermal power balance is obtained for 178 mm lowering of the Neutraliser wrt the Grounded Grid centre as represented by the intersection of the black lines (power on the top and bottom floors) in figure 7.12(c). It can be noted that the maximum power density on these surfaces is very different because of the different impinging angles of particles.

As already shown in figure 7.11, the power density strongly varies along the vertical direction (left and right legs of the graph). For instance, the maximum

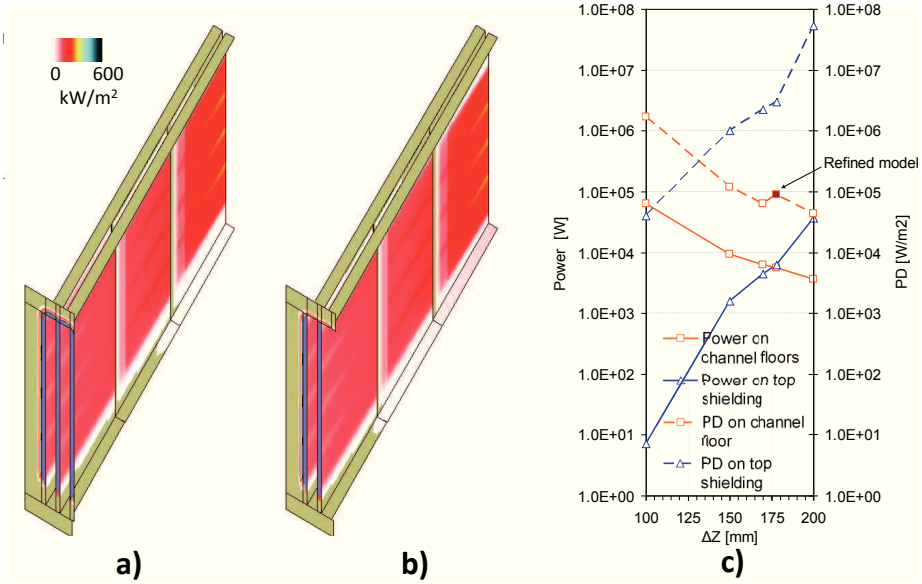


Figure 7.12: Map of power density deposited on Neutraliser walls: (a) 39.2 mdar, (b) 59.2 mrad tilting; (c) power and power density as a function of the vertical position.

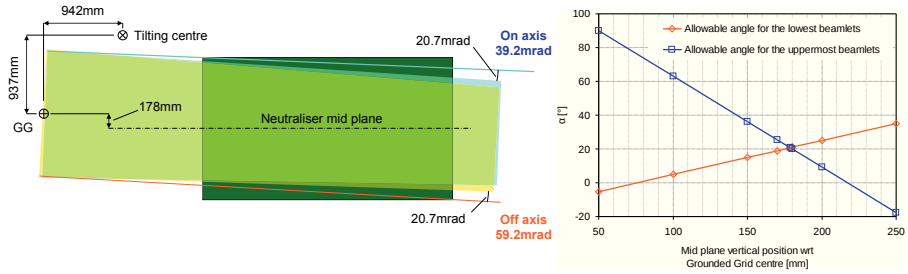
power density on the beam dump element placed at the top of the Neutraliser channels, rapidly increases by two orders of magnitude if the surfaces are shifted by 40 mm along the vertical direction. At the same time, the total power increases by one order of magnitude along the vertical direction. If the Neutraliser is shifted vertically by 8 mm around the nominal position (defined for -178 mm), the total power on the channel floor increases of 15% (see figure 7.12(c)). A feasible tolerance for the vertical positioning of the NED considering manufacturing errors is ±5 mm. A maximum error for the NED vertical positioning of ±5 mm will correspond to a negligible variation of the beam power and power density on the high heat flux elements, so this value is accepted as consistent with the above analyses.

Analytical verification using beam envelops

The margin against direct interference of the beam with the top and bottom floors can be expressed in terms of allowable angle. The calculation consists of defining the beamlet envelop and then equating the allowable angles against direct interception at the top and bottom floors.

Both on-axis and off-axis tilting configurations are analyzed. On-axis aiming is relevant to the interception at the beam entrance section on the top floors, so the top-entrance location represents the reference edge; off-axis setting is relevant to the interaction of the beam at the bottom floors, so the reference edge for this configuration is placed at the bottom-exit. Figure 7.13 shows in a vertical section the beam in the two positions and the channel height, and the optimum vertical position.

Top and bottom beamlets exit the Grounded Grid (GG) with a composite convergence angle of 23.3 mrad [137]; then, adding the tilting angle (39.2 mrad



(a) (b)

Figure 7.13: (a) Geometrical representation of the allowable angle against direct beam interception at the top and bottom floors; allowable angle as a function of the vertical position

or 59.2 mrad), the angles α_{top} and α_{bottom} wrt to the X axis are calculated. A segment between respectively the top GG apertures with the top floors of the Neutraliser, or the bottom GG apertures with the bottom floor is drawn and let β_{top} and β_{bottom} be the slopes of these lines. The allowable angle against direct interception is then calculated as the difference between β angles and α angles; this fraction results to be identical at the top and bottom edges when the Neutraliser is vertically positioned 178 mm below the grounded grid centre.

7.3.3 Vertical positioning of the Electron Dump

The function of the Electron Dump (ED) is to intercept most of the electrons. Their trajectories is influenced by the magnetic fields.

Vertical Magnetic field: in the drift region between the GG and the NED, the maximum acceptable residual field from the tokamak is B_z=0.3 mT. In ITER NBI, residual field coils control the magnetic filed; in MITICA this residual field is created on purpose.

Horizontal Magnetic field: in the drift region, B_y decrease from about -0.7 to -0.1 mT in the "PG17" configuration [196].

Most of the electrons exiting the GG are generated in the last grid gap, and their kinetic energy in in the range of 200 keV. The relativistic effect have to be considered and the kinetic energy E_k becomes:

$$E_k = mc^2(\gamma - 1)$$

being the relativistic factor $\gamma = 1/\sqrt{1-(u/c)^2}$ and u the velocity of the electron. The equation to calculate the gyroradius accounting for the Lorentz force holds for relativistic velocities by correcting $m = m_0/\sqrt{1-(u/c)^2}$:

$$r_g = \frac{mv_\perp}{|q|B}$$

Assuming the length of the drifting region L is 2 m, the displacement D of the footprint due to a transverse magnetic field is:

$$\theta = arcsin(L/r_g), D = r_g(1 - \cos\theta)$$

Considering an uniform $B_\perp$ of 0.3 mT, the transverse displacement would be about 25 cm.

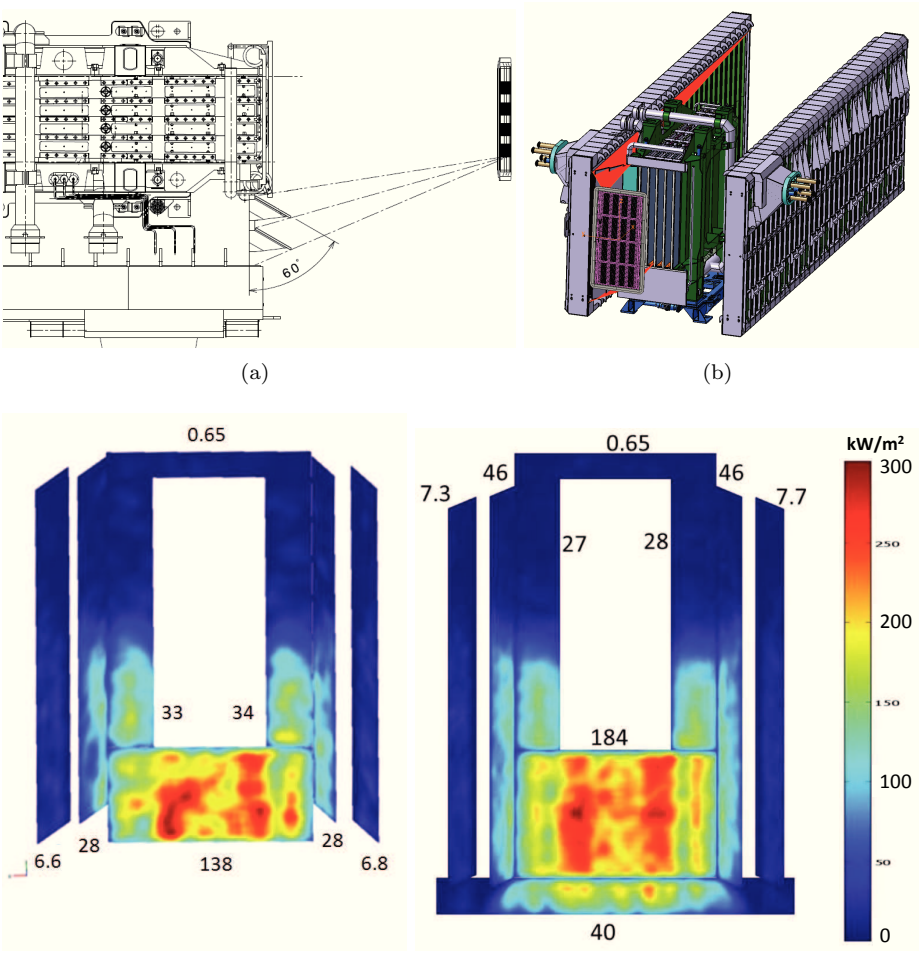


Figure 7.14: (a) Lateral positioning of the LED panels;(b) Vertical positioning of the LED panels; (c) Power density map due to co-accelerated electrons on the Electron Dump on an intermediate design and and (b) on the present design. PD maps taken from [193].

The position and size of the Electron Dump (ED) panels has been evaluated combining various methods. In particular, the position of the Lateral Electron Dump (LED) panels required particular attention: initially their vertical extension was identified tracing straight lines connecting the corner beamlet to the corners of the cryopanels, assuming straight trajectories for the electrons (see figure 7.14(a), 7.14(b)). When a long range horizontal magnetic field was chosen in the design of the beam source to get rid of most of the electrons during the

acceleration, the down-streaming trajectories had to be calculated to identify the proper vertical position. The electron trajectories and the power density maps calculated with BACKSCAT code has been used to adequately position the panels of the Electron Dump (ED). The panels had to be extended down to the floor of the vacuum vessel, in order to directly intercept the down-streaming electrons and the ones that scattered on the floor immediately before the NED (see figure 7.14(c), 7.14(d)).

7.3.4 Total heating power

Both the ion and electron thermal loads shall be considered in the design of the NED. In table 7.1, the total power of electrons exiting the accelerator are compared with the total power of the ions.

The total power deposited by the ions on the NED depends on the beam parameters, and the results of the simulations with TRIGO are presented in table 7.2. The contribution due to ions is the dominant, but not the only one. In figure 7.15, the power deposited by the electrons is given as simulated with BACKSCAT.

	Heat loads on the grids [kW]							Power of the particles at the exit [kW]	
	EG	AG1	AG2	AG3	AG4	GG	Total grids	D^-	e^-
Main beam	85	1318	1497	1090	739	722	5451	**40170**	540
Halo	4	106	149	636	921	794	2610	**1060**	160
Co-extracted electrons	535	10	1	0	0	0	546	**0**	0
Total	601	1436	1309	1329	1769	1349	7793	**42490**	700

Table 7.1: Transmitted and dumped loads given by the electrons generated by stripping, considering the long range magnetic field as in the configuration "PG17" [196, 166]

hmis [mrad]	0	0	0	2	2	2
tilting [mrad]	39.2	49.2	59.2	39.2	49.2	59.2
Total heating power [MW]	5.99	6.00	6.02	6.67	6.68	6.70

Table 7.2: Total heating power on the NED due to beam ions

7.3.5 Power density maps and most thermally loaded elements

The thermomechanical verifications will be carried out only on some of the many elements of the NED: the most loaded elements are identified mainly considering the power deposition by the beam. The rear panels for instance are the most thermally loaded and the thinnest among the wall panels, and therefore can experience higher stresses and strains. The power density maps, such as those shown in figure 7.16, will be imported in the FEM model and applied to the corresponding surfaces.

The scenarios to be considered are a combination of the following parameters: 39.2, 49.2, 59.5 mrad vertical tilting and 0, 2 mrad horizontal misalignment. On the other hand, the most requiring values of beam core divergence and

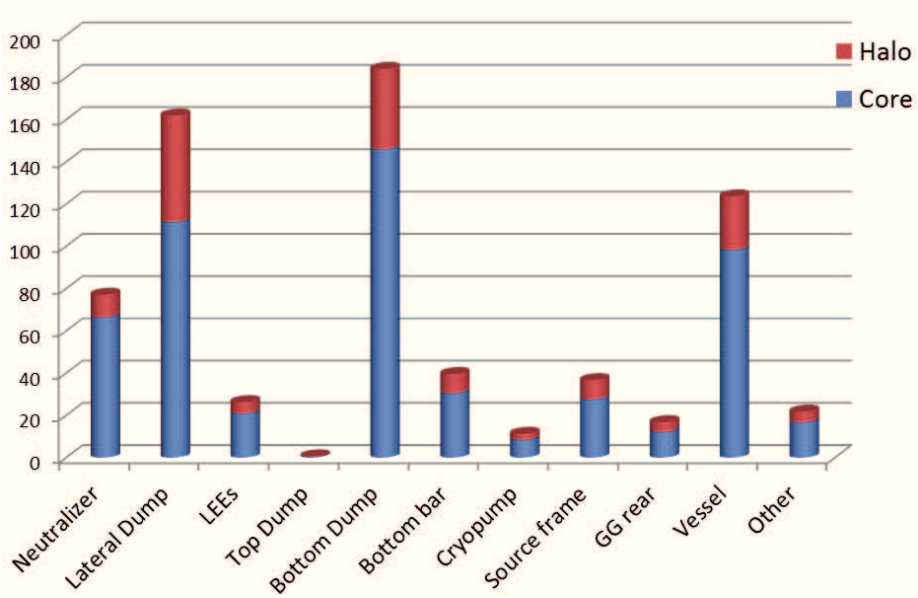
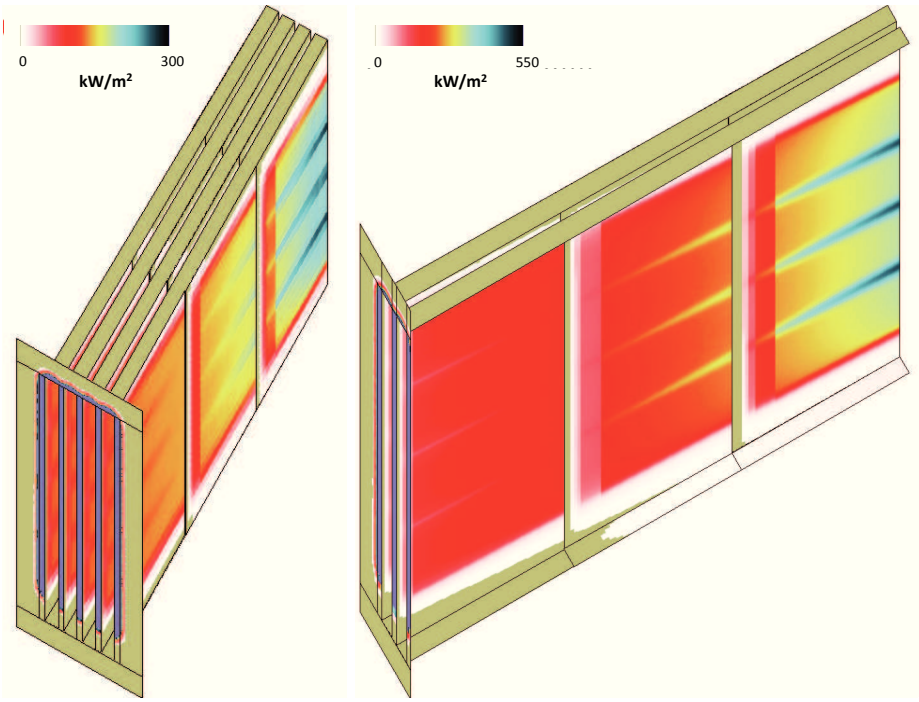


Figure 7.15: Electron power [kW] distributed among the in-vessel component with the present ED design [193].

halo divergence are respectively ω_c=7 mrad, ω_h=30 mrad with a halo power fraction of 0.15. The vertical misalignment can be compensated by the tilting adjustment system. This compensation, foreseen by numerical models, will be calibrated in the early experimental campaign. No adjustment systems are foreseen to correct the horizontal misalignment, therefore it must be considered in the design of the BLCs; the horizontal misalignment also increase the total beam power intercepted by the NED as shown in table 7.2. The maximum power density for an aligned beam is about 290 kW/m^2. In the case of 2 mrad horizontal misalignment it rises up to 530 kW/m^2 on the hot side of the rear wall panels, but on the cold side the maximum power density decreases to 150 kW/m^2. The Leading Edge Elements (LEE) increase the power density from 7.3 MW/m^2 to 10 MW/m^2, with a total power of 1.25÷1.3 MW deposited on the five of them. The vertical tilting only affect the power deposited on the floor of the beam channels, with a maximum of 22 kW on the four floor panels. A simple study of how the beamlet core divergence affect the power deposition is shown in figure 7.17.

Also the power deposited by the electrons is considered in the identification of the most loaded elements. In figure 7.15 the heat load on various elements is presented for a particular physics configuration of the beam source. The total power deposited by the electrons inside the Neutraliser is negligible. The thermal loads on the other elements are, on average, to be considered in the thermomechanical verifications in terms of power densities more than in terms of total power. The important result is that, with the present design of the ED, the cryopumps are protected against thermal loads due to direct and scattered impinging electrons.

The most loaded elements, as identified in these analyses, are listed in table 7.3.



(a) (b)

Figure 7.16: Power density contours, 49.2 mrad tilting, 2 hmis horizontal misalignment. The out-of-scale power density is colored in violet. (a) overall iso view, (b) section view of the left side (hot face in this case) of a middle panel.

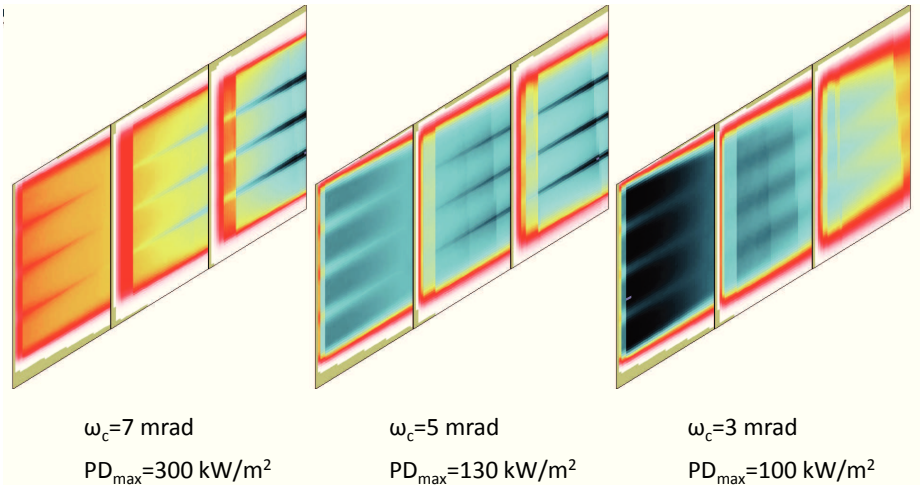


Figure 7.17: Power density on the centre wall panels for no horizontal misalignment, the same tilting and varying core divergence.

Neutraliser element	hmis, tilting [mrad]	Ions		Electrons		Total power [kW]	Note
		Power [kW]	PD [kW/m^2]	Power [kW]	PD [kW/m^2]		
Side wall – rear panel	+2, 49.2	391	532	-	-	391	Non-symmetric load
Centre wall – rear panel	+2, 49.2	525	531	-	-	525	Most loaded panel
Side wall – front panel	+2, 49.2	270	217	-	-	270	Stiffest panel with non-symmetric load
Centre wall – front panel	+2, 49.2	415	217	-	-	415	Stiffest panel with high thermal load
Centre LEE	+2, 49.2	321	?	29	?	321	Most loaded LEE
Side LEE	+2, 49.2	215	?	16	?	215	Non-symmetric geometry
Bottom floors	0, 59.2	5.5	56	-	100**	5.5	Most loaded floors
Top baffle	0, 39.2	31	3014*	4	31	35	Most loaded baffle
Bottom baffle	-	0	0	4	30	4	
Lateral Electron dump– internal panel	+2, 59.2***	22	852	88	204	22	

* Power density is calculated on a surface perpendicular to the X axis (horizontal beam line axis). The actual geometry of the top baffle, with a rounded edge, will strongly reduce this value.

** Value estimated without scattering of electrons.

*** The value of the B_z = 0.3 mT is different from zero only for this row of the table. Indeed, the Bz is relevant only to evaluate the electron deviation.

Table 7.3: Most heated elements: thermal parameters and boundary conditions for the NED elements to be analysed.

8

Heat removal

Most of the elements of ITER and MITICA Neutraliser and Electron Dump are actively cooled in order to withstand the high power and power density they are subjected to. The study of the Flow Rate partitioning and Coolant Temperatures is the starting point for a detail analysis and mechanical verification of the Neutraliser's components.

In this chapter, the current design of the cooling circuit is analysed. A one-dimensional FE model has been developed as a versatile tool in order to have a complete characterisation of the cooling subsystem.

8.1 Overview of the cooling system of beam heated elements

The Neutraliser and Electron Dump (NED) cooling system is sketched in figure 8.2. It includes the inlet and outlet headers, manifolds and all the NED actively cooled elements. The following cooling circuits have been identified:

- The cooling circuits inside the panels are separated into two lines, the front circuit and the rear circuit (A and B circuits of figure fig:heat2). Due to the power density distribution on the panel surfaces, the former is longer than the latter, being constituted by 8 vertical segments instead of 6.
- The cooling circuits inside the LEE that consists of a single channel with a twisted tape inside.
- The cooling circuits inside the top and bottom floors that are realized with U shaped tubes.
- The cooling circuits inside the top and bottom baffles.
- The cooling circuits inside the lateral electron dump (LED).

The operating conditions of the NED cooling circuits are significant for the analysis of any thermal subsystem, in terms of coolant temperature, pressure and especially mass flow partitioning.

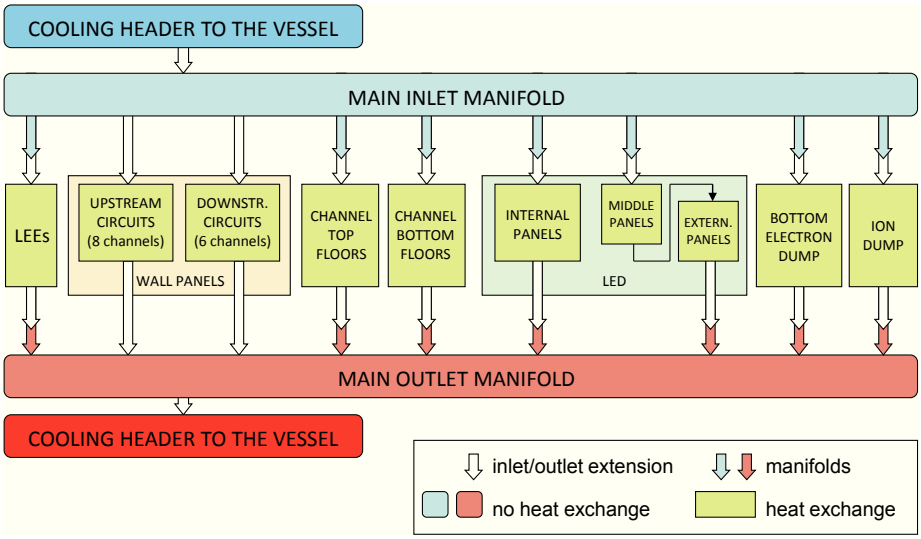


Figure 8.1: Schematic of the NED cooling circuits.

8.2 Thermal loads

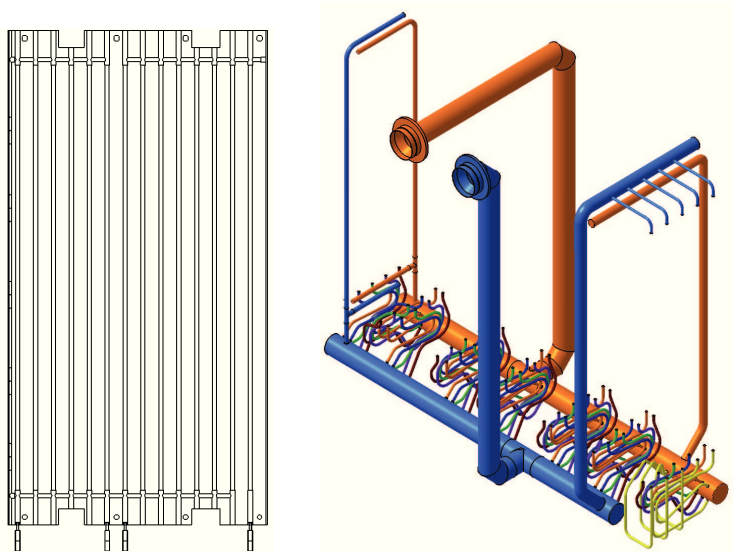
The thermal loads on the actively cooled elements depend on the beam parameters. The reference beamlet divergence (7 mrad beam core divergence, 30 mrad halo divergence with 15% halo power fraction) is considered, but various configurations (see table 8.1) must be taken into account in order to evaluate the worst case for the most heated elements, namely the leading edge elements (LEEs), the Top Ion Baffle and the Bottom Floor; moreover, the horizontal deflection of the electrons will heat asymmetrically the Lateral Electron Dump. The configuration considered for the horizontal misalignment consists of: 2 mrad for ion hmis and Bz effect for electron hmis. The cooling circuit simulation considers as inputs data the values of heat power due to ions and electrons (see previous chapter 7) calculated by means of the codes Trigo and Backscat.

As shown in Figure 8.3, each wall panel is divided into 14 sectors; this subdivision replicates the scheme of the cooling circuits that are composed by 14 vertical segments, thus, the sectors represent the surfaces from which the heat is collected by each single segment. The upstream sector (1/14 of the surface, first from left) of each wall panel is shadowed by the previous panel or by the leading edge element, and receives less beam halo power. In the attempt of uniformly collect the halo power, the positioning of the channel circuit inside the panels is therefore non-symmetrically placed, and the surface is divided in accordance. The power loads due to electrons are listed in table 8.2

The division in sectors has been made in order to obtain temperatures and heat transfer coefficients well suited for a 3D thermo-mechanic FE modelling of panels.

8.3 Parameters of the Hydraulic Circuits

The mass flow rate considered for the thermo-hydraulic verification of the Neutraliser and Electron Dump is 50 kg/s. The remaining mass flow rate given by



(a) (b)

Figure 8.2: (a) Cooling circuit drilled inside a wall panel and (b) Piping up to the interface with the vessel: blue inlet headers, orange outlet headers.

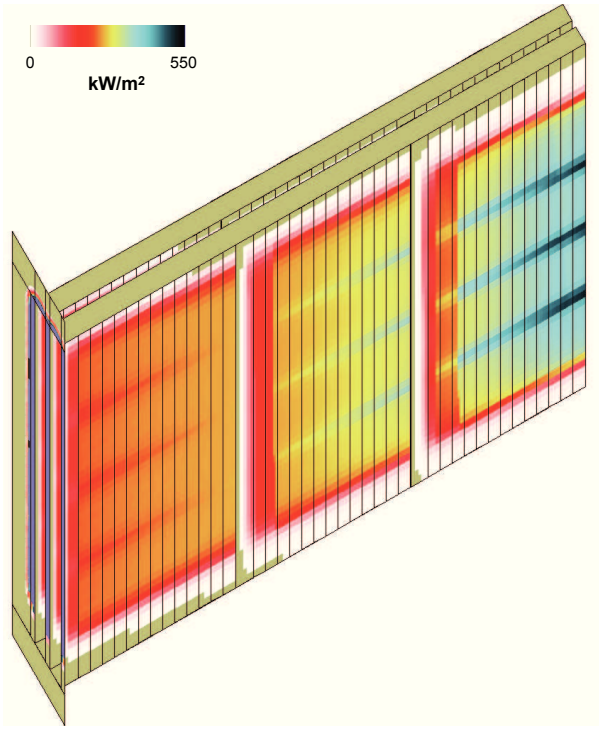


Figure 8.3: Power densities on the surfaces with panels divided into sectors accordingly to the cooling circuit routing

Beam configuration	Tilting [mrad]	Horizontal misalignment [mrad]	BZ for electron steering [mT]
Reference beam configuration	49.2	0	0
On-axis configuration, (Significant for the top ion baffle)	39.2	2	0.3
Off-axis configuration, (Significant for the bottom floor)	59.2	2	0.3

Table 8.1: Considered beam configurations for thermal-hydraulic simulations of elements exposed to the thermal loads.

LED Circuit: panel	Foldable, hot case	Internal, hot case	Internal, cold case	Foldable, cold case
Bz = 0 residual field [kW]	42	80	80	42
Bz = 0.3 mT residual field [kW]	57	88	68	48

Table 8.2: Power due to Electrons on the Electron dump circuits

the cooling system (30 kg/s for the NED operating in MITICA and 50 kg/s in ITER) is considered unnecessary.

The hydraulic characteristics of the model are summed up in table 8.3. All the actively cooled elements of the NED are fed by the main inlet header. They are in parallel among themselves and in series with the inlet/outlet headers which have 152 mm ID and 159 mm OD (SS seamless technical tube with design pressure 5.3 MPa accordingly to ASTM A 213M or A269, suitable factors shall be considered for proper tube material and operating pressure).

8.4 Finite Element model

The hydraulic circuits of the NED have been analyzed in ANSYS. The one-dimensional element type FLUID116 is used to model pipes and manifolds with two degrees of freedom: bulk temperature and pressure.

This fluid element can be used in both heat-exchange segments and adiabatic pipes: it has the ability to conduct heat and transmit fluid between its two primary nodes, and heat flow is calculated considering the conduction within the fluid and the mass transport of the fluid. Heat exchange through convection is accounted for with the use of additional nodes, at which an incoming heat flow is assigned.

In addition, the fluid element can also account for the distributed and localized flow losses. For given dimensions (hydraulic diameter) and parameters

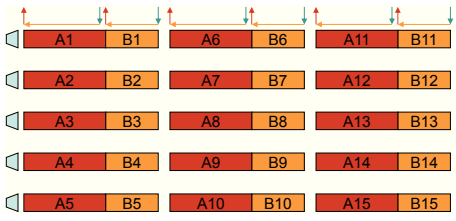


Figure 8.4: Cooling scheme of the Neutraliser Wall Panels; circuit A and B are respectively the front and rear circuits wrt the beam direction

NED element		Circuit			Losses		
		ø [m]	N. of channels	Ltot [m]	Curve N. (1/2 loss factor)	Inlet N. (0.5 loss factor)	Outlet N. (1 loss factor)
Top Floor	channel	0.008	2	6	2	-	-
	inlet extension	0.008	1	0.15	2	1	-
	outlet extension	0.008	1	0.15	2	-	1
	inlet manifold	0.027	1	2.8	1	1	-
	outlet manifold	0.027	1	2.8	1	-	1
Bottom Floor	channel	0.008	2	6	2	-	-
	inlet extension	0.008	1	0.15	2	1	-
	outlet extension	0.008	1	0.15	2	-	1
	inlet manifold	0.027	1	1	1	1	-
	outlet manifold	0.027	1	1	1	-	1
Top baffle	channel	0.018	6	3	4	-	-
	inlet manifold	0.027	1	1	1	1	-
	outlet manifold	0.027	1	1.5	1	-	1
Bottom baffle	channel	0.018	19	9.5	4	-	-
	inlet manifold	0.027	1	0.5	1	1	-
	outlet manifold	0.027	1	0.5	1	-	1
Panel	internal short	0.018	6	9.6	10	-	-
	internal long	0.018	8	12.8	14	-	-
	inlet extension	0.018	1	0.9	2	1	-
	outlet extension	0.018	1	0.9	2	-	1
	manifold	-	-	-	-	-	-
LEE	channel	0.018	1	1.8	-	-	-
	inlet extension	0.018	1	0.7	3	1	-
	outlet extension	0.018	1	0.35	-	-	1
	inlet manifold	0.078	1	1.5	1	1	-
	outlet manifold	0.078	1	0.3	-	-	1
Internal panels of the LED	channel	0.018	4	6.65	6	-	-
	inlet manifold	0.027	1	1.5	1	1	-
	outlet manifold	0.027	1	1.5	1	-	1
Foldable panels of the LED	channel	0.018	8	17.6	16	-	-
	inlet flexible hose	0.018	1	1	-*	1	-
	outlet flexible hose	0.018	1	1	-*	-	1
	inlet manifold	0.027	1	1.5	1	1	-
	outlet manifold	0.027	1	1.5	1	-	1

* still to be characterised in terms of distributed and localised pressure losses

Table 8.3: Parameters of the hydraulic circuits

(surface roughness) it also calculates the heat transfer film coefficient HFLM as a function of temperature and Reynold's number, coefficient that can be used in following detail 3D FE models of Neutraliser components.

Different material properties have been defined for the different heat transfer and friction correlations due to the presence or not of the swirl tube elements and in order to take into account the specific hydraulic diameter.

The first channel of the Baffles and the leading edges use swirl tubes in order to withstand the high power densities. Once the hydraulic diameter of the channel is calculated considering the presence of the twisted tape, the FE modelling of these elements is developed in ANSYS taking into account that:

1. the convective heat transfer coefficient is based on the hydraulic diameter and the twisted component of the coolant velocity;

2. the friction factor is calculated with the modified Colebrook-White formula that considers the hydraulic diameter and the total component of the velocity;

3. the distributed pressure drops are estimated considering the effective coolant path along the twisted tape.

The nonlinear thermal-hydraulic analyses have been carried out considering temperature dependence of the coolant properties (see section 6.2.4).

8.5 Thermal-hydraulic Results

The contour plots of the thermal-hydraulic results are shown in the following. The analyses have been carried out considering all the possible combinations of horizontal misalignment (0÷2 mrad) and beam source tilting (49.2 mrad ±10 mrad) for the load condition 1.1 Beam Operation (see table 6.6).

The maximum pressure drop results of 2.0 bar, the maximum temperature in the wall panels is 115°C and the maximum outlet coolant temperature is 88°C; these results have been obtained with +2 mrad horizontal misalignment.

The coolant pressure and temperature distribution in the overall system is shown in figure 8.5 and figure 8.6 for one of the considered case. A detail of active cooling segments, coloured by temperature, with channel diameter highlighted is shown in figure 8.7. The long, upstream circuits of the wall panels are distinguishable on the left (A), and are segmented in 8 parts, representing the vertical channels; the short, downstream circuits of the wall panels (B) are in the middle and are divided into 6 segments. Next to them, the five LEEs, the Top and Bottom floors (TF,BF), the Top Ion Dump and Bottom Electron Dump (TB,BB), and to the right the circuits of the LED (internal and external foldable panels).

This naming appear in figure 8.8, where the results of the three cases in table 8.1 are compared.

8.5.1 Influence of Vertical Tilting and Horizontal Misalignment

The total power received by all the components of the Neutraliser differs if it is considered the reference condition of 49.2 tilting no horizontal misalignment or the other two cases: +2 mrad horizontal misalignment is considered, and also the vertical tilting, causing the surfaces of the baffle and the bottom floor to be heated.

In the reference condition of 49.2 tilting no horizontal misalignment the total power of about 6.0 MW determines a temperature of the water of 83.8 °C at the outlet of the cooling system; in the case of +2 mrad horizontal misalignment and any vertical tilting, the total power of 6.7 MW heats the coolant up to 87.1 °C. The outlet coolant temperature range for the circuits in the panels and LEEs is 70÷115 °C.

The effect of horizontal misalignment is calculated for a positive misalignment of +2 mrad, which causes a higher heating of the left surface of each beam channels, that is, the right surface of each wall. For this reason, the temperature profiles in figure 8.8 for the side walls are not symmetric.

Considering the reference beam scenario with 0 mrad horizontal misalignment for the wall panels, the maximum coolant temperature is 103÷107 °C at

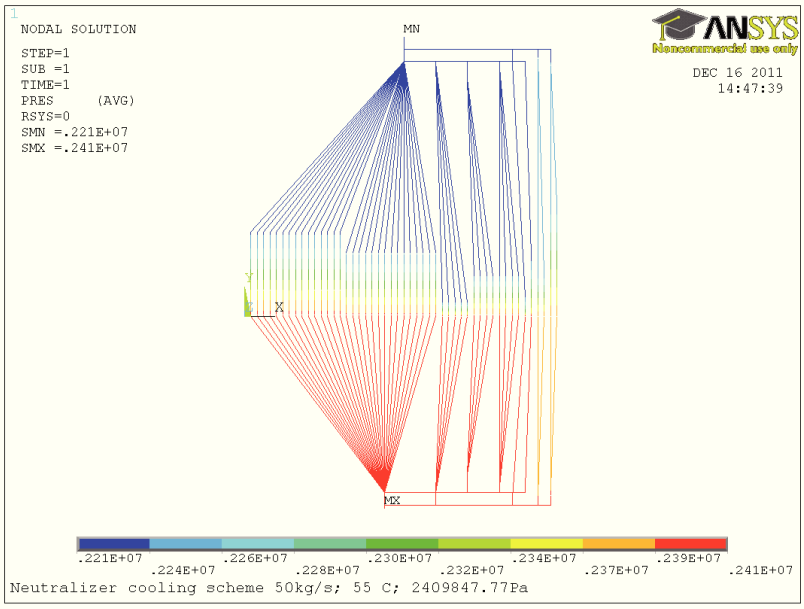


Figure 8.5: Overview of the finite element model with coolant pressure profiles [Pa]

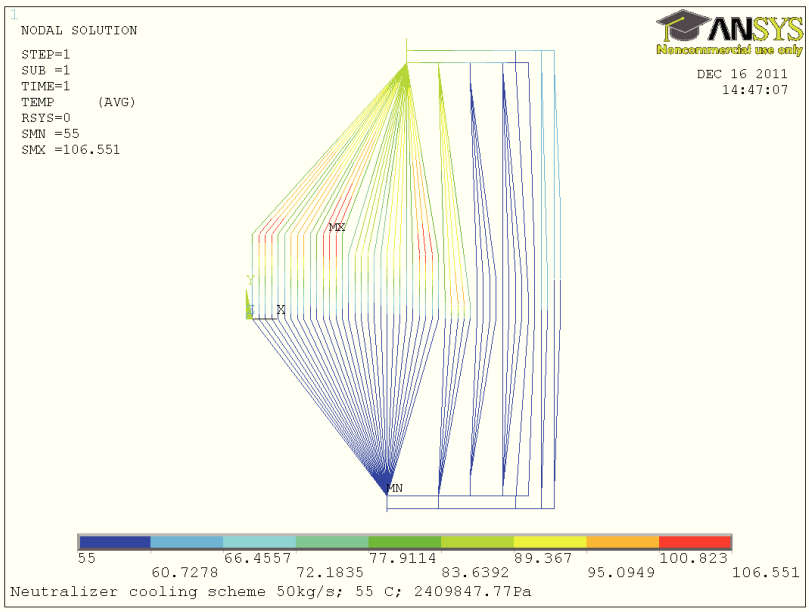


Figure 8.6: Coolant temperature profiles [°C]

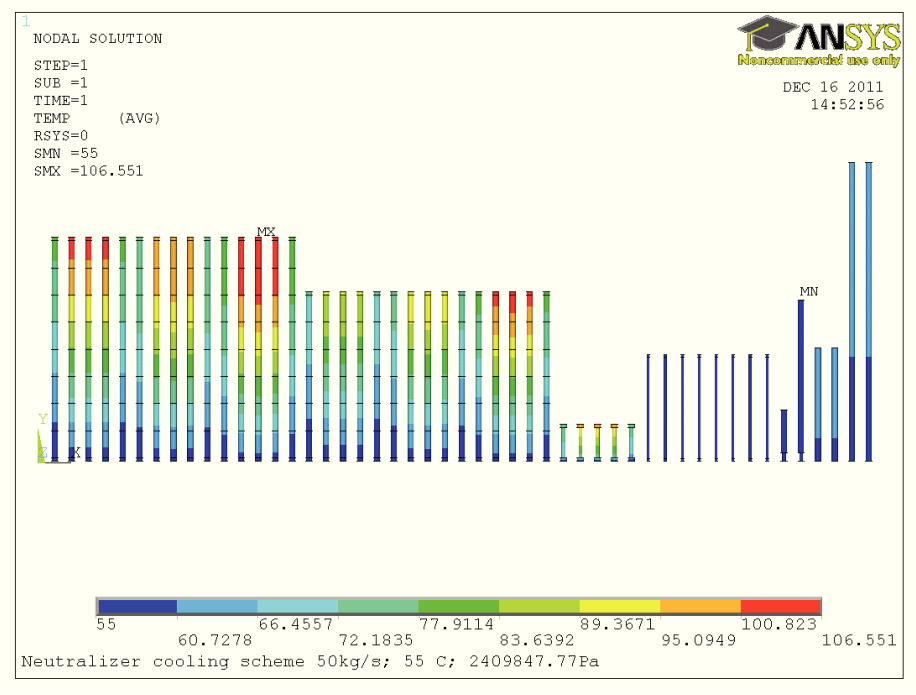


Figure 8.7: Water temperature rise into the wall panels [°C]

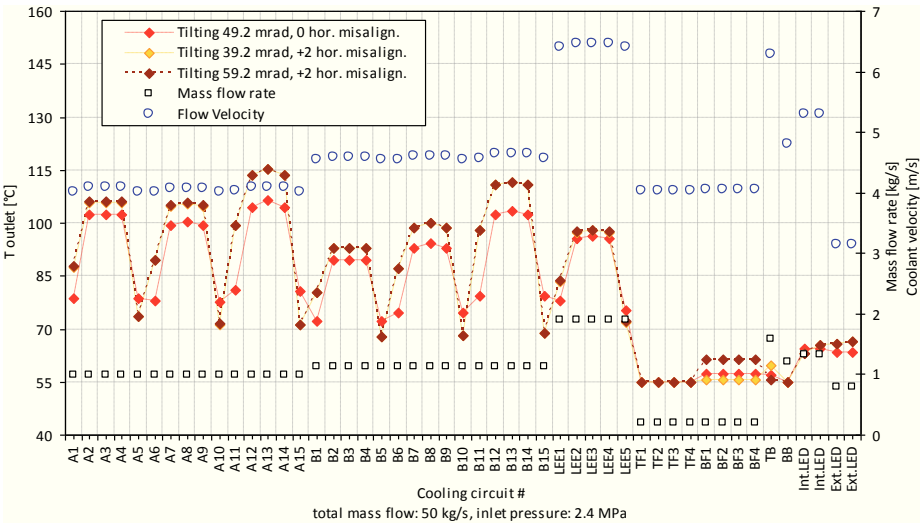


Figure 8.8: Influence of vertical tilting and horizontal misalignment on coolant temperature, mass flow rate and velocity inside channels (50 kg/s total mass flow rate, 2.4 MPa inlet pressure)

the outlet of the two circuits of the centre wall-rear panel. The water velocity is 4.0 m/s in the upstream circuit and 4.6 m/s in the downstream circuit of the centre wall-rear panel realizing a maximum heat transfer coefficient of about 32 kW/(m^{2}K). The maximum coolant temperature increases up to 115 °C for the beam scenarios with 2 mrad horizontal misalignment; the temperature change is opposite between left and right side panels. The tilting of the accelerator has almost no effect on the panels and the LEE heating power and therefore on the coolant outlet temperature.

On the contrary, it is the horizontal misalignment of the beam that do not affect the floors heating power and therefore on the coolant outlet temperature. The top floor does not receive any power contribution from the beam and it is actively cooled only to prevent heating from reflected particles. The temperature rise for TB and BB (top baffle and bottom baffle) is small because the coolant velocity is set to about 6.5 m/s in order to prevent CHF inside channels with twisted tape in the occurrence of focalised electrons. The temperature increase in each LED circuit is low (less than 15 °C) for the same reason.

One should notice that the different outlet temperature of the centre wall panels with respect to the middle wall panels is due to the high value of halo divergence ω_h which determines power deposition from beamlet groups of adjacent channels.

8.5.2 Influence of Water Inlet Temperature

A more comprehensive result is shown in Figure 8.9 where, in order to account for different operating conditions, vertical bars are used to show the calculated water temperature range. The red bars represent the temperature for the Neutraliser actively cooled elements operating in MITICA considering the maximum coolant inlet temperature of 55 °C; the blue bars represent the behaviour with minimum coolant inlet temperature of 20 °C. The vertical bars show the different behaviour of heated elements parametric mainly in horizontal misalignment; only for floors and baffles, the vertical bars represent the temperature variation due to vertical tilting.

8.5.3 Influence of LEE Internal Diameter

Three different diameters for the cooling channels of the LEEs have been analysed in order to evaluate the impact on the flow rate partitioning among all the NED cooling circuits. These analyses were carried out when the design of the lateral electron dump was not finalised, but no significant impact has been detected as the velocity are almost the same shown in the diagrams presented before in this document. In Figure 8.10, three different scenarios are shown: the results were obtained for the off-axis configuration with horizontal misalignment of 2 mrad. Using an ID of 30 mm instead of 18mm would decrease the water velocity by 1/3 and increase the outlet temperature by up to 20% in the panels' circuits. The LEE geometry with 18 mm diameter of the cooling channel was selected since the water velocity and the convective heat transfer coefficient are higher inside all the actively cooled elements.

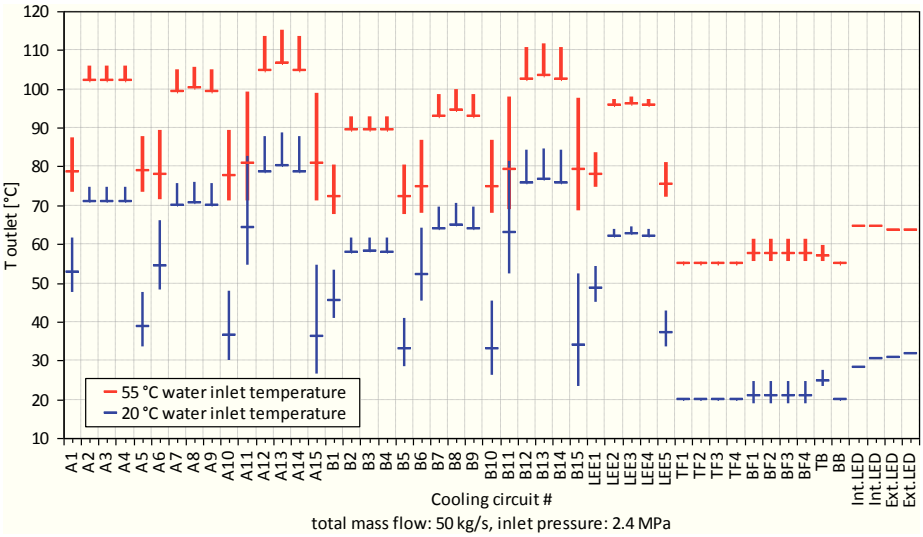


Figure 8.9: Expected coolant temperatures at the exit of each cooling circuit, for 20 °C and 50 °C inlet temperature, 50 kg/s total mass flow rate, 2.4 MPa inlet pressure; the vertical bars represent the variations of temperature due to beam parameters (vertical tilting and horizontal misalignment).

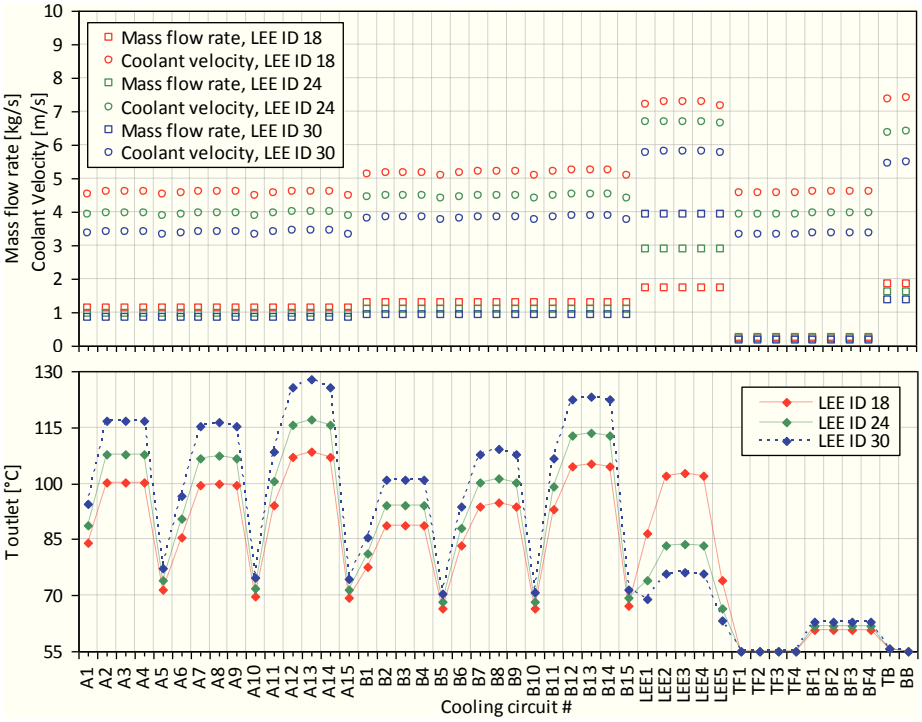


Figure 8.10: Thermal-hydraulic scenarios for different diameter of the LEE cooling channel (50 kg/s total mass flow rate, 2.4 MPa inlet pressure)

9

Thermal and mechanical analyses and verifications

This chapter presents the activities I carried out in the thermo-mechanical analysis of the Neutraliser and Electron Dump. The analyses are aimed at supporting the design development and verify the final design.

At first, the beam facing elements of the NED are studied by using the global boundary conditions described in the previos chapters. In particular the beam facing elements are the Wall panels, the beam channel Floors, the Leading Edge Elements (LEE) and the various panels of the Ion and Electron Dump.

Secondly, the other elements of the NED are studied, i.e. the piping assembly and the support structure.

9.1 Neutraliser wall panels

The Wall Panels are the core elements of the Neutraliser, having the role of splitting the neutralisation volume in four narrow beam channels. The Neutraliser panels must withstand the power density deposition under monotonic and cyclic loads due to interaction with the beam without excessive thermal deformation or stresses. Nonlinear thermal-hydraulic and mechanical analyses have been carried out with the Finite Element code ANSYS in order to evaluate the temperature distribution and the induced stress and strain fields. The compliance with ITER Structural Design Criteria for In-vessel Components (SDC-IC) [140] is verified; the verifications for monotonic type damage are satisfied with a minimum safety factor of 3.6 for all the considered load cases including steady state beam-on with +2 mrad horizontal misalignment and cooling circuit proof test.

The design of the wall panels has been described in section 6.4.

9.1.1 Load cases

The most heated Wall Panels have been identified as described in section 7.3.5: they are the rear panels of the centre and side walls. On these panels, the following load cases have been verified:

1.1 - Beam operation : application of the steady state thermal load; the resulting temperature distribution is verified considering the thermal limit for OFHC copper and the induced stress and strain fields are verified considering the Monotonic Verifications. Breakdown and classification of stresses is performed. Moreover, the cyclic loading conditions beam-on/off and breakdowns are verified considering the Cyclic Verifications.

3.1 - Loss of coolant thermal analysis of the Centre Wall - Rear Panel, as it is the most thermally loaded panel, after a beam-on condition: (1) steady-state beam-on thermal loads are calculated with nominal coolant conditions (flow rate, inlet pressure and temperature); (2) transient temperature profiles are calculated starting from the results obtained at step 1) and considering dried cooling channels (the convective heat transfer coefficient is assumed to be zero). The 2 mrad beam hmis is considered for both the load steps as it yields the highest heating scenario for the Wall Panel.

5.1 - Coolant pressure proof test mechanical verifications of the Wall Panels applying the coolant pressure of 3.5 MPa.

9.1.2 Preliminary analyses

Simplified, preliminary thermo-mechanical analyses have been carried out in order to obtain the thermal displacements of all the wall panels, and to design the slotted holes that will allow free thermal expansions of the wall panels with reference to the support structure. The reaction forces at the panel constraints are used to design the fixing elements and Belleville washers at the Wall Spacer supports. Furthermore, the temperature at the interfaces with the supporting Wall Spacers is used as boundary condition in following verification of the support structure.

The boundary conditions of these models, taken from the global hydraulic model, are the average temperature and heat transfer coefficient (HTC) in each vertical segment of the cooling circuit. Both are uniformly applied in the FE preliminary model together with gravity. Linear elastic material properties are considered for the OFHC Copper.

9.1.3 Model description

The detailed thermo-mechanical analyses of Neutraliser Wall Panels have been carried out in ANSYS Mechanical APDL environment. The solid model was created using the Bottom Up modelling method in order to create a controlled mesh.

Thermo-hydraulic model

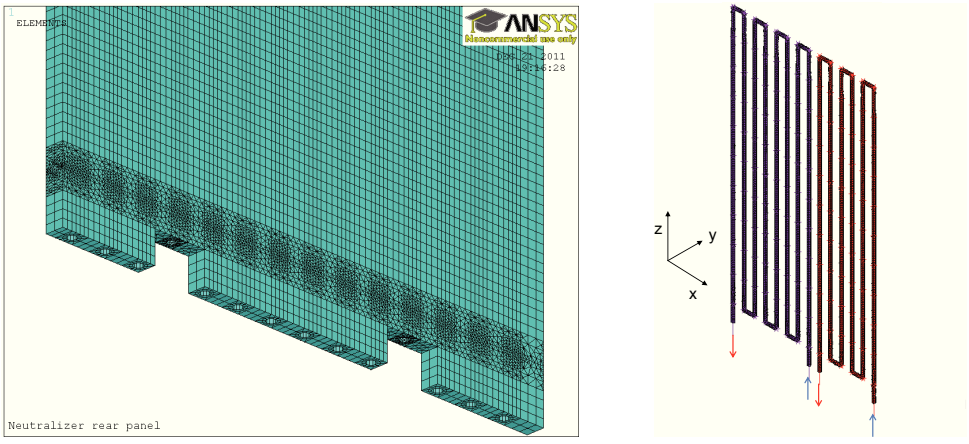
The finite element thermal model in ANSYS takes into account the following input parameters and boundary conditions:

- OFHC copper Panels geometry: elements of the type SOLID90 are used for the thermal analyses, SOLID95 for the structural analyses;

- Power densities (PDs) profiles obtained as described in section 7; the power density profiles on the two faces are imported in ANSYS as a data table, and then applied to the surfaces (or to one surface, in the case of the side wall panels).
- One-dimensional fluid elements FLUID116 are connected in series of many elements per vertical channel, realizing two independent circuits in each Wall Panel.
- water temperature and mass flow rate at the inlet, and pressure at the outlet in the most heating scenario, and estimated as described in 8 using a global hydraulic model, assuming a total water flow of 50 kg/s for the whole Neutraliser and Electron Dump (mass flow rate of 1.13 kg/s for the short rear circuit "B" and 0.99 kg/s for the long front circuit "A" were calculated);
- no heat exchange by thermal radiation;
- the convective heat transfer is calculated using the multiplication factor 1.15 in order to consider non uniform heating around the wetted perimeter of the cooling channels; the use of SURF152 elements covering the inner channel wall allows the interaction between the fluid bulk and the solid elements of the model.

The convective Heat Transfer Coefficient (HTC) α_t is automatically calculated for each surface element and during each substep of the nonlinear analysis as the multiplication of two factors: C_1 is a parameter depending on the geometrical dimensions of the cooling channel and on the mass flow rate (C_1 is constant for each cooling channel); C_2 is function of the coolant bulk temperature and it is automatically calculated along the coolant bulk during each substep of the nonlinear analysis:

$$\alpha_t = C_1 \cdot C_2 \tag{9.1}$$



(a) (b)

Figure 9.1: Meshed bottom-up model (a) and SURF152 element on the walls of the cooling circuit (b).

$$C_1 = 1.15 \cdot 0.027 \cdot \frac{1}{D_h} \left(\frac{4\dot{m}}{P_{wet}} \right)^{0.8} \tag{9.2}$$

$$C_2 = \lambda (1/\mu)^{0.8} Pr^{0.33} \tag{9.3}$$

The mass flow rate of the cooling circuit "A" results different from the one of the cooling circuit "B" inside each Wall Panels that therefore are characterized by different values of the convective heat transfer coefficient as calculated by the elements SURF152.

The elements FLUID116 and SURF152 are shown together in figure 9.1(b). The surfaces of the circuits are divided into segments (i.e. the vertical channels are divided into 10 segments) and the parameters are passed during the iterations from the FLUID116 to SURF152 by means of links realized using the "extra nodes" which are represented with stars in figure 9.1(b); in this way, a spatially accurate definition of the coolant temperature and of the convective HTC is obtained.

In addition, the implementation of a self-consistent model in which both the flowing water and the beam interaction is considered, is mandatory if a time-dependent simulation is to be performed. In the case of the Rear Panel of the Centre Wall for instance, a transient thermal analysis of the beam-on/off and breakdown cycles has been carried out.

This FE model can also be considered as a very accurate sub-modelling of the global hydraulic circuit.

Mechanical model

The boundary conditions are: support in vertical direction at nodes at the bottom, and degree of freedom along the transverse direction constrained on lines at the side of the wall panels, where a continuous contact with the spacer is foreseen (Belleville washers keep the panel adherent to the spacer, but a displacement greater than 0.5 mm determines contact with the nearby spacer on the other side; the initial position causes greater stresses in the material).

The static mechanical analyses have been carried out implementing multi-linear cyclic stress strain curves for OFHC copper; the results are postprocessed with breakdown and classification of stresses. The beam-on/off fatigue analyses are carried out implementing material hardening parameters for OFHC copper and the mechanical results are postprocessed by applying special procedures [189]. In both cases, the SDC-IC [140] criteria are to be verified.

9.1.4 Results

In the following, only the results for rear centre panel will be briefly presented.

Load case 1.1 - Thermal verification

The thermal analyses are carried out applying the maximum coolant inlet temperature (55 °C) and the power density distributions obtained for +2 mrad horizontal misalignment, and for this reason the PD is not symmetric, as partially visible in figure 9.2(a). The steady-state temperature distribution obtained on the hot face with these thermal loads is visible in figure 9.2(b); the water temperature and the corresponding HTC are shown in figure 9.2(c) and (d). The

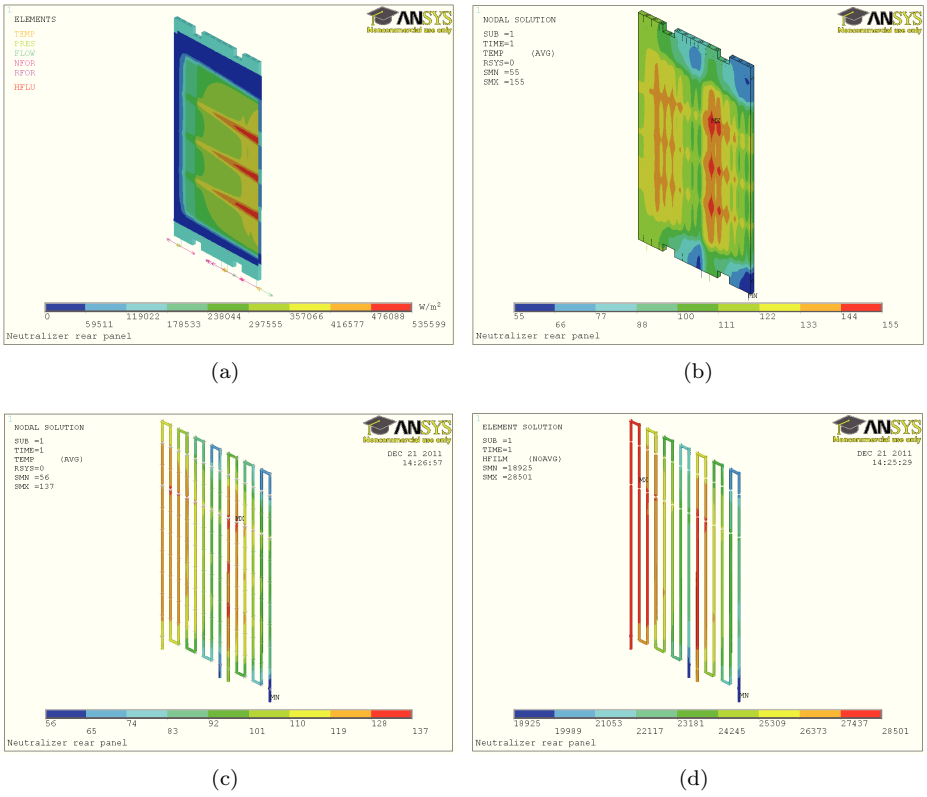


Figure 9.2: Rear Centre Panel: (a) thermal boundary conditions (power density on the hotter surface [W/m^2]) and (b) resulting Temperature distribution at steady-state [°C]; (c) coolant temperature temperature [°C] and (d) HTC [W m^{-2} K^{-1}] at channel walls.

thermal verification of the OFHC copper is satisfied as the maximum panel temperature is 150 °C < 300 °C.

Starting from room temperature, the time evolution of the temperature during beam-on is shown in figure 9.3 with a the calculated characteristic time of $\tau_c = 13.9$ s. The effect of breakdowns in terms of temperature variation is negligible ($\Delta T_{max} < 4$°C), and so the strain range, so Cyclic damage verifications are not performed for breakdown thermal cycles of the Wall Panels. Significant strain ranges can be observed due to beam-on/off temperature variations up to $\Delta T_{max} = 100$°C as described in the following for the beam-on/off thermal cycling.

Load case 1.1 - Monotonic verification

Two boundary conditions are considered for the analysis in order to distinguish the primary stresses from the total ones (primary plus secondary): coolant pressure (2.4 MPa) and gravity loads (beam-off conditions) will yield primary stresses; coolant pressure, gravity, and thermal loads (steady-state beam-on conditions) will yield primary plus secondary stresses. Primary and secondary

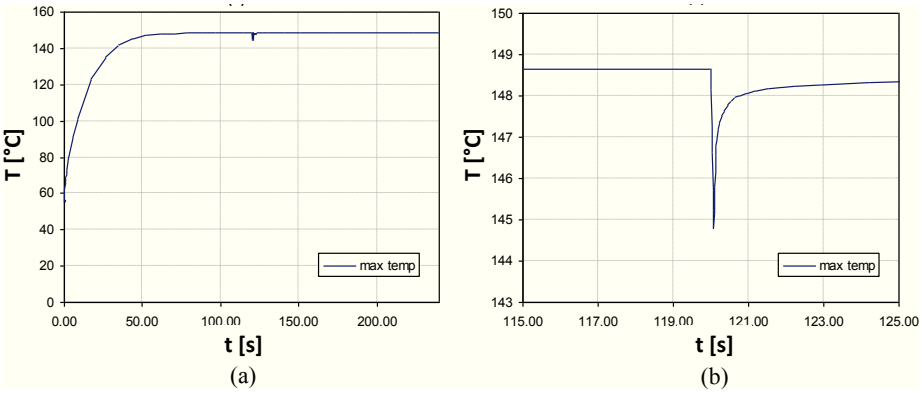


Figure 9.3: Element temperature as a function of time during beam-on (a) and detail of the effect of breakdowns (b).

stresses have been properly considered carrying out the breakdown and classification of stresses for monotonic type (M type) verifications.

The stress field of interest to carry out the monotonic verifications is discovered to be located at the cooling channel intersection shown in figures 9.4(a) and (c), where paths have been identified where to carry out the breakdown and classification of stresses according to ITER SDC-IC [140]: the linearized breakdown along the minimum thickness (MIN_TK) path is shown in figures 9.4(b) and (d).

The results of the M-type verification are detailed in table 9.1 for the presented linearised stresses at MIN_TK. The second rule for the verification of local primary membrane stress is not applicable since overlapped material are not modelled for the panels. A conservative estimate for K_I can be obtained by using the following expression for a single-edge notched plate subjected to a uniform tensile stress σ at infinity [140, App. B]:

$$K_I = \frac{1.122}{\left(1 - \frac{a_0}{h}\right)^{3/2}} \cdot \sigma\sqrt{\pi a_0} \tag{9.4}$$

In the formula, $h = 34$ mm is the thickness of the section and $a_0 = 805$ mm is calculated as $\max(4a_u, h/4)$, where a_u [μm] is the largest undetectable crack by non-destructive techniques to be used, 10 μm in this case.

All the M-type verifications are satisfied. The calculated directional displacements are presented in figure 9.5, where they are compared with results for rear side panels: in particular the out-of-plane deformation is important, since it could determine enhanced interaction with the beam.

Load case 1.1 - Cyclic Verification

The thermo-mechanical results have been imported in the fatigue post-processing code in order to carry out the fatigue verifications considering all the nodal conditions. A reduced selection of elements is used to perform fatigue verification.

Only beam-on/off cycles have a significant effect for reducing the fatigue life, whereas the breakdowns have no impact. The maximum fatigue life consumption is about 7%. The fatigue verification is satisfied.

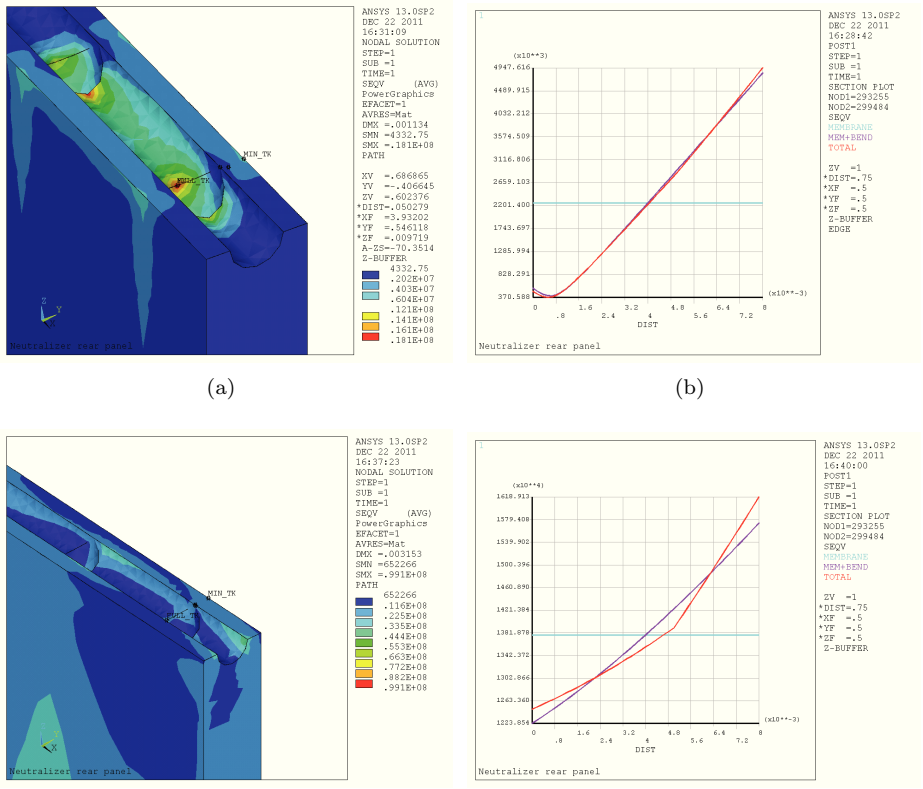


Figure 9.4: Breakdown and classification of stresses along MIN_TK path: (a) distribution and (b) linearized primary Von Mises stresses and (c) distribution and (d) linearized primary plus secondary Von Mises stresses [Pa]

Criterion	Rule	Condition		Limit	Elastic result	Safety factor
Immediate plastic collapse and plastic instability (IC 3211)	Primary membrane and bending stress	$\overline{P_m} \le S_m(T_m, \phi t_m)$	[MPa]	46	2.3	20
		$\overline{P_L + P_b} \le K_{eff} S_m(T_m, \phi t_m)$	[MPa]	69	5	14
	Local primary membrane stress	$\overline{P_L} \le \min\left[1.5 S_m(T_m, \phi t_m), S_{y,\min}(T_m, \phi t_m)\right]$		69	2.3	30
		$\overline{P_L} \le 1.1 S_m(T_m, \phi t_m)$	[MPa]	(not applicable)		
Immediate plastic flow localization (IC 3212)	Primary plus secondary membrane stress	$\overline{P_L + Q_L} \le S_e(T_m, \phi t_m)$	[MPa]	No limit	13.8	OK
Local fracture due to exhaustion of ductility (IC 3213)	Total stress, including peak stress	$\overline{P_L + P_b + Q + F} \le S_d(T, \phi t, r_2)$	[MPa]	No limit	16.2	OK
	Total stress, excluding peak stress	$\overline{P_L + P_b + Q} \le S_d(T, \phi t, r_3)$	[MPa]	No limit	15.7	OK
Fast fracture (IC 3214)	Global fast fracture	$K_I \le 0.33 K_C(T_m, \phi t_m)$	[MPa m$^{1/2}$]	5	0.3	19
	Local fast fracture	$K_I \le 0.67 K_C(T_m, \phi t_m)$	[MPa m$^{1/2}$]	11	0.3	39

Table 9.1: M-type verifications for load case 1.1 at MIN_TK path.

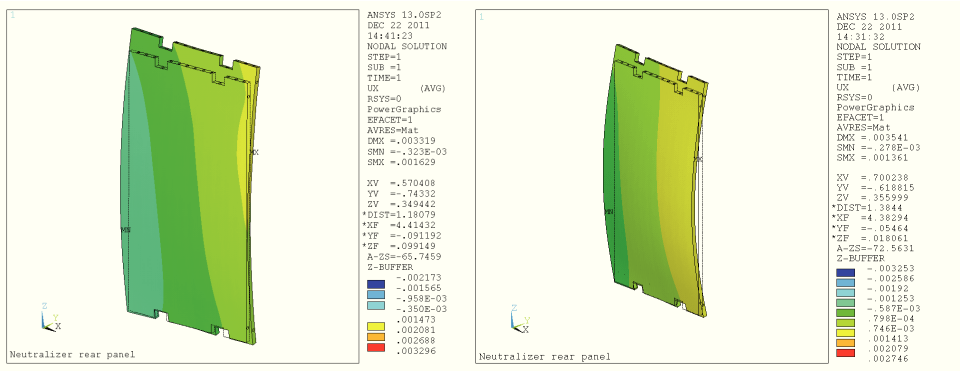


Figure 9.5: Thermally induced directional deformations (respectively longitudinal, transversal, vertical) calculated for Load case 1.1: (a), (c), (e) rear center panel, (b), (d), (f) rear side panel.

Load case 3.1 - Thermal Verification

A thermal transient analysis aimed at the thermal verification of load case 3.1 has been performed, by starting from the steady-state temperature distribution

already calculated for load case 1.1 and then interrupt the cooling action by removing the boundary conditions for convection at all the cooling circuits' surfaces. This represents a complete loss of coolant with dried cooling channels. The beam parameters are: full beam-on power, 49.2 mrad beam source tilting, +2 mrad beam horizontal misalignment.

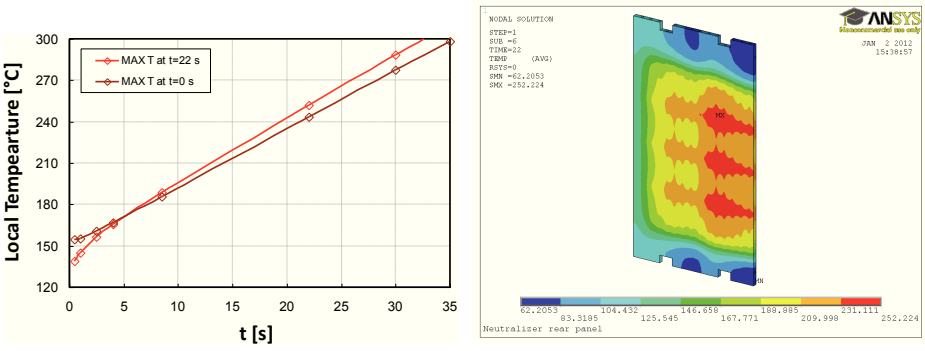
The time duration of the transient analysis is $\delta t = 30$ s. In order to verify the minimum time for reaching the maximum allowable temperature (within the range $250 \div 300$°C for OFHC copper) two nodes are selected: one is the node where the maximum temperature occurs at t = 0 s, and the other node is the one where the maximum temperature occurs at t = 22 sec. The temperature rise is shown in figure 9.6(a) The maximum allowable temperature of 250 °C is reached at $t = 22$ s. The temperature distribution relevant to that time step is shown in figure 9.6(b). A time window of 22 s is high enough to determine a ΔT of ∼100 °C compared with the time constant of thermal sensors.

Load case 5.1 - Monotonic Verification

Cooling circuit proof test is carried out at a coolant pressure of 3.5 MPa. No other mechanical loads are present apart from gravity which is considered negligible. The uniform pressure is applied at the inner surface of the cooling channels. Paths have been identified to carry out the M type verifications and the breakdown and classification of stresses, and all the M type verifications are satisfied.

Investigation of overcooled condition

An operating condition with 20% water flow rate over the reference value of 50 kg/s has been investigated in terms of temperature distribution and maximum deformation of a Side Wall - Rear Panel. The maximum coolant inlet temperature (55 °C) and power density profile for +2 mrad hmis are applied. The maximum temperature reached at steady state conditions is 130 °C instead of 135 °C. The water temperature at the exit of the two cooling circuits is respectively 93.4 °CC and 89.5 °CC for the long and short panel circuit. Basically,



(a) (b)

Figure 9.6: Temperature rise (A) and temperature distribution at t=22 s (b) with maximum T=250 °C.

the out-of-plane displacement do not change; the 20% higher flow rate does not help in reducing the deformations.

9.1.5 Comments

The design of the cooling circuit for the wall panels is functional and all the verifications are satisfied.

9.2 Leading Edge Elements

The five edges of the Neutraliser Walls are subjected to high heat loads due to power deposition from accelerated beam ions and electrons. These edges are protected by Leading Edge Elements (LEEs) that must withstand the power density deposition under monotonic and cyclic loads due to interaction with the beam without excessive thermal deformation or stresses. The material is CuCrZr-IG alloy.

The design of the wall panels has been described in section 6.4; the optimization of their design instead is discussed in the following.

9.2.1 Optimization of the Leading Edge Elements

The thermal power deposition occurs on the external surface, and many cases can be reduced to the six geometries in table 9.2, defined by external radius R_{ext} that is the sum of the tube radius and the wall thickness. The LEE cross section (see figure 9.7(a)) has been designed considering the following constraints:

1. minimum width: the LEEs protects the 10 mm thick front wall panel, so the LEE width is assumed to be 44 mm;

2. wall thickness around channel: thick to allow the deep drilling of the channel, but small enough to minimize thermal paths and avoid thermal island. 4, 5, 6 mm is considered;

3. cooling channel diameter: small enough to reduce the flow rate consumption (18, 20, 22, 24, 30 mm channel diameters have been simulated).

The considered heat loads are:

- Electron thermal loads as calculated by BACKSCAT. The uniform electron power density of 500 kW/m2 has been applied on the LEE surface. This value is applied on the entire LEE surface even if it corresponds to the maximum one; this assumption is based on the following considerations:the range of values for the electrons power density (0 500 kW/m2)

A.	Rext=13 mm (ID 18 mm, TK 4 mm)
B.	Rext=16 mm (ID 24 mm, TK 4 mm; ID 20 mm, TK 6 mm; ID 22 mm, TK 5 mm)
C.	Rext=19 mm (ID 30 mm, TK 4 mm)
D.	Rext=15 mm (ID 18 mm, TK 6 mm; ID 20 mm, TK 5 mm; ID 22 mm, TK 4 mm)
E.	Rext=17 mm (ID 24 mm, TK 5 mm, ID 22 mm, TK 6 mm)
F.	Rext=14 mm (ID 18 mm, TK 5 mm)

Table 9.2: LEE geometries obtained combining different parameters

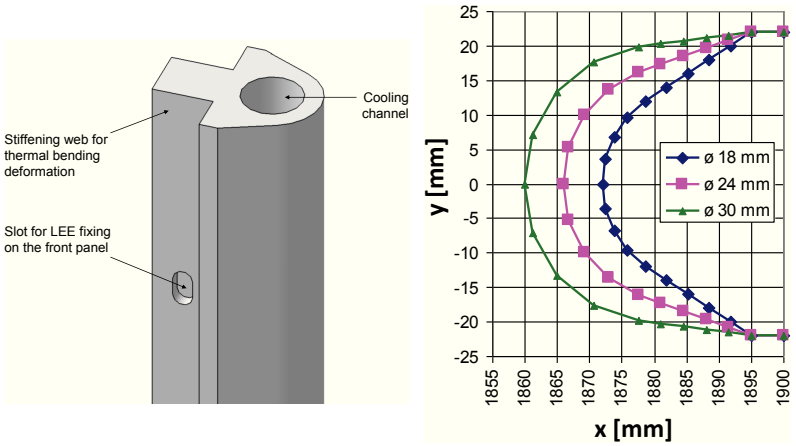
is narrow compared with the ions power density (0 7 MW/m2); the position of the maximum of electron power density can change in the map of Figure 2 -4 due to the large deflection of electron trajectories under external electro-magnetic fields.

- Ion thermal load is obtained from the vectorial code Trigo; Many PD profiles have been generated for both 0 mrad and +2 mrad beam horizontal misalignment and considering. It has been verified that the vertical tilting angle of the beam source is not significant for changing the PD profile, so only the reference value (49.2 mrad) is used in the following cases. A sketch of the LEE parametric cross section and the in plane coordinates are given in figure 9.7(b), for which the calculated ion power density maps are shown in figure 9.8.

A customized version of ANSYS is used for the application of the thermal load on the thermo-hydraulic finite element model, because of the use of STEs. The cross section is selected considering the maximum temperature reached on the FE elements; this criterion is effective at this design stage because the maximum temperature is related to: (1) material aging under localized thermal conditions for the required pulses duration; (2) material creep under thermal and stress conditions for the required pulses duration; and (3) fatigue damage due to the thermal strain and stress conditions under beam-on/off pulses.

R_ext [mm]	name	$R_channel$ [mm]	TK [mm]	T_front [°C]	T_side [°C]
15	D1	9	6	253	214
15	D2	10	5	233	200
15	D3	11	4	214	205

Table 9.3: Selection of the best thermal results obtained among the many considered geometries.



(a) (b)

Figure 9.7: (a) Sketch of the LEE and (b) example of cross-sections considered for the design: the x coordinate refers to the Grounded Grid position, and y to the mid-panel

Among all the above tabulated geometries, the best in term of less temperature are those of case D (see table 9.3, and in particular among the three channel diameter the intermediate one with 20 mm ID is chosen, after comparing the temperature at a front and side node (see figure 9.9(a)). This LEE geometry gives the minimum side temperature, low front temperature, low flow rate consumption (20 mm inner diameter) and the 5 mm wall thickness can be technologically realized by deep drilling.

9.2.2 Verifications

The thermal and mechanical verifications have been carried out for the LEE type D2 identified as the solution best fitting the boundary conditions. The monotonic and cyclic verifications are satisfied for the load case 1.1.

9.3 Floors and wall spacers

The channel floors and the wall spacers they protect are subjected to the direct heating by the beam; their design has been described in section 6.4.2. Their structural function is thus associated with the beam/component interaction, A thermo-hydraulic analysis of the elements has been carried out; at a later stage, the design of the interface with the wall panels has evolved from this configuration.

A submodel was used in order to study the combined thermal behaviour of:

- the channel floors, heated by the beam,
- the wall spacers in contact with the hot wall panels, and
- the cooling channels in between.

The FE model was developed in ANSYS Workbench, as described in the following.

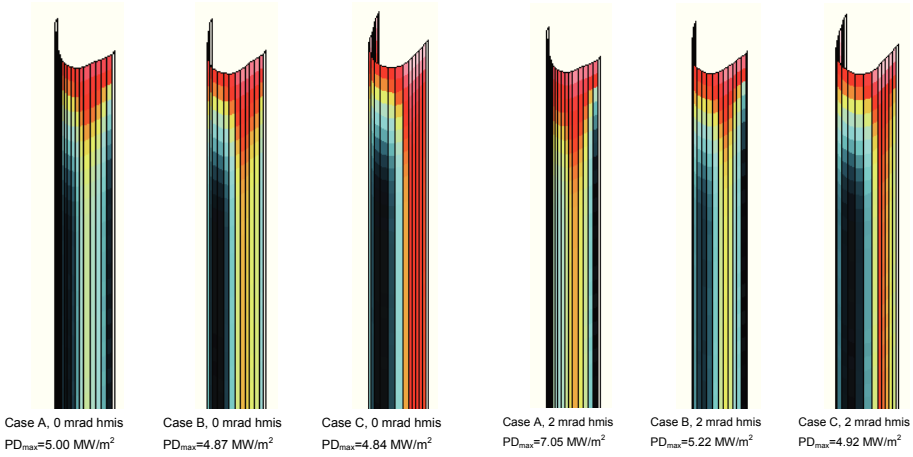
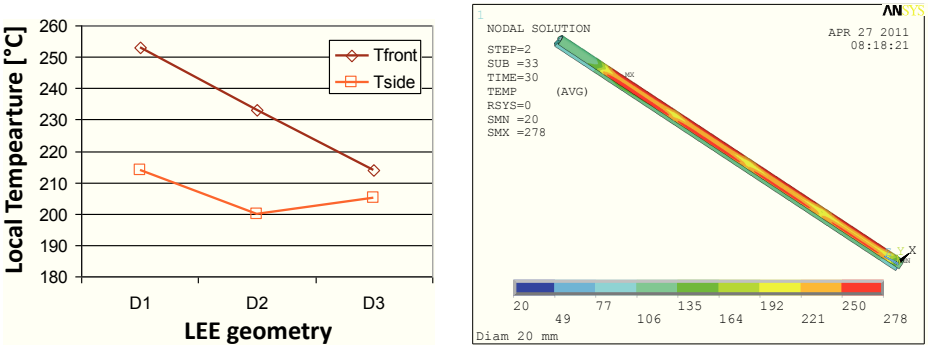
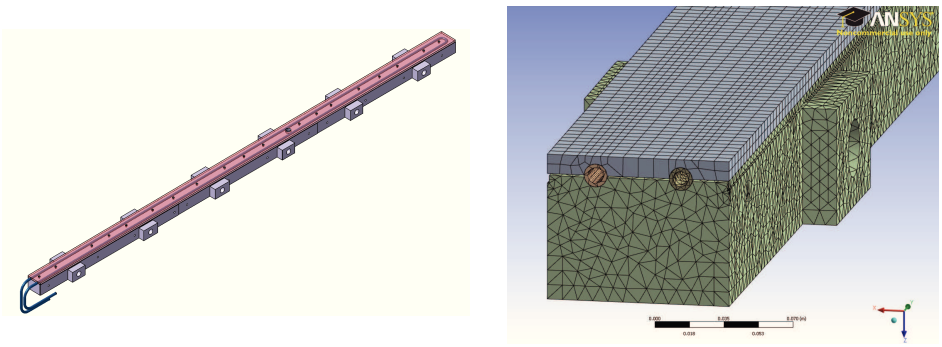


Figure 9.8: Detail of the PD map on three geometries of the LEE; on the left, cases with no hmis, and on the right, cases with 2 mrad hmis.



(a) (b)

Figure 9.9: Temperature rise (A) and temperature distribution at t=22 s (b) with maximum T=250 °C.



(a) (b)

Figure 9.10: Temperature rise (A) and temperature distribution at t=22 s (b) with maximum T=250 °C.

9.3.1 Model description

Thermo-hydraulic model

The heat exchange by radiation is considered negligible, and therefore all the surfaces are adiabatic, apart from:

1. surface of the beam channel floor: the total power of the accelerated ions impacting the component is about P_{beam} = 6 kW and the power density map calculated with Trigo is applied; the contribution due to electrons is negligible (about 80 kW are distributed on the surfaces of the four neutraliser channel by the electrons [193], slightly less than in previous results [151]).

2. thermal contact with the wall panels: the spacer is heated by the wall panels through the fixing screws and washers that hold the panels in the in-plane position and by direct contact at the side (positioning surface of the panels) and at the weight bearing surface (only bottom spacers);

ideal contact is assumed. The local temperature is obtained from the preliminary thermal analyses of the wall panels (see section 9.1.2), and range from 75 to 110 °C as listed in table 9.4.

3. internal walls of the cooling channel: the water inlet temperature is function of the site conditions and it is assumed equal to the highest possible value of 55 °C. Both inlet and outlet of the U-shaped channel are at the rear edge. The local temperature and HTC are calculated in the following.

wall panel	segment #	temperature [°C] at side surfaces	temperatures [°C] at bearing surfaces
Front	1	120	110
	2	105	
	3	105	100
	4	75	
Middle	1	110	100
	2	105	
	3	105	100
	4	75	
Rear	1	110	105
	2	105	
	3	100	95
	4	75	

Table 9.4: Surface temperatures applied as boundary conditions at the areas of contact with wall panel

In a preliminary model, the power input at steady state by heat exchange with the wall panels is quantified in $P_{panels} = 0.5$ kW at the bottom spacers.

The heat balance is expressed by the formula:

$$P_{ions} + P_{panels} = \dot{m} c_p (T_{out} - T_{in}) \tag{9.5}$$

The coolant temperature is calculated analytically for different flow velocity and mass flow rates; with 4 m/s flow velocity and $\dot{m} = 0.2$ kg/s, the water ($c_p = 4184$ J/kg.K) temperature at the exit is 63 °C with an increase of 8 °C, acceptable values indicating a good thermal design.

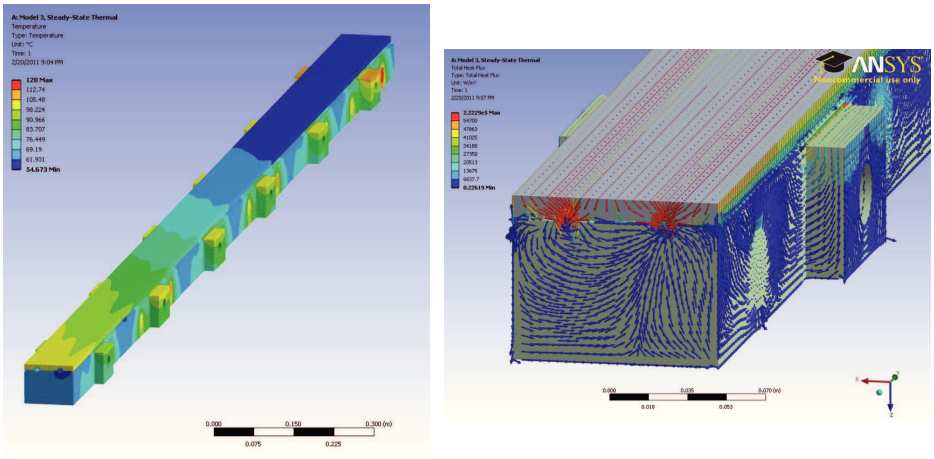
The water bulk temperature is assumed to change linearly from the inlet to the outlet along the U shaped cooling tube; the heat transfer coefficient is assumed to be constant for the entire tube and it has been calculated with the Sieder-Tate formula:

$$\alpha = Nu \frac{\lambda}{ID} = \frac{\lambda}{ID} \cdot 0.027 \cdot Re_H^{0.8} Pr^{1/3} \left(\frac{\mu}{\mu_w} \right)^{0.14} = 23500 \ \frac{\mathrm{W}}{\mathrm{m^2 K}} \tag{9.6}$$

9.3.2 Results

Load Case 1.1 - thermal results

Steady-state thermal analyses are discussed in the following. The heating is asymmetric due to the fact that the continuous contact with panels is realized only on one side; in addition, the water temperature varies along the channel, and therefore it is asymmetric (from 55 °C to 62 °C).



(a) (b)

Figure 9.11: (a) Temperature distribution (wiew from behind) with max T$\sim$ 120°C and Heat flux [W/m^2] in the Wall Spacer assembly (b)

The copper plate can reach about 107 °C; as the temperature depends on the power deposition, it is maximum at the rear edge where there is the maximum interaction with the beam. In the SS spacer, the temperature is dominated by the cooling channels, and varies from 62 °C (at the cooling circuit entrance) to the imposed 120 °C at the side contact with the front panel. Figure 9.11(b) presents the heat flux through the floor, the SS tube and the Wall Spacer. The large difference between the copper and SS thermal conductivity is evident: only 5% of the total heating flow comes from the side contact surface with the wall panels. The high thermal contact conductance is evident around the cooling tube perimeter. The thermal verification of the OFHC copper is satisfied as the maximum panel temperature is < 300°C.

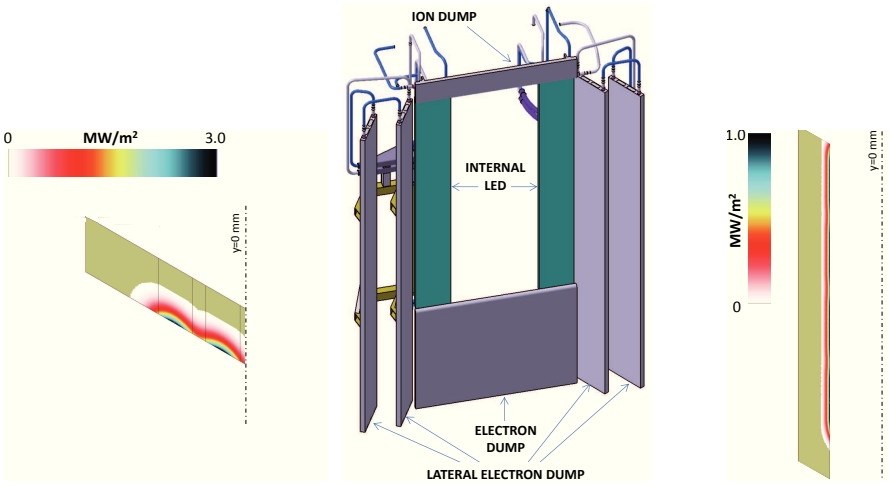
The free deformations of the wall spacer along 3 m in the transverse direction, preliminary calculated on this model, are such that an integrated model of the NED support structure is required to verify the overall assembly and the tie-rods; it has been realized as described in section 9.6.

9.4 Electron Dump panels

This section deals with the thermal and mechanical verifications of the Ion and Electron Dump, named also Particle Baffles to consider the interception necessity of both ion beam halo and accelerated and steered electrons exiting the Beam Source.

The methods described in section 7 are adopted to calculate the thermal boundary conditions.

The layout and naming of the particle dump elements placed out of the Neutraliser core cross-section are sketched in figure 9.12(b), with the ion dump at the top of the beam entrance section, the electron dump at the bottom, and the lateral electron dump. The high-divergence beam halo ions will interact



(a) (b) (c)

Figure 9.12: Layout of the panels constituting the Electron Dump (b); power density deposited by ions on the top (b) and side (c) panels.

with the baffles as shown figure 9.12(a) and (c). In order to absorb this power, STEs are used in the innermost cooling channel of these elements.

9.4.1 Thermo-mechanical model

By applying the calculated heat loads, the OFHC Copper panels are verified and the resulting maximum temperature is less than the maximum allowable temperature for OFHC Copper for all the panels ($< 300\,°C$).

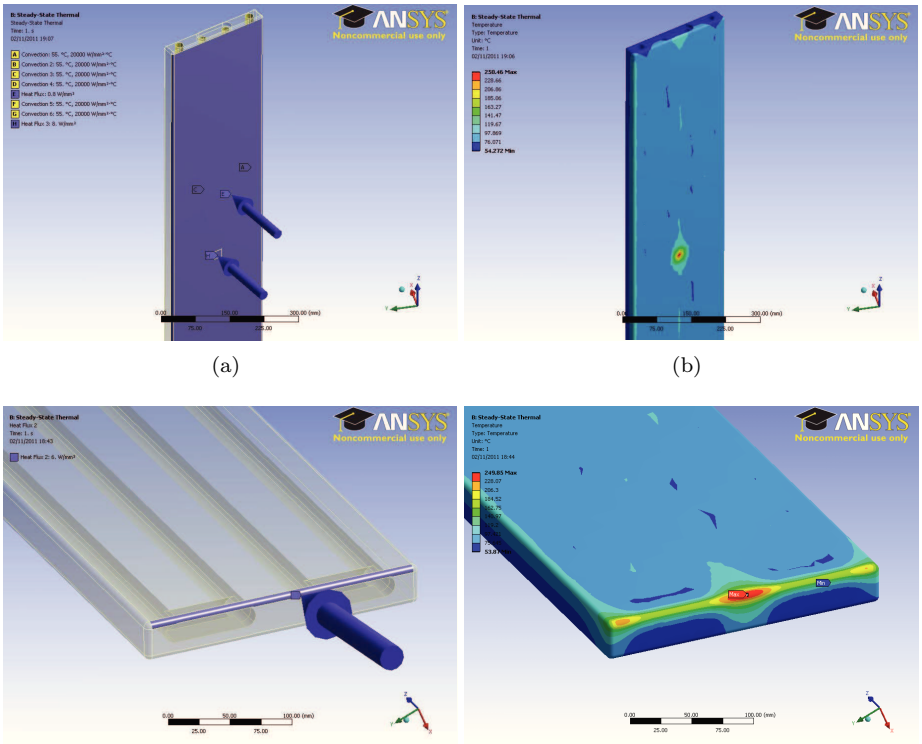
Therefore the criteria that has been used to verify the design of the ED panels uses a somewhat different approach from the ones described until now. A reliable map of the power density deposited by the electron is not available yet, until the final design review of the beam source. Their trajectories, however, are very susceptible to electromagnetic fields and may focus and heat limited, small areas.

A virtual scenario of beam operation has been identified in the case of a lateral electron dump (LED) panel, with particle focusing on a very small surface. The high power density may be localised anywhere on the panel surface facing the beam source. The thermal power is applied on the small surface up to reach the local temperature of 250 °C.

Virtual scenario of beam operation

A coolant pressure of 2.4 MPa is applied to the internal channels. The peak power density on the internal LED panel operating in the virtual scenario can depend on the location of the heat deposition:

i. Limited area in between the cooling channels. The heating condition for the case of localized heating in between two cooling segments results: maximum power 3.2 MW in a square area of 400 mm2 with a power



(a) (b)

(c) (d)

Figure 9.13: (a) boundary conditions and (b) temperature for case i.; (c) boundary conditions and (d) temperature for case ii.

density of 8 MW/m^2, when all around a uniform PD of 0.8 MW/m^2 is applied on the panel's surface. This thermal load determines a maximum Von Mises stress of about 120 MPa all around the heated area.

ii. Limited area at the bottom edge. The thermal contours of the LED innermost panel are plotted in figure 9.13 for operation without localised heating for PDmax = 6 MW/m^2.

9.5 Piping assembly

The structural analyses of the cooling piping assembly of the Neutraliser and Electron Dump are presented, and the studies of different configurations, which helped during the design phase, are quickly discussed. Together with the static thermo-mechanical verifications, results from modal analysis are presented.

Pressure limits for cooling pipework blowing out, draining, and drying are presented considering the PED hazard classification.

A bellows restraining device RH compatible has been developed by RFX to be mounted onto main cooling bellows of MITICA Beam Line Components (BLCs). This device has been proposed to the IO to verify the compatibility

with the RH manipulator and tools. Implementing the required modifications, the system could be mounted also on main cooling bellows of ITER HNB BLCs.

9.5.1 Requirements and preliminary remarks

Requirements for piping

Requirements for the NED piping assembly are then relevant to the accommodation of the manufacturing and positioning errors and to normal and maintenance operations:

- withstand steady state loading conditions including mechanical loads and thermal expansions considering beam-on operation and baking conditions;
- withstand dynamic loadings induced by seismic events;
- allow NED lifting/lowering after/before cutting/welding of pipes for maintenance operations; this means that a bellows shall be interposed between the vessel feedthroughs and the cooling headers, in order to be able to disconnect/connect the tube end sections after/before cutting/welding operations;
- accommodate manufacturing and positioning errors of the interfaced components. These errors could be different in ITER HNBs and MITICA because the ITER beam shall be aligned with respect to the ITER tokamak references.

Use of flexible joint technology

Main cooling headers of MITICA Beam Line Components (BLCs) will present bellows at the vessel feedthroughs: some considerations can be pointed out:

1. The hydrostatic forces are very strong. Forces generated at miters act axially on the expansion joints. For this reason, their elongation shall be contained by tie-rods used for lateral expansion joints in order to transfer the pressure load to the vessel wall. The main advantages of using lateral expansion joints are:
   a. to absorb lateral misalignment for relative positioning errors between the vessel and the beam line components;
   b. to allow cutting/welding operation (axial compression still possible);
   c. to avoid huge transversal forces acting on the beam line components after piping pressurisation (see 7.3).
2. Compensation of manufacturing errors can be made by adjusting the length of the tie-rods.

Fluid forces acting on the pipes

Hydrostatic forces At miters/elbows, there is a force due to the net difference of surface area exposed to the static pressure of the fluid. From the force balance, that force results being equal to the fluid pressure applied to the internal section of the miter inlet (1) and outlet (2):

$$\bar{F} = p_2 A_2 \bar{n}_2 + p_1 A_1 \bar{n}_1 \tag{9.7}$$

In the case of 90° changes of direction with no variation of section, the force acting on the miter/elbow is 45° oriented on the plane of the deflection, and results (with negligible pressure losses):$F = \sqrt{2} \cdot p \cdot A$. If these equations are applied to the case of the NED cooling circuit, in correspondence of the 90° miters of the inlet pipe and the main header, the force results equal to 75 kN obtained as the vector sum of the two perpendicular 53 kN components (2.4 MPa fluid pressure multiplied by 22160 mm^2 section area).

Hydrodynamic forces Hydrodynamic contributions are due to changes in flow direction with the mean velocity calculated as:

$$\bar{F} = \frac{\Delta \bar{p}}{\Delta t} = \frac{m\bar{v}_2}{\Delta t} - \frac{m\bar{v}_1}{\Delta t} = \dot{m}(v_2 - v_1) \tag{9.8}$$

Velocity is given by $v = \dot{m}(\rho A)^{-1}$ In the case of 90° changes of direction, the force acting on the miter/elbow results $F = (\dot{m})^2\sqrt{2}(\rho A)^{-1}$; given the small value of flow velocity, the forces acting on the pipework are negligible with reference to the hydrostatic contribution (hundreds of N).

Drag forces Friction acts on long pipes, giving rise to a drag F_D that can be calculated as follows:

$$F_D = f\rho\frac{v^2}{2}(L\pi d) \tag{9.9}$$

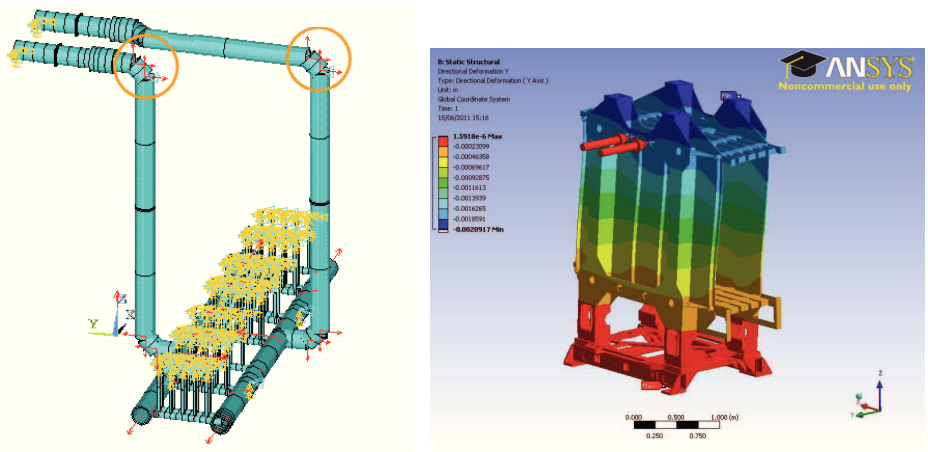
The drag force can be calculated in the case of the longest pipe run, which is the vertical segment of the pipe run proceeding from the vessel. Assuming a friction factor of about f = 0.04 with a water velocity of 4 m/s, for a pipe segment length of 3 m, the drag force along axial direction results about 0.85 kN, and is therefore considered negligible with respect to the hydrostatic contribution.

Need for a tied axial expansion bellows

The typical constraint layout for the anchor of such a system is that an anchor is located after the 90° curve, which allows thermal deformations. If the axial expansion bellows is not limited in its expansion, the NED structure will be loaded with the pressure of the water at the curve, equal to a force $F_Y = A \cdot p =$ 53 kN.

The stiffness to transverse loads of the support structure has been evaluated as shown in figure 9.14. By analogy with a cantilever, the stiffness of the structure results from FEM post-processing considering the applied force and the resulting displacements along Y direction: $k_Y = F_Y/\Delta Y = 10$ kN/mm. The axial adjusting force rate for the pressurised bellows, equal to $c_delta = 365$ N/mm, shall be added to k_Y, calculating the total stiffness $k_{tot} = 10.3$ kN/mm and therefore the net displacement $\Delta Y = F_Y/k_{tot} = 10.2$ mm. This displacement is of course totally unacceptable, not to mention the equivalent (Von Mises) stresses.

This constraint layout is not feasible; the transverse forces cannot be loaded on the NED structure. Therefore, the analysis confirms that the use of tied expansion joints at the interface with the vessel is mandatory.



(a) (b)

Figure 9.14: (a) Example of a piping model in which the transverse constraints are given by the NED, and (b) FEM-characterized transversal displacements caused by the reaction forces.

9.5.2 Design of the bellows restraining device

As described above, a bellows restraining device is needed for the main headers cooling bellows. Bellows axial expansions after piping pressurization up to 20 barA during operation shall be restrained in order to prevent both the damage of bellows due to excessive elongation and the transversal displacement of NED affecting positioning and alignment requirements.

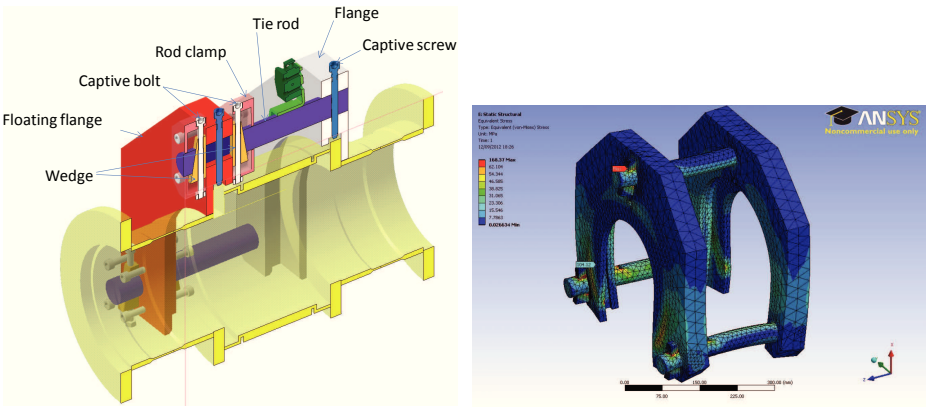
The restraining device is equipped with tie rods and flanges, able to transfer the pressure load to the vessel wall. The length of these tie-rods shall be adjustable, in order to set flanges on actual bellows length and to compensate manufacturing and positioning errors.

The bellows restraining device will be mounted on bellows before piping pressurization and it will be removed before maintenance to allow cutting/welding operations. The bellows restraining device must be RH compatible as per ITER Remote Handling Code of Practice [152]. The removable assembly shall have appropriate interface with ITER manipulator arm and lifting winch. The design is derived from the available ITER RH cut/weld tool [153]; the bellows restraining device is represented in figure 9.15(a).

Bellows expansion is restrained by two flanges that are connected by three tie rods. The distance between flanges can be adjusted on the actual bellows length; indeed the RH tool can engage captive bolts to move vertically the wedges and then change the tie rod shoulders on the floating flange. Wedges can be made of aluminium bronze in order to avoid in vacuum bonding.

Structural analyses have been carried out simulating the pressure load of 51 kN resulting by applying the 20 barA coolant pressure on bellows inner area. The tie rod diameter of 40 mm is proposed and the mean tensile stress results 13.5 MPa in the gross area.

The pressure load is modelled as a remote force centred on the bellow axis and applied on annular areas set as rigid surfaces in order to simulate the contact



(a) (b)

Figure 9.15: (a) Section view of the bellows restraining device and (b) Von Mises stresses [MPa] in the bellows restraining device with applied full pressure load.

with flanges of the removable bellows assembly. Bonded surfaces are assigned at the contacts region between wedges and tie rods and between wedges and the floating flange.

Linear elastic steady state analyses have been carried out to investigate the behaviour of different tie rod diameters. Von Mises stresses on the assembly elements are represented in figure 9.15(b). Structural deformations along the bellows axis have been also investigated.

9.5.3 Design and verifications of the piping assembly

The layout for the piping constraint is studied by means of a global model, which helped in the development of proper supporting and fixing clamps by means of:

- steady state thermo-mechanical analyses simulating thermal expansions; they have been performed to verify the system capability to realise free thermal deformations without stress concentrations due to reaction forces
- modal analyses to verify the system frequencies and to limit the degrees of freedom.

At the same time, the piping assembly realises a mechanical interface between the vessel and the Neutraliser, so integrated structural analyses should be carried out considering the operation of the NED with all possible load combinations.

Piping model description

In ANSYS it is possible to model piping systems and their loads with PIPE elements. Elements PIPE16 or PIPE289 are used in the global piping model, to model the straight pipe run and the mitered bends. The presence of flexible or extensible elements, such as bellows or curls, cannot be easily modeled by pipe segments. Therefore beams with equivalent stiffness are used, such as BEAM4 elements.

	ANSYS element	OD [m]	TK [mm]	A [m^2]	Ixx, Iyy [m^4]
Main headers and pipes	PIPE289	0.1524	3.2	-	-
Panel Expansion joints	PIPE289	0.01905	0.5	-	-
Cutting / welding segment	PIPE289	0.219	3	-	-
Bellows	BEAM4	-	-	3.58E-07	2.48E-11

Table 9.5: Real constants and sections for ANSYS tubing elements

The structure is defined by nodes connected by elements: the pipework geometry has been developed using keypoints and lines in ANSYS, and the coordinates of headers, manifolds and pipes, their length, diameter, and wall thickness are taken from the CAD model design, and are listed in table 9.6. In particular, the equivalent section and inertia of the bellows are estimated from the adjusting-force rate coefficients, in terms of axial elongation c_δ [N/mm] but also both angular bending c_α [N m/deg] and lateral deflection c_λ [N/mm]; a cantilever model is used to convert the adjustment-force rates in the variables E_x, J, A of a beam as:

$$c_\delta = AE/l, \;\; c_\delta = 2EJ/l^2, \;\; c_\delta = 12EJ/l^3 \tag{9.10}$$

The material used for modelling the piping system is AISI 304L. Non-linearity of material properties is not considered, apart for the coefficient of thermal expansion that is expressed by a polynomial of second order:

$$\alpha_T = 15.76 \cdot 10^{-6} + 1.075 \cdot 10^{-8} \cdot T - 4.175 \cdot 10^{-12} \cdot T^2 \tag{9.11}$$

Young's modulus $E_x = 210$ GPa and Poisson ratio 0.3 are used for the piping elements. Virtual bellows elements are modelled with $E_x = 20$ GPa.

The verification criteria for the bellows is the maximum movement absorptions, which is calculated as the sum of the three absorption fractions:

$$\frac{\alpha}{\alpha_0} + \frac{\delta}{\delta_0} + \frac{\lambda}{\lambda_0} \leq 1 \tag{9.12}$$

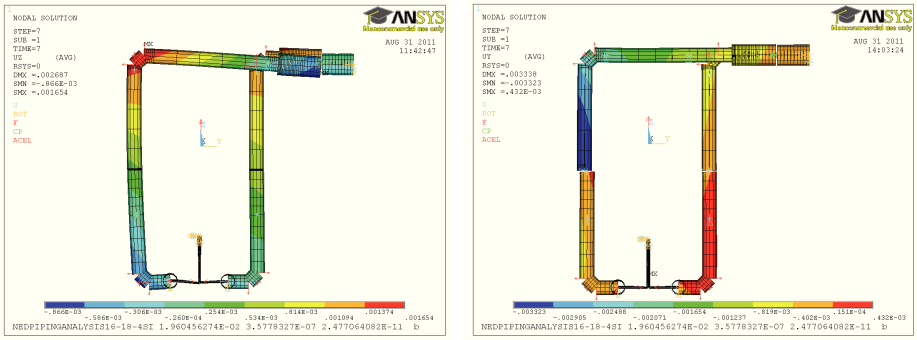
where α, δ and λ are respectively angular, axial and lateral absorption by the corrugate element. The nominal axial movement absorption ($2\delta_N$) can be used to calculate the other two; the obtained correction factors must be used to consider operating pressure and temperature.

Piping alternative concepts

Different concepts were taken into account during the design optimizations. The differences include the presence of secondary manifolds, the way the assembly is supported and constrained, the presence of additional bellows, and son on. Two examples are shown in figure 9.16; in none of them the bellows are verified.

Piping design description

A different concept consists of supporting the whole weight of the piping structure from the top of the Neutraliser. The basic idea is that the expansion tube



(a) (b)

Figure 9.16: Directional displacements in two alternative layouts: (a) vertical support at the bottom manifolds and (b)a lateral expansion bellows in the middle of the vertical headers.

elements designed to connect the headers to the panels can take the vertical elongation of the structure, exerting small forces on the panels; the bellows interfacing Neutraliser and Vacuum Vessel will not be subjected to lateral misalignments during normal operations.

Transversal constraints along the transversal direction (Y axis) are offered from the structure only at the two manifolds. Supports along longitudinal direction (X axis) are placed at the top of the piping assembly, along the horizontal pipe runs, and at the headers, at the support closer to the tee. At last, the weight of the structure is supported by vertical constraints (along Z direction) placed at the top of the side plates of the Neutraliser (one support for the inlet header, two for the outlet header). A simplified geometry has been used to represent the panel expansion joints.

The vertical pipe runs are not constrained along the longitudinal X direction. From modal analysis, it was noticed that the lowest is placed the support in this direction, the minor are the manifolds oscillations; the X constraint is placed at the NED pad closest to the header axis. Manifold vertical oscillation occurs and its frequency is related to the stiffness of the Panel Expansion Joints.

Hyperstatic constraints are avoided. No support along Y direction is placed at the top of the NED, it is at the main manifolds. The structure freely expands vertically and horizontally. The elongations are taken by the panel expansion joints at the bottom of the structure, and not by the bellows at the interface with the vessel.

No reaction forces along X direction are present. Nevertheless, misalignment between the vessel and the Neutraliser will give rise to small forces along axis X and Y.

Beam operations (Load case 1.1)

Pressure, gravity, thermal loads (temperature of the inlet circuit 50 °C, temperature of the outlet circuit 70°C) are applied to the model. Fixed support at the Vessel interface and at the wall panels. Node forces are used to model fluid forces.

element	FX [N]	FY [N]	FZ [N]
Top supports (outlet pipe, inlet pipe)	< 50	-	15÷43, 170
Panel junction	< 10	< 15	645÷665
Vessel	< 10	$\sim$40000	< 175
Header supports	-	< 400	-

Table 9.6: Reaction forces at the Neutraliser elements and interfaces

The results of the vertical displacements and the Von Mises stresses are presented in figure 9.17. The static analysis results show some peak stresses in few areas within 51 MPa that are considered very low compared with the AISI 316L maximum allowable stress $Sm = 115$ MPa. (see Figure 9 -29). The reaction results of this analysis are listed in Table 9 -15. Momentum at panels is always less than 2 Nm in every direction.

For the dynamic verifications, the modal analysis has been carried out in order to identify critical oscillations and frequencies. The dynamic response of the piping assembly has been studied up to a participation mass fraction of 50% and up to 130 Hz. Frequencies are not so low (13% of mass participates to the lowest modes at about 26 Hz) but the system presents a consistent percentage of mass involved in dynamic modes around 50 Hz. The modes with the high mass participation fraction are shown in figure 9.18 All the identified modes are strictly related to vertical oscillations of the two headers.

9.5.4 Design and verification of the Panel Expansion Joints

A complete re-design of the Panel Expansion Joint has been carried out in order to fulfil the new requirements, in particular the Vertical and Horizontal displacements of the piping assembly (namely, Z and X directions) have to be taken by these components and the forces acting on the joints (manifold-pipes and pipes-panels) have to be under a safe threshold.

Beam operations (load case 1.1)

Three cases are considered in order to find the most demanding combination:

A. in the first analysis, only a vertical displacement $Z = 2$ mm at room temperature is considered;

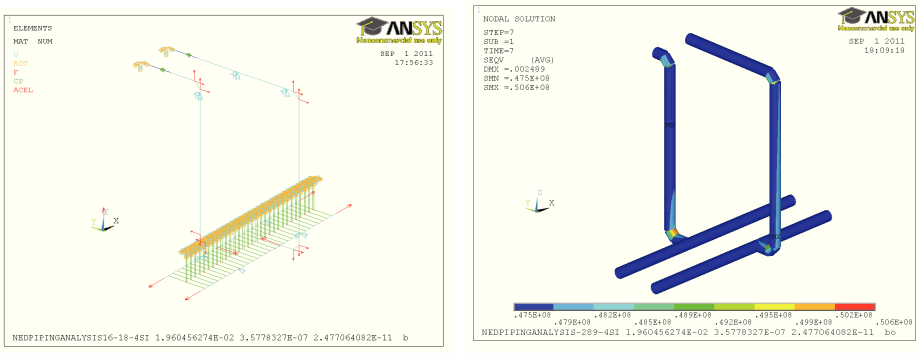
B. in the second one, both a vertical and an horizontal displacement of $Z, X = 2$ mm at room temperature are considered;

C. in the third one, the operating temperature of the components is set to 70 °C, and both the displacements are considered.

The internal pressure of 2.4 MPa is applied in all the cases.

It is found that case B is the most demanding on. The Von Mises stresses and the breakdown and classification at the maximum are shown in figure 9.19. The M-type verifications are satisfied with minimum safey factor of 1.5.

The reaction forces at the interface with the panels and the manifolds are always below 0.7 kN for load case 1.1/B.



(a) (b)

Figure 9.17: Steady-state thermo-mechanical analysis: (a) Displacement vector sum [m] with DOF constraints and (b) Von Mises stresses [Pa] on main headers and manifolds.

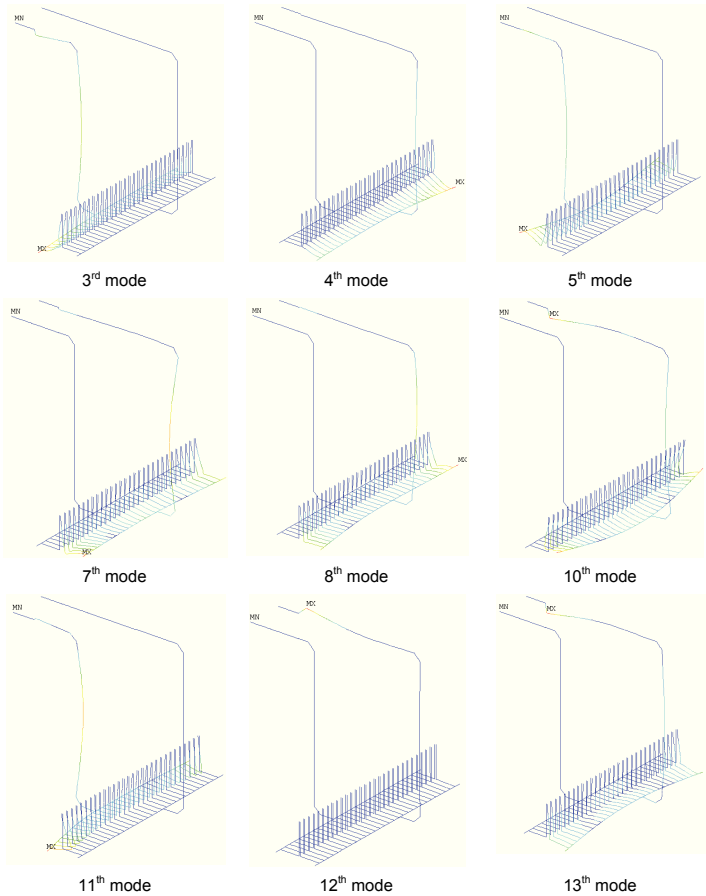
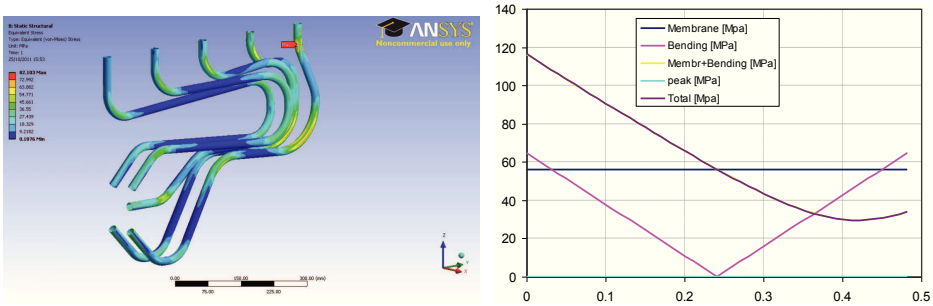


Figure 9.18: Modal analysis, deformed shapes of lowest frequency modes with high mass participation.



(a) (b)

Figure 9.19: Panel expansion joints: (a) Von Mises equivalent stresses and (b) linearized stresses across the tube thickness, at the maximum VM stress.

9.5.5 Draining and drying pressure

If maintenance is required, the component shall be safely removed from the vacuum vessel. Complete drying is required in that case. The cooling channel convolutions inside the wall panels constitute two independent parallel circuits of different length; the blowing out pressure level has to be estimated considering the cooling circuit characteristics.

During blowing out and draining operations, the shorter circuit could be cleared by the gas (nitrogen) flow whereas the longer one could still be filled with coolant("short circuit"). As shown in figure 9.20, the coolant trapped inside the longer circuit will be evacuated only if the pressure difference applied at its opposite boundaries is greater than the pressure given by the coolant column height; inside the NED panels, the latter is (Stevin's law) $p = \rho g h = 1000 \cdot 9.81 \cdot 1.63 = 0.16$ bar; this static pressure must be smaller than the pressure drop for gas flowing across the shorter circuit.

The pressure drop for gas flowing inside the shorter circuit has been estimated considering the channel geometry. The shorter circuit is made by 6 vertical channels, which can be divided into 5 equal U shaped segments. If the pressure drop inside this segment is greater than or equal to 1/5 of the total pressure drop, the minimum configuration for blowing out is considered reached; this verification is carried out considering results from CFD analyses (FLUENT). Analytical estimations are considered for the pressure drop in the rest of the system.

The blowing-out scenarios in table 9.7 have been identified. The operation is possible with a minimum p_{inlet} of about 1.3 bar (absolute).

scenario	$\dot{m}$ [kg/s]	Channel velocity [m/s]	$\Delta p_{to\,tank}$ [bar]	$\Delta p_{manifold}$ [bar]	$\Delta p_{channel}$ [bar]	p_{inlet} [bar]
Low velocity	0.33	27	0.01	0.08	0.2	1.3
Mean velocity	0.41	34	0.016	0.16	0.4	1.6
High velocity	0.65	54	0.04	0.32	0.8	2.2
Very high velocity	0.92	78	0.08	0.56	1.4	3.1

Table 9.7: Nitrogen blowing out parameters for different gas velocity scenarios; $p_{outlet} = 1.02$ bar

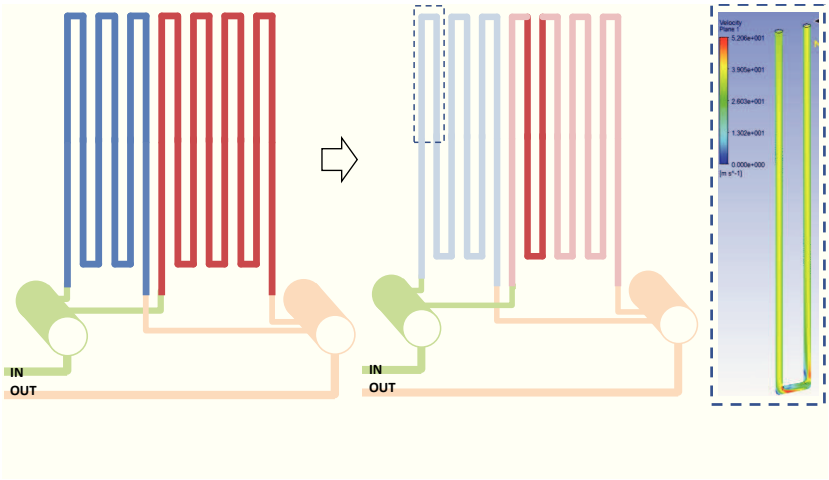


Figure 9.20: Blowing out and draining scheme for parallel cooling circuits of NED panels; the CFD result is shown on the right.

9.6 Support structure

The large dimensions of the NED compel attention in the design of a very massive and wide support structure, mainly made by the side plates, the tie-rods (shown in figure 9.21(a)) and the wall spacers.

An integrated model of the Neutraliser and Electron Dump (NED) structure has been developed in order to carry out verifications for the identified load cases. The verifications of the side plates under various load combinations are presented: they are heated by thermal conduction through the areas interfaced with the spacers that are heated by the wall panels; furthermore, the side plates exchange heat flow by radiation among the NED wall panels, the cryo panels, and the surrounding environment. A considerable attention has been given to the design of the tie-rods that clamp the wall panels and the side plates together; particular analyses had to be carried out in order to perform the verifications, as described in section 9.6.4.

9.6.1 Load cases

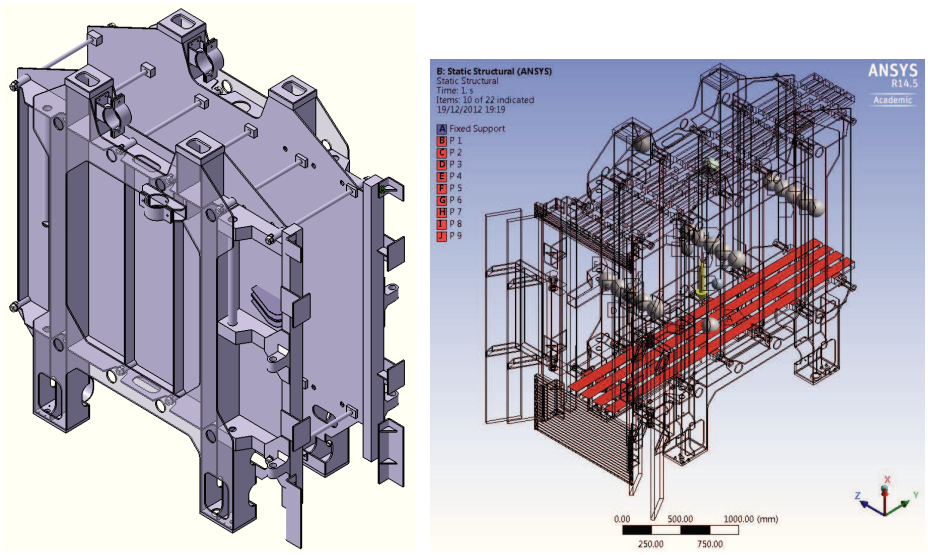
The load cases verified in this section are: **1.1 - Beam operation; 1.2 - Standby trickle flow; 4.1 - Seismic analyses; 5.3 - Bake out; 5.5 - Bed position adjustment**.

9.6.2 Model description

The support structure has been simplified by removing small geometrical features. The elements whose weight is supported by the structure are modelled by masses.

Thermal model

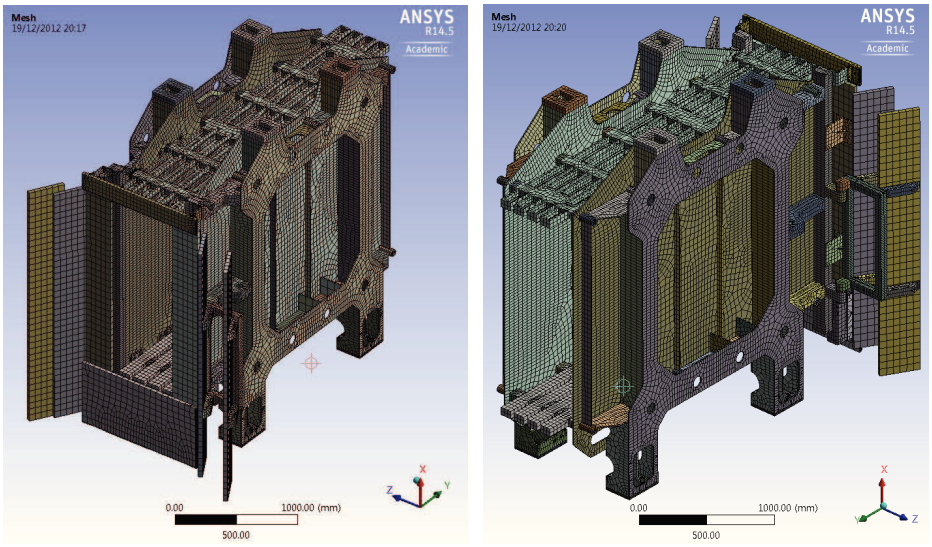
As shown in figure 9.23(a) and (c), the thermal fluxes that have been taken into account consist of:



(a) (b)

Figure 9.21: (a) Model of the support structure, hidden wall spacers and (b) mechanical boundary conditions applied in ANSYS model

a) Conduction with the vessel at fixed temperature of $T_{pad} = 30°C$ towards the four support pads; the vacuum vessel is assumed to be at room temperature, but a slightly higher T_{pad} is chosen in consideration of the thermal



(a) (b)

Figure 9.22: (a) front-top and (b) rear-top view of the meshed model of the support structure

path to the thermal capacity of the vessel, which is assumed to be maintained at room temperature by convection with air;

b) Radiative exchange with the wall panels: the inner face of the side plates are located few centimeters from the side walls, which therefore dominate their radiative exchange. The side wall temperature is assumed $T_{panels} = 100°C$ during beam-on operations and 22 °C (close to the minimum coolant inlet temperature) during beam-off; surface emissivities for copper panels ε_{Cu} and side plates ε_{SS} are set respectively to 0.02 and 0.1, the first being a typical value for copper non-oxidized surfaces (assumed in-vacuum operations only), and the latter being slightly higher than the typical value of smooth stainless-steel surface (< 0.07); in fact, particle deposition could increase the emissivity of this smooth surface.

c) Radiative exchange with the cryopumps: the outer surfaces of the side plates will face the cryopumps, whose external shielding is cooled by cryogenic Nitrogen ($T_{cryo} \sim 87$ K), and in part the internal surfaces of the vacuum vessel (about room temperature). The effective temperature for the environmental radiative exchange is estimated do be -123 °C. with a surface emissivity ε_{CRYO} of about 0.1. The cryopump is made of a backplate aimed at reduction of heat exchange with the background vessel, and triangular shields protecting the charcoal from radiation coming from beam line components. These two protection elements are made of the same material, AISI 304L, with the same surface finishing, and are conditioned at the same temperature during cryopump operations. The surface temperature ranges between 80 and 95 K, with a mean temperature that is expected to be 87 K during beam-on operation and 83 K during beam-off condition. An exhaustive description of the design of the cryopump can be found in [154].

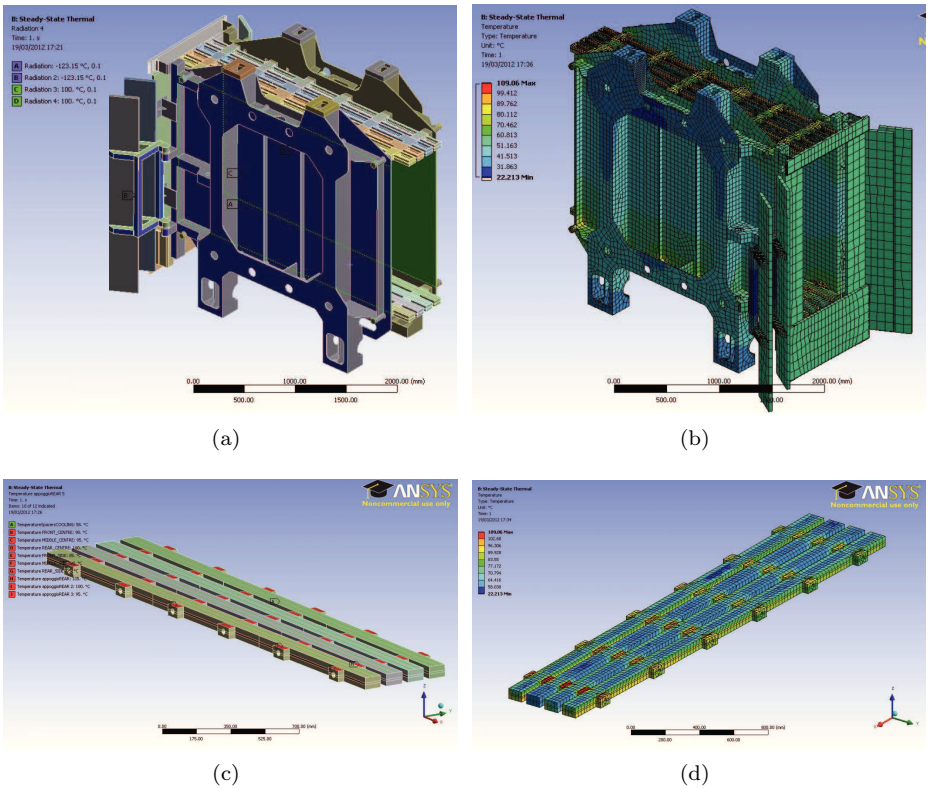
d) Conduction with the panels: the wall spacers are in direct contact with the wall panels, therefore the whole support structure is heated.

Mechanical model

The mechanical boundary constraints applied on the NED pads are shown in figure 9.21(b) and they consist of a fixed constraint on the pads; alternatively the fixed nodes are those at the lifting lugs, if remote handling (RH) operations are considered.

Gravity loads of the NED assembly are primary loads, applied also by using *point masses* of those elements not modeled. The gravity loads are transmitted as friction loads on the side plate by the wall spacers. These friction loads are assured by the pre-load of the tie-rods that apply compression loads to the Neutraliser assembly. The verification regarding this condition is discussed in section 9.6.4.

According to the definition of the load case, the results of the thermal analyses are applied as body temperatures on the mechanical model.



(a) (b)

(c) (d)

Figure 9.23: (a) radiation and (b) fixed temperature boundary conditions; calculated temperature distribution, overall view (c) and detail of the spacers (d).

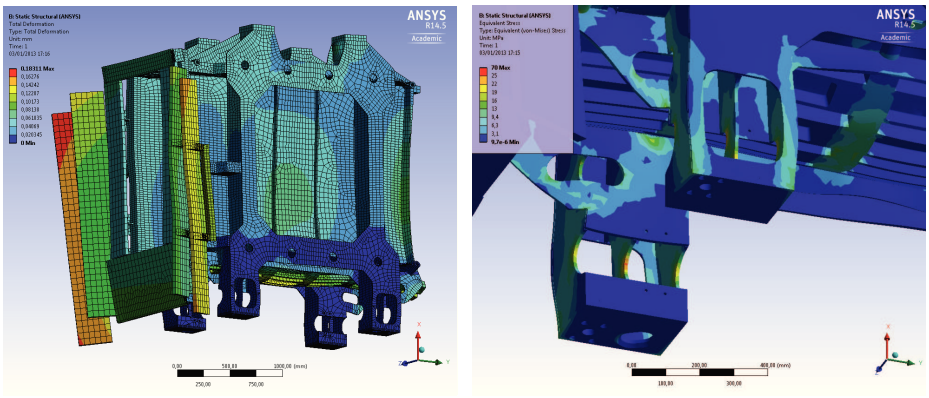
9.6.3 Results for the side plate

Loadcase 1.1 - thermomechanical verifications

The temperature distribution calculated for steady state condition gives a good overview of the NED thermal behaviour (see figure 9.23(b) and (d). The boundary conditions at the contact surfaces between wall spacers and panels and at the spacer cooling channels represent upper limit values, since the coolant temperature is the highest foreseen value (coolant inlet temperature 55°C) and ideal thermal contact is assumed. So, also the calculated thermal expansions are to be considered as maximum expected values. The imposed BCs are listed in table 9.8.

For what concern the primary stresses, a simulation with no thermal load has been carried out. The calculated total displacements are shown in figure 9.24(a). The Von Mises stress concentration at the front pads is shown in figure 9.24(b): the maximum value in this region is about 25 MPa.

The temperature distribution is considered as a body load, to simulate the primary plus secondary stresses. The maximum stress condition occurs at the round housing of the main cooling header; the maximum temperature of this region considering the conditions of load case 1.1 is about 30 °C, so the AISI



(a) (b)

Figure 9.24: Static model: total deformations (a) and Von Mises stress at the front pads (b).

Cooling boundary conditions	
Coolant water temperature:	55 °C
Imposed temperature	
NED pads:	35 °C
Wall spacer cooling channels:	58 °C (accounting for pipe conduction)
Panel vertical supports:	85÷105 °C
Panel lateral contact for centre panels:	90÷100 °C
Panel lateral contact for side panels:	85÷95 °C
Radiation exchange	
Side plate inner surface:	ε=0.1
effective temperature	$T_{inner} = 100$ °C
Side plate external surface:	ε=0.1
effective temperature	$T_{outer} = -123.15$ °C

Table 9.8: Thermal boundary conditions

304L limits are calculated for this temperature.

The linearization of stresses has been carried out in correspondence of the maximum equivalent stress at one pad, and the M-type verifications as for SCD-IC are verified with minimum safety factor 3.

Loadcase 1.1 - Cyclic verifications

Cyclic damage verifications have been carried out for load case 1.1 considering only beam-on/off cycles; indeed NED structures are subjected to mechanical and thermal loadings which will vary periodically during the beam operation. Only beam-on/off cycles could have a thermal impact on the support structure due to the thermal cycles between the load case 1.1 and the load case 1.2; breakdowns cycles are characterized by quick transient events that have no thermal effect on the support structure.

Loadcase 1.2 - Thermomechanical verifications

During standby and trickle flow condition, the cryopumps operate and the coolant continues to flow with reduced mass flow. The temperature of the wall panels is assumed to be room temperature 22 °C.

The minimum temperature of the side plate is found to be 14 °C. No critical regions are identified; the temperature profiles are used as body temperatures for the mechanical model; the M-type verifications as for SCD-IC are carried out on the same path considered before, and are verified with a minimum safety factor of 6.5.

Loadcase 4.1 - Seismic verifications

The seismic verification involves three different types of analyses: static structural to evaluate the prestress condition, modal analysis, and response spectrum analysis. The general purpose of this analysis is to provide a verification of the present NED design considering the seismic action at the ITER site, therefore the acceleration spectra (power spectral density, PSD) are the response spectra of the ITER building at the specific level and location where NBIs are installed.

The seismic analysis is the result of a combination of three types of analysis, where the relationship between these follow a logical order based in the input data and initial conditions for the resolution of differential equations. In this sense, the ANSYS program based in finite element code has been used to carry out the simulations.

The seismic design for the Neutraliser and Electron Dump (NED) is made in agreement with ASME VIII code [138], for the general requirements of Part 5 Design by analysis requirements, and ASCE 7 code [155] for the evaluation of the seismic load case combination. Elastic constitutive behaviour has been considered in the numerical model of the Neutraliser and Electron Dump (NED), in agreement with the ASME Code and ITER SDC-IC [140]. The numerical analyses have assumed the structure to maintain within the elastic field, where the superposition of effects holds, thus allowing the use of a natural frequency analysis and CQC combination as seismic response of the overall structure. Following the ASCE code, the NED structure is considered as non-building structure [155, sec. 15] and the seismic load case is defined by applying spectral analyses in x, y, z direction; in the response spectrum analysis, the equivalent seismic load is calculated using a Complete-Quadratic-Combination (CQC) method. The seismic response E is evaluated [155, sec. 12.4] in accordance with the following expressions:

$$\begin{array}{ll} E_1 = E_x + 0.3E_y + E_z & \text{(full longitudinal effect)} \\ E_2 = 0.3E_x + E_y + E_z & \text{(full transversal effect)} \end{array} \tag{9.13}$$

The safety limit state (SLV) combination represents the safety against the plastic collapse in the ASME design method. The SLV spectral accelerations of the ITER building have been employed [156]. In agreement with the ASCE code, the spectral analyses are expected to include a sufficient number of modes, to obtain a combined modal mass participation of at least 90% of the actual mass in each direction.

The modal analysis is required to characterize the component. A single-point response spectrum (SPRS) analysis has been set in ANSYS in order to

specify one acceleration spectrum curve at the set of all supports identified at the interface between the NED and the Vessel and between the NED and the lifting frame.

Two conditions shall be considered: the NED lays on the four pads fixed onto the Adjustable Bed integral with the vessel, and the NED is lifted during maintenance. Only the results of the former scenario are briefly presented in the following.

Two modes calculated with the modal analyses are shown in figure 9.25(a) and (b), corresponding to the modes involving largest mass respectively along the vertical and longitudinal direction. The two stress fields calculated with the response spectrum analyses of full longitudinal and full transversal effect are shown respectively in figure 9.25(c) and (d), with maximum equivalent (Von Mises) stress localised at the supporting pads. Other peak stress regions are

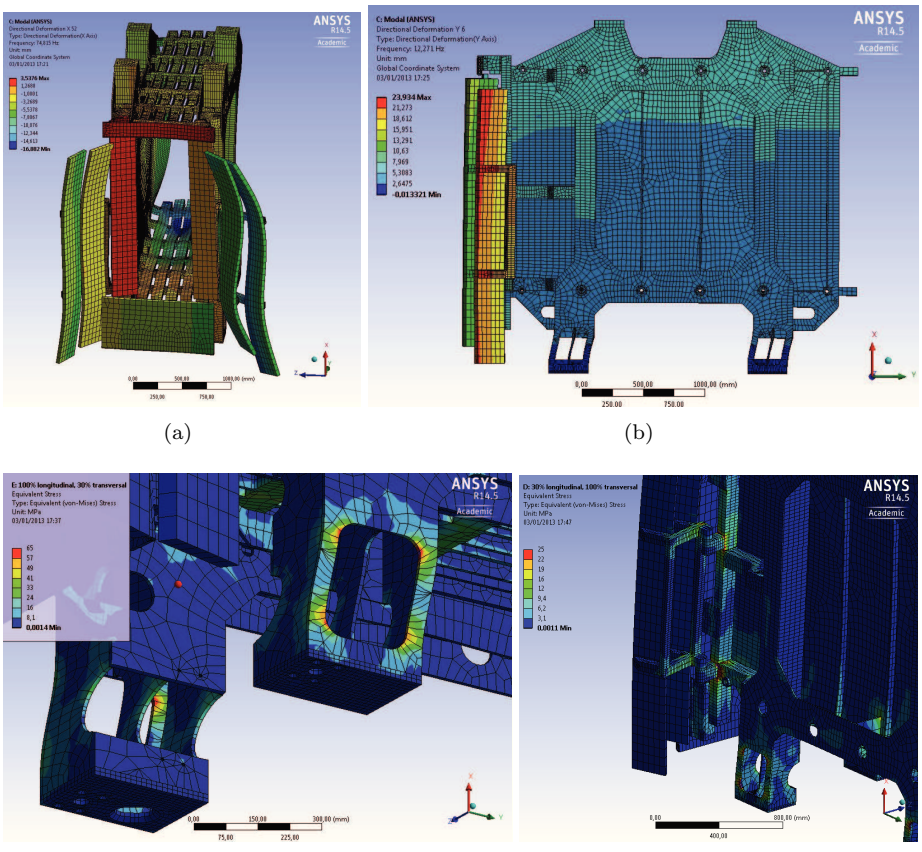


Figure 9.25: (a) deformed shape in vertical direction relevant to mode #52 75 Hz, 35% masses involved (b) deformed shape in longitudinal direction relevant to mode #6 12 Hz, 53% masses involved (c) full longitudinal response spectrum, Von Mises stresses with maximum at 65 MPa at the front pads (d) full transversal response spectrum, Von Mises stresses [MPa] concentration with 25 MPa maximum at the Electron Dump support frame

identified at the interface between Side Plate and Wall Spacers: firstly the Wall Panel supporting areas on Wall Spacers are localised, secondly local peaks at the Side Plate edges are not realist because welding will produce rounded fillet.

The maximum equivalent stress of about 65 MPa is low compared with the maximum allowable stress S_m=115 MPa and with the yield stress of AISI 304L (about 200 MPa) [189], so the mechanical verifications are considered satisfied. The Von Mises peak stress localised at the support for the inlet cooling pipework is not considered significant for damaging of the NED structure because relative displacements occurring between the NED and the cooling pipework are not modelled here and local plasticisation at the support for the inlet cooling pipework will not stress the NED structure.

Loadcase 5.3 - Thermomechanical verifications

The baking procedure determines a volumetric heating on each component up to a temperature of 240°C as specified from ITER requirements [157]. The homogeneity of the volumetric heating and the time taken to reach the heated condition are key issues for differential thermal stresses on the structure: in the case of strong temperature gradients between elements of the supporting structure, thermal stresses could overcome the strength of the materials with permanent distortion. A finite element analysis of the volumetric heating has to be performed on the whole NED structure accurately reproducing the heating conditions.

A free thermal deformation analysis has been carried out in order to quantify the total elongation of the structure as a consequence of the bake out temperature rise. The following thermal elongations have been quantified: the two pads of the side plate separate each other with a displacement of 4 mm considering the closer side of the pads and of 8 mm at the outer side of the pads. This expansion requires free sliding conditions at the supporting pads, and this should be taken into account when the bake-out procedures will be assessed.

Loadcase 5.5 - Bed position adjustment

Adjustment errors could occur during the NED positioning e.g. for wrong selection of shim spacers. This condition is simulated by assuming a maximum difference among the vertical positions of the pad planes of 2 mm, that represents the offset imposed to one pad. All the other mechanical loads are applied as described for load case 1.1; of course no thermal load is considered.

The maximum Von-Mises stress (about 195 MPa) is localized at the round groove housing the main cooling header. The M-type verifications as for SCD-IC are carried out on the same path considered before, and are verified with a minimum safety factor of 1.4.

9.6.4 Results for the tie-rods

The bottom wall spacers form a bed on which the weight of copper panels is applied. These vertical components of forces have to be transmitted by frictional contacts between spacers in order to obtain almost non-deformed supports for panels and to limit shear and bending loads on the tie-rods. It is expected that the four wall spacers will elongate together having almost the same temperature, whereas the relative longitudinal displacement between side plate and wall

spacers will be larger. Plates made of nickel aluminium bronze C63200 can be placed between the side plate and wall spacers in order to permit these expected relative displacements. In addition, slotted holes along the longitudinal direction have been foreseen for the tie-rod housing inside the wall spacers. So at the interface with side plate and wall spacer the vertical components of forces will be, in the wort hypotesis, shear loads on tie-rods.

Load case 1.1 - Tie-rods verification

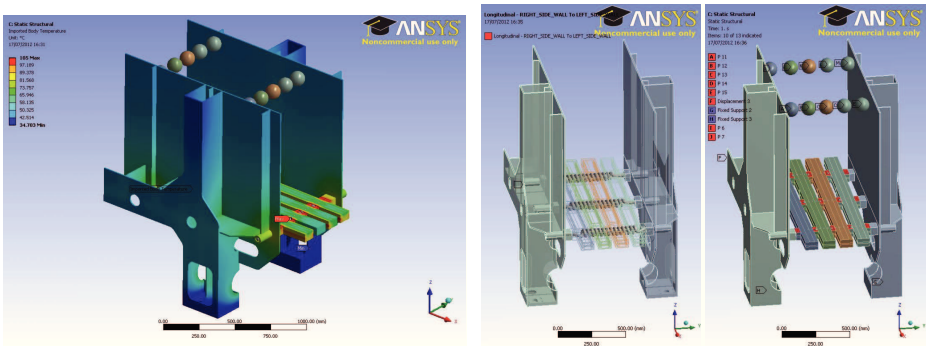
Thermo-mechanical model

Thermal analyses are performed to calculate the maximum temperature the system can reach during beam-on operation. Indeed, boundary conditions at the contact surfaces between wall spacers and panels and at the spacer cooling channels represent an upper limit, since the coolant temperatures considered are the highest acceptable corresponding to 55°C coolant inlet temperature. The calculated results have been compared with the ones obtained from the full size model.

A further thermal analysis has been performed to calculate the maximum temperature the system can reach during beam-on operations (one hour beam-on duration). A transient analysis has been then performed considering the cooling down of the component, starting from the steady state temperature distribution calculated as beam-on condition. The characteristic time of this process has been estimated of about 400 s (less than seven minutes); steady state is reached after 3000 s (50 minutes). The results confirm that, during one hour operation in ideally steady beam-on at maximum power, steady-state thermal conditions are reached. So, the temperature distribution shown in the previous section can be used for verifications.

The max temperature is 110 °C, the minimum temperature 22 °C.

The following analysis has the purpose to identify the conditions that guarantee the tightness of the sandwich-assembled structure against thermal deformation; in other words the tie-rods preload has to keep contact condition



(a) (b)

Figure 9.26: (a) Thermal body loads [°C] and (b) mechanical boundary condition (tie-rods modelled as springs and panels modelled as masses).

between pairs of spaces, so the tie-rod sectional area and the preload have to be suitably assessed.

A reduced model of 1/4 of the Neutraliser has been prepared to verify the contact conditions and forces at (1) the surfaces between spacers and (2) the contact surfaces between side plate and spacers. In the former case, two verifications are needed: (1a) verification for contact condition without detachments between pair of spacers, assuring that panels are vertically supported by the wall spacers; (1b) verification that forces at the spacer interfaces are compatible with the maximum allowable friction force assured by the tie-rod preload;

Different results are obtained using three slightly different models:

- MODEL 1 the diameter of the tie-rods with their axial stiffness;
- MODEL 2 the minimum preload to be applied to the tie-rods;
- MODEL 3 the forces loading the tie-rods.

The general boundary conditions for the 1/4 model are:

- At the cut planes of the quarter model, the following conditions are imposed: symmetry at vertical plane; coupled vertical degrees of freedom at top horizontal plane;
- Fixed supports are imposed at bottom pads.

The maximum allowable preload for a SS M30 screw is 85 kN.

MODEL 1 - FEM model to calculate thermally induced deformations of the wall spacers and sliding forces at the interfaces. Procedure:

1. frictionless, sliding contacts are used; coordinate of some nodes inside tie-rods housing hole, both on the spacer and on the side plate, are coupled together along the vertical direction, in order to be aligned with the same vertical displacements;

2. Absence of gravity in the FEM model; it will be analytically superposed to the thermally induced forces.

3. Tie-rods modelled as springs, their preload in

The forces at the intefaces has been calculated in order to assess the minimum tie-rod preload; results are presented in table 9.9.

MODEL 2 - The minimum tie-rod stiffness, i.e. diameter, and its preload is verified in the following with this procedure:

1. Average tie-rod temperature is assumed; with $\alpha_L = 1.53E-5$ °C$^{-}1$ coefficient of linear thermal expansion, $\Delta L_{thermal} = L_0 \alpha_L \Delta T = 0.57$mm with T'=75 °C; their stiffness is $K_{tie-rod}$ [N/m] = E [N/mm^2] A [mm^2] / L [m];

2. Simulate FEM model with thermal loads, and tie-rods modelled as transversal forces; obtain transversal displacements corresponding to the position of each tie-rod;

3. Calculate reaction force generated by the tie-rods, corresponding to $K \cdot \Delta L_{imposed}$;

Tie-rod #	Interface	$\Delta F_{thermal}$ [kN]	$\Delta F_{gravity}$ [kN]	$\Delta F_{thermal}+$ $\Delta F_{gravity}$ [kN]
1	1-2	0.2	3.0	3.2
	2-3	-0.8	0	-0.8
	3-4	-1.0	-3.0	-4.0
2	1-2	-2.0	2.8	0.8
	2-3	2.9	0	2.9
	3-4	1.0	-2.8	-1.8
3	1-2	6.8	2.8	9.6
	2-3	-0.9	0	-0.9
	3-4	-5.9	-2.8	-8.7
Minimum friction force		7.0	8.2*	9.6
Minimum preload (f=0.35)		20	23.5*	28

Table 9.9: Vertical forces at the interfaces between spacers assuming a friction coefficient f=0.35 (*at the interface with the side plate).

4. Iterate applying the reaction force in the FEM model: convergence is reached if $\Delta L_{imposed}$ does not vary.

In this way the operating condition for the tie-rods is given by the intersection of their stiffness and the stiffness of the rest of the support structure, in particular calculated at the minimum cross section of the the wall spacers. One iteration could be enough, since :

$$\frac{K_{tie-rods}}{K_{spacers}} = \frac{A_{tie-rods}}{A_{spacers}} = 0.07$$

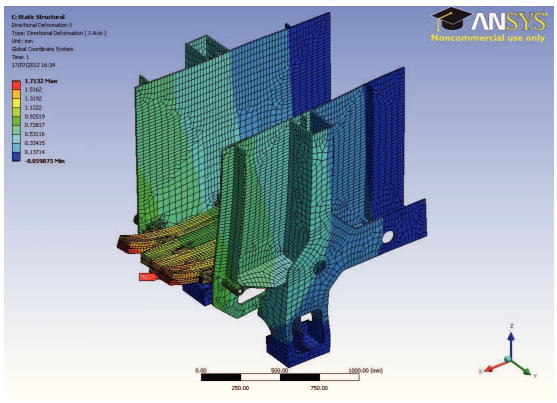
This process has been applied for all the three tie-rods of the quarter model and the results converged to the values summarized in table 9.10. Contact conditions with different preloads are shown in figure 9.27(b). A 30 mm diameter is sufficient.

Tie-rod #	Elongation [mm]	Net tie-rod elongation [mm]	FY (preload + thermal) [kN]
1	0.80	0.23	30+35=65
2	0.80	0.23	30+35=65
3	1.0	0.43	30+65=95

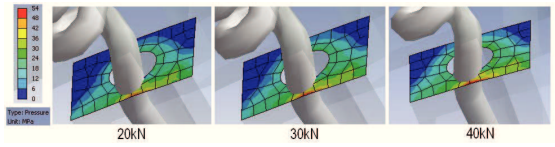
Table 9.10: Transversal forces exerted by tie-rods considering preload and thermal expansion

MODEL 3 - The shear forces acting on the tie-rods and the spacer deformations along the vertical direction (Z axis) are calculated with this procedure.

The four wall spacers will elongate together having almost the same temperature, whereas the relative longitudinal displacement between side plate and wall spacers is about 0.4 mm at the contact surfaces (see figure 9.27(a)). Plates made of nickel aluminium bronze C63200 can be placed between the side plate and wall spacers in order to permit these relative displacements. In addition, slotted holes along the longitudinal direction have been foreseen for the tie-rod housing inside the wall spacers. As calculated before, the wall spacers instead behave as an unique body, as relative sliding does not occur, but this is not



(a)



(b)

Figure 9.27: (a) Longitudinal displacements [mm] along the X axis (30 kN preload, M30) and (b) calculated contact pressure [MPa] at the contact surface between the lateral spacer and the side-plate for various tie-rod preload.

the case of the contact with the side plate. In the FEM, gravity forces are now considered and the contact between the spacers are *bonded*. At the interface between side plate and spacers, the vertical restraining action exterted by tie-rods is simulated by coupling the vertical degree of freedom.

Shear forces obtained from FE modelling by applying thermal and mechanical boundary conditions are compared with analytical calculations considering only gravity contributions in table 9.11. The vertical displacements of the deformed shape are shown in figure 9.27(b).

Tie-rod #		Gravity load	Thermal + Gravity
NED	submodel	[kN]	loads* [kN]
1		8.2	(3.2)
2		8.2	(13.2)
3		7.5	(7.0)
4	1	7.5	7.0
5	2	7.0	12.0
6	3	7.0	2.0

Table 9.11: Shear forces on the tie-rods considering only gravity loads (analytical calculation) and combining thermal deformations and gravity loads (FE modelling); front to rear numbering; *values between brackets have been calculated by using the quarter model thermal forces for the symmetric part of the component

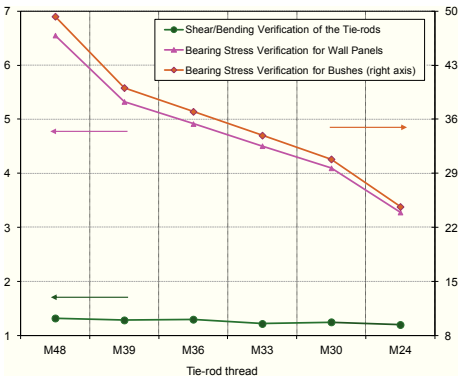


Figure 9.28: Summary for the verifications of the tie-rods; all verifications are satisfied for diameter M30

Load case 1.1 - Tie-rods verification

Each tie rod is made by a cylindrical bar threaded at both ends realizing screws with nominal diameter equal to the rod diameter (i. e. M30 screw for 30 rod). The verification of the tie rods has been carried out satisfying the compliance with different criteria and considering different screw and rod diameters (M24, M30, M33, M36, M39, and M48).

The share verification considers the gravity and thermal loads, and the preload. The verification of the most loaded tie-rod (the N.2), is shown in table 9.12; verifications are satisfied with safety factors indicated.

The bearing stress verification of the bushes has been carried out considering the design force applied on the diametral projection of the rod surface; the correlations used for the verification depend on the ratio between the tie-rod diameter and the height of the shear loaded area.

The bearing stress verification for wall panels has been carried out considering the gravity load of one front panel (the heaviest) applied on a portion of the contact area of one spacer; indeed, the interface area has been reduced in order to account for the effective contact area that will yield possible local plasticization.

The results summary for the considered diameters is represented in figure 9.28. All the verifications are satisfied for the tie-rod diameter M30.

Parameter	Gravity loads		Thermal + gravity loads	
Rod diameter [mm]	30	40	30	40
Thread pre-load [kN]	30	30	30	30
Maximum axial load during beam-on [kN]	65	65	65	65
Design vertical force [kN]	8.2	8.2	13.2	13.2
Rod A_root [mm^2]	596	1107	596	1107
σ_{max} [MPa] (shear stress)	18	10	30	16
σ_{axial} [MPa]	106	106	106	106
$\sigma_{VM,\,shear}$ [MPa] (only shear stress)	32	17	51	28
σ_{VM} [MPa]	111	107	118	110
Safety factor on S_m=147 MPa	1.32	1.36	1.25	1.34

Table 9.12: Shear verification of the most loaded tie-rod (N.2)

10

Thermal diagnostics

The thermal sensors to be installed on the Neutraliser and Electron Dump will be used for different purposes:

a. protect the components from over-temperature;

b. complement the off-vacuum calorimetric measurements by obtaining the thermal power measurement for the cooling circuit of each actively cooled element;

c. quantify the interaction of the particle beam with the exposed surfaces; these thermal measurements will be compared with the ones obtained by other diagnostics like the tomography measurements, complementing the characterisation of some beam parameters e.g. beam source tilting, particle misalignment and steering, power deposition asymmetry.

Only a subset of the NED thermal sensors operating in MITICA will be installed in ITER HNBs after performing experimental operation and identifying the significant measurements for the component protection.

There will be three different kinds of thermal measurements installed on the NED. Calorimetric thermal measurement is an integral indicator of the thermal energy deposition on a component, or in better words, of the heat deposited by the accelerated particles on the region cooled by the specific circuit. Inertial thermal measurement instead is made directly on the heated elements. As boiling detectors, accelerometers are installed to detect vibrations produced by bubble implosion in the subcooled water bulk after reaching nucleate boiling conditions.

The definition of the layout for thermal measurement system of the MITICA NED is presented in this chapter with the analyses that supported its definition. The current configuration and layout are also described distinguishing among the purposes and the characteristics of measurements. A subset of these sensors will be also present on the NED operating in ITER HNBs.

Guidelines and technical solutions for sensor selection, fixing, cabling, and routing inside the vacuum vessel are provided in [197].

10.1 Inertial termocouples

The interaction of the particle beam with the exposed surfaces can be quantified with inertial thermocouples. The component protection from over-temperature is monitored with inertial thermocouples installed on the most heated elements; these thermal measurements are intended mostly for protection against over-heating due to errors in the beam optics for beam horizontal misalignment (hmis) and other sources of power deposition asymmetry. The possibility to characterize the beam properties by inference of thermal measurements is also investigated.

A termocouple array for overheating protection will be installed on the rear edge of the rear wall panels. The maximum power and power density deposition on the NED wall panels occurs at that location in the case of ω_c=7 mrad beam core divergence. In addition, the rear edges of the rear panels are easily accessible for cable routing, sensor installation, and maintenance in MITICA. On the contrary, in the case of limited beam core divergence (ω_c=3 mrad), the most heated panels become the front ones, and the heating is substantially due to the halo fraction of the beam. The power and power densities in this case should be of no harm to the NED.

Termocouples (TCs) will be placed at the inner side of the side wall panels and at both sides of the centre and middle panels, with 8 instrumented wall edges in total. Various parameters are evaluated in the following: many power density analyses have been carried out in order to simulate the effect of different vertical tilting and horizontal misalignment, as reported in section 7.

10.1.1 Dependency on beam source tilting

The analyses investigating the effect of varying the beam source vertical tilting are carried out for 7mrad beam core divergence and 0mrad hmis; the power density (PD) profile along the instrumented, rear edge is plotted in figure 10.1. The displacements of the PD peaks is ±50 mm from the reference position,

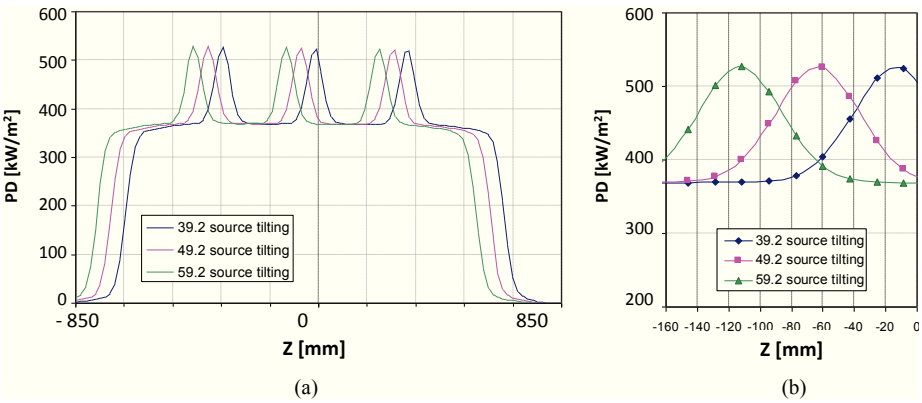


Figure 10.1: (a) power density profiles at the rear edge of the rear wall panels, varying the beam tilting, horiz. misalignment 0 mrad (z=0 at the panel's middle height); (b) close view of the peaks' position.

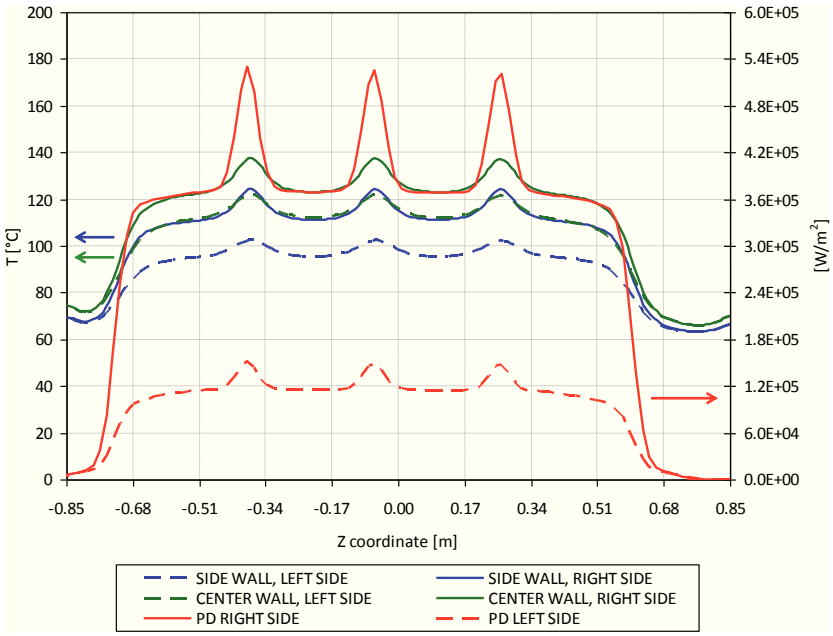


Figure 10.2: Power density and temperature profiles calculated at the rear edge of the rear, centre panel, in the case of 2 mrad horiz. misalignment and 49.2 beam tilting.

which is found to be located at z=-62 mm for the central PD peak. The TC array will be centered on this position.

10.1.2 Dependency on horizontal misalignment

The dependency on horizontal misalignment (hmis), causing an asymmetric interaction with the neutraliser wall panels, is investigated considering not only the power deposition maps but the consequent temperature distribution. The power density profiles presented above are applied to the FE model (see section 9.1) of the rear panels.

The results of both PD and temperature profiles are summarized in figure 10.2. The PD is about three times higher on one side than the other, but the temperature variation due to 2 mrad hmis is 15÷20 °C between different faces of the same panel (or between the same faces of different panels).

10.1.3 Dependency on beam core divergence

The power deposition on the rear panel will change accordingly to the divergence of the beamlet's core. The following analyses have been carried out with 0 mrad hmis and 49.2 mrad beam source vertical tilting. The total power deposition due to H/D beam interaction with the Neutraliser Wall Panels may decrease by more than 35% as a consequence of a reduced beam core divergence ω_c; for instance, in the case of aligned beam, the power decreases from 6MW in the case of ω_c=7 mrad down to 3.7 MW for ω_c=3 mrad. As already stated, the NED rear panels are the most loaded in the case of ω_c=7 mrad but in the case

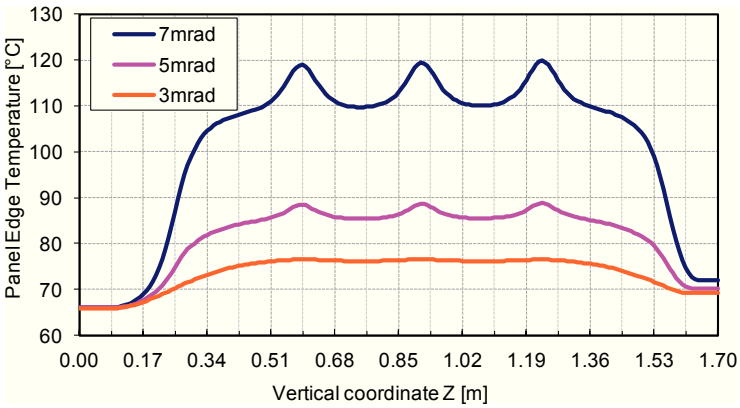


Figure 10.3: Copper panel temperature at the rear edge of the rear panel, hmis=0 mrad.

of limited beam core divergence ω_c=3 mrad, the most heated panels become the front ones, and the heating is substantially due to the halo fraction of the beam (see in particular figure 7.17.

The correlation between the measured temperatures and their variations with the variations in the beam core divergence has been studied. The expected temperatures are plotted in figure 10.3. For what concern the thermocouples positions, the temperature peaks occur at the same positions, even though the peaks are no more measurable in the case of minimum beamlet divergence. Differently, thermocouples positioned at the knees of the profile where the temperature ramps up, could still measure the gradients due to the increase of the beam-wall interaction. This consideration holds also in the case of variable tilting. The minimum temperature ramp-up at the knees of the profile is 15% in the case of minimum beamlet divergence. The temperature profile is obtained assuming the same water temperature (63 °C) at the inlet of the panel cooling circuit, that is the mean water temperature expected in the rear cooling segment in the case of ω_c=7 mrad and 0 mrad hmis.

10.1.4 Identification of PD peak positions

Some consideration drawn from the previous analyses:

a. The power density peak determines a peak of temperature, which can be smooth but detectable. The presented analyses have been performed by assuming constant water temperature and heat transfer coefficient in the vertical cooling channel, and the calculated Copper temperatures of the three peaks are almost the same; in reality, the maximum temperature of top-middle-bottom peaks will slightly differ along the vertical direction for the coolant temperature increase.

b. The temperature distribution along the rear edge changes as the beam source tilting changes, and the inertial TC measurement is able to appreciate a it with different beam core divergences, at the knees of the temperature profile.

c. For hmis smaller than 2 mrad (e.g. 1 mrad), the temperature difference between the panel sides will be smaller, but the vertical position of the peaks will not change.

d. The divergence of each beamlet (in terms of core and halo divergence) determines the power deposition: the maximum value at peaks, and the extension of the hot area, varies with the divergence, but the vertical position does not change.

Assuming the power density shape around maxima is that of a Gaussian distribution, a curve fitting by three segments can be done. The fitting is used to precisely calculate the centre of the hot regions along the panel rear edge. The selection of TC positions is based on the PD profile, which offers enhanced gradients and reduced errors with respect to the temperature profile, calculated with ANSYS. The function used for fitting the power deposition is:

$$f = A + Be^{-\frac{(x-D)^2}{2C^2}} \tag{10.1}$$

Let's consider the case of ω_c=7 mrad. The curve fitting is used to identify the three hot areas, that will be instrumented with 3 TCs each. The temperature variation measured by these TCs is included in the range 90÷140 °C. Rather than in the areas around the PD peaks, the steepest temperature gradient is at the margins, where the beam begin the interaction with the panel and the PD rises from almost 0 up to 350 kW/m^2 and the consequent temperature variation is 40 °C and 50 °C, respectively on the cold face of the panel and on the illuminated one. The temperature increase will be lower at the side panels, about 20÷40 °C, still greater than the Δt$\sim$10 °C that occurs about the PD maxima.

In consideration of this:

- in order to measure the maximum temperature, 9 TCs shall be positioned at Z=260±50 mm, Z=-64±50 mm and Z=-387±50 mm.
- in order to measure the effective source tilting, the most appropriate locations to densely instrument appear to be around Z=595±50 mm and Z=-720±50 mm at the walls' rear edges.

10.1.5 Proposed Layout

The number of TCs that will be used for the protection of MITICA NED can be 112, 72 TCs on the 8 sides of the rear panels and 40 TCs on the 10 sides of the LEEs and Inner Panel of the Lateral Electron Dump; considering that 4 regions of almost constant power density have been identified along the height of the LEEs, 1 TC can be placed in correspondence of each region.

The number of TCs that will be used in the MITICA NED to evaluate the beam source tilting and horizontal misalignment can be 24. In the region of the beam exit section, 24 TCs on both heated sides of the middle wall-rear panels at the top and bottom boundaries of the beam, so 3 top TCs and 3 bottom TCs can be used to measure the beam vertical tilting. This layout will give information for all the beam channels.

The 72+40 TCs for protection can also provide informations about beam horizontal misalignment, together with the 5 calorimetric TCs (see next section) applied on the cooling outlet tubes of LEEs.

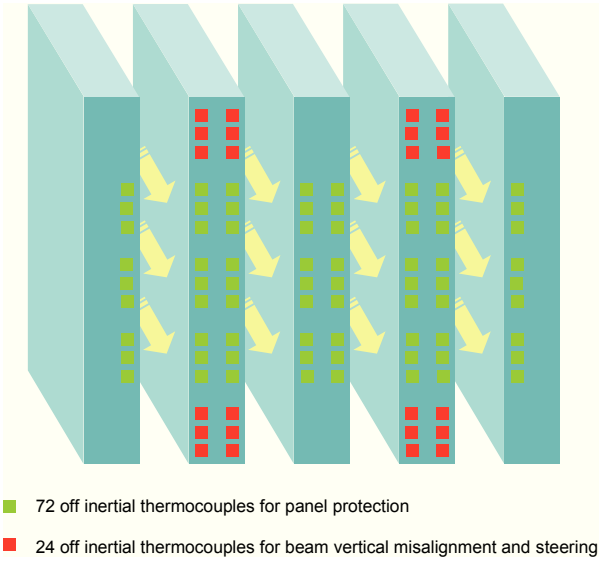


Figure 10.4: Schematic of the thermocouples proposed for the neutraliser panels at the beam exit section.

10.2 Calorimetric thermocouples

Calorimetric thermocouples are proposed to be installed at the outlet of each actively cooled element in order to retrieve thermal power partitioning among the heated components. In fact, the flow rate partitioning among the cooling circuits can be verified by measuring and adjusting the flow rates during factory tests or on-site tests of the component. The following configuration is proposed:

- Panels: two independent parallel cooling circuits will be realized in each Neutraliser panel (double inlet and double outlet are foreseen for each panel). The water temperature measurement will be done at the outlet tube of each cooling circuit in order to provide a calorimetry measurement for thermal power estimation.
- Leading Edge Elements (LEEs): the LEEs will be instrumented with calorimetry TCs positioned at the coolant outlet in order to have measurements for the beam horizontal misalignment.
- Electron Dump (ED): the calorimetric temperatures are the only feasible measurements for the ED panels. Localized heat loads might appear at the particle baffles, but their position can change during the injector operation due to the large deflection of electron trajectories under external electro-magnetic fields. The detection of these heat loads is considered not feasible to be implemented by using local measurements; therefore, only calorimetric TCs will be positioned at the outlet of the cooling tubes of the particle baffles.

The expected temperature range at the exit of the cooling circuits is presented in figure 8.9.

10.2.1 Proposed Layout

The proposed number of calorimetry TCs to be installed for thermal power measurements in the MITICA NED is 53: 30 TCs on the cooling outlet tubes of Wall Panels (5 walls x 3 panels/wall x 2 outlets/panel); 5 TCs on the cooling outlet tubes of LEEs; 8 TCs on the cooling outlet tubes of particle baffles (elements are cooled in series); 8 TCs on the cooling outlet tubes of top and bottom floors (each of the 8 panels will be cooled independently with a U shaped channel); 2 TCs on the main cooling outlet header; this measurement is double for redundancy and it is measured in-vacuum in order to avoid errors due to the thermal conductance of the feedthroughs at the vessel. Ex-vessel measurements are one TC on the main inlet header and one water flow measurement on the main outlet header.

10.3 Boiling detectors

The component protection from over-heating is monitored with boiling sensors installed on the leading edge elements. The boiling sensors for MITICA Beam Line Components will consist of accelerometers. The heat transfer technique in Swirl Tube Elements (STEs) is based on subcooled boiling thermal hydraulics with highest heat transfer coefficient for nucleate boiling conditions. The design of STEs operating in such thermal hydraulic condition, is carried out safeguarding proper margins with respect to experimentally validated formulations that predict the reaching of the critical heat flux and component burnout. In some cases the critical heat flux margin can be low, so the monitoring of the nucleate boiling conditions is needed.

Vibrations transmitted to the structure from the vapour bubble collapsing region can be measured by accelerometers considering that the bubble departure rate that modulates the different bubble pulse mechanisms should be lower than 200 Hz [198], and some additional accelerometers can be positioned on the main feeding cooling manifolds in order to distinguish other sources of vibration and to get better monitoring of boiling.

10.3.1 Proposed Layout

The proposed number of accelerometers to be mounted on the MITICA Neutraliser is 7: 5 accelerometers at the LEEs outlet tube (expected frequency lower than 200 Hz); and 2 additional accelerometers installed on the Neutraliser structure, that will help in distinguishing other sources of vibration.

10.4 Discussion

Two sets of thermocouples are considered for the BLCs operating in MITICA and ITER HNBs: a first group of common thermocouples for ITER HNBs and MITICA, and a second group of additional sensors foreseen only in MITICA. Different cable insulations are proposed for the two sets of thermocouples in order to realise significant cost savings, to guarantee the reliability required in ITER and to verify and compare the cable reliability considering the operation in MITICA and then validate the selected technology for the ITER HNBs:

1. Common thermocouples for ITER HNBs and MITICA for protection: three types of insulation (mineral insulation, Kapton, and Sulzer-type insulation). About the MI, natural cable twisting in the small diameter sheath will limit sufficiently the interferences considering the low magnetic field strength inside the injector. The cables of the common sensors will be grouped together and will terminate on one RH compatible connector.

2. Additional sensors foreseen only in MITICA for beam diagnostics: only Kapton or equivalent organic-vacuum compatible insulation. The cables of the additional sensors foreseen only in MITICA will be grouped in more bundles terminating on LEMO standard connectors.

The two sets of sensors are listed in table 10.1: only protection thermal measurements are foreseen in the NED operating in the ITER HNBs plus the calorimetric measurements at the cooling outlet header where two thermocouples are foreseen for redundancy.

Component	Location	Measurement	ITER HNBs sensor set for protection	MITICA additional sensors
			MI	Kapton insulation
Rear Wall Panels	Rear edge side	Embedded	72	24
Wall Panels	Cooling outlet	Calorimetric	-	30
Electron Dump	Cooling outlet of each panel	Calorimetric	-	8
Inner Panel of the Lateral Electron Dump	Sides	Embedded	8	-
LEEs	Sides	Embedded	32	-
LEEs	Cooling outlet	Calorimetric	5	-
LEEs	Cooling outlet	Vibrations	-	7
Channel floors	Cooling outlet of each panel	Calorimetric	-	8
Cooling outlet header	-	Calorimetric	2	-
Total			119	77

Table 10.1: Summary of thermal sensor layout and characteristics on the Neutraliser and Electron Dump, different configurations for MITICA and ITER HNB

Considering the radiation environment, a mineral-insulated, SS-sheathed thermocouple cable will be used. It is expected that the materials used in these thermocouples can endure, during the entire operational time, neutron fluxes much larger values typical of NB systems. These thermocouples are very robust and currently being installed at JET, but have a delicate manufacturing step in the preparation of the terminations (end of the insulation).

11

The Gas Injection system

The quality of the beam neutralisation depends on the gas parameters and distribution inside the Neutraliser channels delimited by wall panels. The gas injection occurs through nozzles located at the middle panels that are gas fed through the gas feeding lines where the gas is supplied with the proper gas pressure.

Three different injection channels can be used to provide the proper gas target to the nominal negative ion beam inside neutralisation channels. These injection channels are placed at different positions inside the neutraliser panels: 0.5, 0.6, and 0.7 of the panels' length. At each position there is a throughput section, constituted by 5 vertically aligned injection nozzles. The required gas throughputs for deuterium and hydrogen have been correlated to the gas mass flow rate and pressure to be controlled at the interface between the MITICA injector and the Gas Injection System (GIS). The vertical homogeneity of the target thickness has been evaluated elsewhere [127, 50] and [172], but all the evaluations are based on the hypothesis that the same throughput exits from all the injection nozzles. This assumption has been verified in the following.

Also transient events have been analysed, in particular for simulating the abrupt interruption of the gas feeding due to a failure of the last control valve. In this case, the gas shall continue to be injected providing the required gas neutralisation parameters for a minimum time duration: within this time frame the variation of gas pressure/mass flow rate shall be detected and transmitted to the control system in order to interrupt the beam. In fact, a non-neutralised ion beam before will overheat the ERID with possible damage. This can be accomplished thanks to a gas reservoir.

This chapter deals with the following topics:

a. the estimation of the mass flow rate partitioning between the two injection channels, and among the 10 injection nozzles provided at each channel;

b. the estimation of the slot duration that allows to maintain a sufficient high gas flow and throughput after the closure of the last control valve by the use of a gas reservoir.

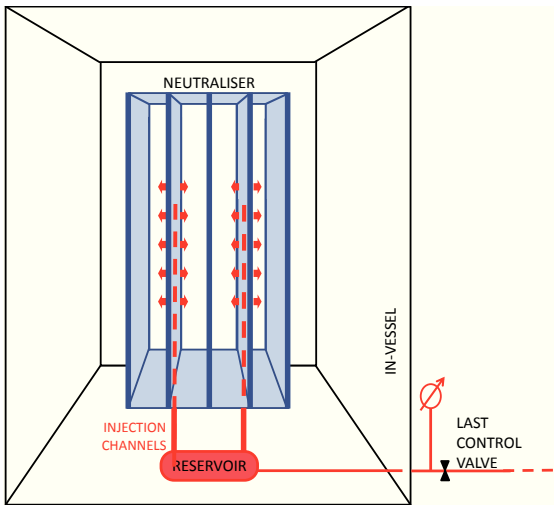


Figure 11.1: Sketch of the gas injection lines considering the contained volume as reservoir that will mitigate the effect of a sudden interruption of the ex-vessel gas supply

The study of the parameters of the gas injection is presented in this chapter, starting from the theoretical basis of gas expansions in vacuum (section 11.2) and the analytical and numerical calculations (see section 11.3). Transient events are analysed in section 11.3.3 in order to simulate a failure at the last control valve considering the gas volume inside feeding lines as reservoir. A possible optimization of the mass flow partitioning among the injection nozzles will also be discussed in section 11.3.2.

11.1 Design description and injection requirements

The quality of the beam neutralisation depends on the gas parameters and distribution inside the Neutraliser channels delimited by wall panels. The gas injection occurs in each beam channel (or gas cell) through 5 nozzles located on each side of the middle panels, totaling 10 nozzle per panel and 20 nozzles feeded in parallel. The middle panels are drilled with injection channel of 18 mm diameter, and the five nozzles are 250 mm vertically spaced.

As stated before, in MITICA there will be 3 gas independent injection sections at 0.5, 0.6 and 0.7 of the Neutraliser length, with 3 gas lines alternatively fed by ex-vessel valves monitored by the control system. One optimum position, confirmed by experiments, will be implemented in ITER NBIs.

A schematic of one gas feeding line is represented in figure 11.1, and the drawings in figure 6.5. The channels of the cooling circuit drilled in the Neutraliser panels had to be carefully arranged in order to be compatible with the three injection channels, and the machining tolerances for the deep-drilling process.

The nominal gas throughputs are 43 Pa m^3/s for hydrogen and 19 Pa m^3/s for deuterium operations: this scenario represents the steady state condition

with neutralization efficiency close to the maximum. The gas flow rate in molecules per second can be calculated from the throughput, if the gas temperature is known, as $\phi = Q/(k_B T)$ and therefore the mass flow rate reads

$$\dot{m} = m \frac{Q}{k_B T} \tag{11.1}$$

being m the mass of a single molecule. The throughputs are defined at room temperature, therefore in table 11.1 the mass flow rates are easily calculated from the nominal throughput for H_2 and D_2 gas. In a gas flow, it is important to choose properly the temperature to be used when calculationg the throughput from the mass flow rate; it must represent both the internal energy but also the kinetic energy associated with the flowing gas fluid, and should therefore be the stagnation temperature.

Gas species	Q [Pa·m^3/s]	T [K]	m [kg]	$\dot{m}$ [kg/s]	$\dot{m}$ per injection channel [kg/s]
Hydrogen Gas (H_2)	43	293	3.38E-27	3.59E-05	1.80E-05
Deuterium Gas (D_2)	19	293	6.75E-27	3.18E-05	1.59E-05

Table 11.1: Total mass flow rate for H_2 and D_2

The beam fraction of positive ions $\Gamma(D^+)$ grows with the gas target thickness and the fraction of negative ions $\Gamma(D^-)$ decreases, and vice-versa. A reduction in terms of gas throughput by 3% causes an increase by 5% in the power deposition on one side of the RID panels due to the D^-, while the same increase caused by the H^- is verified with an increase by 4% [158]. Therefore in the case of failure of the gas control valve a maximum variation by -3% is allowable.

11.2 Flow regions

Three different flow regions can be identified in the overall gas domain of the NBI. A medium-to-high vacuum region is the domain from the cryopumps to the Neutraliser channels, which are by far the main gas source in the system. At the injection nozzles and in the expansion region immediately thereafter, the gas expands in the compressible viscous regime. Upstream in the injection channels and the feeding lines, the flow is incompressible viscous: as a general rule of thumb, if the Mach number is below 0.3, the gas flow can be considered incompressible.

11.2.1 Gas flow in the vacuum

The gas modelling in the vacuum and in the neutraliser channels has been already discussed, in particular in section 5.2.2; additional evaluations can be done, to the purpose of evaluating the evacuation time of the neutralisation channels.

Past calculations [50, App. 3] showed that the life-time of a gas particle injected inside a Neutraliser channel (3 m long) is in the order of 30ms. In AVOCADO, the number of rebounds at solid walls is calculated. By integrating over the two surfaces delimiting the gas cell and dividing by the number of injected particles per beam channel, the average number of times the gas

Parameter	Value
k_B	1.38E-23 J/K
T	293 K
m	6.70E-27 kg
Z_{wall}	6.34E+22
Z_{wall} (2 walls)	1.27E+23
Q	19 Pa m3 s-1
Q per channel	4.75 Pa m^3 s^{-1}
ϕ per channel	1.17E+21 1/s
rebounds Z_{wall}/ϕ	108
average distance per rebound	0.15 m
distance	16 m
v_{RMS}	1346 m/s
t	12 ms

Table 11.2: Physical parameters of the beam

molecules hit the wall is obtained. The average length each molecule covers between consecutive rebounds can be taken as 1.5 times the width of the channel, i.e. 0.15 m. From kinetic theory in a Maxwell-Boltzmann the average RMS velocity at room temperature is:

$$v_{RMS} = \sqrt{\frac{3k_BT}{m}} \tag{11.2}$$

and therefore the time required to exit the gas cell can be estimated. The calculation is shown in Table 11.2: the characteristic time of the process is estimated to be in the order of tens of milliseconds. Compared to other processes in the injection system, this time will be neglected in the transient analyses.

11.2.2 Gas expansion at the injection

As known from fluid-dynamics, the gas flow through an orifice directed into a lower pressure ambient determines a sonic flow and choked velocity condition through the aperture, when the ambient pressure p_{amb} is less than the critical pressure p_c:

$$p_{amb} < p_c = p_0 \left(\frac{\gamma+1}{2}\right)^{\gamma/(1-\gamma)} \tag{11.3}$$

where γ is the specific heat ratio; $p_{amb}/p_0 < 0.528$ in the case of hydrogen, assumed biatomic gas with $\gamma = 1.4$; this means that the gas injection in the beam neutralisation channel always occur in choked conditions. The nozzle of given diameter D and area A will allow a mass flow rate only determined by the upstream pressure p_0 and temperature T_0.

The mass flow rate through an ideal nozzle is slightly different from the mass flow rate expected to flow through a real orifice, since there is no geometry adaptation to the converging flow lines. A *vena contracta* condition typically reduces the actual aperture area, and a coefficient C' (discharge coefficient) is to be applied to the typical equation for a sonic converging nozzle mass flow rate:

$$\dot{m} = C' A p_0 \sqrt{\frac{m}{k_BT}} \sqrt{\gamma \left(\frac{2}{\gamma+1}\right)^{\frac{\gamma+1}{\gamma-1}}} \tag{11.4}$$

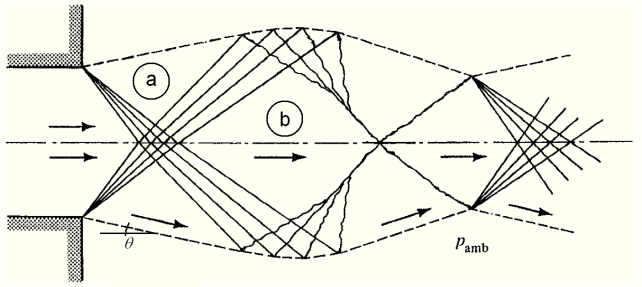


Figure 11.2: Supersonic jet from underexpanded nozzle

Therefore the flow at the injection nozzles determine the throughput and the overall gas flow in the domain.

11.2.3 Gas expansion in the vacuum

This is the case of an underexpanded flow exiting from a nozzle, since the pressure at the injection hole section is higher than the pressure in the beam neutralisation channels. These kinds of flow are constrained by the symmetry axis in the axis of the jet, and by the outer surface in contact with the surrounding ambient, where equilibrium of pressure shall exist.

We may say that the pressure at this boundary is given by the equilibrium between molecules exiting and entering the jet region, and the solution of the molecular flow can give this result in terms of pressure. This is the region (a) in figure 11.2. If we assume a reasonably uniform pressure, this would be in the range of 0.5÷1.0 Pa. Let's consider the equations for a Prandtl-Meyer expansion fan, to give an estimation of the flow parameters.

$$\frac{T_2}{T_1} = \left(\frac{1 + \frac{\gamma-1}{2} M_1^2}{1 + \frac{\gamma-1}{2} M_2^2} \right), \quad \frac{p_2}{p_1} = \left(\frac{1 + \frac{\gamma-1}{2} M_1^2}{1 + \frac{\gamma-1}{2} M_2^2} \right)^{\gamma/(\gamma-1)} \tag{11.5}$$

$$\theta = \nu(M_2) - \nu(M_1), \;\; \nu(M) = \sqrt{\frac{\gamma+1}{\gamma-1}} \cdot \operatorname{atan} \sqrt{\frac{\gamma-1}{\gamma+1}(M^2-1)} - \operatorname{atan} \sqrt{M^2-1} \tag{11.6}$$

If the critical pressure at the nozzle p_c is about 80 Pa, the Mach number shall be about 4 in this region, with a θ angle of about 65°. In the fully expanded region (b) a complete expansion occurs; in this area, the viscous regime is no longer valid. Typically, the wave pattern would cyclically repeat itself. The large velocity difference that exists over the free boundary causes a turbulent shear layer which rather quickly (proportionally to the pressure ratio p_c / p_{amb}) dissipates the wave patterns. In this case, as soon as a molecular flow regime is reached, the pattern could hardly propagate.

These evaluations were carried out assuming continuum fluid equations hold in this region. The following considerations, based on qualitative calculation of the Knudsen number, hold for the various regions: i) at the free jet boundary: $p \geq$1 Pa, M=4, T=70 K, mfp=3 mm (transition flow close to the molecular limit considering the dimension of the nozzle); ii) at the injection hole: $p \geq$75

Pa, M=1, T=250 K, mfp=0.1 mm, Kn=0.03 (viscous flow regime close to the transition flow limit); iii) in the injection channel: $p \geq$200 Pa, T=300 K, Kn=0.003 (viscous flow regime).

11.2.4 Gas flow in the injection channels

The gas flow in the channels is incompressible, since the Mach number $M < 0.3$, and laminar, since $Re = \rho v D/\mu < 2100$, where the dynamic viscosity is calculated with the Sutherland's formula:

$$\mu = \mu_0 \frac{T_0 + C}{T + C} \left(\frac{T}{T_0} \right)^{3/2},$$

For hydrogen gas, the dynamic viscosity at room temperature is $\mu_0 = 8.76 \times 10^{-6}$ Pa s, and C=72 K. The Darcy-Weisbach friction factor for the distributed pressure losses along a duct in laminar flows reads $f = 64/Re$ and the distributed pressure losses are calculated as

$$\Delta p = f \frac{L}{D} \frac{\rho v^2}{2} \tag{11.7}$$

The localised pressure drop for curves or inlets and outlets is

$$\Delta p = k \frac{\rho v^2}{2} \tag{11.8}$$

The gas temperature is assumed constant, and the density is simply calculated at any point as $\rho = pm(k_B T)^{-1}$.

The velocity profile and the consequent Reynolds number and friction factor are calculated. The sound velocity for H_2 and D_2 at room temperature is respectively 1315 m/s and 930 m/s. As presented in the following section 11.3.2, calculated gas velocities are about 0.1 times these velocity and therefore the assumption of incompressible flow is verified.

11.3 Models

Three different models have been developed in order to investigate the gas flow conditions and parameters in each region:

1. The in-vacuum environment has been investigated by using the Avocado model, as already presented in particular in section 5.2.2. The main result that is relevant to the purposes of the present document consists of the evacuation time of the gas cell, to be compared with the timeframe relevant to the maximum allowable reduction of the gas flow due to the closure of the last control valve during beam on operation.

2. The gas injection and the flow through the nozzle is modelled analytically, but to fully characterize the choked flow a CFD model has been developed in FLUENT (in particular to obtain the unknown parameter of the discharge coefficient C').

3. An analytical model has been developed considering the gas flowing through the injection channels and the nozzles. It allows the calculation of the upstream gas parameters. A CFD model of the injection channel (inside the wall panel) is used for comparison with the analytical results.

11.3.1 CFD characterization of the discharge coefficient

The results of analytical models are compared and adjusted considering CFD simulations in FLUENT. Bi-dimensional axis-symmetric and three-dimensional analyses are described in the following.

The axis-symmetric analysis on a high-quality structured grid (see figure 11.3) has been carried out to study the injection and expansion region. The proper dimensions (4 mm aperture diameter, neutraliser channel width ∼100 mm) are considered. The aims of this analysis are to evaluate the expansion parameters and to quantify the discharge coefficient C' to be used in the analytical calculations.

The considered geometry is partially appropriate, because in the 3D geometry the gas gets to the nozzle with transverse velocities. The gas is hydrogen (H_2) in the ideal gas hypothesis; the boundary conditions as illustrated in figure 11.4 are: upstream total pressure (inlet): 600 Pa; downstream pressure (outlet): 3 Pa; no-slip wall in front of the aperture. The mesh is presented in figure 11.3 with a close-up of the mesh at the nozzle.

The velocity distribution are shown in figure 11.4(b). The key result of this simulation is the mass flow rate of the choked nozzle, which is calculated to be 2.72×10^{-6} kg/s. The discharge coefficient C' is found to be 0.58. One should notice that in this axis-symmetric model the inlet gas velocity is parallel to the axis of the nozzle while in the real geometry, with a 90° turn, the vena contracta could determine a smaller effective discharge coefficient.

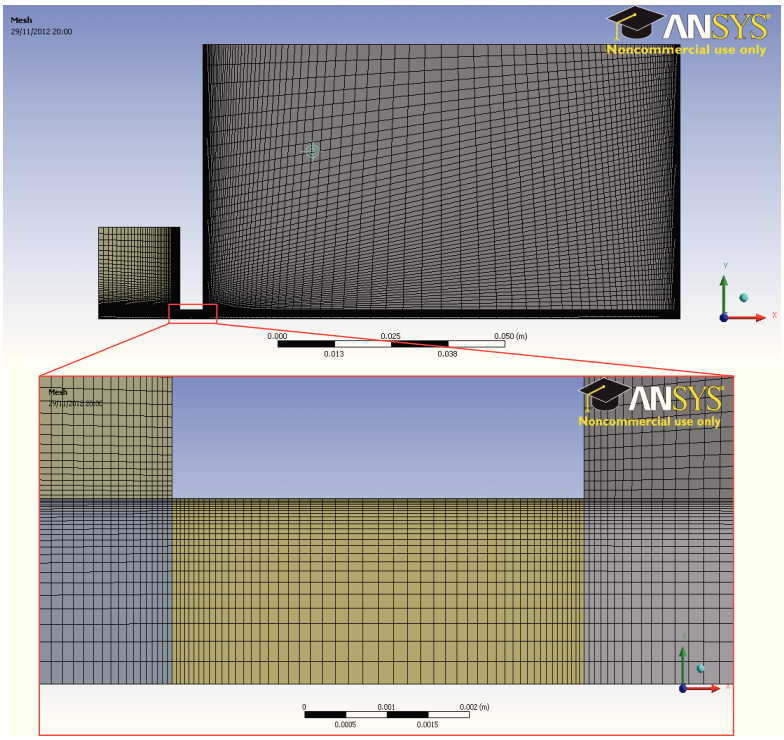
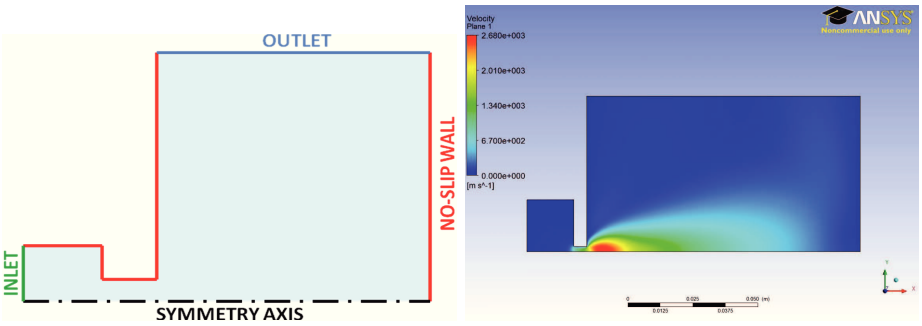


Figure 11.3: Meshed fluid domain.



(a) (b)

Figure 11.4: Sketch of the fluid domain and the boundary conditions (a) and velocity [m/s] distribution (b).

11.3.2 Model of the injection channels and nozzles

The analytical model of the injection channels and the nozzles makes use of the equations and the coefficients defined above. The analytical approach has been used to quickly calculate different configurations. The results for the nominal diameters (4 mm) are presented in the following. The gas flow parameters inside the injection channel are shown in figure 11.7: there are sudden variation in correspondence with the nozzles, because of the net mass flow reduction.

In figure 11.5 the gas throughput normalized to the nominal value is presented; nozzle are numbered from the bottom to the top. The corresponding gas density distribution inside the neutralisation channels is presented in figure 11.6, to evaluate the vertical homogeneity. The results are postprocessed from a dedicated AVOCADO model.

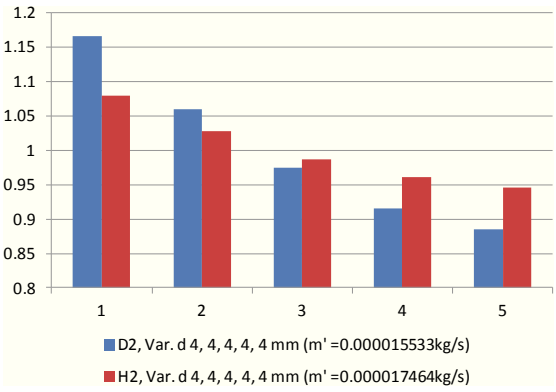


Figure 11.5: Normalized throughput for deuterium and hydrogen at the five injection nozzles, 4mm constant diameter of nozzles.

An optimization of the aperture diameters has been tried; a different optimum operation point is found in the case of hydrogen or deuterium gas. In table 11.4 the maximum difference from the nominal throughput at each nozzle are listed for the considered cases. It has been found that a reduced diameter

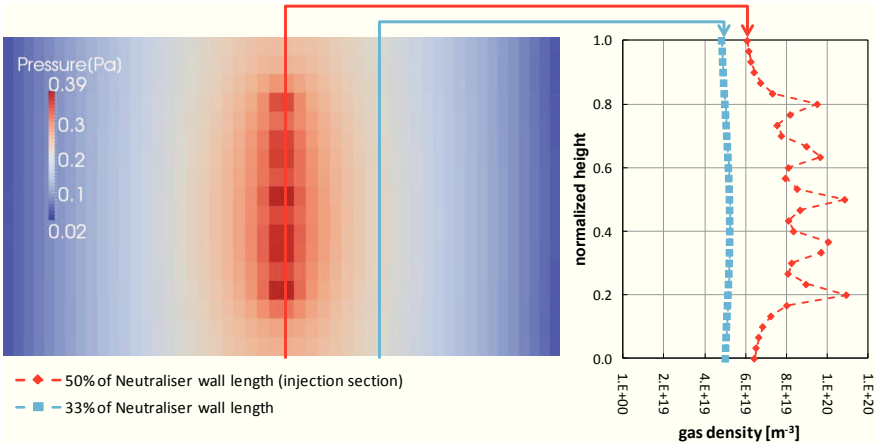


Figure 11.6: Pressure at the Neutraliser wall (left) and corresponding density profiles (right), case: nominal D_2 throughput injected at 0.5 Neutraliser length.

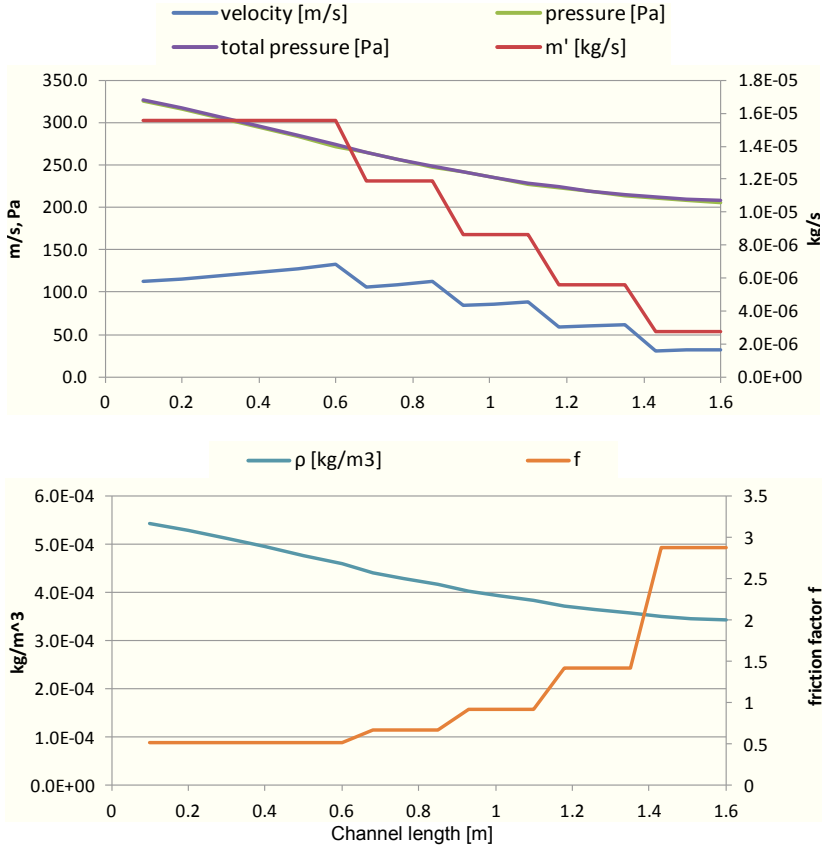


Figure 11.7: Deuterium flow parameters along the injection channel with 4mm constant diameter of nozzles.

would homogenize the flow partitioning.

Gas	D_2	H_2
Nominal diameter (4mm)	16.5%	8%
Optimized diameter for D_2 (3.69,3.87,4.04,4.19,4.27 mm)	0.5%	8%
Optimized diameter for H_2 (3.85,3.94,4.02,4.08,4.12 mm)	8.5%	0.5%
Reduced diameter (2mm)	1.5%	0.5%

Table 11.3: Uniformity of the gas injection among the five injection nozzles. The diameters are listed from the bottom to the top one.

Gas	D_2 [Pa]	H_2 [Pa]
Nominal diameter (4mm)	325	680
Reduced diameter (2mm)	975	2100

Table 11.4: Upstream pressure

The analytical results have been compared to the results calculated with FLUENT of a three-dimensional injection channel in the case of hydrogen. Cylinders have been added to the gas domain downstream the nozzle section: this zone is not meant to fully represent the gas expansion in the beam neutralisation channels, it simply moves the boundary condition away from the significant flow regions. A common downstream pressure, as low as possible, is imposed at the 10 cylindric outlet surfaces. The fluid is compressible hydrogen gas (H_2), ideal gas model in laminar flow. The static pressure at the inlet section is 660 Pa, while the pressure at the outlet was set to 2 Pa; in this way the choked, sonic condition at the nozzles will be verified. The mesh has been refined in particular at the injection nozzles, and it is constituted by 1.3×10^6 elements. The meshed model and the velocity distribution are shown in figure 11.8. A converged solution with residual relative errors below 10^{-5} gives a mass flow rate 30% higher than the analytic calculations. A more significant result would be obtained only with much better meshing and lower residuals.

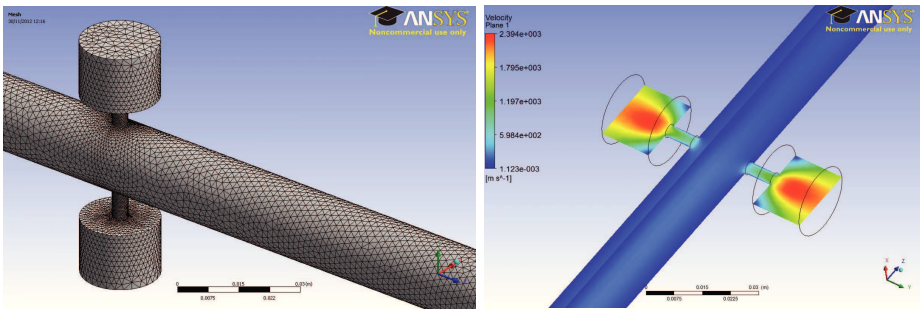


Figure 11.8: Meshed model (left) and velocity module distribution (right)

11.3.3 Model for transient analyses

Having characterized the gas flow through the injection channel and the nozzles allows for a very simple numerically-integrated model of the transient events. The gas properties upstream the injection channels, i.e. the pressure in the gas reservoir, have been characterized also. The deuterium mass contained in the reservoir is reduced by $\dot{m}(t_0)\Delta T$, and the new pressure calculated at the next step determines a different $\dot{m}(t)$ The time steps for the time integration are small with respect to the time interval to be studied.

Generally speaking, the higher is the pressure in the gas reservoir, the longer is the time window before the minimum throughput is reached after the failure of the control valve. As an example, in figure 11.9 the behaviour of the total pressure and the gas throughput as a function of time is presented, for a geometry that has been found to provide more uniform injection and higher pressure in the feedlines, that is injection nozzle diameter of 2 mm. A reservoir volume of 0.1 m^3, compatible with the present design of the NED, is considered.

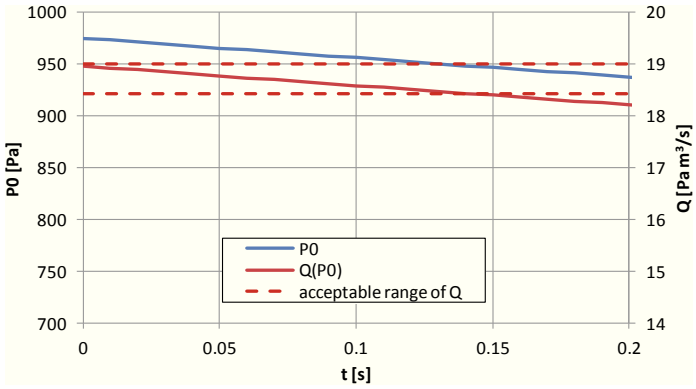


Figure 11.9: Transients of total pressure in the reservoir and total gas throughput after closure of the last control valve, deuterium gas, in the cse of 2mm diameter nozzles and 0.1 m^3 reservoir volume.

11.4 Discussion

The gas domain has been split in three interfaced regions in order to obtain results to be applied as boundary conditions to the contiguous region. Starting from the beam neutralisation cell with molecular flow conditions, the gas expansion at the nozzles has been analysed considering compressible viscous flow. After that, gas parameters have been calculated inside the injection lines considering incompressible viscous flow. The calculations have been done analytically, by simple modelling of the choked nozzles on the basis of well consolidated formulas. The results are supported by CFD simulations.

The mass flow partitioning along the five vertical apertures has been assessed. The non uniformity between the lowest and the uppermost aperture may reach 25% in hydrogen operation with 4mm nozzle diameter. It has been demonstrated that the optimization of the nozzle diameter may improve the vertical homogeneity, but the deuterium and hydrogen operation scenarios are

not fully compatible: if the apertures are optimized for deuterium operation, the non-homogeneity in hydrogen operations would reduce to 15%. The reduction of the nominal diameter down to 2mm is proposed. Two advantages have been identified: (1) the improvement of the gas injection uniformity inside the beam neutralisation channels and (2) the increase of the in-vessel reservoir pressure, which determine a longer timeframe to detect the failure of the last control valve using flow and/or pressure sensors and to interlock the beam power supplies to control the beam interruption scenario.

The gas flow from the injection line volume enclosed downstream the last control valve is considered the first line of defence against too low gas density inside the Neutraliser cell after a failure of such a valve during beam on operation. Different injection line volumes have been considered as reservoirs to simulate the transient event occurring after the closure of the valve.

The main results of these analyses are the estimation of the time window and gas parameters relevant to the maximum allowable reduction of the gas flow (3%) due to the closure of the last control valve. The time constant of the gas cell emptying process has been evaluated to be in the order of tens of microseconds, so it results negligible if compared to the one of the injection lines. The calculated time ranges are (in the case of deuterium gas):

a. 0.04 s with 4 mm injection nozzle diameter and 0.1 m^3 injection lines volume corresponding to the present Neutraliser configuration. During this time range the pressure inside the reservoir varies from 340 Pa down to 330 Pa;

b. 0.15 s with 2 mm injection nozzle diameter and 0.1 m^3 injection lines volume. During this time range the pressure varies inside the reservoir from 975 Pa down to 947 Pa;

c. 0.44 s with 2 mm injection nozzle diameter and considering a possible increase of the injection lines volume up to 0.3 m^3. During this time range the pressure varies inside the reservoir from 975 Pa down to 947 Pa.

At the end of each experimental campaign the gas injection valve will be closed and the gas contained inside the reservoir will be released inside the vessel so increasing the cryopump regeneration frequency. Volumes considered for gas reservoirs (0.10.3m3) are very low if compared with the vessel volume (about $2\times10^2 m^3$), so that the detrimental effect on the cryopump regeneration could be considered negligible; further assessment considering gas flow through the cryopump shall be undertaken.

Part III

SPIDER

12

Thermally induced misalignments and stresses in SPIDER

In today's negative ion sources research it was found that there are optimal temperatures for functional components. The plasma source lateral walls, for instance, shall be kept around 50 °C, while the Plasma Grid shall be maintained around 150 °C, as a trade off between optimum Cesium coverage and good mechanical performance. The acceleration grids, on the contrary, shall be kept at a temperature as low as possible, compatible with the best mechanical performance and minimum deformations in a high heat flux environment.

Generally speaking, the coupling of components that operate at unequal temperatures requires attention. Accommodation of relative elongations may be an issue. Furthermore in the particular case of an electrostatic accelerator, a proper alignment of the grids' apertures shall be maintained within a strict tolerance; for various acceleration voltage, and preferably during all the beam on phases.

The study I performed on the thermal deformations of SPIDER beam source structure is reported in this chapter. A systematic examination of the thermal deformation in time-varying operating condition is performed, as a key issue for both the safety and the performance of the beam source. The peculiarities of the fastening system have to be taken into account if the heat flux is to be estimated. The effects on the aperture misalignment is quantified, and the ceramic insulators with structural function are assessed against these deformations. This activity supported the design of the SPIDER grid frames and its thermal conditioning system.

12.1 SPIDER description

The extraction and acceleration system for the SPIDER ion source is composed of three grids: PG, EG, GG as shown in figure 12.1. A detailed description of SPIDER extractor and accelerator may be found in [40].

The operating temperature, different for each grid, of each grid affects the bulk temperature of the supporting frames: this heating may as well be localized and inhomogeneous in the structure, with a detrimental effect on the alignment between the apertures of two subsequent grids; furthermore the three grid frames at different potentials are connected by ceramic post-insulators, which are fragile components subjected to additional loads due to thermal deformations.

12.1.1 Conceptual description of the Grid Supporting Structure

Three kinds of connection between grid and frame exist, as listed in the following:

- On-plane constraint along Z (beam axis);
- Reference positioning pin, two constraints along X (horizontal) and Y (vertical);
- Vertical positioning pin, Y constraint.

Thermal and electric insulation between grids and frames is realized by means of macor washers. Given the small distances between the support frame and both plasma grid and bias plate, the electric contact could occur bridging through the supporting frame itself, if the thermal deformation overcomes the gaps.

The ceramic post-insulators stand the weight of the extraction and grounded grid assembly, that is about 1300 kg. Their endurance is mandatory. Weibull probability analysis can be used to verify ceramic components, but require the knowledge of some statistic material properties which are affected by certain manufacturing (i.e. thermal loads). For this reason, tests must follow the numerical analysis.

A huge effort was made in the past in order to reduce the deformations of the grids due to heat loads, but the models were based on the assumption that

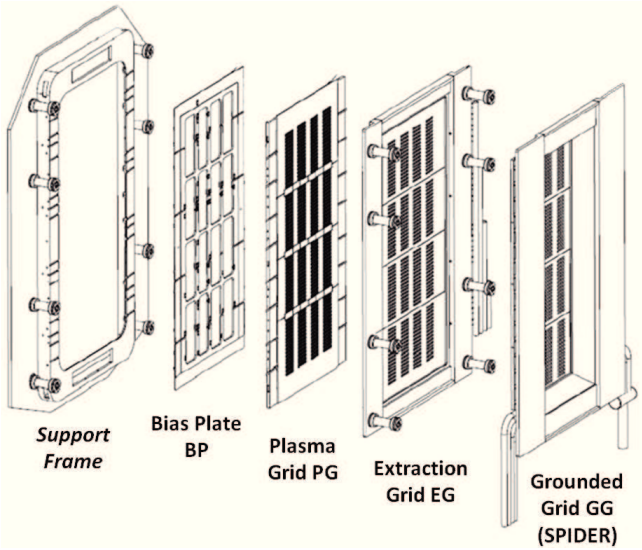
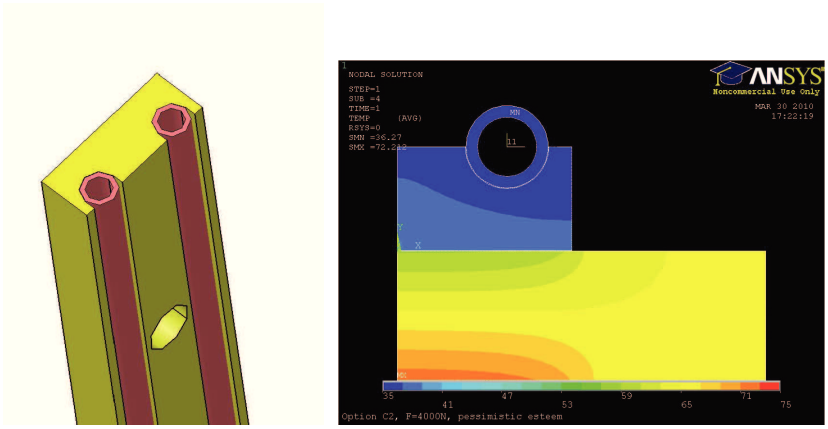


Figure 12.1: SPIDER

the grid was fastened to fixed points. The thermal deformation of the support structure determines a displacement of the fastening points:

- Z direction (grid gaps): The distance along the beam axis in between two consequent grids determines the value of the electric field ($E = -\Delta V/q$): thus, small variations in the distance between grids affect the acceleration of the ions ($F = qE$) and eventually spoil the beam optics. As stated before, there is a linear dependency of the beamlet divergence θ_{rms} on the Z position of the EG grid, and ± 0.2 mm causes a +50% divergence [4];
- Y direction: failure on the alignment may happen as a consequence of deformations along the vertical on-plane direction of the supporting structure;
- X direction: the grid segments are free to expand horizontally, but displacements of the reference positioning pin affect the alignment.

Given the uncertainty on thermal behaviour of the grid supporting structure, the design of a dedicated cooling circuit is required, in the attempt to reduce thermal excursion of the structure by precisely define the temperature in the frames and to allow deformation reduction and control. Two steel pipes brazed to a 27 mm wide copper plate constitutes the SPIDER main frame thermal conditioning system (see figure 12.4(a), bolted to the external frame of the plasma grid; the exact location where to install it has been difficultly determined, since the support frame is heavily drilled (lines of sight for diagnostics). The optimization of this design has been carried out in order to conciliate the need for installing simplicity and thermal effectiveness. In the absence of a dedicated interface inside SPIDER vessel, the coolant has to be derived from another in-vessel hydraulic line: in the present design, the cooling water is taken from the plasma chamber/lateral wall cooling circuit. It is mandatory to clarify whether the requirements of a circuit are always compatibles with the ones of the other or not, in particular in terms of inlet temperature.



(a) (b)

Figure 12.2: (a) design and (b) bi-dimensional thermal model of the Frame Cooling System for SPIDER

12.2 Design requirements

The following design requirements have to be fulfilled:

Safety mechanical requirements on Ceramic insulator that shall withstand both the gravity and operational thermal loads;

Performance Functional requirements for optimum beam generation and transmission, meaning limited and controlled deformations of the support frame.

As a consequence of these requirements, the following design criteria will be considered:

1. Avoiding failure of post insulators, prescribing the properties of the ceramic or by means of proof/qualification tests, and suggesting design modifications;

2. misalignments between apertures shall be limited below the aperture alignment tolerance of ± 0.2 mm;

3. maintain the distance between the plasma and the extraction grid (nominally 6 mm) as steady as possible, because it has a primary effect on the E field and thus on the beam optics; namely, 0.2 mm cause, with a linear behaviour, a beamlet divergence rms of about +50% (see [4]);

4. Prevent direct contact between plasma grid and bias plate, which are prescribed to operate at a slightly different electric potential.

Daily variations during test session, in different initial conditions, shall also be considered.

12.2.1 Operating scenarios and thermal load cycles

The accelerator components undergo a load history of thermal cycles mainly due to beam on/beam off cycles (and breakdown cycles). The duty cycle of beam pulses is expected to be in the ratio 3/4 off, 1/4 on. Considering the thermal path from the grids to the support structure, breakdown events (beam off with durations of about 0.1 sec) are totally negligible.

The temperature of the cooling water at disposal for frame cooling ranges between 20 and 55 °C in PRIMA facility: the maximum temperature is expected in summer, when both SPIDER and MITICA are operating at full power. When one-hour beam operation (worst case) is considered for SPIDER, the temperature of the coolant water is set to 35 °C (average condition). One-hour operation capability shall be demonstrated for SPIDER beam source: this scenario determines the maximum temperatures of the structure.

Element	Dimension
Plate width	27 mm
Plate height	8 mm
Pipe external diameter, dext	6.35 mm
Pipe internal diameter, dint	5.46 mm
Fastening	M5 every 10mm

Table 12.1: Characteristics of the Frame Conditioning System

Grid	Operating temperature [°C] and thermal behaviour of the Grid Segments	thermal behaviour of the Support Frame
PG	Conditioned to 150 °C, negligible ΔT_{water}	Steady state; (τ_c of the frame approx. 2.5 h)
EG	Passive conditioning at grid fastenings: $T_{water,in} = 35$ °C; $T_{water,out} = 55$ °C	Transient to steady state every time the beam is turned on.

Table 12.2: Operating scenario and thermal behaviour of components

The expected temperatures of grid segments are presented in the following table. The characteristic time of grid segments is expected to be negligible compared to the characteristic time τ_c of the support structure (about 2.5 sec. compared to 2 h).

12.3 Thermal Contact Conductance

In vacuum, the thermal Contact Conductance (TCC) h_c is due to the "solid spots" where the surfaces are in touch (h_s), and to radiation at a smaller extent; the contribution due to gas conductance and convection is neglected (h_g). TCC in vacuum depends on the contact pressure, on the material hardness (or at least, on the hardness of the softer material), on the roughness of the surfaces, and on the thermal conductivity of the materials (also temperature at the interface plays a minor role).

TCC is calculated following two procedures, which are in very poor agreement when the solid-spot conductance h_s is considered (a good agreement is found for gas TCC, as h_s becomes less relevant). Taking as example the particular case of Copper/Stainless Steel contacts, following the procedure described in [159, pag.39-43] the following interpolation is found:

$$h_s = (3181 + 3.87T_c) \cdot (0.13309 + p_c) \tag{12.1}$$

where p_c is the pressure and T_c is the average temperature at the interface, respectively expressed in [Pa] and [°C] This result is obtained considering an average roughness and slope at the contact surfaces; one should notice that the TCC is found to be strongly dependent on the latter parameter. Whereas, interpolating the data from [160, 161], a discrepancy up to a factor 8 is found.

The case of Copper-Copper contacts is used as comparison with other data. This procedure gives values 3 to 5 times higher than what is found in [162], where on average the thermal contact conductance between Coppers in Vacuum can be defined roughly as 1×10^4 (W/m^{2}K) at a contact pressure of 1 MPa, or 5 $\times10^4$ (W/m^{2}K) at 10 MPa.

The equipments and techniques used in the experimental measurements strongly influence the results. Considering the variability of the TCC, a sensitivity analysis to verify the dependence of the overall temperature distribution on its value will be carried out; nevertheless, the thermal resistance of the structural elements is such that slight dependence is expected on the TCC at the contacts. A temperature variation below 0.2 °C is found; other assumptions have greater influence on the temperature distribution. The details of this calculation and of the derivation of eq. 12.1 can be found in [199].

12.4 Thermal characterization of the structure

12.4.1 Summary of the analyses

Given the complexity of the system, different kinds of thermal models have been developed to examine the accelerator supporting structure, in order to accurately represent different aspects of the design.

For instance, the use of contacts in FEM requires very detailed geometries and fine mesh. Sub-modeling of small, complex details is a common way to accomplish efficiency in numeric solutions. The number of elements in FE models of the whole SPIDER structure is such that steady-state results are obtainable but transient simulations are not advisable.

The models are strictly correlated between them, and therefore results can be cross-compared as is shown in figure 12.3.

The following models were developed:

1. Thermal contact conductance model;

2. 2D FE models of frame structure;

3. Lumped model for transient analysis in an horizontal section;

4. 3D FE submodels of details of the structure to calculate their equivalent thermal resistance;

5. Global 3D FEM of the support structure - complete of internal and external grid frame and the rigid backbone beams on the back of the plasma source (required to evaluate edge/3D effects of deformations and loads on post-insulators);

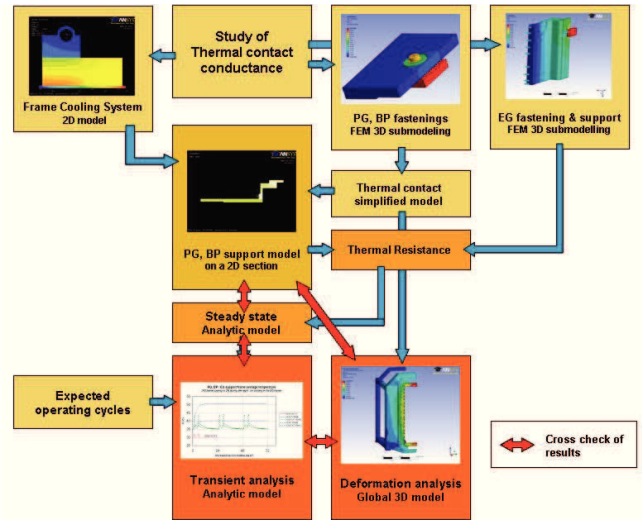
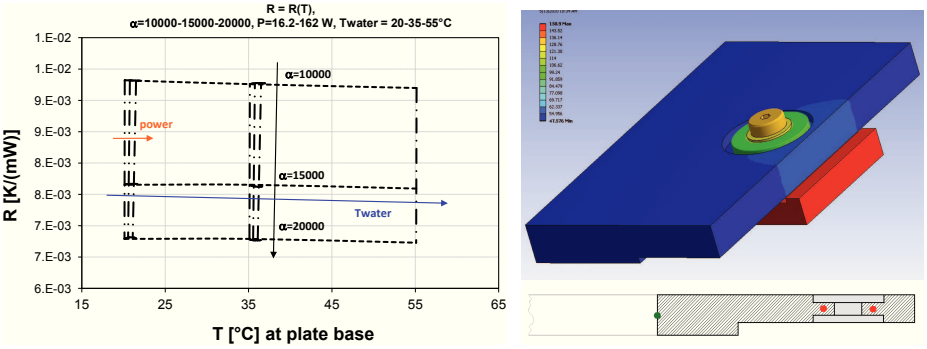


Figure 12.3: Visual summary of the analyses



(a) (b)

Figure 12.4: (a) Linear thermal resistance of the FCS between water and contact with the frame, as a function of the temperature at the copper base plate; (b) 3D sub-model of the PG and BP support fastening.

12.4.2 Frame Conditioning System (2D model)

The FCS conditioning system is composed of two steel pipes brazed to a copper plate. M5 bolts connect the system to the PG external frame, producing an average pressure at the interface of 1.3 MPa. Coolant is water, derived from the lateral wall conditioning circuit of the plasma chamber: its temperature is uncertain and variable, ranging from 20°C to 55°C. The dimensions of the modeled Frame Cooling System are detailed elsewhere [199]. By symmetry, only half of the geometry is modelled.

The following BCs are considered:

- Film coefficient α is calculated analytically (Sieder-Tate formula). Even if its calculated value is about 15000, the heat transfer coefficient α is expected to range between 10000 and 20000 [W m^{-2}K^{-1}];
- Thermal contact conductance in vacuum h_s [W m^{-2}K^{-1}] calculated by means of the following equation:

$$h_c = (6.02e-6 \cdot p_c - 0.318955)T_c + 4.965e-3p_c + 246.475$$

  that interpolates surface property data as described in the previous section; $p_c = 1.3$ MPa, T_c at the interface is obtained by iterating;
- Water temperature: 20, 35, 55 °C;
- The cooling system is coupled to a steel plate; a negative PD is applied to the opposite side of it, on a length corresponding to the width of the copper plate.

The thermal resistance R is very low; it is dominated by α. This means the thermal design of the FCS is adequate; the temperature at the base of the conditioning plate is dominated by the water temperature.

12.4.3 Plasma Grid and Bias Plate fastenings (3D model)

Three dimensional models are used to correctly characterize the fastening geometry and materials. The thermal resistances extrapolated from FEM results,

banally calculated as $R = \Delta T/q$ or $R = \Delta T/(P_D A)$ between two points or surfaces, shall be converted into linear effective resistances in order to be used in bi-dimensional models:

$$R_{linear} = R/L$$

where L is the length of the 3D FE sub-model which is not considered in the 2D model.

The support layout is the same for the Plasma Grid and for the Bias Plate: the contact between frame and grids occurs through three different kinds of fastening. The analysis reported here concern the one realized by means of Macor washers; the other two give negligible contribution of thermal conductance. The pressure on the washers is due to the presence of a Belleville washer.

FEM simulations that use contacts require a fine mesh. Error due to poor mesh quality can be evaluated with a sensitivity analysis; arbitrary refinement of the mesh did not imply notable variation of the effective R with variations within 3%.

The following boundary conditions apply:

- PG/BP homogeneous temperature of 150 °C;
- Negative power density PD at the far edge of the modelled frame portion: the removed heat flow q is computed as $q = P_D \cdot A$, where A is the area of the cross section where the BC is applied;
- Symmetry at side edges (adiabatic surfaces), as the width of the model equals the average distance between two consequent fastening of this kind in the supporting frame.

The effective thermal resistance is computed between the far edge (green dots) and in housing slot (average of red dots, figure 12.4(b)) was considered. The thermal resistance of the fixing assembly (macor washers plus screw) must be obtained subtracting, from the overall resistance of the sub-model, the thermal resistance of the frame.

Being the material properties non-linear but the temperature range small, a plot of R as a function of q, or T_{mean} (as done for the FCS) shows only small variations.

A sensitivity analysis of the uncertainties in the thermal contact conductance is evaluated: R variations range between +5% halving h_s and -4% doubling it with respect to the nominal values h_s, $R*$. If vacuum contact conductance is infinite, $R/R*$=0.92. The thermal insulation capability of the joint depends by less than 10% on the value of h_s. The insulation due to the macor washers is quite good.

In order to have an idea of the insulation quality of this assembly, calculations have been performed using alumina washers instead of macor ones: R drops from 4.27 to 0.65 m K/W, with a remarkable increase of T in the support frames.

12.4.4 Horizontal section of the PG frame (2D model)

A bi-dimensional section on the horizontal middle plane is simulated considering results from the previous sub-model: connections with the PG and BP at the top of the internal frame (on the right), are replaced by a virtual element of equivalent resistance. Thermal resistances at the interfaces are considered also.

The computed thermal resistances R are shown in figure 12.5 for each component.

12.4.5 Extraction Grid fastenings and frames (3D model)

Instead of performing a 3D detail analysis of the fastening and then a 2D analysis of a cross-section, a 3D model of a representative section is used to calculate all the thermal resistances, of three parts of the EG support structure: (1) Fastening, (2) Internal frame, and (3) External frame. Average pressure of interfaces and relative contact conductance are considered. Thermal resistance are converted to linear thermal resistances as already described.

The height of the modeled slice equals a half of the grid segment height; vertical symmetry is valid at the cut section in this geometry. The grid temperature ranges from 35 °C and 50 °C (cooling water exit temperature); in this small interval the thermal behaviour is linear.

The washer spacers are made of a high thermal conductivity material, Aluminium bronze. The role of these elements is to enhance heat transfer between frame and grid. In this way, the active frame temperature control is replaced by a passive thermal conditioning. The material properties are taken from [141]; materials not tabulated there are described in [199, App. A]. A thermal contact conductance of 1730 W/m^2 has been applied to the internal frame/external frame interface.

The following boundary conditions are used:

- an uniform temperature of 50 °C, applied to the portion of the EG that has been modelled;
- a fictitious negative heat flux at the far edge of the frame, with power density PD=-250 W/m^2, with no physical meaning but needed to characterize the heat flux proceeding from the grid: in fact, in a transient analysis the external frame has the largest thermal capacity and absorb the heat flow.

The fastening assembly (the set of bolt, aluminium bronze washers, contact conductance and geometry of the contact) has a thermal resistance that is very low compared to the thermal resistance offered by the internal and external AISI 316 frame.

The linear resistance of the whole assembly is 0.75 Km/W that is very low compared to the one of the PG.

12.5 Transient thermal lumped model of SPIDER beam source

A lumped model which simulate steady-state and transient thermal behaviour of the SPIDER beam source is realized. A set of analyses is needed in or-

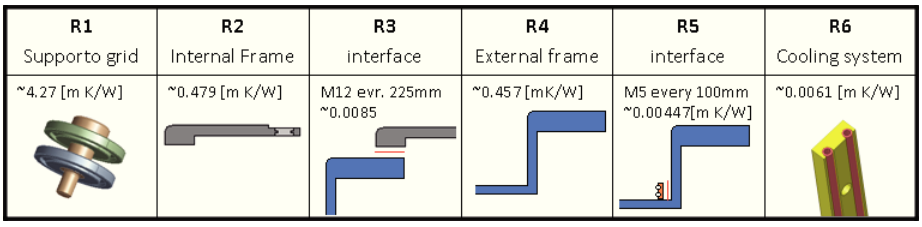
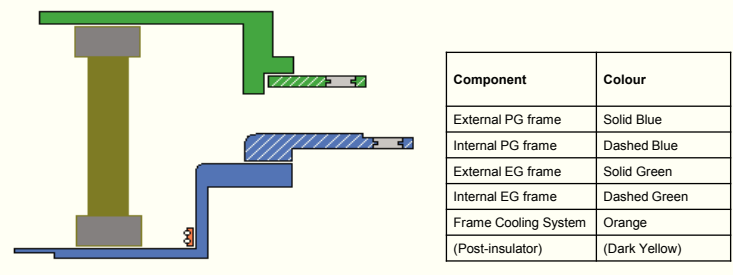


Figure 12.5: Thermal resistances of various components in the horizontal section of SPIDER supporting frames. Note the minimum relevance of interfaces and cooling system.



Component	Colour
External PG frame	Solid Blue
Internal PG frame	Dashed Blue
External EG frame	Solid Green
Internal EG frame	Dashed Green
Frame Cooling System	Orange
(Post-insulator)	(Dark Yellow)

Figure 12.6: Summary of the thermal elements in the considered section and their geometry

der to reduce complex geometries to equivalent thermal resistances, between given points or areas; in this way the accuracy of 3D detailed sub-modeling is conserved in the lumped model. The non-linearities are preserved also, as a relation between thermal resistance and mean temperature of the component can be extrapolated.

The thermal behaviour of the system on time, with alternating boundary conditions (beam on-off), is obtained by analytical computations. Also a preliminary evaluation of thermal elongations at any moment is possible. Results are expected to be accurate, since thermal resistances are obtained from finite element modeling.

The lumped model presented here does not consider radiation, as preliminary computations have been done, and the radiation phenomena are completely negligible.

Transient analyses are quickly solved with this model, and easy to interpret. The lumped model was implemented in MS Visual Basic [163].

12.5.1 Lumped model description

The model performs a simulation of an horizontal cross-section of the support frame, as shown in figure 12.6.

The average temperature of a component is represented by its central node. The node is connected with two equivalent resistances to the nodes nearby, that represent the boundary of the components. Therefore, an element in the simulation is provided with three nodes, a heat capacity, and two thermal resistances R_{sx} and R_{dx} as shown in figure 12.7(a). A thermal contact is an element with no heat capacity.

Such an element can be characterized by calculating the total thermal resistance of the element between two contact points, by FEM calculations; then R_{sx} and R_{dx} are approximately an half.

As the elements are connected one to the other, a finite difference method is constructed as follows. The entering heat fluxes (entering flux: $q > 0$) can be absorbed by the element mass.

$$q_{sx} = \frac{T_{i-1} - T_i}{R_{sx}} = \frac{1}{R_{sx}} T_{i-1} + \frac{-1}{R_{sx}} T_i \tag{12.2}$$

$$q_{dx} = \frac{T_{i+1} - T_i}{R_{dx}} = \frac{1}{R_{dx}} T_{i+1} + \frac{-1}{R_{dx}} T_i \tag{12.3}$$

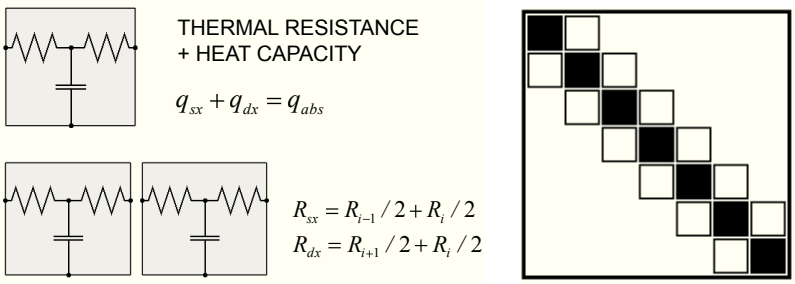


Figure 12.7: Illustration of an element in the simulation (a) and of the B matrix (b)

$$q_{abs} = \frac{c_i \rho_i V_i \Delta T_i}{\Delta t} = \left(-\frac{c_i \rho_i V_i T_{i,OLD}}{\Delta t} \right) + \left(\frac{c_i \rho_i V_i T_i}{\Delta t} \right) \tag{12.4}$$

The heat balance reads

$$\left(\frac{c_i \rho_i V_i T_{i,OLD}}{\Delta t} \right) + \left(-\frac{c_i \rho_i V_i}{\Delta t} - \frac{1}{R_{sx}} - \frac{1}{R_{dx}} \right) T_i + \left(\frac{1}{R_{dx}} \right) T_{i+1} + \left(\frac{1}{R_{sx}} \right) T_{i-1} = 0 \tag{12.5}$$

In the case a nearby node is at a boundary, either the term T_{i+1} or T_{i-1} will be a constant term.

The left terms are a constant term at time t, so the system of element equations can be written as a SISO (single-input single-output) system (figure 12.7(b)):

$$[A] + [B][T] = [0] \tag{12.6}$$

$$\begin{aligned} A_0 &= \frac{c_i \rho_i V_i}{\Delta t} T_{i,OLD} + \left\{ \frac{1}{R_i/2} T_{BC,sx} \right\} \\ A_i &= \frac{c_i \rho_i V_i}{\Delta t} T_{i,OLD} \\ A_{i,max} &= \frac{c_i \rho_i V_i}{\Delta t} T_{i,OLD} + \left\{ \frac{1}{R_i/2} T_{BC,dx} \right\} \end{aligned} \tag{12.7}$$

$$\begin{aligned} &B_{i,i} = -\frac{c_i \rho_i V_i}{\Delta t} T_{i,OLD} - \frac{1}{R_{sx}} - \frac{1}{R_{dx}} \\ &\text{if } i < i_{max},\ B_{i,i+1} = \frac{1}{R_{dx}} \\ &\text{if } i > 0,\ B_{i,i-1} = \frac{1}{R_{sx}} \end{aligned} \tag{12.8}$$

The system is solved using biCGstab algorithm (already discussed in section 3.3.4).

12.5.2 Imposed operating conditions

The calculated operating profiles of an ideal scenario, of one-hour beam-on followed by 3 hours beam standby.

The geometry on the horizontal section of the supporting frame is shown in figure 12.6, where also a brief recap of the thermal elements is presented. The color scheme is maintained in the results shown in figure 12.8.

The considered operating profile, boundary conditions and element properties are the following:

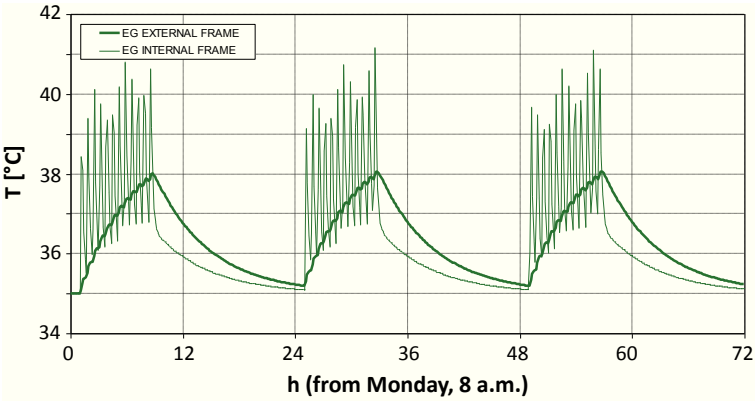
- duty cycle 1/4; most critical profile is 1h ON, 3h OFF;
- frame coolant temperature $T_{in,water} = 35$ °C (constancy and homogeneity of this value is an open issue);
- characteristic time of the grids τ_c ∼few seconds (less than 2.5 sec, instantaneous process compared to frames);
- PG, BP conditioning: $T_{in} = 150$ °C ($\sim T_{out}$) controlled and constant (4/4 cycle); $\rightarrow T_{PG} = 150$ °C (fixed);
- EG conditioning:
  - BEAM OFF: $T_{in} = 35$ °C, $T_{out} = 35$ °C $\rightarrow T_EG = 35$°C,
  - BEAM ON: $T_{in} = 35$ °C, $T_{out} = 51$ °C $\rightarrow T_EG = 53$°C.
- Thermal resistance of components.

12.5.3 Daily-based thermal behaviour

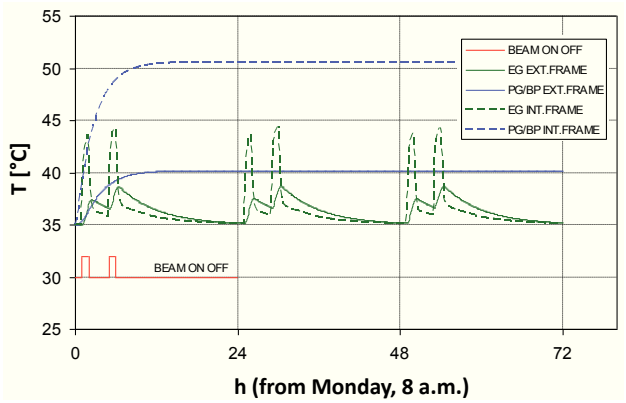
The characteristic time of frames has been calculated. The temperature profiles during a 3 days test session have been calculated in two scenarios.

Figure 12.8 shows the temperature profile during 3 days of test, in the most onerous case (1h on, 3h off). The temperatures of the PG frame are shown in this figure: the PG frames (dashed blue line internal, solid blue line external frame) starting from the uniform temperature of T_{ini}=35 °C, reach a steady state condition in about 12h, with a τ_c of about 2.75 h. The EG frames instead, being passively conditioned by the EG cooling circuit, undergoes a rapid increase of temperature during beam operation. The dashed green line is the calculated mean temperatures of the internal EG frame (with τ_c slightly shorter than PG frame). In 15 min, the frame temperature increase is 63% of the one-hour ΔT (about 10 °C). Also the external EG frame temperature (solid green line) slowly increase of a few degrees.

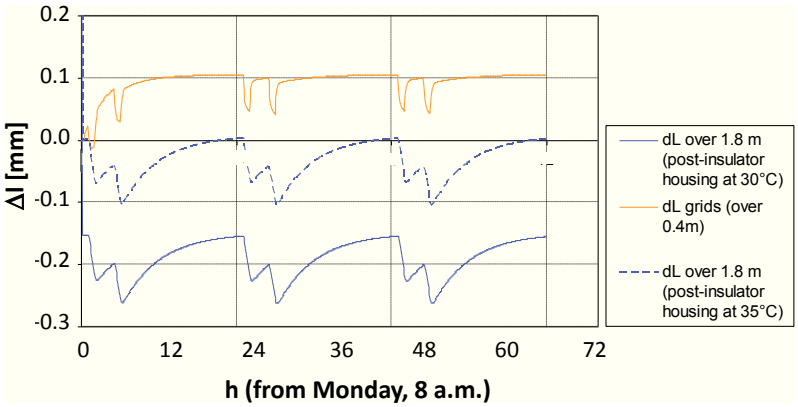
In Figure 4 -22, the mean temperatures of the internal and external EG frame are shown for a 10 minutes beam on / 30 minutes beam off scenario. Basically, there is no difference in the average temperatures at the end of a day if we compare this case to the other, since the amount of heat collected by the frames is the same. Thermal elongation during beam operation, corrected with relative displacements and with two possible boundary condition (temperature at housing slots of post-insulators), seems to have a positive effect on the alignment of beamlet apertures (see Figure 4 -24). Please note that the calculated EG frame elongations are not symmetric (at cooling entrance side, T remains constant). Relative displacement of post-insulator slots vertical position worsens during beam operation. From comparison with 3D FEM results, elongation errors turn out to be about 12% (position of ceramic slots) and 5% (position of grid precision pins).



(a)



(b)



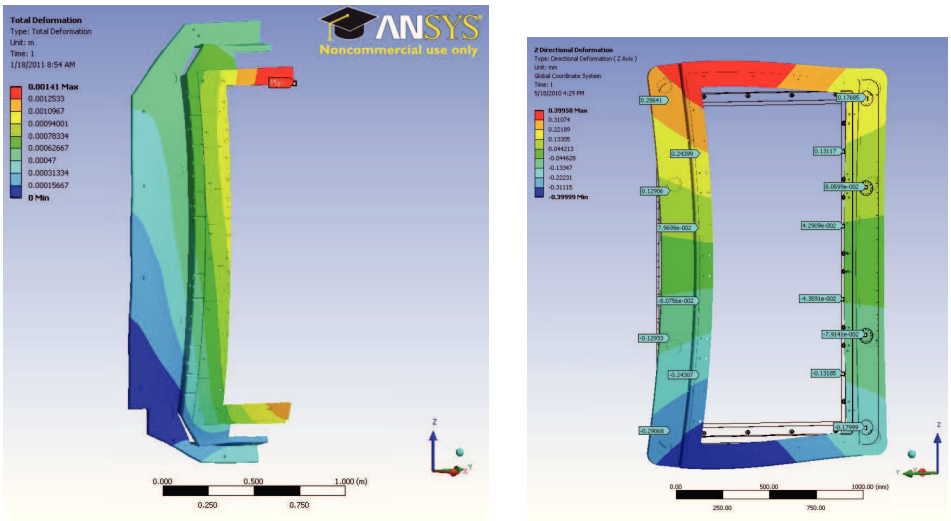
(c)

Figure 12.8: (a) Transient analysis, profile of temperature of the external and internal EG frame in a 3 days, 8 hours per day, 10 min On / 30 min Off cycle; (b) transient analysis, profile of temperature of various components. Areas filled with solid colour in Figure 4 -21 correspond to solid lines, whereas dashed areas in Figure 4 -21 correspond to dashed lines; (c) transient analysis, expected elongation of various components in the case of Figure 4 -23.

In order to reduce thermal excursion and elongation of the EG supports, the possibility of applying an active conditioning to these frames has been considered. Unluckily, a cooling system similar to the one used for the PG frame can be installed only at the external edge of the external frame, in a region far away from where the heat flux is applied. A simulation was carried out and the active cooling resulted useless if set there.

12.6 Analysis of SPIDER structure deformations

It is possible to evaluate three dimensional deformations and edge-effects only by means of a global, finite element, thermo-mechanical model. At first, the thermal deformation of the supporting structures of the Plasma Grid and the Extraction Grid was studied independently, as shown in figure 12.9. The deformations are such that an integrated model, which consider the ceramic elements connecting the frames, is mandatory.



(a) (b)

Figure 12.9: (a) deformation of the internal and external PG frames; (b) Asymmetric deformation of the external and internal EG frames during beam operations (water temperature rises from 35 to 50°C). Deformations are amplified.

The number of elements will be large and the simulation computational costly. Only steady-state analyses will be performed, and the correct boundary conditions will be provided by FE sub-models or by results from the transient lumped model.

Hypothesis:

- Horizontal symmetry on the central vertical plane: this hypothesis is used even though the temperature of the EG is not symmetric;
- The rigid structure behind the main support frame inexorably reach a uniform temperature, which - more or less - corresponds to the temperature of the coolant;

- Four fixed supports uphold the aforementioned structure from the bottom.
- A notable amount of thermal sinks or thermal capacities linked to the main structure is neglected;
- the contact pressure due to bolts is uniformly distributed at the interfaces;

The geometry of the structure is imported from CAD models, where small geometrical features are neglected thus reducing complexity.

12.6.1 Boundary conditions and use of sub-model

Frame Cooling System

The most important results from dedicated analyses are:

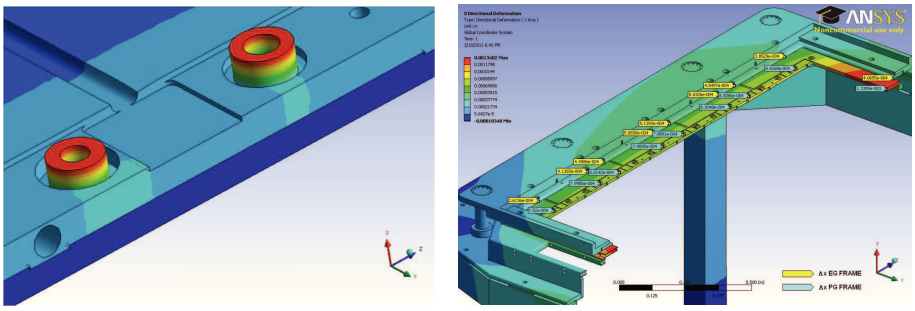
- Temperature at the foot of the cooling system T_{base} is basically uniform and almost completely depends on the coolant temperature T_w.
- Thermal resistance of the component only depends on film coefficient α, and anyhow is not prominent in the system.

On these bases, a very simple boundary condition on temperature is applied directly to two parallel lines on the frame, respectively 35.8 and 35 °C at the inner and outer lines.

Grid fastening sub-modelling

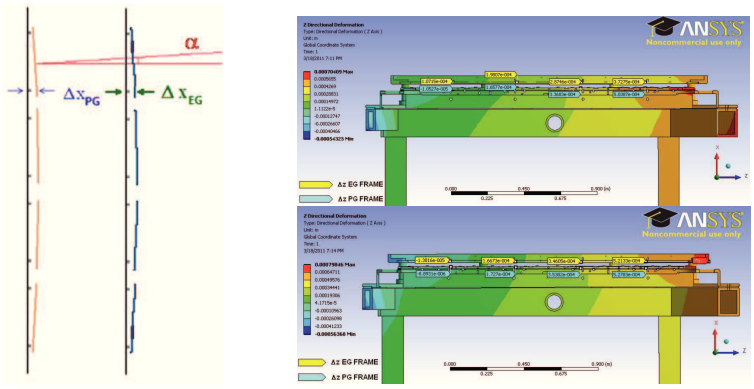
The complex joint is replaced with a tube-shape element of equivalent thermal resistance R [k/W], with height h [m] and cross-section area A [m]. Slot holes on the frame for BP and PG support have different diameter; thus in order to have the same conduction section and use the same fictitious material properties, external diameter is properly calculated. Equivalent linear thermal conductivity λ [W/m K] is calculated as:

$$\lambda = \frac{1}{R}\frac{h}{A} \tag{12.9}$$



(a) (b)

Figure 12.10: (a) Temperature distribution at two virtual elements, replacing in the global model the complex assembly of grid support; the PG/BP is at 150 °C (red) while the bulk of the support frame is below 40 °C (blue contour) and (b) horizontal (out-of-plane) displacements calculated for case A



(a) (b)

Figure 12.11: (a) sketch of grid rotations, as induced by out-of-plane deformations and (b) vertical displacements in cases A and B.

12.6.2 Global integrated model

The need for a precise estimation of relative deformations of PG and EG frames leads to the development of a global model, in which PG and EG supports are coupled together. Only a vertical half of the geometry is modeled. The aim of this simulation is to quantify - and possibly find solutions to heal - the misalignments of the grid apertures, and the forces acting on post-insulators:

A) **Nominal position** alignment is required at the starting up of the beam: the starting temperature will always be different from the reference temperature (22 °C) at which the nominal dimensions are defined. In that condition, horizontal symmetry exists of the structure and its tempearture distribution ($T_EG = 35$ °C).

B) **Forces acting on post insulators** the maximum thermally induced forces are those expected after one hour of beam operation: in that condition, horizontal symmetry does not hold anymore. Loads calculated considering the temperature at the "hot side" are considered ($T_EG = 55$ °C).

Fixed supports are placed at the feet of the main chassis. Mechanical loads estimated at the bounds of post-insulators are used for a successive submodelling. Their material properties, in terms of young modulus and thermal conductivity are the same of average alumina.

The gaps between grid segments of the PG and EG are reduced by 0.5 mm over 6 mm of initial gap. Basically, there is only a small difference in the out of plane deformation in case A and B. The base of the post-insulators moves of about 0.3-0.4 mm.

There is a vertical misalignment between the grids Δz at beam off that progressively reduces as the EG frame heats up. After one hour of operation, when the temperatures in the EG frame are higher, the alignment between PG and EG changes: in figure 12.11(b) at the bottom, the colour contours that represent the vertical displacement are nearly the same in the PG and the EG frame.

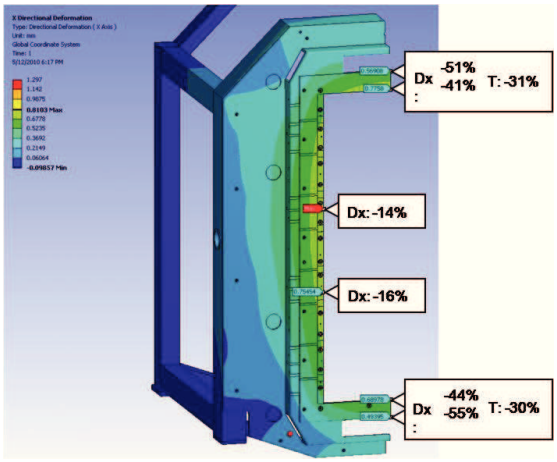


Figure 12.12: Improvements obtainable with the new design (option n.1). Option n.2 determines an additional improvement of 2-3%. Maximum out of plane displacement reduces from 1.3 to 0.8 mm.

This variation of the vertical alignment occurs only at the hot side of the EG frame (maximum temperature 51 °C), that is, the side where the water exits the cooling circuit of the grid segments. At the cold side of the EG frame, the vertical displacements do not vary during beam operation as the BCs do not change.

Prescription of a mechanical offsets for the calibrated pins, reduction of the peak temperatures, stiffening the structure and the use of calibrated washer spacers are some of the solution that have been taken into account to reduce positioning errors due to thermal deformations. Design modifications have been proposed, and the obtainable improvements have been quantified and are shown in figure 12.12.

Vertical displacement of ceramic post-insulators	Vertical displacement of grid reference pins	Out-of-plane deformations: grid gaps reduction	Mechanical forces at the post-insulator interface (the one at the top)
wrt the middle of the frame: +0,2 +0,1 -0,1 -0,2 [mm]	wrt the centre: PG EG 0.27 0.13 0.04 0.04 -0.04 -0.04 -0.27 -0.13 [mm] [mm]	1 mm * 0.5 mm 1 mm * *no spacers for PG here	F (N) M (N mm) X 879 235460 +500 Y -2673 76358 Z 576 100260 -1550 Thermal loads Gravity Loads

Table 12.3: Summary of displacement results for the PG and EG frame - load case (a) - and forces acting on the post-insulators - load case (b).

As listed in table 12.3, the following results were obtained:

- A mechanical offset has been defined for the PG, EG reference pins on the support frame, in order to correct the displacement due to thermal deformation during operation. It has been calculated as $Z_{design} = Z_{nominal} - \Delta Z_{thermal}$. The chosen $\Delta Z_{thermal}$ is the one calculated for beam off configuration (load case a). New dimensions are implemented in CAD drawings;
- Out-of-plane deformations were quantified. Simple design modifications have been proposed, in order to lower the maximum temperature and enhancing the stiffness of the most displaced parts;
- Force and momentum acting on each post-insulator in loadcase B.

12.7 Post-insulator probability of failure analysis

The structural analysis of the post-insulators has been carried out in ANSYS. The post-insulators have the fundamental function of structural support and electric insulation. They are subjected to forces and momentum at the interface with the Grid Frames. The probability of failure analysis of the ceramic material is carried out using the Weibull probabilistic approach, a technique that requires a good statistical basis. The FE analysis is performed using sub-modelling of the component, in which the applied boundary conditions are obtained from the results of the 3D global model.

The grids support structure is iperstatic, and inexactitudes in the assembly, or dimensional tolerances, will affect the post-insulators, which are the fragile elements of the structure.

The post-insulators are described in [50], with are made made of alumina. Six Stainless Steel bushes brazed into each end of the alumina post-insulator form the connection to the metallic structure: the interface between Stainless Steel and ceramic material is a critical key issue of the FE model, and while the external dimensions of the post-insulators are clearly defined, no detailed description of the brazing procedure, nor the material and geometry of the bushes, is given.

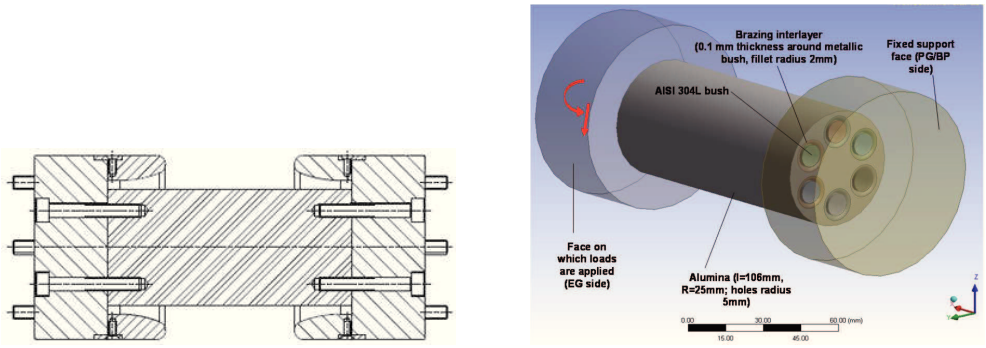
12.7.1 Verification of ceramic material

As in a chain, the reliability of a ceramic material is given by the reliability of every single element constituting the element. For this reason, it is possible to discretize the volume of the ceramic material in elements, and thus to use a Finite-element approach. The Stress Field is first calculated in ANSYS, and the results are post-processed, integrating over the volume the contribution of every element subjected to stress to the total probability. The post-processing is done using a dedicated code I wrote in C++.

This post-processing has a probabilistic approach and uses the Weibull probability density function:

$$P(\sigma) = 1 - e^{(\sigma/\sigma_0)^m} \tag{12.10}$$

where σ_0 and m are properties of the ceramic material obtained from experimental results. In figure 12.14, the probability density and cumulative distribution are shown in the case m=25 and m=10.



(a) (b)

Figure 12.13: SPIDER Alumina post-insulator: section (a) and FE sub-model geometry and imposed loads (b)

One should notice that, in this type of analyses, the model should precisely reproduce the geometry of the component, and the stress field should be as accurate as possible (FE dimensions as small as possible), in particular where the gradient of the stress is high. A good statistic knowledge of the material properties (in terms of σ_0 and m) is mandatory. The experimental data is processed in order to obtain the shape parameter m and the scale parameter σ_0. From [50] we have the following experimental results for the *base* Alumina: $\sigma_0 = 250$ MPa and $m = 24.8$. Those experimental results are -mainly- obtained from a single piece, and the variability of the manufacturing process is therefore not considered.

As it is known from bibliography, any thermal cycle affect both σ_0 and m of the base ceramic material. Reference alumina has $\sigma_0 = 320$ MPa. According to [164] for instance, after different processes of brazing or bonding at temperatures in the range $500 \div 1000$ °C, σ_0 drop to an average value of 170 MPa taking into account pieces that did not survive machining.

In the FE analysis, the stress components $\sigma_{1,i}$, $\sigma_{2,i}$, $\sigma_{3,i}$ are needed for each i-th element, of volume V_i. A correction factor $H_{d,i}$ will be $H_{d,i} = 1$ if $\sigma_{d,i} \geq 0$, or $H_{d,i} = -8$ is $\sigma_{d,i} < 0$, as the ceramic materials have greater compressive strength. The effective stress is summed over all the element:

$$I = \sum_i V_i \left(\left(\frac{\sigma_1}{H_1 \cdot \sigma_0} \right)^m + \left(\frac{\sigma_2}{H_2 \cdot \sigma_0} \right)^m + \left(\frac{\sigma_3}{H_3 \cdot \sigma_0} \right)^m \right) \tag{12.11}$$

The probability of failure of the overall ceramic component will be a function of the Γ function [165] and therefore:

$$P_f = 1 - e^{\{-(\Gamma(1+1/m))^m \cdot I\}} \tag{12.12}$$

12.7.2 Finite Element analysis

In order to obtain results as precise and realistic as possible, the six Stainless Steel bushes brazed into each end of the alumina post-insulator were modeled together with the interlayer of brazing materials. The structural loads are not

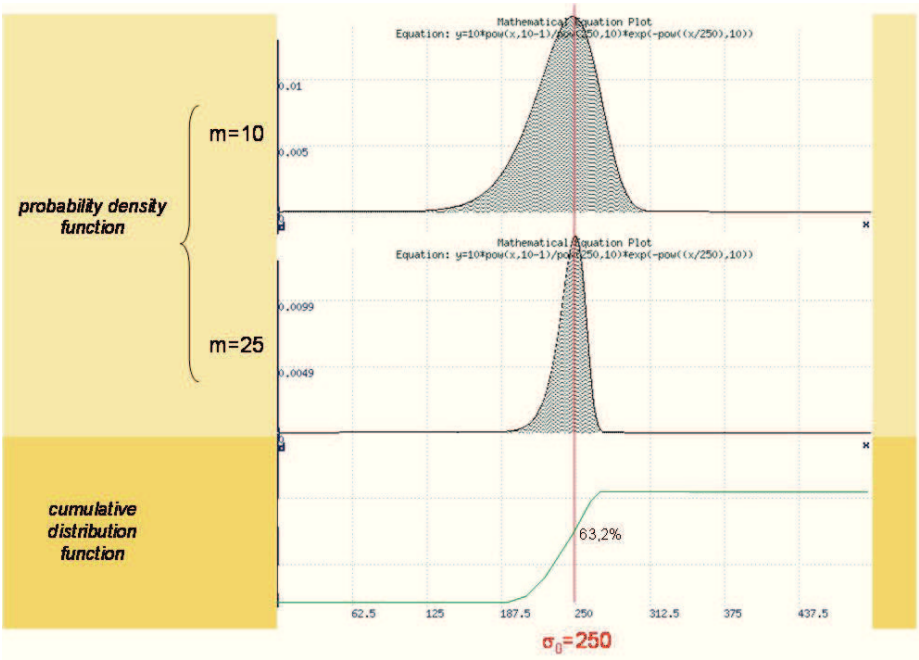


Figure 12.14: Example of Weibull probability function, calculated for constant σ_0, m=10 and 25 (on top), and the cumulative distribution function for m=25 (on bottom)

directly applied on the post-insulator, but on the Stainless Steel base that is used as connector to the structure. The BCs applied are shown in figure 12.13(b).

The effect of the presence of the interlayer in the model has been investigated. On this subject, a sensitivity analysis has been carried out in order to investigate the dependency of the results on the presence and the type of the brazing layer in the model. Only the results obtained from simulations in which the brazing interlayer was modelled were considered acceptable, as the layers of brazing materials:

- avoids geometric discontinuity and sharp edges at the interface;
- redistributes the stress field; in fact, it is usually a ductile material in order to avoid residual stresses after brazing, also with a low Young's modulus. If the layer is not modelled, at the Stainless SteelAlumina interface a stress concentration occurs, and it involves only nodes placed along a circumference.

A fine mesh was used, with 1 million elements, many of which were used to model the brazing interlayer. The stress profile in the metallic bases and bushes was not investigated. The structural loads are summarized in table 12.4.

Boundary conditions for the FE model

Mechanical loads are not multiply by safety coefficient: if needed, it suffices to divide the σ_0 parameter by the safety factor, and use a different curve of the probability of failure graph (figure 12.16). It is important to stress that:

Load type		Obtained from
Externally-applied	Gravity	Analytical estimations considering EG and PG
	Thermo-structural stresses	Global model
Other loads	Thermo-structural stresses	Imposing temperature and gradients obtained from global model
Neglected loads	Residual stresses due to the brazing process.	

Table 12.4: Structural loads applied to the sub-model

- The brazing process and the brazing material is unknown. As stated before, different values of Young's modulus E (and therefore Shear modulus G) were tested. In the purpose of the simulation, values of E in the range of Cusil ABA alloy were chosen.
- Residual stresses that could be stored-up in the brazing process are hard to estimate. The brazing alloy could solidify at high temperature, or could not have enough ductility. In general, a deep knowledge of the applied brazing technique would be mandatory; but this kind of analysis is not in the aim of this study. For these reasons residual stresses due to thermal process were neglected.

The most critical set of loads was chosen considering that:

- from the theory that the relevance to the fragile failure of a compression stress equals 1/8 of a tensile stress.
- a dedicated simulation has been carried out in order to evaluate the effect of shear forces compared to tensile forces when applied to this model. The shear forces (for instance, a Fy or Fz using the coordinate system shown in Figure 7 -50) have an effect on the probability of failure that is qualitatively 1/3 the effect of an axial force.

The post-insulator at the top of the frames are the most stressed. Loads are listed in table 12.5

F_x [N]	879
F_y [N]	-2673
F_z [N]	576
M_x [kN mm]	235
M_y [kN mm]	76
M_z [kN mm]	100

Table 12.5: Forces and momentum acting on the most loaded post-insulator (the one on top): x is axial direction.

Assessment of ceramic material property requirements

In figure 12.16, the probability of failure pf of post-insulator n.1 is shown. Given the uncertainties on the material properties, m and σ_0 of Alumina are parameters. The total loads on the component, as presented before, determine the probability of failure *pf* shown in solid line, while *pf* due to the gravity load alone is the dashed line. For the same Alumina properties, between the two *pf* there are 4÷5 orders of magnitude of difference.

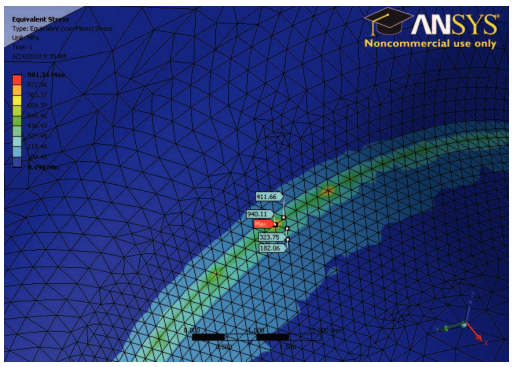


Figure 12.15: Equivalent Stress in the Alumina element is everywhere less than 120 MPa, Although the Von Mises criteria do not apply to Ceramic Materials, it can be used to highlight problems of stress concentration due to finite element errors.

One should first decide the admissible probability of failure, drawing an horizontal line in the plot (for instance, 1/10000), and then find a combination of admissible properties (σ_0 and m) on the machined material, obtained where the horizontal line is crossed. The acceptable pf should be computed considering the number of post-insulators on which the same load is applied (at least the two on the top of the structure: this means, if pf=1/10000, 1 failure every 5000).

Post-insulator n.1 is a post-insulator between PG and EG assembly, placed at the top, and is the critical one (for comparison, the green lines shown in figure are the probabilities of failure of the GG post-insulators).

Also the results from FE model with no brazing interlayer are shown: the probability of failure is given by the blue line.

The minimum required m and σ_0 are very high compared to standard commercial Alumina. If 1/10000 is considered acceptable, for the given geometry and loads: if $\sigma_0 = 250$ MPa, $m > 13$; and if $\sigma_0 = 200$ MPa, m should be higher than 17.

The fatigue mechanism does not apply to ceramics.

12.7.3 Comments

The number of ceramic insulators is low (16 pieces). Instead of making mechanical design and verification of the insulators, the suggestion is to produce the insulators with commercial ceramic powders and then to perform proof/qualification tests reproducing the actual operating conditions (obtained from the analyses in this report) on each piece.

The transitory thermally induced loads are mainly due to the temperature rising in the EG frame; they would be greatly reduced if the EG frame were thermally conditioned to a fixed temperature. It is compulsory however to identify a proper placing for this EG Frame Cooling System: it should be as near as possible to the origin of the heat, in the internal frame, but the presence of many lines of sight and so on makes the task really hard. At present, no proper location has been found.

In order to reduce the thermally induced stresses and the stresses due to imprecision in the assembly, elastic elements (elastic crosses) could be installed

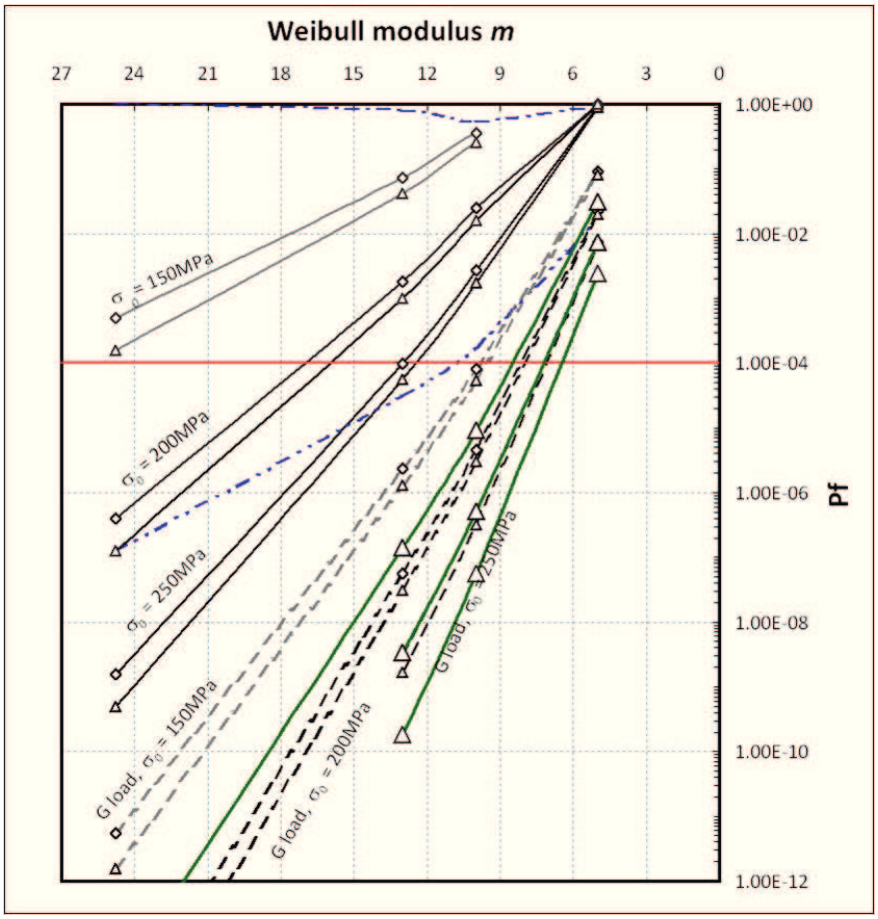


Figure 12.16: Results of the Weibull analysis.

at the base of the post-insulators. Their stiffness would be reduced by both geometry and constituting material; in the iperstatic structure of SPIDER, the role of the elastic cross would be to redistribute stresses between the 8 post-insulators that support each grid frame, absorbing the thermal deformations/displacements with their lower stiffness.

A material with low young's module, and high yield stress (e.g. aluminium bronze), shall be used, together with an optimised geometry enhancing deformability along precise directions.

12.8 Discussion and open issues

The main results of the analyses carried out are summarized in the following.

Frame active cooling is necessary in order to preserve the beam optics and avoid ceramic post-insulators failure: as a matter of fact, SPIDER and MITICA beam sources are expected to operate for much longer pulses than any other accelerator. In addition, coolant temperature should be controlled in a small range (±3 °C). It is currently considered in the design (and assumed for the analyses) to divert the cooling water from a source circuit at constant temperature of 35

°C. Small variations of this temperature may produce important variations of the thermal deformation (i.e., +5 °C means +0.2 mm elongation, causing the increase of stresses and misalignments).

The internal frame supporting the PG reaches a peak temperature of 88 °C. This yields displacements along the beam direction, with two detrimental consequences: a gap reduction of 0.5 mm occurs between PG and EG, and the PG and the PG frame may be extensively in contact (a distance of only 0.5 mm is foreseen between them) with a negative effect on the electric insulation. The gap between PG and EG is small, and its size important for the beam optic. The use of washer spacers with specific, differentiated thickness in EG joints is suggested. The variation in thickness, small even though, could correct irregularities in beam-off configuration that are expected (due to the 150 °C thermal conditioning of the PG).

The heating of the support structure results in a displacement of the points where each grid is fixed onto its frame. Analyses of the grid deformation in "supports-fixed-in-space" hypothesis do not suffice, if a good beam optic is pursued. On-plane deformations yields displacement of the grid support pins. A mechanical offset has been calculated (in beam-off conditions) and already taken into consideration in the CAD drawings. Due to the higher grid temperature at the cooling exit side, the EG frame deformation becomes non-symmetric during beam operation. Fastening displacements, after 1 hour beam-on, are double at the hot side, but, if we consider the displacements of the EG apertures wrt the PG ones, a better alignment is expected to occur on this side.

The temperature rising of the support structure is not homogeneous. Thermo-structural elongations and deformations give rise to forces acting on the post-insulators. Stresses on the post-insulators are expected also in beam stand-by condition. The mechanical loads on the post-insulators were estimated, and requirements on the alumina properties were calculated in terms of the Weibull distribution parameters σ_0 and m. A design solution was also proposed in the technical note [199]: it will help in reducing peak temperatures with no consequences on the design of other components and CAD modelling time saving; in addition, the approach with proof/qualification tests, combined with the use of the "elastic cross" elements should guarantee the survival of the post insulators accomplishing the safety requirement for the system.

Conclusions and perspective

A contribution to the design and development of the ITER HNB was given. New methods and models were developed to approach the phenomena involved, which produced qualitative and quantitative understanding. The knowledge I acquired is transversal to physics and engineering, as the approach I tried to have in the challenges I faced.

Numerical modeling, analyses and code development, design optimization and verification, execution of experimental measurements and benchmarking, were the activities of my PhD research. I now summarize the detailed conclusions, following the outline of the thesis.

Gas density distribution modeling

AVOCADO Two years after I begin its development, the numerical code Avocado is now capable of consistently solve multi-scale molecular flows in temperature -varying domains, and phenomena typical of these cases are correctly and reliably solved. The code has the capability to solve the gas distribution with spatial accuracy at the solid walls, but also in the bulk of the gas domain. The code is optimized for parallel computing with large sparse matrices. It is integrable in the mechanical design, by using new or existing Finite Element models and their mesh. The original contribution of Avocado has been published in Vacuum [5]; another publication regarding the new methods implemented for coherently calculate temperature and density is being submitted [6]. I am also glad to see that the project has been very welcomed at *Consorzio RFX* were I have been working.

ARIANNA In Arianna, geometries relevant to electrostatic accelerators has been prepared, and the gas molecular flows measured. Thanks to Arianna, a deep validation campaign of Avocado has been carried out, with numerical results within few percents from the measured conductances. With this activity, I acquired competences on experimental devices and their planning, in a collaborative environment of a scientific research institute.

Applications to ITER NBI and MITICA Avocado has been applied to the simulation of the gas domain in the large high vacuum system of the ITER Neutral Beam Injector. Results from simulation of the Beam Line and the submodeling of the Beam Source are coherent with previous results. In particular, the simulation of the Beam Source were used for the optimization of its design, as reported in the NIBS conference [7], and is being used in the physics design

[8, 9, 2]. The density profiles along the beamlets give estimates of the stripping losses and their non-uniformities, and the neutralization efficiency. The code is able of solving the three-dimensional MITICA beam source configuration, as its computing capability scaled up by a factor 32 in one year and a half[1].

MITICA Neutraliser and Electron Dump

The integrated final design of the Neutraliser and the Electron Dump (NED) for MITICA has been realized. The heat loads have been quantified, both developing a code to calculate the power deposition maps on the Beam Line Components and considering results from the simulation of relativistic electron trajectories and scattering. The developed method has been described in a publication [3]. The functional parameters of the neutralisation have been assessed. The power deposition by high-energy particles has been considered in the design of the actively cooled elements facing the beam, using numerical methodologies suited to the peculiarity of the subject (e.g. the development of dedicated codes to simulate the accelerated particles, or the integrated thermo-hydraulic finite element modelling).

The design of the functional core of the Neutraliser, i.e. the beam-facing panels but also their support structure and cooling system, has been verified against all load combinations, during beam operations and other procedural or unlikely loads, among them the seismic events. The Electron Dump design has been examined from various points of view, taking into account electrons-intercepting capability and gas flow reduction. Finally, new results have been produced, regarding the gas injection in the gas cells, its uniformity and time-constant.

The design underwent the Preliminary (PDR) and the informal Final Design Review (FDR). The technical specifications for the procurement of the component can now be prepared on the basis of a robust design.

The description of the design and verification activity has been published in Fusion Engineering and Design [10], and in [1] as part of the design of the MITICA accelerator. A vast number of technical notes, delivered to the ITER European domestic agency, details the analyses and the many aspects of the NED that were taken into account. With this multi-disciplinary and wide-ranging activity, I collaborated with the very supportive *NBI team* (which I thank).

SPIDER thermal deformations

The activity on the SPIDER beam source has been carried out in the last months of its design, with the purpose of characterizing the structural behaviour during operation besides validating its design. The thermal deformations of the support structure affecting the beam optics have been estimated [4], and some correction were identified and implemented. The modeling of fragile components, such as ceramic insulators, gave useful indications, to be considered in the design of MITICA beam source.

[1] in terms of number of apertures in the accelerator models, comparing the same simulation time

Other activities

Other minor activities I was engaged in, such as the magnetic analysis of the extraction region in MITICA beam source (see appendix A) leaded to interesting results [11] and increased my skills on the electromagnetic applications.

Further developments

As I am writing the final lines of this thesis, I would like to add some ideas and guidelines for further developments of the activities reported hereafter.

Modeling of gas density distribution Generally speaking, the numerical modeling of the beam source requires the support of the benchmarking activity on the MANITU data that is currently on-going and will, hopefully, proceed next year. Also, further validation in ARIANNA could give additional reliability to the models.

The AVOCADO code itself can be optimized further, in reducing the memory requirements, and adopting graphic-unit algorithms.

Concerning the simulations of the gas density in MITICA beam source, the choices in the design of the grid apertures, in terms of shape, diameters and length, are still open. Data on the updated layout shall be provided.

Design of MITICA NED Even though the mechanical design of the NED is concluded, many technological issues remain open, such as welding and manufacturing of structural components, brazing of thermocouple heads on components, the insertion and fixing of twisted tapes in STEs, and minor details in the remote-handling compatible movement of the lateral Electron Dump.

Many have cynically remarked that the primary purpose of their PhD thesis is to take up space on dusty shelves. I am very glad (to see) that this is not the destiny of my research, which had as primary purpose the *actual construction* of a device and its future installation on a wider, international fusion machine.

I wish to dedicate these three years of full-time working (even though my daily schedule has been shifting into afternoon and evenings) to my daughter and the generations to come. I hope that the considerable efforts that all of us, as a fusion community, are investing into the ITER project will have generous outcomes.

Padova, 31/01/2013

Appendixes

A

Magnetic field in the extraction region of MITICA ion source

Different sources and spatial distributions of the Magnetic Field influence the accelerator performances.

- The *filter field* is a transverse field (usually horizontal) in the Plasma Source in the vicinity of the PG. It reduces the number of co-extracted electrons. Typically it is small and spatially uniform (~ 0.5 mT upstream the PG). It can be produced by current running on the PG and suitable return bus-bars, or by stacks of permanent magnets at the sides of the PG.
- The *suppression field* is a transverse field whose purpose is deflecting and stopping the co-extracted electrons before they pass the EG and are accelerated. Permanent magnets embedded in the EG produce the field; typically they are arranged in horizontal stacks and magnetized with opposite polarity from stack to stack. The field strength upstream and downstream the EG is ~ 10 mT.
- The *compensation field* is designed to compensate in the AGs the deflection of the accelerated ions caused by the suppression field, and to deflect the stripped/secondary electrons along the accelerator. It can be either locally or globally produced (magnets embedded in the grids or long-range fields).
- The *shielding field* is produced by a layer of ferromagnetic material on a grid. It is a preferred "return path" which decouples the upstream and downstream fields generated by embedded magnets.

I took part in the development of concepts for the magnetic field of MITICA beam source. I carried out magnetic analyses in three-dimensional ANSYS models, detailing the geometry of magnet stacks, ferromagnetic layers, the geometry of the PG apertures, as shown in figure A.1.

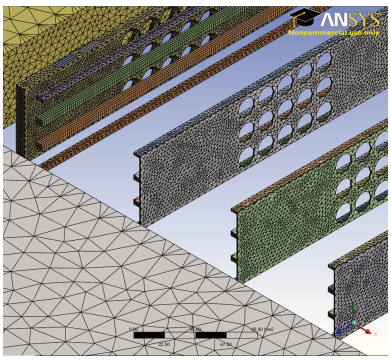
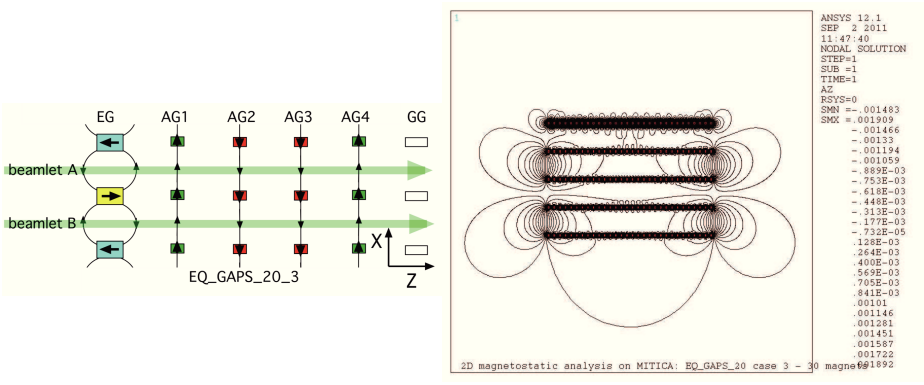


Figure A.1: Three-dimensional meshed model in ANSYS

The results of these analyses are described in [11]. As an example, a particular application of these models is presented here. One of the purposes of the analyses was to evaluate a particular magnetic option, in which the suppression and compensation field magnet stacks are disposed vertically (see figure A.2(a)). This is a layout that was not experimentally tested, and doubts arose concerning the magnetic field in the extraction region; the filter field is typically horizontal while the suppression field is vertical, resulting in a diagonal field entering and exiting the PG conical surfaces.

The preferred approach was to combine the results from 3D models simulating the current through the PG, whose geometry was properly modelled and meshed, and the 2D models simulating the vertical stacks of magnets figure A.2(b). The results of the superposition are shown in figure A.4. The transverse magnetic fields generated by the permanent magnets can be linearly superposed.

Denoting z the beam axis and x the horizontal, transverse direction, the ion deflection $\theta = \partial y/\partial z$ deflection is calculated by numerical integration of the



(a) (b)

Figure A.2: Sketch on the horizontal plane of the magnet layout (a) and results from the bi-dimensional magnetic models in ANSYS, magnetic flux lines (b)

following approximate equation:

$$\frac{\partial^2 y}{\partial z^2} \approx \frac{q\left(B_x(z) + \frac{dy}{dz}\frac{dU}{dz}\right)}{m\sqrt{v_0^2 + \frac{2q}{m}(U_0 - U(z))}} \tag{A.1}$$

The results shown in figure A.3 were one of the best results, in terms of minimum ion deflection, obtained.

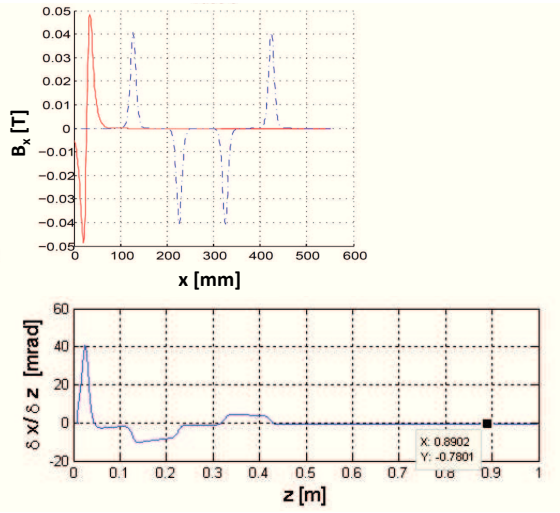


Figure A.3: Magnetic field along the path of a central beamlet originated by the embedded magnets, and ion deflection calculated with the approximate equation for geometry EQ_GAP_20, case 3.

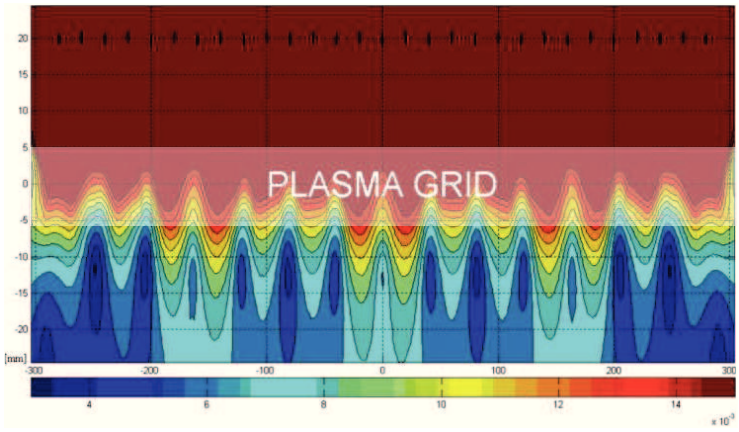
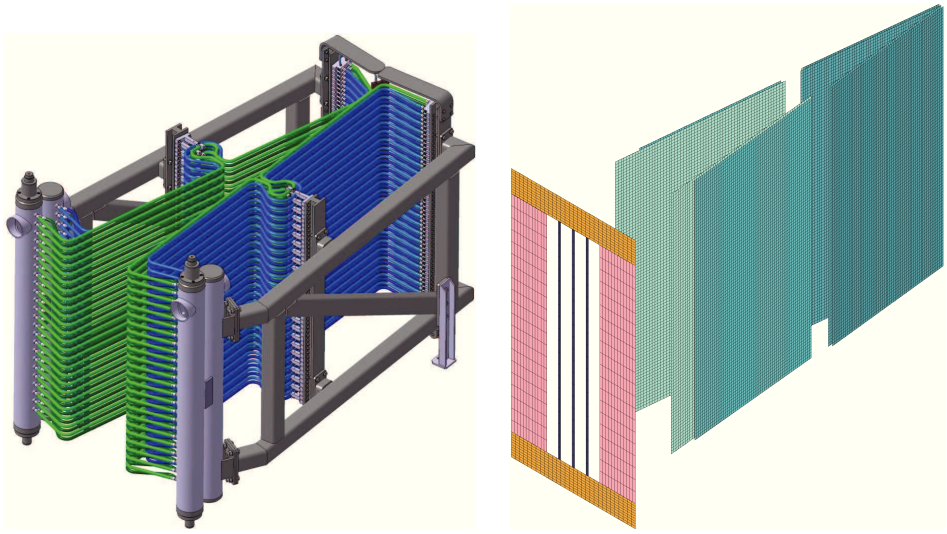


Figure A.4: Magnetic field intensity on the horizontal plane, obtained superposing the results from the 3D and the 2D models; the PG thickness is highlighted; case EQ_GAP_20, case 3.

B

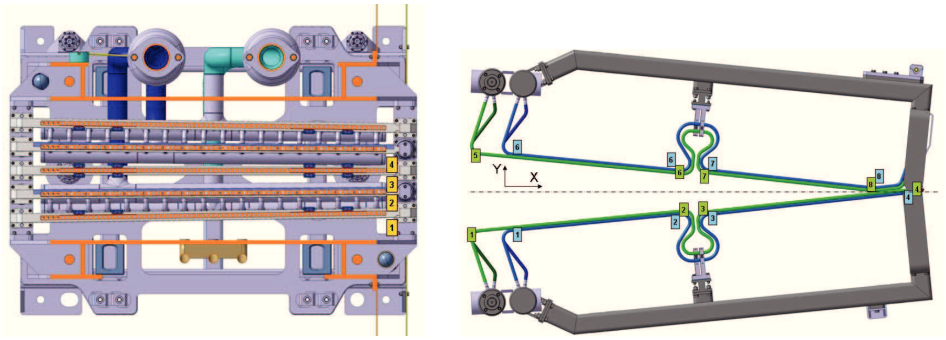
Application of Trigo to the MITICA Calorimeter

The activity I carried out on the analyses of beam interaction with the swirl tubes of MITICA Calorimeter is reported in this appendix. The analyses were focused on the evaluation of the power density deposition on the tube elements using the Trigo code described in section 7. These results will be an input for the development of a neutron diagnostic for the Calorimeter.



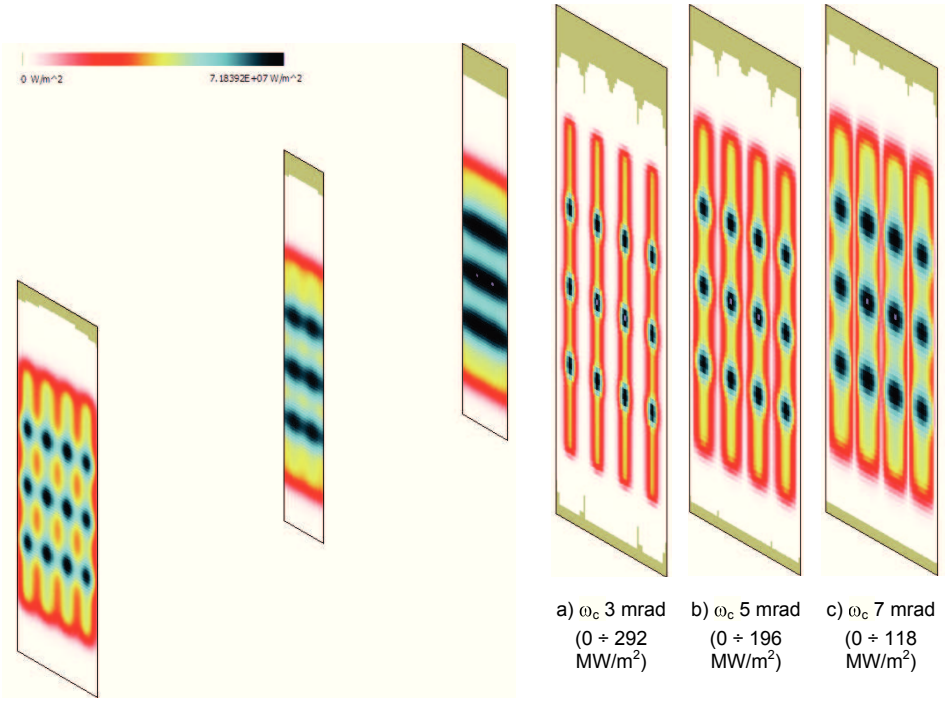
(a) (b)

Figure B.1: (a) overview of the Calorimeter: inner (green) and outer (blue) tubes are visible. The meshed surfaces of the calorimeter in Trigo model shall be considered with the shadowing surfaces of the RID (b) and the Neutraliser, which are not visible.



(a) (b)

Figure B.2: Horizontal section of (a) RID and (b) Calorimeter. The coordinates of the numbered positions are considered in the model.



(a) (b)

Figure B.3: (a) Beam footprint at the entrance, middle, and exit section of the Calorimeter when no shadowing surfaces are considered and (b) beam footprint at the entrance when different core divergence are considered.

Geometry description

A global overview of the two panels of MITICA Calorimeter is given in figure B.1. The reference tilting of the beam defines the design of the panels: these are made of two parallel series of swirl tubes arranged in vertical arrays, having the same nominal vertical tilting as the beam (49.2 mrad). In the following the green tubes are called inner and the blue ones outer, while the panels upstream are called front panels and those downstream rear panels. The horizontal sections of the RID and the Calorimeter are lso shown in figure B.2.

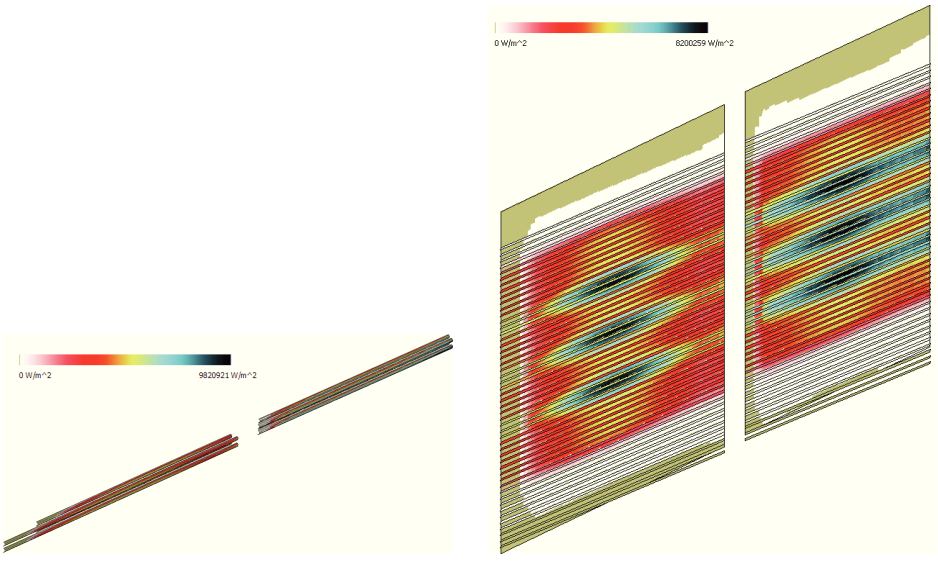
Overview of the results

The complete description of the model and its results is given in the technical note [195].

The beam footprint on three planes at the entrance, middle, and exit section of the Calorimeter are shown in figure B.3(a). A parametric study of the effect of the beamlet divergence is shown in figure B.3(b) and figure B.5, in which the cross-sections and the calorimeter planes are respectively shown.

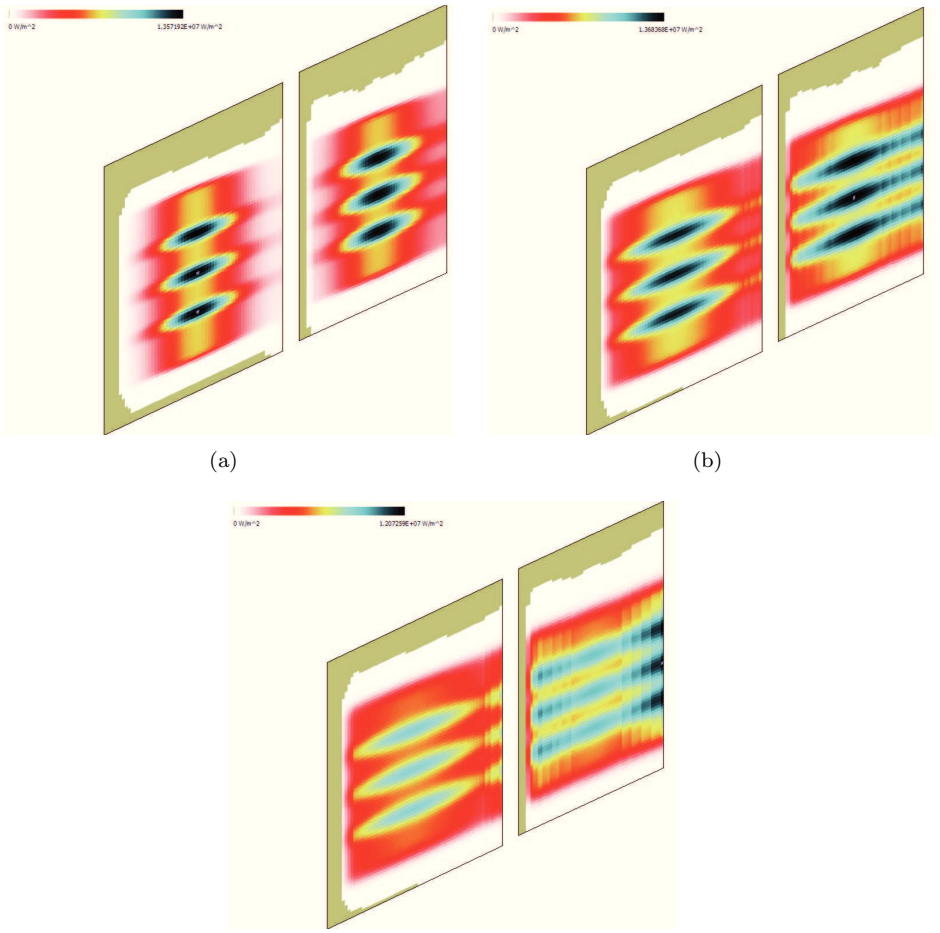
The actual geometry of the tubes has also been considered, simulating the power deposited on a limited set of tube segments as shown in figure B.4(a).

As the study was aimed at the prediction of the neutron production, proportional to the beam interaction with the solid surfaces, the loads on the inter and outer tubes shall be combined projecting the power density maps on the same plane. This was achieved creating an array of shadowing surfaces in front of a plane, representing respectively the inner and outer tubes. Many cases have been considered, by varying the beam misalignment and beamlet divergences. An example is shown in figure B.4(b).



(a) (b)

Figure B.4: Horizontal section of (a) RID and (b) Calorimeter. The coordinates of the numbered positions are considered in the model.



(a) (b)

(c)

Figure B.5: Horizontal section of (a) RID and (b) Calorimeter. The coordinates of the numbered positions are considered in the model.

Publications

[1] P. Sonato *et al.*, "Design of the MITICA neutral beam injector: from physics analysis to engineering design," 2012.

[2] L. Grisham, P. Agostinetti, G. Barrera, P. Blatchford, D. Boilson, J. Chareyre, G. Chitarin, H. de Esch, A. D. Lorenzi, P. Franzen, U. Fantz, M. Gagliardi, R. Hemsworth, M. Kashiwagi, D. King, A. Krylov, M. Kuriyama, N. Marconato, D. Marcuzzi, M. Roccella, L. Rios, A. Panasenkov, N. Pilan, M. Pavei, A. Rizzolo, E. Sartori, G. Serianni, P. Sonato, V. Pilard, M. Tanaka, H. Tobari, P. Veltri, and P. Zaccaria, "Recent improvements to the iter neutral beam system design," *Fusion Engineering and Design*, vol. 87, no. 11, pp. 1805 – 1815, 2012.

[3] P. Veltri, P. Agostinetti, M. D. Palma, E. Sartori, and G. Serianni, "Evaluation of power loads on mitica injector components," *27th Symposium on Fusion Technology submitted to Fusion Engineering and Design*, 2013.

[4] P. Veltri, P. Agostinetti, V. Antoni, M. Cavenago, G. Chitarin, N. Marconato, N. Pilan, E. Sartori, and G. Serianni, "Sensitivity analysis of the off-normal conditions of the spider accelerator," vol. 1390, pp. 594–603, 2011.

[5] E. Sartori and P. Veltri, "Avocado: A numerical code to calculate gas pressure distribution. http://dx.doi.org/10.1016/j.vacuum.2012.09.022," *Vacuum*, vol. 90, pp. 80–88, April 2013.

[6] E. Sartori *et al.*, "Gas density and energy 3D modeling in vacuum systems by view factor technique," *to be submitted to Computer Methods in Applied Mechanics and Engineering.*

[7] E. Sartori, S. Dal Bello, G. Serianni, and P. Sonato, "Distribution of the background gas in the MITICA accelerator," in *NIBS conference*, AIP conf. proceeding., 2012.

[8] H. de Esch, M. Kashiwagi, T. Inoue, G. Serianni, P. Agostinetti, G. Chitarin, N. Marconato, E. Sartori, P. Sonato, P. Veltri, and R. S. Hemsworth, "Physics design of the HNB accelerator for ITER," 2012.

[9] G. Chitarin, P. Agostinetti, D. Marcuzzi, N. Marconato, E. Sartori, G. Serianni, P. Sonato, and P. Veltri, "Optimization of the electrostatic and magnetic field configuration in the MITICA accelerator," *27th Symposium on Fusion Technology, submitted to Fusion Eng. Des.*, 2012.

[10] M. Dalla Palma, E. Sartori, W. Gonzalez, A. Tiso, L. Trevisan, and P. Zaccaria, "Design and r&d for manufacturing the mitica neutraliser and electron dump," *27th Symposium on Fusion Technology submitted to Fusion Engineering and Design*, 2013.

[11] G. Chitarin, P. Agostinetti, N. Marconato, D. Marcuzzi, E. Sartori, G. Serianni, and P. Sonato, "Concepts for the magnetic design of the MITICA neutral beam test facility ion accelerator," *Rev. Sci. Instrum.*, vol. 83, no. 02B107, 2012.

References

[12] D. Meade, "50 years of fusion research," *Nucl. Fusion*, vol. 50, no. 014004, 2010.

[13] J. Wesson, *Tokamaks; 4th ed.* International series of monographs on physics, Oxford: Oxford Univ. Press, 2011.

[14] J. D. Lawson, "Some criteria for a power producing thermonuclear reactor," *Proc. Phys. Soc. B, vol 70*, 1957.

[15] D. M. Meade *Fusion Eng., Proc. 17th IEEE/NPSS Symposium, Vol. 2,752*, 1997.

[16] H. F. Dylla, "The development of ultrahigh and extreme high vacuum technology for physics research,," *J. Vac. Sci. Technol. A 21, S25 ; http://dx.doi.org//1.1599891*, 2003.

[17] "Iter physics basis," *Nuclear Fusion 39, 12*, 1999.

[18] "Agreement on the establishment of the ITER international fusion energy organization for the joint implementation of the ITER project,." Paris, 21/11/2006.

[19] "ITER EDA Documentation Series no. 21.".

[20] K. Tomabechi, J. R. Gillel, Y. A. Sokolov, R. Toschi, and I. Team, "ITER conceptual design,," *Nucl. Fusion*, vol. 31, p. 1135, 1991.

[21] R. Aymar, P. Barabaschi, and Y. Shimomura, "The ITER design," *Plasma Phys. Control*, vol. 44, no. 519, 2002.

[22] H. P. Eubank, "Neutral beam heating of tokamaks: Past performance and future applications," *J. Vac. Sci. Technol. A*, vol. 2, no. 655, 1984.

[23] Wagner *et al. PRL*, vol. 49, p. 1408, 1982.

[24] W. Kraus, *CERN accelerator school - ion sources.* June 2012.

[25] J. Jacquinot and J. Team, "Deuterium-tritium operation in magnetic confinement experiments: results and underlying physics, plasma phys. and contr," *Plasma Phys. and Contr. Fus.*, vol. 41, 1999.

[26] "Efda website (2012) http://www.efda.org.".

[27] T. Oikawa, K. Ushigusa, C. B. Forest, M. Nemoto, O. Naito, *et al.*, "Heating and non-inductive current drive by negative ion based nbi in jt-60u," *Nucl. Fusion*, vol. 40, no. 3Y, pp. 435–443, 2000.

[28] Y. Sakamoto, T. Fujita, S. Ide, A. Isayama, M. Takechi, *et al.*, "Stationary high confinemnet plasmas with large bootstrap current fraction in jt-60u," *Nucl. Fusion*, vol. 45, pp. 574–580, 2005.

[29] A. Kojima, M. Hanada, Y. Tanaka, T. Inoue, K. Watanabe, *et al.*, "Achievement and improvement of the jt-60u negative ion source for jt-60sa," *Proc. of the 13th ICIS, Rev. Sci. Instrum.*, vol. 81, no. 02B112, 2010.

[30] Y. Takeiri, O. Kaneko, K. Tsumori, Y. Oda, K. Ikeda, *et al.*, "High-power and long pulse injection with negative-ion-based neutral beam injectors in the large helical device," *Nucl. Fusion*, vol. 46, pp. S199–S210, 2006.

[31] M. Kuriyama, "Operation of the negative-ion based nbi for jt-60u," *Fusion Engineering and Design*, vol. 39-40, pp. 115–121, 1998.

[32] L. Svensson, "System Requirement Document ver.1.2," Tech. Rep. idm: 2WCCSG, october 2009.

[33] U. Fantz, P. Franzen, and D. Wünderlich, "Development of negative hydrogen ion sources for fusion: Experiments and modelling," *Chemical Physics*, vol. 398, pp. 7–16, April 2012.

[34] I. G. Brown, ed., *The physics and thechnology of ion sources,*. Wiley-VCH Verlag GmbH & Co., Weinheim, 2004.

[35] J. Ishikawa, H. Tsuji, Y. Gotoh, and S. Azegami, "Particles and fields series 53: production and neutralization of negative ions and beams, 6th int. symp.," vol. 287, p. 66.

[36] Y. B. et al, "A powerful injector of neutrals with a surface-plasma source of negative ions," *Nuclear Fusion*, vol. 14, 1974.

[37] G. D. Alton *Surf. Sci.*, vol. 175, no. 226, 1986.

[38] W. G. Graham in *Proc 2nd International Symposium on Production and Neutralization of Negative Hydrogen Ions and Beams*, 1980.

[39] M. Hanada, "Development of negative ion sources for the iter neutral beam injector," *Fusion Eng. Des.*, vol. 56, pp. 505–509, 2001.

[40] P. Agostinetti, V. Antoni, M. Cavenago, G. Chitarin, N. Marconato, D. Marcuzzi, N. Pilan, G. Serianni, P. Sonato, P. Veltri, and P. Zaccaria, "Physics and engineering design of the accelerator and electron dump for spider," *Nucl. Fusion*, vol. 51, no. 6, 2011.

[41] C. F. Barnett, "Atomic data for fusion," Tech. Rep. ORNL-6086/V1, Oak Ridge NAtional Laboratory, TN, USA, 1990.

[42] J. Pamela, "A model for negative ion extraction and comparison of negative ion optics calculations to experimental results," *Rev. Sci. Inst.*, vol. 62, pp. 1163–1172, 1991.

[43] H. de Esch, R. Hemsworth, and P. Massmann, "Updated physics design iter-singap accelerator," *Fusion Eng. Des.*, vol. 73, pp. 329–341, 2005.

[44] D. Ciric, "Permag manual," tech. rep., UKAEA Fusion/Euratom Association, Culham Science Centre, Abingdon, United Kingdom, 2007.

[45] G. Chitarin *et al. IEEE transaction magn.*, vol. 25, p. 4330, 1989.

[46] "Ansys manual." ANSYS Inc., http://www.ansys.com.

[47] G. Fubiani, H. de Esch, A. Simonin, and R. Hemsworth, "Modeling of secondary emission processes in the negative ion based electrostatic accelerator of the international thermonuclear experimental reactor," *Phys. Rev. Special Topics Accelerators and Beams*, vol. 11, no. 014202, 2008.

[48] "Opera website, http://www.cobham.com.".

[49] P. Veltri. PhD thesis, Universita' degli studi di padova, 2011.

[50] "ITER Design Description Document (DDD 5.3), neutral beam heating and current drive system," july 2003.

[51] E. Surrey, "Gas heating in the neutraliser of the iter neutral beam injection systems," *Nucl. Fusion*, vol. 46, pp. S360–S368, 2006.

[52] W. K. et al, "Rf negative ion source development at ipp garching," in *AIP Conf. Proc. 925*, pp. 224–237, 2006.

[53] P. Franzen *et al.*, "Progress of the develpment of the ipp rf negative ion source for the iter neutral beam system," *Nucl. Fusion*, vol. 47, pp. 264–270, 2007.

[54] B. Heinemann *et al.*, "Negative ion test facility elise - status and first results," *in press on Fusion. Eng. Des.*

[55] P. Sonato, P. Agostinetti, G. Anaclerio, V. Antoni, O. Barana, and M. Bigi, "The ITER full size plasma source device design," *Fus. Eng. Des.*, vol. 84, no. 269e74, 2009.

[56] U. Fantz *et al. Plasma Phys. Control. Fus*, vol. 49, p. B563B580, 2007.

[57] K. Jousten, ed., *Handbook of vacuum technology.* Wiley -VCH Verlag, 2008.

[58] G. Lewin and D. Mullaney, "Vacuum symp," in *Trans*, (NY), p. 176, Pergamon, 1963.

[59] H. F. Dylla, "Turbomolecular pump vacuum system for the princeton large torus," *J. Vac. Sci. Technol.*, vol. 15, no. 734, 1978.

[60] D. J. Grove, "Status of tftr with ohmic heating and neutral beam injection," *J. Vac. Sci. Technol. A*, vol. 3, no. 1145, 1985.

[61] G. Duesing, "The vacuum systems of the nuclear fusion facility jet," *Vacuum*, vol. 37, p. 309 to315, 1987.

[62] R. Pearce, A. Antipenkov, B. Boussier, S. Bryan, M. Dremel, B. Levesy, C. Mayaux, and M. Wykes, "The iter divertor pumping system, design evolution, simplification and performance," *to be published in Fusion Eng. Des.*, 2012.

[63] "Iter-feat vacuum pumping and fuelling r&d programmes," in *proc. IAEA*, 2000.

[64] A. S. et al, "Design of the neutral beam injection system for asdex-upgrade,," in *15th SOFT, Utrecht, Vol 1*, pp. 620–624, Sep. 88.

[65] M. Dremel, C. Day, R. Hemsworth, R. Pearce, and C. Mayaux, "Cryopump design for the iter heating neutral beam injector," *Nucl. Fusion*, vol. 49, May 2009.

[66] R. Kersevan, "Analytical and numerical tools for vacuum systems," tech. rep., Proc. Cas - CERN accelerator school and ALBA synchrotron light facility: course on vacuum in accelerators, 2006. and references therein.

[67] J. M. Lafferty, *Foundation of Vacuum Science and Technology.* Wiley Interscience.

[68] B. Ferrario, *Introduzione alla tecnologia del vuoto.* Patron Editore Bologna, 1999.

[69] S. Ohta, N. Yoshimura, and H. Hirano, "Resistor network simulation method for a vacuum system in a molecular flow region," *J. Vac. Sci. Technol. A*, vol. 1, no. 84, 1983.

[70] L. W. Nagel and D. O. Pederson, "Spice (simulation program with integrated circuit emphasis)," Tech. Rep. Memorandum No ERL-M382, University of California, Berkeley, April 1973.

[71] G. Saksaganski, *Molecular flow in complex vacuum systems.* New York: Gordon and Breach, 1988.

[72] R. Kersevan, "Molflow user's guide," Tech. Rep. Tech Report ST/M-91/17, Sincrotrone Trieste, 1991.

[73] A. Pace and A. Poncet *Vacuum*, vol. 41, pp. 1910–1913, 1990.

[74] G. Bird, "Monte carlo simulation of gas flows," *Ann. Rev. Fluid Mech.*, vol. 10, pp. 11–31, 1978.

[75] D. H. Davis, "Montecarlo calculation of molecular flow rates through a cylindrical elbow and pipes of other shapes," *J. Appl. Phys.*, vol. 31, pp. 1169–76, 1960.

[76] G. A. Bird, "Approach to translational equilibrium in a rigid sphere gas," *Phys. Fluids*, vol. 6, p. 1518, 1963.

[77] Molflow, "http://test-molflow.web.cern.ch/.".

[78] "KIT website, http://www.itep.kit.edu/english/434.php.".

[79] "Three dimensional monte carlo simulation of molecular movement and heat radiation in vacuum devices: Computer code movak3d.," Tech. Rep. technical report KFK-4292, 1987.

[80] V. Hauer and C. Day., "ITERVAC - a semiempirical code for calculations in the transitional flow regime," in *51th JVSTA Workshop on Modern Problems and Capability of Vacuum Gas Dynamics*, 2007.

[81] M. Knudsen *Ann Phys (Leipzig)*, vol. 1910; 33:1435 1927; 83:797.

[82] F. R and Y. G., "Knudsen's cosine law and random billiards," *Chem. Eng. Sci.*, vol. 59, no. 1541e56, 2004.

[83] P. Ossipov, "The angular coefficient method for calculating the stationary molecular gas flow for arbitrary reflection law," *Vacuum*, vol. 48, 1997.

[84] A. Bonucci *et al.*, "The method of angular coefficients: a powerful tool to address complex vacuum gas dynamics problems," Proc. of the XVI AIV congress, Catania, 2002.

[85] M. La Fontaine, "Calculation of molecular flow using the heat-transfer analogy, ansys conf," *ANSYS Conf Proc*, vol. 1, pp. 371–378, 1998.

[86] P. Michelato, E. Cavaliere, C. Pagani, E. . Bari, and A. Bonucci, "Vacuum interface analysis of a windowless spallation target for accelerator-driven systems," *Nucl. Sci. Eng*, vol. 157, pp. 95–109, 2007.

[87] H. J. K., "The solution of two molecular flow problems by monte-carlo methods," in *Methods in Computational Physics, Advances in Research and Application, vol. 4, Application in Hydrodynamics*, pp. 109–209, 1965.

[88] R. Kersevan and J.-L. Pons, "Introduction to molflow+: New graphical processing unit-based monte carlo code for simulating molecular flows and for calculating angular coefficients in the compute unified device architecture environment," *J. Vac. Sci. Technol. A*, vol. 27, no. 1017, 2009.

[89] M. S. Smoluchowski *Phil. Mag. and J. Sci.*, vol. 46, p. 192, 1989.

[90] F. O. Goodman and H. Y. Wachman, "Formula for Thermal Accommodation Coefficient," Technical Report AFORR 66-0295, Massachusetts Institute of Technology, 1966.

[91] S. C. Saxena and R. Afshar, "Thermal accommodation coefficient of gases on controlled solid surfaces: Argon-tungsten system," *Int. J. of Thermophysics*, vol. 6, no. 2, pp. 143–163, 1985.

[92] S. Song and M. M. Yovanovich, "Correlation of thermal accommodation coefficient for 'engineering' surfaces," 1987.

[93] A. Rebrov, A. Morozov, M. Y. Plotnikov, N. I. Timoshenko, and A. V. Shishkin, "The Accommodation of the Translational and Rotational Energy of a gas in Knudsen Flow past a thin wire," *J. of Experimental and Theoretical physics*, vol. 97, no. 4, pp. 738–744, 2003.

[94] D. J. Rader, W. M. Trott, *et al.*, "Measurements of Thermal Accommodation Coefficients," Technical Report SAND2005-6084, Sandia National Laboratories, 2005.

[95] A. Gaurav, H. C. Chang, and E. J. Maginn, "Molecular simulations of knudsen wall-slip: effect of wall morphology," *Molecular Simulation*, vol. 29, pp. 697–709, 2003.

[96] K. J. Daun, G. J. Smallwood, and F. Liu, "Molecular dynamics simulations of transitional thermal accommodation coefficients for time-resolved lii," *Appl. Phys. B*, vol. 94, pp. 39–49, 2009.

[97] D. Bruno, M. Cacciatore, S. Long, and M. Rutigliano, "Gas-surface scattering models for particle fluid dynamics: a comparison between analytical approximate models and molecular dynamics calculations," *Chemical Phys. Letters*, vol. 320, pp. 245–254, 2000.

[98] J. Sun and Z. Li, "Two-dimensional molecular dynamic simulations on accommodation coefficients in nanochannels with various wall configurations," *Computer & fluids*, vol. 39, pp. 1345–1352, 2010.

[99] H. Eric, "Point in polygon strategies," in *Heckbert Paul, editor. Graphics gems IV.*, Academic Press, 1994.

[100] "Openmp api, http://openmp.org/." 2012.

[101] "Pbs portable batch system, hpc workload management and job scheduling, http://www.pbsworks.com/." 2012.

[102] *Intel C++ compiler icc, http://software.intel.com/en-us/articles/intel-compilers/.* 2012.

[103] D. Knuth, *The Art of Computer Programming.* Addison-Wesley, 1997.

[104] Y. Saad, "Sparskit: A basic tool kit for sparse matrix computations," technical report, RIACS-90-20, NASA Ames Research Center, Moffett Field, CA, 1990.

[105] F. Gnesotto, P. Sonato, W. R. Baker, and A. D. F. Elio, "The plasma system of rfx," *Fus. Eng. and Design*, vol. 25, pp. 335–372, 1995.

[106] A. Bulu, J. T. Fineman, M. Frigo, J. R. Gilbert, and C. E. Leiserson, "Parallel sparse matrix-vector and matrix-transpose-vector multiplication using compressed sparse blocks," in *Proc. SPAA Calgary, Canada*, 2009.

[107] Y. Saad, *Iterative methods for sparse linear systems.* Philadelphia: SIAM, 2003.

[108] H. A. van der Vorst, "Bi-cgstab: a fast and smootly converging variant of bi-cg for the solution of non-symmetric linear systems," *SIAM Journal on Scientific and Statistical Computing*, vol. 12, pp. 631–644, 1992.

[109] "File formats for vtk version 4.2, http://www.vtk.org/vtk/img/file-formats.pdf." 2012.

[110] "Paraview website, http://www.paraview.org/." 2012.

[111] "The paraview tutorial, http://www.vtk.org/wiki/images/2/2d/paraviewtutorial310.pdf." 2012.

[112] C. P. *Ann Physik*, vol. 12, no. 961, 1932.

[113] P. A. Redhead, J. P. Hobson, and E. V. Kornelsen, *The Physical Basis of Ultrahigh vacuum*. London: Chapman and Hall, 1968.

[114] S. Nishizawa and M. Hirata *Vacuum*, vol. 67, pp. 301–306, 2002.

[115] M. Vargas, M. Wuest, and S. Stefanov *J. of Ph. Conf. Series*, vol. 362, no. 012013, 2012.

[116] B. Baule *Ann. der Physik*, vol. 44, pp. 145–176, 1914.

[117] F. O. Goodman and H. Y. Wachman, "Formula for thermal accommodation coefficients," *Journal of Chemical Physics*, vol. 46, no. 6, p. 2376, 1967.

[118] F. Goodman, "Thermal accommodation," *Progress in Surface Science*, vol. 5 Part 3, p. 261375, 1974.

[119] C. Walck, "Hand-book on statistical distributions for experimentalists," Tech. Rep. SUF-PFY, Universitet Stockholms, 2007.

[120] Y. Zhao, "Brief introduction to the thermostats," Tech. Rep. Research-Note007Thermostat, University of California San Diego.

[121] M. P. Allen and D. J. Tildesley, *Computer simulation of liquids*. New York: Oxford University press, 1989.

[122] A. Krylov and R. S. Hemsworth, "Gas flow and related beam losses in the ITER neutral beam injector," *Fusion Eng. Des.*, vol. 81, pp. 2239–2248, 2006.

[123] D. Wünderlich, "private communication." 2012.

[124] E. Speth *et al.*, "Overview of the rf source development programme at ipp garching," *Nucl. Fusion*, vol. 46, p. S220, 2006.

[125] S. Hanke and S. Papastergiou, "Cryogenic system and cryopump requirements," Tech. Rep. VAC-GQM-090321-QD-0010, Karlsruhe Institute of Technology KIT, 2010.

[126] M. Wnderlich, "Neutral depletion in an h- source operated at high rf power and low input gas flow," *Plasma Sources Sci. Technol.*, no. 045005, 2011.

[127] X. Luo and C. Day, "3D monte carlo vacuum modeling of the neutral beam injection system of ITER," *Fusion Eng. Des.*, vol. 85, pp. 1446–1450, 2010.

[128] U. Fantz, H. Falter, P. Franzen, D. Wünderlich, M. Berger, A. Lorenz, W. Kraus, P. McNeely, R. Riedl, and E. Speth, "Spectroscopy - a powerful diagnostic tool in source development," *Nucl. Fusion*, vol. 46, pp. S297–S306, 2006.

[129] P. Agostinetti, G. Chitarin, P. Franzen, B. Ruf, G. Serianni, and P. Veltri, "Benchmark of the SLACCAD code against data from the MANITU radio frequency ion source at IPP," 2012.

[130] S. Hanke and X. Luo, "Report on gas density calculations for the HNB injection system," Tech. Rep. VAC-GEW- 090321-GC-0001, Karlsruhe Institute of Technology KIT.

[131] M. Porton, E. Shapiro, and D. Drikakis, "Transitional modelling of the neutral gas in the jet neutralizer," *Fusion Eng. Des.*, vol. 85, pp. 789–795, 2010.

[132] J. Wei, C. Hu, L. Liang, and Z. Liu, "Modeling the gas flow in the neutralizer of ITER neutral beam injector using Direct Simulation Monte Carlo approach," *Fusion Eng. Des.*, 2012.

[133] M. Porton, *Exploring continuum computational models for neutral gas flow in the JET neutraliser*. PhD thesis, Cranfield University, School of Engineering, December 2010.

[134] S. Hanke, M. Scannapiego, X. Luo, C. Day, F. Fellin, *et al.*, "The development of the unique and large cryopump system for the heating neutral beam injection of iter," in *IVS-2012, Kolkata (16 Feb 2012)*.

[135] R. Pasqualotto, E. Gazza, G. Serianni, B. Zaniol, M. Agostini, *et al.*, "Spectroscopic diagnostics for the negative ion rf source spider," *Nuclear Instruments and Methods in Physics Research Section A: Accelerators, Spectrometers, Detectors and Associated Equipment*, vol. 623, no. 2, pp. 794–796, 2010.

[136] U. Fantz, P. Franzen, W. Kraus, M. Berger, S. Christ-Koch, H. Falter, M. Fröschle, R. Gutser, B. Heinemann, C. Martens, P. McNeely, R. Riedl, E. Speth, A. Stäbler, and D. Wünderlich, "Physical performance analysis and progress of the development of the negative ion rf source for the ITER NBI system," *Nucl. Fusion*, vol. 49, no. 125007, 2009.

[137] "Beam aiming sheet, iter_d_2dmm9r, rdi-006_hnb_beam_aiming#27d4re - a_sheet03, https://user.iter.org/?uid=2dmm9r.".

[138] "ASME Boiler and Pressure Vessel Code, Sections III and VIII," tech. rep., The American Society of Mechanical Engineers, 2001.

[139] "RCC-MR design and construction rules for mechanical components of FBR nuclear island," tech. rep., AFCEN, 2007.

[140] "ITER Structural Design Criteria - In-vessel Components, SDC-IC," Tech. Rep. 222RHC, ITER Organization.

[141] "ITER Material Properties Handbook," Tech. Rep. G 74 MA 16, ITER Organization.

[142] "NIST database, http://www.nist.gov/," tech. rep., National Institute of Standards and Technology, 2012.

[143] E. N. Sieder and G. E. Tate, "Heat transfer and pressure drop of liquids in tubes," *Ind. Eng. Chem.*, vol. 28, pp. 1429–1435, 1936.

[144] C. F. Colebrook and C. M. White, "Fluid friction in roughened pipes," *Proc. of the Royal Society of London*, vol. 161A, pp. 367–381, august 1937.

[145] "Mpq load specifications iter_d_222qgl v3.5," tech. rep.

[146] M. Dalla Palma, *Multiaxial fatigue design criteria for high heat flux components actively cooled in nucleate boiling conditions*. PhD thesis, december 2006.

[147] "Witzenmann Bellows catalogue.".

[148] E. Dlougach, "Beam transport code btr - user's manual," tech. rep., NFI, 2006.

[149] G. Chitarin, N. Marconato, P. Agostinetti, G. Serianni, and P. Sonato, "Flexible magnetic design of the mitica plasma source and accelerator," *NIBS Conf., submitted to AIP Conf. Proc.*, 2012.

[150] M. Dalla Palma and E. Sartori, "Data, codes, and criteria used for the analyses and verification of the Neutraliser and Electron Dump," Tech. Rep. RFX-MITICA-TN-132, Consorzio RFX, PD, Italy, december 2011.

[151] H. de Esch and M. Singh, "Electron dumps for iter hnb and dnb beamlines," *Fusion Engineering and Design*, vol. 85, no. 5, pp. 707 – 717, 2010.

[152] "ITER Remote Handling Code of Practice RHCP," Tech. Rep. 2E7BC5 ver. 1.2, ITER Organization.

[153] "ITER Interface report for generic pipe tools between NB RH and NB system," Tech. Rep. 6ZJUQ6 ver 1.0, ITER Organization.

[154] "Final report on thermal hydraulic analyses and results," Tech. Rep. VAC-GEW-090321-RD-0D04, Karlsruhe Institute of Technology KIT.

[155] "ASCE 7 minimum design loads for buildings and other structures," tech. rep., The American Society of Civil Engineers, 2001.

[156] "ITER Tender design - Tokamak Complex - Generation of the floor response spectra," Tech. Rep. 3Z5N6P ver. 1.1, ITER Organization.

[157] "ITER Vacuum Handbook," Tech. Rep. 2EZ9UM ver. 2.3, ITER Organization.

[158] "Analyses report - F4E-GRT-313 task 4.4/p4, MITICA Electrostatic Residual Ion Dump (ERID).," Tech. Rep. MIT2-CAL-0001 issue 2, CCFE.

[159] C. V. Madhusudana, *Thermal Contact Conductance*. Springer, New York, 1996.

[160] *Heat Exchanger Design Handbook HEDH*. Hemisphere Publishing Corporation, 1983.

[161] W. M. W.M.Rohsenow *et al.*, *Handbook of heat transfer fundamentals*. McGraw-Hill Company, New York, 1973.

[162] "Heat transfer mechanism of metal surface contacted; 2nd report: Thermal contact resistance in vacuum (in japanese)," *Japan Society of Mechanical Engineering*, pp. 37–299, 1971.

[163] "Microsoft visual basic, webpage http://www.microsoft.com/visualstudio/eng/.".

[164] S. Hong and A. Glaeser, "Reduced-temperature transient-liquid-phase bonding of Alumina using a Ag-Cu-based brazing alloy," 2006.

[165] Zhang and Jin, *Computation of Special Functions*. John Wiley and Sons, 1996.

RFX Technical Notes

[166] P. Agostinetti, G. Chitarin, N. Marconato, D. Marcuzzi, N. Pilan, E. Sartori, G. Serianni, P. Sonato, F. Spada, P. Veltri, and P. Zaccaria, "Single beamlet optics studies and functional optimization of the MITICA accelerator," Tech. Rep. RFX-MITICA-TN-146 rev. 2, Consorzio RFX, PD, Italy, january 2013.

[167] E. Sartori, "AVOCADO, a numerical code for molecular flow calculations," Tech. Rep. RFX-MITICA-TN-74 rev. 1, Consorzio RFX, PD, Italy, december 2012.

[168] E. Sartori, M. Fincato, and W. Gonzalez, "ARIANNA experiment and AVOCADO validation," Tech. Rep. RFX-MITICA-TN-154, Consorzio RFX, PD, Italy, december 2012.

[169] E. Sartori and P. Veltri, "Pressure distribution calculations inside mitica accelerator," Tech. Rep. RFX-MITICA-TN-134 rev. 1, Consorzio RFX, PD, Italy, december 2011.

[170] E. Sartori, "Gas density profile in MITICA beam source," Tech. Rep. RFX-MITICA-TN-145, Consorzio RFX, PD, Italy, december 2012.

[171] P. Agostinetti, V. Antoni, M. Cavenago, E. Sartori, G. Chitarin, N. Marconato, D. Marcuzzi, N. Pilan, G. Serianni, P. Sonato, P. Veltri, and P. Zaccaria, "Physics and engineering analyses on the MITICA accelerator," Tech. Rep. RFX-MITICA-TN-033 rev 5, Consorzio RFX, PD, Italy, december 2011.

[172] E. Sartori, "Gas density distribution in MITICA beam line," Tech. Rep. RFX-MITICA-TN-147, Consorzio RFX, PD, Italy, december 2012.

[173] B. Zaniol, R. Pasqualotto, M. Barbisan, and M. Tollin, "Design description of MITICA optical diagnostics," Tech. Rep. RFX-MITICA-TN-089, Consorzio RFX, PD, Italy, october 2011.

[174] P. Agostinetti, G. Chitarin, P. Franzen, B. Ruf, E. Sartori, G. Serianni, and P. Veltri, "Benchmark of SLACCAD, AVOCADO and EAMCC codes against data from the MANITU testbed at IPP," Tech. Rep. RFX-MITICA-TN-220, Consorzio RFX, PD, Italy, december 2012.

[175] M. Dalla Palma, A. Tiso, E. Sartori, L. Trevisan, and W. Gonzalez, "Final 3d model and 2d drawings of the MITICA Neutraliser and Electron

Dump," Tech. Rep. RFX-MITICA-TN-063 revision 2, Consorzio RFX, PD, Italy, december 2012.

[176] M. Dalla Palma, E. Sartori, and W. Gonzalez, "Neutralizer and electron dump analyses and verifications - Master Document," Tech. Rep. RFX-MITICA-TN-119, Consorzio RFX, PD, Italy, 2012.

[177] E. Sartori and M. Dalla Palma, "Positioning of the neutraliser inside the MITICA and ITER injectors," Tech. Rep. RFX-MITICA-TN-120, Consorzio RFX, PD, Italy, 2011.

[178] E. Sartori, P. Veltri, P. Agostinetti, and M. Dalla Palma, "Identification of the most heated elements of the Neutraliser and Electron Dump," Tech. Rep. RFX-MITICA-TN-121, Consorzio RFX, PD, Italy, december 2011.

[179] E. Sartori and M. Dalla Palma, "Flow rate partitioning and coolant temperatures of the neutraliser and electron dump cooling circuit," Tech. Rep. RFX-MITICA-TN-122, Consorzio RFX, PD, Italy, december 2011.

[180] E. Sartori and M. Dalla Palma, "Verification of the neutraliser wall panels," Tech. Rep. RFX-MITICA-TN-123, Consorzio RFX, PD, Italy, december 2011.

[181] M. Dalla Palma and E. Sartori, "Verification of the neutraliser leading edge elements," Tech. Rep. RFX-MITICA-TN-124, Consorzio RFX, PD, Italy, december 2011.

[182] E. Sartori and M. Dalla Palma, "Ion and electron dump verification," Tech. Rep. RFX-MITICA-TN-125, Consorzio RFX, PD, Italy, december 2011.

[183] E. Sartori and M. Dalla Palma, "Verification of the neutraliser floors and wall panel fixings," Tech. Rep. RFX-MITICA-TN-126, Consorzio RFX, PD, Italy, december 2011.

[184] E. Sartori, M. Dalla Palma, and A. Tiso, "Neutraliser and electron dump: cooling pipework verification," Tech. Rep. RFX-MITICA-TN-127 rev. 2, Consorzio RFX, PD, Italy, december 2012.

[185] E. Sartori, M. Dalla Palma, and W. Gonzalez, "Verification of the support structure of the MITICA neutraliser and electron dump," Tech. Rep. RFX-MITICA-TN-128 rev. 2, Consorzio RFX, PD, Italy, december 2012.

[186] M. Dalla Palma, E. Sartori, and W. Gonzalez, "Seismic verification of the MITICA neutraliser and electron dump," Tech. Rep. RFX-MITICA-TN-129 rev. 2, Consorzio RFX, PD, Italy, december 2012.

[187] E. Sartori and M. Dalla Palma, "Analyses for gas injection in the mitica neutraliser," Tech. Rep. RFX-MITICA-TN-130 rev. 2, Consorzio RFX, PD, Italy, december 2012.

[188] E. Sartori and M. Dalla Palma, "Analyses for the thermal sensor layout in the neutraliser and electron dump operating in MITICA and ITER HNBs," Tech. Rep. RFX-MITICA-TN-131, Consorzio RFX, PD, Italy, december 2011.

[189] M. Dalla Palma and E. Sartori, "Data, codes, and criteria used for the analyses and verification of the Neutraliser and Electron Dump," Tech. Rep. RFX-MITICA-TN-132, Consorzio RFX, PD, Italy, december 2011.

[190] M. Dalla Palma and E. Sartori, "PED conformity assessment and MD329/04 regulation for the NED assembly," Tech. Rep. RFX-MITICA-TN-133 rev. 1, Consorzio RFX, PD, Italy, december 2012.

[191] E. Sartori, "Vector code for calculating the power density maps on beam line components of MITICA & ITER HNBs," Tech. Rep. RFX-MITICA-TN-135, Consorzio RFX, PD, Italy, december 2011.

[192] P. Veltri, P. Agostinetti, M. Dalla Palma, and E. Sartori, "Evaluation of power loads downstream of the MITICA accelerator," Tech. Rep. RFX-MITICA-TN-136, Consorzio RFX, PD, Italy, december 2011.

[193] P. Veltri, P. Agostinetti, M. Dalla Palma, E. Sartori, and G. Serianni, "Evaluation of power loads due to electrons along the MITICA beamline," Tech. Rep. RFX-MITICA-TN-162, Consorzio RFX, PD, Italy, december 2012.

[194] M. Dalla Palma, "Neutraliser and electron dump Development Requirement Document," Tech. Rep. RFX-MITICA-TN-22 revision 2, Consorzio RFX, PD, Italy, september 2011.

[195] E. Sartori and M. Tollin, "MITICA calorimeter - Analyses of power deposition," Tech. Rep. RFX-MITICA-TN-67 rev. 1, Consorzio RFX, PD, Italy, december 2011.

[196] G. Chitarin, N. Marconato, P. Agostinetti, G. Serianni, and P. Sonato, "Flexible magnetic design of the mitica plasma source and accelerator," *NIBS Conf., submitted to AIP Conf. Proc.*, 2012.

[197] M. a. Dalla Palma, "MITICA calorimeter - Analyses of power deposition," Tech. Rep. RFX-MITICA-TN-67 rev. 1, Consorzio RFX, PD, Italy, december 2011.

[198] M. Dalla Palma and N. Pomaro, "Overall system description of the thermal sensors embedded in MITICA components," Tech. Rep. RFX-MITICA-TN-71 rev 1, Consorzio RFX, PD, Italy, december 2011.

[199] E. Sartori and M. Pavei, "Thermo-structural analyses of SPIDER accelerator mechanical structure," Tech. Rep. RFX-SPIDER-TN-126, Consorzio RFX, PD, Italy, march 2011.

Acknowledgements

Thanks to

ANTONIO BUFFA - ALESSANDRO SCAGGION - ANDREA RIZZOLO - ANDREA TISO - GIANLUIGI SERIANNI - GIUSEPPE CHITARIN - ITALO PREDEBON - LAURO TREVISAN - MARCO VERANDA - MAURO DALLA PALMA - MAURO PAVEI - MICHELE FINCATO - NICOLO MARCONATO - PIERLUIGI VELTRI - PIERGIORGIO SONATO - PIERO AGOSTINETTI - POLATO SANDRO - SAMUELE DAL BELLO - WINDER GONZALEZ - WLADI RIGATO

and Giovanna.